CELL TYPE DIVERSITY IN THE NERVOUS SYSTEM: FROM GENES TO FUNCTION

EDITED BY: Miao He, Giordano Lippi and Jiangteng Lu
PUBLISHED IN: Frontiers in Cellular Neuroscience, Frontiers in Molecular Neuroscience, Frontiers in Genetics and Frontiers in Neuroscience

frontiers Research Topics

ISSN 1664-8714
ISBN 978-2-88974-336-0
DOI 10.3389/978-2-88974-336-0

About Frontiers

Frontiers is more than just an open-access publisher of scholarly articles: it is a pioneering approach to the world of academia, radically improving the way scholarly research is managed. The grand vision of Frontiers is a world where all people have an equal opportunity to seek, share and generate knowledge. Frontiers provides immediate and permanent online open access to all its publications, but this alone is not enough to realize our grand goals.

Frontiers Journal Series

The Frontiers Journal Series is a multi-tier and interdisciplinary set of open-access, online journals, promising a paradigm shift from the current review, selection and dissemination processes in academic publishing. All Frontiers journals are driven by researchers for researchers; therefore, they constitute a service to the scholarly community. At the same time, the Frontiers Journal Series operates on a revolutionary invention, the tiered publishing system, initially addressing specific communities of scholars, and gradually climbing up to broader public understanding, thus serving the interests of the lay society, too.

Dedication to Quality

Each Frontiers article is a landmark of the highest quality, thanks to genuinely collaborative interactions between authors and review editors, who include some of the world's best academicians. Research must be certified by peers before entering a stream of knowledge that may eventually reach the public - and shape society; therefore, Frontiers only applies the most rigorous and unbiased reviews.
Frontiers revolutionizes research publishing by freely delivering the most outstanding research, evaluated with no bias from both the academic and social point of view. By applying the most advanced information technologies, Frontiers is catapulting scholarly publishing into a new generation.

What are Frontiers Research Topics?

Frontiers Research Topics are very popular trademarks of the Frontiers Journals Series: they are collections of at least ten articles, all centered on a particular subject. With their unique mix of varied contributions from Original Research to Review Articles, Frontiers Research Topics unify the most influential researchers, the latest key findings and historical advances in a hot research area! Find out more on how to host your own Frontiers Research Topic or contribute to one as an author by contacting the Frontiers Editorial Office: frontiersin.org/about/contact

CELL TYPE DIVERSITY IN THE NERVOUS SYSTEM: FROM GENES TO FUNCTION

Topic Editors:
Miao He, Fudan University, China
Giordano Lippi, The Scripps Research Institute, United States
Jiangteng Lu, Shanghai Jiao Tong University, China

Citation: He, M., Lippi, G., Lu, J., eds. (2022). Cell Type Diversity in the Nervous System: From Genes to Function. Lausanne: Frontiers Media SA.
doi: 10.3389/978-2-88974-336-0

Table of Contents

frontiers in Cellular Neuroscience

ORIGINAL RESEARCH
published: 07 April 2020
doi: 10.3389/fncel.2020.00048

A Brain Signaling Framework for Stress-Induced Depression and Ketamine Treatment Elucidated by Phosphoproteomics

Yan Xiao[1†], Huoqing Luo[2,3,4†], Wen Z. Yang[5,6], Yeting Zeng[1], Yinbo Shen[1], Xinyan Ni[2], Zhaomei Shi[2], Jun Zhong[7], Ziqi Liang[2], Xiaoyu Fu[2,3,4], Hongqing Tu[2,3,4], Wenzhi Sun[8], Wei L. Shen[2], Ji Hu[2]* and Jiajun Yang[1]**

[1]Department of Neurology, Shanghai Jiao Tong University Affiliated Sixth People's Hospital, Shanghai, China, [2]School of Life Science and Technology, Shanghaitech University, Shanghai, China, [3]State Key Laboratory of Neuroscience, CAS Center for Excellence in Brain Science and Intelligence Technology, Shanghai Institutes for Biological Sciences, Chinese Academy of Sciences, Institute of Neuroscience, Shanghai, China, [4]University of Chinese Academy of Sciences, Beijing, China, [5]Shanghai Institute for Advanced Immunochemical Studies & School of Life Science and Technology, Shanghaitech University, Shanghai, China, [6]CAS Key Laboratory of Synthetic Chemistry of Natural Substances, Shanghai Institute of Organic Chemistry, Chinese Academy of Sciences, Shanghai, China, [7]Delta Omics Inc., Baltimore, MD, United States, [8]Chinese Institute For Brain Research, Beijing, China

OPEN ACCESS

Edited by:
Miao He,
Fudan University, China

Reviewed by:
Xiaoke Chen,
Stanford University, United States
Ti-Fei Yuan,
Shanghai Mental Health Center, China
Lianghai Hu,
Jilin University, China

***Correspondence:**
Wei L. Shen
shenwei@shanghaitech.edu.cn
Ji Hu
huji@shanghaitech.edu.cn
Jiajun Yang
yangjiajunfzy@sina.com

[†]These authors have contributed equally to this work

***Specialty section**:*
This article was submitted to Cellular Neurophysiology, a section of the journal Frontiers in Cellular Neuroscience

Received: *12 December 2019*
Accepted: *20 February 2020*
Published: *07 April 2020*

Citation:
Xiao Y, Luo H, Yang WZ, Zeng Y, Shen Y, Ni X, Shi Z, Zhong J, Liang Z, Fu X, Tu H, Sun W, Shen WL, Hu J and Yang J (2020) A Brain Signaling Framework for Stress-Induced Depression and Ketamine Treatment Elucidated by Phosphoproteomics. Front. Cell. Neurosci. 14:48. doi: 10.3389/fncel.2020.00048

Depression is a common affective disorder characterized by significant and persistent low mood. Ketamine, an N-methyl-D-aspartate receptor (NMDAR) antagonist, is reported to have a rapid and durable antidepressant effect, but the mechanisms are unclear. Protein phosphorylation is a post-translational modification that plays a crucial role in cell signaling. Thus, we present a phosphoproteomics approach to investigate the mechanisms underlying stress-induced depression and the rapid antidepressant effect of ketamine in mice. We analyzed the phosphoprotein changes induced by chronic unpredictable mild stress (CUMS) and ketamine treatment in two known mood control centers, the medial prefrontal cortex (mPFC) and the nucleus accumbens (NAc). We initially obtained >8,000 phosphorylation sites. Quantitation revealed 3,988 sites from the mPFC and 3,196 sites from the NAc. Further analysis revealed that changes in synaptic transmission-related signaling are a common feature. Notably, CUMS-induced changes were reversed by ketamine treatment, as shown by the analysis of commonly altered sites. Ketamine also induced specific changes, such as alterations in synapse organization, synaptic transmission, and enzyme binding. Collectively, our findings establish a signaling framework for stress-induced depression and the rapid antidepressant effect of ketamine.

Keywords: depression, chronic unpredictable mild stress (CUMS), ketamine, LC-MS/MS, phosphoproteomics, brain signaling

INTRODUCTION

Depression is a devastating disease characterized by a combination of symptoms such as inferiority, loss of appetite, low energy and unexplained discomfort (Gould et al., 2019). This diagnosis occurs at some stage in the life of approximately 16% of the world's population and is related to severe health and socioeconomic consequences (Li and Vlisides, 2016). The cause of depression has been suggested to be maladaptive changes in specific brain circuits

in response to environmental stimuli, such as stressful events. Meanwhile, functional magnetic resonance imaging (fMRI) showed increased activation in response to negative vs. neutral stimuli in the medial prefrontal cortex (mPFC), and increased activation of the nucleus accumbens (NAc) and the amygdala in depression patients (Anand et al., 2005; Harvey et al., 2005; Roberson-Nay et al., 2006). Clinically, the lag time of the therapeutic efficacy is a remarked limit for the conventional antidepressants including selective serotonin reuptake inhibitors (SSRIs) and selective norepinephrine reuptake inhibitors (SNRIs; Dale et al., 2015). Recently, the N-methyl-D-aspartate (NMDA) receptor antagonist ketamine was found to elicit antidepressant effects only several hours after a single administration, and these effects lasted for several days in both major depressive disorder (MDD) patients and animal models of depression (Diazgranados et al., 2010; Autry et al., 2011; Murrough et al., 2013; Zanos et al., 2016; Cui et al., 2018; Yang et al., 2018). Mechanistically, both conventional antidepressants and ketamine promoted neural plasticity, including increased expression of brain-derived neurotrophic factor (BDNF; Moda-Sava et al., 2019), activation of cAMP response element-binding protein (CREB; Duman and Voleti, 2012; Reus et al., 2016), and activation of mammalian target of rapamycin (mTOR) signaling in the mPFC (Li et al., 2010). Rapid and persistent enhancement of neural plasticity, for example, *via* immediate suppression of eukaryotic elongation factor 2 (eEF2) or Ca^{2+}/calmodulin-dependent protein kinase II (CaMKII) signaling to induce global protein synthesis in the hippocampus, is also required for the rapid antidepressant activity of ketamine (Monteggia et al., 2013; Taha et al., 2013; Adaikkan et al., 2018). Conversely, impairment of neural plasticity is fundamental for the development of depression (Duman, 2002; Quiroz and Manji, 2002; Liu et al., 2017). However, the cellular basis of depressive disorders is still unclear.

Currently, mass spectrometry (MS)-based proteomics approaches have been used as a powerful tool in systems biology research and have identified many important signaling proteins related to various diseases (Ye et al., 2016; Liu et al., 2018; Wang et al., 2018; Eckert et al., 2019; Noberini and Bonaldi, 2019). Therefore, a comprehensive characterization of phosphorylation events in the whole brain will enable us to obtain an integrated blueprint to understand the cellular mechanism of depression. Herein, we applied this technology along with behavioral and pharmacological investigations to achieve a systemic view of the molecular signaling dysfunctions in depressive conditions and the antidepressant state induced by ketamine. We first demonstrated that the chronic unpredictable mild stress (CUMS) induced depressive-like states, and ketamine produced rapid antidepressant effects in mice, mimicking clinical observations. Then, we identified more than 8,000 phosphorylation sites. Among them, 3,988 sites in the mPFC and 3,196 sites in the NAc were quantifiable. From these experiments, we obtained a systemic overview of the synaptic proteins altered by CUMS in the mPFC and the NAc and found that ketamine reversed these. Altogether, phosphoproteomics combined with pharmacological—approaches helped us to—unveil signaling pathways involved in the phosphorylation-mediated rapid antidepressant effects. Consequently, our approach reveals a novel strategy for the discovery of phosphorylated protein-based therapeutics.

MATERIALS AND METHODS

Animals

All animal care and experimental procedures were approved by the Animal Care and Use Committee of ShanghaiTech University, Shanghai Model Organisms Center, Inc. C57BL/6J mice were housed at 20–22°C and the humidity between 50% and 60%, under a 12:12 h light/dark cycle (light on between 7:00 AM–19:00 PM), Mice had *ad libitum* access to food and water. All behavioral assays were performed on animals 12–16 weeks old which were purchased from Shanghai JieSiJie Experiment Animal Company Limited. Forced Swim Test (FST) and Tail Suspension Test (TST) were performed during the light phase. The Sucrose Preference Test (SPT) began during the dark phase to maximize the consumption of the solution. All behavioral analyses were performed blinded to experimental conditions.

Drug and Reagents

Ketamine was dissolved in 0.9% saline for intraperitoneal (IP) injection (10 mg/kg). The 0.9% saline was used as the vehicle. EDTA-free protease inhibitor cocktail tablets (#05892791001) and Phosphatase inhibitor cocktail tablets (#04906837001) were purchased from Roche (Basel, Switzerland). Pierce™ BCA Protein Assay Kit (#23225) and anti-phospho-Csnk1a1 (#PA5-36790) were purchased from Thermo Fisher Scientific (Waltham, MA, USA). Titansphere Phos-TiO_2 kit (#5010-21312) and Monospin C18 (#5010-21701) were purchased from GL Sciences (Japan). Anti-GAPDH (#sc-32233) was purchased from Santa Cruz (Dallas, TX, USA). HRP-conjugated Goat Anti-Rabbit IgG (#D110058) and HRP-conjugated Goat Anti-Mouse IgG (#D110087) were purchased from the Sangon Biotech (Shanghai, China). RNAscope 2.5 HD detection reagent kit (#322350) and Prkcg probe (#417911) were purchased from Advanced Cell Diagnostics (Newark, NJ, USA). Urea (U0631), ammonium bicarbonate (ABC) and other materials were obtained from Sigma–Aldrich (St. Louis, MO, USA) unless otherwise indicated.

Chronic Unpredictable Mild Stress (CUMS)

The depression model was described previously with a slight modification (Gu et al., 2014). CUMS-induced mice groups were exposed to different stressors for 21 days. The CUMS procedure followed a random weekly schedule of commonly used mild stressors: (1) food or water deprivation (24 h); (2) soiled cages (200 ml water in the sawdust bedding, 24 h); (3) 45° angle cage tilt (24 h); (4) tail clipping (1 h); (5) foot shock (1.75 mA, 40 min); (6) overnight illumination (12 h); (7) social attack (15 min); and (8) restraint in a 50-ml tube (6–8 h). The stressors intensity increased gradually to avoid mice to adapt to stress. After the last CUMS procedure, mice received a series of behavioral tests as indicated. Mice rested at least 2 h between two different behavioral tests.

Sucrose Preference Test (SPT)

Animals were singly housed and accustomed to two bottles of water for 3 days, followed by two bottles of 2% sucrose for 3 days. Animals were then deprived of water for 24 h and then exposed to two bottles for choice, with one of 1% sucrose and another of water for 2 h in the dark phase. During the test, the positions of the bottle were switched after 1 h to avoid any preference of bottle positions (Opal et al., 2014). Total consumption of each fluid was measured on days 7, 14, 21, 28 during the CUMS, respectively. The sucrose consumption ratio was defined as the total consumption of sucrose divided by the total consumption of water and sucrose. The sucrose preference referred to the average sucrose consumption ratio during the 2 h.

Forced Swim Test (FST)

Mice were individually placed in a cylinder (20 cm diameter, 40 cm height) filled with water (26–27°C) and swam for six min under normal light (Gigliucci et al., 2013). The water depth was set to 15 cm to prevent the tail or hind limbs of the mouse from touching the bottom of the pool. Mice behaviors were tracked from the top (Shanghai Jiliang Software Technology). The time that mice stay floating or motionless under the actions necessary to maintain balance in the water was defined as "immobile time" and was counted offline by an observer blinded to animal treatment during the last four min in the test.

Tail Suspension Test (TST)

TST behavior was recorded by a computerized device allowing four animals to be tested at one time. Mice were suspended 50 cm above the floor by adhesive tape placed approximately 1 cm from the tip of the tail in a soundproof chamber. Meantime, the activities of mice were recorded using cameras and the total duration of immobility was analyzed during the last four min in the six min by an observer blinded to animal treatment test.

Ketamine Experiment

Ketamine was dissolved in saline (0.9%) and administered intraperitoneally (IP). The concentration of ketamine was 10 mg/kg for mice. After ketamine delivery, CUMS mice were respectively used for SPT or FST and TST behavioral assays after 1 or 24 h.

Phosphoproteomics Sample Preparation

In phosphoproteomics experiments, each experimental group included four mice. The saline and ketamine (10 mg/kg) were injected intraperitoneally (IP) into mice. After 1 h, animals were killed by cervical displacement, and then the brains were removed from the skull and microdissected immediately. The mPFC and NAc were flash-frozen in liquid nitrogen after dissection. Samples were then stored at −80°C for subsequent phosphoproteomic analysis. Frozen brain tissues were transferred into tubes, which contained 200 μl of lysis buffer (8 M urea, 50 mM ABC, pH 8) with protease inhibitor (10 ml/tablet) and phosphatase inhibitor (10 ml/tablet) added. Samples were then sonicated for 2 min on ice. The supernatant was extracted after centrifuged for at 4°C for 5 min at 14,000 *g*. The bicinchoninic acid (BCA) assay was used to determine the protein concentration of the lysates. Next, dithiothreitol (DTT, 5 mM) was added to the same quality samples and put it on a 37°C shaker for 2 h. After cooling to room temperature, iodoacetamide (IAM, 1 M) was added and protected from light for 40 min. Samples were treated with trypsin (#V5113, Promega) at 37°C overnight and the ratio of protein-to-enzyme was 50:1. The protein digestion was stopped by adding 10% trifluoroacetic acid (TFA) until a pH <2 was reached. Then, the supernatant was collected after centrifuged at 25°C for 5 min at 14,000 *g*. The peptides were desalted using Monospin C18 according to the protocol. Briefly, tips were washed with 100 μl of buffer B (0.1% formic acid, 50% acetonitrile) followed by 100 μl of buffer A (0.1% formic acid). Peptides were then loaded onto the tips and centrifuged at 1,000 *g* for 5 min and repeated once. Then, the samples were eluted with buffer B after washed with buffer A. Next, the resulting peptide solution dried with a SpeedVac apparatus. After this step, the phosphopeptides were enriched and then purified using the Titansphere Phos-TiO_2 kit according to the protocol (Forget et al., 2018). In Brief, tips were washed with 100 μl of TiO_2 buffer A (0.4% TFA, 80% acetonitrile) followed by 100 μl of TiO_2 buffer B (25% lactic acid, 75% TiO_2 buffer A). Peptides were then loaded onto the tips and centrifuged at 1,000 *g* for 5 min and repeated once. The 100 μl of TiO_2 buffer B and 100 μl of TiO_2 buffer A were used to wash the tips, respectively. Then, the samples were eluted by the elution buffer (5% NH_4OH, 40% acetonitrile). Finally, the eluates were dried by a SpeedVac apparatus and then analyzed by LC-MS/MS.

LC-MS/MS Analysis of Enriched Peptides

Peptides were resuspended with 5 μl mobile phase A (0.1% formic acid in 2% acetonitrile), then separated by nanoLC (Easy-nLC 1000 system) and analyzed by on-line electrospray tandem mass spectrometry (Q Exactive HF-X, Thermo Fisher Scientific). Three microliter peptide sample was loaded and separated by the analytical column (75 μm × 50 cm, Thermo Fisher Scientific) using a flow rate of 250 nl/min. A 90-min gradient was set up using mobile phase A and mobile phase B (0.1% formic acid in 98% acetonitrile), among them, from 4% to 28% B in 79-min, 28% to 60% B in 1-min, and climbing to 90% B in 1-min, then holding at 90% for the last 9-min. The electrospray was used to ionize the peptides at 2.1 kV. A completed MS spectrum in the range of 375–1,500 m/z was obtained at a resolution of 120,000 at m/z 200 and a maximum ion accumulation time of 20 ms. 30 s was the dynamic exclusion setting parameter and the 15,000 was the resolution for HCD MS/MS spectra at m/z 200. The AGC of MS1 was set at 3E6 and that of MS2 was 1E5. HCD selected the 20 strongest ions above the 2.5E4 count threshold for the fragmentation, and the maximum ion accumulation time was 80 ms. MS2 isolation width was 1.6 m/z units. MS/MS removed single and unassigned charged ions. The normalized collision energy was 27% for HCD.

MS Data Analysis

Tandem mass spectra were processed by MaxQuant (v.1.6.5.0), and the database used for database searches was the mouse protein database (release 2016_07, 49,863 sequences). There allowed two missed cleavage sites for the enzyme of trypsin. The mass error of the precursor ions was 5 ppm and that of

the fragment ions was 0.02 Da. The fixed modification was carbamidomethylation on Cys, and the variable modifications were oxidation (M), acetylation (Protein N-term), and phosphorylation (STY). The thresholds of false discovery rate (FDR) for protein, peptide, and modification sites were set at 1% and 7 was the minimum length of the peptide. The three options including "Second peptides," "Match between runs" and "Dependent peptides" selected the enable and all other parameters retained the setting of default values. Moreover, Student's *t*-test was performed to test the significance of the differences between each comparison group.

Bioinformatics Analysis

We only chose the commonly identified phosphorylation sites across samples for further quantitative analysis for each type of brain parts. Then, the two comparisons have been carried out: CUMS + saline vs. Control + saline, CUMS + ketamine vs. CUMS + saline, and CUMS + ketamine vs. Control + saline. We chose the ratio of 1.2-fold change and the probability of 0.05 as a cut-off for differentially expressed proteins or sites as indicated. The multi-omics data analysis tool, OmicsBean, was used to analyze the obtained phosphoproteins data[1], in which distributions in biological process, cell component and molecular function were assigned to each protein based on Gene Ontology (GO) categories. Protein-protein interaction (PPI) analysis was performed also using OmicsBean. The DAVID (Database for Annotation, Visualization, and Integrated Discovery) functional annotation tool was used to analyze the Kyoto Encyclopedia of Genes and Genomes (KEGG; Kanehisa et al., 2014) pathway[2] mapping of phosphoproteins (Huang da et al., 2009).

Western Blot Analysis

For western blot analysis, the protein samples were resolved and transferred onto nitrocellulose filter (NC) membranes. After blocking with 5% BSA in TBS-tween 20 at room temperature for 2 h, the membranes were performed using specific primary antibody anti-phospho-Csnk1a1 (1:2,000) and anti-GAPDH (1:1,000) at 4°C overnight. The membranes were then incubated with HRP-conjugated Goat Anti- Rabbit IgG (1:2,000) and HRP-conjugated Goat Anti-Mouse (1:2,000) at room temperature for 2 h. Western blot signals were quantified using Amersham Imager 600 (GE Healthcare), and band signals were expressed as relative protein amounts compared to GAPDH.

In situ Hybridization

The RNAscope 2.5 HD Detection Kit was used to RNAscope *in situ* hybridization according to the manufacturer's protocol. After the mice were anesthetized, they were perfused with PBS followed by 4% PFA. The brains of the mice were removed and immediately placed in freshly prepared 4% PFA, and fixed at 4°C for 24 h. Brain tissues were immersed in 1× PBS containing 30% sucrose for 2 days at 4°C until the tissues sink to the bottom of the container. Then the brain tissues embedded the OCT and placed at -20°C for 1 h. Sections of 14 μm thickness were prepared using a cryostat. The slides were washed in 1× PBS for 5 min to remove OCT. Two to four drops of hydrogen peroxide were added to each section and incubated at room temperature for 10 min. The slides were immersed in boiling 1× target repair reagent to repair 5 min and then washed with fresh distilled water twice followed by 100% ethanol. Two to four drops of protease plus were added in the hydrophobic circle on each brain slice and incubated at 40°C for 30 min. The slides were washed with fresh distilled water twice. And then about four drops of Prkcg probe were added to each brain slice in the hydrophobic circle and incubated at 40°C for 2 h. The slides were washed with 1× wash buffer 2 times at room temperature for 2 min. Amp 1 (incubated at 40°C for 30 min), Amp 2 (incubated at 40°C for 15 min), Amp 3 (incubated at 40°C for 30 min), Amp 4 (incubated at 40°C for 15 min), Amp 5 (incubated at room temperature for 30 min), and Amp 6 (incubated at room temperature for 15 min) were performed in sequence, and finally the RED working solution was added to detect the signal.

Statistical Analysis

Statistical analysis was carried out using the GraphPad Prism 8.0 software. No methods of randomization were used to allocate animals to experimental groups. All experiments were blind to the experimenter. Two-tailed Student's *t*-test (95% confidence), one-way ANOVA and two-way ANOVA, with Bonferroni's *post hoc* multiple comparison test, were performed as required, respectively. Two by two comparisons were two-tailed. P-value < 0.05 was considered statistically significant.

RESULTS

Experimental Workflow and Depression-Like States Induced by CUMS

To investigate the phosphorylation changes related to depression and the antidepressant effect of ketamine, we used CUMS to induce depression-like states in mice (Deng et al., 2015; Jin et al., 2015; Ma et al., 2016) and then treated with ketamine before performing the phosphoproteomics analysis (**Figure 1A**). Briefly, the mice were subjected to unpredictable mild stress, including food or water deprivation, soiled cages, 45° angle cage tilt, tail clipping, foot shock, overnight illumination, social attack, and restraint in a 50-ml tube for 21 days. Age-matched wild-type littermates that did not receive the stress treatment were used as controls. The body weight and sucrose preference were monitored weekly during the protocol (**Figure 1A**). As expected, the CUMS group showed progressive decreases in body weight and sucrose preference (**Figures 1B,C**), which are the typical signs of depression (Burstein and Doron, 2018). Furthermore, we performed the forced swim test (FST) and tail suspension test (TST) to assess the depressive state. As expected, the CUMS group exhibited an increased immobility time during the FST (**Figure 1D**) and TST (**Figure 1E**), indicative of a depression-like state (Castagné et al., 2011). After successfully establishing the CUMS model, we intraperitoneally (IP) administered saline to the control group and saline or ketamine to the CUMS group (**Figure 1A**). Notably, 1 h after ketamine injection, the sucrose preference was significantly reversed to control levels

[1]http://www.omicsbean.cn/
[2]https://www.genome.jp/kegg/pathway.html

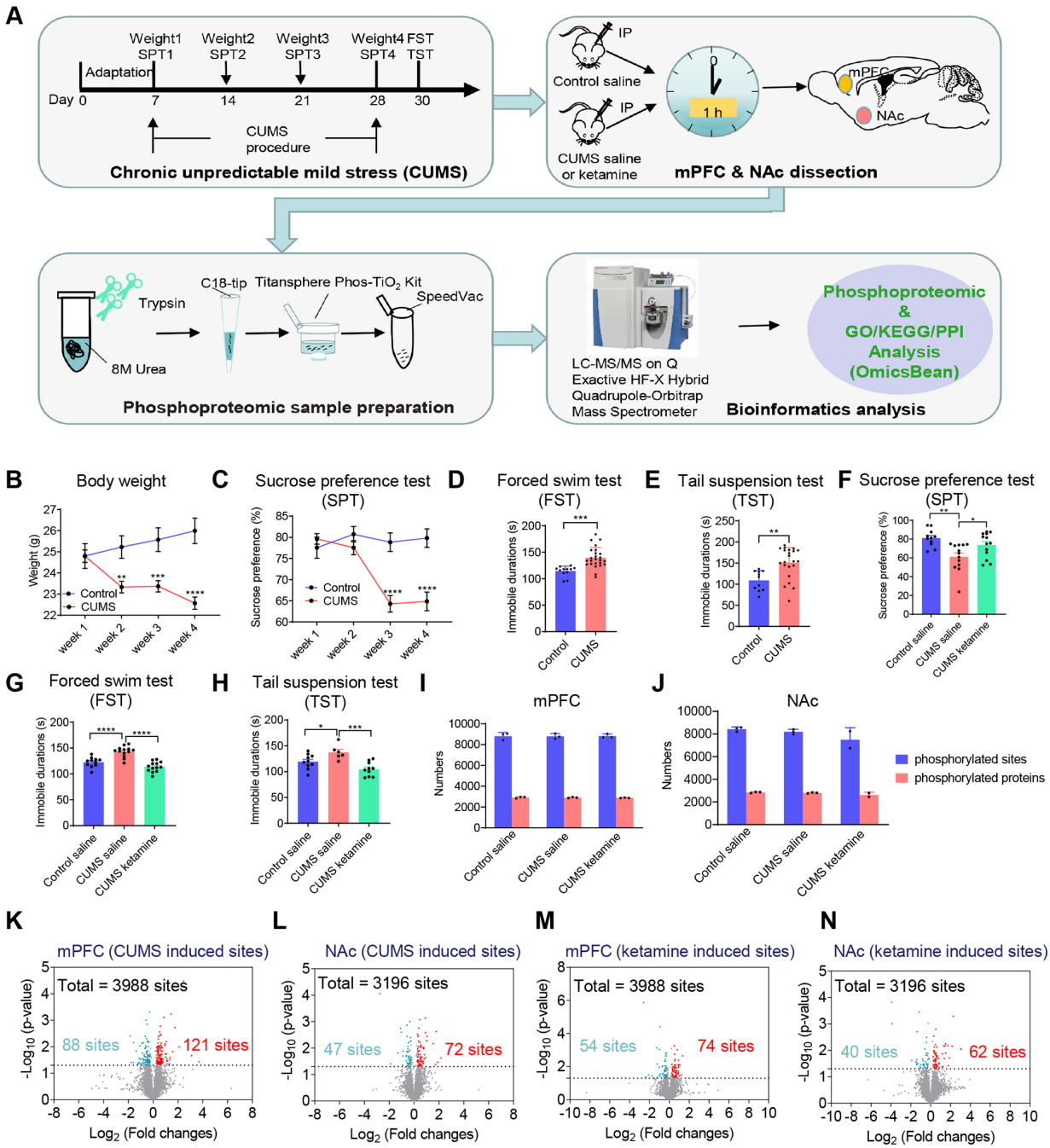

FIGURE 1 | Overview of the experimental workflow, related behavioral tests, and summary of phosphorylation changes induced by chronic unpredictable mild stress (CUMS) and ketamine. **(A)** The protocol of using CUMS to induce depression-like state and performing phosphoproteomic analysis afterward. First, the mice were subjected to CUMS protocol as indicated. SPT, sucrose preference test; FST, forced swim test; TST, tail suspension test. Second, ketamine or saline was administrated intraperitoneally (IP) to CUMS and control mice as indicated. All mice were killed 1-h after injection (n = 4 per group). Two brain regions (mPFC, NAc) were dissected and processed for phosphoproteomic analysis. mPFC, medial prefrontal cortex; NAc, nucleus accumbens. Third, proteins for phosphoproteomic analysis were tryptic digested in solution, and peptides were loaded onto the tips using Monospin C18 and phosphopeptides from each fraction were enriched by Titansphere Phos-TiO_2 Kit. Finally, the samples were subjected to LC and Q-Exactive HF-X analysis, following by bioinformatics analysis [Gene Ontology (GO)/Kyoto Encyclopedia of Genes and Genomes (KEGG)/protein-protein interaction (PPI) analysis]. **(B)** Bodyweight changes during the CUMS protocol (Control, n = 12; CUMS, n = 25, two-way ANOVA, $^{**}P < 0.01$, $^{***}P < 0.001$, $^{****}P < 0.0001$ compared with control group). **(C–E)** Behavioral evaluations after the CUMS to confirm the depression-like state. The preference value in the SPT was shown in (**C**; Control, n = 12; CUMS, n = 25, two-way ANOVA, $^{****}P < 0.0001$ compared with control group). The duration of immobility in the FST was shown in (**D**; Control, n = 12; CUMS, n = 25, t-test, $^{***}P < 0.001$ compared with control group). The duration of immobility in the TST was shown in (**E**; Control, n = 11; CUMS, n = 22, t-test, $^{**}P < 0.01$ compared with control group). **(F–H)** Behavioral evaluations after

(*Continued*)

FIGURE 1 | Continued
ketamine injection (IP) to CUMS mice to confirm the antidepressant effect. The preference value in the SPT was shown in (**F**; Control + saline, $n = 11$; CUMS + saline, $n = 13$; CUMS + ketamine, $n = 13$, one-way ANOVA, $^{**}P < 0.01$ for CUMS + saline compared with Control + saline; $^{*}P < 0.05$ for CUMS + saline compared with CUMS + ketamine). The duration of immobility in the FST was shown in (**G**; Control + saline, $n = 11$; CUMS + saline, $n = 13$; CUMS + ketamine, $n = 13$, one-way ANOVA, $^{****}P < 0.0001$ for CUMS + saline compared with Control + saline; $^{****}P < 0.0001$ for CUMS + saline compared with CUMS + ketamine). The duration of immobility in the TST was shown in (**H**; Control + saline, $n = 10$; CUMS + saline, $n = 6$; CUMS + ketamine, $n = 10$, one-way ANOVA, $^{*}P < 0.05$ for CUMS + saline compared with Control + saline; $^{***}P < 0.001$ for CUMS + saline compared with CUMS + ketamine). All data are shown as mean ± SEM. **(I,J)** The number of identified phosphorylated sites and proteins in different groups (Control + saline, CUMS + saline, and CUMS + ketamine) in the mPFC **(I)** and the NAc **(J)**, respectively. **(K,L)** The number of quantified differential phosphorylated sites between CUMS and controls without treatment in the mPFC **(K)** and the NAc **(L)**. **(M,N)** The number of quantified differential phosphorylated sites from CUMS mice between ketamine and saline injections in the mPFC **(M)** and the NAc **(N)**. The ratio of 1.2-fold change and the probability of 0.05 as a cut-off for differential expressed sites with statistical significance. The differential phosphorylated sites are shown in red (up-regulated) and blue (down-regulated).

(**Figure 1F**). The immobilization phenotypes in the FST and TST were also corrected 24-h post-injection (**Figures 1G,H**; Franceschelli et al., 2015).

Since we have confirmed the depression-like behaviors and the antidepressant effect of ketamine, 1-h after ketamine or saline injection, we quickly dissected two brain areas, the mPFC and the NAc, which have been associated with mood control (Rive et al., 2013; Floresco, 2015; Lieberman et al., 2019). The brain tissues from the two areas in a group of four mice were then homogenized and digested with trypsin. The phosphopeptides were extracted according to the procedure shown in **Figure 1A**. To ensure the reliability of the quantitative profiling results, the samples were prepared and the fractions were collected from three biological replicates per group. All samples were subjected to parallel label-free phosphoproteomics analysis using liquid chromatography-tandem mass spectrometry (LC-MS/MS). Unfortunately, one of the biological triplicates from the NAc group treated with ketamine was discarded due to poor sample processing.

Systematic Examination of Phosphorylation Changes Induced by CUMS and Ketamine

After phosphoproteomics analysis, we successfully identified ∼8,800 different phosphorylated sites mapping to ∼2,900 proteins from the mPFC groups (**Figure 1I**) and ∼8,000 phosphorylated sites mapping to ∼2,750 proteins from the NAc groups (**Figure 1J**). To test the reproducibility of our study, we performed Pearson correlation analysis between each biological replicate and discovered that the Pearson correlation between the experimental repeats was >0.85 in the mPFC (**Supplementary Figure S1A**) and >0.79 in the NAc (**Supplementary Figure S1B**), indicating robust reproducibility. In the meantime, we analyzed the overlapped phosphorylation sites between each replicate within a group and found that the percentage of the overlapped phosphorylation sites identified between every two repeats was approximately 80% (**Supplementary Table S1**). Next, we defined the differential phosphorylation sites between the CUMS group and the control as CUMS-induced phosphorylation and those between the CUMS group treated with ketamine and saline as ketamine-induced phosphorylation. We found that 3,988 and 3,196 of the identified phosphorylation sites were quantifiable in the mPFC and the NAc, respectively. Then, the ratio of 1.2-fold change and the probability of 0.05 as a cut-off for differential expressed sites with statistical significance. Therefore, for CUMS-induced changes, we quantified 209 differential phosphorylation sites from the mPFC and 119 differential phosphorylation sites from the NAc. There were 121 up-regulated and 88 down-regulated phosphorylation sites from the mPFC (**Figure 1K**; **Supplementary Data Sheet S1**), and 72 up-regulated and 47 down-regulated sites from the NAc (**Figure 1L**; **Supplementary Data Sheet S1**). For ketamine-induced changes, we quantified 128 differential phosphorylation sites from the mPFC, of which 74 were up-regulated and 54 were down-regulated (**Figure 1M**; **Supplementary Data Sheet S1**), and we quantified 102 differential phosphorylation sites from the NAc, of which 62 were up-regulated and 40 were down-regulated (**Figure 1N**; **Supplementary Data Sheet S1**). Moreover, we analyzed the differential phosphorylation between CUMS + ketamine vs. Control + saline. We quantified 270 differential phosphorylation sites from the mPFC, of which 173 were up-regulated and 97 were down-regulated (**Supplementary Figure S2A**; **Supplementary Data Sheet S1**), and quantified 108 differential phosphorylation sites from the NAc, of which 69 were upregulated and 39 were down-regulated (**Supplementary Figure S2B**; **Supplementary Data Sheet S1**).

Protein-Protein Interaction (PPI) Networks for CUMS- and Ketamine-Induced Changes

After the quantification of differential phosphorylation, we wonder whether there are interactions between the proteins carrying these quantified sites as it might help to identify key signaling pathways for depression induction and its treatment. Therefore, we used the OmicsBean analysis tool to investigate PPI networks. Interestingly, we found several pathway hubs in the PPI networks. For example, there were nine pathways induced by CUMS in the mPFC: "Synaptic vesicle cycle," "Endocrine and other factor-regulated calcium reabsorption," "Endocytosis," "Cholinergic synapse," "GABAergic synapse," "Glutamatergic synapse," "Retrograde endocannabinoid signaling," "Aldosterone synthesis and secretion," and "Morphine addiction" (**Figure 2A**). A total of 10 pathways were induced by ketamine in the mPFC: "Fc gamma R-mediated phagocytosis," "Taste transduction," "Endocytosis," "Ras signaling pathway," "Type II diabetes mellitus," "Synaptic vesicle cycle," "Nicotine addiction," "Amyotrophic lateral sclerosis (ALS)," "Regulation of actin cytoskeleton," and "Axon guidance" (**Figure 2B**). In the NAc, there were also 10 pathways induced

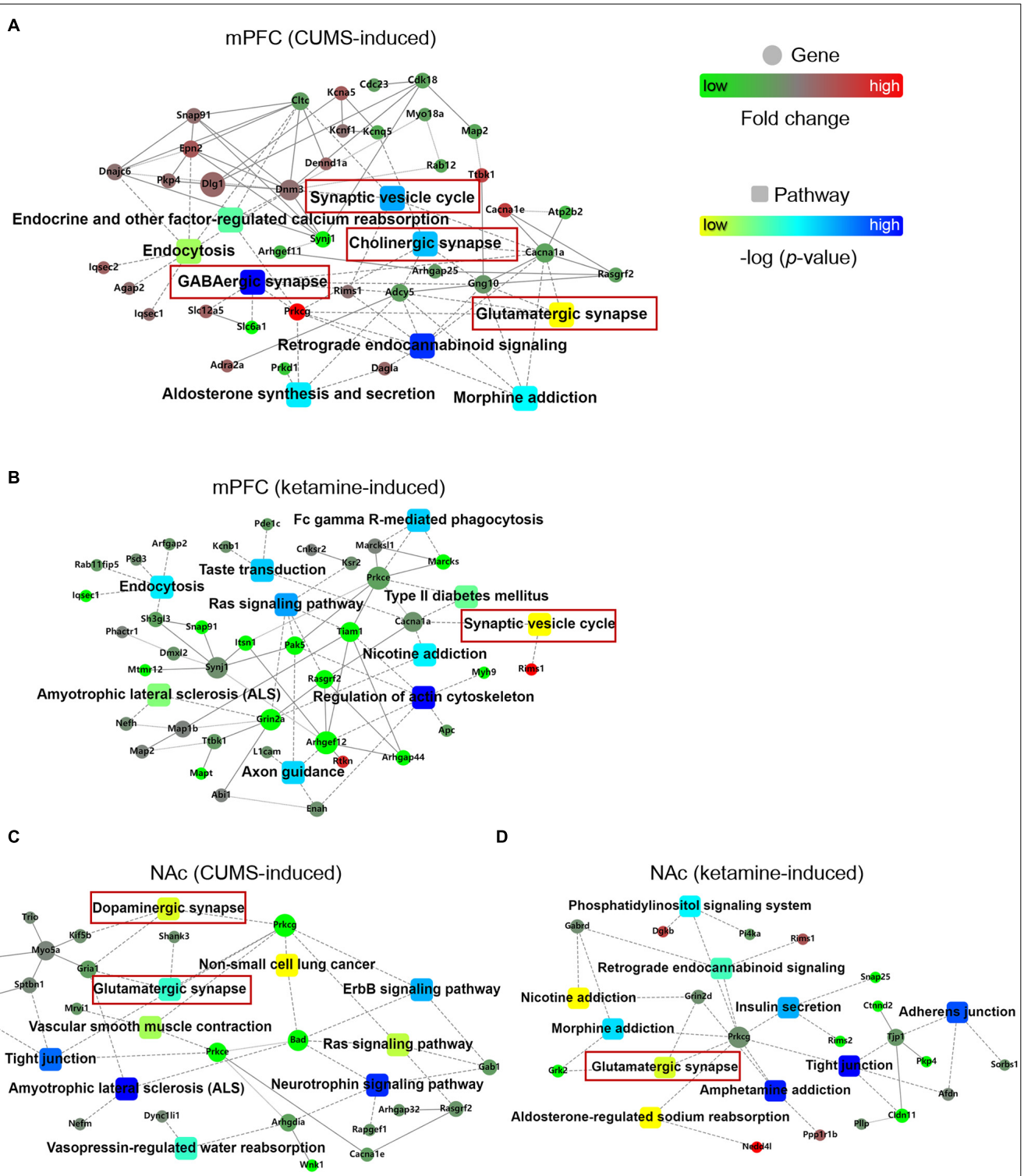

FIGURE 2 | PPI networks for CUMS- and ketamine-induced changes. **(A,B)** The PPI networks for proteins corresponding to quantified phosphorylation sites in the mPFC induced by CUMS **(A)** and ketamine **(B)**. **(C,D)** The PPI networks for proteins corresponding to quantified phosphorylation sites in the NAc induced by CUMS **(C)** and ketamine **(D)**. The PPI analysis is based on fold changes of genes expression, PPIs, and KEGG pathway enrichments. Fold changes of genes are indicated by circle nodes with gradient color (red, up-regulated; green, down-regulated). Rectangles indicate KEGG pathways, which are colored with a yellow to the blue gradient (smaller to larger *p*-values, respectively). The scales are indicated next to PPI networks. The red boxes represent the pathways associated with different synapses.

by CUMS: "Dopaminergic synapse," "Non-small cell lung cancer," "Glutamatergic synapse," "ErbB signaling pathway," "Vascular smooth muscle contraction," "Tight junction," "Ras signaling pathway," "ALS," "Neurotrophin signaling pathway," and "Vasopressin-regulated water reabsorption" (**Figure 2C**). A total of 10 pathways were induced by ketamine: "Phosphatidylinositol signaling system," "Retrograde endocannabinoid signaling," "Nicotine addiction," "Insulin secretion," "Morphine addiction," "Adherens junction," "Glutamatergic synapse," "Tight junction," "Amphetamine addiction," and "Aldosterone-regulated sodium reabsorption" (**Figure 2D**).

Furthermore, we wonder whether there is a common feature in these hubs across brain regions and treatments. Interestingly, we found "synapse" as a shared hub feature. As follow, the CUMS-induced PPI hubs in the mPFC included "Glutamatergic synapse," "GABAergic synapse," "Cholinergic synapse," and "Synaptic vesicle cycle" (**Figure 2A**). The ketamine-induced PPI hub in the mPFC included the "Synaptic vesicle cycle" (**Figure 2B**). Similarly, the CUMS-induced PPI hubs in the NAc included "Glutamatergic synapse" and "Dopaminergic synapse" (**Figure 2C**). The ketamine-induced PPI hub in the NAc included "Glutamatergic synapse" (**Figure 2D**). Thus, our data suggest that synaptic function changes might be an important hallmark for depression progression and treatment, which is consistent with previous reports (Elizalde et al., 2010; Li et al., 2011; Duman and Aghajanian, 2012; Duman et al., 2016).

Synaptic Signaling Changes Induced by CUMS and Ketamine

To unveil the critical synapse-related signaling pathways identified from the PPIs, we classified the relevant protein phosphorylation sites according to their synaptic types, which included glutamatergic, GABAergic, cholinergic and dopaminergic (**Figures 3A,B**). For glutamatergic synapses, Cacna1a (T1888), Gng10 (S8), and Adcy5 (S156) were down-regulated by CUMS, while Prkcg (S322) was up-regulated in the mPFC (**Figure 3A**). Grin2a (S929) was down-regulated by ketamine, while Cacna1a (T1888; S2153) was up-regulated in the mPFC (**Figure 3A**). Gria1 (S849) and Shank3 (S450) were up-regulated, while Prkcg (S342) was down-regulated by CUMS in the NAc (**Figure 3B**). Grin2d (S1049) and Prkcg (S342) were up-regulated by ketamine in the NAc (**Figure 3B**). These genes are involved in regulating synaptic plasticity and postsynaptic excitability (Lee et al., 2000; Shuvaev et al., 2011; Ryan et al., 2013; Perszyk et al., 2016; Kellermayer et al., 2018). For GABAergic synapses, Cacna1a (T1888), Gng10 (S8), Adcy5 (S156), and Slc6a1 (T15) were down-regulated, while Prkcg (S322) and Slc12a5 (S1047) were up-regulated by CUMS in the mPFC (**Figure 3A**). Cacna1a (T1888; S2153) and Plcl1 (S570) were up-regulated by ketamine in the mPFC (**Figure 3A**). Prkcg (S342) was down-regulated by CUMS in the NAc (**Figure 3B**). Gabrd (S390) and Prkcg (S342) were up-regulated by ketamine in the NAc (**Figure 3B**). These genes are involved in regulating postsynaptic hyperpolarization (Yanagihori et al., 2006; Oláh et al., 2009; Shuvaev et al., 2011; Schwale et al., 2016). For cholinergic synapses, Cacna1a (T1888), Gng10 (S8), Adcy5 (S156), and Kcnq5 (S79) were down-regulated, while CUMS up-regulated Prkcg (S322) in the mPFC (**Figure 3A**). Cacna1a (T1888; S2153) was up-regulated by ketamine in the mPFC (**Figure 3A**). Chrm4 (S379) and Prkcg (S342) were down-regulated by CUMS in the NAc (**Figure 3B**). Prkcg (S342) was up-regulated, while Kcnq2 (S645) was down-regulated by ketamine in the NAc (**Figure 3B**). These genes are involved in regulating synaptic plasticity (Shuvaev et al., 2011; Niday et al., 2017). For dopaminergic synapses, Cacna1a (T1888), Gng10 (S8), and Adcy5 (S156) were down-regulated, while CUMS up-regulated Prkcg (S322) in the mPFC (**Figure 3A**). Grin2a (S929) was down-regulated, while Cacna1a (T1888; S2153) was up-regulated by ketamine in the mPFC (**Figure 3A**). Prkcg (S342) was down-regulated, while CUMS up-regulated Gria1 (S849) and Kif5b (S933) in the NAc (**Figure 3B**). Prkcg (S342), Grin2d (S1049) and Ppp1r1b (S46) were up-regulated by ketamine in the NAc (**Figure 3B**). These genes are involved in regulating synaptic plasticity (Calabresi et al., 2000; Lee et al., 2000; Shuvaev et al., 2011; Ryan et al., 2013; Perszyk et al., 2016; Kellermayer et al., 2018).

Intriguingly, protein kinase C gamma (Prkcg), which has been implicated in long-term alterations in synaptic efficacy (Saito and Shirai, 2002; McNamara and Lenox, 2004), was drastically enriched by CUMS induction in the mPFC (8.5-fold, **Figure 3C**) and by ketamine in the NAc (1.47-fold, **Figure 3D**) and is involved in all four synaptic types (**Figures 3A,B**). Another highly enriched phosphoprotein was protein phosphatase 1 regulatory subunit 1B (Ppp1r1b), also known as dopamine- and cAMP-regulated neuronal phosphoprotein (DARPP-32), which was enriched 2.4-fold in the NAc by ketamine treatment (**Figure 3D**). Interestingly, Ppp1r1b has been shown to play an important role in long-term synaptic plasticity in the NAc (Calabresi et al., 2000; Stipanovich et al., 2008). Overall, our data identified the critical changes in synaptic signaling induced by CUMS and ketamine.

Bioinformatics Analysis of the Shared and Differential Phosphorylation Changes Between the CUMS-Induced and Ketamine-Induced Groups

As the shared and differential phosphorylation changes induced by CUMS and ketamine might be important for the antidepressant effect of ketamine, we analyzed these changes by (GO: biological process, cell component, and molecular function) and KEGG pathways using the OmicsBean analysis tool. First, we found that 13 phosphorylation sites overlapped between the CUMS-induced and ketamine-induced changes in the mPFC (**Figures 4A,B**). Interestingly, opposite changes for these overlapping sites were observed between the two groups (**Figure 4B**). Seven sites down-regulated by CUMS and up-regulated by ketamine, while the remaining six sites were changed in the opposite direction (**Figure 4B**), suggesting that the altered phosphorylation induced by CUMS was corrected by ketamine treatment. Among them, regulating synaptic membrane exocytosis protein 1 (Rims1) is a member of the

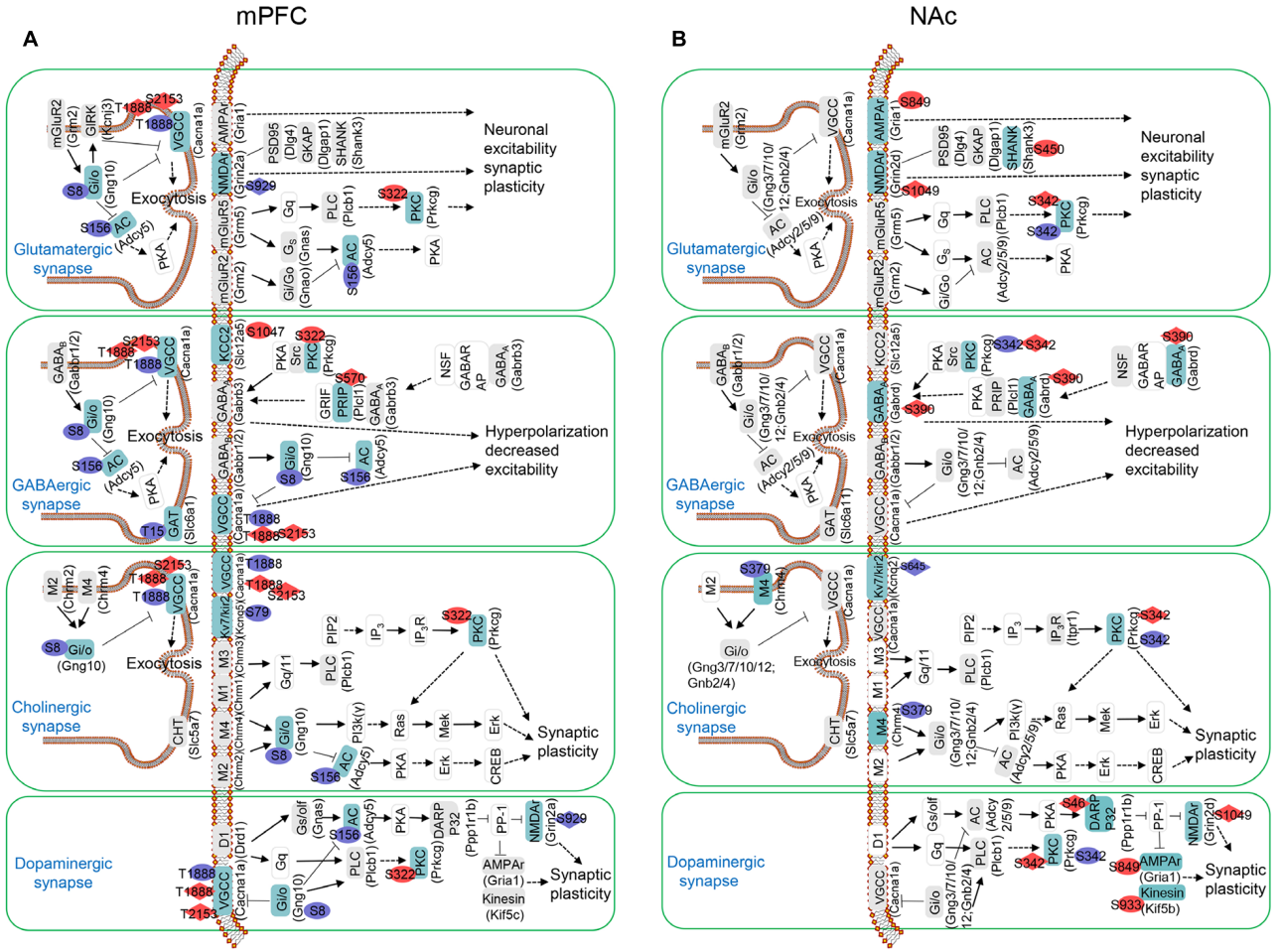

C

The changes of phosphorylated genes/sites in **A**

Groups \ Genes (Sites)	VGCC Cacna1a (T1888)	VGCC Cacna1a (S2153)	Gi/o Gng10 (S8)	AC Adcy5 (S156)	NMDAr Grin2a (S929)	PKC Prkcg (S322)	GAT Slc6a1 (T15)	KCC2 Slc12a5 (S1047)	PRIP Plcl1 (S570)	Kv7/Kir2 Kcnq5 (S79)
CUMS induced	0.71	N	0.81	0.74	N	8.50	0.29	1.66	N	0.67
ketamine induced	1.41	1.41	N	N	0.78	N	N	N	1.94	N

D

The changes of phosphorylated genes/sites in **B**

Groups \ Genes (Sites)	AMPAr Gria1 (S849)	NMDAr Grin2d (S1049)	SHANK Shank3 (S450)	PKC Prkcg (S342)	$GABA_A$ Gabrd (S390)	M4 Chrm4 (S379)	DARPP32 Ppp1r1b (S46)	Kinesin Kif5b (S933)	Kv7/Kir2 Kcnq2 (S645)
CUMS induced	1.26	N	1.46	0.79	N	0.64	N	1.47	N
ketamine induced	N	1.49	N	1.47	1.54	N	2.36	N	0.67

Red color : up-regulated Blue color : down-regulated N : not differential

FIGURE 3 | Summary of CUMS- and ketamine-induced signaling pathways at synapses. **(A,B)** Proteins assigned to different KEGG pathways, with particular phosphorylated sites of each protein indicated in ovals (CUMS-induced) and rhombuses (ketamine-induced). The corresponding genes were shown in brackets. The aqua green, gray, and white rectangles indicate differential, not differential, and not identified phosphoproteins in our study, respectively. Four types of synapses were analyzed, including the glutamatergic synapse, the GABAergic synapse, the cholinergic synapse, and the dopaminergic synapse. Red and blue ovals indicate up-regulated and down-regulated phosphorylation induced by CUMS in the mPFC, respectively. Red and blue rhombuses demonstrate up-regulated and down-regulated phosphorylation induced by CUMS and ketamine in the NAc, respectively. **(C)** The phosphorylation list for **(A)**, where red, blue colors and N indicate up-, down-regulated, and not differential, respectively. **(D)** The phosphorylation list for **(B)**, where red, blue colors and N indicate up-, down-regulated, and not differential, respectively.

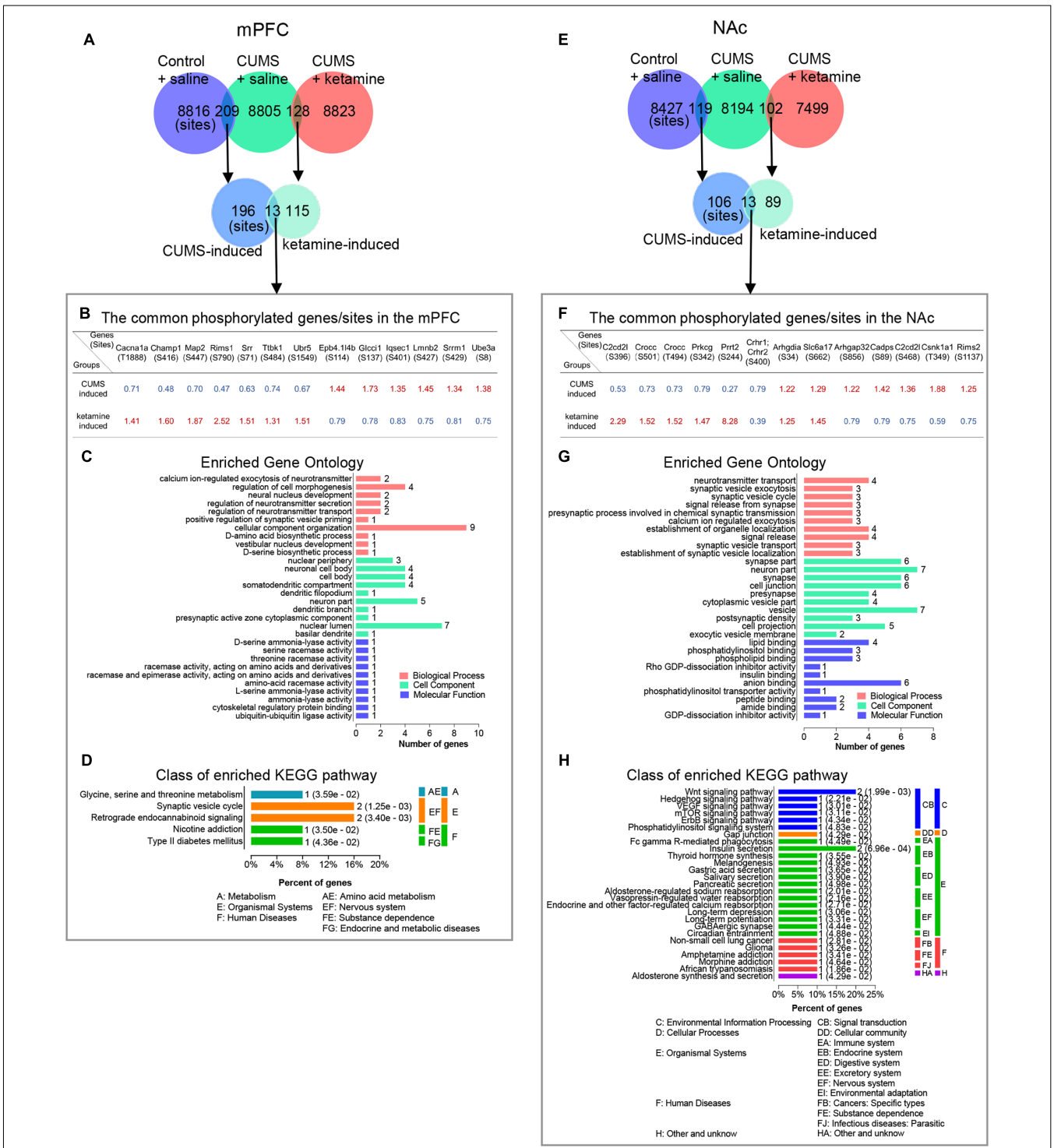

FIGURE 4 | Bioinformatics analysis of the overlapped phosphorylation changes between CUMS- and ketamine-induced. **(A)** The overlapping of identified phosphorylated sites for indicated experimental groups in the mPFC. **(B–D)** Bioinformatics analysis of the proteins corresponding to the common phosphorylation sites between CUMS-induced and ketamine-induced in the mPFC. The genes/sites list, GO analysis, and KEGG pathway analysis are shown in **(B–D)**, respectively. **(E)** The overlapping of identified phosphorylated sites for indicated experimental groups in the NAc. **(F–H)** Bioinformatics analysis of the proteins corresponding to the common phosphorylation sites between CUMS-induced and ketamine-induced in the NAc. The genes/site lists, GO analysis, and KEGG pathway analysis are shown in **(F–H)**, respectively. The red and blue colors indicate up- and down-regulated in **(B,F)**, respectively. Enriched GO analysis shows the 10 most significantly enriched terms of biological process, cell component, and molecular function, respectively. Enriched KEGG pathway analysis shows the number of involved genes in a specific pathway, and corresponding *p*-values are shown on the right side of the column.

Ras superfamily of genes and plays an important role in neurotransmitter release (Wang et al., 1997; Calakos et al., 2004). Rims1 had the largest fold change, with approximately half-fold repression by CUMS and a 2.5-fold enrichment by ketamine (**Figure 4B**). Moreover, microtubule-associated protein 2 (Map2), a protein that stabilizes microtubule activity and regulates neuronal axons and dendritic microtubule networks (Sánchez et al., 2000), was also repressed by CUMS and enriched by ketamine (**Figure 4B**). Serine racemase (Srr), a D-serine synthesis enzyme involved in the regulation of synaptic plasticity (Miya et al., 2008), showed similar changes to Map2 (**Figure 4B**). Next, we performed GO analysis and found that the top enriched categories were "cellular component organization," followed by "neuron part" and "nuclear lumen" (**Figure 4C**). Besides, we performed KEGG pathway analysis and found that "Synaptic vesicle cycle" and "Retrograde endocannabinoid signaling" were the top enriched categories (**Figure 4D**). All other categories from the GO and KEGG analyses are shown in (**Figures 4C,D**). Additionally, we analyzed CUMS induced sites with phosphorylation levels precisely restored to control levels by ketamine treatment. We obtained 10 phosphorylation sites in mPFC (**Supplementary Table S2**) and eight sites in the NAc (**Supplementary Table S3**).

Similarly, we found 13 phosphorylation sites that overlapped between CUMS-induced and ketamine-induced changes in the NAc (**Figures 4E,F**). Among them, 10 sites were regulated in the opposite direction by CUMS and ketamine (**Figure 4F**), with five sites downregulated and five sites upregulated by CUMS. The opposite changes were induced by ketamine (**Figure 4F**). These results confirm that the altered phosphorylation by CUMS was reversed by ketamine treatment. Interestingly, several synaptic plasticity genes, including Proline-rich transmembrane protein 2 [Prrt2 (Michetti et al., 2017)] and Calcium-dependent secretion activator [Cadps (Shinoda et al., 2016)], were involved. Further bioinformatics analysis showed that the top enriched GO annotations were "neuron part" and "vesicle," followed by "synapse part," "synapse," "cell junction," and "anion binding" (**Figure 4G**), suggesting that synaptic changes might be important for the depression-like state and the antidepressant effect of ketamine. From the KEGG pathway analysis, the "Wnt signaling pathway" and "Insulin secretion" were the top enriched categories (**Figure 4H**). All other categories from the GO and KEGG analyses are shown in **Figures 4G,H**.

In addition, we found that 31 phosphoproteins overlapped between the CUMS-induced and ketamine-induced changes in the mPFC (**Supplementary Figure S3A**; **Supplementary Data Sheet S2**). The top enriched GO categories were "cellular component organization" and "cellular component organization or biogenesis" in biological process. "neuron part" and "protein binding" were the top enriched categories in cell component and molecular function, respectively (**Supplementary Figure S3B**). For the KEGG pathway analysis, we found that "Retrograde endocannabinoid signaling" and "Synaptic vesicle cycle" were the top enriched categories (**Supplementary Figure S3C**). All other categories from the GO and KEGG analyses are shown in **Supplementary Figures S3B,C**. In the NAc, 13 phosphoproteins overlapped between the CUMS-induced and ketamine-induced changes (**Supplementary Figure S3D**; **Supplementary Data Sheet S2**). After GO analysis, we found that "localization" was the top enriched category in biological process, and "neuron part" and "vesicle" were the top enriched categories in cell components. For molecular function, "lipid binding" was the top enriched category (**Supplementary Figure S3E**). For the KEGG pathway analysis, the top enriched signaling pathways included the "Wnt signaling pathway" and "Insulin secretion" (**Supplementary Figure S3F**). All other categories from the GO and KEGG analyses are shown in **Supplementary Figures S3E,F**.

Furthermore, we analyzed the differential phosphorylation changes induced by ketamine, but not by CUMS, as these changes might also be important for the antidepressant effect of ketamine. We identified 115 phosphorylation sites in the mPFC (**Figure 5A**; **Supplementary Data Sheet S3**). After GO analysis, we found that several synaptic transmission-related signaling pathways were enriched in biological processes, such as "synapse organization," "modulation of synaptic transmission," and "chemical synaptic transmission," suggesting synaptic changes might be a hallmark of ketamine treatment. For cell component, many synapse-related structure proteins were enriched in "synapse," "postsynaptic specialization," "postsynaptic density" and "neuron part," suggesting that changes in the synaptic structure might be important after ketamine treatment. For molecular function, "binding" was the top enriched category, followed by "protein binding," "enzyme binding," and "cytoskeletal protein binding" (**Figure 5B**), suggesting that a series of intracellular signaling pathways were rapidly activated after ketamine injection (1 h). For KEGG analysis, the top enriched signaling pathways included "Regulation of actin cytoskeleton." In addition, the "Ras signaling pathway" and "Axon guidance" were enriched (**Figure 5C**). All other categories from the GO and KEGG analyses are shown in **Figures 5B,C**. For the NAc, we identified 89 phosphorylation sites that were induced by ketamine, but not by CUMS (**Figure 5D**; **Supplementary Data Sheet S3**). After GO analysis, we found that the "single-organism cellular process" was the top enriched category in biological process, followed by "cellular component organization" and "cellular component organization or biogenesis." For cell component, "whole membrane," "synapse," and "cell junction" were among the top categories, followed by "synapse part" and "postsynapse." For molecular function, we found that "binding" was also the top enriched categories, including "protein binding," "enzyme binding," "cytoskeletal protein binding," and "GTPase binding" (**Figure 5E**). These results suggested that a series of intracellular signaling pathways were rapidly activated following ketamine injection. For KEGG analysis, we found that the top enriched signaling pathways included "cAMP signaling," "Adherens junction" and "Tight junction," followed by "Phosphatidylinositol signaling" and "Synaptic vesicle cycle" (**Figure 5F**), suggesting that a different set of signaling pathways was activated in the NAc compared to the mPFC following ketamine treatment. All other categories from the GO and KEGG analyses are shown in **Figures 5E,F**.

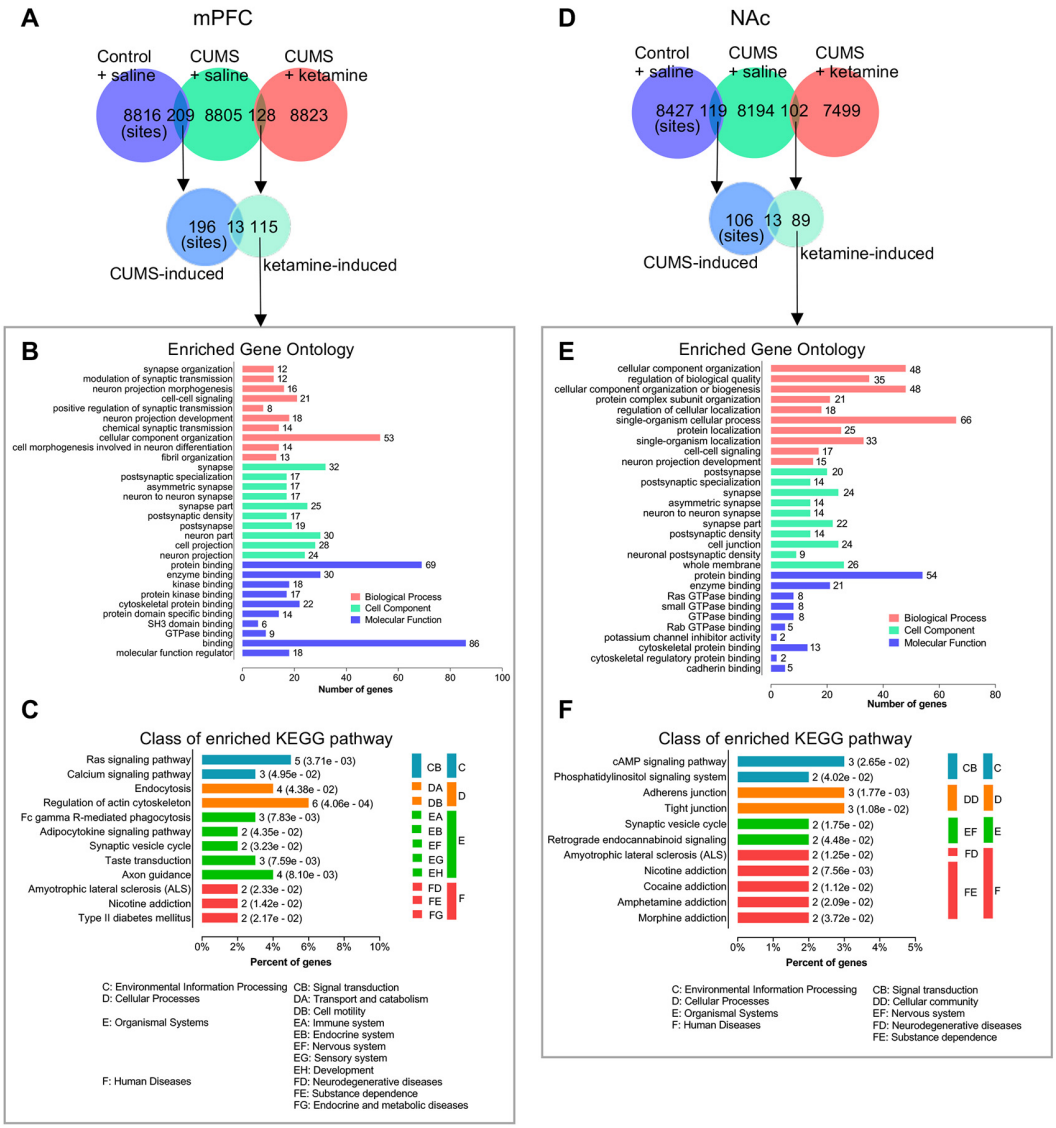

FIGURE 5 | Bioinformatics analysis of the phosphorylation site changes induced selectively by ketamine, but not by CUMS. **(A)** The overlapping of identified phosphorylated sites for indicated experimental groups in the mPFC. **(B,C)** Bioinformatics analysis of the proteins corresponding to phosphorylation sites induced selectively by ketamine, but not by CUMS in the mPFC. The GO and KEGG pathway analyses are shown in **(B,C)** respectively. **(D)** The overlapping of identified phosphorylated sites for indicated experimental groups in the NAc. **(E,F)** Bioinformatics analysis of the proteins corresponding to phosphorylation sites induced selectively by ketamine, but not by CUMS in the NAc. The GO and KEGG pathway analyses are shown in **(E,F)** respectively. Enriched GO analysis shows the 10 most significantly enriched terms of biological process, cell component, and molecular function, respectively. Enriched KEGG pathway analysis indicates the number of involved genes in a specific pathway, and corresponding *p*-values are shown on the right side of the column.

In addition, we analyzed the differential phosphoprotein changes induced by ketamine but not by CUMS. We identified 81 phosphoproteins in the mPFC (**Supplementary Figure S4A**; **Supplementary Data Sheet S4**). After GO analysis, we found that "positive regulation of biological process," "cytoplasm," and "protein binding" were the top enriched categories in biological process, cell component, and molecular function, respectively (**Supplementary Figure S4B**). We found that "Regulation of actin cytoskeleton" was the top enriched category in KEGG pathway analysis (**Supplementary Figure S4C**). All other categories from the GO and KEGG analyses are shown in **Supplementary Figures S4B,C**. In the NAc, we identified 80 phosphoproteins for GO and KEGG pathway analyses (**Supplementary Figure S4D**; **Supplementary Data Sheet S4**). For GO analysis, "single-organism cellular process," "whole membrane," and "protein binding" were the top enriched categories in biological process, cell component, and molecular function, respectively (**Supplementary Figure S4E**). We found that the "cAMP signaling pathway," "Adherens junction," and "Tight junction" were the top enriched categories in

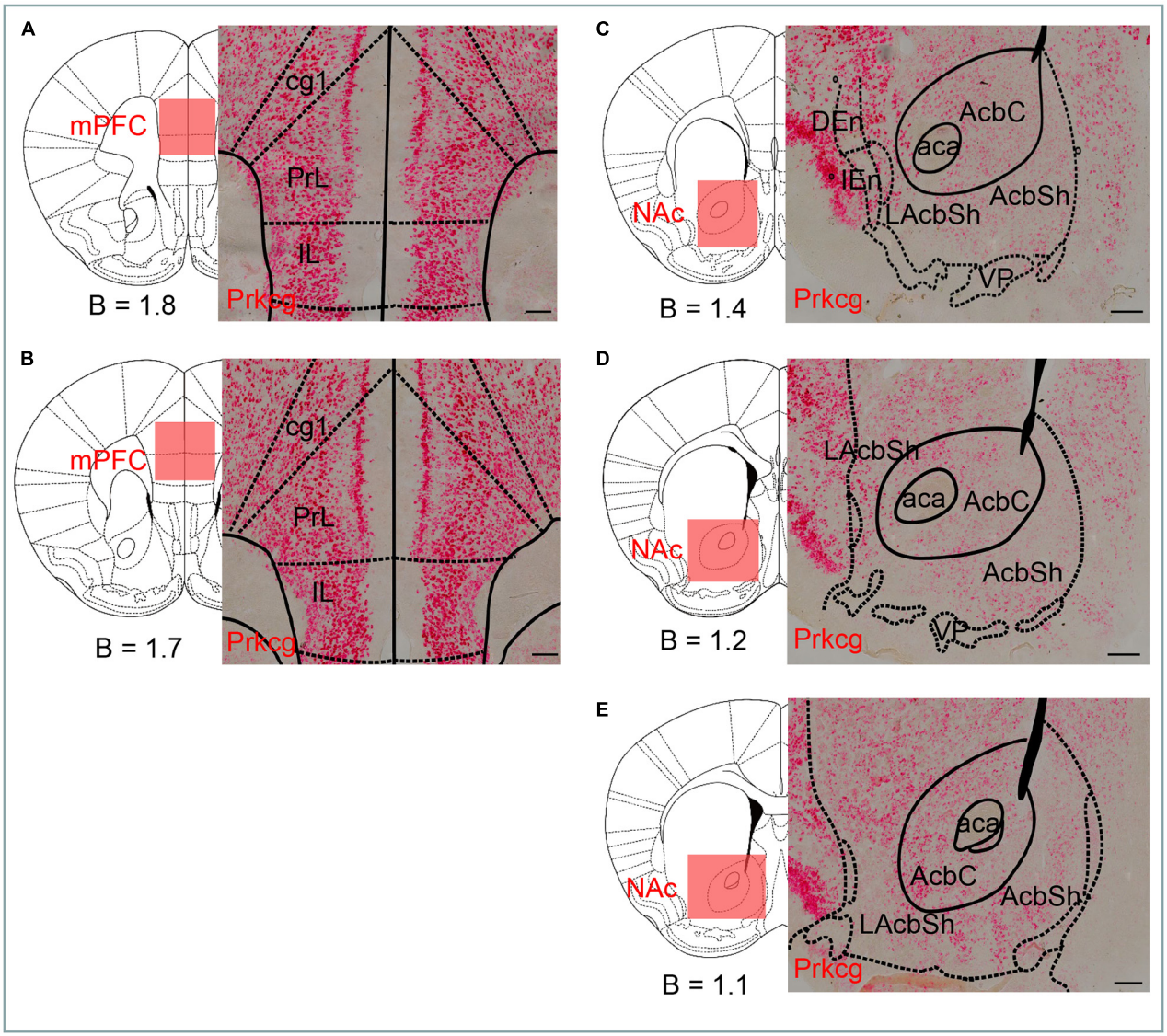

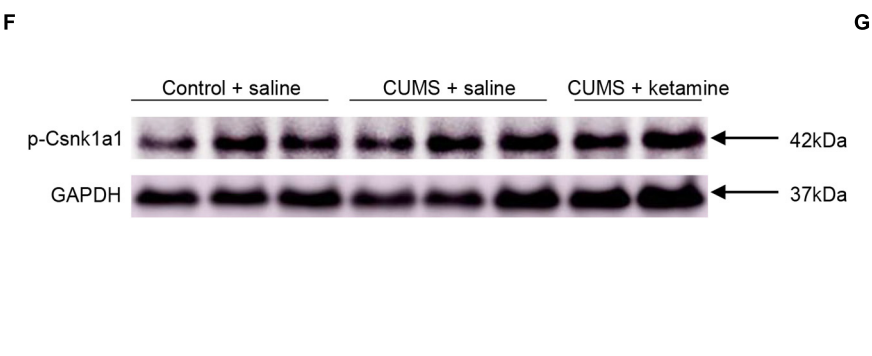

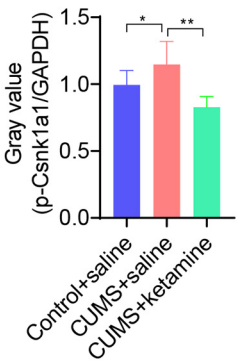

FIGURE 6 | Candidate verification by RNA in situ or western blot. **(A–E)** RNAscope in situ hybridization was performed on coronal sections of wild-type mouse brains in the mPFC and NAc with a Prkcg probe. Prkcg mRNA was expressed in both the mPFC and the NAc. Scale bars are 200 μm. B, bregma; cg1, cingulate cortex, area 1; PrL, prelimbic cortex; IL, infralimbic cortex; aca, anterior commissure, anterior part; AcbC, accumbens nucleus, core; LAcbSh, lateral accumbens shell; AcbSh, accumbens nucleus, shell; DEn, dorsal endopiriform claustrum; IEn, intermediate endopiriform claustrum; VP, ventral pallidum. **(F–G)** Western blot analysis for the phosphorylation of Csnk1a1 at T321. All data are shown as mean ±SEM. $^{*}P < 0.05$, one-way ANOVA tests for CUMS + saline compared with Control + saline; $^{**}P < 0.01$, one-way ANOVA tests for CUMS + saline compared with CUMS + ketamine.

KEGG pathway analysis (**Supplementary Figure S4F**). All other categories from the GO and KEGG analyses are shown in **Supplementary Figures S4E,F**.

Nevertheless, we analyzed the overlapping phosphorylation sites between the mPFC and the NAc. We found that only three sites were common for CUMS-induced changes: Dync1li1 (S510), Jag2 (S1125) and Gpm6a (S267; **Supplementary Figure S5A**). Dync1li1 (S510) and Jag2 (S1125) were up-regulated by CUMS in the mPFC and the NAc, and Gpm6a (S267) was up-regulated in the mPFC but down-regulated in the NAc (**Supplementary Figure S5A**). Cytoplasmic dynein 1 light intermediate chain 1 (Dync1li1) is a subunit of cytoplasmic dynein that moves cellular components toward the minus ends of microtubules and determines the distribution of vesicular organelles (Tynan et al., 2000; Sivaram et al., 2009). Jagged-2 (Jag2) is one of several ligands that activates Notch and related receptors, and the Notch signaling pathway plays an important role in neuronal plasticity (Shimizu et al., 2000; Monsalve et al., 2014). Neuronal membrane glycoprotein M6-a (Gpm6a) is a transmembrane protein that plays an important role in neurite/filopodium outgrowth and synapse formation (Alfonso et al., 2005). For ketamine-induced changes, there were four sites in common between the two brain regions: Rims1 (S790), Hdgfrp2 (S635), Set (S30) and Arhgap44 (S598; **Supplementary Figure S5B**). Rims1 (S790) was up-regulated by ketamine in the mPFC and the NAc, Hdgfrp2 (S635) was up-regulated in the mPFC but down-regulated in the NAc, and Set (S30) and Arhgap44 (S598) were down-regulated in both brain regions (**Supplementary Figure S5B**). Regulating synaptic membrane exocytosis protein 1 (Rims1) is a member of the Ras superfamily and plays an important role in neurotransmitter release (Wang et al., 1997; Calakos et al., 2004). Hepatoma-derived growth factor-related protein 2 (Hdgfrp2) binds to histone marks characteristic of transcriptionally silent chromatin and recruits the homologous recombination repair machinery to active genes silenced upon DNA damage (Baude et al., 2016). Set nuclear proto-oncogene (Set) interacts with numerous proteins involved in histone modification and plays a pivotal role in neurogenesis (Stevens et al., 2018). Rho GTPase activating protein 44 (Arhgap44) is a GTPase-activating protein for the small GTPases RAC1 and CDC42 and is involved in cell spreading and migration (Xu et al., 2017). The few overlapping sites between the two brain regions suggest that they use different signaling mechanisms in response to ketamine treatment.

Candidate Verification by RNA *in situ* or Western Blot

We sought to verify the expression and phosphorylation levels of some candidate proteins by RNA *in situ* and western blot. We checked the expression pattern of Prkcg by RNAscope in situ hybridization since it is a kinase that was drastically enriched by CUMS in the mPFC (8.5-fold, **Figure 3C**) and by ketamine in the NAc (1.47-fold, **Figure 3D**) and was involved in all four synaptic types (**Figures 3A,B**). As expected, the RNA *in situ* revealed that Prkcg mRNA was expressed in both the mPFC and the NAc, with a stronger expression in the mPFC (**Figures 6A–E**). It might be interesting to check the function of this protein kinase in depression in the future.

Besides, we searched antibodies for identified phosphoproteins and found suitable antibodies for p-Csnk1a1 (T321). The level of p-Csnk1a1 (T321) was up- regulated after CUMS treatment and was restored by ketamine (**Figures 6F,G**), which is consistent with the results from the LC-MS/MS analysis (**Supplementary Data Sheet S1**). Csnk1a1 is one of the vital components of the Wnt/β-catenin signaling pathway and is a serine/threonine kinase that inhibits β-catenin (Jiang et al., 2018). It is a tumor suppressor gene for colon cancer and melanoma, and controls proliferation through regulating the β-catenin activity (Sinnberg et al., 2010; Elyada et al., 2011). Epithelial cells lacking Csnk1a1 also exhibits many of the characteristics of human colorectal tumors, particularly induces DNA damage responses and cellular senescence (Carreras Puigvert et al., 2013). It might be interesting to check whether this kinase plays a vital role in depression.

DISCUSSION

Protein phosphorylation, one of the most common intracellular protein modifications, controls a variety of cellular processes, such as kinase-mediated addition of high-energy phosphate groups to serine, threonine, or tyrosine residues on proteins to participate in cells signaling (Martins-de-Souza et al., 2012). Large-scale analyses and quantification of phosphoproteins and their phosphorylation sites using mass spectrometric analysis allow us to systematically analyze the functional role of proteins, such as those involved in signal transduction (Mann et al., 2002). In the present study, we used a highly efficient method to perform phosphorylation proteomic analysis combining TiO_2 phosphopeptide enrichment with LC-MS/MS analysis. We analyzed 17 samples and identified ∼8,800 phosphorylated sites mapping to ∼2,900 proteins from the mPFC groups (**Figure 1I**) and ∼8,000 phosphorylated sites mapping to ∼2,750 proteins from the NAc groups (**Figure 1J**). By analyzing these differential phosphorylation sites among Control, CUMS and CUMS + ketamine, we provided a list of phosphoproteins and their phosphorylation sites that will help elucidate the signaling changes in different brain regions in depressive conditions and following ketamine treatment. Noticeably, it would be interesting to include a ketamine-treated control to see whether ketamine treatment-induced changes are specific to depression states over normal states. Also, it would be more informative to include a regular protein mass spectra for comparison to check whether changes in protein concentration contribute to the changes in protein phosphorylation.

Intriguingly, our findings support the role of synaptic function in depression induction and treatment, as shown by PPI networks. Unexpectedly, we found that "synapse" was the common feature, including glutamatergic, GABAergic, cholinergic, dopaminergic, and synaptic vesicle cycle, as indicated (**Figures 2**, **3**). Another interesting finding is the opposite changes in phosphorylation between the CUMS-induced and ketamine-induced groups, suggesting

that the altered phosphorylation induced by CUMS was reversed by ketamine treatment. Consistent with these changes, several corresponding proteins have been reported to play a role in depression. For example, Cacna1a encodes the transmembrane pore-forming subunit of the P/Q-type or CaV2.1 voltage-gated calcium channel, which regulates the efficiency of synaptic transmission at presynaptic membrane active zones (Lübbert et al., 2017, 2019). The protein levels of Map2 in the hippocampus of CUMS model rats were down-regulated, which could be reversed by Ro41-5253 or fluoxetine treatment (Ke et al., 2019). Another interesting protein is Prkcg, a PKC that is activated by Ca^{2+} and diacylglycerol in the presence of phosphatidylserine (Saito and Shirai, 2002). It is expressed in both the mPFC and the NAc (**Figures 6A–E**). Selective blockade of the PLCb1-PKCg signaling pathway produced an antidepressant-like phenotype in mice (Galeotti and Ghelardini, 2011), consistent with the significant increase of Prkcg (S322) induced by CUMS in the mPFC in our data (**Figure 3C**). However, Prkcg (S342) showed the opposite change in the NAc (**Figure 3D**), which implies that different phosphorylation sites in different brain regions may play different roles in depression. Furthermore, Prrt2 (S244) in the NAc attracted our attention due to its dramatic changes, although this protein's function is still unclear. Some evidence suggests a functional role at synapses, such as its coexpression with synaptic markers (Lee et al., 2012) or interaction with synaptic vesicle cycling (Rossi et al., 2016). Interestingly, our study also found that prrt2 is involved in the synapse-related process (**Figure 4G**), such as neurotransmitter transport and synaptic vesicle exocytosis.

Notably, regarding the differential phosphorylation changes induced by ketamine, but not by CUMS, "synapse" still accounts for a large proportion of the categories from the GO analysis (**Figures 5B,E**). Consistent with our study, many previous studies have shown that ketamine can reverse the synaptic deficits caused by stress (Li et al., 2011; Belujon and Grace, 2014; Ghosal et al., 2017). Surprisingly, only a few phosphorylation sites were overlapping between the mPFC and the NAc induced by CUMS and ketamine, respectively (**Supplementary Figure S5**). We found that only three sites, Dync1li1 (S510), Jag2 (S1125) and Gpm6a (S267), were in common between the two brain regions induced by CUMS (**Supplementary Figure S5A**). For ketamine-induced changes, there were four sites in common: Rims1 (S790), Hdgfrp2 (S635), Set (S30) and Arhgap44 (S598; **Supplementary Figure S5B**). These findings may indicate that the two brain regions respond differently to depression and ketamine treatment.

Here, we identified the global phosphoproteomic changes in CUMS-induced depressive states and ketamine treatment. Through different analyses, we found that many of the phosphorylated proteins quantified in our study were involved in synaptic functions, including glutamatergic, GABAergic, cholinergic and dopaminergic synapses. The CUMS-induced phosphorylation changes were reversed by ketamine treatment. Hence, our research further supports the role of the synaptic machinery in neuropsychiatric disorders and predicts signaling mechanisms for treating depression *via* ketamine, which may provide a foundation for the development of novel treatment strategies (Duman and Aghajanian, 2012; Martins-de-Souza et al., 2012; Duman et al., 2016).

DATA AVAILABILITY STATEMENT

The mass spectrometry proteomics data have been deposited to the ProteomeXchange Consortium (http://proteomecentral.proteomexchange.org) *via* the iProX partner repository (Ma et al., 2019) and the dataset identifier is PXD016302.

ETHICS STATEMENT

The animal study protocol was reviewed and approved by the Animal Care and Use Committee of ShanghaiTech University, Shanghai Model Organisms Center, Inc.

AUTHOR CONTRIBUTIONS

YX and HL performed most of the experiments. HL and YZ performed the behavioral evaluations. YX, HL, ZS, WY, and XN prepared the phosphoproteomics samples and LC-MS/MS analysis. YX, JZ, ZL, XF, YS, and HT performed the bioinformatics analysis. WLS, JH, JY, YX, HL, and WS designed the experiments. YX, HL, JH, and WLS wrote the manuscript.

FUNDING

This study is funded by the Shanghai University of Medicine and Health Sciences Seed Fund National Project Cultivation Special Project (JY, SFP-18-20-14-006), the Shanghai Science and Technology Commission Western Medicine Guidance Project (JY, 19411971400), National Nature Science Foundation of China (WS, 31771169 and 91857104), Innovation Program of Shanghai Municipal Education Commission (WS).

ACKNOWLEDGMENTS

We sincerely thank the participants of this study for their cooperation. We also thank the following individuals: all members of the Shen and Hu Lab of the School of Life Science and Technology, ShanghaiTech University for valuable discussion, the Proteomics technology platform of the School of Life Science and Technology, ShanghaiTech University for mass spectrometric analysis, the staff members of the Animal Facility at the National Facility for Protein Science in Shanghai (NFPS), Zhangjiang Lab, China for providing technical support and assistance, and JZ, the member of Delta Omics Inc., United States for analyzing the mass spectrometry data.

SUPPLEMENTARY MATERIAL

The Supplementary Material for this article can be found online at: https://www.frontiersin.org/articles/10.3389/fncel.2020.00048/full#supplementary-material.

REFERENCES

Adaikkan, C., Taha, E., Barrera, I., David, O., and Rosenblum, K. (2018). Calcium/calmodulin-dependent protein kinase II and eukaryotic elongation factor 2 kinase pathways mediate the antidepressant action of ketamine. *Biol. Psychiatry* 84, 65–75. doi: 10.1016/j.biopsych.2017.11.028

Alfonso, J., Fernández, M. E., Cooper, B., Flugge, A. C., and Frasch, A. C. (2005). The stress-regulated protein M6a is a key modulator for neurite outgrowth and filopodium/spine formation. *Proc. Natl. Acad. Sci. U S A* 102, 17196–17201. doi: 10.1073/pnas.0504262102

Anand, A., Li, Y., Wang, Y., Wu, J., Gao, S., Bukhari, L., et al. (2005). Activity and connectivity of brain mood regulating circuit in depression: a functional magnetic resonance study. *Biol. Psychiatry* 57, 1079–1088. doi: 10.1016/j.biopsych.2005.02.021

Autry, A. E., Adachi, M., Nosyreva, E., Na, E. S., Los, M. F., Cheng, P. F., et al. (2011). NMDA receptor blockade at rest triggers rapid behavioural antidepressant responses. *Nature* 475, 91–95. doi: 10.1038/nature10130

Baude, A., Aaes, T. L., Zhai, B., Al-Nakouzi, N., Oo, H. Z., Daugaard, M., et al. (2016). Hepatoma-derived growth factor-related protein 2 promotes DNA repair by homologous recombination. *Nucleic Acids Res.* 44, 2214–2226. doi: 10.1093/nar/gkv1526

Belujon, P., and Grace, A. A. (2014). Restoring mood balance in depression: ketamine reverses deficit in dopamine-dependent synaptic plasticity. *Biol. Psychiatry* 76, 927–936. doi: 10.1016/j.biopsych.2014.04.014

Burstein, O., and Doron, R. (2018). The unpredictable chronic mild stress protocol for inducing anhedonia in mice. *J. Vis. Exp.* 140:e58184. doi: 10.3791/58184

Calabresi, P., Gubellini, P., Centonze, D., Picconi, B., Bernardi, G., Chergui, K., et al. (2000). Dopamine and cAMP-regulated phosphoprotein 32 kDa controls both striatal long-term depression and long-term potentiation, opposing forms of synaptic plasticity. *J. Neurosci.* 20, 8443–8451. doi: 10.1523/JNEUROSCI.20-22-08443.2000

Calakos, N., Schoch, S., Sudhof, T. C., and Malenka, R. C. (2004). Multiple roles for the active zone protein RIM1α in late stages of neurotransmitter release. *Neuron* 42, 889–896. doi: 10.1016/j.neuron.2004.05.014

Carreras Puigvert, P., von Stechow, L., Siddappa, R., Pines, A., Bahjat, M., Haazen, L. C., et al. (2013). Systems biology approach identifies the kinase Csnk1a1 as a regulator of the DNA damage response in embryonic stem cells. *Sci. Signal* 6:ra5. doi: 10.1126/scisignal.2003208

Castagné, V., Moser, P., Roux, S., and Porsolt, R. D. (2011). Rodent models of depression: forced swim and tail suspension behavioral despair tests in rats and mice. *Curr. Protoc. Neurosci.* Chapter 8:Unit 8.10A. doi: 10.1002/0471142301.ns0810as55

Cui, Y., Yang, Y., Ni, Z., Dong, Y., Cai, G., Foncelle, A., et al. (2018). Astroglial Kir4.1 in the lateral habenula drives neuronal bursts in depression. *Nature* 554, 323–327. doi: 10.1038/nature25752

Dale, E., Bang-Andersen, B., and Sanchez, C. (2015). Emerging mechanisms and treatments for depression beyond SSRIs and SNRIs. *Biochem. Pharmacol.* 95, 81–97. doi: 10.1016/j.bcp.2015.03.011

Deng, X. Y., Li, H. Y., Chen, J. J., Li, R. P., Qu, R., Fu, Q., et al. (2015). Thymol produces an antidepressant-like effect in a chronic unpredictable mild stress model of depression in mice. *Behav. Brain Res.* 291, 12–19. doi: 10.1016/j.bbr.2015.04.052

Diazgranados, N., Ibrahim, L., Brutsche, N. E., Newberg, A., Kronstein, P., Khalife, S., et al. (2010). A randomized add-on trial of an N-methyl-D-aspartate antagonist in treatment-resistant bipolar depression. *Arch. Gen. Psychiatry* 67, 793–802. doi: 10.1001/archgenpsychiatry.2010.90

Duman, R. S. (2002). Synaptic plasticity and mood disorders. *Mol. Psychiatry* 7, S29–S34. doi: 10.1038/sj.mp.4001016

Duman, R. S., and Aghajanian, G. K. (2012). Synaptic dysfunction in depression: potential therapeutic targets. *Science* 338, 68–72. doi: 10.1126/science.1222939

Duman, R. S., Aghajanian, G. K., Sanacora, G., and Krystal, J. H. (2016). Synaptic plasticity and depression: new insights from stress and rapid-acting antidepressants. *Nat. Med.* 22, 238–249. doi: 10.1038/nm.4050

Duman, R. S., and Voleti, B. (2012). Signaling pathways underlying the pathophysiology and treatment of depression: novel mechanisms for rapid-acting agents. *Trends Neurosci.* 35, 47–56. doi: 10.1016/j.tins.2011.11.004

Eckert, M. A., Coscia, F., Chryplewicz, A., Chang, J. W., Hernandez, K. M., Pan, S., et al. (2019). Proteomics reveals NNMT as a master metabolic regulator of cancer-associated fibroblasts. *Nature* 569, 723–728. doi: 10.1038/s41586-019-1173-8

Elizalde, N., Pastor, P. M., Garcia-García, A. L., Serres, F., Venzala, E., Huarte, J., et al. (2010). Regulation of markers of synaptic function in mouse models of depression: chronic mild stress and decreased expression of VGLUT1. *J. Neurochem.* 114, 1302–1314. doi: 10.1111/j.1471-4159.2010.06854.x

Elyada, E., Pribluda, A., Goldstein, R. E., Morgenstern, Y., Brachya, G., Cojocaru, G., et al. (2011). CKIalpha ablation highlights a critical role for p53 in invasiveness control. *Nature* 470, 405–413. doi: 10.1038/nature09673

Floresco, S. B. (2015). The nucleus accumbens: an interface between cognition, emotion, and action. *Annu. Rev. Psychol.* 66, 25–52. doi: 10.1146/annurev-psych-010213-115159

Forget, A., Martignetti, L., Puget, S., Calzone, L., Brabetz, S., Picard, D., et al. (2018). Aberrant ERBB4-SRC signaling as a hallmark of group 4 medulloblastoma revealed by integrative phosphoproteomic profiling. *Cancer Cell* 34, 379.e7–395.e7. doi: 10.1016/j.ccell.2018.08.002

Franceschelli, A., Sens, J., Herchick, S., Thelen, C., and Pitychoutis, P. M. (2015). Sex differences in the rapid and the sustained antidepressant-like effects of ketamine in stress-naive and "depressed" mice exposed to chronic mild stress. *Neuroscience* 290, 49–60. doi: 10.1016/j.neuroscience.2015.01.008

Galeotti, N., and Ghelardini, C. (2011). Antidepressant phenotype by inhibiting the phospholipase $C\beta_1$—protein kinase Cγ pathway in the forced swim test. *Neuropharmacology* 60, 937–943. doi: 10.1016/j.neuropharm.2011.01.037

Ghosal, S., Hare, B., and Duman, R. S. (2017). Prefrontal cortex GABAergic deficits and circuit dysfunction in the pathophysiology and treatment of chronic stress and depression. *Curr. Opin. Behav. Sci.* 14, 1–8. doi: 10.1016/j.cobeha.2016.09.012

Gigliucci, V., O'Dowd, G., Casey, S., Egan, D., Gibney, S., and Harkin, A. (2013). Ketamine elicits sustained antidepressant-like activity *via* a serotonin-dependent mechanism. *Psychopharmacology* 228, 157–166. doi: 10.1007/s00213-013-3024-x

Gould, T. D., Zarate, C. A. Jr., and Thompson, S. M. (2019). Molecular pharmacology and neurobiology of rapid-acting antidepressants. *Annu. Rev. Pharmacol. Toxicol.* 59, 213–236. doi: 10.1146/annurev-pharmtox-010617-052811

Gu, H. F., Nie, Y. X., Tong, Q. Z., Tang, Y. L., Zeng, Y., Jing, K. Q., et al. (2014). Epigallocatechin-3-gallate attenuates impairment of learning and memory in chronic unpredictable mild stress-treated rats by restoring hippocampal autophagic flux. *PLoS One* 9:e112683. doi: 10.1371/journal.pone.0112683

Harvey, P. O., Fossati, P., Pochon, J. B., Levy, R., Lebastard, G., Lehéricy, S., et al. (2005). Cognitive control and brain resources in major depression: an fMRI study using the n-back task. *NeuroImage* 26, 860–869. doi: 10.1016/j.neuroimage.2005.02.048

Huang da, W., Sherman, B. T., and Lempicki, R. A. (2009). Systematic and integrative analysis of large gene lists using DAVID bioinformatics resources. *Nat. Protoc.* 4, 44–57. doi: 10.1038/nprot.2008.211

Jiang, S., Zhang, M., Sun, J., Yang, X. (2018). Casein kinase 1alpha: biological mechanisms and theranostic potential. *Cell Commun. Signal* 16:23. doi: 10.1186/s12964-018-0236-z

Jin, P., Yu, H. L., Tian, L., Zhang, F., and Quan, Z. S. (2015). Antidepressant-like effects of oleoylethanolamide in a mouse model of chronic unpredictable mild stress. *Pharmacol. Biochem. Behav.* 133, 146–154. doi: 10.1016/j.pbb.2015.04.001

Kanehisa, M., Goto, S., Sato, Y., Kawashima, M., Furumichi, M., and Tanabe, M. (2014). Data, information, knowledge and principle: back to metabolism in KEGG. *Nucleic Acids Res.* 42, D199–D205. doi: 10.1093/nar/gkt1076

Ke, Q., Li, R., Cai, L., Wu, S. D., and Li, C. M. (2019). Ro41–5253, a selective antagonist of retinoic acid receptor α, ameliorates chronic unpredictable mild stress-induced depressive-like behaviors in rats: involvement of regulating HPA axis and improving hippocampal neuronal deficits. *Brain Res. Bull.* 146, 302–309. doi: 10.1016/j.brainresbull.2019.01.022

Kellermayer, B., Ferreira, J. S., Dupuis, J., Levet, F., Grillo-Bosch, D., Bard, L., et al. (2018). Differential nanoscale topography and functional role of

GluN2-NMDA receptor subtypes at glutamatergic synapses. *Neuron* 100, 106.e7–119.e7. doi: 10.1016/j.neuron.2018.09.012

Lee, H., Barbarosie, M., Kameyama, K., Bear, M., and Huganir, R. (2000). Regulation of distinct AMPA receptor phosphorylation sites during bidirectional synaptic plasticity. *Nature* 405, 955–959. doi: 10.1038/35016089

Lee, H.-Y., Huang, Y., Bruneau, N., Roll, P., Roberson, E. D. O., Hermann, M., et al. (2012). Mutations in the gene PRRT2 cause paroxysmal kinesigenic dyskinesia with infantile convulsions. *Cell Rep.* 1, 2–12. doi: 10.1016/j.celrep.2011.11.001

Li, N., Lee, B., Liu, R. J., Banasr, M., Dwyer, J. M., Iwata, M., et al. (2010). mTOR-dependent synapse formation underlies the rapid antidepressant effects of NMDA antagonists. *Science* 329, 959–964. doi: 10.1126/science.1190287

Li, N., Liu, R. J., Dwyer, J. M., Banasr, M., Lee, B., Son, H., et al. (2011). Glutamate N-methyl-D-aspartate receptor antagonists rapidly reverse behavioral and synaptic deficits caused by chronic stress exposure. *Biol. Psychiatry* 69, 754–761. doi: 10.1016/j.biopsych.2010.12.015

Li, L., and Vlisides, P. E. (2016). Ketamine: 50 years of modulating the mind. *Front. Hum. Neurosci.* 10:612. doi: 10.3389/fnhum.2016.00612

Lieberman, M. D., Straccia, M. A., Meyer, M. L., Du, M., and Tan, K. M. (2019). Social, self (situational), and affective processes in medial prefrontal cortex (MPFC): causal, multivariate, and reverse inference evidence. *Neurosci. Biobehav. Rev.* 99, 311–328. doi: 10.1016/j.neubiorev.2018.12.021

Liu, W., Ge, T., Leng, Y., Pan, Z., Fan, J., Yang, W., et al. (2017). The role of neural plasticity in depression: from hippocampus to prefrontal cortex. *Neural Plast.* 2017:6871089. doi: 10.1155/2017/6871089

Liu, J. J., Sharma, K., Zangrandi, L., Chen, C., Humphrey, S. J., Chiu, Y. T., et al. (2018). *In vivo* brain GPCR signaling elucidated by phosphoproteomics. *Science* 360:eaao4927. doi: 10.1126/science.aao4927

Lübbert, M., Goral, R. O., Keine, C., Thomas, C., Guerrero-Given, D., Putzke, T., et al. (2019). $Ca_V2.1$ α_1 subunit expression regulates presynaptic $Ca_V2.1$ abundance and synaptic strength at a central synapse. *Neuron* 101, 260–273. doi: 10.1016/j.neuron.2018.11.028

Lübbert, M., Goral, R. O., Satterfield, R., Putzke, T., van den Maagdenberg, A. M., Kamasawa, N., et al. (2017). A novel region in the $Ca_V2.1$ α_1 subunit C-terminus regulates fast synaptic vesicle fusion and vesicle docking at the mammalian presynaptic active zone. *Elife* 6:e28412. doi: 10.7554/eLife.28412

Ma, J., Chen, T., Wu, S., Yang, C., Bai, M., Shu, K., et al. (2019). iProX: an integrated proteome resource. *Nucleic Acids Res.* 47, D1211–D1217. doi: 10.1093/nar/gky869

Ma, K., Xu, A., Cui, S., Sun, M. R., Xue, Y. C., and Wang, J. H. (2016). Impaired GABA synthesis, uptake and release are associated with depression-like behaviors induced by chronic mild stress. *Transl. Psychiatry* 6:e910. doi: 10.1038/tp.2016.181

Mann, M., Ong, S., Grønborg, M., Steen, H., Jensen, O., and Pandey, A. (2002). Analysis of protein phosphorylation using mass spectrometry deciphering the phosphoproteome. *Trends Biotechnol.* 20, 261–268. doi: 10.1016/s0167-7799(02)01944-3

Martins-de-Souza, D., Guest, P. C., Vanattou-Saifoudine, N., Rahmoune, H., and Bahn, S. (2012). Phosphoproteomic differences in major depressive disorder postmortem brains indicate effects on synaptic function. *Eur. Arch. Psychiatry Clin. Neurosci.* 262, 657–666. doi: 10.1007/s00406-012-0301-3

McNamara, R. K., and Lenox, R. H. (2004). Acute restraint stress reduces protein kinase C γ in the hippocampus of C57BL/6 but not DBA/2 mice. *Neurosci. Lett.* 368, 293–296. doi: 10.1016/j.neulet.2004.07.028

Michetti, C., Castroflorio, E., Marchionni, I., Forte, N., Sterlini, B., Binda, F., et al. (2017). The PRRT2 knockout mouse recapitulates the neurological diseases associated with PRRT2 mutations. *Neurobiol. Dis.* 99, 66–83. doi: 10.1016/j.nbd.2016.12.018

Miya, K., Inoue, R., Takata, Y., Abe, M., Natsume, R., Sakimura, K., et al. (2008). Serine racemase is predominantly localized in neurons in mouse brain. *J. Comp. Neurol.* 510, 641–654. doi: 10.1002/cne.21822

Moda-Sava, R. N., Murdock, M. H., Parekh, P. K., Fetcho, R. N., Huang, B. S., Huynh, T. N., et al. (2019). Sustained rescue of prefrontal circuit dysfunction by antidepressant-induced spine formation. *Science* 364:eaat8078. doi: 10.1126/science.aat8078

Monsalve, E. M., García-Gutiérrez, M. S., Navarrete, F., Giner, S., Laborda, J., and Manzanares, J. (2014). Abnormal expression pattern of Notch receptors, ligands and downstream effectors in the dorsolateral prefrontal cortex and amygdala of suicidal victims. *Mol. Neurobiol.* 49, 957–965. doi: 10.1007/s12035-013-8570-z

Monteggia, L. M., Gideons, E., and Kavalali, E. T. (2013). The role of eukaryotic elongation factor 2 kinase in rapid antidepressant action of ketamine. *Biol. Psychiatry* 73, 1199–1203. doi: 10.1016/j.biopsych.2012.09.006

Murrough, J. W., Iosifescu, D. V., Chang, L. C., Al Jurdi, R. K., Green, C. E., Perez, A. M., et al. (2013). Antidepressant efficacy of ketamine in treatment-resistant major depression: a two-site randomized controlled trial. *Am. J. Psychiatry* 170, 1134–1142. doi: 10.1176/appi.ajp.2013.13030392

Niday, Z., Hawkins, V. E., Soh, H., Mulkey, D. K., and Tzingounis, A. V. (2017). Epilepsy-associated KCNQ2 channels regulate multiple intrinsic properties of layer 2/3 pyramidal neurons. *J. Neurosci.* 37, 576–586. doi: 10.1523/JNEUROSCI.1425-16.2016

Noberini, R., and Bonaldi, T. (2019). Epigenetic drug target deconvolution by mass spectrometry-based technologies. *Nat. Struct. Mol. Biol.* 26, 854–857. doi: 10.1038/s41594-019-0279-x

Oláh, S., Füle, M., Komlósi, G., Varga, C., Báldi, R., Barzó, P., et al. (2009). Regulation of cortical microcircuits by unitary GABA-mediated volume transmission. *Nature* 461, 1278–1281. doi: 10.1038/nature08503

Opal, M. D., Klenotich, S. C., Morais, M., Bessa, J., Winkle, J., Doukas, D., et al. (2014). Serotonin 2C receptor antagonists induce fast-onset antidepressant effects. *Mol. Psychiatry* 19, 1106–1114. doi: 10.1038/mp.2013.144

Perszyk, R. E., DiRaddo, J. O., Strong, K. L., Low, C. M., Ogden, K. K., Khatri, A., et al. (2016). GluN2D-containing N-methyl-d-aspartate receptors mediate synaptic transmission in hippocampal interneurons and regulate interneuron activity. *Mol. Pharmacol.* 90, 689–702. doi: 10.1124/mol.116.105130

Quiroz, J. A., and Manji, H. K. (2002). Enhancing synaptic plasticity and cellular resilience to develop novel, improved treatments for mood disorders. *Dialogues Clin. Neurosci.* 4, 73–92.

Reus, G. Z., Abaleira, H. M., Titus, S. E., Arent, C. O., Michels, M., da Luz, J. R., et al. (2016). Effects of ketamine administration on the phosphorylation levels of CREB and TrKB and on oxidative damage after infusion of MEK inhibitor. *Pharmacol. Rep.* 68, 177–184. doi: 10.1016/j.pharep.2015.08.010

Rive, M. M., van Rooijen, G., Veltman, D. J., Phillips, M. L., Schene, A. H., and Ruhe, H. G. (2013). Neural correlates of dysfunctional emotion regulation in major depressive disorder. A systematic review of neuroimaging studies. *Neurosci. Biobehav. Rev.* 37, 2529–2553. doi: 10.1016/j.neubiorev.2013.07.018

Roberson-Nay, R., McClure, E. B., Monk, C. S., Nelson, E. E., Guyer, A. E., Fromm, S. J., et al. (2006). Increased amygdala activity during successful memory encoding in adolescent major depressive disorder: an FMRI study. *Biol. Psychiatry* 60, 966–973. doi: 10.1016/j.biopsych.2006.02.018

Rossi, P., Sterlini, B., Castroflorio, E., Marte, A., Onofri, F., Valtorta, F., et al. (2016). A novel topology of proline-rich transmembrane protein 2 (PRRT2): hints for an intracellular function at the synapse. *J. Biol. Chem.* 291, 6111–6123. doi: 10.1074/jbc.m115.683888

Ryan, T. J., Kopanitsa, M. V., Indersmitten, T., Nithianantharajah, J., Afinowi, N. O., Pettit, C., et al. (2013). Evolution of GluN2A/B cytoplasmic domains diversified vertebrate synaptic plasticity and behavior. *Nat. Neurosci.* 16, 25–32. doi: 10.1038/nn.3277

Saito, N., and Shirai, Y. (2002). Protein kinase C γ (PKC γ): function of neuron specific isotype. *J. Biochem.* 132, 683–687. doi: 10.1093/oxfordjournals.jbchem.a003274

Sánchez, C., Díaz-Nido, J., and Avila, J. (2000). Phosphorylation of microtubule-associated protein 2 (MAP2) and its relevance for the regulation of the neuronal cytoskeleton function. *Prog. Neurobiol.* 61, 133–168. doi: 10.1016/s0301-0082(99)00046-5

Schwale, C., Schumacher, S., Bruehl, C., Titz, S., Schlicksupp, A., Kokocinska, M., et al. (2016). KCC2 knockdown impairs glycinergic synapse maturation in cultured spinal cord neurons. *Histochem. Cell Biol.* 145, 637–646. doi: 10.1007/s00418-015-1397-0

Shimizu, K., Chiba, S., Hosoya, N., Kumano, K., Saito, T., Kurokawa, M., et al. (2000). Binding of Delta1, Jagged1, and Jagged2 to Notch2 rapidly induces cleavage, nuclear translocation, and hyperphosphorylation of Notch2. *Mol. Cell. Biol.* 20, 6913–6922. doi: 10.1128/mcb.20.18.6913-6922.2000

Shinoda, Y., Ishii, C., Fukazawa, Y., Sadakata, T., Ishii, Y., Sano, Y., et al. (2016). CAPS1 stabilizes the state of readily releasable synaptic vesicles to fusion

competence at CA3-CA1 synapses in adult hippocampus. *Sci. Rep.* 6:31540. doi: 10.1038/srep31540

Shuvaev, A. N., Horiuchi, H., Seki, T., Goenawan, H., Irie, T., Iizuka, A., et al. (2011). Mutant PKCγ in spinocerebellar ataxia type 14 disrupts synapse elimination and long-term depression in Purkinje cells *in vivo*. *J. Neurosci.* 31, 14324–14334. doi: 10.1523/JNEUROSCI.5530-10.2011

Sinnberg, T., Menzel, M., Kaesler, S., Biedermann, T., Sauer, B., Nahnsen, S., et al. (2010). Suppression of casein kinase 1alpha in melanoma cells induces a switch in beta-catenin signaling to promote metastasis. *Cancer Res.* 70, 6999–7009. doi: 10.1158/0008-5472.CAN-10-0645

Sivaram, M. V., Wadzinski, T. L., Redick, S. D., Manna, T., and Doxsey, S. J. (2009). Dynein light intermediate chain 1 is required for progress through the spindle assembly checkpoint. *EMBO J.* 28, 902–914. doi: 10.1038/emboj.2009.38

Stevens, S. J. C., van der Schoot, V., Leduc, M. S., Rinne, T., Lalani, S. R., Weiss, M. M., et al. (2018). De novo mutations in the SET nuclear proto-oncogene, encoding a component of the inhibitor of histone acetyltransferases (INHAT) complex in patients with nonsyndromic intellectual disability. *Hum. Mutat.* 39, 1014–1023. doi: 10.1002/humu.23541

Stipanovich, A., Valjent, E., Matamales, M., Nishi, A., Ahn, J. H., Maroteaux, M., et al. (2008). A phosphatase cascade by which rewarding stimuli control nucleosomal response. *Nature* 453, 879–884. doi: 10.1038/nature06994

Taha, E., Gildish, I., Gal-Ben-Ari, S., and Rosenblum, K. (2013). The role of eEF2 pathway in learning and synaptic plasticity. *Neurobiol. Learn. Mem.* 105, 100–106. doi: 10.1016/j.nlm.2013.04.015

Tynan, S. H., Purohit, A., Doxsey, S. J., and Vallee, R. B. (2000). Light intermediate chain 1 defines a functional subfraction of cytoplasmic dynein which binds to pericentrin. *J. Biol. Chem.* 275, 32763–32768. doi: 10.1074/jbc.M001536200

Wang, Z., Ma, J., Miyoshi, C., Li, Y., Sato, M., Ogawa, Y., et al. (2018). Quantitative phosphoproteomic analysis of the molecular substrates of sleep need. *Nature* 558, 435–439. doi: 10.1038/s41586-018-0218-8

Wang, Y., Okamoto, M., Schmitz, F., Hofmann, K., and Südhof, T. C. (1997). Rim is a putative Rab3 effector in regulating synaptic-vesicle fusion. *Nature* 388, 593–598. doi: 10.1038/41580

Xu, J., Jiao, J., Xu, W., Ji, L., Jiang, D., Xie, S., et al. (2017). Mutant p53 promotes cell spreading and migration *via* ARHGAP44. *Sci. China Life Sci.* 60, 1019–1029. doi: 10.1007/s11427-016-9040-8

Yanagihori, S., Terunuma, M., Koyano, K., Kanematsu, T., Ho Ryu, S., and Hirata, M. (2006). Protein phosphatase regulation by PRIP, a PLC-related catalytically inactive protein—implications in the phospho-modulation of the GABAA receptor. *Adv. Enzyme Regul.* 46, 203–222. doi: 10.1016/j.advenzreg.2006.01.006

Yang, Y., Cui, Y., Sang, K., Dong, Y., Ni, Z., Ma, S., et al. (2018). Ketamine blocks bursting in the lateral habenula to rapidly relieve depression. *Nature* 554, 317–322. doi: 10.1038/nature25509

Ye, J., Zhang, H., He, W., Zhu, B., Zhou, D., Chen, Z., et al. (2016). Quantitative phosphoproteomic analysis identifies the critical role of JNK1 in neuroinflammation induced by Japanese encephalitis virus. *Sci. Signal.* 9:ra98. doi: 10.1126/scisignal.aaf5132

Zanos, P., Moaddel, R., Morris, P. J., Georgiou, P., Fischell, J., Elmer, G. I., et al. (2017). NMDAR inhibition-independent antidepressant actions of ketamine metabolites. *Nature* 533, 481–486. doi: 10.1038/nature17998

Conflict of Interest: JZ was employed by the company Delta Omics Inc.

The remaining authors declare that the research was conducted in the absence of any commercial or financial relationships that could be construed as a potential conflict of interest.

frontiers in Molecular Neuroscience

ORIGINAL RESEARCH
published: 25 May 2020
doi: 10.3389/fnmol.2020.00083

Single-Cell RNA Analysis of Type I Spiral Ganglion Neurons Reveals a *Lmx1a* Population in the Cochlea

Fiorella Carla Grandi[1], *Lara De Tomasi*[2] *and Mirna Mustapha*[2,3]*

[1]Cancer Biology Program, Stanford University, Stanford, CA, United States, [2]Department of Biomedical Science, University of Sheffield, Sheffield, United Kingdom, [3]Department of Otolaryngology-Head and Neck Surgery, Stanford University School of Medicine, Stanford, CA, United States

In the mature cochlea, each inner hair cell (IHC) is innervated by multiple spiral ganglion neurons of type I (SGNI). SGNIs are morphologically and electro-physiologically diverse. Also, they differ in their susceptibility to noise insult. However, the molecular underpinnings of their identity and physiological differences remain poorly understood. In this study, we developed a novel triple transgenic mouse, which enabled the isolation of pure populations of SGNIs and the analysis of a 96-gene panel *via* single-cell qPCR. We found three distinct populations of Type I SGNs, which were marked by their exclusive expression of *Lmx1a, Slc4a4*, or *Mfap4/Fzd2*, respectively, at postnatal days P3, P8, and P12. Our data suggest that afferent SGN subtypes are established genetically before the onset of hearing and that the expression of key physiological markers, such as ion channels, is heterogeneous and may be underlying the heterogeneous firing proprieties of SGNIs.

Keywords: type I spiral ganglion neurons, single-cell transcriptome, Lmx1a, development, cochlea

OPEN ACCESS

Edited by:
Jiangteng Lu,
Shanghai Jiao Tong University, China

Reviewed by:
Agnieszka J. Szczepek,
Charité–Universitätsmedizin Berlin, Germany
Sangyong Jung,
*Singapore Bioimaging Consortium (A*STAR), Singapore*

***Correspondence:**
Mirna Mustapha
mirna.m@sheffield.ac.uk

Received: *06 March 2020*
Accepted: *24 April 2020*
Published: *25 May 2020*

Citation:
Grandi FC, De Tomasi L and Mustapha M (2020) Single-Cell RNA Analysis of Type I Spiral Ganglion Neurons Reveals a Lmx1a Population in the Cochlea. Front. Mol. Neurosci. 13:83. doi: 10.3389/fnmol.2020.00083

INTRODUCTION

The inner and outer hair cells (IHC and OHC) of the organ of Corti allow us to perceive sound using spiral ganglion neurons (SGNs). SGNs type I and type II, which innervate the IHC and OHC, respectively, are structurally and functionally different. Type I SGNs (SGNI) make up 90–95% of SGNs and are the main cells that transmit complex sound information to the brain (Berglund and Ryugo, 1987; Nayagam et al., 2011). The remaining 5–10% of type II SGNs (SGNII) are the sensory drive for the olivocochlear efferent reflex (Froud et al., 2015).

In the mature cochlea, each IHC is innervated by multiple SGNI fibers that have varying morphological and electrophysiological properties, such as low and high thresholds of sound detection. Heterogeneous electrophysiological features of postnatal SGNI can be distinguished tonotopically and within the same cochlear region (Davis and Liu, 2011). In addition to their functional and morphological differences, studies have suggested that SGNIs also exhibit differential vulnerability to aging and noise-induced excitotoxicity. Single-fiber recording studies have shown a selective reduction of high-threshold neurons in noise-exposed and aging rodents, resulting in auditory synaptopathy (Kujawa and Liberman, 2015) The mechanisms, as to why high-threshold fibers are predominantly affected by noise remain elusive.

SGNs and vestibular ganglion neurons (VGNs), which are both derived from the proneurosensory tissue, are defined early in development by the transcription factor networks of GATA3 and TLX3, respectively (Appler and Goodrich, 2011). However, little is known about the subsequent mechanisms involved in specifying the terminal differentiation of SGNIs to low- and high-threshold neurons. The identities of other molecular selectors, be they intrinsic or extrinsic to the cell, remain unknown. Recent studies of the retina may provide clues about the developmental regime operating in the inner ear. Lineage tracing studies of retinal progenitor cells have determined that they are multipotent and they differentiate *via* defined, irreversible states (Goetz et al., 2014). Although these progenitors can, to some degree, be influenced by extrinsic cues, a growing list of transcription factors have been suggested as intrinsic regulators of retinal cell specification. Many of these genes also affect hearing, leading us to hypothesize that SGNI subtypes are also genetically defined by intrinsic cues.

Validating this hypothesis requires the ability to specifically sort out and profile single SGNIs from cochlear tissue. With this goal, we established a transgenic mouse model capable of differentially fluorescently labeling SGNI and SGNII. This allowed us to isolate pure, single-cell populations and perform single-cell transcriptomic analysis. The single-cell transcriptomic analysis is a powerful tool to understand cellular diversity in complex tissues, and has been successfully used in the inner ear (Durruthy-Durruthy et al., 2014; Waldhaus et al., 2015; Petitpré et al., 2018; Shrestha et al., 2018; Sun et al., 2018). However, these previous studies focused primarily on adult SGNs. To test our hypothesis about the intrinsic genetic definition of SGN subtypes before the onset of hearing, we profiled SGNs at postnatal day 3 (P3) and P8, before the onset of hearing and at P12, around the onset of hearing in most mice. Using a 96-gene targeted single-cell RT-PCR platform, we identified and validate three main clusters of SGNIs in the neonatal ear. *Lmx1a*, *Slc4a4*, and *Mfap4*/*Fzd2* designate the three clusters, respectively. This targeted approach allowed us to amplify low-abundance genes that were absent from other studies.

MATERIALS AND METHODS

A Mouse Model for SGN Labeling

All the animal experiments were performed following institutional and governmental regulations approved by the Stanford University Institutional Animal Care and Use Committee. A triple transgenic mouse line was generated by systematically crossing three lines: Ai14-tdTomato (Jax:007908) mice were crossed with Bhlhb5-cre mice, a neuronal-specific transcriptional factor (Lu et al., 2011). These mice were subsequently crossed with peripherin (*Prph*)-GFP mice (McLenachan et al., 2008; Huang et al., 2014) to generate triple transgenic *Ai14*-tdTomato, *Bhlhb5*-cre, *Prph*-GFP mice. Peripherin is a type III intermediate filament protein expressed in SGNIIs (Hafidi et al., 1993). In this scheme, SGNI cells are labeled in red, and SGNII is labeled in red and green. We have used a similar approach to create the *Lmx1a* reporter line. We have crossed a *Lmx1a*-cre (Chizhikov et al., 2010) to *Ai14*-tdTomato and *Prph*-GFP mouse line.

Cochlea Dissociation and Cell Culture

For single-cell experiments, 4–6 of each of the postnatal ages P3, P8 or P12 cochleae were incubated in digestion solution [50 μM kynurenic acid (Sigma–Aldrich, K3375), 10 mM $MgCl_2$, 10 mM glucose in MEM Hanks (Life Technologies, 11575-032)] with 50 μg/ml collagenase (Roche, 10269638001) and 6 μg/ml DNAseI (Worthington, LS002004) for 15 min at 37°C with continuous shaking at 50 rpm (Excella E24 Incubator Shaker Series, New Brunswick Scientific). Tissue was dissociated with gentle pipetting four to six times during digestion. Subsequently, trypsin (Gibco, 15090046) was added to a final concentration of 0.05%, and tissues were and incubate for another 15 min at 37°C and 50 rpm. For P12 cochleae, we replaced trypsin with milder recombinant enzyme 0.05% TrypLE Select (Gibco, A12177-01) for better cell viability. After digestion, the cell suspension was placed on ice and remaining clumps were dissociated by pipetting. The enzymatic digestion was stopped using the fetal bovine serum. The samples were centrifuged at 0.8× *g* for 5 min at 4°C, and cells were resuspended in 500 μl HBSS (Hyclone, ADD20159) and passed through a 35 μm cell strainer (Corning, 352235) and used directly for fluorescence-activated cell sorting (FACS) analysis or culture.

To prepare neuronal cultures, the cells were resuspended in Neurobasal-A media supplemented with glutamax (Gibco, 35050079), 1× B27 (Gibco, 17504-044), 10 ng/ml BDNF (Sigma, B3795) and 10 ng/ml NT-3 (Sigma, N1905), and cultured overnight on 0.5 mg/ml poly-D-lysine (Sigma, P6407) coated coverslip in a 35 mm cell culture dish.

Immunostaining and Neuron Quantification

Cells cultured overnight were fixed with 4% paraformaldehyde in PBS for 30 min at room temperature, then were washed three times for 10 min in room temperature PBS. Cells were blocked with 5% BSA/0.5% Triton-X 100/PBS for 1 h at room temperature, then washed three times in PBS. Cells were incubated overnight with the TUJ1 antibody (BioLegend, 801202) at a 1:500 dilution at 4°C, then washed three times with 0.1% Tween20 in PBS for 10 min at room temperature, before incubating with secondary antibody for 1 h and repeating wash steps. Slides were mounted with anti-fade mounting media with DAPI (Invitrogen, 1010789). Cells were manually counted from different areas on coverslip under a 20× fluorescent microscope.

Single Neuron Sorting by Fluorescence-Activated Cell Sorting (FACS)

Cochleae were dissected out from triple transgenic animals and enzymatically dissociated as described in the cochlea dissociation section. Cells were then stained with Sytox red (Life Technologies, S34859) and sorted on the FACS Aida and FACS Falstaff (BD Biosciences) at the Stanford FACS core facility. Cells debris and dead cells were removed by gating forward scatter area (FSC-A) and side scatter area (SSC-A; **Supplementary Figures S1D–H** for FACS gating strategies). Finally, tdTomato

and GFP positive cells were gated and high tomato positive cells were sorted into 96-wells plate, with each well, containing 5 μl of 2× reaction mix (Invitrogen, CellsDirect, 1753-500) mixed with 0.05 units of SUPERase-In RNase inhibitor (Ambion, PN AM2696) and stored at −80°C until use. The total time from animal sacrifice to single-cell sorting was ∼2.5 h. A subset of cells was always kept for culture to ensure minimal cell stress to the cells being analyzed by single-neuron qRT-PCR.

Single-Neuron Multiplex qRT-PCR

Single-neuron multiplex qRT-PCR assays were performed on sorted cells following the manufacturer's guidelines (Fluidigm manual-PN 68000088 L) and as previously described (Durruthy-Durruthy et al., 2014). Briefly, each cell was placed in a well containing CellsDirect reagents (Invitrogen, CellsDirect, 11753-500) to isolate RNA. RNA was then transcribed to cDNA, and specific target genes were pre-amplified with one step PCR using SuperScript III RT Platinum Taq Mix and 500 nM primer (DELTAgene). Samples were treated with ExoI (NEB, M0293L) to cleave off single-stranded DNA. Exo-treated samples were diluted five times with nuclease-free water. Samples were then prepared for qRT-PCR analysis as per manufacturer specifications (Fluidigm, 85000736). qRT-PCR experiments were performed on the Biomark HD (Fluidigm manual, PN 68000088 L1) with pre-defined protocol GE96.96 Fast PCR+Melt v2.PCI for 30 cycles using the 96.96 dynamic arrays integrated fluidic circuit chip (IFC, Fluidigm). Data are available in **Supplementary Table S1**. For P3, the data represent 203 single cells aggregated from three independent runs. For P8, the data represent 383 single cells aggregated from seven independent runs, and for P12, data represents 230 single cells aggregated from three runs. Each run consists of four to six pups pooled from a litter.

Data Processing and Bioinformatics

A series of preliminary experiments were conducted to validate that: (a) the primers amplify single amplicons in the expected size range; (b) the target mRNA is indeed expressed in neonatal and young cochlea; and (c) to determine the limit of detection (LOD), which is the cycle threshold (Ct value) for each primer/gene combination. Quantitative single-cell RT-PCR cannot be normalized to a single housekeeping gene or groups of genes, but rather to the individually determined detection limit for each primer pair. Ultimately, quantitative gene expression for each primer pair and cell is presented as expression level above detection limit on a log scale using Log2Ex values [Log2Ex = Ct(LOD) − Ct(measured); Durruthy-Durruthy et al., 2014]. In simple terms, Log2Ex for a gene represents transcript level above background in log base 2. LOD Ct values for each primer pair were determined in dilutions of bulk cochlear cDNA (neonatal and P21) over 16 orders of magnitude. Primers that did not meet the three above stated validation requirements were eliminated. A list of 96 genes (**Supplementary Table S1**) was used for gene expression profiling, and the Log2Ex values were used for downstream analysis.

Before clustering, the data set was cleaned by removing cells with low expression of housekeeping genes *Gapdh* and *Actb*, as well as removing any non-neuronal contaminants by selecting cells, which expressed *Map2* and *Tubb3*. We used HDBSCAN, implemented in python, to cluster single cells obtained from P3, P8, and P12 cochlea, and obtained six clusters. In selecting our clustering method, we sought to find a method that would agree with our underlying assumptions about the cell populations, namely that: (1) the variance between different cell populations might not be the same; (2) the size of each subpopulation may be different; (3) some rare cell populations might not be sufficiently sampled; and (4) variance in the data can be introduced by additional factors, such as RNA degradation. HDBSCAN (McInnes et al., 2017) has many advantages over traditional k-means clustering, including its ability to deal with data with variable density and variance, fulfilling goals (1) and (2), and the ability to deal with noisy data by assigning some points to no cluster, fulfilling conditions (3) and (4). We restricted our analysis to five of these six clusters, as the sixth was found not to express any of the selected genes. To visualize the cells, we utilized UMAP, a dimensionality-reducing algorithm, to project the cells into 2D space and mapped the HDBSCAN called cluster identities. Here, we present all cells, including those cells that HDBSCAN did not cluster due to low confidence about their identity. Enrichment for a particular marker gene was tested using a one-factor ANOVA with correction for multiple hypothesis testing (alpha = 0.05/96), and then each significant ANOVA was tested using the *post hoc* Tukey test. Statistical analysis was performed in Python and Prism (Graphpad).

We also repeated the same clustering process using PCA analysis plus K-means clustering and hierarchical clustering. K-means clustering was applied in each data sets using the algorithm "Hartigan-Wong" with one thousand iterations (iter.max = 1,000) in R. Hierarchical clustering was computed by Ward's minimum variance method (Ward.D2). The numbers of stable clusters generated were assessed by gap statistic (Tibshirani et al., 2001).

RNAscope *in situ* Hybridization and Conventional *in situ* Hybridization

RNAscope *in situ* hybridization was performed according to RNAscope guidelines (ACD, document number, 320293; Wang et al., 2012). Briefly, temporal bones were removed in ice-cold PBS and cleaned. Cochleae were placed in 4% PFA at 4°C for 22–24 h with gentle shaking. After fixation, samples were washed 2× with PBS and dehydrated overnight with 30% sucrose at 4°C, for 24 h, the mounted in OCT. Fourteen micrometer cochlear section was cut using a cryostat. The manufacturer designed probes were used for double fluorescent labeling (*Cacna1a*: 493141-C2, *Mfap4*: 421391, *Kcnd2*: 452581-C3) according to manufacturer specifications. Conventional *in situ* hybridization procedures for *Cacna1a* and *Nefm* were performed as described (Mendus et al., 2014). Briefly, *in situ* probes were cloned into the pGEM-T vector (Promega, Madison, WI, USA), with the following primers: *Cacna1a*: GAGAGAATTCGGGCGCACTGCAAATGATAA and GAGAAAGCTTGTCCCAAGCCCACGTTTTTC. *In situ* hybridization was carried out as previously described (Schwander et al., 2007).

Confocal Imaging and Signal Quantification

Images were acquired on a confocal microscope (Zeiss, LMS700) as previously described (Mendus et al., 2014). A 0.5 μm z-stack of images was collected. The signals for specific genes such as *Cacna1a*, *Mfap4*, and *Kcnd2* in each cell were visualized in Velocity 3D image analysis software (PerkinElmer, Inc., Waltham, MA, USA). The boundary of a cell was defined by merging fluorescent images with bright-field images and manually tracing cell borders. The numbers of fluorescent signals in each defined boundary were quantified manually.

RESULTS

Isolation of Type I and Type II SGNs From the Cochlea

To prepare single-cell suspensions of SGNs from the cochlea, we utilized a triple transgenic mouse model in which Type I and II SGNs are uniquely labeled with different fluorescent reporters. Briefly, we crossed *Ai14*-tdTomato to *Bhlhb5*-cre mice and *Prph*-GFP mice (see "Materials and Methods" section). This resulted in cochlear tissues where SGNIs are labeled red and SGNIIs are marked red and green (**Figures 1A–E**). We then isolated pure cell populations by FACS for subsequent single-cell transcriptome analysis. To validate our dissociation and sorting strategy, we immunostained cells with the neuronal marker TUJ1 (**Supplementary Figures S1A,B**). Our dissociation protocol resulted in 85.6% cell viability after sorting (**Supplementary Figure S1C**). As expected, tdTomato/GFP double-positive cells (SGNIIs) compose only 0.05% of the final viable fraction (**Supplementary Figures S1D–H**). Cells were directly sorted into 96-well plates and analyzed using the Fluidigm single-cell platform (**Supplementary Figures S2A–F**). The panel of 96 genes (**Supplementary Table S1**) was preselected using microarray expression profiles generated from the same mouse model and contained genes hypothesized to be either selectors or effectors for SGNI subpopulations.

After quality control and filtering (see "Materials and Methods" section), the single-cell data was visualized using the UMAP projection, which visualizes high-dimensional data on a 2D axis and whose utility for single-cell data has been recently shown (McInnes et al., 2018; Becht et al., 2019). We analyzed 203 cells at P3, 383 cells at P8, and 230 cells at P12.

Zic1, *Pax6*, and *Nfix* Serve as Novel Markers of Type I SGNs

We first sought to determine the broad molecular features separating Type I and Type II SGNs at postnatal day 8 (P8), before the onset of hearing. Mapping the FACs gating information onto the UMAP projection of SGNs, we observed that Cluster I is enriched for tdTomato/GFP expressing cells, suggesting that this cluster corresponds to Type II SGNs (**Supplementary Figure S3A**). Classically, SGNII has been defined by the expression of *Prph* (Hafidi et al., 1993). Cells in Cluster I were enriched for *Prph* expression (**Figure 2A**) as well as *Mafb* and *Gata3* (**Figures 2B,C**), which also have been suggested as markers of postnatal Type II cells (Petitpré et al., 2018; Shrestha et al., 2018; Sun et al., 2018). We also found *Gata3*/*Mfab* positive cells that are not *Prph* positive (**Figures 2A–C**), as has been observed by other studies (Petitpré et al., 2018; Shrestha et al., 2018; Sun et al., 2018). The ambiguity of this expression highlights the need for better molecular markers to distinguish between Type I and Type II SGNs.

With this goal, we focused on the transcription factors in our panel to find those that might act as selectors to designate Type II vs. Type I cells. We observed that Type I cells were strongly enriched for *Pax6, Nfix*, and *Zic1* (**Figures 2E–G**), while Type II cells were enriched for *Foxg1* (**Figure 2D**). In contrast, *Zic5*, although highly expressed in Type I cells, was also mildly expressed by Type II cells (**Figure 2H**). We observed that while *Zic1* expression was highest in early development (P3) and decreased slightly with time, *Pax6* and *Nfix* expression stayed constant from P3 to P12 (**Figures 2E–H**), suggesting they would be optimal markers to identify Type I and II cells over time. In addition to these transcription factors, we find that *Cadps2* and *Tmem178* are broadly enriched in Type I SGNs (**Supplementary Figure S3B**), as well as *Cacna1g*, which although expressed in Type II SGNs, is more strongly expressed in Type I cells (**Supplementary Figure S3B**) in contrast to previous findings. Collectively, these data provide us with novel genetic markers for Type I and II SGNs (**Figures 2I,J**).

Type I SGNs Cluster Into Three Major Subtypes

We next focused our attention on identifying subsets of Type I SGNs at post-natal day 8 (P8). Previous work has shown a variety of physiologically distinct SGNI cells (Taberner and Liberman, 2005; Davis and Liu, 2011) and we hypothesize that these cells should have unique molecular signatures. Therefore, we used machine learning to cluster all the Type I SGNs based on their 96-dimensional gene expression profiles. We chose to use HDBSCAN clustering because it can deal with data of variable density and variance (see "Materials and Methods" section). After data transformation, we selected cells that expressed the housekeeping genes *B-actin* and *Gapdh*, as well as high levels of neuronal markers *Map2* and *Tubb3* (**Supplementary Figures S3C–F**). HDBSCAN was run on this set of Type I SGNs and provided five high confidence clusters (II-VI), of varying sizes (**Supplementary Figures S3G–I**). Three of these clusters contained a substantial number of cells with clear delineating markers, which we termed Type IA, IB, and IC (**Figure 3A**). Similar delineations were found using k-means clustering following PCA analysis (**Supplementary Figure S4**) as well as hierarchical clustering (**Supplementary Figure S5**), validating our findings. Type IA, B, and C cells were distinguished by their expression of the *Lmx1a* (**Figure 3B**), *Slc4a4* (**Figure 3E**), and *Mfap4 and Fzd2* (**Figures 3F,G**), respectively. Both Type IA and IB cells express *Cacna1a* (**Figure 3C**) and *Kcnd2* (**Figure 3D**). The additional two subtypes were characterized by a complex pattern of gene expression (**Supplementary Figure S6**). For completeness, we projected all cells, including those that were not assigned to any subset, onto the UMAP axes when displaying gene expression.

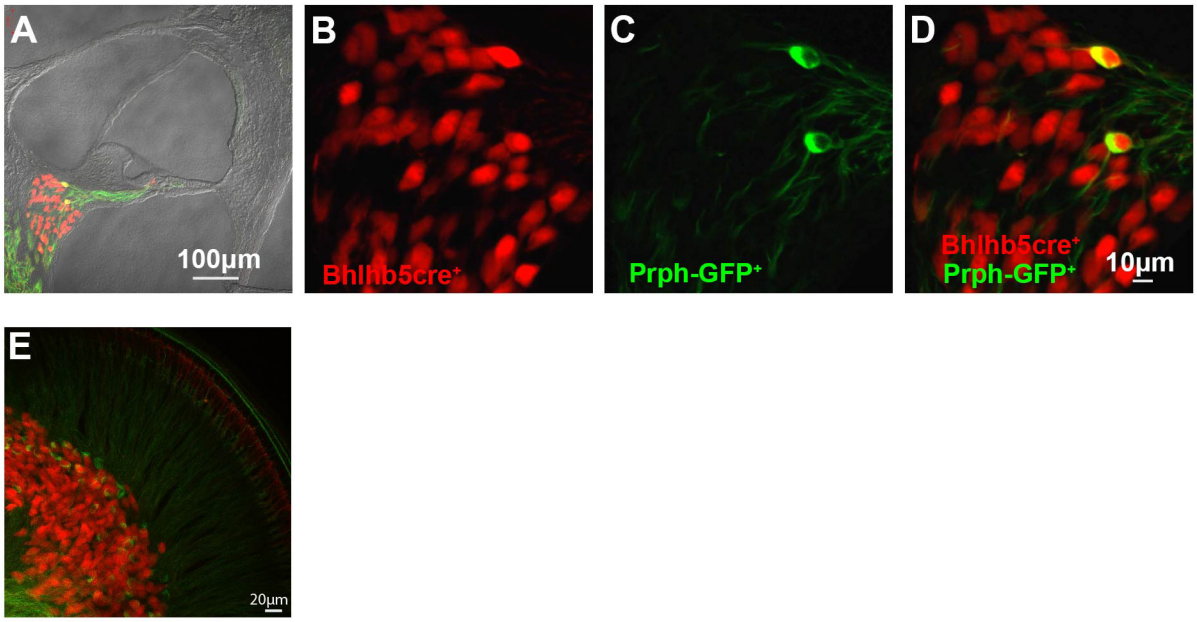

FIGURE 1 | Transgenic mouse model for spiral ganglion neuron (SGN) Type I and Type II Isolation. **(A)** Cross-section of the organ of Corti showing SGNs showing tdTomato; bhlhb5Cre (SGNIs) and Prph-GFP (SGNIIs) from cryopreserved tissue. **(B,C)** Fluorescent imaging of tdTomato and GFP. **(D)** Merge of panels **(B,C)**. **(E)** Whole-mount of the organ of Corti showing cell body and projections of SGN type I (red) and type II (green) from cryopreserved tissues. All images are representative fields from experiments repeated three times (n = 3).

Some of these marker genes have been previously implicated in SGN biology, in particular *Lmx1a* and *Cacna1a. Lmx1a* belongs to the family of LIM-domain containing transcription factors (Rétaux and Bachy, 2002) and is known to play roles in regulating fate decisions, and defining neural boundaries and domains in both the central and peripheral nervous system and the inner ear (Millonig et al., 2000; Chizhikov and Millen, 2004; Nichols et al., 2008; Koo et al., 2009). *Cacna1a* (encoding CAV2.1) has been shown to control fast excitatory synaptic transmission and low threshold exocytosis in the CNS (Jun et al., 1999; Pagani et al., 2004; Weiss and Zamponi, 2013), and its expression in SGNs has been determined by whole-cell and single-channel recordings (Lv et al., 2012, 2014; Stephani et al., 2019). Less is known about *Slc4a4* in SGNs, however, mutations in the human *SLC4A4* gene have been associated with neurosensory disorders including glaucoma and hereditary sensory neuropathy type I (Kok et al., 2003; Dinour et al., 2004). Although the *Fzd2* gene has not been characterized in SGNs, its ligand WNT5A plays an important role in planar cell polarity and cochlear development (Qian et al., 2007; Munnamalai and Fekete, 2013). Therefore, our identified marker genes are instrumental to distinguish functional subsets of SGN cells.

The Abundance of IA, IB and IC SGNIs Changes During Neonatal Development

We next sought to trace the number and fate of these subpopulations over-development by performing single-cell qPCR on SGNIs, before and at the onset of hearing from P3 and P12 cochlea, respectively. We clustered these cells together with P8 neurons and projected them onto the same UMAP embedding. At P3 and P12, we can see cells belonging to all the clusters we described (**Figure 4A**). However, we observed age-related changes in their abundance. IA cells are abundant at pre-hearing stages (P3, P8) representing 85% and 38% of the total SGNs analyzed, and decrease after the onset of hearing to 9% (**Figure 4B**). On the other hand, IB and IC cells are low at P3 (0.9% and 2.8%) and increase significantly at P8 (20% and 32%), stabilizing by P12 (35% and 35%; **Figure 4B**). The expression markers genes for the IB and IC subtypes stayed fairly constant from P8 to P12, after the large increase in these cell populations (**Figures 4D–H**). In contrast, expression levels of *Lmx1a* also decreased mildly with the concurrent loss of IA cells (**Figure 4C**). The loss of the IA population may either reflect differentiation or death with development or increased sensitivity of these cells to manipulation with age. Intriguingly, *Lmx1a* expression was not found by single-cell SGN studies focusing on the adult cochlea (Petitpré et al., 2018; Shrestha et al., 2018; Sun et al., 2018).

SGNI Subtypes Have Distinct Physiological and Signaling Properties

We next sought to understand the unique functions or properties of the Type I SGN subtypes by analyzing the expression patterns of the other genes beyond those defining the subtypes in our assay. As demonstrated by our PCA analysis (**Supplementary Figure S4D**), none of these genes has a role in exclusively defining a particular subtype, but several are enriched in only

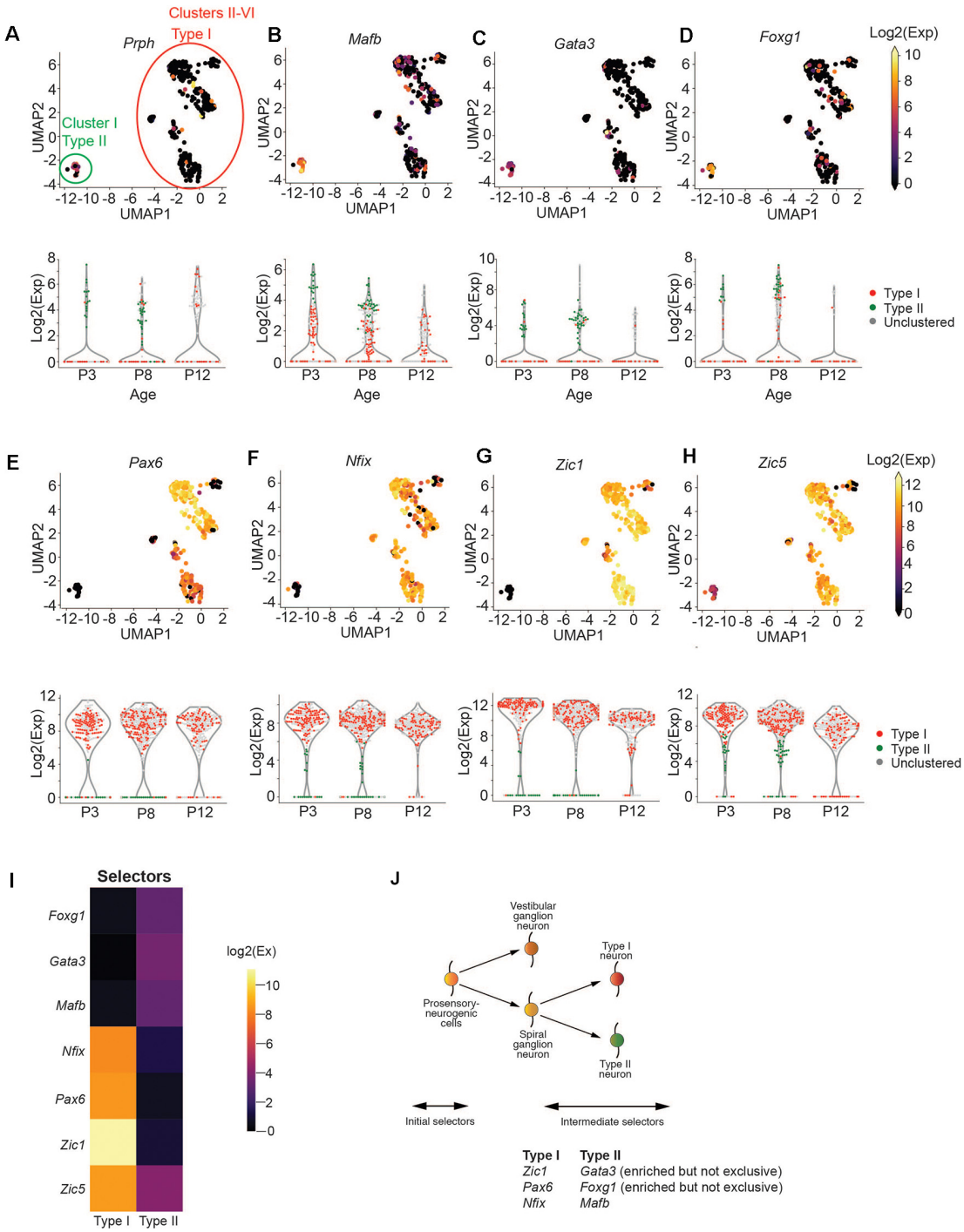

FIGURE 2 | *Zic1, Zic5, Pax6*, and *Nfix* are Type I SGN markers. **(A–D)** UMAP projection of all SGNs from postnatal day 8 cochlea (*n* = 383 cells, pooled from 7 technical runs representing 28 animals). Each point represents a single cell. Type I and Type II cells are circled in red and green, respectively. Cells are colored by the expression of *Prph* **(A)**, *Mafb* **(B)**, *Gata3* **(C)**, and *Foxg1* **(D)**. The expression scale is given on the right. Violin plots for each gene are given below the UMAP plot. Each point represents a cell. Cells are colored either red (Type I), green (Type II), or gray (unclustered). **(E–H)** UMAP projections and violin plots as in (a) for *Pax6* **(E)**, *Nfix* **(F)**, *Zic1* **(G)**, and *Zic5* **(H)**. **(I)** Heatmap for effector genes. **(J)** Proposed schematic for Type I and Type II specification based on data above.

one or two of the subtypes. Genes were classified by their broad functions: *transcription factor*, *signaling, physiology, guidance, and adhesion* (**Supplementary Figure S6**). Overall, we observed that transcription factor expression (beside *Lmx1a* and *Zeb1*) from our selected gene set was generally homogenous between all three identified subsets of Type I SGNs, while some of

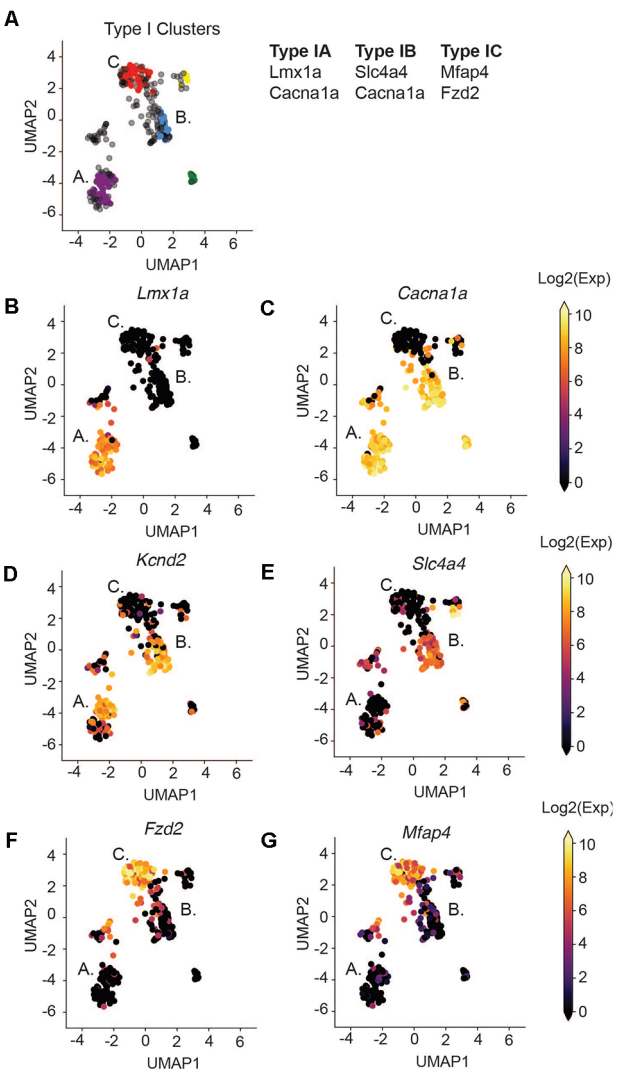

FIGURE 3 | Type I SGNs cluster into three subtypes. **(A)** UMAP projection of the Type SGNs at postnatal day 8. Each point represents a cell. Cells clustering to Type IA, IB, IC are colored in purple, blue, and red, respectively. The major gene markers for each subtype are given on the right. Two additional clusters were found (in yellow and green) but are not considered in this analysis as they did not have clear marker genes. Cells in gray were not clustered into any of the subgroups. **(B–G)** UMAP projection of Type I cells. Each cell is colored by the expression of **(B)** *Lmx1a*, **(C)** *Cacna1a*, **(D)** *Kcnd2*, **(E)** *Slc4a4*, **(F)** *Fzd2*, **(G)** *Mfap4*. The expression scale is given on the right.

the signaling and physiology related genes have more distinct expression patterns among the subtypes.

We found that subtype IA cells were enriched for a variety of sodium channels, including *Scn1a* (Nav1.1) *Scn2b* (Nav1.5), and *Scn9a* (Nav1.7; **Figures 5A,G**, **Supplementary Figure S6**). These channels activate at a more negative membrane potential than the other Nav channels and therefore may contribute to making fibers sensitive to the lower intensity of sound (Royeck et al., 2008; Fryatt et al., 2009; Browne et al., 2017). In addition to these channels, the IA subtype differentially express channels that mediate SGNI resting membrane potential and control neuronal excitability such as hyperpolarization-activated cyclic nucleotide-gated channel α-subunit 2 and 4 (HCN2 and HCN4; **Figures 5A,C**) and the K+-selective leak channels (KCNK9; **Figure 5E**; Welker and Woolsey, 1974; Mo and Davis, 1997; Kim and Holt, 2013; Liu et al., 2014).

IA cells were also enriched for markers related to neural branching and patterning, suggesting that these cells may still be migrating or differentiating into their mature forms between P3 and P12. In IA cells, we find enrichment for *Plxna1* and *Plxnb1* (**Figure 5A**). *Plxna1*, the receptor for class 3 semaphorin (*Sema3a*) was recently shown to be involved in SGNI branching and refinement during postnatal synapse maturation (Katayama et al., 2013; Jung et al., 2019). *Plxnb1* also plays a role in axonal guidance through *Sema2a* in the CNS (Ayoob et al., 2006). Finally, IA cells are enriched in *Nrp1* (**Figures 5A,F**), a receptor involved in neural pathfinding, survival, and maintenance (Cariboni et al., 2011; Guaiquil et al., 2014). Together these genes expressed by the IA subtype, in addition to *Lmx1a*, maybe representing a subset of mid or low threshold neurons that are refining their final connections with target cells.

Subtype IB was enriched in physiological markers involved in increased neural excitability such as *Kcnd2* (Kv4.2; **Figures 4E**, **5A**), a potassium voltage-gated channel. Interestingly, Kv4.2 expression in the SGNs is regulated by neurotrophins (Adamson et al., 2002). This channel is activated at membrane potentials that are below the threshold for action potentials (Shibata et al., 2000; Chen et al., 2006; Granados-Fuentes et al., 2012). Kv4.2 functions downstream of the metabotropic glutamate receptor GRM5 and plays a role in nociception mediated by activation of GRM5 (Hu et al., 2007). *Grm5* is enriched in both type IA and IB as compare to IC (**Figures 5A,G**). IB cells are also enriched for *Gria4* at P8 (**Figure 5A**), another glutamate receptor known to control the frequency, amplitude, and kinetics of the spontaneous excitatory postsynaptic channels of the reticular thalamic nucleus (nRT) neurons (Paz et al., 2011, p. 4). Taken together with the highest expression of *Cacna1* in type IB SGNI, this subtype may be a representative of the mid to low-threshold SGNI.

Additionally, subtype IB cells had the highest expression of Ca^{2+}-dependent activator protein for secretion 2 (*Cadps2*; **Figure 5A**), which is involved in cell survival and the activity-dependent release of the brain-derived neurotrophic factor (BDNF; Sadakata et al., 2004; Shinoda et al., 2011). BDNF is involved in neuronal maturation and synaptic plasticity (Sadakata et al., 2007, 2013). Intriguingly, *Bdnf*, and *Ntf3* expression, as well as their receptor *Ntrk2*, are high in type IB, although present in the other subtypes (**Figure 5A**, **Supplementary Figure S7**). Previous studies have shown a graded expression of neurotrophins in the cochlea, with BDNF expression being highest at the basal turn, while NTF3 is highest at the apical edge (Adamson et al., 2002; Schimmang et al., 2003), suggesting that type IB cells originate from many tonotopic areas. Although expression analysis cannot definitively establish electrophysiological properties, these patterns suggest that IA and IB are more closely related molecularly than IC and may the low or mid-low neurons.

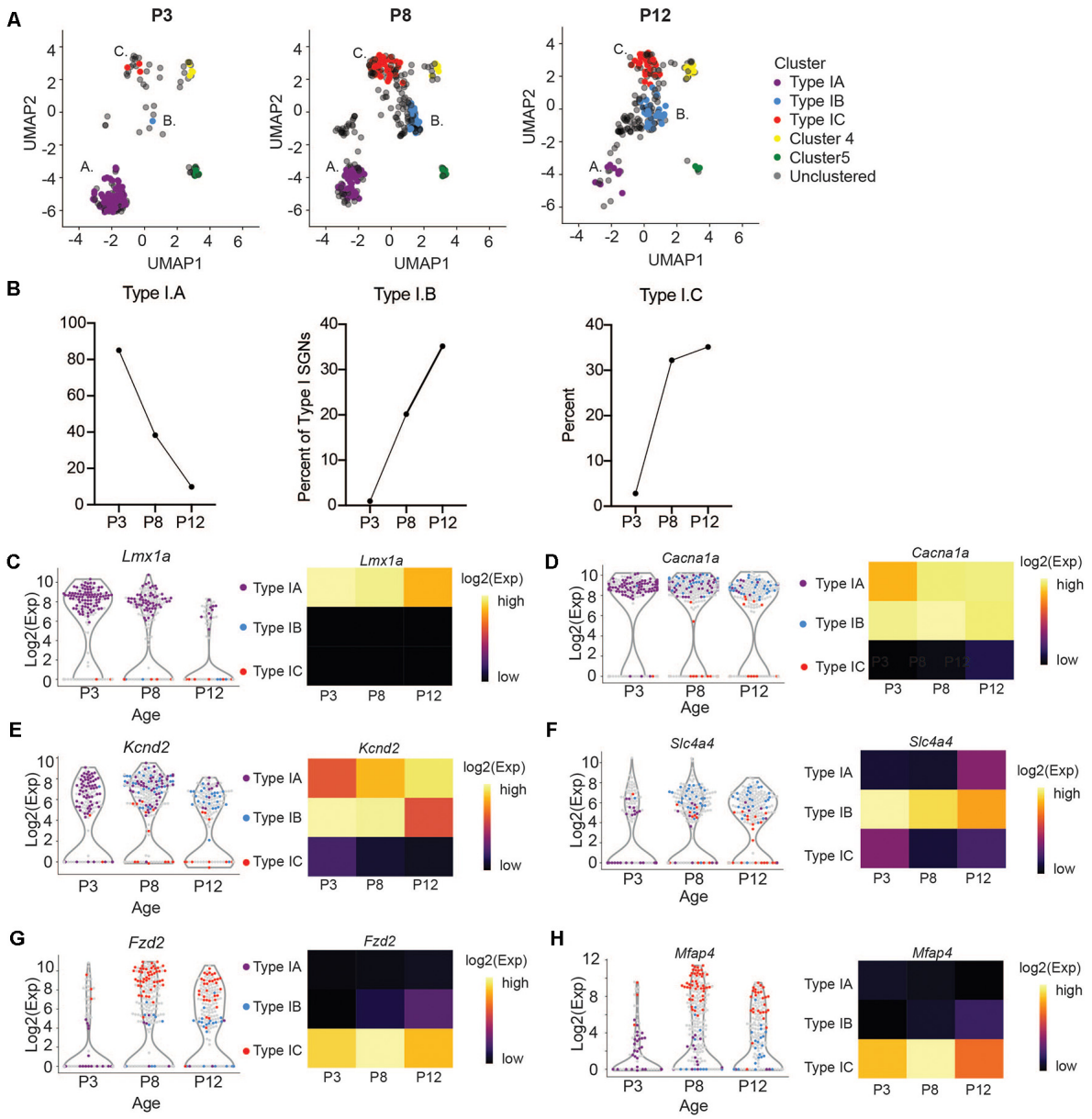

FIGURE 4 | Subtypes of Type I change in abundance at the onset of hearing. **(A)** UMAP projections of Type I SGNs colored by subtypes at postnatal days 3, 8, and 12 (n = 203 single cells at P3 and n = 230 single cells at P12, representing three independent technical runs, each with four to six animals). Postnatal day 8 is reproduced from **Figure 3A** for clarity. **(B)** Quantification of the percentage of Type IA, IB, and IC cells as a fraction of the total Type I SGNs at each age. **(C–H)** Violin plot of **(C)** *Lmx1a*, **(D)** *Cacna1a*, **(E)** *Kcnd2*, **(F)** *Slc4a4*, **(G)** *Fzd2*, **(H)** *Mfap4*. Each point represents a single cell, colored according to its subtype or gray if outside the IA, IB, IC. On the right, a heatmap of the same data. The expression scale is giving on the right side.

Subtype IC cells are defined by their specific expression of adhesion and signaling molecules *Mfap4* and *Fzd2*. They are also enriched for two members of the Tcf transcription factor family: *Zeb1* (*Tcf8*) and *Tcf12* (**Figure 5A**), which may be involved in establishing the IC cluster during early development. Several members of the hedgehog-signaling pathway, *Ptch1*, *Ptch2*, and *Yes1*, are also enriched in this subtype (**Figure 5A**). *Ptch2* expression (**Figure 5I**) has previously been shown to influence neural cell fate decisions and regulate synaptic plasticity and neuronal activity in the CNS (Konířová et al., 2017, p. 2; Herholt et al., 2018). Type IC cells also expressed high platelet-derived growth factor receptor alpha (*Pdgrfa*; **Figure 5J**). PDGF receptors and their ligands play essential roles in neuronal differentiation during embryonic stages and in adult neuronal maintenance (Funa and Sasahara, 2014). PDGF receptors were elevated in cochlear tissues, including SGNs, following noise injury (Fetoni et al., 2014; Bas et al., 2015), suggesting their role in cochlear tissue protection following noise trauma. These expression

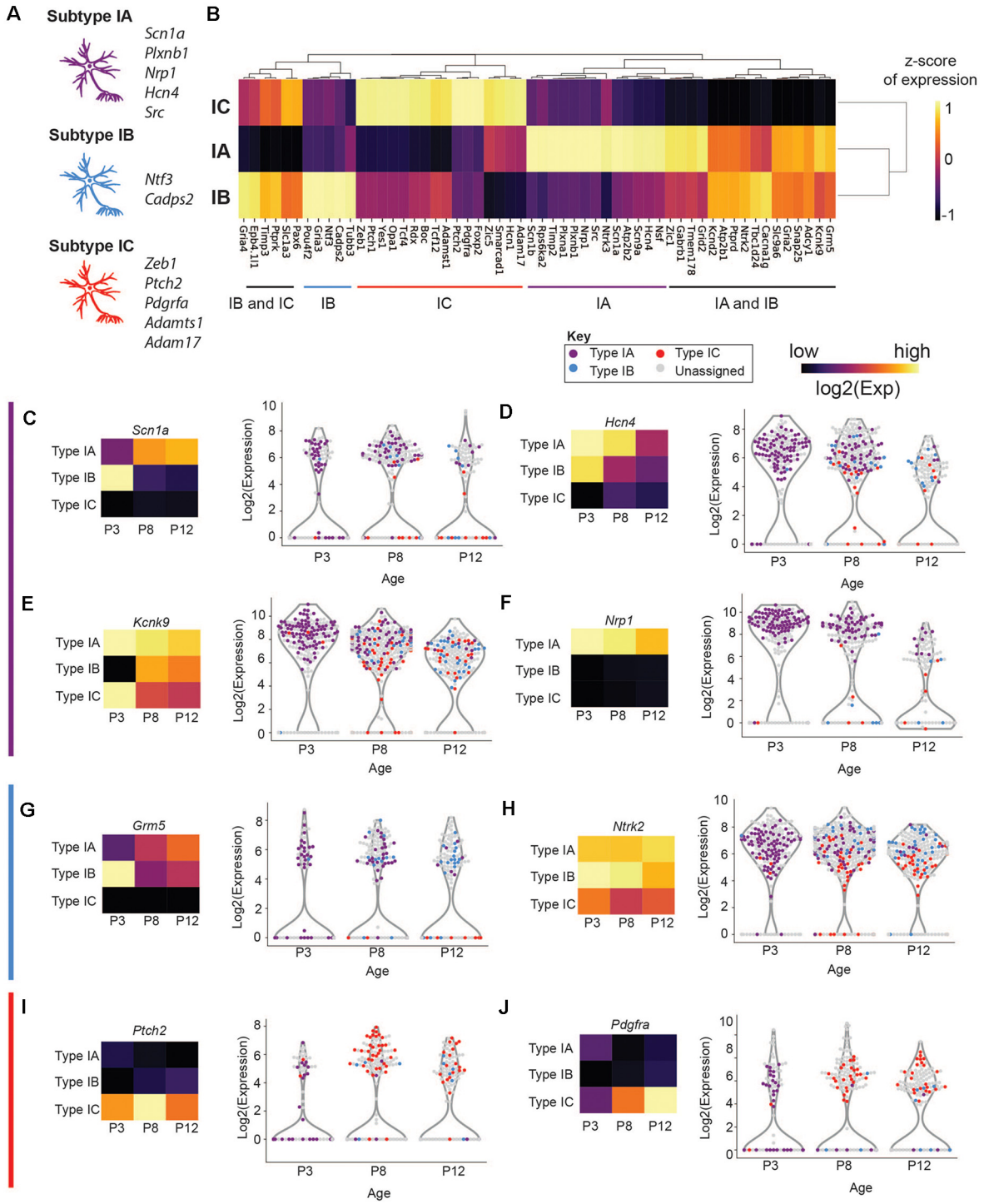

FIGURE 5 | Expression of physiologically relevant genes in SGN Type I subtypes. **(A,B)** Hierarchical clustering of genes that are differentially enriched in Type I **(A,B,C)** SGNs and schematic of the most important effectors (on the left). **(C–J)** Violin plot of **(C)** *Scn1a*, **(D)** *Hcn4*, **(E)** *Kcnk9*, **(F)** *Nrp1*, **(G)** *Grm5*, **(H)** *Ntrk2*, **(I)** *Ptch2*, and **(J)** *Pdgfra*. Each point represents a single cell, colored according to its subtype or gray if outside the IA, IB, IC. On the left, a heatmap of the same data. Each square has the average expression of cells in that subtype. The expression scale and color key are on the top of the page.

patterns indicate that IC neurons may be the high-threshold SGNIs. Collectively, our findings suggest that the three SGNI subtypes defined by their distinctive transcriptional profiles represent physiologically distinct subpopulations.

Validation of Type I SGNs in the Mouse Cochlea

After identifying IA, IB, and IC to be the main three subpopulations arising from our single-cell dataset, we sought to validate these three populations *in vivo*. First, we designed *in situ* probes against *Cacna1a*, which we observed to be enriched in both the IA and IB subtypes. Indeed, we see a strong signal of *Cacna1a* in cochlear tissues at both P3 and P8 (**Supplementary Figures S6D,E**). However, due to the low resolution of traditional *in situ*, we were not able to localize the expression of more than one gene to individual populations of neurons. Therefore, we opted to use RNA-scope technology, an *in situ* hybridization approach with low background signal, that allows us to visualize and/or co-localize two or more probes (Wang et al., 2012). We designed and tested probes against several of the defining population markers (see "Materials and Methods" section). For the validated probes, we were able to observe subpopulations of SGNs that exclusively expressed *Cacna1a*, representing Type IA and Type IB cells and *Mfap4* expressing cells, representing Type IC cells (**Figures 6A,B**). We also tested the co-localization of *Cacna1a* and *Kcnd2*. From the single-cell data, we expected to observe two populations, one that would only express the *Cacna1a* representing Type IA cells without *Kcnd2* (**Figure 4G**) and those expressing *Cacna1a* and *Kcnd2*, pooled both from Type IA and Type IB. In concordance with this data, in RNA-scope images of the cochlea, we observed both cells only expressing *Cacna1a* and others expressing both *Cacna1a* and *Kcnd2* (**Figures 6C,D**).

Previous studies had established a role for *Lmx1a* in inner ear cell fate decisions (Nichols et al., 2008; Koo et al., 2009). However, we were unable to establish robust probes for *Lmx1a*. Therefore, to validate the existence of SGNI cells which expressed *Lmx1a*, we established a new triple transgenic mouse line using a *Lmx1a*-cre line (Chizhikov et al., 2010) crossed to the *Ai14*-tdTomato reporter line and *Peripherin*-GFP lines. Our *in vivo* data revealed that only a subset of SGNIs (i.e., cells not showing GFP expression) was red at P8 (**Figure 7A**), validating that IA cells are indeed a unique subset of SGNIs distinct from the SGNII (**Figure 7B**). Further studies need to be performed on this mouse model to analyze the dynamics of this cell population over time (**Figure 7C**).

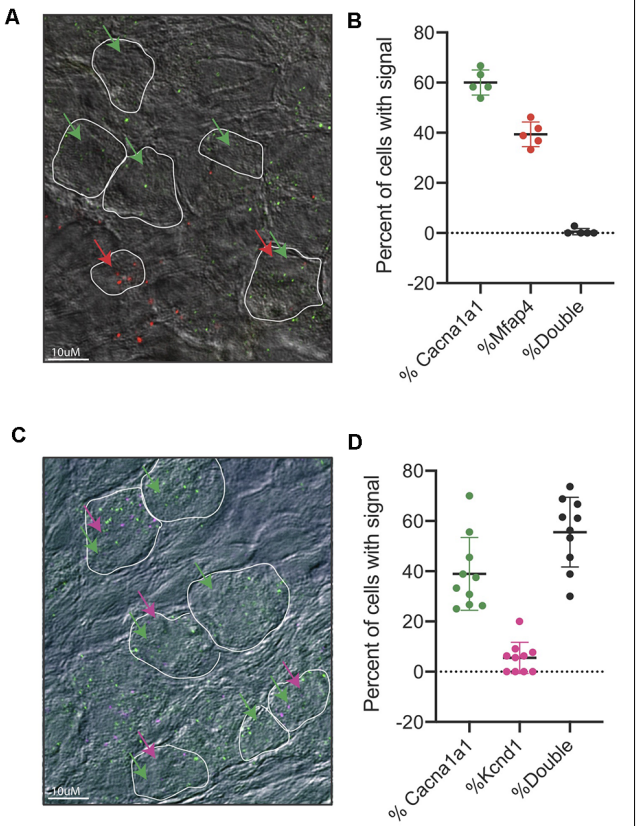

FIGURE 6 | RNA-scope of *Cacna1a* and *Kcnd2*. **(A)** Representative image from RNAscope *in situ* hybridizations of *Cacn1a1* (green) and *Mfap4* (red) with bright field merge at postnatal day 8 from cryopreserved cochlear tissue. White boundaries indicate cells; green arrows indicate cells expressing *Cacna1a*, and red arrows indicate cells expressing *Mfap4*. **(B)** Quantification of cells expressing either *Cacna1* only (60% ± 5%) or *Mfap4* only (39.4% ± 4.8%) or both (0.6% ±1.25%) as percentage of all cells scored per image. Cells were considered positive if they had >1 dot per cell, 5 independent images (n = 5 mice) were scored. Each point represents a scored image; all data presented as average ± STD. **(C)** Representative image from RNAscope *in situ* hybridizations of *Cacn1a1* (green) and *Kcnd2* (purple) with bright field merge at postnatal day 8. White boundaries indicate cells; green arrows indicate cells expressing *Cacna1a*, and purple arrows indicate cells expressing *Kcnd2*. **(D)** Quantification of cells expressing either *Cacna1* only (38% ± 14.5%) or *Kcnd2* only (5% ± 6%) or both (55.9% ±13.9%) as a percentage of all cells scored per image. Cells were considered positive if they had >1 dot per cell, 10 independent images (n = 10 mice) were scored. Each point represents a scored image; all data presented as average ± STD.

Comparison to a Previously Published Dataset of P3 SGNs

We next sought to compare our study to the previously published results from whole-genome single-cell studies (Petitpré et al., 2018; Shrestha et al., 2018; Sun et al., 2018). Of these, two focused primarily on adult SGNs, and therefore were not suitable for comparison with our study, as neuronal properties are known to change from neonate to adult (Crozier and Davis, 2014). We thus chose to compare our work to the *Pvalb-cre* P3 neurons sequenced by Petitpré et al. (2018) although the two studies use different transgenic mouse models for sorting.

In both the adult and P3 data, Petitpré et al. (2018) found three subtypes of SGNs, characterized by their expression of *Calb1, Runx1, and Calb2* (Type IA), *Lypd1, Grm8 and Runx1* (Type IB) and, *Trim54, Pcdh20, Rxrg and Calb2* (Type IC). We did not have any of these markers in our targeted panel, except *Calb1*, whose expression we compared (**Supplementary Figures S7A,B**). We see a more limited expression of *Calb1*, although it is enriched in Type IA (*Lmx1a* positive) neurons at P3, suggesting that these two subtypes may be similar (**Supplementary Figure S7B**). However, by P8, we observe the majority of the *Calb1* expressing cells to be Type II cells (**Supplementary Figure S7C**).

We next wanted to determine if we could sort out our subtypes using the Petitpré et al.'s (2018) data. Thus, we

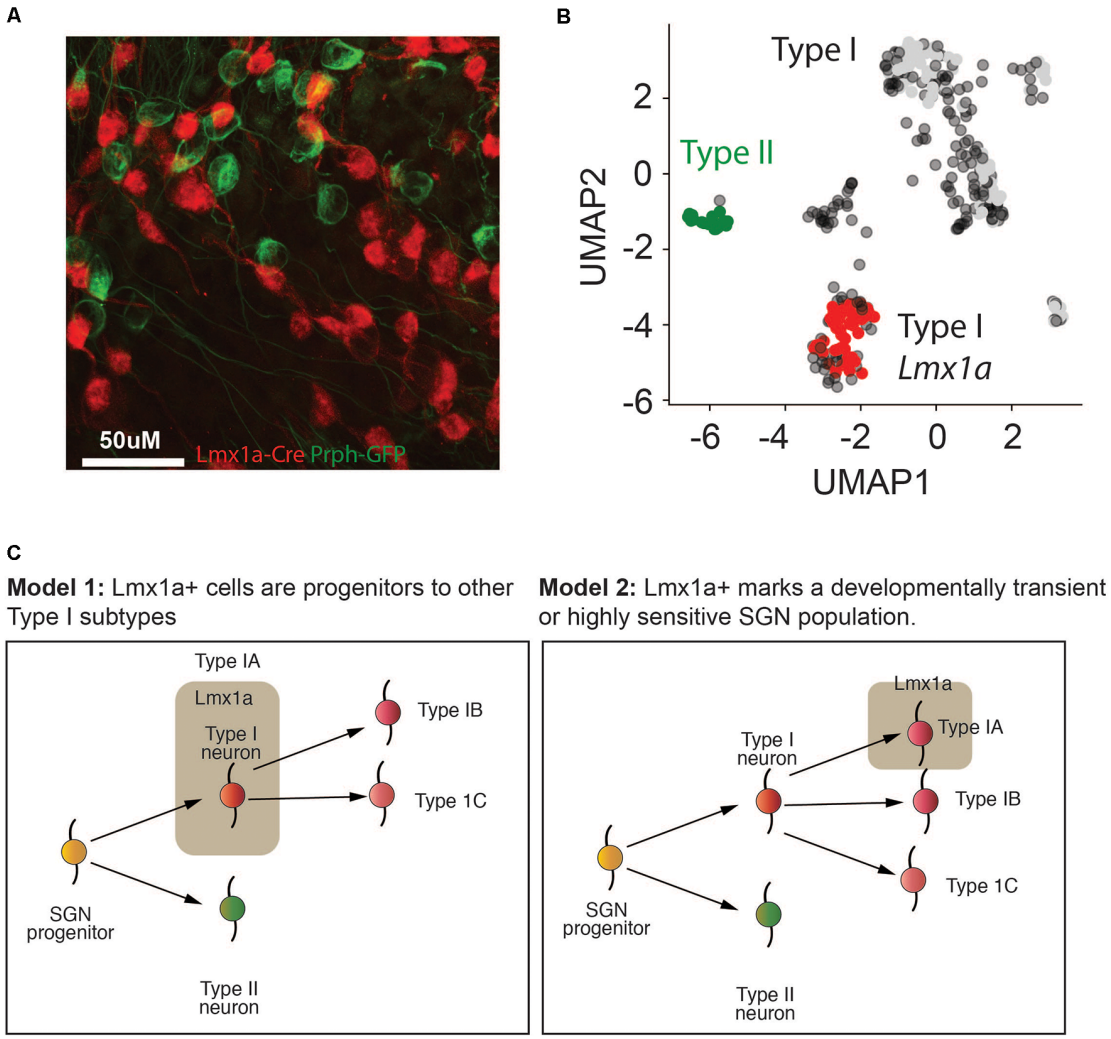

FIGURE 7 | *Lmx1a* marks a distinct population of Type I SGNs. **(A)** Representative fluorescent image of *Lmx1a*-tdTomato x GFP-Prph at P8 from cryopreserved tissue. Magnification at 66×. **(B)** UMAP of P8 SGN Type I and Type II cells, colored according to the mouse model in **(A)**. **(C)** Two putative models for how the different Type I SGN subtypes identified in this article might form in the cochlea. In model 1, the Type IA *Lmx1a* cells form an early progenitor population that is more immature and gives rise to the Type IB and Type IC cells, thereby explaining the age-related decline in these cells. In model 2, the Type IA *Lmx1a* cells are an independent subtype, but they are either more sensitive to stress at later ages, because they are more sensitive, or they are a developmentally transient population that begins to decline by P8.

selected the same 96 genes found in our panel, and projected and clustered the cells as before, but were not able to form the same clusters. We noted several differences between our data and Petitpré et al. (2018): (1) SGNI markers *Zic1* and *Zic5* were not expressed (**Supplementary Figures S7D,E**), although they are expressed in previous studies of bulk SGN tissues at P0 and P6 (**Supplementary Figure S7F**, Lu et al., 2011). (2) Two of our marker genes (*Lmx1a* and *Mfap4*) were not expressed (**Supplementary Figures S7G,H**). *Fzd2* was lowly expressed by a few of their Type IC cells, but these did not cluster together in our analysis (**Supplementary Figure S7F**). Finally, *Slc4a4* and *Cacna1a* were broadly expressed across all subtypes (**Supplementary Figures S7J,K**).

These discrepancies in the two datasets may suggest that transcripts like *Lmx1a* and *Mfap4* may be low-abundance and therefore need to be pre-amplified to be detected. The limited detection of low-abundance transcripts is a known problem with both the 10× and Smart-seq2 pipelines, as these transcripts are not efficiently converted into cDNA. Thus, our dataset complements previous whole sequencing studies that set the outlines of SGN subtypes with the detection of these low abundance transcripts.

DISCUSSION

In the mature cochlea, each IHC is innervated by multiple spiral ganglion neuron subtype-I (SGNI) cells that are morphologically

and physiologically diverse. SGNIs possess complex endogenous firing properties that enable them to rapidly and faithfully transmit the wide dynamic range of sound information to the auditory brainstem (Taberner and Liberman, 2005; Davis and Liu, 2011). However, the factors that define the molecular and physiological diversity of SGNIs remain poorly understood. In this study, we identified marker genes that distinctively label different neonatal SGNI neuron subtypes by using a novel transgenic reporter mouse. This model was designed to distinguish the SGNI and II by their already known exclusive markers and allowed us to isolate pure populations of SGNI (*Bhlhb5*-cre × tdTomato) and SGNII (*Peripherin*-GFP) neurons by FACS. This step facilitated the construction of single-cell transcriptomes of SGNIs and SGNIIs neurons.

Using our single-cell dataset of SGNI cells from P3, P8 and P12 cochlea's we identified three distinct populations: Type IA, marked by *Lmx1a* expression, Type IB marked by *Slc4a4* and Type IC marked by *Mfap4/Fzd2*. Although, we observed all three subtypes of Type I SGNs at each developmental age, their relative sizes varied throughout development. This might be due to the differentiation of progenitor-like SGNs at earlier time points, or selective loss of certain subtypes that are more sensitive to stress (**Figure 7C**). Previous work has highlighted the existence of three electrophysiological categories whose proportions changed between early postnatal (P0-P3) and adult (Crozier and Davis, 2014). Intriguingly, although a previous study also found three subtypes of SGNs at postnatal day 3 (P3; Petitpré et al., 2018), we found little overlap between the marker genes defining the populations. In particular, *Lmx1a* expression was absent from this dataset. This discrepancy between the datasets may be due to the qPCR-based technique allowing pre-amplification of low abundance transcripts, the technique of cochlear dissociation, or the choice of transgenic mouse models. These differences, however, highlight the importance of using several orthogonal methods to investigate complex biological systems, as each technique can reveal unique and complementary features of the tissue.

Previous studies have established that type I SGNs have a variety of physiological phenotypes, corresponding to the so-called low, mid and high threshold neurons (Adamson et al., 2002; Taberner and Liberman, 2005; Liu et al., 2014; Kujawa and Liberman, 2015). We hypothesized that these identities were genetically encoded early in the development of the cochlea, before the onset of hearing. Our observation that we can sort out at least three distinct subsets of neurons at P3, based on 96-gene markers, is in line with this hypothesis. To characterize the physiological identity of these subtypes, we analyzed the expression of effectors that could define and maintain a particular SGNI subtype's electrophysiological characteristics. We found both heterogeneities between SGNI subtypes (**Figure 5**) and also variable expression between SGNI cells of the same subtype.

A recent modeling study of spinal dorsal horn neurons showed that within a single neuron population, varying the densities of just two ion channels could reproduce five patterns of neuronal firing (Balachandar and Prescott, 2018). This work implied that subtle changes in ion channel expression can cause changes to cell physiology and that multiple combinations of ion channel densities may give similar firing patterns. This study, taken in combination with our findings in SGNs, suggests that while specific *selector* molecules may establish subtypes (IA, IB, IC), each subtype may represent a wide variety of excitation potentials. The heterogeneity in the expression of ion channels was also observed in the ganglion retinal cells and has been suggested to allow neuron populations to encode more information (Berry et al., 2018). The heterogeneity we observe in these ion channels may be due to cells originating in different tonotopic regions of the cochlea.

Among the three subtypes, the IA cells drew our attention the most, due to their expression of *Lmx1a*. The *Lmx1* family of genes is known to act as selector molecules in a variety of different developmental contexts, including the development of the CNS (Chizhikov et al., 2010; Kee et al., 2017). *Lmx1a* is one of the early determinants of the fate of midbrain dopaminergic (mDA) neuronal generation (Chizhikov et al., 2010; Deng et al., 2011; Yan et al., 2011). Also, to its role development, it was recently shown to play an important role in maintaining adult mDA circuitry (Doucet-Beaupré et al., 2015). *Lmx1a* expression has long been seen in the mammalian inner ear and cochlea. Data from human studies reported that loss of function mutations lead to deafness in human populations (Schrauwen et al., 2018; Wesdorp et al., 2018). Furthermore, mutations in *Lmx1a* in mice lead to the improper establishment of the sensory-non-sensory regions of the ear, leading to altered ear morphology (Koo et al., 2009). *Lmx1a* has been suggested to be part of the transcription factor network, together with *Gata3*, that define SGN from the VGN population in early development stages (Appler and Goodrich, 2011). Besides, loss of *Lmx1a* also leads to an expansion of the vestibular ganglion region of the inner ear (Huang et al., 2018). Despite these reports, which establish the importance of *Lmx1a* in the inner ear, little attention has been paid to the expression of *Lmx1a* in the SGN population. Our single-cell high-throughput qPCR reveals a population of *Lmx1a* positive cells at P3, whose abundance decreased with age toward P12. We further validated the selective expression of *Lmx1a* in Type IA SGNs by generating a triple transgenic mouse model using *Lxm1a*-Cre X tdTomato and *Prph*-GFP. We observed that the subset of Type I SGNs was labeled in red, but not the Type II *Prph*-GFP.

To fully establish the *bona fide* role of IA neurons, future studies will have to assess the electrophysiological properties of these *Lmx1a* positive cells. From their expression of *Snap25* and *Grm5*, we hypothesize that IA cells will represent neurons with a high spontaneous firing rate property. However, it is also possible that *Lmx1a* will not define a physiologically homogeneous subpopulation (i.e., only high or low threshold cells), as we observe that they have varied expression patterns of effectors genes such as *Scn1a, Scn9a, Scn1b, and Grm5*. These heterogeneous features will be better explored by deep-sequencing studies that can assess the full transcriptome

of each IA SGN, and by electrophysiology experiments using specific blocking agents against each channel.

Taken together, our data provide several novel markers of Type I cells (*Zic1, Pax6*, and *Nfix)* and their subtypes (*Lmx1a, Mfap4, Fzd2, Slc4a4, Cacna1a*) and will enable future efforts to generate subtype-specific reporter lines. These tools will allow the study of the precise interplay of intrinsic genetic factors and extrinsic cues in defining SGNI diversity and their differential susceptibility to noise-induced hearing impairment.

DATA AVAILABILITY STATEMENT

All datasets generated for this study are included in the article/**Supplementary Material**.

ETHICS STATEMENT

The animal study was reviewed and approved by Stanford University Institutional Animal Care and Use Committee.

AUTHOR CONTRIBUTIONS

FG analyzed and visualized the data and wrote the manuscript. LDT collected the data. MM conceptualized and oversaw the study and data analysis and wrote the manuscript.

FUNDING

This work was supported by research grants from the National Institute in Deafness and other Communicative Disorders: R01 DC09590 (to MM) and the Mauritius Research Council: MR/S002510/1(to MM). FG is supported by the National Science Foundation Graduate Fellowship (GRFP).

ACKNOWLEDGMENTS

We sincerely thank Drs. Stefan Heller and Marta Milo for help with data analysis, and Dr. Walter Marcotti for helpful discussion. We also thank Dr. Kathleen J. Millen for generously providing the Lmx1a-cre mice and Dr. Theresa Zwingman for answering the many questions we had concerning these mice (Seattle Children's Research Institute Center for Integrative Brain Research, The University of Washington). We thank Dr. Joseph P. Sarsero (Murdoch Children's Research Institute, Australia) for sharing Peripherin-GFP mice with us and Dr. Lin Gan (Flaum Eye Institute, University of Rochester School of Medicine) for sharing Bhlhb5-cre line.

SUPPLEMENTARY MATERIAL

The Supplementary Material for this article can be found online at: https://www.frontiersin.org/articles/10.3389/fnmol.2020.00083/full#supplementary-material.

FIGURE S1 | **(A)** P8 cultured SGN neurons immunostained for TUJ1, in red. **(B)** P8 cultured SGN neurons stained with DAPI, in blue. **(C)** Quantification of total cultured cells after dissection as determined by DAPI and neurons determined by TUJ1 with and without Trypsin (n = 3 independent neuronal cultures). **(D–H)** Representative FACS gating strategy for separation of type I spiral ganglion neurons. Percentage (%) of cells in each gate **(D–H)** are shown in red. Cell debris was removed by plotting FSC and SSC to remove doublets and tissue clumps **(D–F)**. Dead cells were removed by staining cells with Sytox Red **(G)**. Finally, we gated tdTomato and GFP cells **(H)** and collected high tdTomato positive cells (outlined in the box).

FIGURE S2 | Spiral ganglion neurons single-cell multiplex qRT-PCR quality control. **(A)** *B-actin* **(B)** *Gapdh*, **(C)** percentage of genes expressed per cell. **(D)** Summary of P8 healthy cells, negative control, death, and doublet cells. **(E)** Cells were excluded based on *B-actin* and *Gapdh* expression, lower Log2Ex values indicate death cells or empty wells, and higher Log2Ex values indicate doublet. **(F)** Healthy cells expressed 52.2 ± 13.6% genes, death cells expressed 13.8 ± 4.3% genes, and doublet cells expressed 85.93 ± 0.7% genes of 96 genes analyzed in 96 cells.

FIGURE S3 | **(A)** UMAP projection of SGN cells, colored by the FACs gating, green for GFP-Prph, red for tdTomato. **(B)** UMAP projection of SGN cells at P8. Each cell is colored by the expression of genes enriched in Type I cells: *Cadps2*, *Tmem178*, and *Cacna1a*. The expression scale is given on the right. **(C–F)** UMAP projection of SGN cells at P8. Each cell is colored by the expression of **(C)** *Bactin*, **(D)** *Map2*, **(E)** *Gapdh*, and **(F)** *Tubb3*. The expression scale is given on the right. **(G)** UMAP projection of the Type SGNs at postnatal day 8. Each point represents a cell. Cells clustering to Type IA, IB, IC are colored in purple, blue, and red, respectively. Type II cells are colored in brown. The major gene markers for each subtype are given on the right. Two additional clusters were found (in yellow and green) but are not considered in this analysis as they did not have clear marker genes. Cells in gray were not clustered into any of the subgroups. Partially reproduced from **Figure 3A** for clarity. **(H)** Probability calculated by HDBSCAN that each cell belongs to the cluster assigned in **(G)**. The color key is given to the right. **(I)** Clustering tree generated by the HDBSCAN algorithm to generate clusters in **(G)**.

FIGURE S4 | **(A)** Principal components were analyzed, and PC1 to PC10 were plotted in X-axis with the respective variance in Y-axis. **(B)** K-means clustering was performed. The stable numbers of clusters were chosen based on Gap statistic. The dotted line indicates three stable clusters. **(C)** K-means clustering of PC1 and PC2 with pre-defined three clusters (K = 3). Black, red, and green dots represent cluster-1, cluster-2, and cluster-3 respectively. PC1 and PC2 are plotted in X-axis and Y-axis, respectively. **(D)** Cluster-1 specific genes are *Cacna1a*, *Lmx1a*, *Nrp1*, *Snap25* and *Timp2*. The cluster-2 specific genes are *Gria3*, *Sclc4a4*, *Cacna1a*. The cluster-3 specific genes are *Fzd2* and *Mfap4*. **(E–J)** representative genes in each cluster were plotted in PC1 and PC2. A color key (horizontal bar) with red, green, and gray colors represents high, low, and not detectable of genes expression respectively in cells.

FIGURE S5 | Hierarchical clustering of the same cells analyzed for Kmeans clustering. Three clusters labeled in black, red, and green.

FIGURE S6 | **(A–C)** Heat maps of gene expression in Type II, Type IA, Type IB, and Type IC Genes are grouped by transcription factors, signaling, physiology, and guidance and adhesion and **(A)** P3, **(B)** P8, **(C)** P12. Each square represents the average expression in each cell category. **(D–E)** Representative images of *in situ* hybridizations of *Cacna1a* at **(D)** P3 and **(E)** P8 in the cryopreserved whole cochlea. **(F)** Representative images of *in situ* hybridization for *Nefm* at P8 as a positive control.

FIGURE S7 | **(A)** UMAP projection of SGN cells at P3 from Peptitpre et al. Each point represents a cell, which is colored by the gene count of *Calb1*. The scale is given at the right. **(B)** UMAP projection of SGN cells at P3 from this study colored by expression of *Calb1*. **(C)** Violin plots of the expression level of *Calb1* at P3, P8, and P12. The different subtypes are colored and indicated on the top. **(D–E)** Data presented as in **(A)** for *Zic1* and *Zic5*. **(F)** Microarray values for *Zic1* and *Zic5* at P0 and P6 in bulk SGN samples taken from Lu et al. (2011). **(G–K)** Data presented as in **(A)** for *Lmx1a, Mfap4, Fzd2, Slc4a4* and *Cacna1a*.

TABLE S1 | Raw data + clustering.

REFERENCES

Adamson, C. L., Reid, M. A., and Davis, R. L. (2002). Opposite actions of brain-derived neurotrophic factor and neurotrophin-3 on firing features and ion channel composition of murine spiral ganglion neurons. *J. Neurosci.* 22, 1385–1396. doi: 10.1523/JNEUROSCI.22-04-01385.2002

Appler, J. M., and Goodrich, L. V. (2011). Connecting the ear to the brain: molecular mechanisms of auditory circuit assembly. *Prog. Neurobiol.* 93, 488–508. doi: 10.1016/j.pneurobio.2011.01.004

Ayoob, J. C., Terman, J. R., and Kolodkin, A. L. (2006). *Drosophila* plexin B is a Sema-2a receptor required for axon guidance. *Development* 133, 2125–2135. doi: 10.1242/dev.02380

Balachandar, A., and Prescott, S. A. (2018). Origin of heterogeneous spiking patterns from continuously distributed ion channel densities: a computational study in spinal dorsal horn neurons. *J. Physiol.* 596, 1681–1697. doi: 10.1113/jp275240

Bas, E., Goncalves, S., Adams, M., Dinh, C., Bas, J. M., Van De Water, T. R., et al. (2015). Spiral ganglion cells and macrophages initiate neuro-inflammation and scarring following cochlear implantation. *Front. Cell. Neurosci.* 9:303. doi: 10.3389/fncel.2015.00303

Becht, E., McInnes, L., Healy, J., Dutertre, C.-A., Kwok, I. W. H., Ng, L. G., et al. (2019). Dimensionality reduction for visualizing single-cell data using UMAP. *Nat. Biotechnol.* 37, 38–44. doi: 10.1038/nbt.4314

Berglund, A. M., and Ryugo, D. K. (1987). Hair cell innervation by spiral ganglion neurons in the mouse. *J. Comp. Neurol.* 255, 560–570. doi: 10.1002/cne.902550408

Berry, M. J. II., Lebois, F., Ziskind, A., and da Silveira, R. A. (2018). Functional diversity in the retina improves the population code. *Neural Comput.* 31, 270–311. doi: 10.1162/neco_a_01158

Browne, L., Smith, K. E., and Jagger, D. J. (2017). Identification of persistent and resurgent sodium currents in spiral ganglion neurons cultured from the mouse cochlea. *eNeuro* 4:ENEURO.0303–17.2017. doi: 10.1523/eneuro.0303-17.2017

Cariboni, A., Davidson, K., Dozio, E., Memi, F., Schwarz, Q., Stossi, F., et al. (2011). VEGF signalling controls GnRH neuron survival *via* NRP1 independently of KDR and blood vessels. *Development* 138, 3723–3733. doi: 10.1242/dev.063362

Chen, X., Yuan, L.-L., Zhao, C., Birnbaum, S. G., Frick, A., Jung, W. E., et al. (2006). Deletion of *Kv4.2* gene eliminates dendritic A-type K^+ current and enhances induction of long-term potentiation in hippocampal CA1 pyramidal neurons. *J. Neurosci.* 26, 12143–12151. doi: 10.1523/JNEUROSCI.2667-06.2006

Chizhikov, V. V., Lindgren, A. G., Mishima, Y., Roberts, R. W., Aldinger, K. A., Miesegaes, G. R., et al. (2010). Lmx1a regulates fates and location of cells originating from the cerebellar rhombic lip and telencephalic cortical hem. *Proc. Natl. Acad. Sci. U S A* 107, 10725–10730. doi: 10.1073/pnas.0910786107

Chizhikov, V. V., and Millen, K. J. (2004). Control of roof plate formation by Lmx1a in the developing spinal cord. *Development* 131, 2693–2705. doi: 10.1242/dev.01139

Crozier, R. A., and Davis, R. L. (2014). Unmasking of spiral ganglion neuron firing dynamics by membrane potential and neurotrophin-3. *J. Neurosci.* 34, 9688–9702. doi: 10.1523/JNEUROSCI.4552-13.2014

Davis, R. L., and Liu, Q. (2011). Complex primary afferents: what the distribution of electrophysiologically-relevant phenotypes within the spiral ganglion tells us about peripheral neural coding. *Hear. Res.* 276, 34–43. doi: 10.1016/j.heares.2011.01.014

Deng, Q., Andersson, E., Hedlund, E., Alekseenko, Z., Coppola, E., Panman, L., et al. (2011). Specific and integrated roles of Lmx1a, Lmx1b and Phox2a in ventral midbrain development. *Development* 138, 3399–3408. doi: 10.1242/dev.065482

Dinour, D., Chang, M.-H., Satoh, J., Smith, B. L., Angle, N., Knecht, A., et al. (2004). A novel missense mutation in the sodium bicarbonate cotransporter (NBCe1/SLC4A4) causes proximal tubular acidosis and glaucoma through ion transport defects. *J. Biol. Chem.* 279, 52238–52246. doi: 10.1074/jbc.m406591200

Doucet-Beaupré, H., Ang, S.-L., and Lévesque, M. (2015). Cell fate determination, neuronal maintenance and disease state: The emerging role of transcription factors Lmx1a and Lmx1b. *FEBS Lett.* 589, 3727–3738. doi: 10.1016/j.febslet.2015.10.020

Durruthy-Durruthy, R., Gottlieb, A., Hartman, B. H., Waldhaus, J., Laske, R. D., Altman, R., et al. (2014). Reconstruction of the mouse otocyst and early neuroblast lineage at single-cell resolution. *Cell* 157, 964–978. doi: 10.1016/j.cell.2014.03.036

Fetoni, A. R., Lattanzi, W., Eramo, S. L. M., Barba, M., Paciello, F., Moriconi, C., et al. (2014). Grafting and early expression of growth factors from adipose-derived stem cells transplanted into the cochlea, in a guinea pig model of acoustic trauma. *Front. Cell. Neurosci.* 8:334. doi: 10.3389/fncel.2014.00334

Froud, K. E., Wong, A. C. Y., Cederholm, J. M. E., Klugmann, M., Sandow, S. L., Julien, J.-P., et al. (2015). Type II spiral ganglion afferent neurons drive medial olivocochlear reflex suppression of the cochlear amplifier. *Nat. Commun.* 6:7115. doi: 10.1038/ncomms8115

Fryatt, A. G., Vial, C., Mulheran, M., Gunthorpe, M. J., and Grubb, B. D. (2009). Voltage-gated sodium channel expression in rat spiral ganglion neurons. *Mol. Cell. Neurosci.* 42, 399–407. doi: 10.1016/j.mcn.2009.09.001

Funa, K., and Sasahara, M. (2014). The roles of PDGF in development and during neurogenesis in the normal and diseased nervous system. *J. Neuroimmune Pharmacol.* 9, 168–181. doi: 10.1007/s11481-013-9479-z

Goetz, J. J., Farris, C., Chowdhury, R., and Trimarchi, J. M. (2014). Making of a retinal cell: insights into retinal cell-fate determination. *Int. Rev. Cell Mol. Biol.* 308, 273–321. doi: 10.1016/B978-0-12-800097-7.00007-5

Granados-Fuentes, D., Norris, A. J., Carrasquillo, Y., Nerbonne, J. M., and Herzog, E. D. (2012). IA channels encoded by Kv1.4 and Kv4.2 regulate neuronal firing in the suprachiasmatic nucleus and circadian rhythms in locomotor activity. *J. Neurosci.* 32, 10045–10052. doi: 10.1523/JNEUROSCI.0174-12.2012

Guaiquil, V. H., Pan, Z., Karagianni, N., Fukuoka, S., Alegre, G., and Rosenblatt, M. I. (2014). VEGF-B selectively regenerates injured peripheral neurons and restores sensory and trophic functions. *Proc. Natl. Acad. Sci. U S A* 111, 17272–17277. doi: 10.1073/pnas.1407227111

Hafidi, A., Després, G., and Romand, R. (1993). Ontogenesis of type II spiral ganglion neurons during development: peripherin immunohistochemistry. *Int. J. Dev. Neurosci.* 11, 507–512. doi: 10.1016/0736-5748(93)90024-8

Herholt, A., Brankatschk, B., Kannaiyan, N., Papiol, S., Wichert, S. P., Wehr, M. C., et al. (2018). Pathway sensor-based functional genomics screening identifies modulators of neuronal activity. *Sci. Rep.* 8:17597. doi: 10.1038/s41598-018-36008-9

Hu, H.-J., Alter, B. J., Carrasquillo, Y., Qiu, C.-S., and Gereau, R. W. (2007). Metabotropic glutamate receptor 5 modulates nociceptive plasticity *via* extracellular signal-regulated kinase-Kv4.2 signaling in spinal cord dorsal horn neurons. *J. Neurosci.* 27, 13181–13191. doi: 10.1523/JNEUROSCI.0269-07.2007

Huang, Y., Hill, J., Yatteau, A., Wong, L., Jiang, T., Petrovic, J., et al. (2018). Reciprocal negative regulation between lmx1a and Lmo4 is required for inner ear formation. *J. Neurosci.* 38, 5429–5440. doi: 10.1523/JNEUROSCI.2484-17.2018

Huang, L., Hu, F., Feng, L., Luo, X.-J., Liang, G., Zeng, X.-Y., et al. (2014). Bhlhb5 is required for the subtype development of retinal amacrine and bipolar cells in mice. *Dev. Dyn.* 243, 279–289. doi: 10.1002/dvdy.24067

Jun, K., Piedras-Rentería, E. S., Smith, S. M., Wheeler, D. B., Lee, S. B., Lee, T. G., et al. (1999). Ablation of P/Q-type Ca^{2+} channel currents, altered synaptic transmission, and progressive ataxia in mice lacking the α_{1A}-subunit. *Proc. Natl. Acad. Sci. U S A* 96, 15245–15250. doi: 10.1073/pnas.96.26.15245

Jung, J. S., Zhang, K. D., Wang, Z., McMurray, M., Tkaczuk, A., Ogawa, Y., et al. (2019). Semaphorin-5B controls spiral ganglion neuron branch refinement during development. *J. Neurosci.* 39, 6425–6438. doi: 10.1523/JNEUROSCI.0113-19.2019

Katayama, K., Imai, F., Suto, F., and Yoshida, Y. (2013). Deletion of Sema3a or plexinA1/plexinA3 causes defects in sensory afferent projections of statoacoustic ganglion neurons. *PLoS One* 8:e72512. doi: 10.1371/journal.pone.0072512

Kee, N., Volakakis, N., Kirkeby, A., Dahl, L., Storvall, H., Nolbrant, S., et al. (2017). Single-cell analysis reveals a close relationship between differentiating dopamine and subthalamic nucleus neuronal lineages. *Cell Stem Cell* 20, 29–40. doi: 10.1016/j.stem.2016.10.003

Kim, Y.-H., and Holt, J. R. (2013). Functional contributions of HCN channels in the primary auditory neurons of the mouse inner ear. *J. Gen. Physiol.* 142, 207–223. doi: 10.1085/jgp.201311019

Kok, C., Kennerson, M. L., Spring, P. J., Ing, A. J., Pollard, J. D., and Nicholson, G. A. (2003). A locus for hereditary sensory neuropathy with cough

and gastroesophageal reflux on chromosome 3p22–p24. *Am. J. Hum. Genet.* 73, 632–637. doi: 10.1086/377591

Konířová, J., Oltová, J., Corlett, A., Kopycińska, J., Kolář, M., Bartněk, P., et al. (2017). Modulated DISP3/PTCHD2 expression influences neural stem cell fate decisions. *Sci. Rep.* 7:41597. doi: 10.1038/srep41597

Koo, S. K., Hill, J. K., Hwang, C. H., Lin, Z., Millen, K. J., and Wu, D. K. (2009). Lmx1a maintains proper neurogenic, sensory, and nonsensory domains in the mammalian inner ear. *Dev. Biol.* 333, 14–25. doi: 10.1016/j.ydbio.2009.06.016

Kujawa, S. G., and Liberman, M. C. (2015). Synaptopathy in the noise-exposed and aging cochlea: primary neural degeneration in acquired sensorineural hearing loss. *Hear. Res.* 330, 191–199. doi: 10.1016/j.heares.2015.02.009

Liu, Q., Lee, E., and Davis, R. L. (2014). Heterogeneous intrinsic excitability of murine spiral ganglion neurons is determined by Kv1 and HCN channels. *Neuroscience* 257, 96–110. doi: 10.1016/j.neuroscience.2013.10.065

Lu, C. C., Appler, J. M., Houseman, E. A., and Goodrich, L. V. (2011). Developmental profiling of spiral ganglion neurons reveals insights into auditory circuit assembly. *J. Neurosci.* 31, 10903–10918. doi: 10.1523/JNEUROSCI.2358-11.2011

Lv, P., Kim, H. J., Lee, J.-H., Sihn, C.-R., Gharaie, S. F., Mousavi-Nik, A., et al. (2014). Genetic, cellular and functional evidence for Ca^{2+} inflow through $Ca_v1.2$ and $Ca_v1.3$ channels in murine spiral ganglion neurons. *J. Neurosci.* 34, 7383–7393. doi: 10.1523/JNEUROSCI.5416-13.2014

Lv, P., Sihn, C.-R., Wang, W., Shen, H., Kim, H. J., Rocha-Sanchez, S. M., et al. (2012). Posthearing Ca^{2+} currents and their roles in shaping the different modes of firing of spiral ganglion neurons. *J. Neurosci.* 32, 16314–16330. doi: 10.1523/JNEUROSCI.2097-12.2012

McInnes, L., Healy, J., and Astels, S. (2017). hdbscan: hierarchical density based clustering. *J. Open Source Softw.* 2:205. doi: 10.21105/joss.00205

McInnes, L., Healy, J., and Melville, J. (2018). UMAP: uniform manifold approximation and projection for dimension reduction. *ArXiv180203426 Cs Stat*. Available online at: http://arxiv.org/abs/1802.03426. Accessed September 24, 2019.

McLenachan, S., Goldshmit, Y., Fowler, K. J., Voullaire, L., Holloway, T. P., Turnley, A. M., et al. (2008). Transgenic mice expressing the Peripherin-EGFP genomic reporter display intrinsic peripheral nervous system fluorescence. *Transgenic Res.* 17, 1103–1116. doi: 10.1007/s11248-008-9210-7

Mendus, D., Sundaresan, S., Grillet, N., Wangsawihardja, F., Leu, R., Müller, U., et al. (2014). Thrombospondins 1 and 2 are important for afferent synapse formation and function in the inner ear. *Eur. J. Neurosci.* 39, 1256–1267. doi: 10.1111/ejn.12486

Millonig, J. H., Millen, K. J., and Hatten, M. E. (2000). The mouse Dreher gene Lmx1a controls formation of the roof plate in the vertebrate CNS. *Nature* 403, 764–769. doi: 10.1038/35001573

Mo, Z.-L., and Davis, R. L. (1997). Heterogeneous voltage dependence of inward rectifier currents in spiral ganglion neurons. *J. Neurophysiol.* 78, 3019–3027. doi: 10.1152/jn.1997.78.6.3019

Munnamalai, V., and Fekete, D. M. (2013). Wnt signaling during cochlear development. *Semin. Cell Dev. Biol.* 24, 480–489. doi: 10.1016/j.semcdb.2013.03.008

Nayagam, B. A., Muniak, M. A., and Ryugo, D. K. (2011). The spiral ganglion: connecting the peripheral and central auditory systems. *Hear. Res.* 278, 2–20. doi: 10.1016/j.heares.2011.04.003

Nichols, D. H., Pauley, S., Jahan, I., Beisel, K. W., Millen, K. J., and Fritzsch, B. (2008). Lmx1a is required for segregation of sensory epithelia and normal ear histogenesis and morphogenesis. *Cell Tissue Res.* 334, 339–358. doi: 10.1007/s00441-008-0709-2

Pagani, R., Song, M., McEnery, M., Qin, N., Tsien, R. W., Toro, L., et al. (2004). Differential expression of α1 and β subunits of voltage dependent Ca^{2+} channel at the neuromuscular junction of normal and p/q Ca^{2+} channel knockout mouse. *Neuroscience* 123, 75–85. doi: 10.1016/j.neuroscience.2003.09.019

Paz, J. T., Bryant, A. S., Peng, K., Fenno, L., Yizhar, O., Frankel, W. N., et al. (2011). A new mode of corticothalamic transmission revealed in the $Gria4^{-/-}$ model of absence epilepsy. *Nat. Neurosci.* 14, 1167–1173. doi: 10.1038/nn.2896

Petitpré, C., Wu, H., Sharma, A., Tokarska, A., Fontanet, P., Wang, Y., et al. (2018). Neuronal heterogeneity and stereotyped connectivity in the auditory afferent system. *Nat. Commun.* 9:3691. doi: 10.1038/s41467-018-06033-3

Qian, D., Jones, C., Rzadzinska, A., Mark, S., Zhang, X., Steel, K. P., et al. (2007). Wnt5a functions in planar cell polarity regulation in mice. *Dev. Biol.* 306, 121–133. doi: 10.1016/j.ydbio.2007.03.011

Rétaux, S., and Bachy, I. (2002). A short history of LIM domains (1993–2002): from protein interaction to degradation. *Mol. Neurobiol.* 26, 269–281. doi: 10.1385/mn:26:2-3:269

Royeck, M., Horstmann, M.-T., Remy, S., Reitze, M., Yaari, Y., and Beck, H. (2008). Role of axonal NaV1.6 sodium channels in action potential initiation of CA1 pyramidal neurons. *J. Neurophysiol.* 100, 2361–2380. doi: 10.1152/jn.90332.2008

Sadakata, T., Mizoguchi, A., Sato, Y., Katoh-Semba, R., Fukuda, M., Mikoshiba, K., et al. (2004). The secretory granule-associated protein CAPS2 regulates neurotrophin release and cell survival. *J. Neurosci.* 24, 43–52. doi: 10.1523/JNEUROSCI.2528-03.2004

Sadakata, T., Shinoda, Y., Sato, A., Iguchi, H., Ishii, C., Matsuo, M., et al. (2013). Mouse models of mutations and variations in autism spectrum disorder-associated genes: mice expressing *Caps2/Cadps2* copy number and alternative splicing variants. *Int. J. Environ. Res. Public Health* 10, 6335–6353. doi: 10.3390/ijerph10126335

Sadakata, T., Washida, M., Iwayama, Y., Shoji, S., Sato, Y., Ohkura, T., et al. (2007). Autistic-like phenotypes in Cadps2-knockout mice and aberrant CADPS2 splicing in autistic patients. *J. Clin. Invest.* 117, 931–943. doi: 10.1172/JCI29031

Schimmang, T., Tan, J., Müller, M., Zimmermann, U., Rohbock, K., Köpschall, I., et al. (2003). Lack of Bdnf and TrkB signalling in the postnatal cochlea leads to a spatial reshaping of innervation along the tonotopic axis and hearing loss. *Development* 130, 4741–4750. doi: 10.1242/dev.00676

Schrauwen, I., Chakchouk, I., Liaqat, K., Jan, A., Nasir, A., Hussain, S., et al. (2018). A variant in LMX1A causes autosomal recessive severe-to-profound hearing impairment. *Hum. Genet.* 137, 471–478. doi: 10.1007/s00439-018-1899-7

Schwander, M., Sczaniecka, A., Grillet, N., Bailey, J. S., Avenarius, M., Najmabadi, H., et al. (2007). A forward genetics screen in mice identifies recessive deafness traits and reveals that pejvakin is essential for outer hair cell function. *J. Neurosci.* 27, 2163–2175. doi: 10.1523/JNEUROSCI.4975-06.2007

Shibata, R., Nakahira, K., Shibasaki, K., Wakazono, Y., Imoto, K., and Ikenaka, K. (2000). A-type K^+ current mediated by the Kv4 channel regulates the generation of action potential in developing cerebellar granule cells. *J. Neurosci.* 20, 4145–4155. doi: 10.1523/JNEUROSCI.20-11-04145.2000

Shinoda, Y., Sadakata, T., Nakao, K., Katoh-Semba, R., Kinameri, E., Furuya, A., et al. (2011). Calcium-dependent activator protein for secretion 2 (CAPS2) promotes BDNF secretion and is critical for the development of GABAergic interneuron network. *Proc. Natl. Acad. Sci. U S A* 108, 373–378. doi: 10.1073/pnas.1012220108

Shrestha, B. R., Chia, C., Wu, L., Kujawa, S. G., Liberman, M. C., and Goodrich, L. V. (2018). Sensory neuron diversity in the inner ear is shaped by activity. *Cell* 174, 1229.e17–1246.e17. doi: 10.1016/j.cell.2018.07.007

Stephani, F., Scheuer, V., Eckrich, T., Blum, K., Wang, W., Obermair, G. J., et al. (2019). Deletion of the Ca^{2+} channel subunit $\alpha_2\delta3$ differentially affects $Ca_v2.1$ and $Ca_v2.2$ currents in cultured spiral ganglion neurons before and after the onset of hearing. *Front. Cell. Neurosci.* 13:278. doi: 10.3389/fncel.2019.00278

Sun, S., Babola, T., Pregernig, G., So, K. S., Nguyen, M., Su, S.-S. M., et al. (2018). Hair cell mechanotransduction regulates spontaneous activity and spiral ganglion subtype specification in the auditory system. *Cell* 174, 1247.e15–1263.e15. doi: 10.1016/j.cell.2018.07.008

Taberner, A. M., and Liberman, M. C. (2005). Response properties of single auditory nerve fibers in the mouse. *J. Neurophysiol.* 93, 557–569. doi: 10.1152/jn.00574.2004

Tibshirani, R., Walther, G., and Hastie, T. (2001). Estimating the number of clusters in a data set *via* the gap statistic. *J. R. Stat. Soc. Ser. B Stat. Methodol.* 63, 411–423. doi: 10.1111/1467-9868.00293

Waldhaus, J., Durruthy-Durruthy, R., and Heller, S. (2015). Quantitative high-resolution cellular map of the organ of corti. *Cell Rep.* 11, 1385–1399. doi: 10.1016/j.celrep.2015.04.062

Wang, F., Flanagan, J., Su, N., Wang, L.-C., Bui, S., Nielson, A., et al. (2012). RNAscope: a novel in situ RNA analysis platform for formalin-fixed, paraffin-embedded tissues. *J. Mol. Diagn.* 14, 22–29. doi: 10.1016/j.jmoldx.2011.08.002

Weiss, N., and Zamponi, G. W. (2013). Control of low-threshold exocytosis by T-type calcium channels. *Biochim. Biophys. Acta* 1828, 1579–1586. doi: 10.1016/j.bbamem.2012.07.031

Welker, C., and Woolsey, T. A. (1974). Structure of layer IV in the somatosensory neocortex of the rat: description and comparison with the mouse. *J. Comp. Neurol.* 158, 437–453. doi: 10.1002/cne.901580405

Wesdorp, M., de Koning Gans, P. A. M., Schraders, M., Oostrik, J., Huynen, M. A., Venselaar, H., et al. (2018). Heterozygous missense variants of LMX1A lead to nonsyndromic hearing impairment and vestibular dysfunction. *Hum. Genet.* 137, 389–400. doi: 10.1007/s00439-018-1880-5

Yan, C. H., Levesque, M., Claxton, S., Johnson, R. L., and Ang, S.-L. (2011). Lmx1a and Lmx1b function cooperatively to regulate proliferation, specification, and differentiation of midbrain dopaminergic progenitors. *J. Neurosci.* 31, 12413–12425. doi: 10.1523/JNEUROSCI.1077-11.2011

Conflict of Interest: The authors declare that the research was conducted in the absence of any commercial or financial relationships that could be construed as a potential conflict of interest.

frontiers in Molecular Neuroscience

CORRECTION
published: 05 May 2021
doi: 10.3389/fnmol.2021.686790

Corrigendum: Single-Cell RNA Analysis of Type I Spiral Ganglion Neurons Reveals a *Lmx1a* Population in the Cochlea

Fiorella Carla Grandi[1], *Lara De Tomasi*[2] *and Mirna Mustapha*[2,3]*

[1] Cancer Biology Program, Stanford University, Stanford, CA, United States, [2] Department of Biomedical Science, University of Sheffield, Sheffield, United Kingdom, [3] Department of Otolaryngology-Head and Neck Surgery, Stanford University School of Medicine, Stanford, CA, United States

Keywords: type I spiral ganglion neurons, single-cell transcriptome, *Lmx1a*, development, cochlea

OPEN ACCESS

Approved by:
Frontiers Editorial Office, Frontiers Media SA, Switzerland

***Correspondence:**
Mirna Mustapha
mirna.m@sheffield.ac.uk

Specialty section:
This article was submitted to Molecular Neuroscience Archive, a section of the journal Frontiers in Molecular Neuroscience

Received: *27 March 2021*
Accepted: *01 April 2021*
Published: *05 May 2021*

Citation:
Grandi FC, De Tomasi L and Mustapha M (2021) Corrigendum: Single-Cell RNA Analysis of Type I Spiral Ganglion Neurons Reveals a Lmx1a Population in the Cochlea. Front. Mol. Neurosci. 14:686790. doi: 10.3389/fnmol.2021.686790

A Corrigendum on

Single-Cell RNA Analysis of Type I Spiral Ganglion Neurons Reveals a *Lmx1a* Population in the Cochlea

by Grandi, F. C., De Tomasi, L., and Mustapha, M. (2020). Front. Mol. Neurosci. 13:83. doi: 10.3389/fnmol.2020.00083

In the original article, there was an error. Dr. Gopal Pramanik was acknowledged without his agreement. As per his request, we are removing his name and contribution from the acknowledgment paragraph.

A correction has been made to the *Acknowledgments*. The corrected paragraph is shown below.

"We sincerely thank Drs. Stefan Heller and Marta Milo for help with data analysis, and Dr. Walter Marcotti for helpful discussion. We also thank Dr. Kathleen J. Millen for generously providing the Lmx1a-cre mice and Dr. Theresa Zwingman for answering the many questions we had concerning these mice (Seattle Children's Research Institute Center for Integrative Brain Research, The University of Washington). We thank Dr. Joseph P. Sarsero (Murdoch Children's Research Institute, Australia) for sharing Peripherin-GFP mice with us and Dr. Lin Gan (Flaum Eye Institute, University of Rochester School of Medicine) for sharing Bhlhb5-cre line."

The authors apologize for this error and state that this does not change the scientific conclusions of the article in any way. The original article has been updated.

frontiers in Cellular Neuroscience

ORIGINAL RESEARCH
published: 09 October 2020
doi: 10.3389/fncel.2020.579349

Improved Separation of Odor Responses in Granule Cells of the Olfactory Bulb During Odor Discrimination Learning

Dejuan Wang†, Yang Chen†, Yiling Chen†, Xiaowen Li, Penglai Liu, Zhaoyang Yin and Anan Li**

Jiangsu Key Laboratory of Brain Disease and Bioinformation, Research Center for Biochemistry and Molecular Biology, Xuzhou Medical University, Xuzhou, China

OPEN ACCESS

Edited by:
Jiangteng Lu,
Shanghai Jiao Tong University, China

Reviewed by:
Zhonghua Lu,
Chinese Academy of Sciences (CAS), China
Veronica Egger,
University of Regensburg, Germany
Yiqun Yu,
Fudan University, China

***Correspondence:**
Dejuan Wang
wangdj@xzhmu.edu.cn
Anan Li
anan.li@xzhmu.edu.cn

†These authors have contributed equally to this work

Specialty section:
This article was submitted to Cellular Neurophysiology, a section of the journal Frontiers in Cellular Neuroscience

Received: *02 July 2020*
Accepted: *14 September 2020*
Published: *09 October 2020*

Citation:
Wang D, Chen Y, Chen Y, Li X, Liu P, Yin Z and Li A (2020) Improved Separation of Odor Responses in Granule Cells of the Olfactory Bulb During Odor Discrimination Learning. Front. Cell. Neurosci. 14:579349. doi: 10.3389/fncel.2020.579349

In the olfactory bulb, olfactory information is translated into ensemble representations by mitral/tufted cells, and these representations change dynamically in a context-dependent manner. In particular, odor representations in mitral/tufted cells display pattern separation during odor discrimination learning. Although granule cells provide major inhibitory input to mitral/tufted cells and play an important role in pattern separation and olfactory learning, the dynamics of odor responses in granule cells during odor discrimination learning remain largely unknown. Here, we studied odor responses in granule cells of the olfactory bulb using fiber photometry recordings in awake behaving mice. We found that odors evoked reliable, excitatory responses in the granule cell population. Intriguingly, during odor discrimination learning, odor responses in granule cells exhibited improved separation and contained information about odor value. In conclusion, we show that granule cells in the olfactory bulb display learning-related plasticity, suggesting that they may mediate pattern separation in mitral/tufted cells.

Keywords: granule cells, fiber photometry, odor representation, go/no go, go/go

INTRODUCTION

Interpreting the dynamic environment precisely to facilitate appropriate behavior is crucial for animal survival. To accomplish this complex task, sensory systems in the brain encode dynamic information in the activity of neuronal ensembles. Such representations in the sensory system form an important constituent of information processing in the brain (Andermann et al., 2010; Komiyama et al., 2010; Harvey et al., 2012; Huber et al., 2012; Kato et al., 2015). As the first processing center in the olfactory system, the olfactory bulb (OB) plays an important role in odor detection and discrimination (Wilson et al., 2017; Chong and Rinberg, 2018; Li et al., 2020). Odor representation in the OB is highly dynamic and is modulated by various types of olfactory experience (Kass et al., 2013; Abraham et al., 2014; Kass et al., 2016; Hu et al., 2020b; Li et al., 2020). Previous studies have established that odor representations in OB output neurons (mitral/tufted cells, M/T cells) display improved pattern separation during active odor discrimination learning

(Nunez-Parra et al., 2014; Yamada et al., 2017; Wang et al., 2019) when mice have learned to discriminate two odors, the representation of those odors in M/T cells becomes more divergent. This process is thought to convey information about odor value and improve odor discrimination learning (Nunez-Parra et al., 2014; Li et al., 2015). Nevertheless, it remains unknown how pattern separation in M/T cells arises.

Pattern separation could arise from the native OB network during odor discrimination learning. In the OB, olfactory information relayed by the olfactory sensory neurons (OSNs) is transmitted to M/T cells, which in turn send their axons to higher brain areas (Uchida et al., 2014; Vaaga and Westbrook, 2016). Studies have shown a lack of odor experience-dependent plasticity and learning-related pattern separation in the OSN input (Kato et al., 2012; Chu et al., 2017), indicating that pattern separation in M/T cells is not inherited from changes in the OSN inputs to the OB. Rather, it may be due to plasticity downstream of the OSN inputs, e.g., within the synaptic interactions with the interneurons in the OB. The activity of M/T cells is extensively modified by dynamic interactions with GABAergic and dopaminergic interneurons within the OB (Burton, 2017). These interneurons form both dendro-dendritic reciprocal synapses and axo-dendritic synapses with M/T cells and mediate lateral and recurrent inhibition onto M/T cells (Margrie et al., 2001; Aungst et al., 2003; Hu et al., 2017, 2020a), which play a major role in transforming odor representations (Nusser et al., 2001; McGann, 2013). Previous studies have shown that odor enrichment can induce response changes in the inhibitory interneurons of the OB (Mandairon et al., 2008) and that GABAergic inhibition onto M/T cells is crucial for pattern separation and odor discrimination (Abraham et al., 2010; Godde et al., 2016).

Granule cells (GCs) are a major class of GABAergic interneurons in the OB and provide feedback inhibition to M/T cells through reciprocal dendrodendritic synapses (Isaacson and Strowbridge, 1998; Abraham et al., 2010). Importantly, GCs not only regulate OB output to other brain regions but also mediate top-down modulation of sensory processing in the OB (Boyd et al., 2012; Nunez-Parra et al., 2013). Previous studies have shown that GCs exhibit strong odor responses and impose a sparse and temporally dynamic structure on the ensemble activity of M/T cells (Kato et al., 2012; Cazakoff et al., 2014). Exciting or inhibiting GCs in the OB bidirectionally alters pattern separation in the M/T cells and olfactory discrimination (Gschwend et al., 2015; Nunes and Kuner, 2015). The important role of GCs in pattern separation raises the possibility that GCs may mediate pattern separation in M/T cells. However, little is known about how odor responses in OB GCs change during odor discrimination learning.

In this study, we used fiber photometry to characterize the activity of the GCs population in awake behaving mice engaged in an odor discrimination task. We found that odor responses in GCs were excitatory and reliable. When mice were proficient in the discrimination task, odor responses in GCs exhibited improved separation, suggesting that odor responses of GCs in the OB display context-dependent plasticity and contain information about odor value.

MATERIALS AND METHODS

Animals

C57BL/6J male mice aged 10–14 weeks old were used for fiber photometry recordings. Before surgery, mice were housed under a 12/12 h light/dark cycle and housed in groups. After surgery, they were housed individually for at least 2 weeks for recovery before further experiments. All mice were given *ad libitum* access to chow and water except during the behavioral sessions. During the behavioral sessions, mice were weighed daily and received sufficient water to maintain > 80% of their pre-water-restriction weight. Animal care and use conformed to protocols submitted to and approved by the Xuzhou Medical University Institutional Animal Care and Use Committee.

Virus Injection and Fiber Implant

We used the genetically encoded Ca^{2+} indicator GCaMP6s to monitor the activity of neurons. EGFP-expressing animals were used as controls for comparison with GCaMP6s-expressing animals. AAVs used in this study, including AAV-VGAT1-Cre (AAV2/9, 5.26 × e+12 vg/mL), AAV-DIO-GCaMP6s (AAV2/9, 5.33 × e+12 vg/mL), and AAV-DIO-EGFP (AAV2/9, 4.98 × e+12 vg/mL) were purchased from BrainVTA (Wuhan, China). For targeted viral delivery, mice were fixed in a stereotactic frame (RWD, Shenzhen, China) under pentobarbital sodium anesthesia (i.p. 90 mg/kg). A small craniotomy was made and a calibrated pulled-glass pipette (Sutter Instrument) was lowered to the OB (coordinates 4.28 mm from lambda, 1.00 mm from the midline, and 1.20 mm ventral to lambda). A total volume of 300 nl of virus (AAV-VGAT1-Cre and either AAV-DIO-GCaMP6s or AAV-DIO-EGFP, in a 1:2 mixture) was injected with a microsyringe pump (Stoelting Quintessential Injector) at a rate of 40 nl/min. The injection pipette was left in place for ten additional minutes before being withdrawn slowly.

For optical manipulation, following virus injection mice were implanted with custom-built fiber connectors [0.37 numerical aperture (NA), 200 μm diameter; Newdoon]. The tip of the fiber was lowered to the injection site in the OB. The optical fiber was fixed in place with dental acrylic and a custom-made aluminum head-plate was attached to the skull to enable head-fixation. After surgery, mice were housed individually for at least 2 weeks to allow sufficient time for transgene expression and animal recovery. At the end of the behavioral analyses, we sacrificed the subject mice, performed standard histology, and confirmed the efficiency of both AAV infection and fiber placement.

Fiber Photometry Recording

Fiber photometry was performed using a previously described system (Zhou et al., 2017; Sun et al., 2019; Wang et al., 2019, 2020; Wu et al., 2020). To record fluorescent signals, the beam from a 488 nm laser (OBIS 488LS, Coherent) was reflected by a dichroic mirror (MD498, Thorlabs), focused by an objective lens (10×, NA: 0.3; Olympus), and then coupled to an optical commutator (Doric Lenses). An optical fiber

(200 mm o.d., NA: 0.37, 1.5 m long) coupled the light between the commutator and the implanted optical fiber. GCaMP6s fluorescence was collected by the same fiber and objective, then bandpass-filtered (MF525–39, Thorlabs) and detected by a photomultiplier tube (R3896, Hamamatsu). An amplifier (C7319, Hamamatsu) converted the photomultiplier tube current output to a voltage signal, which was further filtered through a low-pass filter (35 Hz cut-off; Brownlee, 440). The analog voltage signals were digitized at 500 Hz and recorded by fiber photometry software (Thinkerbiotech, Nanjing, China) for the duration of each behavioral session.

Odor Delivery

Odors were dissolved in mineral oil at 1% (v/v) dilution. Similar to our previous studies (Wang et al., 2019; Liu et al., 2020), eight odors that always induce frequent responses were used during passive exposure: isoamyl acetate, 2-heptanone, phenyl acetate, benzaldehyde, dimethylbutyric acid, n-heptane acid, n-pentanol, and 2-pentanone (Sinopharm Chemical Reagent). In the go/no go task, only the first two pairs of odors (isoamyl acetate versus 2-heptanone and phenyl acetate versus benzaldehyde) were used. As in our previous studies (Wang et al., 2019; Liu et al., 2020), isoamyl acetate and phenyl acetate were defined as S+ odors, and 2-heptanone and benzaldehyde as S– odors. Odors were presented by an odor delivery system (Thinkerbiotech, Nanjing, China). A stream of charcoal-filtered air flowed over the oil and was then diluted to 1/20 by an olfactometer. Odor presentation was synchronously controlled by the data acquisition system via a solenoid valve driven by a digital-to-analog converter. Air or odorized air was delivered at a constant rate of 1 l/min to eliminate the effect of airflow. The duration of each odor presentation was 2 s and the inter-trial interval was 30 s.

Overview of Training and Behavioral Tasks

After recovering from surgery, mice were head-fixed with two horizontal bars but were able to maneuver on an air-supported free-floating Styrofoam ball (**Figure 4A**). During passive exposure, the eight odorants were delivered randomly, with 15 trials for each odorant. Before starting the behavioral tasks (a go/go task and a go/no go task), mice were water restricted and their weight was maintained at 80–85% of their initial weight. During the behavioral task, mice performed daily sessions that lasted 200 trials, or until the mouse disengaged, whichever came first. On each trial, one of two odorants was pseudorandomly delivered (maximum of two trials in a row with the same odorant). Each trial consisted of a 2 s odorant delivery period, followed by a 0.5 s answer period, during which the mouse could choose whether or not to lick a lickport (**Figure 4B**). Mice were trained to perform a go/go task during which a water reward was delivered from the lick-port when either of the odorants was delivered on a trial and the mouse responded by licking the lickport during the answer period. A 15 s inter-trial interval followed the answer period, and there was no punishment on error trials.

Next, the mice were trained to perform a go/no go task in which they were required to discriminate the reinforced odor (S+) from the unreinforced odor (S–) to receive the water reward. In this task, mice learned to lick the lickport when an S+ was presented and to not lick the lickport when an S– was presented. Thus, if an S+ was presented and the mouse responded with licking (Hit), a water reward was delivered through the lickport; if they failed to lick in response to the S+ (Miss) the water reward was not delivered. If an S– was presented, water was never delivered, regardless of the mouse's actions [licking in response to an S– was classed as a false alarm (FA); not licking in response to an S– was classed as a correct rejection (CR); see **Figure 4C**]. Hits and CRs were classed as correct responses, whereas Misses and FAs were classed as incorrect responses. The performance was evaluated in blocks of 20 trials, with 10 S+ and 10 S– trials presented at random. The percentage correct value for each block represents the percentage of trials in which the odors were correctly discriminated and associated with the appropriate behavioral action. Each session included 6–10 blocks of 20 trials. Calcium signals were recorded simultaneously throughout the behavioral tasks.

Immunohistochemistry

For verification of viral expression, frozen brain sections were prepared. The mice were deeply anesthetized with pentobarbital sodium (i.p. 90 mg/kg) and perfused intracardially with 0.9% saline, followed by 4% paraformaldehyde (PFA) in PBS (0.1 M, pH 7.4). The brains were subsequently removed and postfixed in 4% PFA at 4°C overnight. After cryoprotection with 30% (w/v) sucrose, brain tissue was then embedded in OCT compound and coronal sections (30 μm) were cut on a cryostat (Leica CM1860). Sections were incubated with blocking solution (5% normal goat serum, 0.3% Triton X-100 in PBS) and incubated for 2 h at room temperature. Primary antibodies (anti-GAD67, 1:250, MAB5406, Millipore) were diluted in blocking solution and applied overnight at 4°C. Sections were washed three times with PBS and incubated with fluorescent secondary antibodies for 2 h at room temperature. After washing three times in PBS, slides were incubated with DAPI for nuclear staining and coverslipped with a 50% glycerol mounting medium. Images were obtained by confocal scanning microscopy (Zeiss, LSM710) and were processed via ZEN 2011 (Zeiss).

Statistical Analysis

Behavioral Performance

For the go/go and go/no go tasks, the performance in each block was calculated as follows: (number of Hit trials + number of CR trials)/total number of trials, including all Hit, Miss, CR, and FA trials.

Analysis of Fiber Photometry Data

Data were exported as MATLAB .mat files and segmented according to the onset of odor stimulation on individual trials. We derived the values of fluorescence change (ΔF/F) by calculating $(F - F_0)/F_0$, where F_0 is the baseline fluorescent signal averaged over a 5 s long control time window, which

preceded the onset of odor stimulation. Averaged ΔF/F values for 5 s from the onset of odor delivery are presented as heat maps or trial-averaged plots. In the go/go and go/no go tasks, the first 30 trials in the first session were classified as "naïve" trials, and the last 30 trials in the last session were classified as "proficient" trials.

ROC Analysis

Receiver operating characteristic (ROC) analysis was used to assess the classification of the responses evoked by odor pairs. ROCs were estimated using the roc function from the MATLAB exchange. The area under the ROC (auROC) is a nonparametric measure of the discriminability of two distributions. We used auROC to assess the classification of two odors within an odor pair. The area under the ROC curve was defined as ranging from 0.5 to 1.0. A value of 0.5 indicates completely overlapping distributions, whereas a value of 1.0 indicates perfect discriminability.

Calculation of Differences in ΔF/F

We used the difference in ΔF/F to assess the extent of the divergence in the responses to two odors within an odor pair. The responses evoked by the two odors were defined as Res A and Res B, respectively. The difference in ΔF/F was calculated as follows: ABS (Res A—Res B)/Res A, where ABS represents the absolute value and Res A and Res B represent the responses evoked by odor A and odor B, respectively.

All statistical analyses were performed with MATLAB or Prism. The Shapiro-Wilk test was used to assess the normality of the data. We used the Friedman test, Mann-Whitney test, Wilcoxon's sign rank test, and paired *t*-test; all tests were two-sided. All data in the present study are presented as the mean ± SEM.

RESULTS

Excitatory Responses to Odors in GCs Recorded With Fiber Photometry

First, we recorded odor-evoked response profiles in GCs. It is reported that VGAT is expressed in all GABAergic neurons (Vong et al., 2011) and the VGAT-Cre animal line has been used to study the activity of GCs in the OB (Fukunaga et al., 2014; Wienisch and Murthy, 2016). Neuronal activity of GCs was monitored with the genetically encoded Ca^{2+} indicator GCaMP6s in awake head-fixed mice using fiber photometry. GCaMP6s expression was genetically restricted to GCs by injecting a composite virus solution (AAV-VGAT1-Cre and AAV-DIO-GCaMP6s) into the granule cell layer of the OB in C57BL/6J mice (**Figure 1A**). Three weeks after viral injection there was an extensive expression of GCaMP6s in the granule cell layer and the external plexiform layer where the dendrites of granule cells are distributed (**Figures 1B,C**). GCaMP6s fluorescence in the granule cell layer represents expression in GCs while GCaMP6s fluorescence in the mitral cell layer and the external plexiform layer largely reflects dendrites of GCs. GCaMP6s expression was restricted to GCs as shown by colocalization with immunolabeling of GAD67 in the granule cell layer (**Figure 1B**). We observed an increase of Ca^{2+} levels during and after odor application in the GC population of the OB (**Figure 1D**). C57 BL/6J mice injected with a mixture of AAV-VGAT1-Cre and AAV-DIO-EGFP served as controls (**Figures 1E,F**): no calcium signal was detected in these mice (**Figure 1G**, $n = 4$ mice). Thus, this method allowed us to selectively record odor-evoked responses from GCs located beneath the optical fiber.

Previous fiber photometry and two-photon Ca^{2+} imaging studies have shown that M/T cells display both excitatory and inhibitory responses to odors (Yamada et al., 2017; Wang et al., 2019). Unlike M/T cells, GCs showed only increases in Ca^{2+} levels in response to odor delivery (**Figures 2A–C**, from 0.71 to 9.86%, average: 2.94 ± 0.252%, $n = 70$ animal-odor pairs from ten mice). To investigate how GCs respond to different odorants, we compared the odor responses between the different odorants. We found that the averaged ΔF/F was significantly different for different odorants (**Figures 2D,E**, Friedman test, $P = 0.00460$; odor 1 versus odor 4, $P = 0.00106$; odor 4 versus odor 7, $P = 0.0428$). Therefore, different odors induce different excitatory responses in the GC population of the OB.

To further investigate whether odorants are differentially represented in the GC population, we computed the Pearson's correlation coefficient. This measures the similarity between pairs of population vectors constructed from the responses to pairs of different odors. **Figure 3A** shows the odor responses evoked by four different odorants in an individual mouse. We found that the correlation between responses to different odors (between odors) was low (**Figures 3B,C**, $r = 0.252 \pm 0.0595$). To exclude the possibility that recorded differences were caused by the instability of fiber photometry recording, we calculated the correlation coefficient for different trials within individual odorants (within odor) (**Figures 3D–F**, $r = 0.726 \pm 0.0197$). We found that the within-odor correlation coefficients were much larger than the between-odors correlation coefficients (**Figure 3G**, Mann–Whitney test, $P < 0.0001$). These results suggest that odor responses in GCs is different between odors while remaining stable within the same odor. Next, we investigated whether the responses to the same odor were distinct in different animals. We found that the correlation between responses to the same odor in different animals was low (**Figures 3H,I**, $r = 0.0365 \pm 0.0141$). This suggests that the different animals display distinct odor responses recorded with fiber photometry.

Previous studies using two-photon calcium imaging have shown that daily odor experience could induce a gradual weakening of mitral cell activity (Kato et al., 2012; Yamada et al., 2017). We examined whether GC odor responses display such experience-dependent change in response strength over days. We repeated the passive odor application for 7 consecutive days. We observed a slight weakening of odor responses in GCs at days 3 and 4 (**Figures 3J,K**, Friedman test, $P = 0.000164$; day 1 versus day 3, $P = 5.96 \times 10^{-5}$; day 1 versus day 4, $P = 0.0281$). This result suggests that similar to that in mitral

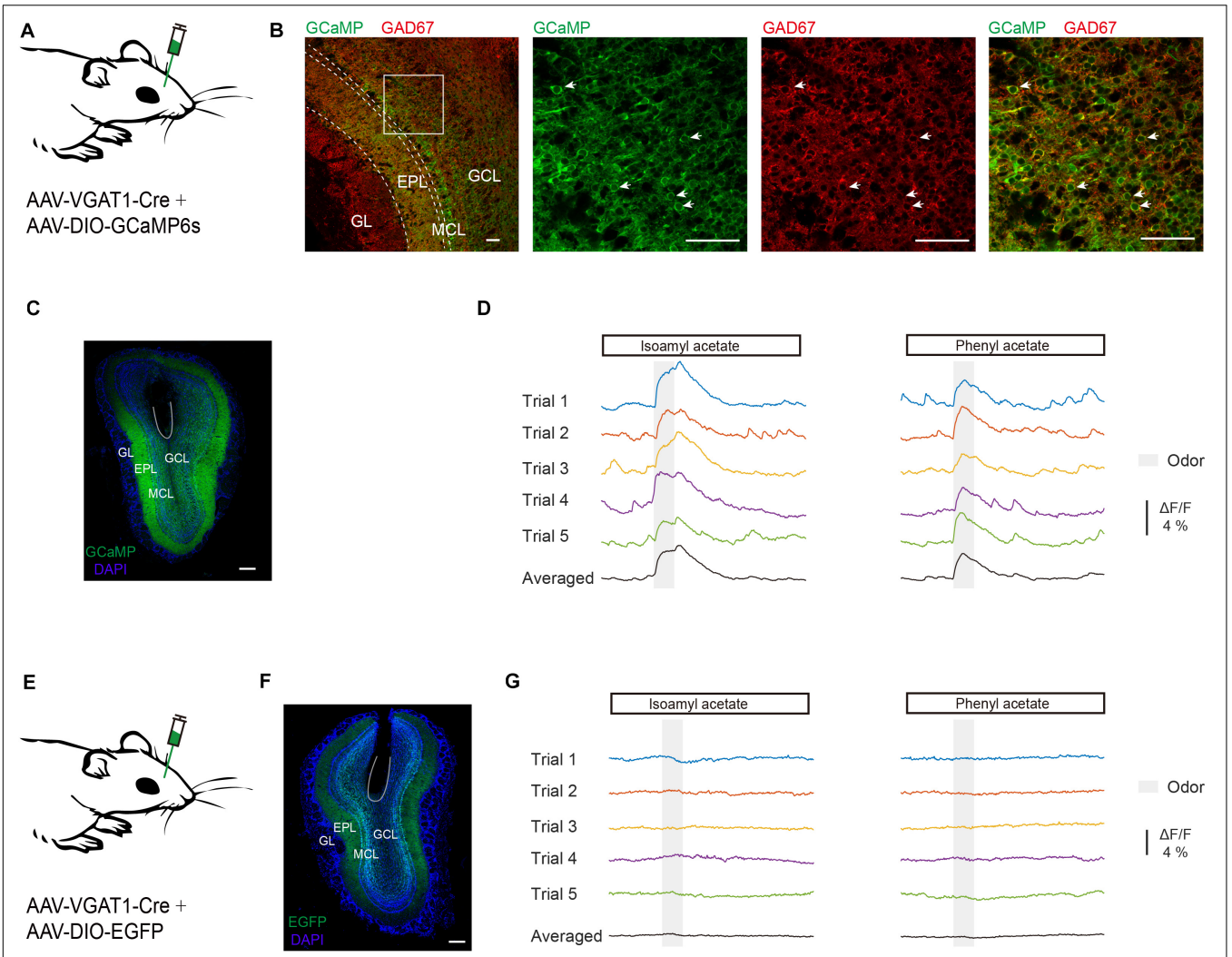

FIGURE 1 | Odor-evoked responses are recorded in GCs of the OB. **(A)** Diagram of virus injection. To record the odor-evoked calcium responses of granule cells, AAV-VGAT1-Cre and AAV-DIO-GCaMP6s were injected into the OB of C57BL/6J mice. **(B)** Expression pattern in the OB following virus injection. Note the dense labeling in the granule cell layer and the external plexiform layer. Expression of GCaMP6s in the granule cell layer co-localizes with immunolabeling of GAD67. GL, Glomerular layer; EPL, external plexiform layer; MCL, mitral cell layer; GCL, granule cell layer. Scale bar = 50 μm. **(C)** Representative viral transduction (GCaMP6s) and fiber location. Expression of GCaMP6s in the OB. Within the OB, GCaMP6s is expressed in the granule cells. Scale bar = 200 μm. **(D)** Typical traces and trial-averaged traces of the calcium responses evoked by isoamyl acetate and phenyl acetate. **(E)** Diagram of virus injection. AAV-VGAT1-Cre and AAV-DIO-EGFP were injected into the OB of C57BL/6J mice. **(F)** Representative viral transduction (EGFP) and fiber location. Scale bar = 200 mm. **(G)** Odors evoked no response in a control mouse.

cells, GC responses also display an experience-dependent change in response strength.

Improved Separation of Odor Responses in GCs After Odor Discrimination Learning

In addition to encoding information about odor identity, M/T cells display enhanced separation of odor representations when animals are learning an odor discrimination task (Nunez-Parra et al., 2014; Yamada et al., 2017; Wang et al., 2019), and GCs play an important role in that separation (Gschwend et al., 2015). We therefore asked whether odor responses in the GC population show increased separation when mice have learned to discriminate a pair of odors. To address this question, mice were trained on a go/no go discrimination task (**Figure 4A**). First, mice underwent a pre-training period to learn a go/go paradigm, in which they were presented with two odorants, both of which were paired with the water reward. Mice were trained to lick the lick-port in response to odorants to obtain the water reward. After reaching the learning threshold in the go/go task (80% correct), mice were then trained to perform a go/no go discrimination task in which they eventually learned to lick in response to the rewarded odorant (S+) to obtain a water reward while refraining from licking to the unrewarded odorant (S–), which was not paired with a water reward (**Figures 4B,C**). Behavioral

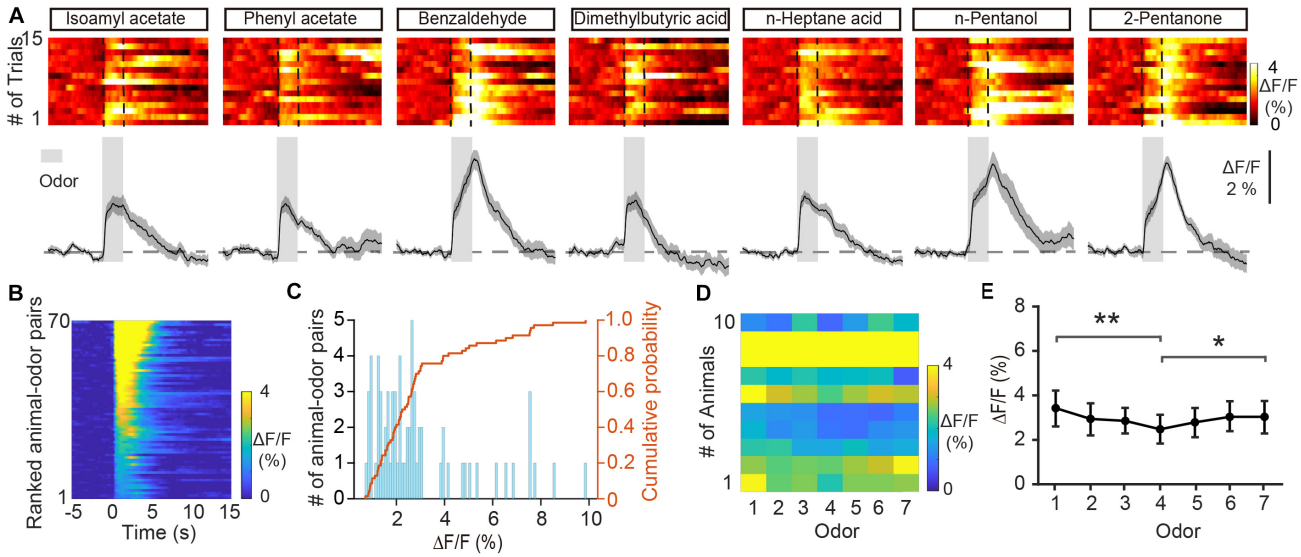

FIGURE 2 | Odor-evoked responses in GCs of the OB are excitatory. **(A)** Trial-to-trial pseudocolored heat maps (top) and trial-averaged traces (bottom) of the calcium responses evoked by different odors. **(B)** Heat maps of ΔF/F averaged across all trials and further averaged across odorants for each mouse, ranked by mean ΔF/F. **(C)** Histograms and cumulative probability of ΔF/F. **(D,E)** Pseudo-color heat-map of ΔF/F **(D)** and averaged ΔF/F **(E)** evoked by different odors. [Friedman test: $\chi^2(6, 54) = 18.8$, $P = 0.0046$, odor 1 versus odor 4, $P = 0.00106$, odor 4 versus odor 7, $P = 0.0428$]. $^*P < 0.05$, $^{**}P < 0.01$.

performance was assessed by calculating the percentage of correct responses to S+ and S– in each 20-trial block with mice completing 6–10 blocks per session. Performance gradually improved over the week-long training period. On the last day of go/no go training, performance improved from near chance levels (50% correct) in Block 1 to well above the learning threshold (80% correct) in Block 6 (**Figure 4D**).

Figure 4E shows odor-evoked responses in GCs from an individual mouse performing the go/no go task. The traces are sorted into trials where the mouse was learning to differentiate the odorants (left, first 30 trials of the first session, naïve) and trials where mice were proficient in discriminating the odorants (right, last 30 trials of the last session, proficient). The difference in odor responses evoked by S+ and S– increased once the mouse had learned to discriminate the odorants (**Figure 4E**). Analysis of ΔF/F evoked by S+ and S– showed that the auROC values were larger during the proficient period than during the naïve period (**Figure 4F**). The separation of odor responses evoked by S+ and S– was observed consistently for other animal-odor pairs. The averaged ΔF/F values during the naïve and proficient periods for all animal-odor pairs (n = 10 animal-odor pairs from nine mice) are shown in **Figure 4G**. Both the auROC values and the difference in ΔF/F increased when mice became proficient in the go/no go task (**Figures 4H–J**, auROC: paired t-test, $P = 0.0118$; difference in ΔF/F: Wilcoxon's sign rank test, $P = 0.00980$). These data demonstrate that odor responses in GCs display enhanced separation after odor discrimination learning. We also analyzed the ΔF/F rise time and half time during the go/no go task and found that there is no significant difference in the auROC values of ΔF/F rise time or half time between the naïve period and proficient period (**Figure 4K**, paired t-test, $P = 0.127$; **Figure 4L**, paired t-test, $P = 0.221$).

Lack of Improved Separation of Odor Responses in GCs During the Go/Go Task

To exclude the possibility that the improved separation in the go/no go task is due to general behavioral state (such as thirst) differences between the naïve period and the proficient period, we compared the odor responses during these two periods in the go/go task where mice also received water and became satiated. **Figure 5A** shows the behavioral performance of all mice performing the go/go task (n = 13 animal-odor pairs from ten mice). Odor responses showed no increase in separation during the proficient period (**Figures 5B–D**). Further analysis indicated that neither the auROC values nor the difference in ΔF/F was significantly different between naïve trials and proficient trials during the go/go task (**Figures 5E–G**, auROC, Wilcoxon's sign rank test, $P = 0.622$, difference in ΔF/F, Wilcoxon's sign rank test, $P = 0.636$). Therefore, the improved separation of odor responses in GCs during the go/no go task is established by learning-related plasticity as opposed to behavioral states.

GCs Encode Odorant Value

Previous studies have shown that both odor-induced oscillations in the OB and odor responses in M/T cells differ between FA and CR trials (Ramirez-Gordillo et al., 2018; Wang et al., 2019), which are incorrect and correct responses to the same odorant (S–), respectively. Using the methods described above, we analyzed GC activity during the Hit, FA, and CR trials in the last session of the go/no go task. **Figure 6A** shows that activity on the CR trials was well separated from activity on both the Hit and FA trials. We then performed an ROC analysis using FA/CR and Hit/CR trials. The auROC was significantly different from zero (the diagonal)

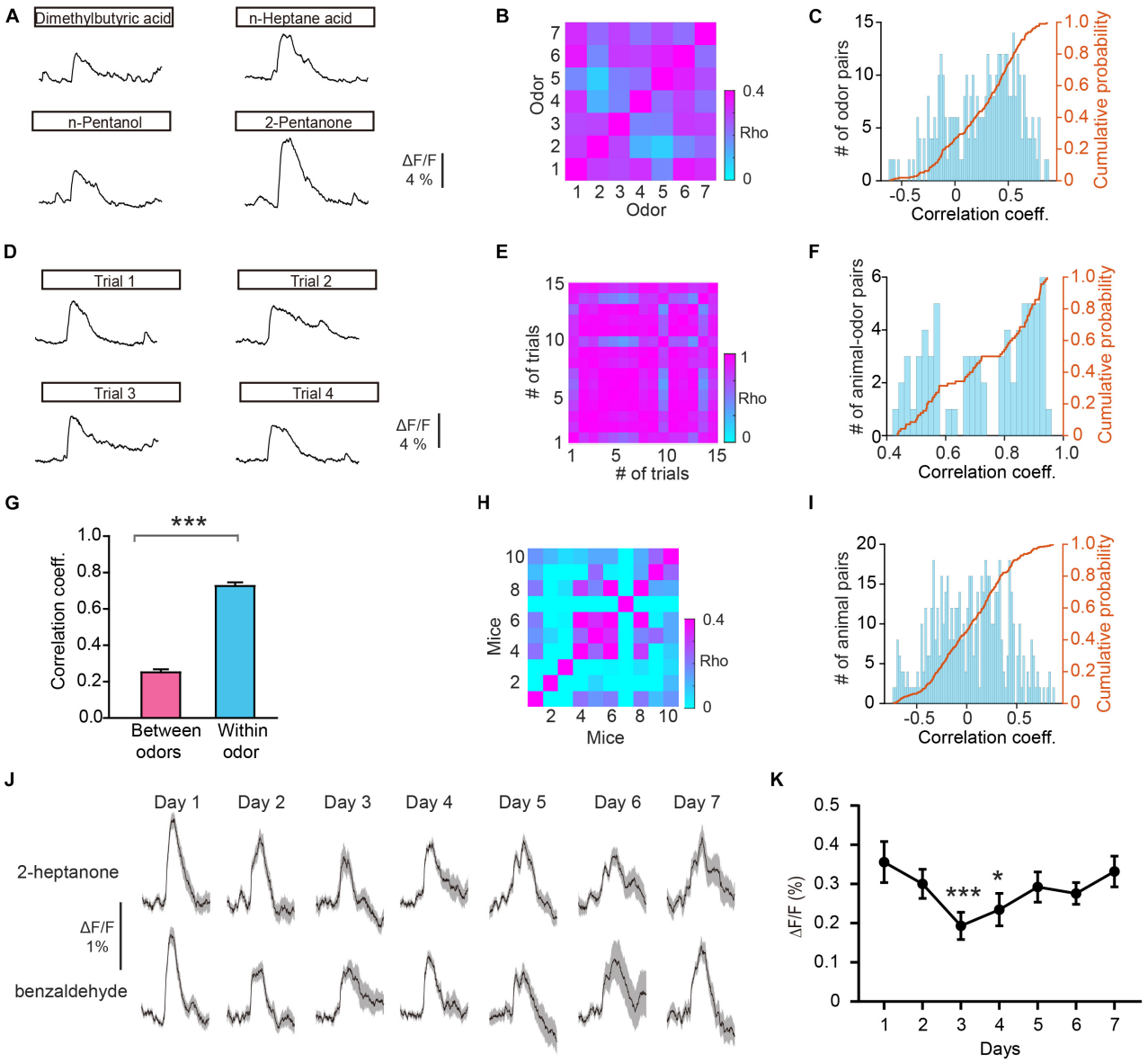

FIGURE 3 | Odor responses differ between odors. **(A)** Odor responses evoked by four odorants in an individual mouse. **(B,C)** Heat map **(B)**, histograms **(C)**, and cumulative probability **(C)** of the correlation coefficients for the ΔF/F induced by different odorants. **(D)** Odor responses evoked by the same odorant (n-Pentanol) in different trials in an individual mouse. **(E,F)** Heat map **(E)**, histograms **(F)**, and cumulative probability **(F)** of the correlation coefficients for the ΔF/F from different trials with the same odorant. **(G)** Comparison of the correlation coefficients for the "between odors" and "within odor" conditions (Mann-Whitney test, U = 2706, $P < 0.0001$). **(H,I)** Heat map **(H)**, histograms **(I)**, and cumulative probability **(I)** of the correlation coefficients for the ΔF/F induced by the same odor in different animals. **(J)** Representative GC odor responses over 7 days of passive exposure. **(K)** Averaged ΔF/F over days. [Friedman test: $\chi^2(6, 138) = 26.7$, $P = 0.000164$, odor 1 versus odor 4, $P = 5.96 \times 10^{-5}$, odor 4 versus odor 7, $P = 0.0281$]. $^*P < 0.05$, $^{***}P < 0.001$.

for both FA/CR and Hit/CR [Hit/CR, $t_{(9)} = 6.13$, $P = 0.0002$; FA/CR, $t_{(9)} = 11.5$, $P < 0.0001$, one-sample t-test, **Figures 6B,C**]. Thus, the calcium signal can distinguish correct (CR) from incorrect (FA) responses relatively well, even though both are responses to the same odorant (S–). This indicates that odor responses in GCs reflect odor value as opposed to odor identity.

To investigate this further, we asked whether GCs display improved separation in the go/go task, in which both odorants delivered are rewarded. To address this, we analyzed data from mice performing the go/go task and then the go/no go task with the same odor pair. As shown in **Figure 6D**, odor responses evoked by the two odors during the proficient period in the go/go task did not display separation. Both the auROC and the difference in ΔF/F were significantly greater in the go/no go task than in the go/go task (**Figures 6E,F**, paired t-test, $P = 0.0146$; **Figure 6G**, Wilcoxon's sign rank test, $P = 0.0273$, $n = 9$ animal-odor pairs from eight mice). In other words, no separation was observed when odorant valences were

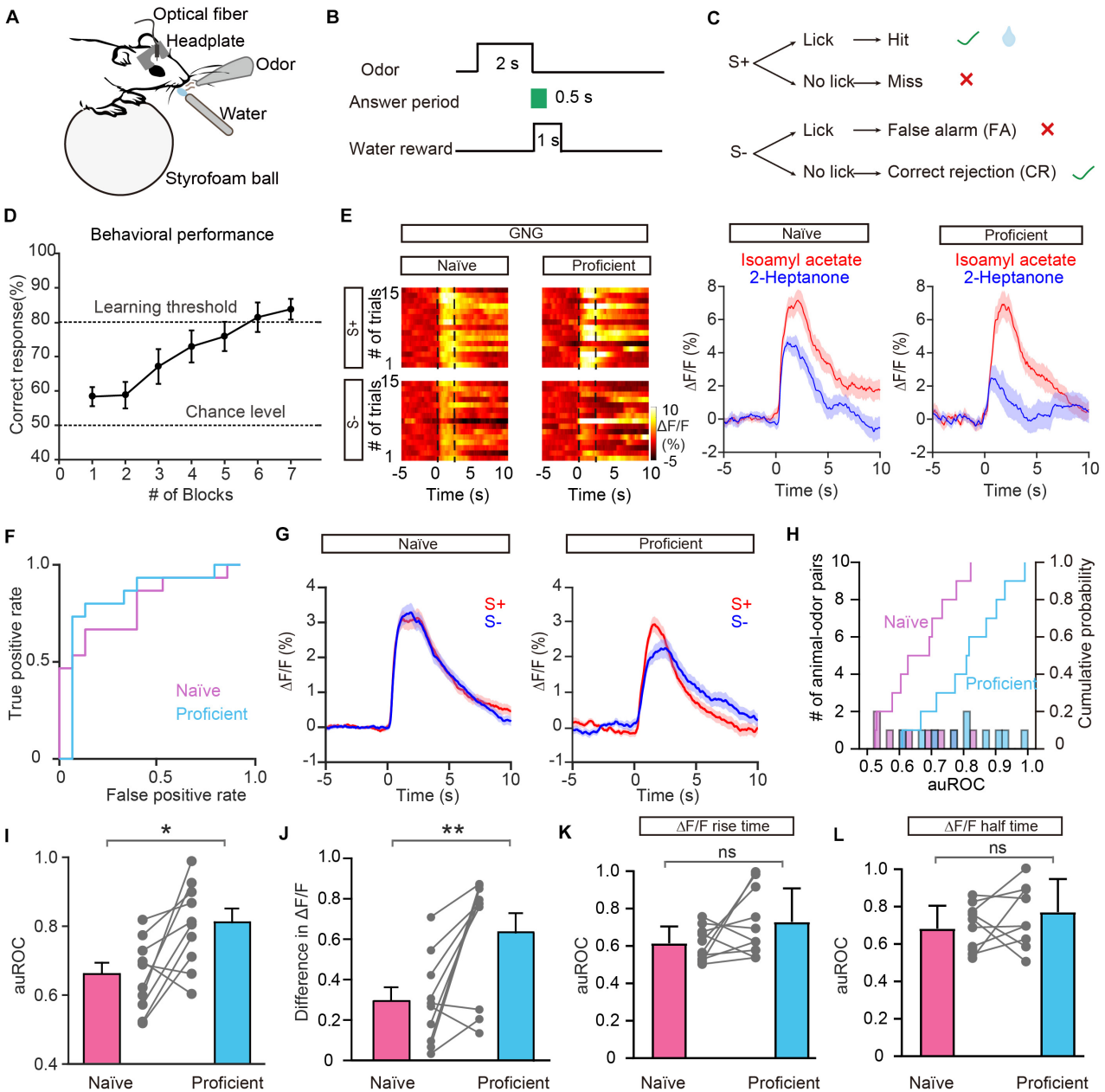

FIGURE 4 | Odor responses in GCs show improved separation in the go/no go (GNG) task. **(A)** Diagram of the experimental set-up. **(B)** Timeline for a single trial. Each trial consisted of a 2 s odorant delivery period, followed by a 0.5 s answer period during which the mouse could choose whether or not to lick a lickport. A water reward was delivered if the stimulus was rewarded (S+) and the mouse licked during the answer period. **(C)** Schematic of behavioral paradigm. If an S+ was presented and the mouse responded with licking, a water reward was delivered. If an S– was delivered, no water reward was delivered regardless of the mouse's actions. **(D)** Odor discrimination performance during the last session in the go/no go task. The mean percentage correct responses are plotted for each block of 20 trials. The chance level and learning threshold are indicated by dashed lines. **(E,F)** Heat maps **(E)**, peri-event plots **(E)**, and ROC graph **(F)** of Ca^{2+} signals from an individual mouse induced by S+ and S– in the naïve stage and in the proficient stage during the go/no go task. **(G)** Averaged traces of odor responses across all animal-odor pairs (n = 10 animal-odor pairs from nine mice). **(H)** Histograms and cumulative probability of auROCs in the naïve stage and the proficient stage. **(I,J)** auROCs **(I)** and difference in ΔF/F **(J)** are larger in the proficient stage than in the naïve stage. [**I:** paired t-test, $t_{(9)} = 3.15$, $P = 0.0118$; **J:** Wilcoxon's sign rank test, $W = -49.0$, $P = 0.00980$.] **(K,L)** Comparison of the auROC values of ΔF/F rise time **(K)** and half time **(L)** between the naïve stage and proficient stage. [**(K)** paired t-test, $t_{(9)} = 1.68$, $P = 0.127$; **(L)** paired t-test, $t_{(9)} = 1.32$, $P = 0.221$]. $^*P < 0.05$, $^{**}P < 0.01$.

the same (in the go/go task) but significant separation was observed when odorant valences were different (in the go/no go task). Therefore, similar to studies showing that odor value is encoded by M/T cell activity (Nunez-Parra et al., 2014; Wang et al., 2019), odor responses in GCs also contain information about odor value.

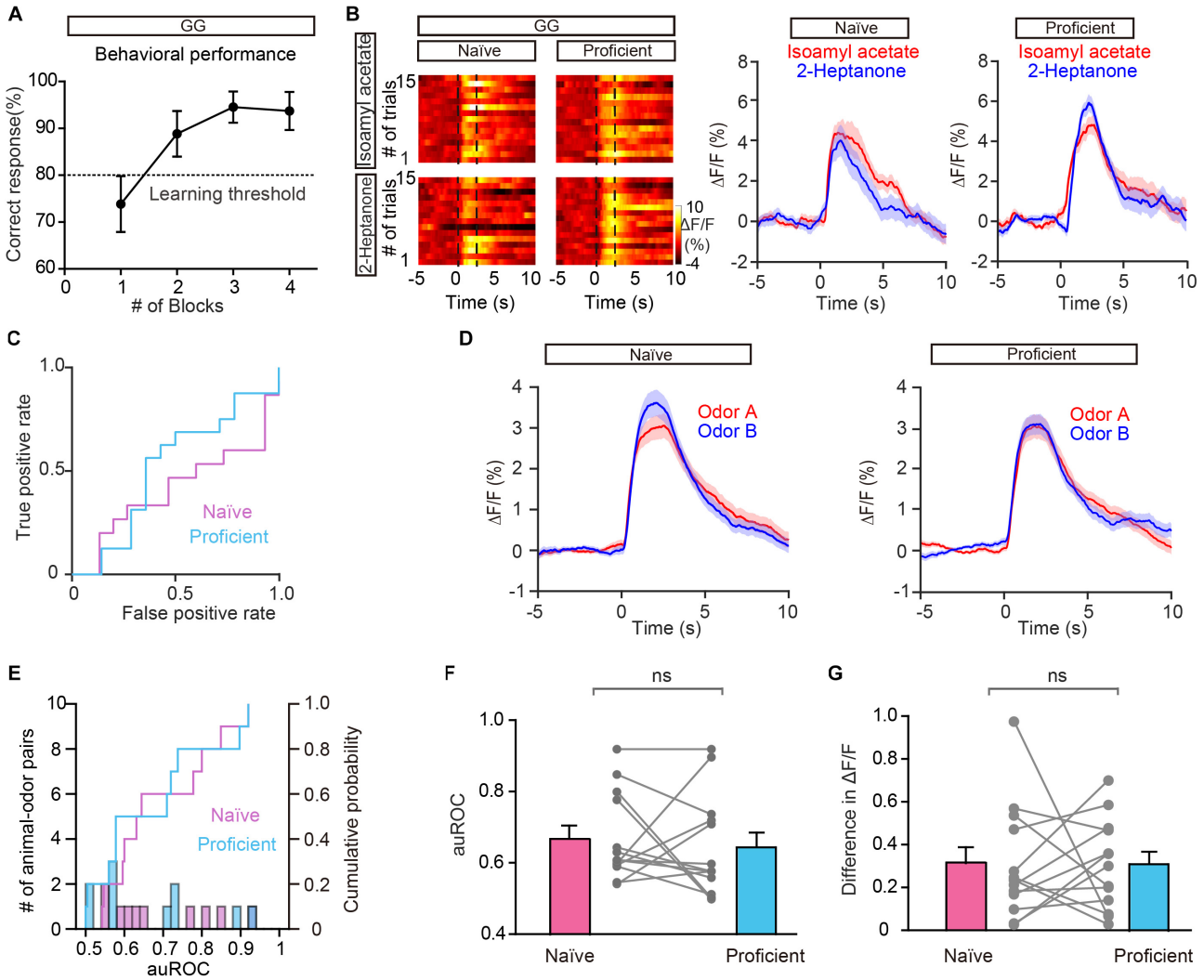

FIGURE 5 | Odor responses in GCs do not show separation during the go/go (GG) task. **(A)** Percentage of correctly answered trials in the last session of the go/go task. **(B,C)** Heat map **(B)**, peri-event plot **(B)**, and ROC graph **(C)** of Ca^{2+} signals from an individual mouse in the naïve stage and in the proficient stage of the go/go task. **(D)** Averaged traces of odor responses across all animal-odor pairs (n = 13 animal-odor pairs from ten mice). Odor A and odor B represent the two rewarded odors delivered during the go/go task. **(E)** Histograms and cumulative probability of auROCs in the naïve stage and the proficient stage. **(F,G)** auROCs **(F)** and the difference in ΔF/F **(G)** are not significantly different between the naïve stage and the proficient stage. [**(F)** Wilcoxon's sign rank test, W = 14.0, P = 0.622; **(G)** Wilcoxon's sign rank test, W = -15.0, P = 0.636].

DISCUSSION

Studies have shown that the neural activity of M/T cells displays improved pattern separation during active learning and conveys information about odor value (Doucette and Restrepo, 2008; Doucette et al., 2011; Gschwend et al., 2015; Wang et al., 2019). Here, we explored the change of odor responses of OB granule cells during odor discrimination learning. Using fiber photometry, we characterized the basic odor response properties of GCs and, then tracked the long-term changes in population odor responses: we discovered that GC responses to pairs of odors display improved separation during a go/no go task. The responses of the same odor differed on FA and CR trials and improved separation was not observed during the go/go task, suggesting that GC activity contains information about odor value. Therefore, odor responses in GCs display learning-related plasticity and may mediate the pattern separation observed in M/T cells.

Although GCs are the major class of GABAergic interneurons in the OB, direct *in vivo* measurement of GC activity in awake animals has been limited to only a few studies demonstrating that GC activity is modulated by brain state and respiration (Kato et al., 2012; Cazakoff et al., 2014; Youngstrom and Strowbridge, 2015). To our knowledge, there have been no studies on GC activity in awake behaving animals. Here, we used fiber photometry a sensitive but easy method of detecting changes in fluorescence in a population of cells to monitor GC activity in mice engaging in a go/no go task. Although the population

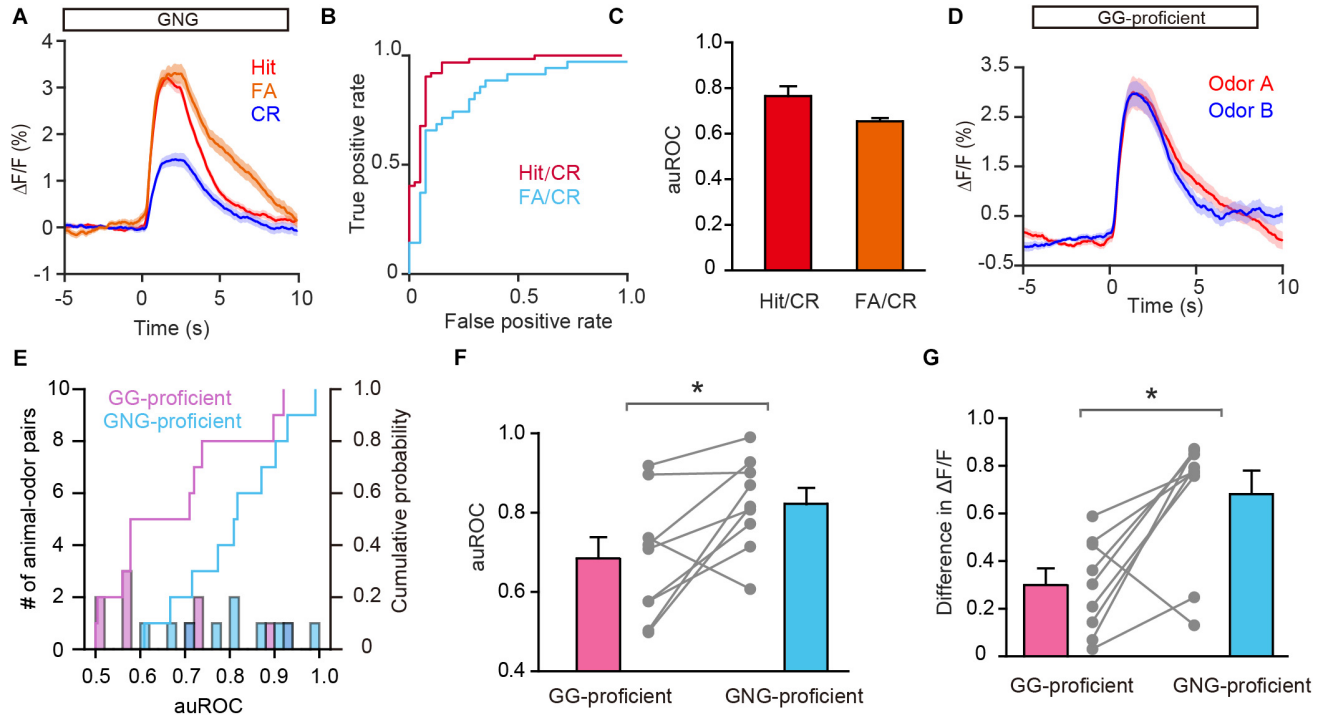

FIGURE 6 | Odor responses in GCs reflect odor value as opposed to odorant identity. **(A)** Averaged traces for Hit, FA, and CR trials during the go/no go (GNG) task across all animal-odor pairs. **(B)** ROC analysis for Hit/CR and FA/CR from an individual mouse. **(C)** The auROCs for Hit/CR trials and FA/CR trials across all mice performing the go/no go task. **(D)** Averaged traces of odor responses during the go/go (GG) task (n = 9 animal-odor pairs from eight mice), odor A and odor B represent the rewarded odors delivered during the go/go task. **(E)** Histograms and cumulative probability of auROCs in the proficient stage for the go/go task and the go/no go task. **(F,G)** The auROCs **(F)** and difference in ΔF/F **(G)** in the proficient stage for the go/go task and the go/no go task. [**F:** paired t-test, $t_{(9)}$ = 3.01, P = 0.0146; **G:** Wilcoxon's sign rank test, W = -37.0, P = 0.0273]. *P < 0.05.

recorded may contain a small fraction of short axon cells, another interneuron subtype in the granule cell layer (Eyre et al., 2008; Nagayama et al., 2014), the vast majority of GABAergic neurons in this layer are GCs. Robust and reliable responses were recorded in all mice tested and the calcium signals changed when different odors were presented while remaining stable across different trials of the same odor, indicating that this method works well for characterizing odor-evoked neural activity in GCs.

Studies from electrophysiological recording, two-photon imaging, and fiber photometry recording consistently demonstrate both excitatory and inhibitory responses to passive odor exposure in M/T cells (Yamada et al., 2017; Wang et al., 2019; Liu et al., 2020). By contrast, we observed only excitatory responses to passive odor exposure in GCs, consistent with our previous study (Sun et al., 2019). Indeed, excitatory odor responses have also been found in previous studies using two-photon calcium imaging and extracellular recording (Kato et al., 2012; Cazakoff et al., 2014). There are mainly two types of glutamatergic inputs onto GCs in the OB: the dendrodendritic input from mitral cells in the external plexiform layer and the axodendritic input from the olfactory cortex in the granule cell layer (Balu et al., 2007; Pressler and Strowbridge, 2017, 2019). Both of these two inputs may contribute to the odor responses in GCs. The optical fibers were embedded in the granule cell layer and GCs show several types of dendritic spikes that might not necessarily reach the soma (Zelles et al., 2006; Lin et al., 2007). In addition, a recent study has revealed that the unitary dendrodendritic input is relatively weak with highly variable release probability but cortical input to GCs is more powerful and less variable (Pressler and Strowbridge, 2017). Thus, the excitatory responses recorded in this study mainly reflect the cortical feedback input from the olfactory cortex onto GCs. Our previous studies have shown that odors always evoke excitatory responses in the pyramidal neurons of the piriform cortex (Zhou et al., 2017; Wang et al., 2020). Given that granule cells in the OB receive extensive glutamatergic feedback from the olfactory cortex (Boyd et al., 2012), the excitatory response in GCs mainly derive from the olfactory cortex. In future studies, more direct evidence could be provided by recordings focused on more subtle processing in the external plexiform layer of the OB in behaving animals. Although previous studies have shown a lack of learning-related plasticity in the piriform cortex (Zinyuk et al., 2001; Wang et al., 2019), whether the cortical inputs to GCs display such plasticity is unknown. Indeed, long-term plasticity has been induced in the cortical feedback inputs to GCs (Gao and Strowbridge, 2009; Cauthron and Stripling, 2014) and an olfactory circuitry model suggests that changes in the weight of top-down feedback contribute to pattern separation (Chen and Padmanabhan, 2020).

Therefore, changes in the weight of cortical inputs may regulate the plasticity in GCs during odor discrimination learning.

Since the separation of odor responses in OSN inputs remains stable during perceptual learning (Chu et al., 2017), the circuits within and/or beyond the OB must be responsible for the increase in pattern separation with learning in M/T cells. Here we find that odor responses in GCs also display improved separation, suggesting that granule cells may mediate the pattern separation in M/T cells. There are several lines of evidence in support of this hypothesis. (1) Disruption of GABAergic inhibition onto M/T cells impairs pattern separation in M/T cells and odor discrimination (Godde et al., 2016). Furthermore, bidirectional manipulation of GC activity affected pattern separation in M/T cells and odor discrimination performance (Gschwend et al., 2015; Nunes and Kuner, 2015). (2) Cortical feedback enhances pattern separation in mitral cells through inhibitory circuits (Otazu et al., 2015). Since granule cells are the main target of the feedback fibers, they may contribute to the cortical regulation of mitral cell pattern separation. (3) Indeed, it was recently shown that cortical feedback via granule cells in the OB could account for the learning-related pattern separation in mitral cells (Yamada et al., 2017). These studies combined with our findings suggest that GCs in the OB likely mediate the pattern separation in M/T cells. This hypothesis is further supported by a recent study showing that odor-induced changes in the power of local field potential oscillations in the OB also display learning-related separation (Ramirez-Gordillo et al., 2018). A previous study has shown that GC-specific silencing does not alter the firing rate of mitral cell (Fukunaga et al., 2014). In the future, it would be important to examine whether and how GCs mediate the pattern separation in M/T cells.

Furthermore, neuromodulatory inputs to the OB, including noradrenergic, serotonergic, and cholinergic fibers, have been demonstrated to shape the responses of mitral cells to odor and play an important role in olfactory-related behavior (Doucette and Restrepo, 2008; Escanilla et al., 2010; Ma and Luo, 2012; Nunez-Parra et al., 2013; Kapoor et al., 2016). Optogenetic silencing of noradrenergic axons in the OB disrupts learning-related separation in OB oscillations (Ramirez-Gordillo et al., 2018). Raphe activation, and presumed subsequent increases in endogenous serotonin release, leads to increased pattern separation in mitral cell odor codes (Kapoor et al., 2016). Future studies are needed to determine whether and how neuromodulation regulates the improved pattern separation observed in the OB during olfactory discrimination.

In summary, the present study provides direct evidence that odor responses of granule cells in the OB show improved separation during odor discrimination learning, suggesting task-dependent plasticity in the response of granule cells to odors. This finding is important for understanding the function of different cell types in the OB and how the OB processes odor information in the ever-changing real environment.

DATA AVAILABILITY STATEMENT

The raw data supporting the conclusions of this article will be made available by the authors, without undue reservation, to any qualified researcher.

ETHICS STATEMENT

The animal study was reviewed and approved by the Xuzhou Medical University Institutional Animal Care and Use Committee.

AUTHOR CONTRIBUTIONS

DW and AL designed the research and wrote the manuscript. YaC, DW, XL, and ZY performed the research. DW, YaC, YiC, and PL analyzed the data. All authors contributed to the article and approved the submitted version.

FUNDING

This work was supported by the National Natural Science Foundation of China (NSFC, 31872771 and 32070995 to AL, 31700895 and 32071024 to DW), the Natural Science Foundation of Jiangsu Province (BK20170260 to DW), the Innovative Entrepreneurship Training Program for National College Students (202010313079Y to YaC and XL), and the National Demonstration Center for Experimental Basic Medical Science Education (Xuzhou Medical University).

REFERENCES

Abraham, N. M., Egger, V., Shimshek, D. R., Renden, R., Fukunaga, I., Sprengel, R., et al. (2010). Synaptic inhibition in the olfactory bulb accelerates odor discrimination in mice. *Neuron* 65, 399–411. doi: 10.1016/j.neuron.2010.01.009

Abraham, N. M., Vincis, R., Lagier, S., Rodriguez, I., and Carleton, A. (2014). Long term functional plasticity of sensory inputs mediated by olfactory learning. *eLife* 3:e02109.

Andermann, M. L., Kerlin, A. M., and Reid, R. C. (2010). Chronic cellular imaging of mouse visual cortex during operant behavior and passive viewing. *Front. Cell. Neurosci.* 4:3. doi: 10.3389/fncel.2010.00003

Aungst, J. L., Heyward, P. M., Puche, A. C., Karnup, S. V., Hayar, A., Szabo, G., et al. (2003). Centre-surround inhibition among olfactory bulb glomeruli. *Nature* 426, 623–629. doi: 10.1038/nature02185

Balu, R., Pressler, R. T., and Strowbridge, B. W. (2007). Multiple modes of synaptic excitation of olfactory bulb granule cells. *J. Neurosci.* 27, 5621–5632. doi: 10.1523/jneurosci.4630-06.2007

Boyd, A. M., Sturgill, J. F., Poo, C., and Isaacson, J. S. (2012). Cortical feedback control of olfactory bulb circuits. *Neuron* 76, 1161–1174. doi: 10.1016/j.neuron.2012.10.020

Burton, S. D. (2017). Inhibitory circuits of the mammalian main olfactory bulb. *J. Neurophysiol.* 118, 2034–2051. doi: 10.1152/jn.00109.2017

Cauthron, J. L., and Stripling, J. S. (2014). Long-term plasticity in the regulation of olfactory bulb activity by centrifugal fibers from Piriform cortex. *J. Neurosci.* 34, 9677–9687. doi: 10.1523/jneurosci.1314-14.2014

Cazakoff, B. N., Lau, B. Y., Crump, K. L., Demmer, H. S., and Shea, S. D. (2014). Broadly tuned and respiration-independent inhibition in the olfactory bulb of awake mice. *Nat. Neurosci.* 17, 569–576. doi: 10.1038/nn.3669

Chen, Z., and Padmanabhan, K. (2020). Top-down control of inhibitory granule cells in the main olfactory bulb reshapes neural dynamics giving rise to a diversity of computations. *Front. Comput. Neurosci.* 14:59. doi: 10.3389/fncom.2020.00059

Chong, E., and Rinberg, D. (2018). Behavioral readout of spatio-temporal codes in olfaction. *Curr. Opin. Neurobiol.* 52, 18–24. doi: 10.1016/j.conb.2018.04.008

Chu, M. W., Li, W. L., and Komiyama, T. (2017). Lack of pattern separation in sensory inputs to the olfactory bulb during perceptual learning. *eNeuro* 4:ENEURO.0287-17.2017.

Doucette, W., Gire, D. H., Whitesell, J., Carmean, V., Lucero, M. T., and Restrepo, D. (2011). Associative cortex features in the first olfactory brain relay station. *Neuron* 69, 1176–1187. doi: 10.1016/j.neuron.2011.02.024

Doucette, W., and Restrepo, D. (2008). Profound context-dependent plasticity of mitral cell responses in olfactory bulb. *PLoS Biol.* 6:e258. doi: 10.1371/journal.pbio.0060258

Escanilla, O., Arrellanos, A., Karnow, A., Ennis, M., and Linster, C. (2010). Noradrenergic modulation of behavioral odor detection and discrimination thresholds in the olfactory bulb. *Eur. J. Neurosci.* 32, 458–468. doi: 10.1111/j.1460-9568.2010.07297.x

Eyre, M. D., Antal, M., and Nusser, Z. (2008). Distinct deep short-axon cell subtypes of the main olfactory bulb provide novel intrabulbar and extrabulbar GABAergic connections. *J. Neurosci.* 28, 8217–8229. doi: 10.1523/jneurosci.2490-08.2008

Fukunaga, I., Herb, J. T., Kollo, M., Boyden, E. S., and Schaefer, A. T. (2014). Independent control of gamma and theta activity by distinct interneuron networks in the olfactory bulb. *Nat. Neurosci.* 17, 1208–1216. doi: 10.1038/nn.3760

Gao, Y., and Strowbridge, B. W. (2009). Long-term plasticity of excitatory inputs to granule cells in the rat olfactory bulb. *Nat. Neurosci.* 12, 731–733. doi: 10.1038/nn.2319

Godde, K., Gschwend, O., Puchkov, D., Pfeffer, C. K., Carleton, A., and Jentsch, T. J. (2016). Disruption of Kcc2-dependent inhibition of olfactory bulb output neurons suggests its importance in odour discrimination. *Nat. Commun.* 7:12043.

Gschwend, O., Abraham, N. M., Lagier, S., Begnaud, F., Rodriguez, I., and Carleton, A. (2015). Neuronal pattern separation in the olfactory bulb improves odor discrimination learning. *Nat. Neurosci.* 18, 1474–1482. doi: 10.1038/nn.4089

Harvey, C. D., Coen, P., and Tank, D. W. (2012). Choice-specific sequences in parietal cortex during a virtual-navigation decision task. *Nature* 484, 62–68. doi: 10.1038/nature10918

Hu, B., Geng, C., and Hou, X. Y. (2017). Oligomeric amyloid-beta peptide disrupts olfactory information output by impairment of local inhibitory circuits in rat olfactory bulb. *Neurobiol. Aging* 51, 113–121. doi: 10.1016/j.neurobiolaging.2016.12.005

Hu, B., Jin, C., Zhang, Y. Q., Miao, H. R., and Wang, F. (2020a). In vivo odorant input induces distinct synaptic plasticity of GABAergic synapses in developing zebrafish olfactory bulb. *Biochem. Biophys. Res. Commun.* 531, 160–165. doi: 10.1016/j.bbrc.2020.07.106

Hu, B., Wang, J. J., and Jin, C. (2020b). In vivo odorant input induces spike timing-dependent plasticity of glutamatergic synapses in developing zebrafish olfactory bulb. *Biochem. Biophys. Res. Commun.* 526, 532–538. doi: 10.1016/j.bbrc.2020.03.126

Huber, D., Gutnisky, D. A., Peron, S., O'Connor, D. H., Wiegert, J. S., Tian, L., et al. (2012). Multiple dynamic representations in the motor cortex during sensorimotor learning. *Nature* 484, 473–478. doi: 10.1038/nature11039

Isaacson, J. S., and Strowbridge, B. W. (1998). Olfactory reciprocal synapses: dendritic signaling in the CNS. *Neuron* 20, 749–761. doi: 10.1016/s0896-6273(00)81013-2

Kapoor, V., Provost, A. C., Agarwal, P., and Murthy, V. N. (2016). Activation of raphe nuclei triggers rapid and distinct effects on parallel olfactory bulb output channels. *Nat. Neurosci.* 19, 271–282. doi: 10.1038/nn.4219

Kass, M. D., Guang, S. A., Moberly, A. H., and McGann, J. P. (2016). Changes in olfactory sensory neuron physiology and olfactory perceptual learning after odorant exposure in adult mice. *Chem. Senses* 41, 123–133.

Kass, M. D., Rosenthal, M. C., Pottackal, J., and McGann, J. P. (2013). Fear learning enhances neural responses to threat-predictive sensory stimuli. *Science* 342, 1389–1392. doi: 10.1126/science.1244916

Kato, H. K., Chu, M. W., Isaacson, J. S., and Komiyama, T. (2012). Dynamic sensory representations in the olfactory bulb: modulation by wakefulness and experience. *Neuron* 76, 962–975. doi: 10.1016/j.neuron.2012.09.037

Kato, H. K., Gillet, S. N., and Isaacson, J. S. (2015). Flexible sensory representations in auditory cortex driven by behavioral relevance. *Neuron* 88, 1027–1039. doi: 10.1016/j.neuron.2015.10.024

Komiyama, T., Sato, T. R., O'Connor, D. H., Zhang, Y. X., Huber, D., Hooks, B. M., et al. (2010). Learning-related fine-scale specificity imaged in motor cortex circuits of behaving mice. *Nature* 464, 1182–1186. doi: 10.1038/nature08897

Li, A., Gire, D. H., and Restrepo, D. (2015). Upsilon spike-field coherence in a population of olfactory bulb neurons differentiates between odors irrespective of associated outcome. *J. Neurosci.* 35, 5808–5822. doi: 10.1523/jneurosci.4003-14.2015

Li, A., Rao, X., Zhou, Y., and Restrepo, D. (2020). Complex neural representation of odour information in the olfactory bulb. *Acta Physiol.* 228:e13333.

Lin, B. J., Chen, T. W., and Schild, D. (2007). Cell type-specific relationships between spiking and $[Ca^{2+}]$i in neurons of the *Xenopus* tadpole olfactory bulb. *J. Physiol.* 582, 163–175. doi: 10.1113/jphysiol.2006.125963

Liu, P., Cao, T., Xu, J., Mao, X., Wang, D., and Li, A. (2020). Plasticity of sniffing pattern and neural activity in the olfactory bulb of behaving mice during odor sampling, anticipation, and reward. *Neurosci. Bull.* 36, 598–610. doi: 10.1007/s12264-019-00463-9

Ma, M., and Luo, M. (2012). Optogenetic activation of basal forebrain cholinergic neurons modulates neuronal excitability and sensory responses in the main olfactory bulb. *J. Neurosci.* 32, 10105–10116. doi: 10.1523/jneurosci.0058-12.2012

Mandairon, N., Didier, A., and Linster, C. (2008). Odor enrichment increases interneurons responsiveness in spatially defined regions of the olfactory bulb correlated with perception. *Neurobiol. Learn. Mem.* 90, 178–184. doi: 10.1016/j.nlm.2008.02.008

Margrie, T. W., Sakmann, B., and Urban, N. N. (2001). Action potential propagation in mitral cell lateral dendrites is decremental and controls recurrent and lateral inhibition in the mammalian olfactory bulb. *Proc. Natl. Acad. Sci. U.S.A.* 98, 319–324. doi: 10.1073/pnas.98.1.319

McGann, J. P. (2013). Presynaptic inhibition of olfactory sensory neurons: new mechanisms and potential functions. *Chem. Senses* 38, 459–474. doi: 10.1093/chemse/bjt018

Nagayama, S., Homma, R., and Imamura, F. (2014). Neuronal organization of olfactory bulb circuits. *Front. Neural Circuits* 8:98. doi: 10.3389/fncir.2014.00098

Nunes, D., and Kuner, T. (2015). Disinhibition of olfactory bulb granule cells accelerates odour discrimination in mice. *Nat. Commun.* 6:8950.

Nunez-Parra, A., Li, A., and Restrepo, D. (2014). Coding odor identity and odor value in awake rodents. *Prog. Brain Res.* 208, 205–222. doi: 10.1016/b978-0-444-63350-7.00008-5

Nunez-Parra, A., Maurer, R. K., Krahe, K., Smith, R. S., and Araneda, R. C. (2013). Disruption of centrifugal inhibition to olfactory bulb granule cells impairs olfactory discrimination. *Proc. Natl. Acad. Sci. U.S.A.* 110, 14777–14782. doi: 10.1073/pnas.1310686110

Nusser, Z., Kay, L. M., Laurent, G., Homanics, G. E., and Mody, I. (2001). Disruption of GABA(A) receptors on GABAergic interneurons leads to increased oscillatory power in the olfactory bulb network. *J. Neurophysiol.* 86, 2823–2833. doi: 10.1152/jn.2001.86.6.2823

Otazu, G. H., Chae, H., Davis, M. B., and Albeanu, D. F. (2015). Cortical feedback decorrelates olfactory bulb output in awake mice. *Neuron* 86, 1461–1477. doi: 10.1016/j.neuron.2015.05.023

Pressler, R. T., and Strowbridge, B. W. (2017). Direct recording of dendrodendritic excitation in the olfactory bulb: divergent properties of local and external glutamatergic inputs govern synaptic integration in granule cells. *J. Neurosci.* 37, 11774–11788. doi: 10.1523/jneurosci.2033-17.2017

Pressler, R. T., and Strowbridge, B. W. (2019). Functional specialization of interneuron dendrites: identification of action potential initiation zone in axonless olfactory bulb granule cells. *J. Neurosci.* 39, 9674–9688. doi: 10.1523/jneurosci.1763-19.2019

Ramirez-Gordillo, D., Ma, M., and Restrepo, D. (2018). Precision of classification of odorant value by the power of olfactory bulb oscillations is altered by optogenetic silencing of local adrenergic innervation. *Front. Cell. Neurosci.* 12:48. doi: 10.3389/fncel.2018.00048

Sun, C., Tang, K., Wu, J., Xu, H., Zhang, W., Cao, T., et al. (2019). Leptin modulates olfactory discrimination and neural activity in the olfactory bulb. *Acta Physiol.* 227:e13319.

Uchida, N., Poo, C., and Haddad, R. (2014). Coding and transformations in the olfactory system. *Annu. Rev. Neurosci.* 37, 363–385. doi: 10.1146/annurev-neuro-071013-013941

Vaaga, C. E., and Westbrook, G. L. (2016). Parallel processing of afferent olfactory sensory information. *J. Physiol.* 594, 6715–6732. doi: 10.1113/jp272755

Vong, L., Ye, C., Yang, Z., Choi, B., Chua, S. Jr., and Lowell, B. B. (2011). Leptin action on GABAergic neurons prevents obesity and reduces inhibitory tone to POMC neurons. *Neuron* 71, 142–154. doi: 10.1016/j.neuron.2011.05.028

Wang, D., Liu, P., Mao, X., Zhou, Z., Cao, T., Xu, J., et al. (2019). Task-demand-dependent neural representation of odor information in the olfactory bulb and posterior piriform cortex. *J. Neurosci.* 39, 10002–10018. doi: 10.1523/jneurosci.1234-19.2019

Wang, D., Wang, X., Liu, P., Jing, S., Du, H., Zhang, L., et al. (2020). Serotonergic afferents from the dorsal raphe decrease the excitability of pyramidal neurons in the anterior piriform cortex. *Proc. Natl. Acad. Sci. U.S.A.* 117, 3239–3247. doi: 10.1073/pnas.1913922117

Wienisch, M., and Murthy, V. N. (2016). Population imaging at subcellular resolution supports specific and local inhibition by granule cells in the olfactory bulb. *Sci. Rep.* 6:29308.

Wilson, C. D., Serrano, G. O., Koulakov, A. A., and Rinberg, D. (2017). A primacy code for odor identity. *Nat. Commun.* 8:1477.

Wu, H., Yan, X., Tang, D., Gu, W., Luan, Y., Cai, H., et al. (2020). Internal states influence the representation and modulation of food intake by subthalamic neurons. *Neurosci. Bull.* doi: 10.1007/s12264-020-00533-3 [Epub ahead of print].

Yamada, Y., Bhaukaurally, K., Madarasz, T. J., Pouget, A., Rodriguez, I., and Carleton, A. (2017). Context- and output layer-dependent long-term ensemble plasticity in a sensory circuit. *Neuron* 93, 1198–1212.e5.

Youngstrom, I. A., and Strowbridge, B. W. (2015). Respiratory modulation of spontaneous subthreshold synaptic activity in olfactory bulb granule cells recorded in awake, head-fixed mice. *J. Neurosci.* 35, 8758–8767. doi: 10.1523/jneurosci.0311-15.2015

Zelles, T., Boyd, J. D., Hardy, A. B., and Delaney, K. R. (2006). Branch-specific Ca2+ influx from Na+-dependent dendritic spikes in olfactory granule cells. *J. Neurosci.* 26, 30–40. doi: 10.1523/jneurosci.1419-05.2006

Zhou, Y., Wang, X., Cao, T., Xu, J., Wang, D., Restrepo, D., et al. (2017). Insulin modulates neural activity of pyramidal neurons in the anterior piriform cortex. *Front. Cell. Neurosci.* 11:378. doi: 10.3389/fncel.2017.00378

Zinyuk, L. E., Datiche, F., and Cattarelli, M. (2001). Cell activity in the anterior piriform cortex during an olfactory learning in the rat. *Behav. Brain Res.* 124, 29–32. doi: 10.1016/s0166-4328(01)00212-1

Conflict of Interest: The authors declare that the research was conducted in the absence of any commercial or financial relationships that could be construed as a potential conflict of interest.

frontiers in Neuroscience

ORIGINAL RESEARCH
published: 27 October 2020
doi: 10.3389/fnins.2020.562292

Human iPSC-Derived Neuronal Cells From *CTBP1*-Mutated Patients Reveal Altered Expression of Neurodevelopmental Gene Networks

*S. Vijayalingam[1], Uthayashanker R. Ezekiel[2], Fenglian Xu[3], T. Subramanian[1], Elizabeth Geerling[1], Brittany Hoelscher[3], KayKay San[2], Aravinda Ganapathy[2], Kyle Pemberton[3], Eric Tycksen[4], Amelia K. Pinto[1], James D. Brien[1], David B. Beck[5], Wendy K. Chung[6], Christina A. Gurnett[7] and G. Chinnadurai[1]**

[1] Department of Molecular Microbiology and Immunology, Saint Louis University School of Medicine, Edward A. Doisy Research Center, St. Louis, MO, United States, [2] Department of Clinical Health Sciences, Doisy College of Health Science, Saint Louis University School of Medicine, Saint Louis, MO, United States, [3] Department of Biology and Henry and Amelia Nasrallah Center for Neuroscience, Saint Louis University, St. Louis, MO, United States, [4] McDonnell Genome Institute, Washington University School of Medicine, St. Louis, MO, United States, [5] National Human Genome Research Institute, National Institutes of Health, Bethesda, MD, United States, [6] Department of Pediatrics and Medicine, Columbia University Medical Center, New York, NY, United States, [7] Department of Neurology, Washington University School of Medicine, St. Louis, MO, United States

OPEN ACCESS

Edited by:
Giordano Lippi,
The Scripps Research Institute, United States

Reviewed by:
Subhabrata Sanyal,
California Life Company (Calico), United States
Zhexing Wen,
Emory University, United States

***Correspondence:**
G. Chinnadurai
g.chinnadurai@health.slu.edu

Specialty section:
This article was submitted to Neurogenomics, a section of the journal Frontiers in Neuroscience

Received: 15 May 2020
Accepted: 01 October 2020
Published: 27 October 2020

Citation:
Vijayalingam S, Ezekiel UR, Xu F, Subramanian T, Geerling E, Hoelscher B, San K, Ganapathy A, Pemberton K, Tycksen E, Pinto AK, Brien JD, Beck DB, Chung WK, Gurnett CA and Chinnadurai G (2020) Human iPSC-Derived Neuronal Cells From CTBP1-Mutated Patients Reveal Altered Expression of Neurodevelopmental Gene Networks. Front. Neurosci. 14:562292. doi: 10.3389/fnins.2020.562292

A recurrent *de novo* mutation in the transcriptional corepressor *CTBP1* is associated with neurodevelopmental disabilities in children (Beck et al., 2016, 2019; Sommerville et al., 2017). All reported patients harbor a single recurrent *de novo* heterozygous missense mutation (p.R342W) within the cofactor recruitment domain of CtBP1. To investigate the transcriptional activity of the pathogenic *CTBP1* mutant allele in physiologically relevant human cell models, we generated induced pluripotent stem cells (iPSC) from the dermal fibroblasts derived from patients and normal donors. The transcriptional profiles of the iPSC-derived "early" neurons were determined by RNA-sequencing. Comparison of the RNA-seq data of the neurons from patients and normal donors revealed down regulation of gene networks involved in neurodevelopment, synaptic adhesion and anti-viral (interferon) response. Consistent with the altered gene expression patterns, the patient-derived neurons exhibited morphological and electrophysiological abnormalities, and susceptibility to viral infection. Taken together, our studies using iPSC-derived neuron models provide novel insights into the pathological activities of the *CTBP1* p.R342W allele.

Keywords: transcriptional repression, CtBP, *de novo* mutation, interferon response, intellectual and developmental disabilities, transcriptome analysis

INTRODUCTION

The C-terminal Binding Protein (CtBP) family consists of two highly related paralogs, CtBP1 and CtBP2 (and their splice forms) in vertebrates (Chinnadurai, 2007). The nuclear isoforms of CtBP1 (CtBP1-L, NM_001328.2) and CtBP2 (CtBP2-L, NM_022802.2) function as transcriptional corepressors (reviewed in Chinnadurai, 2007). CtBPs mediate transcriptional repression by

targeting various chromatin-modifying enzymes to the promoter regions and by interacting with DNA-bound repressors. CtBPs bind with the chromatin modifying factors and various repressors through a high-affinity protein-binding interface known as PXDLS-binding cleft. In addition, an auxiliary protein-binding interface termed RRT-binding groove in CtBPs is involved in interaction with certain Zinc-finger-containing transcription factors. The CtBP1 corepressor complex mediates coordinated histone modifications by deacetylation and methylation of histone H3K9 and demethylation of histone H3K4 (Shi et al., 2003). CtBPs also activate transcription under certain specific contexts (Fang et al., 2006; Paliwal et al., 2012; Bajpe et al., 2013; Itoh et al., 2013; Ray et al., 2014). Since CtBPs are NAD(H)-binding proteins (Kumar et al., 2002; Nardini et al., 2003), the intracellular levels of NAD(H) dinucleotides differentially regulate their transcriptional activity through oligomerization (Zhang et al., 2002).

Studies on mice with disruptions in the *ctbp* genes, showed that *ctbp1* and *ctbp2* play overlapping and unique transcriptional roles during development (Hildebrand and Soriano, 2002). While homozygous deletion of the *ctbp2* gene was embryonic lethal affecting brain and heart development, homozygous deletion of *ctbp1* resulted in viable mice with reduced size and lifespan. In humans, overexpression of *CTBP1* and *CTBP2* was reported in a number of epithelial cancers and was associated with transcriptional activity that leads to epithelial to mesenchymal transformation (reviewed by Chinnadurai, 2002; Byun and Gardner, 2013; Dcona et al., 2017). A role of *CTBP1* in human neurodevelopment was revealed with the discovery of a recurrent *de novo* missense mutation in *CTBP1* (c.991C → T, p.R331W in NM_001012614.1; p.R342W c.1024 C → T in NM_001328.2) in patients with neurodevelopmental features including intellectual disability, ataxia, hypotonia, as well as tooth enamel defects (Beck et al., 2016, 2019; Sommerville et al., 2017). The neurodevelopmental phenotypes conferred by the *CTBP1* mutant allele provide genetic evidence that *CTBP1* is important for normal human brain development. Previous biochemical studies also suggested that CtBPs might be important for certain brain developmental functions (Sahu et al., 2017; Shen et al., 2017). CtBP1 has been reported to mediate transcriptional repression of a number of neuronal genes involved in synaptic activities of the inner ear hair cells, the retina (Ivanova et al., 2015) and the synaptic ribbon complex (Tom Dieck et al., 2005).

The mechanism by which the pathogenic *CTBP1* mutant allele contributes to neurodevelopmental disease is not known. The mutation (referred here as p.R342W) maps within an α-helical region (α-5) of CtBP1 that forms a part of the PXDLS-protein interaction cleft. In a glioblastoma cell line with exogenously expressed *CTBP1* p.R342W, the interactions of various CtBP-cofactors were reduced with the mutant protein (Beck et al., 2019). In order to determine the altered transcriptional profiles in patient-derived cell models, we generated iPSCs from dermal fibroblasts, differentiated them into early stage neurons, and determined their transcriptional profiles by RNA-seq. The morphological and physiological changes inferred from the altered gene expression profiles of patient-derived cells were also determined. Here, we report that genes involved in neurodevelopment, adhesion and antiviral-response pathways are downregulated in *CTBP1* heterozygous p.R342W neurons. Consistent with the transcriptome data, patient-derived heterozygous p.R342W neurons also showed morphological and physiological abnormalities and susceptibility to neurotropic viral pathogenesis.

RESULTS

Neuronal Cell Models

Since the *CTBP1* p.R342W mutation is associated with neurodevelopmental disabilities, we designed experiments to compare the transcriptional profiles of patient and healthy control derived neuronal cell models. We generated iPSCs from the dermal fibroblasts of two patients with the *CTBP1* p.R342W heterozygous mutation and two age-matched normal donors using Sendai virus delivery of the Yamanaka factors (Klf-4, Sox-2, Oct3/4, and c-Myc) (Ban et al., 2011; Nayler et al., 2017). We further differentiated the iPSC (**Supplementary Figure 1A**) into neural stem cells (NSC) (**Supplementary Figure 1B**) and early (14-days of differentiation) neurons (**Figure 1**) using neural differentiation media. These neurons were used for transcriptional profiling and morphological and electrophysiological comparisons.

The phase contrast images of iPSC/NSC-derived neurons of normal donors and patients revealed typical neuronal morphology, exhibiting ability to grow and extend robust neurites and form inter- connections (**Figure 1**). To quantify the differences in neurite length and number, phase contrast images were measured using the ImageJ software, NeuronJ (Meijering et al., 2004; Pemberton et al., 2018). While there were no significant differences between patient and control cells in these outgrowth parameters (**Figures 1D,E**), analysis of neurite thickness demonstrated a significantly decreased primary neurite thickness in patient cells compared to control cells (**Figure 1A**, arrows; **Figure 1F**). The neurons were also analyzed by immunocytochemistry labeling of the cytoskeletal markers beta-3 Tubulin (green) (**Figure 1B**) and Microtubule-Associated Protein 2 (MAP2, red) (**Figure 1C**). This analysis confirmed robust and extensive internetworks formed by both control- and patient-derived neurons. We also quantified the staining of nuclei with DAPI (blue). Compared to controls, patient cultures had, in general, fewer DAPI-positive cells (**Figure 1G**). Together, these results indicated that neurons derived from *CTBP1*-mutated stem cells survived less in culture. Although they were able to form and extend neurites, like control neurons, the neurites of patient neurons were significantly thinner.

Transcriptomic Profiling of iPSC/NSC-Derived Neurons

To determine the transcriptional profiles altered by the *CTBP1* mutant allele (p.R342W) in patient-derived cell models, we prepared RNA from the neurons (14-days after differentiation) generated from two different patient-derived NSC and two

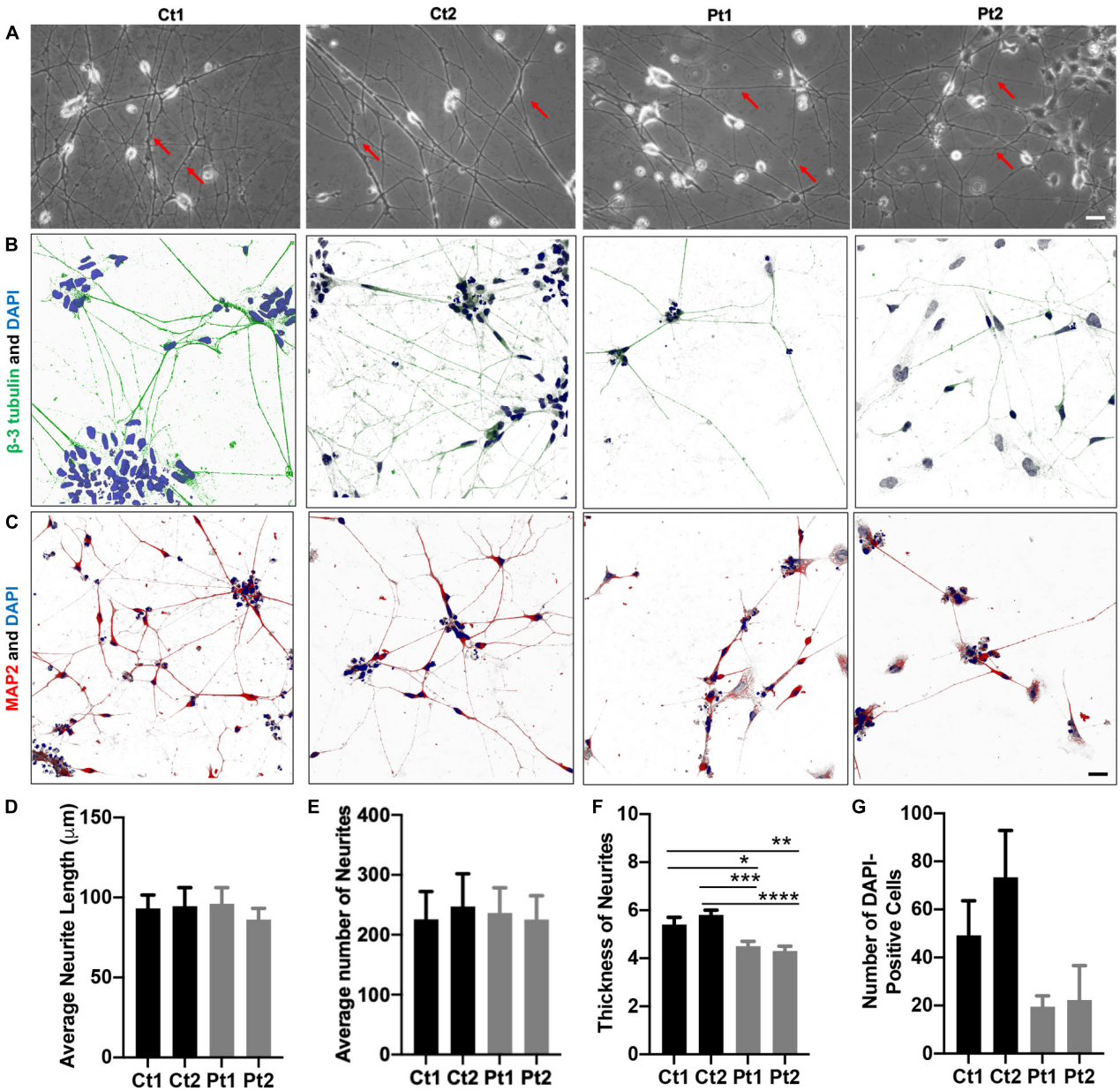

FIGURE 1 | Morphology of iPSC/NSC-derived neurons. Neurite networks of healthy donor control (Ct1 and Ct2) and patient (Pt1 and Pt2) neurons were revealed by phase contrast imaging **(A)** and immunofluorescence imaging of cells stained with antibodies to cytoskeletal proteins beta-3-Tubulin **(B)** and MAP2 **(C)**. The length **(D)**, number **(E)** and thickness **(F)** of neurites were measured from phase contrast images and quantified. There were no significant differences in either the number or the length of neurites between control or patient-cells. Specifically, the average neurite length **(D)** of different cells was: Ct1, 93.2 ± 8.4 μm; Ct2, 94.6 ± 11.6 μm; Pt1, 96.1 ± 10.1 μm; and Pt2, 86.2 ± 7.0 μm ($p = 0.882$; $n = 5$). The average number **(E)** of neurites per image was: Ct1, 225.8 ± 46.4; Ct 2, 247.2 ± 54.6: Pt1, 236.0 ± 42.4; and Pt2, 225.4 ± 39.8 ($p = 0.985$; $n = 5$). The average neurite thickness **(F)** in Ct1 was 5.4 ± 0.3 μm, Ct2 was 5.8 ± 0.2 μm, Pt1 was 4.5 ± 0.2 μm, and Pt2 was 4.3 ± 0.2 μm ($p = 0.03$ for Ct1 vs Pt1; p = 0.00045 for Ct2 vs Pt1; $p = 0.005$ for Ct1 vs Pt2; $p = 0.00004$ for Ct2 vs Pt2; $n = 10$ primary neurites measured in 5 phase contrast images for all conditions, totaling 50 neurites measured per condition). * Indicates a significance level of $p < 0.05$, $^{**}p < 0.01$, $^{***}p < 0.001$, and $^{****}p < 0.0001$. **(G)** Number of DAPI-Positive Cells Bar Graph. DAPI staining of nuclei revealed fewer patient neurons adhered to the culture dish. Number of DAPI-positive cells in Ct1 was 49.2 ± 14.4, in Ct2 was 73.4 ± 19.5, in Pt1 was 19.5 ± 4.5, and in Pt2 was 22.3 ± 14.3 ($p = 0.0507$; $n = 6, 6, 5$, and 3 fluorescent images analyzed for Ct1, Pt1, Ct2, and Pt2, respectively). Scale bar is 25 μm.

healthy donor NSC lines. The cDNA generated from RNA derived from the early neurons were sequenced on an Illumina HiSeq 3000 with single-end 50 base pair reads. The sequence reads were aligned with STAR (Dobin et al., 2013), and were quantitated with Subread (Liao et al., 2014). The gene counts were analyzed using established methods for quantifying gene expression: the R/Bioconductor package Limma (Ritchie et al., 2015) and SVA (Leek et al., 2012). Our analysis revealed that out

of 15,942 gene transcripts robustly expressed at greater than 1 count-per-million in at least 5 samples, 7,141 were differentially expressed between patient and control neurons (FDR $\leq$ 0.05). Among these transcripts, 6,500 genes were protein-coding. As depicted in the volcano plot, among the differentially expressed protein-coding transcripts, 161 were down-regulated and 36 were up-regulated by 3-fold or more in patient-derived neurons (**Figure 2A**). All genes were then tested for perturbations in gene ontology (GO) biological processes (**Figure 2B**).

The differentially expressed genes were then subjected to Weighted Gene Correlation Network Analysis (WGCNA) (Langfelder and Horvath, 2008). A matrix of *de novo* color-coded modules found by WGCNA and correlated with the mutation are shown in **Figure 2C**. The modules with high correlations (Pearson correlations >75%) to *CTBP1* p.R342W mutant cells were selected for further analysis; darkturquoise (**Figure 3**), pink (**Supplementary Figure 2**) and white (**Supplementary Figure 3**). The correlation of the eigengenes for every cluster revealed a highly negative correlated module labeled in darkturquoise containing 102 transcripts and highly positively correlated modules labeled in pink (451 transcripts) and white (78 transcripts). GO enrichment analysis of the darkturquoise module revealed highly significant down regulation of genes involved in neuronal development/functions, synaptic cell adhesion, and type 1 interferon signaling and response (**Figures 3A,B**). A heat-map of these highly correlated genes confirmed that the genes associated with these biological processes were down-regulated across all *CTBP1* mutant samples (**Figure 3C**). The genes that were significantly up-regulated in patient cells in the pink cluster (**Supplementary Figures 2A–C**) appear to be involved in diverse biological processes such as protein synthesis and protein targeting/localization, RNA catabolic process and apoptosis signaling. The white module of up-regulated genes in *CTBP1* mutant cells were significantly enriched for metabolic processes, transcriptional initiation and translation as shown in **Supplementary Figures 3A–C**.

Considering the neuronal developmental phenotypes, including intellectual disability exhibited by patients with the *CTBP1* p.R342W mutation and adherence phenotypes of the mutant cells observed while differentiating NSC to neurons (not shown), we pursued RNA sequencing and observed the suppression of genes involved in neuronal development and cell adhesion (**Figure 4A** and **Supplementary Table 1**). We then focused on the genes of down-regulated biological processes for validation by RT-qPCR analysis (**Figure 4**). The down-regulated transcriptional pattern was prominent in the transcriptome data analysis and the expression patterns of a number of transcripts were readily validated by RT-qPCR analysis. Further, the known functions of several down-regulated genes appeared to be relevant to the patient phenotypes (see **Supplementary Table 2**). In contrast to the down-regulated transcripts, up-regulated transcripts were diverse (see below). The down-regulated genes included those involved in neuronal development and cell adhesion (**Figure 4A** and **Supplementary Table 1**). In agreement with the RNA-seq data sets, RT-qPCR analysis revealed that several genes involved in type I interferon-response were also repressed in patient neurons (**Figure 4B** and **Supplementary Table 1**). In contrast to the negatively correlated and down-regulated genes in darkturquoise, the more variable heatmaps and lower statistical significance of genes in the positively correlated up-regulated pink and white clusters were diverse. Query with RT-qPCR analysis of several up-regulated genes suggested that these clusters did not merit further pursuit (data not shown). However, the possibility of up-regulation of isolated genes (none identified here) cannot be ruled out.

Physiological and Biological Activities of *CTBP1* p.R342W-Mutated Neurons

Calcium transients: The above transcriptome analysis revealed down-regulation of neurodevelopmental and interferon response genes, we carried out additional assays to examine whether *CTBP1* p.R342W mutation affects factors such as cytosolic calcium (Ca^{2+}) levels and plasma membrane ion currents that are involved in normal neuronal functions. It is well known that brief and repetitive elevations of intracellular calcium levels (spontaneous calcium transients) are important in regulating various neural developmental processes, including neural survival, differentiation, neurite outgrowth, synaptic transmission and plasticity (Spitzer et al., 1994; Spitzer, 2006; Rosenberg and Spitzer, 2011). To assess the effect of *CTBP1* p.R342W on calcium transients, we performed fluorescent calcium imaging experiments on control donor and patient neurons. Our results revealed that neurons derived from patients exhibited differences in the frequency and/or amplitude of Ca^{2+} transients as compared to control neurons (**Figure 5**). Specifically, both control neurons (Ct1 and Ct2) exhibited regular compound patterns of calcium oscillations, and showed regular spiking activity with the ability to return to the baseline between spikes (indicated by blue arrows in **Figure 5**, left two panels). Interestingly, the patient neurons (Pt1 and Pt2) showed either more sustained elevation of intracellular Ca^{2+} with significantly reduced amplitude ($p < 0.05$, **Figure 5**) or more frequent, irregular patterns of Ca^{2+} transients with the calcium levels rarely returning to baseline (indicated by blue arrows in **Figure 5**, right two panels). These results indicate that *CTBP1* p.R342W impacts internal Ca^{2+} oscillations, either affecting their amplitudes or spiking patterns leading to dysregulation of Ca^{2+} homeostasis in patient neurons. We note that in spite of the inter-patient variations between the two patient-derived cell lines (Pt1 and Pt2), they both exhibited consistent irregular Ca^{2+} transients. It is possible that the effect of *CTBP1*-mutation might be additionally influenced by other stochastic intra-patient environments.

Because spontaneous Ca^{2+} transients are normally driven by active firing of neuronal action potentials mediated by the functional expression of inward sodium (Na^{+}) and outward potassium (K^{+}) currents, we next examined whether the *CTBP1* p.R342W mutation alters these currents in neurons. We specifically focused on the impact of *CTBP1* p.R342W on the voltage-gated Na^{+} currents, which are essential for the ability of neurons to generate action potentials. Our whole cell patch clamping data (**Supplementary Figure 4**) showed that

neurons from control donors exhibited normal expression of Na^+ currents. However, the neurons derived from one patient (Pt1) expressed little or no Na^+ currents in all neurons examined and the neurons derived from the second patient (Pt2) exhibited either smaller or much larger Na^+ currents (**Supplementary Figure 4**). As in the case Ca^{2+} transient measurements, both Pt1 and Pt2 cells showed inter-patient variations in Na^+ current measurements. Taken together, our data suggest that the *CTBP1* p.R342W mutation may affect the normal neuronal functions such as intracellular Ca^{2+} homeostasis and membrane excitability, two fundamental factors that mediate neuronal communications in the nervous system.

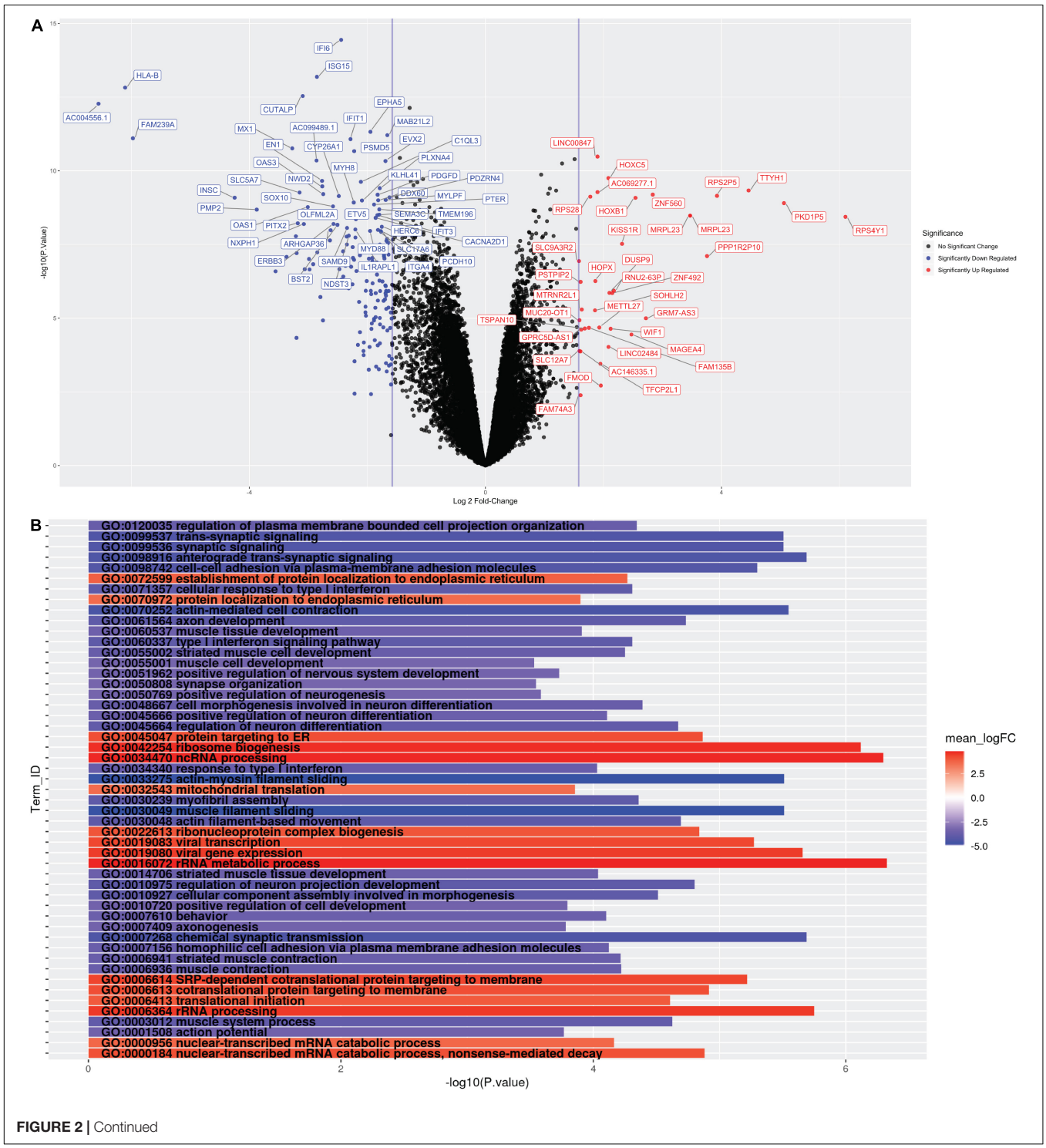

FIGURE 2 | Continued

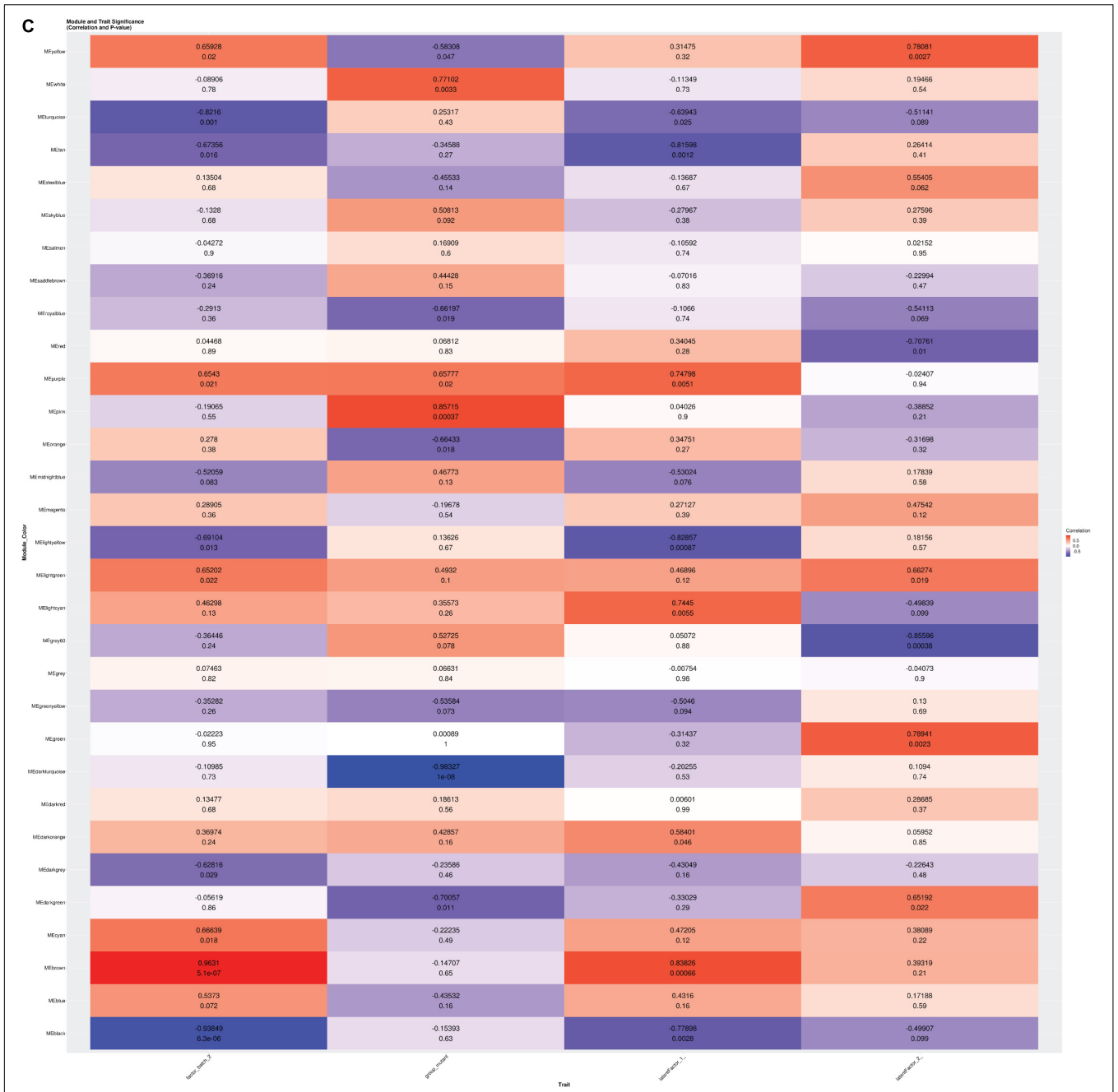

FIGURE 2 | (A) Volcano Plot: Volcano plot of 15,942 gene transcripts with log 2 fold changes observed by Limma. 7,141 were differentially expressed between patient and control neurons (FDR $\leq$ 0.05). Among these transcripts, 6,500 genes were protein-coding. Out of these, 161 were down-regulated (Blue) and 36 were up-regulated (Red) by 3-fold or more. **(B)** Global GO Biological Process Perturbation Bar Plot: All 15,942 transcripts were interrogated by Gage for level perturbations across all known GO biological process gene sets. The significance and mean log 2 fold change of each term was evaluated by *t*-tests. **(C)** Module and Trait Eigengene Correlation and Significance Matrix: Matrix of *de novo* color coded modules found by WGCNA and their respective eigengene Pearson correlation (top value in each cell) and p-values (bottom value in each cell) for the mutation and statistical covariates. Bright red modules are high positively correlated and bright deep blue are high negatively correlated transcripts. Modules with absolute value Pearson correlations greater than 75% to the mutant samples (pink, white, and darkturquoise) were considered the best candidates for further investigation.

Adhesion activities: While performing routine cell culture procedures, we observed that *CTBP1*-mutated cells exhibited increased ability to become detached from the culture surface as individual cells when treated with cell detachment agents. Our transcriptome analysis revealed down-regulation of several adhesion molecules involved in cell-cell and synaptic adhesion (**Figure 3B** and **Supplementary Table 2**). To experimentally determine whether the *CTBP1* p.R342W neurons exhibit less

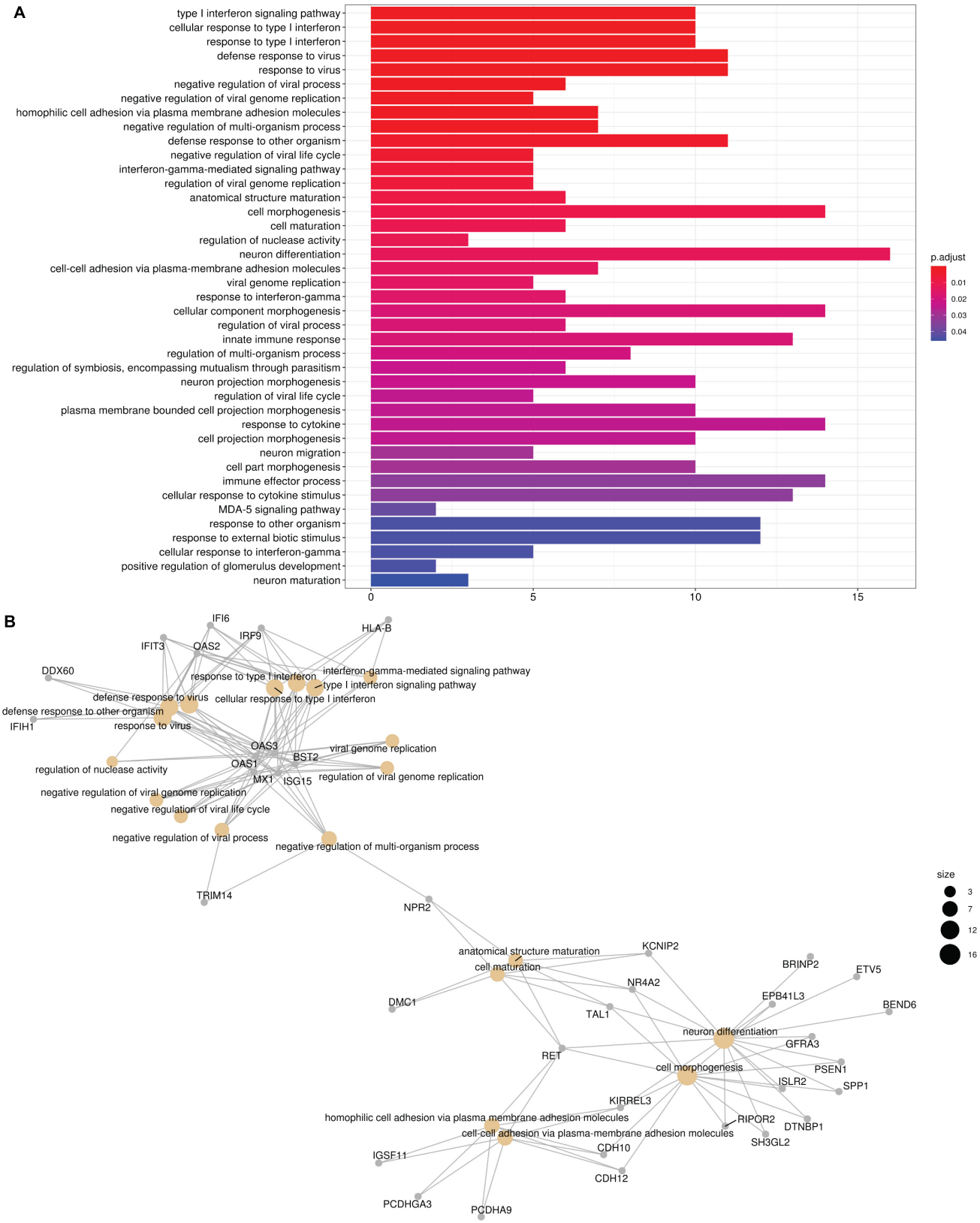

FIGURE 3 | Continued

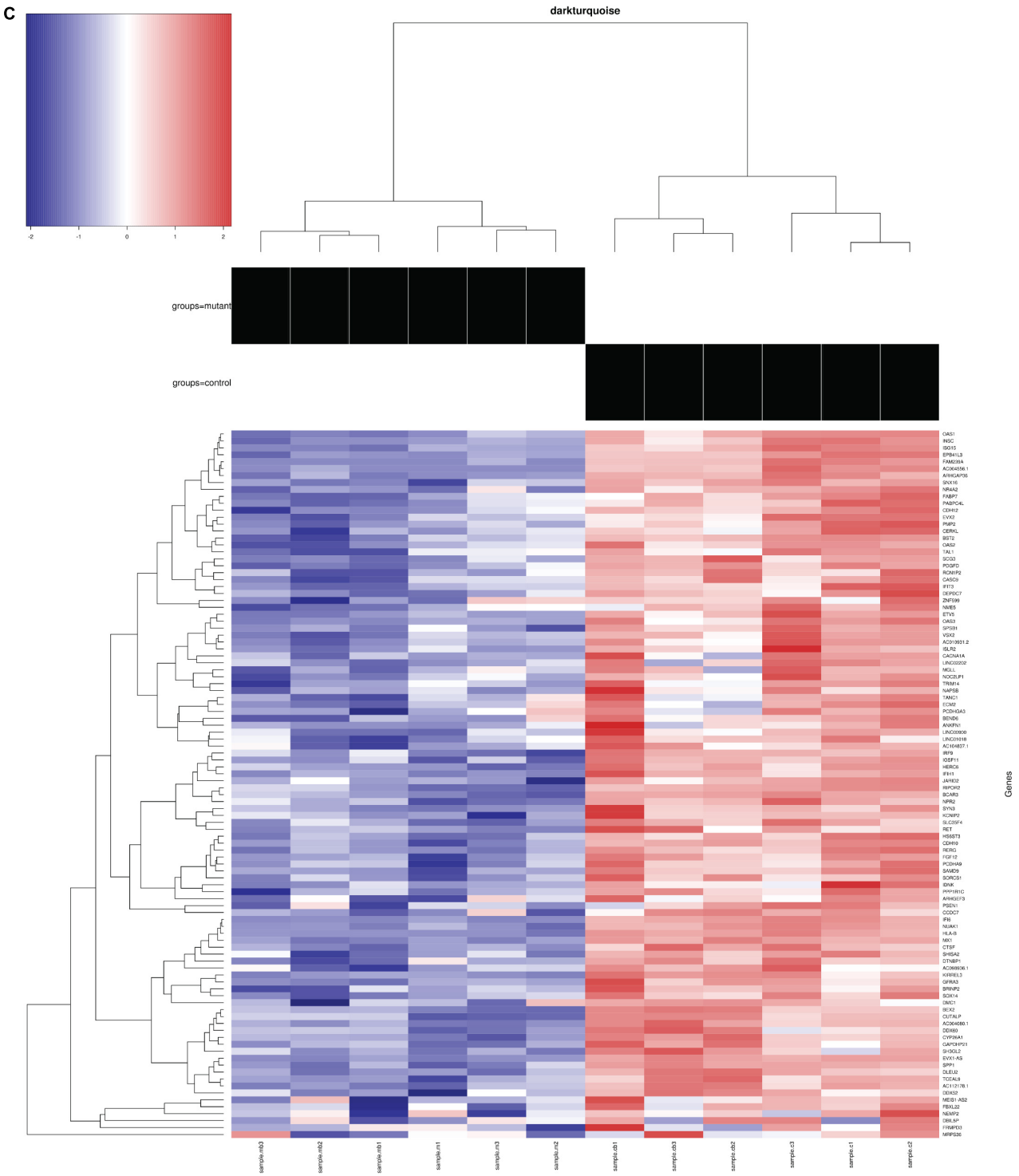

FIGURE 3 | GO network plot for down-regulated genes and heat maps: **(A)** Darkturquoise GO Biological Process Enrichment Bar Plot. All 102 negatively correlated WGCNA *de novo* clustered darkturquoise genes were tested for enrichment across known GO biological processes with the R/Bioconductor package clusterProfiler. The color illustrates the significance of the enrichment and the size of each bar characterizes the number of genes for each enriched term. The down regulation and negative correlation of darkturquoise module genes alludes to the down regulation represented by each significant term. **(B)** GO Category Network Plot: The negatively correlated genes clustered into a WGCNA *de novo* network labeled as darkturquoise were tested for enrichment across known GO biological processes with the R/Bioconductor package clusterProfiler. Significant terms with overlapping genes are clustered together while the overlapping genes represented in the darkturquoise network module illustrate the connections between those terms. **(C)** Heat map: Heat map representing 102 genes in the darkturquoise WGCNA module whose z-scores illustrate their down regulation and high negative correlation across all mutant samples.

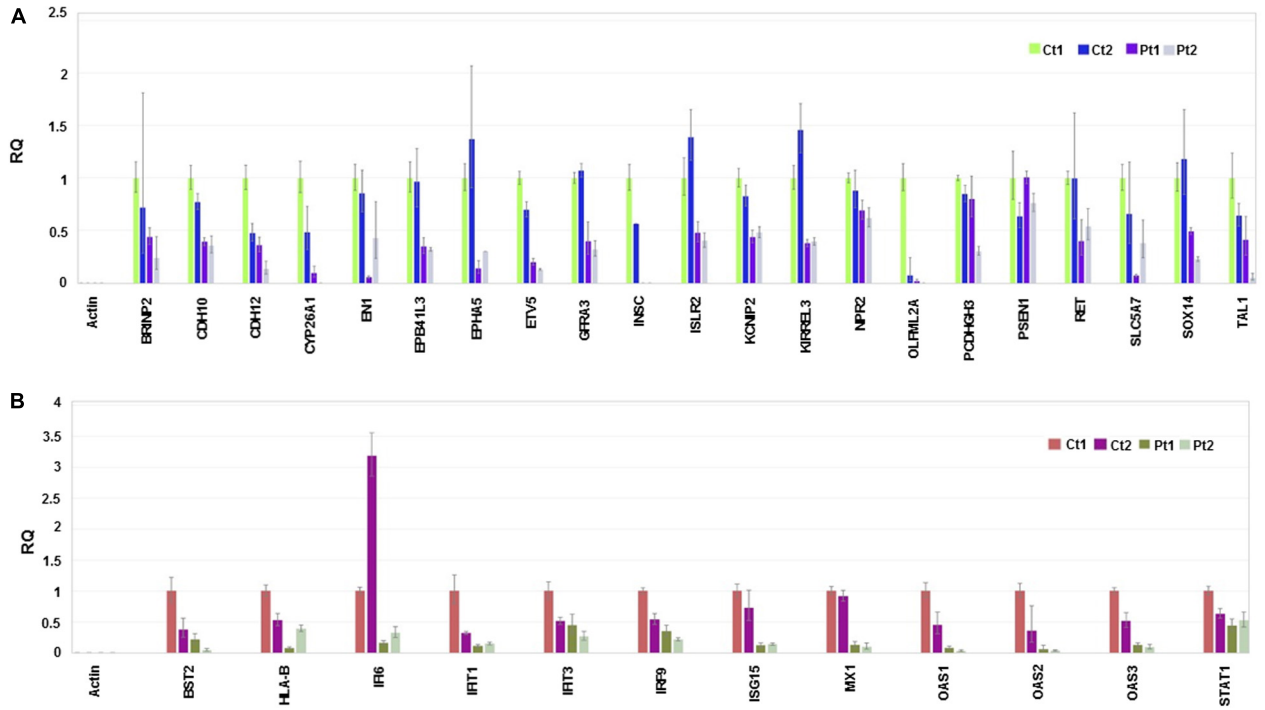

FIGURE 4 | RT-qPCR validation. The experiment was carried out in triplicate and the relative quantification (RQ) values are plotted and the data analysis done in Thermo Fisher Connect™ (Cloud) https://www.thermofisher.com/us/en/home/digital-science.html. Endogenous and reference control used in the experiment is Actin and control (Ct1), respectively. **(A)** Relative quantification of genes involved in neuronal development and cell adhesion. **(B)** Relative quantification of genes involved in Interferon responses.

adhesion activities, we carried out a "flipping" assay (Langhe et al., 2016). The control and patient cells were plated onto Geltrex coated chamber slides and incubated. After short culture time, the adherent and non-adherent cells were determined by flipping one set of plates. The cells in both flipped and un-flipped plates were fixed and stained with DAPI and MAP2-antibody. The percentage of adhered (flipped) cells was calculated based on un-flipped cells. We found that the percent of adherent cells were statistically lower in patient-derived neurons. As shown in **Figure 5B**, the patient-derived neurons exhibited significantly less adhesion than controls (Pt1-$p < 0.05$; Pt2-$p < 0.01$). As cadherins function in cell-cell contacts, reduced adherence of patient neurons suggest that the expression of these molecules may be affected. This *in vitro* result correlates with our transcriptome analysis where several cadherins (CDH10, CDH12 and KRREL3) are down-regulated (**Supplementary Table 2**).

Response to neurotropic virus infection: Our transcriptome analysis revealed prominent down regulation of homeostatic levels of interferon-stimulated genes. West Nile Virus infection is known to directly infect neurons both in mice (Shrestha et al., 2003) and in humans (Diamond et al., 2009) and can cause neuronal injury by direct cytopathic effect. Multiple studies have demonstrated that WNV is highly susceptible to antiviral interferon stimulated genes (ISG), which can act to reduce viral titer and alter cell susceptibility (Jiang et al., 2010). Therefore, we hypothesized that *CTBP1* p.R342W neuronal cells would be more susceptible to WNV replication as compared to healthy control neurons. To test this, we performed a single step growth curve using WNV on both patient and healthy control-derived neurons (**Figure 6**). We noted that there was a higher level of WNV replication in the patient-derived *CTBP1* p.R342W neuronal cells as compared to healthy control neurons from 4 h post infection until the end of the assay. These results were statistically significant at 20 h post infection ($p \leq 0.01$). We interpret these results to mean that the *CTBP1* p.R342W neurons might be more susceptible to WNV infection as the virus replicated to higher titers in mutant neurons compared to control neurons for most of the time points tested (about 100-fold at 20 h after infection). These results are consistent with the levels of expression of various anti-viral response genes in the patient neurons.

DISCUSSION

A specific *W342* mutation in the transcriptional corepressor *CTBP1* leads to prominent neurodevelopmental manifestations including intellectual disability, ataxia, and hypotonia in affected patients (Beck et al., 2016, 2019; Sommerville et al., 2017). The neurodevelopmental phenotypes conferred by the *CTBP1* p.R342W allele provide genetic evidence that *CTBP1* is important for normal human neurodevelopment. We employed patient iPSC-derived neuronal cell models to determine the transcriptional activities of the pathogenic *CTBP1* p.R342W allele and the potential link to functional abnormalities in neurons. By using iPSC-derived "early" neurons of two different patients with *CTBP1* p.R342W mutations (out of 12 known

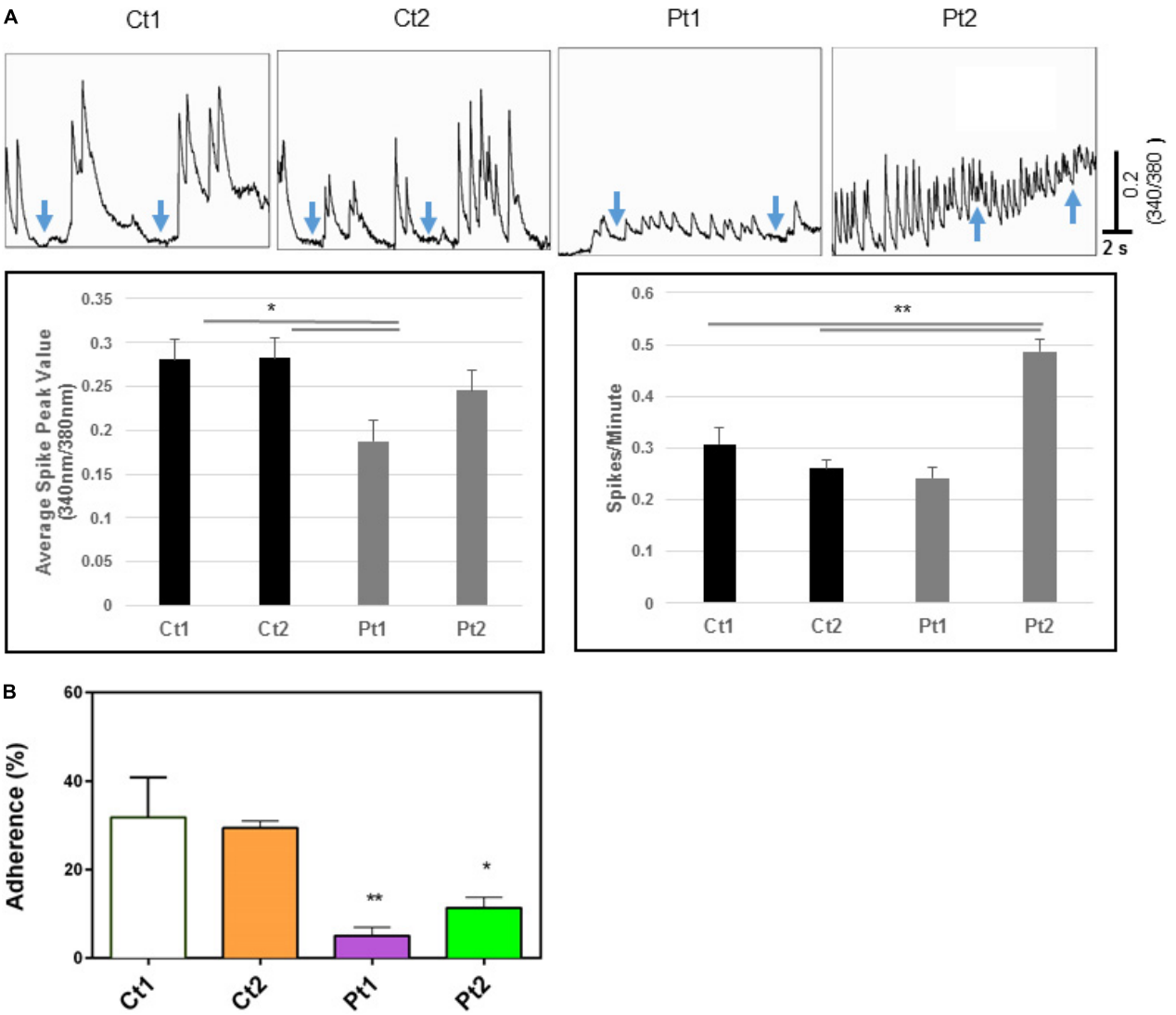

FIGURE 5 | (A) Calcium imaging data. Top panels show raw traces of spontaneous calcium transients recorded from neurons of control donors and patients. Bottom bar graphs are quantitative data of the mean peak amplitudes and spiking frequency of calcium transients. Our data show that neurons from patients (Pt1 and Pt2) exhibited significant changes in either the amplitude or the frequency of calcium transients with the inability to return to basal levels compared to their matched donor controls (Ct1 and Ct2). Arrows indicate basal levels between calcium transcients. **(B)** Adhesion activity of neurons. Control (Ct1 and Ct2) and patient-derived (Pt1 and Pt2) neurons (6-days after differentiation from NSC) were plated onto Geltrex coated 8-well glass slide Chamber and incubated at 37°C for 30 min, the dishes were flipped to remove non-adherent cells. The adherent neurons were stained with an antibody specific to MAP2 and DAPI and MAP2-expressing cells were counted. Percentage of adherent (flipped) cells was calculated based on un-flipped cells. Patient-derived cells exhibited statistically less adhesion than control cells Ct1 and Ct2: Pt1 ($p < 0.05$) and Pt2 (<0.01). $n = 3$.

patients) and two healthy age-matched donors, we determined the transcriptional profiles through RNA-seq analysis. These results revealed down-regulation of genes involved in three major neuronal functions: including cell adhesion, neurodevelopment, and antiviral (type I interferon) response (**Figure 3**). The altered gene expression profiles appear to be consistent with intellectual and movement disorder phenotypes seen in patients with *CTBP1* mutations (Beck et al., 2016, 2019; Sommerville et al., 2017).

Our results revealed down-regulation of several neuronal adhesion genes such as *KIRREL3*, *CDH10* and *CDH12* (**Figure 4A** and **Supplementary Table 1**). Reduced expressions of these genes or specific mutations in these genes have previously been implicated in intellectual disabilities (see citations in **Supplementary Table 2**). For example, the intellectual disability gene *KIRREL3* was shown to regulate target-specific mossy fiber synapse development in the hippocampus, and cadherin 12 (CDH12) was shown to mediate calcium dependent cell-cell adhesion. The neuronal adhesion genes appear to exert their effects through alterations of synaptic adhesion of neurons. Similarly, the expression of several genes involved in neurodevelopment (e.g., *SOX14*), ion channel activities

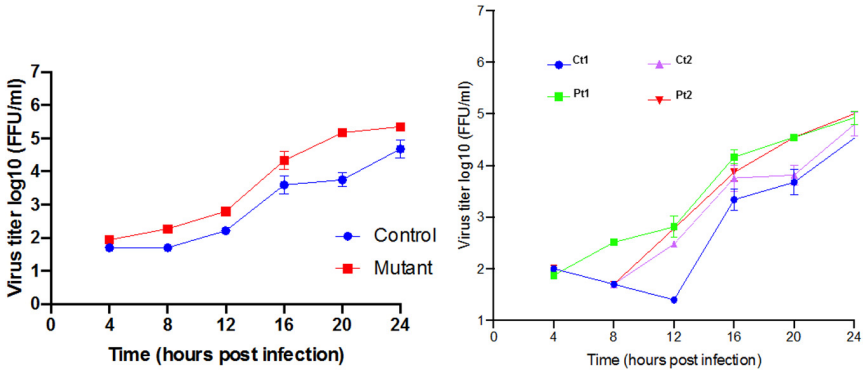

FIGURE 6 | Single step growth curves for WNV replication in neurons: The single step growth curves were generated by determining the viral titers at different times after infection in triplicates. The media supernatants of infected cells were collected at indicated times during 24 h of infection and stored at –80°C prior to viral titer analysis by focus forming assay. The average mean (±SD) of controls (Ct1 and Ct2) and patient cells (Pt1 and Pt2) are on the left. The values for the individual control and patient cells are on the right.

(e.g., *BRINP2* and *KCNIP2*) and neuronal receptors (*GFRA3*, *NR4A2*, *RET* and *ISLR2*) is also reduced in our patient-derived neurons. Mice lacking *Brinp2* were reported to exhibit neurodevelopmental phenotypes while *Kcnip2* and associated subunits were shown to regulate homeostatic neuronal excitability (ref. in **Supplementary Table 2**). Additionally, the expressions of certain neuronal transcription factors that are involved in neuronal development and survival (*ETV5*, *TAL1* and *EN1*) were also reduced in patient neurons. These results suggest that the neurodevelopmental phenotypes caused by the *CTBP1* p.R342W allele may be related to global down regulation of a number of genes that are involved in neuron survival, growth, membrane excitability, synaptic transmission and plasticity.

Here, we have used physiologically relevant patient-derived and age-matched control neuronal cell models to determine the transcriptional profiles of primary iPSC-derived neurons. Many human neuronal diseases (including *CTBP1*p.R342W-mutated developmental defects; our unpublished data) do not appear to manifest phenotypes in the mouse models. In the lack of suitable animal models, human neuronal cell models are most relevant. However, we acknowledge the limitations of our study. It involved cells derived from a limited number of patients (2 out of 12 known patients that were available) and these cell models exhibited inherent inter-patient differences. However, application of suitable data analysis approaches revealed a prominent patient-centric transcriptional pattern that was validated by RT-qPCR analysis. We note that the transcriptional patterns of iPSC-derived patient cell models is somewhat different from that of a reconstituted exogenously introduced *CTBP1*p.R342W mutant allele (Beck et al., 2019), suggesting that the cell type (glioblastoma vs primary neuron) and/or the endogenous chromatin context influence the gene expression of the *CTBP1* mutant allele.

Our phase contrast images and immunostaining of DAPI and cytoskeletal β-tubulin and MAP2 markers revealed that patient neurons exhibited thinner neuritic processes and fewer cell bodies as compared to those in control donor neurons. This decrease in DAPI-positive cells in patient cultures could be the result of a decrease in cell survival, proliferation or a change in cell fate. This could be due to the aforementioned compromised cell adhesion genes/proteins in CtBP1 patients' neurons because adhesion molecules have been reported to play important roles in various neuronal developmental processes including neural precursor cell proliferation, differentiation, growth cone pathfinding, neural excitability, and cell-cell communications (Dihne et al., 2003; Valente et al., 2016). The significant thinner neuritic processes in patients' neurons may indicate smaller neuritic surface areas for housing ionic channels and transmitter receptors, resulting in the decreased efficiency of neuronal conductivity and synaptic communication. These data suggest that *CTBP1* p.R342W mutation may negatively impact the production of key molecular components of neural cytoskeletal structures. Although no studies have demonstrated a direct link between CtBP1 and the cytoskeleton in mammalian cells, it has been reported that a "CtBP/BARS-like" protein in plants has a direct activity on the microtubule cytoskeleton (Folkers et al., 2002). Specifically, the plant CtBP homolog, Angustifolia (AN) was reported to control polar elongation of leaf cells *via* regulation of microtubule cytoskeleton proteins and mutations in AN caused aberrant development and distribution of the microtubules. Thus, our results along with previously published data suggest that CtBP1 may be important for normal development of neural cytoskeletal structures which in turn contribute to neural morphogenesis and synaptic function. The pathological phenotypes in patients with *CTBP1* p.R342W mutations may be caused by impairments in microtubule development and neuronal connections.

In addition to its roles in neuron morphological development, CtBPs also regulate genes involved in neuronal excitability. For example, CtBPs affect gene expression in epileptogenesis (Hubler et al., 2012; Goldberg and Coulter, 2013; Liu et al., 2017), and are highly expressed in many brain regions where they may play a role in synaptic transmission and plasticity (Tom Dieck et al., 2005; Jose et al., 2008). We showed here that neurons derived from patients with *CTBP1* p.R342W mutations had altered spontaneous Ca^{2+} waves and whole-cell Na^{+} currents, further

implying its involvement in neural excitability and synaptic function. Intracellular Ca^{2+} is essential to many developmental events including neural survival, differentiation, proliferation, and neurite outgrowth as well as synapse formation, synaptic transmission, and plasticity (Rosenberg and Spitzer, 2011; Grienberger and Konnerth, 2012). It is becoming increasingly clear that the common pattern of Ca^{2+} signaling in neurons is a pattern of spiking activities (Ca^{2+} transients), and the amplitude and frequency of Ca^{2+} transients are key determinants for normal neuronal development and function (O'Donovan, 1999; Dupont et al., 2011; Gasperini et al., 2017). For example, Ca^{2+} transients but not sustained Ca^{2+} elevations play important roles in axon growth and branching, growth cone turning, and cytoskeletal stabilization in developing mammalian neurons (Tang et al., 2003). Interestingly, our study revealed that Ca^{2+} in neurons derived from *CTBP1*- mutated patients exhibited more sustained patterns, and the amplitude and frequency of Ca^{2+} were significantly altered compared to those in control donor neurons (**Figure 5A**). Because of the central role of Ca^{2+} in neuronal physiology, even moderate alterations of Ca^{2+} homeostasis may lead to profound functional impairments as shown in several neuronal disorders (Wojda et al., 2008; Kawamoto et al., 2012; Oliveira et al., 2014). Therefore, the *CTBP1* mutation-mediated alteration in Ca^{2+} transients may in turn contribute to the morphological abnormalities in the neuritic cytoskeleton observed in our study. In line with this postulation is a study showing that CtBP1 was a molecular constituent of the subfamily 2 of voltage-gated Ca^{2+} channel (Ca_V2) proteome in the rat brain, which co-purified with cytoskeletal proteins. These results raised the possibility that CtBP1 may regulate Ca^{2+} signaling *via* Ca_V and could play a role in regulating cytoskeletal function. However, future studies are warranted to investigate the exact mechanistic action of CtBP1 on the functions of Ca_V and cytoskeletal proteins.

Here, we also provide evidence that *CTBP1* mutation alters whole cell ionic currents including voltage-gated Na^+ (Na_V) currents. Na_V channels are essential for neuronal electrical activity generation and propagation. The abnormal Na_V currents detected in *CTBP1*-mutated neurons in our study suggest that CtBP1 may interact with Na_V channels and regulate its expression and/or function in neurons. Furthermore, our RNA-seq data showed that the *CTBP1* p.R342W mutation down regulated KCNIP, a gene encoding a Ca^{2+}-binding protein that is an integral subunit component of K_V4 (Burgoyne, 2007). Activity of K_V4 currents contributed to neuronal excitability in response to changes in intracellular Ca^{2+} (Burgoyne, 2007). Together these studies provide insights into the involvement of specific ions such as Ca^{2+}, Na^+, or K^+. Altering the homeostasis of these ions is indicative of changes in action potentials in neurons. However, future studies on direct measurement and comparison of action potentials using isogenic cell models would be of interest to elucidate misregulation of neuronal activities by altered ionic homeostasis.

Brain imaging results have been reported for a subset of patients with *CTBP1* p.R342W mutations and those studies revealed cerebellar volume reduction in consecutive scans (Beck et al., 2016; Sommerville et al., 2017). Among the various human tissues, *CTBP1* is highly expressed in the cerebellum[1]. It was reported that CtBP(1/2) proteins play an anti-apoptotic role in primary cerebellar granule cells as well as in dopaminergic neuron-like cells (Stankiewicz et al., 2013). Our results showed that the patient neurons expressed reduced levels of the homeodomain transcription factor, Engrailed 1 (EN1). The activity of EN1 is required for normal cerebellar differentiation (Wurst et al., 1994; Joyner, 1996) and survival of dopaminergic neurons (Chi et al., 2003; Alvarez-Fischer et al., 2011), suggesting the possibility that reduced expression of EN1 in patients might contribute to the cerebellar pathology of *CTBP1*-mutated patients, hence future investigation of *CTBP1* mutation in cerebellar function is also much wanted.

The effect of *CTBP1* p.R342W on interferon-response genes was unexpected since patients have not demonstrated any increased susceptibility toward infections although this has not been characterized in detail. Our results suggest that the iPSC-derived "early" neurons express constitutive basal levels of type I interferon-response genes and that the expression is diminished in patient-derived "early" neurons. Although the interferon signaling pathway in neurons is not well-studied, homeostatic expression of type I interferon response genes in neurons have been reported (Cavanaugh et al., 2015; Drokhlyansky et al., 2017). Developing neurons respond to pathogenesis by neurotropic viruses *via* production of type I interferon (reviewed by Chakraborty et al., 2010; Nallar and Kalvakolanu, 2014). Since the expression of interferon response genes is lower in *CTBP1*-mutated early neurons compared to the constitutive levels in control cells, our results suggest a role for *CTBP1* in the regulation of interferon response in early neurons. Thus far, a direct role for CtBP1 in regulating the expression of interferon-response genes has not been identified. However, the histone methyltransferase PRDM16 which interacts with CtBPs was reported to repress type I interferon response genes in adipocytes (Kissig et al., 2017) in intestinal epithelium (Stine et al., 2019). PRDM16 also plays critical roles in neuronal development and was previously shown to control embryonic and post-natal neural stem cell maintenance and differentiation in the brain (Inoue et al., 2017; Shimada et al., 2017). It is possible that the *CTBP1* p.R342W allele may augment the activities of repressors such as PRDM16 to reduce the level of constitutive interferon signaling in early neurons. Additionally, it remains to be seen whether peripheral blood from patients demonstrates a similar decrease in interferon-response to neurons. Our results suggest that patients with *CTBP1* mutations may have an additional risk factor of increased susceptibility to neuronal viral pathogens.

The mechanism by which the *CTBP1* p.R342W allele regulates transcription in neuronal cells remains to be determined. All known *CTBP1*-mutated patients contained the same c.C991→T (*CTBP1*-S) transition within the *CTBP1* gene. Since the mutation is heterozygous, it appears that the mutation may either act as a dominant negative or gain of function. An *in silico* prediction suggests potential dominant negative phenotype for the *CTBP1* p.R342W allele (Beck et al., 2016). There have been multiple

[1]www.proteinatlas.org/ENSG00000159692-CTBP1/tissue

reports of frame-shift mutations in individuals who are not affected (ExAC database: PMID:27535533), implying that one allele of *CTBP1* is enough to avoid neurologic phenotype. Potential dominant negative activity of the mutant allele may affect functions of both CtBP1 and CtBP2 (**Figure 7**). It should be noted that Arg at residue 342 is conserved in most vertebrate (including CtBP2) and invertebrate CtBPs, suggesting a pivotal role for it in CtBP functions. The mutation *CTBP1*p.R342W is located within the major protein-interaction cleft (known as PXDLS-binding cleft) that is involved in binding with different transcriptional repression molecules of the CTBP1/2-repression complex (Chinnadurai, 2007), and the mutation was shown to impair such interactions (Beck et al., 2019). Recently, two different *CTBP1*-mutated patients with two different mutations within CTBP1 protein sequences that involved interaction with the components of the CTBP-repression complex have also been identified (David Beck; Nijala Al-Sweel; personal communications). It is possible that the heterozygous *CTBP1* mutant alleles may function as dominant repressors by not dissociating from the target gene promoters (**Figure 7**). Alternative models may include compromised transcriptional repression activity of the heterozygous *CTBP1* alleles, resulting in relief of repression of a master transactional repressor. Such a repressor may directly repress different neuronal target genes.

Phenotypes caused by the *CTBP1* p.R342W allele partially overlap with some core phenotypes of Wolf-Hirschhorn syndrome (WHS). WHS patients exhibit deletions in the chromosomal region (chromosome 4p16.3) that spans chromosome *CTBP1* locus (Battaglia et al., 2008; Zollino et al., 2008). In certain patients with the smallest micro-deletions in 4p16.3, a cluster of four genes including *NSD2* and *CTBP1* is deleted, implicating *CTBP1* in neurodevelopmental disorders including epilepsy in some WHS patients (Misceo et al., 2012). Thus, it appears that deleting *CTBP1* may contribute to some WHS phenotypes, in addition to mutations in WHS genes. Disrupting *C. elegans* CtBP1 also results in exploration and movement phenotypes (Reid et al., 2015; Yeon et al., 2018). Thus, multiple investigations, including our current transcriptional profiling studies, indicate an emerging importance of CtBP1 in normal neuronal development and activities.

MATERIALS AND METHODS

Fibroblasts: The human dermal fibroblasts from patients (CSC43 and CSC44, designated here as Pt1 and Pt2, respectively) and healthy donors (LE028 and NT011, designated Ct1 and Ct2, respectively) were received from Columbia University, Department of Pediatrics and Medicine and were grown in DMEM supplemented with 10% fetal bovine serum. Informed consent was obtained from all individual participants included in the study.

Stem cells: Patient and donor iPSCs were generated by reprogramming dermal fibroblasts by transduction of Sendai virus (SeV) vectors expressing the Yamanaka factors. Fibroblasts were transduced with CytoTune SeV reprogramming vectors. Eight days after transduction with SeV, colonies were harvested and re-plated on Mouse Embryonic Fibroblast (MEF) culture dishes. The transduced cells were expanded on MEF culture dishes and were then shifted to iPSC medium (ThermoFisher Scientific). The medium was composed of Dulbecco's Modified Eagle Medium F-12 Mixture (DMEM/F-12), KnockOut Serum Replacement (KnockOut SR), Non-Essential Amino Acids, Basic Fibroblast Growth Factor (FGF-Basic), and 2-mercaptoethanol. Colonies were stained with live cell imaging agent TRA-1-60 Alexa flour 594 conjugate antibody (ThermoFisher Scientific) and picked for further propagation and characterized by immunocytochemistry using iPSC marker, SOX2. In order to convert iPSCs to Neural Stem Cells (NSCs), the cells were plated on Geltrex coated plates and grown with PSC Neural induction media as per the protocol (ThermoFisher Scientific). The differentiated NSC cells were characterized by immunocytochemistry using NSC makers, Nestin.

Early neurons: Early neurons were generated by differentiation of NSC. For this, NSCs were first plated on poly-ornithine and laminin coated plates and grown using NSC Serum Free Media (SFM) (ThermoFisher Scientific) for the first 2 days. The NSC SFM was composed of Knockout DMEM/F-12, Stempro Neural Supplement, Recombinant FGF-Basic (Human), GlutaMAX^{TM}-I Supplement, and recombinant EGF (Human). After 2 days, they were grown in differentiation medium, which is composed of 1X neurobasal medium, serum free B-27 supplement, and GlutaMAX^{TM}-I supplement.

RNA sequencing and data analysis: Cells were grown in a 6-well plate. Cell culture media was aspirated and cells were lysed with Trizol (Zymo Research, Irvine, CA, United States). Total RNA was purified using the Direct- Zol RNA kit (Zymo Research, Irvine, CA, United States) following the manufacturer's protocol. Library preparation was performed with 1 μg of total RNA, concentration was determined by Qubit and integrity was determined using an Agilent tapestation or bioanalyzer. Ribosomal RNA was removed by a hybridization method using Ribo-ZERO kits (Illumina). Depletion and mRNA yield was confirmed by bioanalyzer. mRNA was then fragmented in buffer containing 40 mM Tris acetate pH 8.2, 100 mM potassium acetate and 30 mM magnesium acetate and heating to 94 degrees for 150 s. mRNA was reverse transcribed to yield cDNA using SuperScript III RT enzyme (Life Technologies, per manufacturer's instructions) and random hexamers. A second strand reaction was performed to yield ds-cDNA. cDNA was blunt ended, had an A base added to the 3'ends, and then had Illumina sequencing adapters ligated to the ends. Ligated fragments were then amplified for 12–15 cycles using primers incorporating unique index tags. Library molarity was determined by Qubit assay for concentration and tapestation for size. An equimolar pool was made of all libraries with unique indices. Fragments were sequenced on an Illumina HiSeq-3000 using single reads extending 50 bases.

Basecalls and demultiplexing were performed with Illumina's bcl2fastq software and a custom python demultiplexing program with a maximum of one mismatch in the indexing read. RNA-seq reads were then aligned to the Ensembl release 76 top-level assembly with STAR version 2.0.4b. Gene counts were derived from the number of uniquely aligned unambiguous

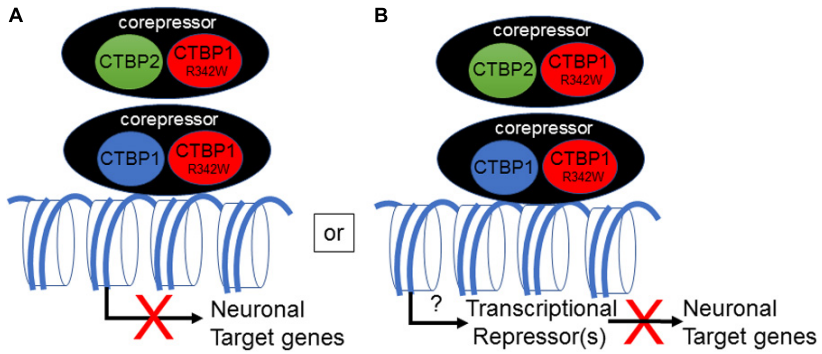

FIGURE 7 | Model for transcriptional down-regulation of neuronal target genes by *CTBP1* mutant allele. CTBP1 mutant protein may homo/heterodimerize with CTBP1 wt or CTBP2 wt. The homo/heterodimeric/oligomeric CTBP-complex may lead to enhanced repression of neuronal target genes as a result of defective dissociation from the target gene promoters directly or indirectly through reduced expression of transcriptional activators **(A)**. Alternatively, the heterodimeric complex may result in up-regulation of a certain transcriptional repressors that may repress a battery of neuronal target genes **(B)**. The down-regulated neurodevelopmental genes function in cell-cell/synaptic adhesion, neuronal transcription, axon growth, ion channel and anti-viral response genes. The transcriptional model does not exclude any potential cytosolic effects of CTBP1 mutant protein indirectly influencing the transcriptional outcome.

reads by Subread:featureCount version 1.4.5. All gene counts were then imported into the R/Bioconductor package EdgeR and TMM normalization size factors were calculated to adjust for samples for differences in library size. Ribosomal genes and genes not expressed in at least five samples greater than one count-per-million were excluded from further analysis. The TMM size factors and the matrix of counts were then imported into the R/Bioconductor package Limma. Weighted likelihoods based on the observed mean-variance relationship of every gene and samples were then calculated for all samples with the voomWithQualityWeights. Unknown latent effects were estimated with surrogate variable analysis and differential expression analysis was then performed to analyze for differences between conditions and the results were filtered for only those genes with Benjamini-Hochberg false-discovery rate adjusted p-values less than or equal to 0.05. Global log 2 fold-change perturbations in known Gene Ontology (GO) terms and KEGG pathways were detected using the R/Bioconductor package GAGE and deemed significant with Benjamini-Hochberg false-discovery rate adjusted p-value less than or equal to 0.05.

To find the most critical genes, the raw counts were variance stabilized with the R/Bioconductor package DESeq2 and then interrogated via weighted gene correlation network analysis with the R/Bioconductor package WGCNA. Briefly, all genes were correlated across each other by Pearson correlations and clustered by expression similarity into unsigned modules using a power threshold empirically determined from the data. An eigengene was then created for each *de novo* cluster and its expression profile was then correlated across all coefficients of the model matrix. Because these clusters of genes were created by expression profile rather than known functional similarity, the clustered modules were given the names of random colors where gray is the only module that has any pre-existing definition of containing genes that do not cluster well with others. For modules where the eigengene correlation exceeded 75%, the modules of genes were tested for functional enrichment of known GO terms with hypergeometric tests available in the R/Bioconductor package clusterProfiler. Significant terms with Benjamini-Hochberg adjusted *p*-values less than 0.05 were then collapsed by similarity into clusterProfiler category network plots to display the most significant terms for each module of hub genes in order to interpolate the function of each significant module. The hub genes for each significant module were then assessed for whether or not those features were also found to be significantly differentially expressed using Limma.

Confocal imaging and immunocytochemistry: Phase contrast images of iPSC/NSC-derived neurons were taken on an inverted microscope (Olympus CKX53). Images were taken under a 20× objective lens and image acquisition parameters were kept consistent between control and patient neurons. After imaging, cells were fixed for 30 min with 4% paraformaldehyde and subsequently washed three times with 1× PBS, permeabilized for 5 min with 0.3% Triton in 1× PBS, and blocked with 5% goat serum diluted in 1× PBS for 1 h. Preparations were then incubated overnight with monoclonal anti-beta-3 Tubulin or anti-MAP2 antibodies produced in mouse (1:500) (Sigma, T0198 for anti-beta-3 Tubulin and Invitrogen, 13-1500 for MAP2). Cells were rinsed three times with 1× PBS the next day. Cells were then incubated with either Alexa Fluor 488 goat anti-mouse IgG secondary antibody (1:500) (ThermoFisher Scientific, A11029) for labeling beta-3 Tubulin or Alexa Fluor 546 goat anti-mouse IgG secondary antibody (1:500) (ThermoFisher Scientific, A11030) for labeling MAP2 for 1 h at room temperature (21–22°C) under dark conditions. Cells were rinsed three times with 1× PBS, and mounted using MOWIOL mounting media with 4′6-diamidino-2-phenylindole dihydrochloride (Sigma, F6057). Samples were acquired and viewed using laser scanning confocal microscopy (Leica TCS SP8 STED 3X super-resolution system) under a 40× oil objective at 488 nm excitation (green, beta-3 Tubulin) with a 515/30 emission filter and 543 nm excitation (red, MAP2) with a 590/50 emission filter. Stack images of 0.7 μm were first collected and compressed into single 3D images. Image acquisition parameters for control and patients' neurons were kept the same.

To quantify morphological differences between patient and control cells, ImageJ and its plugin NeuronJ were utilized as previously described (Meijering et al., 2004; Pemberton et al., 2018). For neuronal growth parameters (neurite length, number and thickness), phase contrast images were taken of 14-day differentiated neurons as described above. The NeuronJ software was programmed to output length of each neurite (μm) and number of neurites measured in each phase contrast image. For neurite thickness analyses, primary neurites extending directly from a cell body were identified. In each phase contrast image, 10 primary neurites were randomly identified, and the thickest part of the neurite was measured and averaged. To determine differences in the number of DAPI-positive cells between patients and controls, confocal images were analyzed in ImageJ, and the number of DAPI-stained cells was counted. A one-way analysis of variance (ANOVA) was completed to statistically analyze all data followed by Tukey's HSD *Post hoc* test as appropriate. Data are presented as mean ± SEM.

Ca^{2+} Imaging: Ca^{2+} imaging experiments were performed using Fura-2 acetoxymethyl ester (AM) ratiometric Ca^{2+} indicator for monitoring basal intracellular Ca^{2+} levels in iPSC/NSC cells derived from control and patients. Cells differentiated into neurons for about 14 days were loaded with 5 μM Fura-2 AM (ThermoFisher Scientific Cat #: F1201) in HBSS for 30 min at 37°C followed by four 10 min washes in HBSS. Cells sat for 15 min to ensure full conversion of the dye before imaging. Images of each wavelength were taken once every second on an inverted microscope (Olympus IX73) installed with a Retiga R1 camera (Qimage). Excitation wavelengths of 340 and 380 nm were delivered using a LAMBDA XL equipped with high-speed wavelength switcher (Sutter Instrument, Novato, CA, United States) through a 40× objective for 10–20 min. The emitted fluorescence signal was collected at 510 nm by the Retiga R1 camera. Images were acquired with the MetaFluor Imaging software (Olympus) and processed and analyzed using ImageJ. Comparisons were made between individual control and mutant samples using student's *t*-Test with Benjamini-Hochberg procedure to control for multiple comparisons.

Whole-Cell Patch-Clamp Recordings: Whole-cell patch-clamp recordings of voltage-dependent ionic currents were performed on neurons after 14 days of differentiation in culture using a Multiclamp 700B amplifier (Axon Instruments; Sunnyvale, CA, United States) connected to an analog-to-digital interface Digidata 1500A (Axon Instruments). Signals were acquired and stored through pClamp 10.6 software (Axon Instruments). Whole-cell currents were recorded under voltage-clamp mode with the holding potential of −70 mV. Currents were evoked by voltage steps ranging from −90 mV to +60 mV in 10 mV increments. The external solution contained (in mM) NaCl, 135; $CaCl_2$, 3; KCl, 5; $MgCl_2$, 2; HEPES, 10; D-Glucose, 10; pH adjusted to 7.3 with NaOH. The internal pipette solution was composed of (in mM) CsCl, 130; $MgCl_2$, 0.3; HEPES, 10; EGTA, 0.1, ATP-Mg, 3; GTP-Na, 0.6; pH adjusted to 7.3 with CsOH. The osmolarity for internal solution was approximately 300 mOsm (295–305) and for external solution approximately 330 mOsm (320–340). Borosilicate glass pipettes were pulled using a horizontal micropipette puller (Model P-1000, Sutter instrument Co., United States) and had a tip resistance ranging from 3 to 6 MΩ after filling with internal solutions. Only cells with series resistances less than ∼20 MΩ and leaks less than ∼80 pA were selected for the analysis. Traces were processed using Clampfit 10.6 software (Axon Instruments).

Cell adhesion assay: The adherence activity of control and *CTBP1*-mutated neurons was determined by a "flipping" assay (Langhe et al., 2016). NSCs were differentiated to neurons (6 days) and dissociated using StemPro Accutase. Cells were counted and plated (1×10^4 cells) onto Geltrex coated Lab-Tek II Chamber 8-well glass slides and incubated for 30 min at 37°C. One set of dishes was flipped over and shaken to remove non-adherent cells. The adherent cells were fixed and stained with DAPI and immunostained with MAP2 antibody. The numbers of adherent cells were determined by counting 3 independent areas for each experiment. The cells were counted using Cytation 3 Cell Imaging Multi-Mode Reader (BioTek). The percentage of adhered (flipped) cells was calculated based on un-flipped cells. Comparisons between control and mutant adherence were performed using one-way analysis of variance (ANOVA) with Bonferroni Multiple Comparisons *post hoc* test. All experimental data were reported as mean ± SEM and three independent experiments were performed. $P < 0.05$ was considered statistically significant.

West Niles Virus (WNV) replication assay: WNV-NY (strain 3000.0259) passaged once in Vero cells (African green monkey kidney epithelial cells) was purchased from American Type Culture Collection (ATCC CCL-81). The virus was titered using a standard focus forming assay (FFA) on Vero cells as previously described (Pinto et al., 2014). WNV replication was determined by single step growth in human *CTBP1*-mutated or healthy control neurons. The 14-days differentiated neurons were infected with WNV at MOI = 1 and allowed to incubate for 1 h before the virus was removed. The progeny viral titers were determined by focus forming assay (FFA) as described (Pinto et al., 2014).

DATA AVAILABILITY STATEMENT

The original contributions presented in the study are publicly available. This data can be found here: https://www.ncbi.nlm.nih.gov/geo/query/acc.cgi?acc=GSE158754.

AUTHOR CONTRIBUTIONS

GC designed and directed the project, and wrote the manuscript. SV performed the transcriptome analysis, validation, imaging of neurons and cell adhesion assay. TS participated in the characterization of patient-derived cells. UE generated the stem cells from patient fibroblasts and participated in the transcriptome analysis. KS and AG participated in the generation of stem cells from patient fibroblasts along with UE and FX performed electrophysiological experiments and wrote sections of the manuscript. BH and KP participated in cell and calcium imaging studies. EG, AP, and JB designed the studies on response of neurons to WNV infection. ET performed RNA-seq data analysis. DB, WC, and CG

along with GC designed, supervised the project and edited the manuscript. All authors contributed to the article and approved the submitted version.

FUNDING

WC is supported from grants from SFARI and the JPB Foundation. KS and AG were supported by a grant from the DeNardo Education and Research Foundation. FX was supported by a National Science Foundation (NSF) research grant (Award Number 1916563).

ACKNOWLEDGMENTS

We thank the families of patients with *CTBP1* mutations for their generous contributions. We thank Cure, C. and Anne Rutkowski with their help in patient recruitment. Research reported in this publication was supported by the Eunice Kennedy Shriver National Institute of Child Health and Human Development of the National Institutes of Health under Award Number U54 HD087011 to the Intellectual and Developmental Disorders Research Center at Washington University and the Washington University Institute of Clinical and Translational Sciences grant UL1TR002345 from the National Center for Advancing Translational Sciences (NCATS) of the National Institutes of Health (NIH) and a Presidential Research support from Saint Louis University. The content is solely the responsibility of the authors and does not necessarily represent the official view of the NIH.

SUPPLEMENTARY MATERIAL

The Supplementary Material for this article can be found online at: https://www.frontiersin.org/articles/10.3389/fnins.2020.562292/full#supplementary-material

Supplementary Figure 1 | iPSC and NSC immunostaining.

Supplementary Figure 2 | GO network plot for positively regulated genes and heat maps. **(A)** GO Biological Process Enrichment Bar Plot (pink): All 454 positively correlated WGCNA *de novo* clustered pink genes were tested for enrichment across known GO biological processes with the R/Bioconductor package clusterProfiler. The color illustrates the significance of the enrichment and the size of each bar characterizes the number of genes for each enriched term. The up-regulation and positive correlation of pink module genes alludes to the up regulation represented by each significant term. **(B)** Module GO Category Network Plot: Positively correlated genes clustered and labeled as pink and tested for enrichment across known GO biological processes with the R/Bioconductor package clusterProfiler. Significant terms with overlapping genes are clustered together while the overlapping genes represented in the pink network module illustrate the connections between those terms. **(C)** Heat map: Heat map representing positively correlated genes in the pink module whose z-scores illustrate their up regulation and high positive correlation across all mutant samples.

Supplementary Figure 3 | (A) GO Biological Process Enrichment Bar Plot (white): All 81 negatively correlated WGCNA *de novo* clustered white genes were tested for enrichment across known GO biological processes with the R/Bioconductor package clusterProfiler. The color illustrates the significance of the enrichment and the size of each bar characterizes the number of genes for each enriched term. The up-regulation and positive correlation of white module genes alludes to the up-regulation represented by each significant term. **(B)** White Module GO Category Network Plot: All 81 correlated genes clustered into a WGCNA *de novo* network labeled as white were tested for enrichment across known GO biological processes with the R/Bioconductor package clusterProfiler. Significant terms with overlapping genes are clustered together while the overlapping genes represented in the white network module illustrate the connections between those terms. **(C)** White Heat map: Heat map representing 81 genes in the white WGCNA module whose z-scores illustrate their up-regulation and high positive correlation across all mutant samples.

Supplementary Figure 4 | Whole-cell patch-clamping. Whole-cell patch-clamp currents were elicited by step depolarizations, and the peak inward currents at −10 mV were analyzed. Left panels show representative raw traces recorded and right panels show the statistical data. Our results, comparing to the matched control donors (Ct1 and Ct2), showed that *CTBP1* mutation either significantly reduced the inward sodium currents in neurons from one patient (Pt1), or induced much larger sodium currents in the other patient (Pt2). Note that Pt2 cells expressed excessively robust inward current which reached to ≥4 nA.

Supplementary Table 1 | List of highly down-regulated genes in patient neurons.

Supplementary Table 2 | Neurodevelopmental genes down-regulated in *CTBP1*-mutated patient neurons.

REFERENCES

Abudureyimu, S., Asai, N., Enomoto, A., Weng, L., Kobayashi, H., Wang, X., et al. (2018). Essential role of linx/Islr2 in the development of the forebrain anterior commissure. *Sci. Rep*. 8:7292.

Achim, K., Peltopuro, P., Lahti, L., Tsai, H. H., Zachariah, A., Astrand, M., et al. (2013). The role of Tal2 and Tal1 in the differentiation of midbrain GABAergic neuron precursors. *Biol. Open* 2, 990–997. doi: 10.1242/bio.20135041

Alvarez-Fischer, D., Fuchs, J., Castagner, F., Stettler, O., Massiani-Beaudoin, O., Moya, K. L., et al. (2011). Engrailed protects mouse midbrain dopaminergic neurons against mitochondrial complex I insults. *Nat. Neurosci.* 14, 1260–1266. doi: 10.1038/nn.2916

Bajpe, P. K., Heynen, G. J., Mittempergher, L., Grernrum, W., de Rink, I. A., Nijkamp, W., et al. (2013). The corepressor CTBP2 is a coactivator of RAR/RXR in retinoic acid signaling. *Mol. Cell Biol.* 33, 3343–3353. doi: 10.1128/mcb.01213-12

Ban, H., Nishishita, N., Fusaki, N., Tabata, T., Saeki, K., Shikamura, M., et al. (2011). Efficient generation of transgene-free human induced pluripotent stem cells (iPSCs) by temperature-sensitive Sendai virus vectors. *Proc. Natl. Acad. Sci. U.S.A.* 108, 14234–14239. doi: 10.1073/pnas.1103509108

Battaglia, A., Filippi, T., and Carey, J. C. (2008). Update on the clinical features and natural history of Wolf-Hirschhorn (4p-) syndrome: experience with 87 patients and recommendations for routine health supervision. *Am. J. Med. Genet. C Semin. Med. Genet.* 148C, 246–251. doi: 10.1002/ajmg.c.30187

Beck, D. B., Cho, M. T., Millan, F., Yates, C., Hannibal, M., O'Connor, B., et al. (2016). A recurrent de novo CTBP1 mutation is associated with developmental delay, hypotonia, ataxia, and tooth enamel defects. *Neurogenetics* 17, 173–178. doi: 10.1007/s10048-016-0482-4

Beck, D. B., Subramanian, T., Vijayalingam, S., Ezekiel, U. R., Donkervoort, S., Yang, M. L., et al. (2019). A pathogenic CtBP1 missense mutation causes altered cofactor binding and transcriptional activity. *Neurogenetics* 20, 129–143. doi: 10.1007/s10048-019-00578-1

Berkowicz, S. R., Featherby, T. J., Whisstock, J. C., and Bird, P. I. (2016). Mice lacking brinp2 or brinp3, or both, exhibit behaviors consistent with neurodevelopmental disorders. *Front. Behav. Neurosci.* 10:196.

Bhalla, K., Luo, Y., Buchan, T., Beachem, M. A., Guzauskas, G. F., Ladd, S., et al. (2008). Alterations in CDH15 and KIRREL3 in patients with mild to severe intellectual disability. *Am. J. Hum. Genet.* 83, 703–713. doi: 10.1016/j.ajhg.2008.10.020

Burgoyne, R. D. (2007). Neuronal calcium sensor proteins: generating diversity in neuronal Ca^{2+} signalling. *Nat. Rev. Neurosci.* 8, 182–193. doi: 10.1038/nrn2093 doi: 10.1038/nrn2093

Byun, J. S., and Gardner, K. (2013). C-terminal binding protein: a molecular link between metabolic imbalance and epigenetic regulation in breast cancer. *Int. J. Cell Biol.* 2013:647975.

Cavanaugh, S. E., Holmgren, A. M., and Rall, G. F. (2015). Homeostatic interferon expression in neurons is sufficient for early control of viral infection. *J. Neuroimmunol.* 279, 11–19. doi: 10.1016/j.jneuroim.2014.12.012

Chakraborty, S., Nazmi, A., Dutta, K., and Basu, A. (2010). Neurons under viral attack: victims or warriors? *Neurochem. Int.* 56, 727–735. doi: 10.1016/j.neuint.2010.02.016

Chi, C. L., Martinez, S., Wurst, W., and Martin, G. R. (2003). The isthmic organizer signal FGF8 is required for cell survival in the prospective midbrain and cerebellum. *Development* 130, 2633–2644. doi: 10.1242/dev.00487

Chinnadurai, G. (2002). CtBP, an unconventional transcriptional corepressor in development and oncogenesis. *Mol. Cell* 9, 213–224. doi: 10.1016/s1097-2765(02)00443-4

Chinnadurai, G. (2007). Transcriptional regulation by C-terminal binding proteins. *Int. J. Biochem. Cell Biol.* 39, 1593–1607. doi: 10.1016/j.biocel.2007.01.025

Dcona, M. M., Morris, B. L., Ellis, K. C., and Grossman, S. R. (2017). CtBP- an emerging oncogene and novel small molecule drug target: advances in the understanding of its oncogenic action and identification of therapeutic inhibitors. *Cancer Biol. Ther.* 18, 379–391. doi: 10.1080/15384047.2017.1323586

Diamond, M. S., Mehlhop, E., Oliphant, T., and Samuel, M. A. (2009). The host immunologic response to West Nile encephalitis virus. *Front. Biosci. (Landmark Ed.)* 14:3024–3034. doi: 10.2741/3432

Dihne, M., Bernreuther, C., Sibbe, M., Paulus, W., and Schachner, M. (2003). A new role for the cell adhesion molecule L1 in neural precursor cell proliferation, differentiation, and transmitter-specific subtype generation. *J. Neurosci.* 23, 6638–6650. doi: 10.1523/jneurosci.23-16-06638.2003

Dobin, A., Davis, C. A., Schlesinger, F., Drenkow, J., Zaleski, C., Jha, S., et al. (2013). STAR: ultrafast universal RNA-seq aligner. *Bioinformatics* 29, 15–21. doi: 10.1093/bioinformatics/bts635

Drokhlyansky, E., Goz Ayturk, D., Soh, T. K., Chrenek, R., O'Loughlin, E., Madore, C., et al. (2017). The brain parenchyma has a type I interferon response that can limit virus spread. *Proc. Natl. Acad. Sci. U.S.A.* 114, E95–E104.

Dupont, G., Combettes, L., Bird, G. S., and Putney, J. W. (2011). Calcium oscillations. *Cold Spring Harbor Perspect. Biol.* 3:a004226.

Fang, M., Li, J., Blauwkamp, T., Bhambhani, C., Campbell, N., and Cadigan, K. M. (2006). C-terminal-binding protein directly activates and represses Wnt transcriptional targets in *Drosophila*. *EMBO J.* 25, 2735–2745. doi: 10.1038/sj.emboj.7601153

Folkers, U., Kirik, V., Schobinger, U., Falk, S., Krishnakumar, S., Pollock, M. A., et al. (2002). The cell morphogenesis gene ANGUSTIFOLIA encodes a CtBP/BARS-like protein and is involved in the control of the microtubule cytoskeleton. *EMBO J.* 21, 1280–1288. doi: 10.1093/emboj/21.6.1280 doi: 10.1093/emboj/21.6.1280

Fontanet, P. A., Rios, A. S., Alsina, F. C., Paratcha, G., and Ledda, F. (2018). Pea3 Transcription factors, Etv4 and Etv5, are required for proper hippocampal dendrite development and plasticity. *Cereb Cortex* 28, 236–249. doi: 10.1093/cercor/bhw372

Gasperini, R. J., Pavez, M., Thompson, A. C., Mitchell, C. B., Hardy, H., Young, K. M., et al. (2017). How does calcium interact with the cytoskeleton to regulate growth cone motility during axon pathfinding? *Mol. Cell. Neurosci.* 84, 29–35. doi: 10.1016/j.mcn.2017.07.006

Goldberg, E. M., and Coulter, D. A. (2013). Mechanisms of epileptogenesis: a convergence on neural circuit dysfunction. *Nat. Rev. Neurosci.* 14, 337–349. doi: 10.1038/nrn3482

Grienberger, C., and Konnerth, A. (2012). Imaging calcium in neurons. *Neuron* 73, 862–885. doi: 10.1016/j.neuron.2012.02.011

Guerin, A., Stavropoulos, D. J., Diab, Y., Chenier, S., Christensen, H., Kahr, W. H., et al. (2012). Interstitial deletion of 11q-implicating the KIRREL3 gene in the neurocognitive delay associated with Jacobsen syndrome. *Am. J. Med. Genet. A* 158A, 2551–2556. doi: 10.1002/ajmg.a.35621

Hildebrand, J. D., and Soriano, P. (2002). Overlapping and unique roles for C-terminal binding protein 1 (CtBP1) and CtBP2 during mouse development. *Mol. Cell Biol.* 22, 5296–5307. doi: 10.1128/mcb.22.15.5296-5307.2002

Hubler, D., Rankovic, M., Richter, K., Lazarevic, V., Altrock, W. D., Fischer, K. D., et al. (2012). Differential spatial expression and subcellular localization of CtBP family members in rodent brain. *PLoS One* 7:e39710. doi: 10.1371/journal.pone.0039710

Inoue, M., Iwai, R., Tabata, H., Konno, D., Komabayashi-Suzuki, M., Watanabe, C., et al. (2017). Prdm16 is crucial for progression of the multipolar phase during neural differentiation of the developing neocortex. *Development* 144, 385–399. doi: 10.1242/dev.136382

Itoh, T. Q., Matsumoto, A., and Tanimura, T. (2013). C-terminal binding protein (CtBP) activates the expression of E-box clock genes with CLOCK/CYCLE in Drosophila. *PLoS One* 8:e63113. doi: 10.1371/journal.pone.0063113

Ivanova, D., Dirks, A., Montenegro-Venegas, C., Schone, C., Altrock, W. D., Marini, C., et al. (2015). Synaptic activity controls localization and function of CtBP1 via binding to Bassoon and Piccolo. *EMBO J.* 34, 1056–1077. doi: 10.15252/embj.201488796

Jiang, D., Weidner, J. M., Qing, M., Pan, X. B., Guo, H., Xu, C., et al. (2010). Identification of five interferon-induced cellular proteins that inhibit west nile virus and dengue virus infections. *J. Virol.* 84, 8332–8341. doi: 10.1128/jvi.02199-09

Jose, M., Nair, D. K., Altrock, W. D., Dresbach, T., Gundelfinger, E. D., and Zuschratter, W. (2008). Investigating interactions mediated by the presynaptic protein bassoon in living cells by Foerster's resonance energy transfer and fluorescence lifetime imaging microscopy. *Biophys. J.* 94, 1483–1496. doi: 10.1529/biophysj.107.111674 doi: 10.1529/biophysj.107.111674

Joyner, A. L. (1996). Engrailed, Wnt and Pax genes regulate midbrain–hindbrain development. *Trends Genet.* 12, 15–20. doi: 10.1016/0168-9525(96)81383-7

Kawamoto, E. M., Vivar, C., and Camandola, S. (2012). Physiology and pathology of calcium signaling in the brain. *Front. Pharmacol.* 3:61. doi: 10.3389/fphar.2012.00061

Kissig, M., Ishibashi, J., Harms, M. J., Lim, H. W., Stine, R. R., Won, K. J., et al. (2017). PRDM16 represses the type I interferon response in adipocytes to promote mitochondrial and thermogenic programing. *EMBO J.* 36, 1528–1542. doi: 10.15252/embj.201695588

Kumar, V., Carlson, J. E., Ohgi, K. A., Edwards, T. A., Rose, D. W., Escalante, C. R., et al. (2002). Transcription corepressor CtBP is an NAD(+)-regulated dehydrogenase. *Mol. Cell* 10, 857–869. doi: 10.1016/s1097-2765(02)00650-0

Langfelder, P., and Horvath, S. (2008). WGCNA: an R package for weighted correlation network analysis. *BMC Bioinformatics* 9:559. doi: 10.1186/1471-2105-9-559

Langhe, R. P., Gudzenko, T., Bachmann, M., Becker, S. F., Gonnermann, C., Winter, C., et al. (2016). Cadherin-11 localizes to focal adhesions and promotes cell-substrate adhesion. *Nat. Commun.* 7:10909.

Lee, B., Lee, M., Song, S., Loi, L. D., Lam, D. T., Yoon, J., et al. (2017). Specification of neurotransmitter identity by Tal1 in thalamic nuclei. *Dev. Dyn.* 246, 749–758. doi: 10.1002/dvdy.24546

Leek, J. T., Johnson, W. E., Parker, H. S., Jaffe, A. E., and Storey, J. D. (2012). The sva package for removing batch effects and other unwanted variation in high-throughput experiments. *Bioinformatics* 28, 882–883. doi: 10.1093/bioinformatics/bts034

Liao, Y., Smyth, G. K., and Shi, W. (2014). featureCounts: an efficient general purpose program for assigning sequence reads to genomic features. *Bioinformatics* 30, 923–930. doi: 10.1093/bioinformatics/btt656

Liu, D., Liu, Z., Liu, H., Li, H., Pan, X., and Li, Z. (2016). Brain-derived neurotrophic factor promotes vesicular glutamate transporter 3 expression and neurite outgrowth of dorsal root ganglion neurons through the activation of the transcription factors Etv4 and Etv5. *Brain Res. Bull.* 121, 215–226. doi: 10.1016/j.brainresbull.2016.02.010

Liu, Y., Lai, S., Ma, W., Ke, W., Zhang, C., Liu, S., et al. (2017). CDYL suppresses epileptogenesis in mice through repression of axonal Nav1.6 sodium channel expression. *Nat. Commun.* 8:355. doi: 10.1038/s41467-017-00368-z

Lu, C. C., Cao, X. J., Wright, S., Ma, L., Oertel, D., and Goodrich, L. V. (2014). Mutation of Npr2 leads to blurred tonotopic organization of central auditory circuits in mice. *PLoS Genet.* 10:e1004823. doi: 10.1371/journal.pgen.1004823

Martin, E. A., Muralidhar, S., Wang, Z., Cervantes, D. C., Basu, R., Taylor, M. R., et al. (2015). The intellectual disability gene Kirrel3 regulates target-specific mossy fiber synapse development in the hippocampus. *Elife* 4:e09395.

Martinez, S., Andreu, A., Mecklenburg, N., and Echevarria, D. (2013). Cellular and molecular basis of cerebellar development. *Front. Neuroanat.* 7:18.

Meijering, E., Jacob, M., Sarria, J. C., Steiner, P., Hirling, H., and Unser, M., (2004). Design and validation of a tool for neurite tracing and analysis in fluorescence microscopy images. *Cytometry. A: J. Int. Soc. Anal. Cytol.* 58, 167–176. doi: 10.1002/cyto.a.20022

Misceo, D., Baroy, T., Helle, J. R., Braaten, O., Fannemel, M., and Frengen, E. (2012). 1.5Mb deletion of chromosome 4p16.3 associated with postnatal growth delay, psychomotor impairment, epilepsy, impulsive behavior and asynchronous skeletal development. *Gene* 507, 85–91. doi: 10.1016/j.gene.2012.07.021

Moon, M., Jung, E. S., Jeon, S. G., Cha, M. Y., Jang, Y., Kim, W., et al. (2019). Nurr1 (NR4A2) regulates Alzheimer's disease-related pathogenesis and cognitive function in the 5XFAD mouse model. *Aging Cell* 18:e12866. doi: 10.1111/acel.12866

Nallar, S. C., and Kalvakolanu, D. V. (2014). Interferons, signal transduction pathways, and the central nervous system. *J. Interferon Cytokine Res.* 34, 559–576. doi: 10.1089/jir.2014.0021

Nardini, M., Spano, S., Cericola, C., Pesce, A., Massaro, A., Millo, E., et al. (2003). CtBP/BARS: a dual-function protein involved in transcription co-repression and Golgi membrane fission. *EMBO J.* 22, 3122–3130. doi: 10.1093/emboj/cdg283

Nassal, D. M., Wan, X., Liu, H., Laurita, K. R., and Deschenes, I. (2017). KChIP2 regulates the cardiac Ca2+ transient and myocyte contractility by targeting ryanodine receptor activity. *PLoS One* 12:e0175221. doi: 10.1371/journal.pone.0175221

Nayler, S. P., Powell, J. E., Vanichkina, D. P., Korn, O., Wells, C. A., Kanjhan, R., et al. (2017). Human iPSC-derived cerebellar neurons from a patient with ataxia-telangiectasia reveal disrupted gene regulatory networks. *Front. Cell. Neurosci.* 11:321.

O'Donovan, M. J. (1999). The origin of spontaneous activity in developing networks of the vertebrate nervous system. *Curr. Opin. Neurobiol.* 9, 94–104. doi: 10.1016/s0959-4388(99)80012-9

Oliveira, A. M., Bading, H., and Mauceri, D. (2014). Dysfunction of neuronal calcium signaling in aging and disease. *Cell Tissue Res.* 357, 381–383. doi: 10.1007/s00441-014-1954-1 doi: 10.1007/s00441-014-1954-1

Orvis, G. D., Hartzell, A. L., Smith, J. B., Barraza, L. H., Wilson, S. L., Szulc, K. U., et al. (2012). The engrailed homeobox genes are required in multiple cell lineages to coordinate sequential formation of fissures and growth of the cerebellum. *Dev. Biol.* 367, 25–39. doi: 10.1016/j.ydbio.2012.04.018

Paliwal, S., Ho, N., Parker, D., and Grossman, S. R. (2012). CtBP2 promotes human cancer cell migration by transcriptional activation of tiam1. *Genes Cancer* 3, 481–490.

Panza, P., Sitko, A. A., Maischein, H. M., Koch, I., Flotenmeyer, M., Wright, G. J., et al. (2015). The LRR receptor Islr2 is required for retinal axon routing at the vertebrate optic chiasm. *Neural Dev.* 10:23.

Pemberton, K., Mersman, B., and Xu, F. (2018). Using ImageJ to assess neurite outgrowth in mammalian cell cultures: Research data quantification exercises in undergraduate neuroscience lab. *J. Undergrad. Neurosci. Edu.* 16, A186–A194.

Pinto, A. K., Ramos, H. J., Wu, X., Aggarwal, S., Shrestha, B., Gorman, M., et al. (2014). Deficient IFN signaling by myeloid cells leads to MAVS-dependent virus-induced sepsis. *PLoS Pathog* 10:e1004086. doi: 10.1371/journal.ppat.1004086

Prekop, H. T., Kroiss, A., Rook, V., Zagoraiou, L., Jessell, T. M., Fernandes, C., et al. (2018). Sox14 is required for a specific subset of cerebello-olivary projections. *J. Neurosci.* 38, 9539–9550. doi: 10.1523/jneurosci.1456-18.2018

Ray, S. K., Li, H. J., Metzger, E., Schule, R., and Leiter, A. B. (2014). CtBP and associated LSD1 are required for transcriptional activation by NeuroD1 in gastrointestinal endocrine cells. *Mol. Cell Biol.* 34, 2308–2317. doi: 10.1128/mcb.01600-13

Redies, C., Hertel, N., and Hubner, C. A. (2012). Cadherins and neuropsychiatric disorders. *Brain Res.* 1470, 130–144. doi: 10.1016/j.brainres.2012.06.020

Reid, A., Sherry, T. J., Yucel, D., Llamosas, E., and Nicholas, H. R. (2015). The C-terminal binding protein (CTBP-1) regulates dorsal SMD axonal morphology in Caenorhabditis elegans. *Neuroscience* 311, 216–230. doi: 10.1016/j.neuroscience.2015.10.026

Ritchie, M. E., Phipson, B., Wu, D., Hu, Y., Law, C. W., Shi, W., et al. (2015). limma powers differential expression analyses for RNA-sequencing and microarray studies. *Nucleic Acids Res.* 43:e47. doi: 10.1093/nar/gkv007

Rivera, M., Wu, Q., Hamerlik, P., Hjelmeland, A. B., Bao, S., and Rich, J. N. (2015). Acquisition of meiotic DNA repair regulators maintain genome stability in glioblastoma. *Cell Death Dis.* 6:e1732. doi: 10.1038/cddis.2015.75

Rosenberg, S. S., and Spitzer, N. C. (2011). Calcium signaling in neuronal development. *Cold Spring Harbor Perspect. Biol.* 3:a004259.

Sahu, S. K., Tiwari, N., Pataskar, A., Zhuang, Y., Borisova, M., Diken, M., et al. (2017). FBXO32 promotes microenvironment underlying epithelial-mesenchymal transition via CtBP1 during tumour metastasis and brain development. *Nat. Commun.* 8:1523.

Schaller, S., Buttigieg, D., Alory, A., Jacquier, A., Barad, M., Merchant, M., et al. (2017). Novel combinatorial screening identifies neurotrophic factors for selective classes of motor neurons. *Proc. Natl. Acad. Sci. U.S.A.* 114, E2486–E2493.

Shen, Y., Kapfhamer, D., Minnella, A. M., Kim, J. E., Won, S. J., Chen, Y., et al. (2017). Bioenergetic state regulates innate inflammatory responses through the transcriptional co-repressor CtBP. *Nat. Commun.* 8:624.

Shi, Y., Sawada, J., Sui, G., Affar El, B., Whetstine, J. R., Lan, F., et al. (2003). Coordinated histone modifications mediated by a CtBP co-repressor complex. *Nature* 422, 735–738. doi: 10.1038/nature01550

Shimada, I. S., Acar, M., Burgess, R. J., Zhao, Z., and Morrison, S. J. (2017). Prdm16 is required for the maintenance of neural stem cells in the postnatal forebrain and their differentiation into ependymal cells. *Genes Dev.* 31, 1134–1146. doi: 10.1101/gad.291773.116

Shrestha, B., Gottlieb, D., and Diamond, M. S. (2003). Infection and injury of neurons by West Nile encephalitis virus. *J. Virol.* 77, 13203–13213.

Sommerville, E. W., Alston, C. L., Pyle, A., He, L., Falkous, G., Naismith, K., et al. (2017). De novo CTBP1 variant is associated with decreased mitochondrial respiratory chain activities. *Neurol. Genet.* 3: e187. doi: 10.1212/nxg.0000000000000187

Souza, R. P., Romano-Silva, M. A., Lieberman, J. A., Meltzer, H. Y., MacNeil, L. T., Culotti, J. G., et al. (2010). Genetic association of the GDNF alpha-receptor genes with schizophrenia and clozapine response. *J. Psychiatr Res.* 44, 700–706. doi: 10.1016/j.jpsychires.2010.01.002

Spitzer, N. C. (2006). Electrical activity in early neuronal development. *Nature* 444, 707–712. doi: 10.1038/nature05300

Spitzer, N. C., Gu, X., and Olson, E. (1994). Action potentials, calcium transients and the control of differentiation of excitable cells. *Curr. Opin. Neurobiol.* 4, 70–77. doi: 10.1016/0959-4388(94)90034-5

Stankiewicz, T. R., Schroeder, E. K., Kelsey, N. A., Bouchard, R. J., and Linseman, D. A. (2013). C-terminal binding proteins are essential pro-survival factors that undergo caspase-dependent downregulation during neuronal apoptosis. *Mol. Cell. Neurosci.* 56, 322–332. doi: 10.1016/j.mcn.2013.07.004

Stine, R. R., Sakers, A. P., TeSlaa, T., Kissig, M., Stine, Z. E., Kwon, C. W., et al. (2019). PRDM16 maintains homeostasis of the intestinal epithelium by controlling region-specific metabolism. *Cell Stem Cell* 25, 830–845.e8.

Tang, F., Dent, E. W., and Kalil, K. (2003). Spontaneous calcium transients in developing cortical neurons regulate axon outgrowth. *J. Neurosci.* 23, 927–936. doi: 10.1523/jneurosci.23-03-00927.2003

Ter-Avetisyan, G., Dumoulin, A., Herrel, A., Schmidt, H., Strump, J., Afzal, S., et al. (2018). Loss of axon bifurcation in mesencephalic trigeminal neurons impairs the maximal biting force in Npr2-deficient mice. *Front. Cell Neurosci.* 12:153.

Tom Dieck, S., Altrock, W. D., Kessels, M. M., Qualmann, B., Regus, H., Brauner, D., et al. (2005). Molecular dissection of the photoreceptor ribbon synapse: physical interaction of Bassoon and RIBEYE is essential for the assembly of the ribbon complex. *J. Cell Biol.* 168, 825–836.

Tomuschat, C., and Puri, P. (2015). RET gene is a major risk factor for Hirschsprung's disease: a meta-analysis. *Pediatr. Surg. Int.* 31, 701–710. doi: 10.1007/s00383-015-3731-y

Valente, P., Lignani, G., Medrihan, L., Bosco, F., Contestabile, A., Lippiello, P., et al. (2016). Cell adhesion molecule L1 contributes to neuronal excitability regulating the function of voltage-gated Na+ channels. *J. Cell Sci.* 129, 1878–1891. doi: 10.1242/jcs.182089

Wang, H. G., He, X. P., Li, Q., Madison, R. D., Moore, S. D., McNamara, J. O., et al. (2013). The auxiliary subunit KChIP2 is an essential regulator of homeostatic excitability. *J. Biol. Chem.* 288, 13258–13268. doi: 10.1074/jbc.m112.434548

Wang, K., Zhang, H., Ma, D., Bucan, M., Glessner, J. T., Abrahams, B. S., et al. (2009). Common genetic variants on 5p14.1 associate with autism spectrum disorders. *Nature* 459, 528–533.

Williams, M. J., Klockars, A., Eriksson, A., Voisin, S., Dnyansagar, R., Wiemerslage, L., et al. (2016). The *Drosophila* ETV5 homologue Ets96B: molecular link between obesity and bipolar disorder. *PLoS Genet.* 12:e1006104. doi: 10.1371/journal.pgen.1006104

Wojda, U., Salinska, E., and Kuznicki, J. (2008). Calcium ions in neuronal degeneration. *IUBMB Life* 60, 575–590. doi: 10.1002/iub.91 doi: 10.1002/iub.91

Wurst, W., Auerbach, A. B., and Joyner, A. L. (1994). Multiple developmental defects in Engrailed-1 mutant mice: an early mid-hindbrain deletion and patterning defects in forelimbs and sternum. *Development* 120, 2065–2075.

Yeon, J., Kim, J., Kim, D. Y., Kim, H., Kim, J., Du, E. J., et al. (2018). A sensory-motor neuron type mediates proprioceptive coordination of steering in *C. elegans* via two TRPC channels. *PLoS Biol.* 16:e2004929. doi: 10.1371/journal.pbio.2004929

Zhang, Q., Piston, D. W., and Goodman, R. H. (2002). Regulation of corepressor function by nuclear NADH. *Science* 295, 1895–1897.

Zollino, M., Murdolo, M., Marangi, G., Pecile, V., Galasso, C., Mazzanti, L., et al. (2008). On the nosology and pathogenesis of Wolf-Hirschhorn syndrome: genotype-phenotype correlation analysis of 80 patients and literature review. *Am. J. Med. Genet. C Semin. Med. Genet.* 148C, 257–269. doi: 10.1002/ajmg.c.30190

Conflict of Interest: The authors declare that the research was conducted in the absence of any commercial or financial relationships that could be construed as a potential conflict of interest.

frontiers in Neuroscience

ORIGINAL RESEARCH
published: 19 November 2020
doi: 10.3389/fnins.2020.586452

Microglia Play an Essential Role in Synapse Development and Neuron Maturation in Tissue-Engineered Neural Tissues

*Huimin Zhu†, Xin Qiao†, Wei Liu, Changyong Wang and Yuwei Zhao**

Tissue Engineering Research Center, Academy of Military Medical Sciences and Department of Neural Engineering and Biological Interdisciplinary Studies, Institute of Military Cognition and Brain Sciences, Academy of Military Medical Sciences, Beijing, China

In the process of constructing engineered neural tissues, we often use mixed primary neural cells, which contain microglia in the cell culture. However, the role that microglia play in the construction of engineered neural tissue has not been well studied. Here, we generated three-dimensional (3D) engineered neural tissues by silk fibroin/collagen composite scaffolds and primary mixed cortical cells. We depleted microglial cells by magnetic separation. Then, we analyzed the neural growth, development, mature and synapse-related gene, and protein expressions compared with the control engineered neural tissues with the microglia-depleted engineered neural tissues. We found that the engineered neural tissues constructed by magnetic separation to remove microglia showed a decrease in the number of synaptic proteins and mature neurons. These findings link microglia to neuron and synaptic maturation and suggest the importance of microglia in constructing engineered neural tissues *in vitro*.

Keywords: 3D culture, microglia, neuron, reconstruction, tissue engineering, silk fibroin

OPEN ACCESS

Edited by:
Miao He,
Fudan University, China

Reviewed by:
Bo Peng,
Chinese Academy of Sciences (CAS), China
Jennie Leach,
University of Maryland, Baltimore County, United States

***Correspondence:**
Yuwei Zhao
zhaoyuwei158@163.com

†These authors have contributed equally to this work

Specialty section:
This article was submitted to Neural Technology, a section of the journal Frontiers in Neuroscience

Received: *23 July 2020*
Accepted: *15 October 2020*
Published: *19 November 2020*

Citation:
Zhu H, Qiao X, Liu W, Wang C and Zhao Y (2020) Microglia Play an Essential Role in Synapse Development and Neuron Maturation in Tissue-Engineered Neural Tissues. Front. Neurosci. 14:586452. doi: 10.3389/fnins.2020.586452

INTRODUCTION

Most of the *in vitro* approaches for constructing neuronal networks are based on two-dimensional (2D) cultures, which cannot recapitulate three-dimensional (3D) organizations, cell–cell interaction, or their network functions *in vivo* (Swistowski et al., 2010; Yang et al., 2016; Martin et al., 2018). *In vitro* methods to construct 3D neuronal networks that mimic both the structures and functions of neural tissues have been pursued by researchers in various fields, such as neural tissue engineering, neurodegenerative disease studies, and artificial intelligence. Several 3D *in vitro* research models in the form of cerebral organoids (Lancaster et al., 2013; Bagley et al., 2017; Birey et al., 2017), neurospheroids (Fennema et al., 2013; Jeong et al., 2015; van Pel et al., 2018), and hydrogel cultures (Irons et al., 2008; Ma et al., 2008; Koutsopoulos and Zhang, 2013; Sun et al., 2017) have been developed to study the specific processes of the brain that are challenging to investigate and manipulate *in vivo* in animal models or *ex vivo* in brain slices.

Silk protein has received recent attention for neural tissue engineering applications due to its excellent biocompatibility, controllable degradability, controllable mechanical properties, and the ability to be processed into multiple material forms (Kasoju and Bora, 2012; Kundu et al., 2013; Abbott et al., 2016; Huang et al., 2018). The unique silk protein properties protect the neurons from excitotoxicity and maintenance of adequate transfer because of biocompatibility and porous

structure. The construction of the bioengineered neural tissues based on the silk fibroin (SF)–collagen composite scaffold can recapitulate functional neural networks (Tang-Schomer et al., 2014; Chwalek et al., 2015a,b).

The significant categories of cell sources for 3D neural cultures are pluripotent stem cells, neural stem cells, or primary cortical cells. Researchers often do not use a single type of cell for cell seeding, mainly because brain tissue is composed of different types of cells. *In vitro*, different types of brain cells play distinct roles in the process of neural cell remodeling and reassembly. Microglia are glial cells from the myeloid lineage. When brain tissue is damaged, microglia migrate to the site of damage and engulf the cellular debris. The recent discovery is that microglia also play some role in the uninjured brain. Microglia have shown that they can remove dead neurons as well as synapses (Schafer et al., 2012). New evidence suggests that microglia in the brain play an essential role in the synaptic organization, control of neuronal excitability, and trophic support during brain development (Stephan et al., 2012; Parkhurst et al., 2013; Grabert et al., 2016; Weinhard et al., 2018). However, in the tissue-engineered neural tissue model, the function of microglia, the neuron–microglia interactions are still unclear.

Here, we aimed to study the influence of microglia removal on neuronal survival, synapse development, and functional maturation of the neural network in engineered neural tissue constructed *in vitro* and tried to explain the interaction relationship between microglia and neurons in engineered neural tissue.

MATERIALS AND METHODS

Preparation and Characterization of Silk Fibroin Porous Scaffolds

The silk solution was prepared as previously described (Rockwood et al., 2011). Briefly, silkworm cocoons were boiled in 0.02 M Na_2CO_3 for 30 min and washed with ddH_2O to extract the sericin. The degummed silk was dissolved in 9.3 M Libr at 60°C for 4–6 h. The solution was dialyzed in ddH_2O for 48 h and centrifuged at 12,000 rpm for 30 min to remove the aggregates. Then, 4 g NaCl (particle size ∼500 μm) was added to 2 ml of 8% SF solution in the containers for 48 h. The mixture was immersed in water for 48 h to extract the NaCl. Porous scaffolds were made as previously described (Altman et al., 2003). The SF scaffolds were sterilized and coated with poly-L-lysine before cell seeding.

The mechanical properties of the SF scaffolds were tested by an Instron mechanical tester (Instron 5900) and compared with rat and mouse brain tissues. All samples were applied 0.2 N load and compressed by the stress-relaxation tests, which was compressed stepwise at 5% of the height and relaxed for 500 s to establish equilibrium. The compressive load–compressive strain diagram was recorded. The compressive modulus was calculated as the minimum linear slope. All scaffolds and tissue samples were cut into 5 mm diameter and 2 mm height. Adult rat and mouse brain tissues were dissected from adult animals, stored in sterile PBS at 4°C, and tested within 4 h of animal euthanasia.

The SF scaffolds were dehydration treated, and then the morphology was analyzed by scanning electron microscopy (Hitachi S-3400N) at 5 kV. Samples were placed onto a copper plate, and gold sputtering was treated on the samples before observation.

Isolation of Primary Cortical Cells

Isolation of primary cortical cells was assessed as previously described (Pacifici and Peruzzi, 2012). Briefly, primary rat cortical cells were isolated from embryonic day 16–18 SD rats. Cortical tissues were isolated, dissociated with trypsin (0.05%) followed with trypsin inhibition, centrifuged, and resuspended in NeuroBasal media with B-27 supplement and 2 mM L-glutamine.

Magnetic Labeling and Separation of Microglial Cells

The isolated primary cortical cells were centrifuged and suspended in 80 μl buffer [0.5% bovine serum albumin (BSA) in phosphate buffered saline (PBS)] and 20 μl CD11b/c Microbeads (MACS, rat, 130-105-634) per 1×10^7 cells for 15 min at 4°C and then resuspended in 500 μl buffer. LD column was placed in the magnetic field of a MACS Separator. The cell suspension was applied onto the column, and the flow-through unlabeled cells were collected, which were called microglia-depleted cortical cells. The magnetically labeled cells flushed out were microglia. The microglia were grown in Dulbecco's Modified Eagle's Medium (DMEM)–F12 plus 10% fetal bovine serum (FBS).

Construct Assembly, Culture, and Evaluation

The concentrated cortical cells and microglia-depleted cortical cells were seeded on the SF scaffolds (5 mm diameter, 1 mm height) for 24 h, immersed with 200 μl collagen (3 mg/ml) for 30 min at 37°C, and adjusted pH to 7 by NaOH. The inside and edges of the scaffolds were immersed in collagen, and there were no bubbles in the added collagen. The construct seeded mixed cortical cells were called the control group, and the construct seeded microglia-depleted cortical cells were called the depleted group. For control cultures used for cell viability measurement and axon length assays, cells were seeded at 1×10^6, 5×10^6, and 1×10^7 cells/composite scaffold. For control cultures and microglia-depleted group used for microtubule-associated protein 2 (MAP2) positive immunofluorescence staining, neural maturation, synapse development-related gene, and protein expressions based on SF/collagen scaffolds, cells were seeded at 5×10^6 cells/composite scaffold.

Cell Viability Evaluation

A Live/Dead Kit (Invitrogen) was used to evaluate cell viability. Constructs were incubated with Calcein AM and EthD-1 at 37°C for 15–30 min. After incubation, cells were washed three times with PBS and imaged through a confocal microscope (Nikon A1). The images were taken from the surface to 10 μm deep at 2 μm intervals.

Cell Counting Kit-8 (CCK-8) assay (Dojindo) was used to assess the cell viability of 3D engineered tissue cultures and 2D

cultures. CCK-8 was mixed in culture media (1:10) at different time points (day *in vitro* 1, 3, and 7 and one time every week up to 6 weeks) and incubated for 2 h at 37°C. Fluorescence was read at 450 nm on a microplate spectrophotometer (Molecular Devices). Three samples were used for each experiment.

Immunofluorescence Staining

After harvest, the samples were fixed with 4% paraformaldehyde for 30 min, washed with PBS, and treated with 0.3% Triton X-100 including 5% normal goat serum for 30 min, followed by incubation of primary antibodies overnight at 4°C. The next day after three 5 min washes, samples were incubated with secondary antibodies for 2 h at room temperature. Antibodies included anti-Tuj1, anti-CD11b/c, anti-IBA1, anti-MAP2, and goat anti-mouse or anti-rabbit secondary antibodies. **Table 2** shows the information of the primary antibodies. Cell nuclei were stained with DAPI. Samples were again washed thoroughly with PBS before imaging. Fluorescence images were acquired by a Nikon A1 confocal microscope. The images were taken from the surface to 50–60 μm deep at 5 μm intervals.

Real-Time PCR Analysis

We assessed the expression level of genes (NCAM-L1, MAP2, Tuj1, NF-L, synaptophysin, GABAR1, etc.) associated with the neuron growth and microglial inflammatory response using real-time PCR. Briefly, total RNA was extracted with TRIzol reagent, and PCRs were carried out using a LightCycler 96 real-time quantitative thermal cycler (Roche) with SYBR Green PCR Mix (Toyobo). GAPDH was used as an internal reference. **Table 1** shows all the primer sequences used in this study. All reactions were run in triplicate. The fluorescence intensity was recorded under the setting as follows: 20 s at 95°C and 30 s at 58°C for 40 cycles. Finally, the gene expression value of individual constructs was carefully calculated relative to *GAPDH* expression using the $2^{-\Delta\Delta Ct}$ method.

Western Blotting

Western blot analysis was carried out using control or microglia-depleted samples from day 7 and day 14 engineered tissues. The samples were treated in liquid nitrogen for 20 min, and then proteins extracted by Laemmli were homogenized on ice.

TABLE 2 | Information of antibodies used in this study.

Antibody	Type	Dilution	Source
Tuj1	Poly-rabbit	1:500	Abcam ab18207
CD11b/c	Poly-mouse	1:200	Abcam ab1211
MAP2	Poly-rabbit	1:500	Abcam ab32454
IBA1	Poly-mouse	1:200	Abcam ab15690
Synaptophysin	Poly-rabbit	1:200	Abcam ab32127

TABLE 3 | Abbreviations that appeared in this study.

Acronyms	Full acronym
NCAM	Neural cell adhesion molecule
GAP-43	Growth-associated protein-43
SNP-25	Synaptosomal-associated protein-25
SF	Silk fibroin
3D	Three-dimensional
2D	Two-dimensional
CNS	Central nervous system
MAP2	Microtubule-associated protein 2
BSA	Bovine serum albumin
GABA	Gamma aminobutyric acid

The supernatant was collected after centrifugation at 12,000 rpm for 10 min. The concentration of proteins was detected by BCA Protein Assay Kit (Invitrogen). Equal amounts (60 μg) were separated on 12% SDS-PAGE gels and transferred to nitrocellulose membrane. The membranes were blocked with 5% defatted milk for 1 h, incubated with primary antibodies overnight at 4°C, and incubated with appropriate secondary antibodies for 1 h at room temperature. **Table 2** shows the information of the primary antibodies. The labeled proteins were detected by enhanced chemiluminescence reagent (Applygen). GAPDH was used as the control to correct the band intensity.

Statistical Analyses

All quantitative analyses were performed at least in triplicate, and the mean values were obtained. Results presented were based on the averages of data and standard error of the mean as error bars. The analysis used the Student's *t*-test.

TABLE 1 | Primer sequences in this study.

Genes	Forward primer	Reverse primer
Tuj1	GCCAAGTTCTGGGAGGCTCATC	GTAGTAGACACTGTAGCGTTCCA
GAP-43	AACGGAGACTGCAGAAAGCA	GCCTCGGGGTCTTCTTTACC
SNP-25	TGGATGAGCAAGGCGAACAA	TCCTGATTATTGCCCCAGGC
NCAM	CACCAGTGAGAGGGTGAGTG	CTCCAGTACATGGTGTCCTTT
NF-L	AATAAGTCGACGCTGCAGGACCTCAACCA	GATCTGAATTCCTGAGCCTGGTCTCTTC
MAP2	GAGAAGGAGGCCCAACACAA	TCTTCGAGGCTTCTTCCAGTG
IL-10	TTTAGGCGAGAAGCTGAAGG	TCTTCACAGGGCAGGAATCT
IL-1β	GACCTGTTCTTTGAGGCTGAC	TAGCCACGCCTTCTGTGACTCTAACT
TGF-β1	CCCGCATCCCAGGACCTCTCT	CGGGGGACTGGCGAGCCTTAG
IL-6	GACTGATGTTGTTGAGAGCCACTG	TAGCCACGCCTTCTGTGACTCTAACT
Synaptophysin	CATTCATGCGCGCACCTCCA	TTGCTGCCCATAGTCGCCCT
GABAR1	GTGCAAGTTAAATTGCGCTGCA	GCTTCCCAATATCCAATCTGCAGC
GAPDH	GATGGTGAAGGTCGGTGTGA	GGGATCTCGCTCCTGGAAG

Ethics Statement

All animal care and experimental protocols complied with the Animal Management Rule of the Ministry of Health, People's Republic of China (Documentation No. 55, 2001). All procedures were approved by the Institutional Animal Care and Use Committee of the Academy of Military Medical Sciences, Beijing, China.

Table 3 shows all the abbreviations that appeared in this study.

RESULTS

Scaffold Characterization

The overall fabrication process from SF extraction to aqueous-based sponges is shown in **Figure 1A**. The pore size of the scaffolds was about <500 μm. The bright-field microscope image (**Figure 1B**) and SEM image (**Figure 1C**) showed the high porosity of the scaffolds, which allowed sufficient exchange of nutrients, oxygen, and wastes. The mechanical stiffness of the scaffolds and the cortical tissues of mouse and rat were tested by confined compression tests. The respective load-strain trace is shown in **Figure 1D**. The SF scaffolds had a modulus of 32.2 ± 9.7 kPa higher than a rat brain of 12.1 ± 2 kPa and a mouse brain of 3.1 ± 0.1 kPa.

Biofabrication of 3D Engineered Neural Tissues

Since we have fabricated the SF sponges, the isolated primary cortical cells were cultured on the SF sponge. After the cortical cells were attached to the SF sponges, the scaffolds were filled with the collagen matrix to allow axon outgrowth and network formation. The 3D constructs viability of different cell seeding densities at 3 days of culture were stained with Live/Dead to evaluate the cell viability (**Figures 2A,B**). Confocal images showed that the dead cells percentage gradually increased as the cell seeding density increased. The 3D constructs growth of different cell seeding densities after 7 days of culture were immunostained with anti-Tuj1 fluorescent. The results showed that the protein expression of Tuj1 protein of different cell seeding densities was dissimilar. As cell seeding density increases, the more complex the neural network is formed morphologically (**Figures 2C,D**). The engineered neural tissue viability and axon outgrowth were found to be affected by cell density. **Figure 2** shows that the most suitable cell seeding density was 5×10^6 cells/scaffold, which showed the prolonged axon and higher proportion of live cells.

3D Engineered Neural Tissues Growth

Further, we observed the cells viability, axon growth of the engineered neural tissues *in vitro* compared with 2D culture. By confocal images, we observed that the axon growth of the

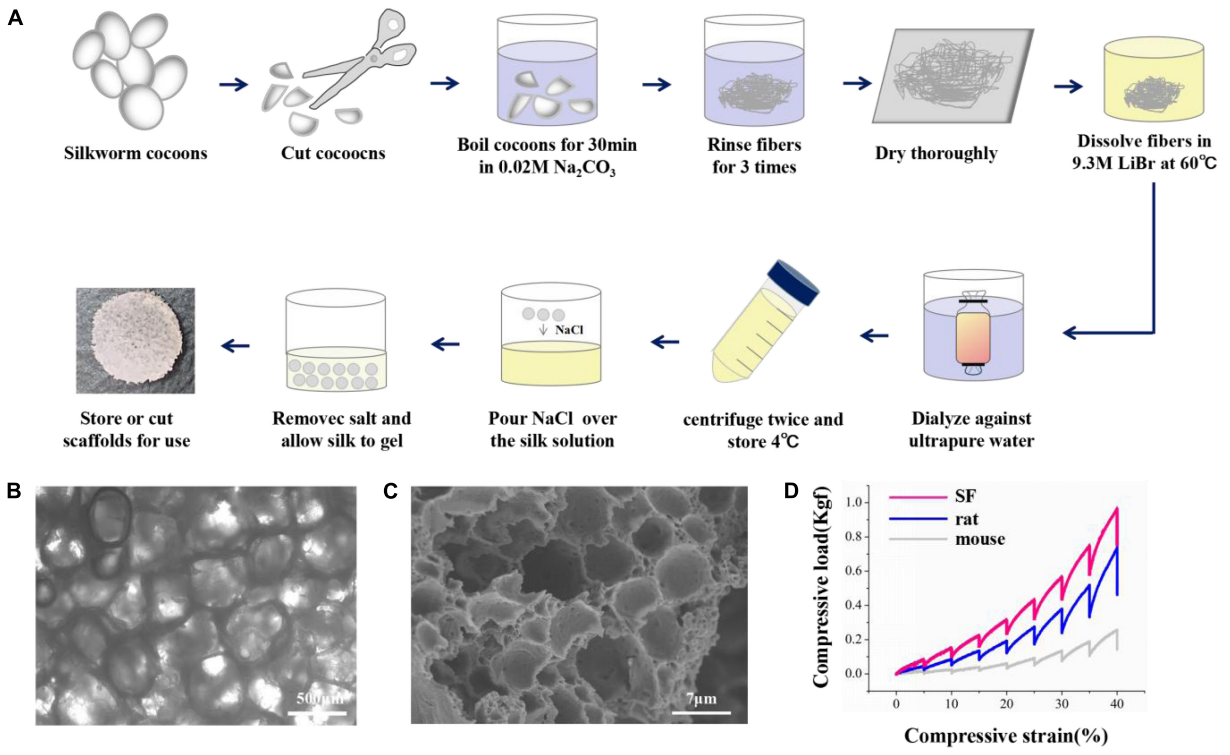

FIGURE 1 | The preparation and characterization of the silk fibroin porous scaffolds. **(A)** Schematic from the silk fibroin extraction to the porous scaffolds. It takes about 4 days from the silk cocoons to the final silk fibroin porous sponges. **(B,C)** The bright-field microscope image and the scanning electron microscopy image show the inner structure of the SF sponges. **(D)** Compressive load-strain traces of the SF sponge, rat, and mouse cortical tissues.

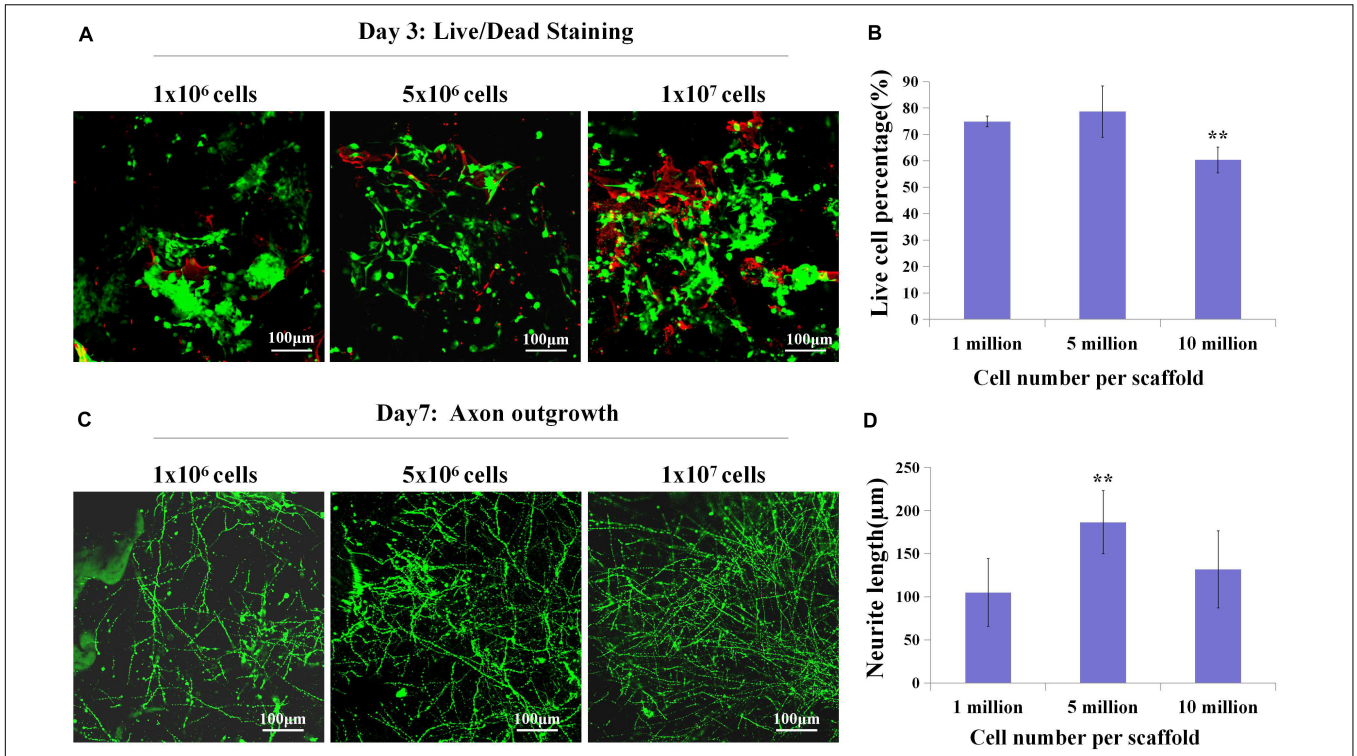

FIGURE 2 | The live cell percentage and axon length with different cell densities. **(A,B)** Live (green)/Dead (red) staining showed live cell percentage with different cell densities on the SF sponges on day 3. **(C,D)** Immunochemistry with anti-Tuj1 indicated the neuronal axon length of different cell densities at day 7. $^{**}p < 0.01$.

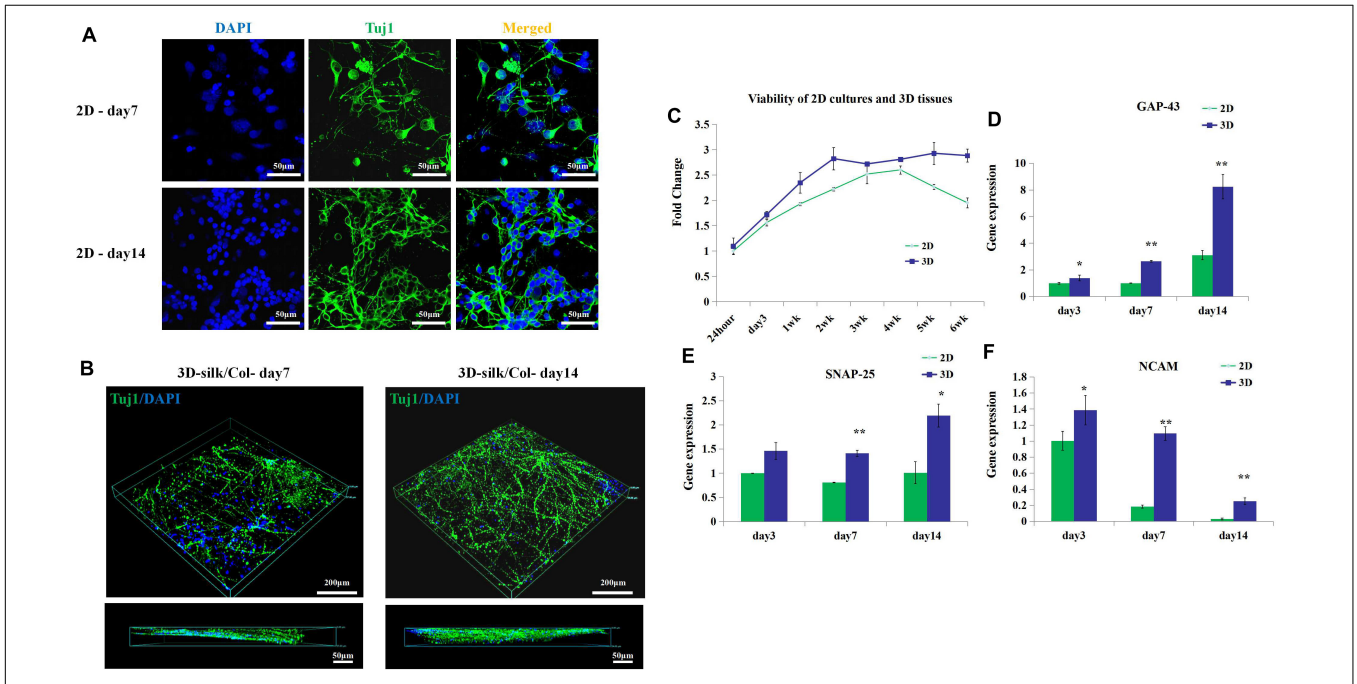

FIGURE 3 | 3D engineered neural tissue growth compared with 2D cultures. **(A)** Fluorescence images of 2D cultures on day 7 and day 14. **(B)** Fluorescence images of 3D fluorescence images of confocal z stacks of day 7 and day 14 neuronal axon on the SF sponges immunostained with Tuj1 in green and DAPI in blue. **(C)** Viability of 2D cultures and 3D engineered neural tissue cultures at 24 h, 3, 7 days, and 2–6 weeks assayed with CCK-8 and expressed relative to 24-h levels. **(D–F)** Expression of growth-associated protein 43 (GAP-43), neural cell adhesion molecule L1 (NCAM-L1), and synaptosomal-associated protein 25 (SNP-25) mRNA in 2D culture (green) and 3D engineered neural tissues culture (deep blue) at day 7 and day 14 relative to day 3 expression. $^{*}p < 0.05$ and $^{**}p < 0.01$.

engineered neural tissues was opposite from the 2D cultures (**Figures 3A,B**). The nucleus was anchored on the surface of porous sponges, and the axons penetrated the gel along with culture time. 3D engineered neural tissue culture showed a more prolonged axon than 2D culture.

The viability of 3D engineered neural tissues and 2D cultures was assayed by the CCK-8 at 24 h, 3, 7 days, 2, 3, 4, 5, and 6 weeks. 3D engineered neural tissue culture showed higher viability by OD value (**Figure 3C**). After 4 weeks, cortical cells viability in 2D cultures showed a decrease, and cortical cells in 3D cultures still maintained high viability. This result demonstrated that the SF scaffold would promote long-term cell survival compared with 2D cultures. Gene expression also showed the differences between 2D cultures and 3D cultures.

After 3 days of culture, the expression of growth-associated protein 43 (GAP-43) and NCAM-L1 was observed to be significantly upregulated for 3D cultures grown on SF/collagen composite materials compared with 2D cultures (1.4-fold). Similarly, after 7 days of culture, the expression of GAP-43, SNAP-25, and NCAM-L1 was observed to be significantly upregulated for 3D cultures compared with 2D cultures (2. 7-, 1. 8-, and 6-fold, respectively). The calculated expression levels of GAP-43, SNAP-25, and NCAM-L1 at 14 days of culture amounted to 2. 7-, 2. 2-, and 8.8-fold for 3D cultures compared with 2D cultures (**Figures 3D–F**). 3D engineered neural tissues showed higher expression levels of regenerative growth (GAP-43), synaptogenesis (SNAP-25), and neuronal adhesion (NCAM-L1) compared with 2D cultures at day 3, day 7, and day 14.

Depletion of Primary Microglia by Magnetic Separation

Schematic images of magnetic separation of primary microglia are shown in **Figure 4A**. Immunofluorescence studies were performed to evaluate the depletion of the microglia after magnetic separation. The magnetically labeled cells flushed out showed IBA1 positive, indicating that the labeled cells were microglia, and most of the microglia were depleted by magnetic separation. We called the engineered neural tissues containing microglia the control group and the engineered neural tissues depleting microglia the depleted group (**Figure 4B**).

The Maturation of Neurons and Synapse Development Were Decreased in the Microglia-Depleted 3D Tissues

By flow cytometry (**Figure 5A**), the proportion of the neurons in the isolated primary cortical cells is about

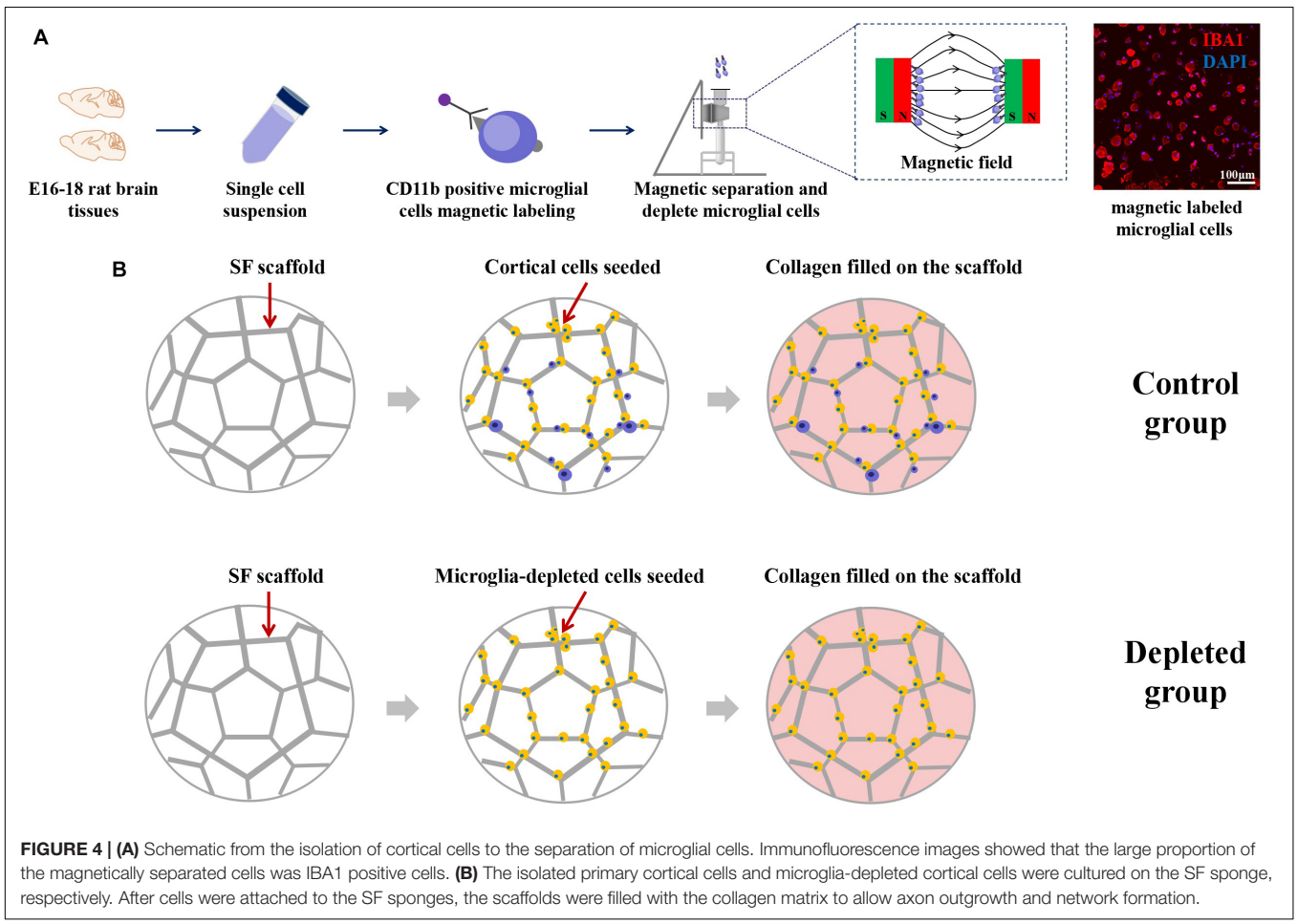

FIGURE 4 | (A) Schematic from the isolation of cortical cells to the separation of microglial cells. Immunofluorescence images showed that the large proportion of the magnetically separated cells was IBA1 positive cells. **(B)** The isolated primary cortical cells and microglia-depleted cortical cells were cultured on the SF sponge, respectively. After cells were attached to the SF sponges, the scaffolds were filled with the collagen matrix to allow axon outgrowth and network formation.

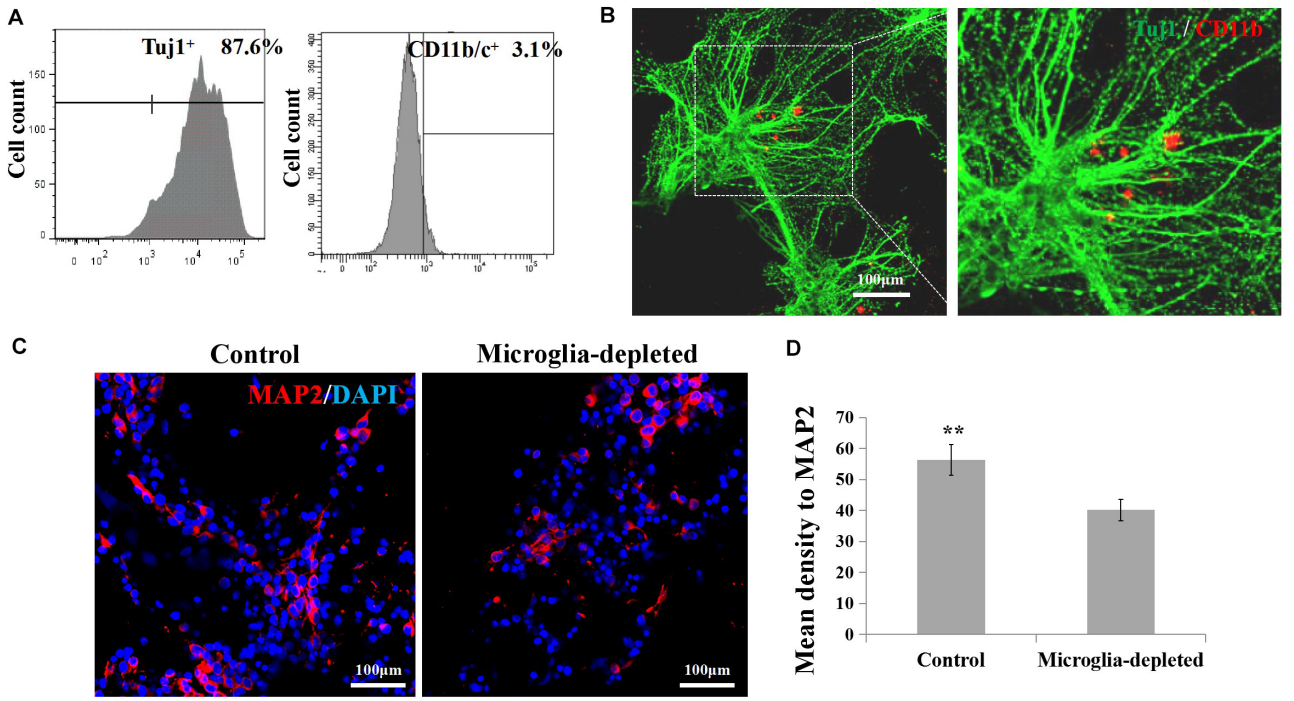

FIGURE 5 | (A,B) Proportion and morphological distribution of neurons and microglia of the primary cortical cells. **(C)** Fluorescence images of day 7 axons immunostained with MAP2 in red and DAPI in blue. **(D)** Expression of microglia-related pro-inflammatory factor (IL-1β, IL-6) and inflammatory factor (IL-10, TGF-β) in the 3D engineered neural tissues (control group) and 3D engineered microglia-depleted neural tissues (depleted group). $^{**}p < 0.01$.

87.6 ± 5.2% ($n = 3$); the proportion of microglia is about 3.1 ± 0.25% ($n = 3$). To visualize microglia and neuron in the engineered neural tissues, we labeled microglia with CD11b/c, a neuron with Tuj1 using immunofluorescence staining. The Tuj1 and CD11b/c double-stained results of the control group revealed that in some cases, microglia were surrounded by neuron cell body and axon (**Figure 5B**). After 7 days of culture, the expression levels of MAP2 of the depleted group were lower than those of the control group (**Figures 5C,D**).

3D neural tissues (control group) tended to have higher expression level of the neuron (Tuj1), mature neuron (MAP2), neuronal adhesion molecular (NCAM-L1), synaptogenesis (synaptophysin), neurofilament (NF-L), and receptors for gamma-aminobutyric acid (GABAR1) than the microglia-depleted 3D neural tissues (depleted group) as shown in **Figure 6A**. Especially after 4 days of culture, the expression of GABAR1 and Tuj1 was significantly upregulated for the control group compared with the microglia-depleted group (2.9- and 2.5-fold, respectively). The expression of NF-L after 7 days and GABAR1 after 14 days was significantly upregulated for the control group compared with the microglia-depleted group (4.3- and 2.4-fold, respectively). The expression levels of MAP2 and synaptophysin of the depleted group were lower than those of the control group at day 7 and day 14, respectively. These results of gene expression were consistent with the results of protein expression by Western blot (**Figure 6B**), suggesting that microglia play an essential role in synapse development and neuron maturation in tissue-engineered neural tissues.

In summary, we generated 3D engineered neural tissues based on the SF–collagen scaffolds. We compared the viability, the axon outgrowth length, and the expression from different cell densities. On this basis, we depleted microglia by magnetic separation and seeded the cortical cells, which remove microglia on the SF–collagen composite scaffold. The effect of the microglia depletion on the structure, gene, and protein expression was determined by immunocytochemical method, mRNA gene expression, and Western blot. We demonstrated that the maturation of neurons and synapse development were decreased in the microglia-depleted 3D tissues group compared with the control group. It is proven that microglia play an essential role in synapse development and neuron maturation in tissue-engineered neural tissues.

DISCUSSION

In this study, we mainly studied the role of microglia in the construction of 3D tissue-engineered neural tissues. We found that the depletion of microglia affects the synapse development and neuron maturation in the 3D neural tissues. This indicated that it is best to use mixed cortical cells of cells differentiated from neural progenitor/stem cells as seeded cells in the construction of engineered neural tissues, which is beneficial to constructing the functional engineered organization.

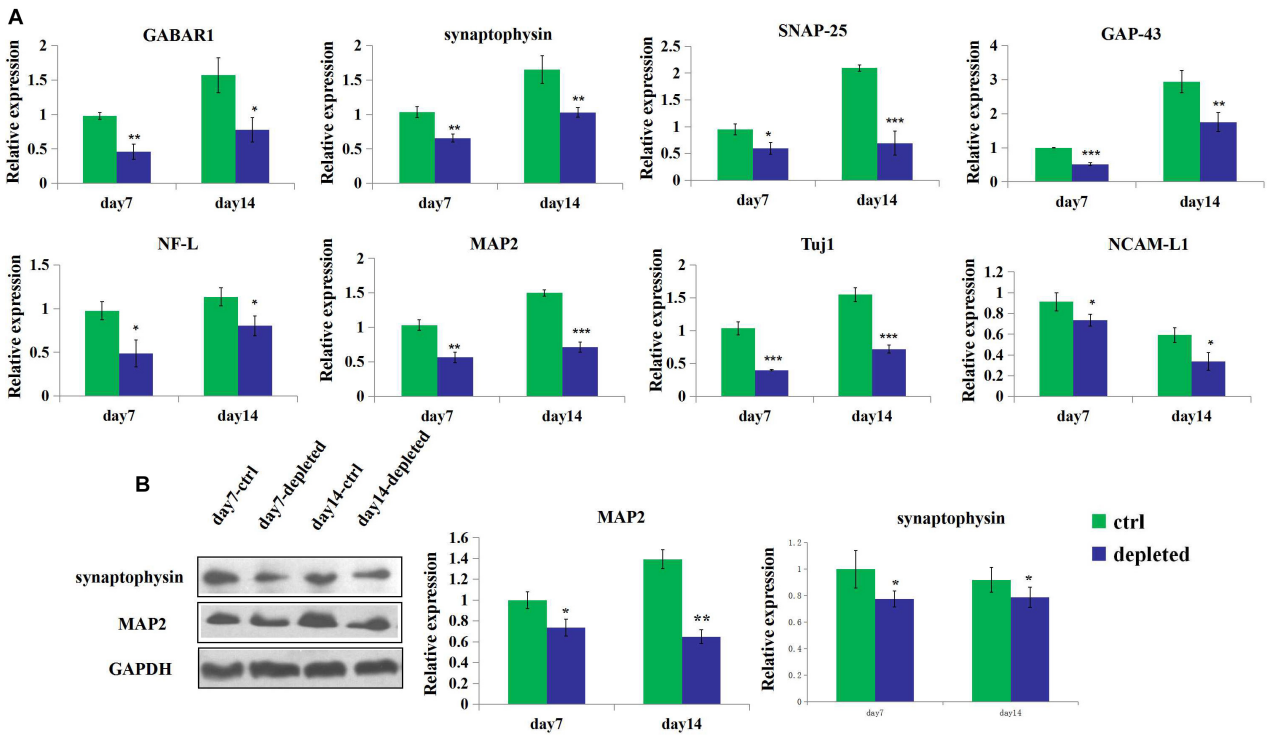

FIGURE 6 | Gene and protein expression of the 3D engineered neural tissues. **(A)**. Expression of GABAR1, synaptophysin, SNAP-25, GAP-43, NCAM-L1, NF-L, MAP2, and Tuj1 mRNA in the control group (light blue) and the microglia-depleted group (deep blue) at day 14 relative to the day 7 expression. **(B)** Expression of synaptophysin, MAP2, and GAPDH protein in the control group (green) and the microglia-depleted group (deep blue) at day 14 relative to the day 7 expression. $^{*}p < 0.05$, $^{**}p < 0.01$, and $^{***}p < 0.001$.

Microglia are homologous macrophage cells that, in addition to providing surveillance and clearance role, can engulf synapses in uninjured brains and achieve synaptic pruning during postnatal development (Prinz and Priller, 2014; Dong et al., 2018; Jung and Chung, 2018; Surinkaew et al., 2018). Paolicelli et al. demonstrated that microglia are involved in the development of brain wiring in newborn mice, and that disrupting microglia–synapse interactions delays the maturation of synaptic circuits (Paolicelli et al., 2011; Norris et al., 2018).

Engineered neural tissue construction is a hot topic in recent years. In recent years, researchers studied microglia-related inflammation or fractal analysis in tissue engineering (Jiang et al., 2016; Koss et al., 2017). However, until now, the role of microglia in the engineered neural tissue construction *in vitro* has not been clarified. Clarifying the role of microglia in the 3D engineered neural tissues contributes significantly to the engineered tissue construction and 3D models in neuroscience.

Obtaining or isolating microglia *in vitro* is different because of the cellular heterogeneity. Researchers usually use the method that is divided into three sections: mixed microglial, astroglial, and oligodendroglial cell culture; culture maintaining; and isolation of other cells except for microglia by shaking or digestion method (Ni and Aschner, 2010; Tamashiro et al., 2012; Roy, 2018). Here, we used a magnetic separation for isolation of primary microglia from primary mixed cortical cells. This method can highly and efficiently remove pure microglia from the mixed cortical cells by magnetic separation. The removed microglia obtained by this method were fully functional and morphologically like microglia obtained by conventional isolation methods.

In summary, microglia play a critical role in synapse development and neuron maturation in tissue-engineered neural tissues. Based on our findings, the maturation of neurons and synapse development were decreased in the microglia-depleted 3D bioengineered neural tissues. Microglia affect engineered neural tissues neuron maturation and synapse development probably through three ways: (1) microglia can remove dead and dying neurons and further affect the viability and remodeling of the engineered neural tissues; (2) in addition to some pro-inflammatory and inflammatory factors, microglia also secrete some neurotrophic factors; and (3) microglia remodel, run, or engulf synapse. However, further research is needed to illuminate the mechanisms on how the microglia affect neuron maturation and synapse development and related signal pathway.

DATA AVAILABILITY STATEMENT

The original contributions presented in this study are included in the article, further inquiries can be directed to the corresponding author.

ETHICS STATEMENT

The animal study was reviewed and approved by the Institutional Animal Care and Use Committee of Academy of Military Medical Sciences.

AUTHOR CONTRIBUTIONS

HZ, XQ, and YZ designed the project. HZ wrote the manuscript and performed the experiments. HZ and XQ analyzed the data. CW supervised the project. All authors contributed to the article and approved the submitted version.

FUNDING

This work was supported by the Key Program of the National Key Research and Development Program of China (no. 2016YFY1101303), the Key Program of National Natural Science Foundation of China (no. 31830030), and the Joint Funds for National Natural Science Foundation of China (no. U1601221).

REFERENCES

Abbott, R. D., Kimmerling, E. P., Cairns, D. M., and Kaplan, D. L. (2016). Silk as a biomaterial to support long-term three-dimensional tissue cultures. *ACS Appl. Mater. Interfaces* 8, 21861–21868. doi: 10.1021/acsami.5b12114

Altman, G. H. I., Diaz, F., Jakuba, C., Calabro, T., Horan, R. L., Chen, J., et al. (2003). Silk-Based-Biomaterials. *Biomaterials* 24, 401–416. doi: 10.1016/s0142-9612(02)00353-8

Bagley, J. A., Reumann, D., Bian, S., Lévi-Strauss, J., and Knoblich, J. A. (2017). Fused cerebral organoids model interactions between brain regions. *Nat. Methods* 14, 743–751. doi: 10.1038/nmeth.4304

Birey, F., Andersen, J., Makinson, C. D., Islam, S., Wei, W., Huber, N., et al. (2017). Assembly of functionally integrated human forebrain spheroids. *Nature* 545, 54–59. doi: 10.1038/nature22330

Chwalek, K., Sood, D., Cantley, W. L., White, J. D., Tang-Schomer, M., and Kaplan, D. L. (2015a). Engineered 3D Silk-collagen-based model of polarized neural tissue. *J. Vis. Exp.* 105:e52970. doi: 10.3791/52970

Chwalek, K., Tang-Schomer, M. D., Omenetto, F. G., and Kaplan, D. L. (2015b). In vitro bioengineered model of cortical brain tissue. *Nat. Protoc.* 10, 1362–1373. doi: 10.1038/nprot.2015.091

Dong, P., Zhao, J., Li, N., Lu, L., Li, L., Zhang, X., et al. (2018). Sevoflurane exaggerates cognitive decline in a rat model of chronic intermittent hypoxia by aggravating microglia-mediated neuroinflammation via downregulation of PPAR-γ in the hippocampus. *Behav. Brain Res.* 347, 325–331. doi: 10.1016/j.bbr.2018.03.031

Fennema, E., Rivron, N., Rouwkema, J., van Blitterswijk, C., and de Boer, J. (2013). Spheroid culture as a tool for creating 3D complex tissues. *Trends Biotechnol.* 31, 108–115. doi: 10.1016/j.tibtech.2012.12.003

Grabert, K., Michoel, T., Karavolos, M. H., Clohisey, S., Baillie, J. K., Stevens, M. P., et al. (2016). Microglial brain region-dependent diversity and selective regional sensitivities to ageing. *Nat. Neurosci.* 19, 504–516. doi: 10.1038/nn.4222

Huang, W., Ling, S., Li, C., Omenetto, F. G., and Kaplan, D. L. (2018). Silkworm silk-based materials and devices Silkworm silk-based materials and devices generated using bio-nanotechnology. *Chem. Soc. Rev.* 47, 6486–6504. doi: 10.1039/c8cs00187a

Irons, H. R., Cullen, D. K., Shapiro, N. P., Lambert, N. A., Lee, R. H., and Laplaca, M. C. (2008). Three-dimensional neural constructs a novel platform for neurophysiological investigation. *J. Neural Eng.* 5, 333–341. doi: 10.1088/1741-2560/5/3/006

Jeong, G. S., Chang, J. Y., Park, J. S., Lee, S. A., Park, D., Woo, J., et al. (2015). Networked neural spheroid by neuro-bundle mimicking nervous system created by topology effect. *Mol. Brain* 8:17. doi: 10.1186/s13041-015-0109-y

Jiang, Z., Song, Q., Tang, M., Yang, L., Cheng, Y., Zhang, M., et al. (2016). Enhanced migration of neural stem cells by microglia grown on a three-dimensional graphene scaffold. *ACS Appl. Mater. Interfaces* 8, 25069–25077. doi: 10.1021/acsami.6b06780

Jung, Y. J., and Chung, W. S. (2018). Phagocytic roles of glial cells in healthy and diseased brains. *Biomol. Ther.* 26, 350–357. doi: 10.4062/biomolther.2017.133

Kasoju, N., and Bora, U. (2012). Silk fibroin in tissue engineering. *Adv. Healthc. Mater.* 1, 393–412. doi: 10.1002/adhm.201200097

Koss, K. M., Churchward, M. A., Jeffery, A. F., Mushahwar, V. K., Elias, A. L., and Todd, K. G. (2017). Improved 3D hydrogel cultures of primary glial cells for in vitro modelling of neuroinflammation. *J. Vis. Exp.* 130:56615. doi: 10.3791/56615

Koutsopoulos, S., and Zhang, S. (2013). Long-term three-dimensional neural tissue cultures in functionalized self-assembling peptide hydrogels. Matrigel and Collagen I. *Acta Biomater.* 9, 5162–5169. doi: 10.1016/j.actbio.2012.09.010

Kundu, B., Rajkhowa, R., Kundu, S. C., Wang, X., Kundu, B., Rajkhowa, R., et al. (2013). Silk fibroin biomaterials for tissue regenerations. *Adv. Drug Deliv. Rev.* 65, 457–470. doi: 10.1016/j.addr.2012.09.043

Lancaster, M. A., Renner, M., Martin, C. A., Wenzel, D., Bicknell, L. S., Hurles, M. E., et al. (2013). Cerebral organoids model human brain development and microcephaly. *Nature* 501, 373–379. doi: 10.1038/nature12517

Ma, W., Tavakoli, T., Chen, S., Maric, D., Liu, J. L., O'Shaughnessy, T. J., et al. (2008). Reconstruction of Functional Cortical-like Tissues from Neural Stem and Progenitor Cells. *Tissue Eng. Part A* 14, 1673–1686. doi: 10.1089/ten.tea.2007.0357

Martin, A. D., Chua, S. W., Au, C. G., Stefen, H., Przybyla, M., Lin, Y., et al. (2018). Peptide nanofiber substrates for long-term culturing of primary neurons. *ACS Appl. Mater. Interfaces* 10, 25127–25134. doi: 10.1021/acsami.8b07560

Ni, M., and Aschner, M. (2010). Neonatal rat primary microglia isolation, culturing, and selected applications. *Curr. Protoc. Toxicol.* 43, 12.17.1–12.17.16. doi: 10.1002/0471140856.tx1217s43

Norris, G. T., Smirnov, I., Filiano, A. J., Shadowen, H. M., Cody, K. R., Thompson, J. A., et al. (2018). Neuronal integrity and complement control synaptic material clearance by microglia after CNS injury. *J. Exp. Med.* 215, 1789–1801. doi: 10.1084/jem.20172244

Pacifici, M., and Peruzzi, F. (2012). Isolation and culture of rat embryonic neural cells: a quick protocol. *J. Vis. Exp.* 63:e3965. doi: 10.3791/3965

Paolicelli, R. C., Bolasco, G., Pagani, F., Maggi, L., Scianni, M., Panzanelli, P., et al. (2011). Synaptic pruning by microglia is necessary for normal brain development. *Science* 333, 1456–1458. doi: 10.1126/science.1202529

Parkhurst, C. N., Yang, G., Ninan, I., Savas, J. N., Yates, J. R., Lafaille, J. J., et al. (2013). Microglia promote learning-dependent synapse formation through brain-derived neurotrophic factor. *Cell* 155, 1596–1609. doi: 10.1016/j.cell.2013.11.030

Prinz, M., and Priller, J. (2014). Microglia and brain macrophages in the molecular age: from origin to neuropsychiatric disease. *Nat. Rev. Neurosci.* 15, 300–312. doi: 10.1038/nrn3722

Rockwood, D. N., Preda, R. C., Yücel, T., Wang, X., Lovett, M. L., and Kaplan, D. L. (2011). Materials fabrication from Bombyx mori silk fibroin. *Nat. Protoc.* 6, 1612–1631. doi: 10.1038/nprot.2011.379

Roy, J. (2018). Primary microglia isolation from mixed cell cultures of neonatal mouse brain tissue. *Brain Res.* 1689, 21–29. doi: 10.1016/j.brainres.2018.03.018

Schafer, D. P., Lehrman, E. K., Kautzman, A. G., Koyama, R., Mardinly, A. R., Yamasaki, R., et al. (2012). Microglia sculpt postnatal neural circuits in an activity and complement-dependent manner. *Neuron* 74, 691–705. doi: 10.1016/j.neuron.2012.03.026

Stephan, A. H., Barres, B. A., and Stevens, B. (2012). The complement system: an unexpected role in synaptic pruning during development and disease. *Annu. Rev. Neurosci.* 35, 369–389. doi: 10.1146/annurev-neuro-061010-113810

Sun, W., Incitti, T., Migliaresi, C., Quattrone, A., Casarosa, S., and Motta, A. (2017). Viability and neuronal differentiation of neural stem cells encapsulated in silk fibroin hydrogel functionalized with an IKVAV peptide. *J. Tissue Eng. Regen. Med.* 11, 1532–1541. doi: 10.1002/term.2053

Surinkaew, P., Sawaddiruk, P., Apaijai, N., Chattipakorn, N., and Chattipakorn, S. C. (2018). Role of microglia under cardiac and cerebral ischemia/reperfusion (I/R) injury. *Metab. Brain Dis.* 33, 1019–1030. doi: 10.1007/s11011-018-0232-4

Swistowski, A., Peng, J., Liu, Q., Mali, P., Rao, M. S., Cheng, L., et al. (2010). Efficient generation of functional dopaminergic neurons from human induced pluripotent stem cells under defined conditions. *Stem Cells* 28, 1893–1904. doi: 10.1002/stem.499

Tamashiro, T. T., Dalgard, C. L., and Byrnes, K. R. (2012). Primary microglia isolation from mixed glial cell cultures of neonatal rat brain tissue. *J. Vis. Exp.* 66:e3814. doi: 10.3791/3814

Tang-Schomer, M. D., White, J. D., Tien, L. W., Schmitt, L. I., Valentin, T. M., Graziano, D. J., et al. (2014). Bioengineered functional brain-like cortical tissue. *Proc. Natl. Acad. Sci. U.S.A.* 111, 13811–13816. doi: 10.1073/pnas.1324214111

van Pel, D. M., Harada, K., Song, D., Naus, C. C., and Sin, W. C. (2018). Modelling glioma invasion using 3D bioprinting and scaffold-free 3D culture. *J. Cell. Commun. Signal.* 12, 723–730. doi: 10.1007/s12079-018-0469-z

Weinhard, L., di Bartolomei, G., Bolasco, G., Machado, P., Schieber, N. L., Neniskyte, U., et al. (2018). Microglia remodel synapses by presynaptic trogocytosis and spine head filopodia induction. *Nat. Commun.* 9:1228. doi: 10.1038/s41467-018-03566-5

Yang, K., Lee, J., Lee, J. S., Kim, D., Chang, G. E., Seo, J., et al. (2016). Graphene oxide hierarchical patterns for the derivation of electrophysiologically functional neuron-like cells from human neural stem cells. *ACS Appl. Mater. Interfaces* 8, 17763–17774. doi: 10.1021/acsami.6b01804

Conflict of Interest: The authors declare that the research was conducted in the absence of any commercial or financial relationships that could be construed as a potential conflict of interest.

frontiers in Cellular Neuroscience

ORIGINAL RESEARCH
published: 25 November 2020
doi: 10.3389/fncel.2020.610741

Phase Coupled Firing of Prefrontal Parvalbumin Interneuron With High Frequency Oscillations

Yanting Yao[1], Mengmeng Wu[1], Lina Wang[1], Longnian Lin[1,2,3] and Jiamin Xu[1]**

[1] Shanghai Key Laboratory of Brain Functional Genomics (Ministry of Education), School of Life Sciences, East China Normal University, Shanghai, China, [2] NYU–ECNU Institute of Brain and Cognitive Science, New York University Shanghai, Shanghai, China, [3] Brain and Spinal Cord Clinical Center, Tongji University, Shanghai, China

The prefrontal cortex (PFC) plays a central role in executive functions and inhibitory control over many cognitive behaviors. Dynamic changes in local field potentials (LFPs), such as gamma oscillation, have been hypothesized to be important for attentive behaviors and modulated by local interneurons such as parvalbumin (PV) cells. However, the precise relationships between the firing patterns of PV interneurons and temporal dynamics of PFC activities remains elusive. In this study, by combining *in vivo* electrophysiological recordings with optogenetics, we investigated the activities of prefrontal PV interneurons and categorized them into three subtypes based on their distinct firing rates under different behavioral states. Interestingly, all the three subtypes of interneurons showed strong phase-locked firing to cortical high frequency oscillations (HFOs), but not to theta or gamma oscillations, despite of behavior states. Moreover, we showed that sustained optogenetic stimulation (over a period of 10 s) of PV interneurons can consequently modulate the activities of local pyramidal neurons. Interestingly, such optogenetic manipulations only showed moderate effects on LFPs in the PFC. We conclude that prefrontal PV interneurons are consist of several subclasses of cells with distinct state-dependent modulation of firing rates, selectively coupled to HFOs.

Keywords: optogenetics, prefrontal cortex, parvalbumin interneurons, firing pattern, high frequency oscillation

OPEN ACCESS

Edited by:
Miao He,
Fudan University, China

Reviewed by:
Han Xu,
Zhejiang University, China
Wen-Jun Gao,
Drexel University, United States

****Correspondence:***
Longnian Lin
lnlin@brain.ecnu.edu.cn
Jiamin Xu
xujiamin@bio.ecnu.edu.cn

Specialty section:
This article was submitted to Cellular Neurophysiology, a section of the journal Frontiers in Cellular Neuroscience

Received: *27 September 2020*
Accepted: *29 October 2020*
Published: *25 November 2020*

Citation:
Yao Y, Wu M, Wang L, Lin L and Xu J (2020) Phase Coupled Firing of Prefrontal Parvalbumin Interneuron With High Frequency Oscillations. Front. Cell. Neurosci. 14:610741. doi: 10.3389/fncel.2020.610741

INTRODUCTION

The prefrontal cortex (PFC) is a critical region responsible for higher cognitive functions including decision making, value estimation, attention, social cognition, working memory and motor control (Miller, 2000). The excitation/inhibition (E/I) balance of cortical circuits plays an important role in information processing during cognitive behaviors. Moreover, E/I balance has been suggested to contribute to the modulation of neural network oscillations (Atallah and Scanziani, 2009; Xue et al., 2014). Local field potential oscillations in the neocortex of mammalians, such as delta (1–4 Hz), theta (4–8 Hz), gamma (30–80 Hz), and the recently reported high-frequency oscillations (HFOs > 100 Hz), are related to various cognitive processes (Ward, 2003). Theta oscillations have been observed in the PFC during spatial memory, working memory and attention tasks (Tamura et al., 2017). Theta-associated gamma rhythms are considered to be involved in cognitive processes including working memory, sensory and visual responses (Cardin et al., 2009; Tamura et al., 2017). HFOs have been observed when the cortex received excitatory inputs (Engel et al., 2009). But the mechanism of HFO generation and their function in cortical information processing is still elusive.

Inhibitory inputs provided by GABAergic interneurons are essential for optimizing the E/I ratio. The loss of PFC GABAergic inhibitory inputs will lead to an elevation in the E/I ratio of pyramidal neurons, which is considered to be one etiology of cognitive impairments such as schizophrenia and autism (Yizhar et al., 2011). As one of the main sources of inhibitory inputs, PV-positive GABAergic interneurons constitute about 40% of the total cortical interneurons (Tremblay et al., 2016). Previous studies have shown that PV interneurons provide powerful inhibitory innervations onto postsynaptic pyramidal neurons (Pfeffer et al., 2013). They are also involved in regulating a variety of cognitive behaviors (Kim et al., 2016). Electrophysiological recordings in brain slices have stated that PV interneurons in medial prefrontal cortex (mPFC) mediate the feedforward inhibition circuits, which is crucial for maintaining cortical E/I balance (Lee et al., 2014). Moreover, neuronal firing activity of some PFC PV interneurons have been reported to be phase-locked to gamma oscillations (Kim et al., 2016). But still, little is known toward the *in vivo* firing patterns of cortical PV interneurons across behavioral states. We set to investigate whether and how PV interneurons may participate in regulating LFP dynamics, including gamma oscillation, under distinct behavioral states.

To answer the above two questions, we performed *in vivo* electrophysiological recording in the mPFC region of free moving mice across various behavioral states, including active wakefulness (AW), quiet wakefulness (QW), rapid-eye-movement (REM) sleep and slow-wave sleep (SWS) states. With the help of optogenetic tools, we described the *in vivo* firing patterns of PFC PV interneurons, and investigated their relationship with LFP oscillations. We further examined the effects of optogenetic manipulations of PV cells on E/I balances and local neural network dynamics.

MATERIALS AND METHODS

Animals

All experiment procedures were carried out in accordance with protocols approved by the Laboratory Animal Management Committee at East China Normal University (Huashishe [2014] No. 6). Two mouse lines [PV-IRES-Cre, Jax No. 008069 (Hippenmeyer et al., 2005) and Ai32 Jax No. 012569 (Madisen et al., 2012)] were used to generate PV-ChR2-EYFP transgenic mice. All animals are offered with 12 h alternating day and night illumination and free access to food and water.

Animal Behavioral State Assessment

We choose four basic behavioral states for further analysis: active wakefulness (AW), quiet wakefulness (QW), rapid-eye-movement (REM) sleep, and slow-wave sleep (SWS). The animal behavioral states were identified through videos recorded via a camera over the recording arena, assisted by simultaneously recorded LFP signals from the PFC and hippocampal dCA1. The AW state was the periods when mice performed proactive physical movements. The appearance of sleeping posture and cortical sleep spindles (7–12 Hz) marks sleep states. During sleep, the periods when slow waves (<1 Hz) and delta rhythms constantly existed in both recording sites (and with hippocampal sharp wave ripple events occurred occasionally) were identified as SWS state, while periods with continuous theta rhythms were classified as REM state. The QW state was defined as the periods when no obvious physical movement, sleeping posture, or sleep spindles in the filtered LFP signal could be detected.

In vivo Electrophysiological Recordings

Microdrive electrodes of 64 or 96 channels were designed for recording across multiple brain regions. The microdrive foundation was adopted from our previous work (Lin et al., 2006). For 64-channel, a few (no more than 4) tetrodes were placed in a bundle targeting hippocampal dorsal CA1 (dCA1), and the others were placed in a bundle targeting mPFC. For 96-channel microdrive electrodes, 16 were placed in mPFC. and 8 tetrodes were placed in dCA1 to help characterize the basic behavioral states such as REM and SWS based on hippocampal LFP dynamics. The tetrode tips were trimmed and electroplated with plating liquid (24K gold, Promex Industries, United States) to reach a final impedance of 500–800 kΩ via an electrode impedance tester (IMP-I, Bak Electronics, United States). An optical fiber was inserted in the middle of the tetrode bundle (optrode), targeting the mPFC with an 0.5 mm indentation from the tetrode tips.

The mice used for recording were housed individually in a rectangular cage (470 mm length × 315 mm width × 260 mm height) with free access to water and food pellets, and handled for a week before surgery (30 min per day). A total number of nineteen PV-ChR2-EYFP mice (2–4 months old, ranging 22–28 grams prior to the implantation surgery, no preference on sex) were surgically implanted with microdrive electrode according to the protocols described in Lin et al. (2006). The tetrode bundles were implanted in unilateral mPFC (AP + 1.94 mm, ML + 0.50 mm, DV −1.50 to −1.90 mm, targeting layer 2 to layer 5 of the prelimbic area of mPFC) as well as the ipsilateral hippocampal dCA1(AP −2.30 mm, ML + 2.00 mm, DV −1.00 mm).

After a recovery of 4–7 days post the surgery, mice underwent electrophysiological observations. Electrophysiology signals were recorded by Plexon MAP system while animal movement was monitored via a video camera. The signals from electrodes were filtered through the preamplifiers (400–7,000 Hz for neuronal spikes, 0.7–300 Hz for LFP), and then sampled at 40 kHz (spikes) or 1 kHz (LFP). The electrode bundles were advanced at a rate of no more than 70 μm every 3 days. We started recording when the spikes of putative interneurons (narrow waveforms with a mean firing rate higher than 5 Hz) were detected in mPFC, and characteristic LFP signals of stratum pyramidale (i.e., sharp wave ripples, Buzsaki et al., 1992) were evident in dCA1.

Optogenetic Stimulation

Blue laser stimulator (DPSS Laser, 470 nm, Inper, China) was used to activate neurons labeled with ChR2 in the PV-ChR2-EYFP mice. Unless otherwise specified, the laser power was set to optimum (usually 5–20 mW), with 5 ms pulse width at 1 Hz frequency for 100 trials for each neuron.

Spikes fired within 10 ms after laser onset were considered to be light evoked spikes. We calculated the light triggered spiking probability by measuring the proportion of the number of trials in which at least one spike was triggered by light stimulation over the total number of trials. Neurons with a light-induced firing probability over 60% were identified as PV positive interneurons. For laser power test, laser power was set to 5, 10, 15, and 20 mW. For laser frequency test, stimulus frequency was set to 0.5, 1, 2, 10, 20, and 40 Hz. For sustained stimulation, the laser stimulation was continuously delivered for 10 s.

Immunohistochemistry and Microscopy

After all recording experiments were completed, mice were deeply anesthetized with pentobarbital sodium (0.1 mg/g body weight) and perfused transcardially with 0.01 M PBS followed by 4% paraformaldehyde (w/v, in PBS). The brain was stripped out and underwent gradient dehydration in 20 and 30% sucrose solution (w/v, in PBS). Coronal sections (30 μm) were prepared with a freezing microtome (CM1520, Leica, United States). Sections were penetrated with 0.5% Triton X-100 (in PBS) at room temperature for half an hour, followed by goat serum (16210-064, Gibco, Life Technologies, Thermo Fisher Scientific, United States) at room temperature for 1 h. Sections were first incubated with primary antibodies (Rabbit IgG anti-PV, PV27, SWant, CH, 1:1,000; Mouse Monoclonal IgG anti-GFP, 600-301-215, Rockland, United States, 1:500) diluted in the antibody diluent solution (003118, Life technologies) overnight at 4℃. Following a 3 × 10 min PBST washing, the sections were then incubated with second antibody (Alexa Fluor 594 Goat anti Rabbit IgG, A-11012, Life Technologies, Thermo Fisher Scientific, United States, 1:500; Alexa Fluor 488 Goat anti Mouse IgG, A-11001, Life Technologies, Thermo Fisher Scientific, United States, 1:500) for 2 h and DAPI (C1006, Beyotime, CN, 1:1,000) for 10 min at room temperature. Following another 3 × 10 min PBST washing, the sections were mounted with 30% glycerol and characterized by confocal microscopy (TCS SP8, Leica, United States).

Data Processing

Spike sorting was performed with Offline Sorter 2.0 software (Plexon, Dallas, TX) as previously described (Zhang et al., 2012). Spikes of single units were converted into *.nex files together with original LFP signals for further processing with MATLAB.

The mPFC LFP signals were band-pass filtered in the delta (2–5 Hz), theta (4–8 Hz), slow gamma (30–50 Hz), fast gamma (50–80 Hz) and high-frequency (100–250 Hz) bands using elliptic filter. To detect HFO events, the root mean square of the filtered signal was calculated by sliding a 10 ms window every 1 ms. Epochs with 2 standard deviations above the background mean power were designated as HFO episodes. Then the time window was moved forward and backward to detect the beginning and the end of each HFO episode, the threshold was set to 1 standard deviation above the background mean power. In addition, the dCA1 LFP signals were band-pass filtered in the delta (2–4 Hz), theta (4–12 Hz), gamma (30–80 Hz) and ripple (100–250 Hz) bands using elliptic filter. To detect ripple events, the root mean square of the filtered ripple signal was calculated by sliding a 10 ms window every 1 ms. Epochs with 5 standard deviations above the background mean power were designated as ripple events. Then the time window was moved forward and backward to detect the beginning and the end of each ripple episode, the threshold was set to 2 standard deviations above the background mean power.

Power Spectrum Analysis

Welch Method were employed for LFP power spectral density (PSD) analysis, with 512 points fast Fourier transform (FFT), 512-ms 1/4 overlapping Hanning window. The power spectrograms in **Figures 3–5** were conducted based on adaptive autoregressive (AAR) model and Kalman filtering (Arnold et al., 1998). Define X_t as the time sequence of LFP, the AAR model of the order p of X_t can be expressed as:

$$X_t = \sum_{k=1}^{p} A_t^{(k)} X_{t-k} + E_t$$

in which t is time, $A_t^{(k)}$ is the parameter. E_t is zero mean Gaussian noise process whose variance is Σ_t. Given the state vector $A_t = \left(A_t^{(1)}, A_t^{(2)}, ..., A_t^{(p)}\right)^T$, and the observed variable $H_t = \left(X_{t-1}, X_{t-2}, ..., X_{t-p}\right)^T$, T represents matrix transpose. Then X_t can be expressed as:

$$X_t = H_t^T A_t + E_t.$$

The change of state can be described by random walk model $A_{t+1} = A_t + W_t$, here E_t and W_t are uncorrelated zero mean Gaussian noise processes, whose variances are $V_{e_t} = \sigma_{e_t}^2$ and $V_{w_t} = \sigma_{w_t}^2$ separately, Then the first step forecast is:

$$\hat{A}_{t|t-1} = E\left[A_t | X_0, X_1, ..., X_{t-1}\right].$$

Here, Kalman filtering is introduced for parameter estimation. The Kalman filtering equations are as follows (Andreassen et al., 1979):

$$\hat{A}_{t|t-1} = (I - K_t H_t^T)\hat{A}_{t|t-1} + K_t X_t,$$

$$K_t = \sum_{t|t-1} H_t \left(H_t^T \sum_{t|t-1} H_t + \sigma_{e_t}\right)^{-1},$$

$$\sum_{t+1|t} \Delta E\left[\left(A_{t+1} - \hat{A}_{t+1|t}\right)\left(A_{t+1} - \hat{A}_{t+1|t}\right)|X_t\right] =$$

$$\sum_{t|t-1} -K_t H_t^T \sum_{t|t-1} +\sigma_{\omega_t},$$

$$\hat{A}_{t|t} = \hat{A}_{t|t-1} + K_t\left(X_t - H_t^T \hat{A}_{t|t-1}\right),$$

$$\sum_{t|t} = \sum_{t|t-1} -K_t H_t^T \sum_{t|t-1},$$

in which I is identity matrix, K_t is Kalman gain matrix.

Then the state vector A_t can be estimated as:

$$\hat{A}_{t|N} = E\left[A_t|X_0, X_1, ..., X_N\right], 0 \le t \le N,$$

a fixed-interval smoothing procedure was applied to avoid the time-lag in the estimates (Tarvainen et al., 2004). And the real-time PSD of signal X_t at frequency ω can be given by:

$$f(t, \omega) = \frac{\sigma_e^2(t)}{f_s\left|1 - \sum_{j=1}^{p} A_t^{(j)} e^{-2i\pi\omega j/f_s}\right|^2},$$

where f_s is the sampling frequency.

Phase-Locking Analysis

Phase-locking analysis was performed according to a previous study (Siapas et al., 2005). The amplitude $A(t)$ and phase $\phi(t)$ of LFP signals were extracted by applying the Hilbert transform. Phase of spike trains at times $S = \{\tau_k | k \in \{1, 2, ..., n\}\}$ is then given by $\phi_s = \{\phi(t) | t \in S\}$. To evaluate the presence of phase-locking, Rayleigh test for circular uniformity was performed. Briefly, the preferred phase μ is given by the mean direction of ϕ_s. $\overline{R}$ is the mean resultant length of unit vector ϕ_s. The Rayleigh statistic is $Z = n\overline{R}^2$. And the probability for the presence of phase-locking is given by

$$P = e^{-Z}\left(1 + \frac{2Z - Z^2}{4n} - \frac{24Z - 132Z^2 + 76Z^3 - 9Z^4}{288n^2}\right).$$

Here we take $P < 0.001$ as significant phase-locking. The phase of spike trains was fit with a von Mises distribution with density

$$f(\phi) = \frac{1}{2\pi I_0(\kappa)} e^{\kappa\cos(\phi - \mu)}, (-\pi \le \phi < \pi, 0 \le \kappa < \infty).$$

The concentration parameter κ can be solved from the equation $I_1(\kappa)/I_0(\kappa) = \overline{R}$ by applying a numerical zero finding routine. $I_i(x)$ is the modified Bessel function of order i.

Pairwise Phase Consistency

Pairwise phase consistency (PPC) is a bias-free measurement of the phase synchronization of neuronal spiking in relation to LFP (Vinck et al., 2010, 2012). For a given frequency f, the PPC of a spike train is defined as:

$$PPC = \frac{\sum_{j=1}^{N}\sum_{k\neq j}^{N}(\sin\theta_j \sin\theta_k + \cos\theta_j \cos\theta_k)}{N(N-1)},$$

in which θ_j and θ_k denote phase of the j-th and k-th spike at frequency f, N denotes the total number of spikes.

RESULTS

Cell-Type-Specific Labeling and Activation of PV Interneurons in the PFC

In order to study the *in vivo* firing properties of PV interneurons, we need to first identify the PV interneurons in the PFC in freely moving mice. Optogenetic tagging of neuronal firing has been proven to be practical for such identification. Tetrode arrays together with an optical fiber (optrode) were stereotaxically implanted into mPFC in PV-ChR2-EYFP double transgenic mice (**Figure 1A**), which were produced by crossing a PV-IRES-Cre line (Jax No. 008069) (Hippenmeyer et al., 2005) with the Ai32 ChR2/EYFP line (Jax No. 012569) (Madisen et al., 2012).

We first examined the co-expression profile of PV and ChR2 in the PFC. We found that 98.63% ± 1.28% of the neurons labeled with ChR2 were positive with PV antibody, while 57.82% ± 13.67% of the PV + neurons co-expressed ChR2 (**Figures 1B,C**).

We then applied laser pulse stimulations via the optical fiber in mPFC during electrophysiological recordings. Indeed, some neurons exhibited stable light evoked spiking responses upon 470 nm laser stimulation. Importantly, the waveforms of spontaneous and optogenetically evoked spikes are almost identical, confirming these cells as PV interneurons (**Figure 1D**). Laser pulse stimulation induced spiking activities of PV neurons, followed by a brief suppression of firing activities right after the light evoked responses (1 Hz, 5 ms laser pulse, **Figure 1E**). Neurons with a light-induced firing probability over 60% were identified as PV positive interneurons. Under this criterion, we identified a total number of 18 PV interneurons in 10 mice.

To better understand the impact of laser stimulation on the firing activities of PV interneurons, we tested various laser stimulation parameters. First, we tested the effect of laser power on spike responses of 4 PV interneurons. As expected, PV interneurons were more effectively activated with higher laser power (**Figure 1F**). Some even fired more than one spike within a single trial, which led to a saturation of the firing probability at higher laser power (**Figure 1G**). We next measured the latency of light evoked response to laser power, which is defined as the duration from the laser onset to the first evoked spike. We found that response latency slightly decreased as the light stimulation power increased (**Figure 1H**). This is consistent with previous study showing that higher light intensity benefits the rapid activation of ChR2 (Ishizuka et al., 2006).

We also tested the effects of laser stimulation frequency (0.5–40 Hz) on the firing responses of PV interneurons. When PV interneurons were stimulated at a lower frequency (i.e., 0.5, 1, and 2 Hz), the cycle of laser stimulation was much longer than the intrinsic suppression time of PV interneurons. As such, the corresponding firing probabilities were able to remain at a higher level (**Figure 1J**). In contrast, when PV interneurons were stimulated at a higher frequency (i.e., 10, 20 or 40 Hz), the suppression-phase time-duration of the laser-triggered suppression responses were artificially shortened and masked by the rapid laser cycles (**Figure 1I**). This came at a cost of the dramatic decline in firing probability (**Figure 1J**), whereas the latency in PV cells did not show such drastic changes (**Figure 1K**).

Behavioral State-Dependent Firing Patterns of PFC PV Interneurons

Neuronal activities are often associated with different behavioral and cognitive states. We carried out long-period continuous

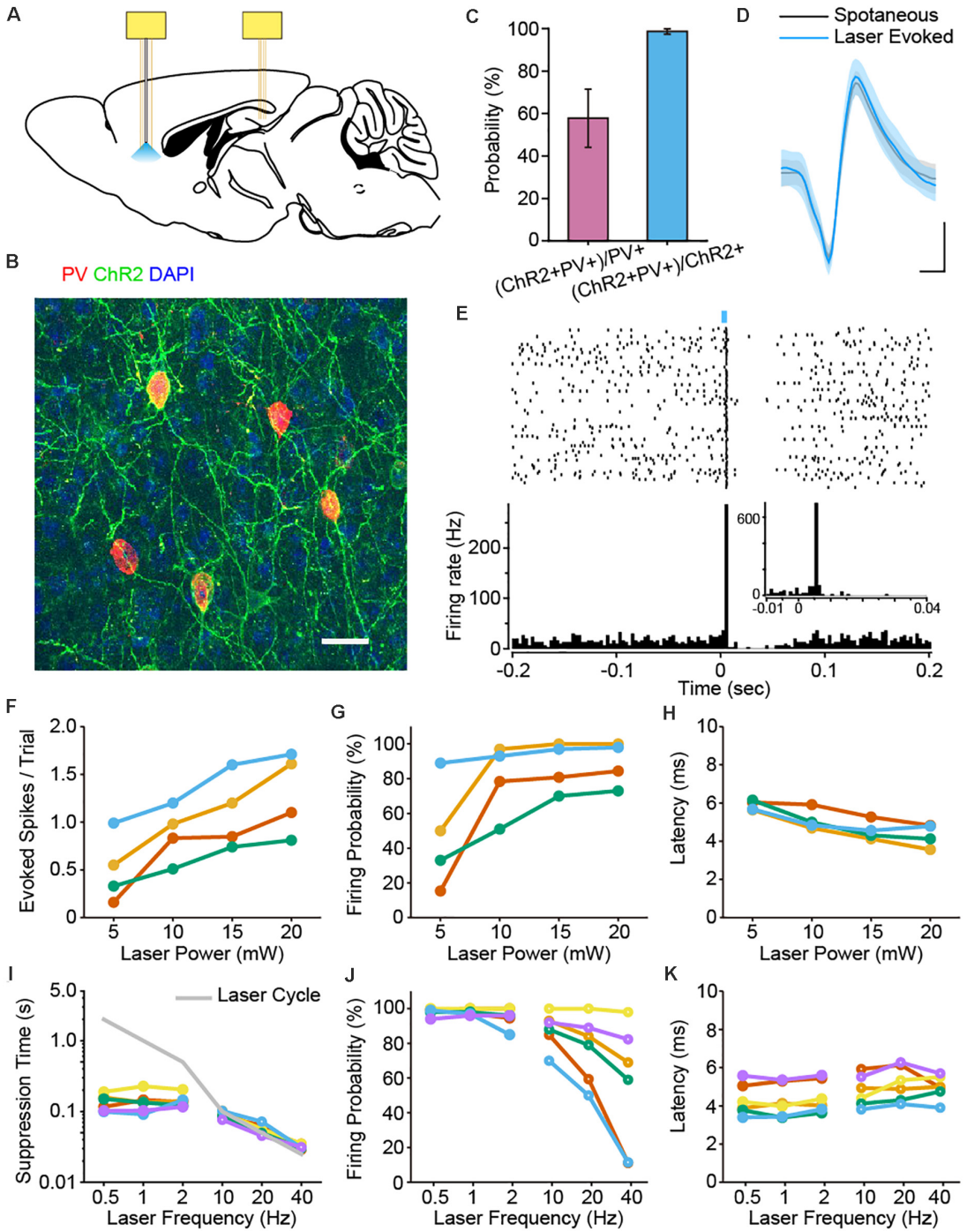

FIGURE 1 | Optogenetic identification of PFC PV interneurons and characterization of laser stimulation parameters. **(A)** Schematic diagram of the placement of two electrode bundles: an optrode targeting the PFC and a tetrode bundle in the dCA1 of the hippocampus. **(B)** Immunostaining of PV (red), EYFP (green) and DAPI (blue) confirmed the co-localization of PV and ChR2 in the PFC of PV-ChR2-EYFP transgenic mice. Scale: 50 μm. **(C)** Expression efficiency statistics revealed that 98.63% ± 1.28% of the ChR2 + neurons were PV+, whereas 57.82% ± 13.67% of the labeled PV neurons were ChR2 + (n = 7 mice). **(D)** Example spike waveforms from one PV neuron. The waveforms of the spontaneous (black) and laser-evoked spikes (blue) were almost identical (mean ± SD of 100 spikes, Pearson Correlation, R = 0.998, p = 1.27e-62). Scale: 0.2 ms, 0.2 mV. **(E)** Peri-stimulus raster and histogram of an example PV interneuron upon laser pulse stimulation (1 Hz, 5 ms pulse, 100 trials, bin = 3 ms). Note the brief suppression response right after the laser evoked firing of PV neuron. Enlarged view shows light-induced spike latency around 6 ms (1 Hz, 5 ms pulse, 100 trials, bin = 1 ms). **(F–H)** The impact of laser power on the number of evoked spikes per trial **(F)**, firing probability **(G)** and spike latency **(H)** for PV interneurons. Each color corresponds to a single neuron, the same below (n = 4 neurons). Neuronal firing responses increased with higher laser stimulation power. **(I–K)** The impact of laser frequency on suppression time **(I)**, firing probability **(J)** and latency **(K)** for PV interneuron activation. Solid circles, lower frequency; open circles, higher frequency (n = 6 neurons). Neuronal firing probability decreased at higher stimulation frequencies **(J)**.

recordings for the 18 opto-tagged PFC PV interneurons to investigate temporal firing dynamics across behavior states. Neuronal firing activity of 3 example PV neurons over 1 h recording across different behavioral states was illustrated in **Figure 2** (light blue histogram), along with spectrograms for the simultaneously recorded LFP at the bottom of each example neurons. Based on neuronal firing kinetics during the four basic behavioral states, we categorized PV interneurons into three subtypes. The first subtype (example Neuron #1 in **Figure 2A**) exhibited a higher firing rate during AW state over other states

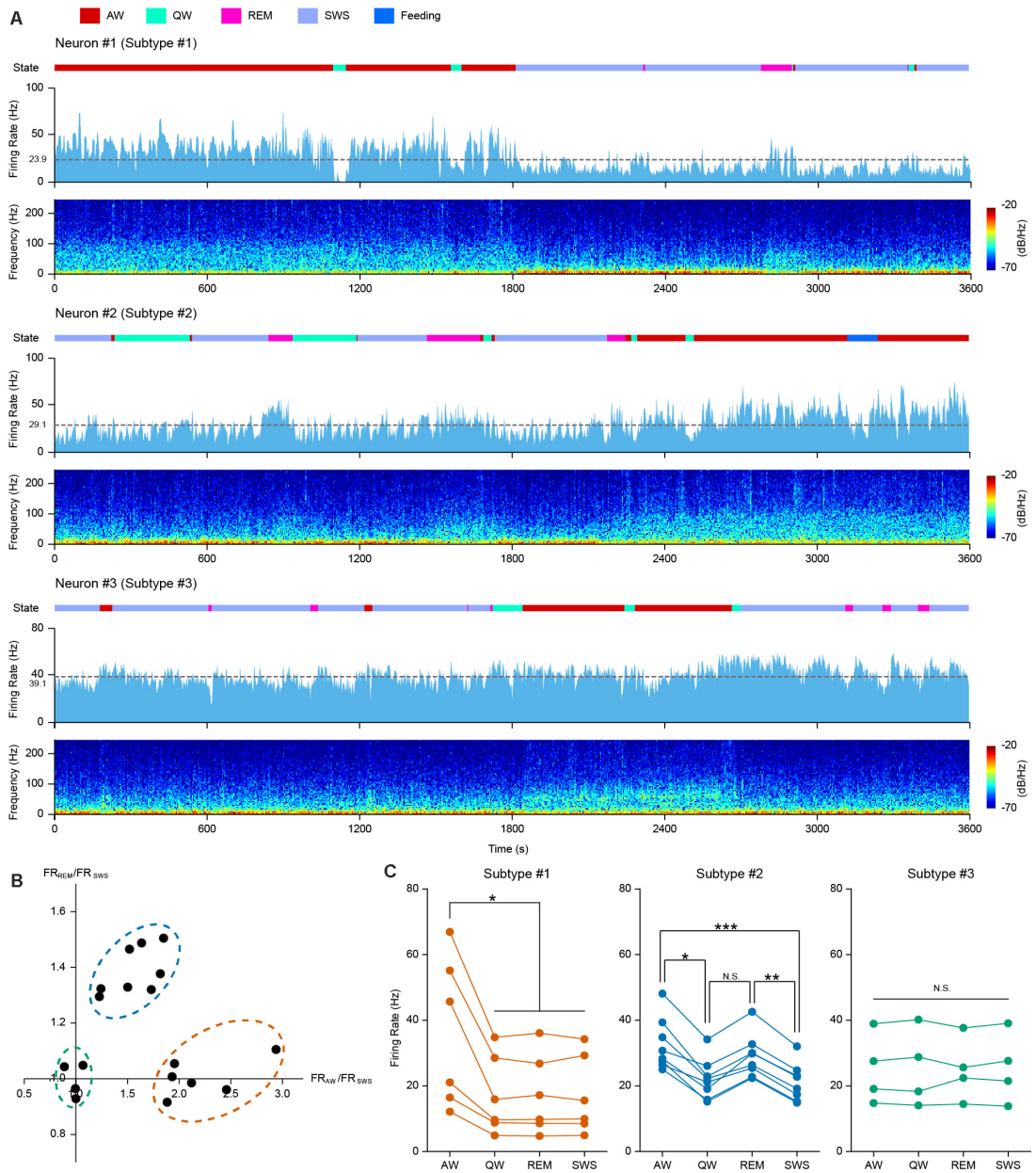

FIGURE 2 | PFC PV interneurons exhibited behavior state-dependent firing patterns. **(A)** One hour continuous monitoring of the firing activities of 3 example PFC PV interneurons. Each example neuron represents one interneuron subtype, showing behavior state-dependent firing patterns. Different behavioral states were associated with changes in neuronal firing rates and LFP power spectrograms. Top row, color coded behavior states (color scheme at the top of the figure); middle row, neuronal firing rate histogram (bin = 2 s) and mean firing rate (dashed gray line, average firing rate on the left); bottom row, LFP power spectrogram. **(B)** Relationship between FR_{AW}/FR_{SWS} and FR_{REM}/FR_{SWS}, each dot represents one opto-tagged PV interneuron. 18 PV neurons were clustered into three subtypes (shown in dashed circles. orange, subtype #1; blue, subtype #2; green, subtype #3). **(C)** Mean firing rate of all the 18 recorded PV interneurons under different behavior states, clustered into 3 subtypes (color coded in orange, blue and green, n = 6, 8, and 4 neurons in each subtype). Each line connecting 4 dots represents one single neuron. Note the difference in behavior state-dependent firing rate change of each interneuron subtype (Friedman Test, $p_{subtype\#1}$ = 0.013, $p_{subtype\#2}$ = 9.80e-5, $p_{subtype\#3}$ = 0.96; Dunn-Bonferroni *post hoc*, $^{*}p < 0.05$, $^{**}p < 0.01$, $^{***}p < 0.001$, N.S., not significant).

(**Figure 2C**, left). The second subtype of PV cells (example Neuron #2 in **Figure 2A**) tended to fire in a higher rate during both AW and REM states (**Figure 2C**, middle). The third subtype of PV interneurons (example Neuron #3 in **Figure 2A**) did not show significant firing rate changes across all behavior states (**Figure 2C**, right).

To quantitatively measure these differences, we compared the mean firing rates during AW and REM states against that during SWS state for each opto-tagged PV interneuron. FR_{AW}/FR_{SWS} versus FR_{REM}/FR_{SWS} of each PV neuron were plotted, where FR stands for the mean firing rate of each state (**Figure 2B**). The 18 PV neurons could be evidently clustered into three subtypes according to their behavior state-dependent firing properties.

PV interneuron subtype #1 has 6 neurons (orange circle in **Figure 2B**), showing high firing rates during AW state. The firing rate during AW state was significantly higher than that during the other three states. Interestingly, the firing rates during SWS, REM and QW states were consistently lower (**Figure 2C**, left panel. Friedman Test, n = 6 neurons, p = 0.013; Dunn-Bonferroni *post hoc*, p_{AW-QW} = 0.044, p_{AW-REM} = 0.044, p_{AW-SWS} = 0.044). Therefore, we speculate that subtype #1 PV cells may be associated with the modulation of active behaviors. Subtype #2 PV cells exhibited higher firing rates during AW and REM states. The FR_{AW}/FR_{SWS} and the FR_{REM}/FR_{SWS} ratio plot indicated that 8 neurons fall into the class of subtype #2 (blue circle in **Figure 2B**). The mean firing rate plot in **Figure 2C** showed higher firing rates of subtype #2 neurons during both AW and REM states in comparison to QW and SWS states (**Figure 2C**, middle panel. Friedman Test, n = 8 neurons, p = 9.8e-5; Dunn-Bonferroni *post hoc*, $p_{AW\text{-}QW}$ = 0.022, $p_{AW\text{-}SWS} < 0.001$, $p_{REM\text{-}SWS}$ = 0.006). The remaining four PV interneurons belonged to subtype #3 (green circle in **Figure 2B**), showing comparable firing rates across all four behavior states (**Figure 2C**, right panel. Friedman Test, n = 4 neurons, p = 0.96).

Taken together, these results suggested that PV cells in the PFC likely reflect multiple distinct groups of interneurons. Some of these subtypes clearly exhibited behavior state-dependent firing rate modulation.

Phase Coupling of PV Cells With High-Frequency Oscillations During AW State

To evaluate the relationship of the temporal dynamics of PV neuronal firing with LFP, we examined whether and how the activities of PV interneurons were associated with different oscillation components of the LFP, namely theta (4–8 Hz), slow and fast gamma (30–50 and 50–80 Hz), and high frequency oscillations and a recently reported 4 Hz oscillation component (Fujisawa and Buzsaki, 2011; Karalis et al., 2016; **Figure 3A**). Theta oscillations occur frequently during AW state in the mouse PFC, constantly accompanied by gamma and high-frequency rhythms (**Figure 3B**). We performed firing phase analysis between PV interneuronal firing and different components of LFP oscillations. We found 5 PV interneurons with significant phase-locked firing with 4 Hz oscillation (**Figure 3C**, left panel). Previous reports have shown that the firing activities of some hippocampal PV interneurons were highly correlated with hippocampal theta rhythms (Klausberger et al., 2003). Unlike the situation in the hippocampus, we found that most of the PFC PV cells (17/18) did not show significant phase-locked firing to theta oscillations (**Figure 3C**, second left panel). Among the 18 recorded PV neurons, 7 of them showed significant phase-locked firing to slow gamma oscillation, and 11 of them showed significant phase-locked firing to fast gamma oscillation (**Figures 3C**, middle panel and second right panel). Interestingly, we found that the activity of PV interneurons showed a strong correlation with LFP HFOs. They increased their firing rate when the power of HFO increased (**Figure 3A**). All the recorded PV interneurons were significantly phase-locked to the trough of HFOs during AW state (mean preferred phase 221.91°± 23.61°, **Figure 3C**, right panel). The phase-locked firing of PV interneurons with HFOs were much stronger than that with other oscillations (**Figure 3D**, Friedman Test, p = 4.19e-10, Dunn-Bonferroni *post hoc*, $p_{4Hz\text{-}HFOs} < 0.001$, $p_{theta\text{-}HFOs} < 0.001$, $p_{slowgamma\text{-}HFOs} < 0.001$, n = 18 neurons).

To further quantify the strength of phase-locked firing of PFC PV interneurons with HFOs, we measured pairwise phase-consistency (PPC) of each recorded neuron. PPC is a bias-free measurement of the phase synchronization of neuronal spiking in relation to LFP (Vinck et al., 2010). Our analyses suggested that the three PV interneuron subtypes show equal phase-locked firing with different oscillations, as the PPCs between interneuron subtypes did not show any significant difference (Kruskal-Wallis Test, $p_{4\,Hz}$ = 0.099, p_{theta} = 0.607, $p_{slowgamma}$ = 0.691, $p_{fastgamma}$ = 0.890, p_{HFOs} = 0.443; Median Test, $p_{4\,Hz}$ = 0.160, p_{theta} = 0.472, $p_{slowgamma}$ = 0.558, $p_{fastgamma}$ = 0.558, p_{HFOs} = 0.558). However, comparisons of PPCs between different frequency-bands showed that the rhythmic firing of PV interneurons occurred more robustly at high-frequency range rather than at other frequency ranges (**Figures 3E**, Friedman Test, p = 7.77e-9, Dunn-Bonferroni *post hoc*, $p_{4\,Hz\text{-}HFOs} < 0.001$, $p_{theta\text{-}HFOs} < 0.001$, $p_{slowgamma\text{-}HFOs} < 0.001$, $p_{fastgamma\text{-}HFOs}$ = 0.016, n = 18 neurons). These results suggested that neural dynamics of PV interneurons are prominently related to, or modulated by, HFOs during AW state.

Phase Coupling of PV Cells With Delta and HFOs During SWS State

Both cortical and hippocampal PV interneurons are mainly derived from medial ganglionic eminences (MGE) during development (Xu et al., 2004). The activities of PV interneurons in the hippocampus are strongly phase-locked to LFP sharp wave ripples (100–250 Hz) during SWS (Klausberger et al., 2003). We wonder whether similar features could be found between the firing of PFC PV interneurons and high frequency oscillations.

The LFP signals in the PFC during SWS were mainly composed of delta and high frequency oscillations (**Figures 4A,B**). We first investigated the relationship between PV interneuronal firings and delta rhythms. Population analysis revealed that all opto-tagged PV interneurons exhibited significant phase-locked firing to delta oscillations, with the

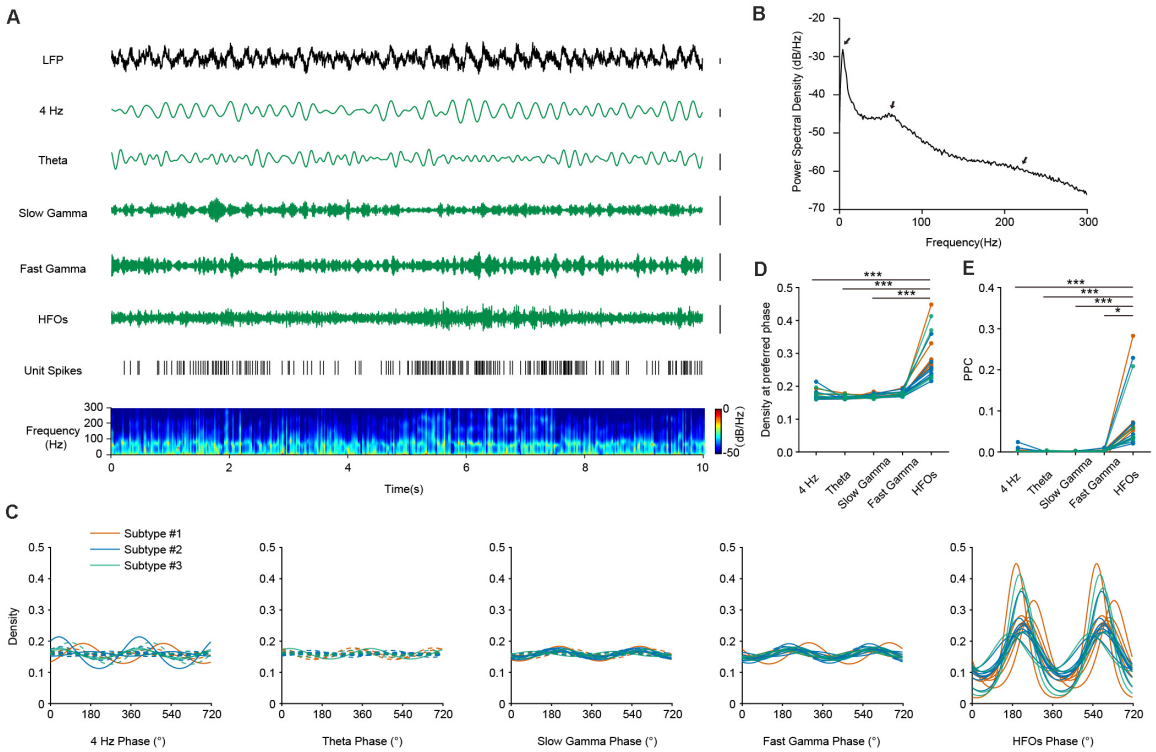

FIGURE 3 | The firing phase-coupling of PFC PV interneurons to LFP HFOs during AW state. **(A)** Example traces showing PV interneuron spikes and different LFP oscillation components during AW state. From top to bottom, LFP signal recorded in the PFC, cortical 4 Hz oscillation, theta oscillation, slow and fast gamma oscillation, HFOs filtered from LFP, PV interneuron spiking activity (each stick represents one action potential fired by the neuron), and power spectrogram of LFP (10 s of data is shown, scale, 0.1 mV). Note the co-activity of elevated neuronal firing and increased power of HFO components in the power spectrogram (e.g., from 5 to 8 s). **(B)** Power spectral density during AW state of one example recording. Theta, gamma and HFO components exhibited prominent power (marked by arrows). **(C)** Firing phase distributions of 3 subtypes of PV interneurons with different oscillation components. Significant phase-locking is shown with solid lines, and non-significant phase-locking shown with dashed lines (Rayleigh's test, $p < 0.001$ as significant phase-locking). Each colored line represents one single PV neuron ($n = 18$ neurons). PV interneurons fire significantly phase-locked to HFOs during AW state, compared to that with other oscillations. **(D)** Peak phase coupling density with different oscillations at preferred phase of PV interneuron spikes during AW states (Friedman Test, $p = 4.19e\text{-}10$, Dunn-Bonferroni *post hoc*, ***, $p_{4\ Hz\text{-}HFOs} < 0.001$, $p_{theta\text{-}HFOs} < 0.001$, $p_{slowgamma\text{-}HFOs} < 0.001$, $n = 18$ neurons). **(E)** Comparison of pairwise phase consistency (PPC) analysis. Note that the phasic firing of PV interneurons to HFOs was much more predominant than that to other oscillations during AW state (Friedman Test, $p = 7.77e\text{-}9$, Dunn-Bonferroni *post hoc*, ***, $p_{4\ Hz\text{-}HFOs} < 0.001$, $p_{theta\text{-}HFOs} < 0.001$, $p_{slowgamma\text{-}HFOs} < 0.001$, *, $p_{fastgamma\text{-}HFOs} = 0.016$, $n = 18$ neurons).

mean preferred firing phase at 160.24°± 44.69° (**Figure 4C**, left panel). Furthermore, the three PV interneuron subtypes showed similar PPC levels with delta frequency (Kruskal-Wallis Test, $p = 0.272$; Median Test, Median = 0.031, $p = 0.435$).

We then turned to investigate the temporal dynamics of PV neuronal firing with HFOs. We found that the two signals exhibited high correlations, as the spiking of an example PV interneuron temporally coincides with HFOs during SWS (**Figure 4A**). All the recorded PV interneurons exhibited significant phase-locked firing to HFOs, with a mean preferred firing phase of 218.85°± 22.78° (**Figure 4C**, right panel). There is no significant difference between the PPCs of the three neuronal subtypes at high frequency (Kruskal-Wallis Test, $p = 0.354$; Median Test, Median = 0.085, $p = 0.558$). Neuronal phase-locked firing of PV interneurons was much stronger with HFOs than that with delta oscillations (**Figure 4E**, Wilcoxon Signed Ranks Test, $p = 3.27e\text{-}4$, $n = 18$ neurons). Comparisons of PPCs at different frequency also showed that the PPCs at high frequency were significantly higher than that at delta frequency (**Figure 4F**, Wilcoxon Signed Ranks Test, $p = 1.96e\text{-}4$, $n = 18$ neurons), indicating that the phase preference of PV interneurons to HFOs were much more robust than that to delta oscillations.

Optogenetic Stimulation of PFC PV Interneurons Suppressed Pyramidal Neuron Activities

In order to investigate the role of PV interneurons in regulating cortical network dynamics, we employed optogenetic strategies to see whether neuronal activities and field potential oscillations were altered upon such manipulation. We noted that laser pulse stimulations of certain frequency typically triggered artificial increases across certain LFP frequencies. As a result, we decided to use sustained optogenetic stimulations to avoid such evoked phenomena.

Figures 5A,B illustrated the laser induced firing responses of two representative PV interneurons to sustained optogenetic stimulations (470 nm laser, 10 s duration) during AW and SWS

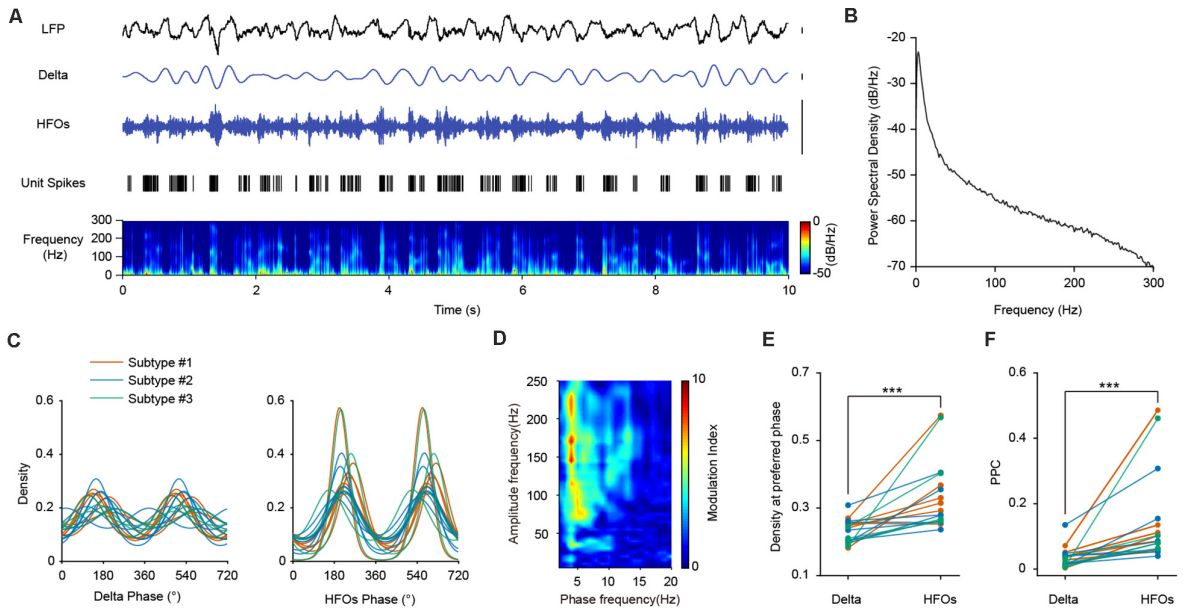

FIGURE 4 | The firing phase-coupling of PFC PV interneurons to LFP HFOs during SWS state. **(A)** Example traces showing PV interneuron spikes and different LFP oscillation components during SWS. The illustrated PV interneuron exhibited correlated firing with HFO events. Traces from top to bottom, PFC LFP signal, delta oscillation, HFOs filtered from LFP, PV interneuron spiking activity (each stick represents one action potential fired by the neuron), and power spectrogram of LFP (10 s of data is shown, scale, 0.1 mV). Note the highly correlated activities of neuronal spiking and HFOs. **(B)** Power spectral density during SWS state of one example recording. **(C)** Firing phase distribution of 3 subtypes of PV interneuron spikes with delta and HFO during SWS. Each colored line represents one single neuron (n = 18 neurons). The firing activities of all the recorded interneurons are significantly phase-locked to both delta and HFOs. **(D)** Phase-amplitude coupling analysis of mPFC LFP during SWS. **(E)** Peak phase coupling density with different oscillations at preferred phase of PV interneuron spikes during SWS state (Wilcoxon Signed Ranks Test, ***, p = 3.27e-4, n = 18 neurons). **(F)** Comparison of PPC of PV interneuron spikes with delta and HFOs during SWS states (Wilcoxon Signed Ranks Test, ***, p = 1.96e-4, n = 18 neurons).

states, respectively. The PV neurons exhibited robust transient burst firing at the laser onset. After the initial burst, the laser evoked firing of PV neurons decreased to an elevated firing level (in comparison to the baseline firing rate). Firing rate during the stimulation period remained either stable elevation (example Neuron #a) or tampered off gradually (example Neuron #b). After the laser stimulation offset, the firing rate of PV neurons returned to baseline.

Next, we checked the effect of laser stimulation on the firing activities of local pyramidal neurons. As expected, the firing activities of all the simultaneously recorded pyramidal neurons were greatly suppressed during laser stimulation (see individual example cells in the second row in **Figures 5A,B**). At the neuronal population level, the mean firing rate of pyramidal neurons was significantly decreased from 1.34 ± 1.43 to 0.05 ± 0.14 Hz (**Figure 5C**, Wilcoxon Signed Ranks Test, Laser OFF-Laser ON, n = 65 neurons from 6 mice, p = 3.52e-12, Z = −6.955, based on negative ranks).

At the field potential level, PSD analysis revealed a slight decrease in the power of field potential oscillations, especially at higher frequency range during SWS state (**Figure 5D**). Statistical analysis confirmed that LFP power was significantly decreased at gamma and high frequency oscillation, but not at delta oscillation range upon laser stimulation (**Figure 5E**, Wilcoxon Signed Ranks Test, p_{delta} = 0.123, p_{gamma} = 0.012, p_{HFOs} = 0.049, n = 8 trials). The strong coupling of PV interneurons with LFP HFOs might contribute to the decreased oscillation power at high frequency range caused by prolonged optogenetic stimulation of PV interneurons in the PFC.

DISCUSSION

Combining Cre-mediated optogenetics with multi-channel tetrode recording, we were able to describe the *in vivo* firing patterns of mPFC PV interneurons in mice during four basic behavioral states. Most of the mPFC PV interneurons (14 out of 18) are modulated in a behavior state-dependent manner, often with elevated firing rates during AW and/or REM states in comparison to that during QW and SWS states. We identified three subtypes of PV interneurons based on their firing patterns: subtype #1 interneurons showed significant higher firing rate during AW than any other behavior states; subtype #2 interneurons showed elevated firing under AW and REM states compared to QW and SWS states; the firing rate of subtype #3 interneurons is stable across all behavioral states. Using parvalbumin as a molecular marker to categorize cortical interneurons only gives us a sketchy classification of interneuron types. In fact, our findings supported the fact that PV interneurons can be further categorized into subtypes based on morphological characteristics and detailed molecular expression profiles (Kepecs and Fishell, 2014; Zeisel et al., 2015).

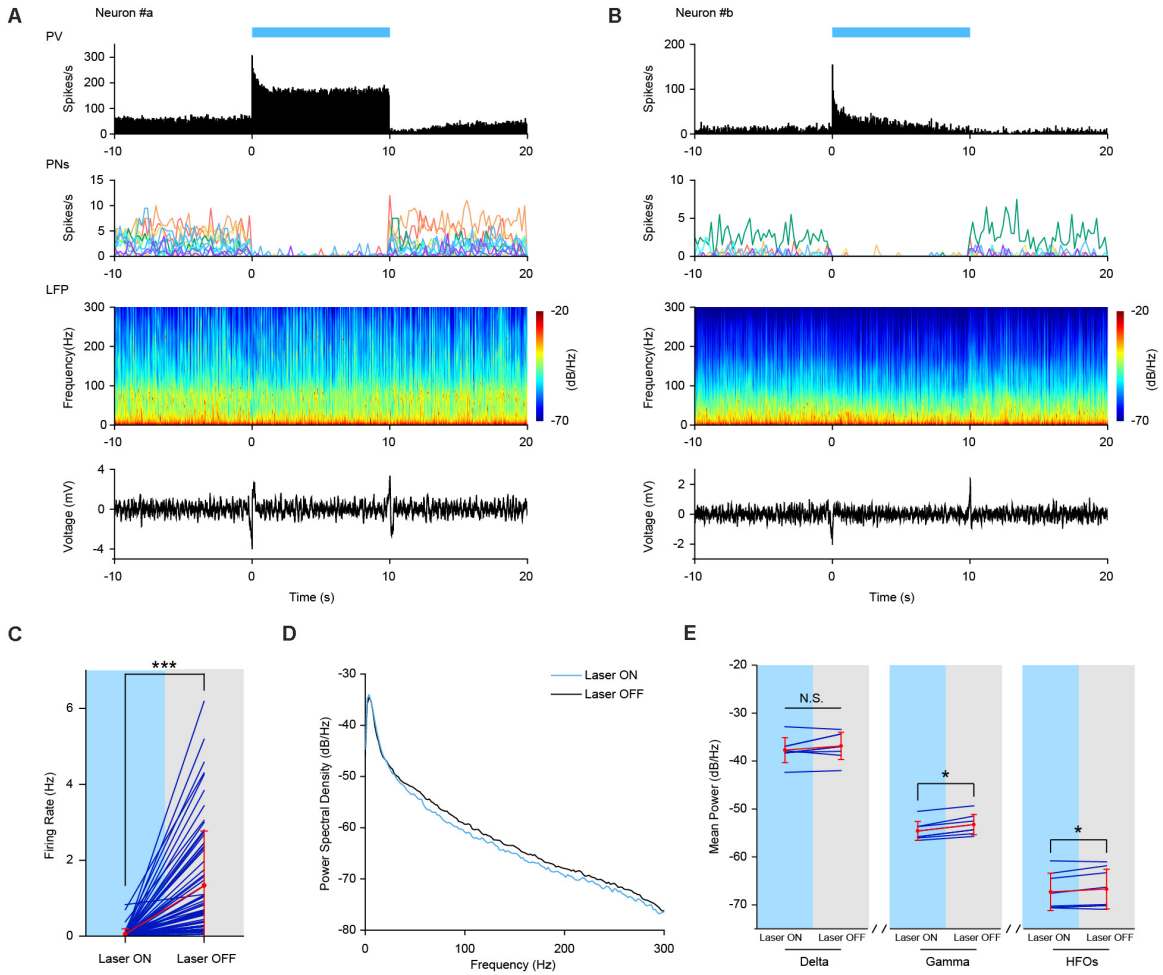

FIGURE 5 | Increased Firing activities of PV interneurons by sustained optogenetic stimulation. **(A,B)** Neuronal firing activities of two example PV interneurons upon optogenetic stimulation in PV-ChR2-EYFP mice during AE and SWS state, respectively. Top row, neuronal firing responses of PV interneurons to sustained laser stimulation (10 s, bin = 0.05 s). Second row, neuronal firing activities of simultaneously recorded pyramidal neurons (PNs). Each colored line represents firing rate activities of one pyramidal neuron [n = 11 PNs in **(A)** and n = 7 PNs in **(B)**, bin = 0.2 s]. Third row, power spectrogram of PFC LFP. Bottom row, responses of PFC LFP to sustained laser stimulation. **(C)** Mean firing rate of simultaneously recorded prefrontal pyramidal neurons during sustained laser stimulation of PV interneurons. Red, mean ± SD; navy, individual; the same below (Wilcoxon Signed Ranks Test, ***, p = 3.5e-12, based on negative ranks, n = 65 neurons). **(D)** PSD of PFC LFP upon laser stimulation of PV interneurons during SWS state. Oscillation power at high frequency range (including gamma and high frequency oscillations) was slightly lower than that without stimulation. **(E)** Statistical test of mean power of different oscillations with and without sustained laser stimulation (Wilcoxon Signed Ranks Test, p_{delta} = 0.123, *, p_{gamma} = 0.012, p_{HFOs} = 0.049, n = 8 trials).

Various studies have demonstrated that fast-spiking interneurons, especially PV positive interneurons, are crucial for the rhythmogenesis and function of mPFC gamma oscillations. Previous study in anesthetized rats has identified two sets of fast-spiking interneurons, firing at early and late phase of cortical UP states, respectively (Puig et al., 2008). Increased synchrony of fast-spiking interneurons at gamma frequency during cortical UP states is reported in both brain slice and anesthetized mice (Salkoff et al., 2015). Furthermore, computational studies predicted that PV interneurons play a crucial role in shaping cortical oscillations. Interconnected PV interneurons are expected to induce gamma oscillations (Buzsaki and Wang, 2012; Keeley et al., 2017). Dysfunction of PV interneurons shortened the duration of cortical UP state in PV-GAD67 mice (Kuki et al., 2015). Synchronized mPFC PV activities are characteristic during attention, accompanied by elevated power of slow gamma oscillation. The firing activities of mPFC PV interneurons are also phase-locked to slow gamma (30–40 Hz) oscillations during attention (Kim et al., 2016). Furthermore, optogenetic stimulation of mPFC PV interneurons at theta-gamma coupled frequency can positively modulate social behaviors (Cao et al., 2018). In our study, we investigated the *in vivo* firing pattern of single PV interneuron and their firing phase relationship with slow and fast gamma oscillation under natural behavior states (but not under attention or memory tasks). Consistent with previous reports, we found that some PV interneurons showed significant phase-locked firing with both slow and fast gamma oscillations. But the strength of such

phase-locked firing with gamma oscillations are much weaker compared to that with cortical HFOs (**Figures 3D,E**). Further experiments would focus on unveiling the causal relationship between PV interneuronal firing and cortical gamma oscillations with optogenetic approaches. In our preliminary experiment, the sustained optogenetic activation of PV interneurons moderately decreased the power of gamma oscillation in the PFC during sleep. We speculate that cortical PV interneurons play a limited role in regulating gamma oscillations.

By applying phase analysis methods, we showed that PV cells in the PFC exhibited robust phase-locked firing to high-frequency oscillations (100–250 Hz) and delta rhythms (1–4 Hz), but poor coupling to gamma (30–80 Hz) or theta (4–8 Hz) oscillations. Moreover, PV interneurons change their firing pattern when behavior state altered, yet they always remain phase-locked to the troughs of high-frequency component of LFP. Ripple oscillations (100–250 Hz) in the hippocampal CA1 region reflect summed IPSPs in ensemble pyramidal neurons. They play an essential role in memory consolidation during sleep. Ripple oscillations always cooccur with large depolarizing activities, called sharp waves, forming sharp wave-ripple complex (Ylinen et al., 1995). The generation of sharp wave ripple events requires inhibitory inputs from local interneurons (Stark et al., 2014). Many hippocampal interneuron subtypes, including PV basket cells, have been reported to be coupled with sharp wave ripples (100–250 Hz) (Klausberger and Somogyi, 2008). Cortical high-frequency oscillations and hippocampal ripple oscillations share several common features: (1) They show overlaps in frequency band, both ranging from 100 to 250 Hz. (2) They are both prominent during SWS states (Buzsaki et al., 1992). (3) Hippocampal pyramidal ensemble burst out synchronous discharge at ripple troughs (Klausberger et al., 2003), while cortical pyramidal population exhibit synchronized spiking activities during HFO periods (Scheffer-Teixeira et al., 2013). (4) The coupling of PFC PV interneurons with high frequency oscillation bears a strong resemblance to that of hippocampal PV basket cells with ripple oscillations. These studies, together with our present results, suggest that PV interneurons in the hippocampus and PFC share good similarities in this regard. They may both involve in the generation and modulation of cortical and hippocampal high frequency oscillations (Tort et al., 2013).

All the simultaneously recorded pyramidal neurons (n = 65) showed significantly reduced firing rate during sustain laser stimulation (**Figure 5C**), confirming that PV interneurons in the PFC exhibit robust inhibition onto pyramidal cells. The prolonged stimulation of PV interneurons increased inhibitory driving force onto postsynaptic pyramidal neurons, hence reducing their firing activities as well as field potential oscillations. The optogenetic stimulation induced moderate effects on LFP power might also be resulted from the possibility of limited numbers of PV interneurons that were activated by laser stimulation through the optic fiber.

Technically speaking, our present study provides several useful perspectives in terms of optogenetic methods in the PFC. It is quite difficult for PV interneurons to follow a strand of laser stimulation at frequencies higher than 10 Hz, although some PV neurons were able to fire at a rate higher than 40 Hz under natural physiological conditions. Unlike physiological conditions, laser stimulation would induce a synchronized firing in PV population. Such synchronized activation of PV interneuron population may result in a strong temporal summation of inhibitory inputs. It may take tens of milliseconds for the membrane potential of PV interneurons to recover to the resting potential, consequently preventing PV interneurons from further adapting to the pace of the optogenetic stimulation frequency. This phenomenon of abundant inhibitory innervations between cortical PV interneurons had been reported by several previous studies as well (Anikeeva et al., 2011; Kvitsiani et al., 2013). Thus, such characterization argues that investigators should prefer to use stimulation frequencies lower than 10 Hz as a way to artificially enhance the function of PV interneurons.

In summary, we found that PV interneurons in the mouse PFC are consisted of at least three subclasses with distinct behavior state-dependent firing patterns. Moreover, activities of PFC PV interneurons were closely coupled to HFOs and delta band. PFC PV interneurons can readily regulate the firing of local pyramidal neurons, and high frequency components of the LFPs.

DATA AVAILABILITY STATEMENT

The raw data supporting the conclusions of this article will be made available by the authors, without undue reservation, to any qualified researcher.

ETHICS STATEMENT

The animal study was reviewed and approved by the Laboratory Animal Management Committee at East China Normal University.

AUTHOR CONTRIBUTIONS

YY and LL conceived this project and designed the experiments. YY performed *in vivo* electrophysiological recording, immunohistochemistry experiments, and data analysis. LW helped with immunohistochemistry experiments and data analysis. YY and MW performed raw data processing. YY, LL, and JX wrote the manuscript. All authors contributed to the article and approved the submitted version.

FUNDING

This work was supported by the National Natural Science Foundation of China (Grant No. 31800890).

ACKNOWLEDGMENTS

We thank J. Tsien for critically reading the manuscript. We thank L. Zhang from Georgia Institute of Technology for the advice on data analysis.

REFERENCES

Andreassen, S., Stein, R. B., and Oguztoreli, M. N. (1979). Application of optimal multichannel filtering to simulated nerve signals. *Biol. Cybern.* 32, 25–33. doi: 10.1007/BF00337448

Anikeeva, P., Andalman, A. S., Witten, I., Warden, M., Goshen, I., Grosenick, L., et al. (2011). Optetrode: a multichannel readout for optogenetic control in freely moving mice. *Nat. Neurosci.* 15, 163–170. doi: 10.1038/nn.2992

Arnold, M., Miltner, W. H. R., Witte, H., Bauer, R., and Braun, C. (1998). Adaptive AR modeling of nonstationary time series by means of Kalman filtering. *IEEE Trans. Biomed. Eng.* 45, 553–562. doi: 10.1109/10.668741

Atallah, B. V., and Scanziani, M. (2009). Instantaneous modulation of gamma oscillation frequency by balancing excitation with inhibition. *Neuron* 62, 566–577. doi: 10.1016/j.neuron.2009.04.027

Buzsaki, G., Horvath, Z., Urioste, R., Hetke, J., and Wise, K. (1992). High-frequency network oscillation in the hippocampus. *Science* 256, 1025–1027. doi: 10.1126/science.1589772

Buzsaki, G., and Wang, X. J. (2012). Mechanisms of gamma oscillations. *Annu. Rev. Neurosci.* 35, 203–225. doi: 10.1146/annurev-neuro-062111-150444

Cao, W., Lin, S., Xia, Q. Q., Du, Y. L., Yang, Q., Zhang, M. Y., et al. (2018). Gamma oscillation dysfunction in mPFC leads to social deficits in neuroligin 3 R451C knockin mice. *Neuron* 97, 1253–1260.e7. doi: 10.1016/j.neuron.2018.02.001

Cardin, J. A., Carlen, M., Meletis, K., Knoblich, U., Zhang, F., Deisseroth, K., et al. (2009). Driving fast-spiking cells induces gamma rhythm and controls sensory responses. *Nature* 459, 663–667. doi: 10.1038/nature08002

Engel, J. Jr., Bragin, A., Staba, R., and Mody, I. (2009). High-frequency oscillations: what is normal and what is not? *Epilepsia* 50, 598–604. doi: 10.1111/j.1528-1167.2008.01917.x

Fujisawa, S., and Buzsaki, G. (2011). A 4 Hz oscillation adaptively synchronizes prefrontal. VTA, and hippocampal activities. *Neuron* 72, 153–165. doi: 10.1016/j.neuron.2011.08.018

Hippenmeyer, S., Vrieseling, E., Sigrist, M., Portmann, T., Laengle, C., Ladle, D. R., et al. (2005). A developmental switch in the response of DRG neurons to ETS transcription factor signaling. *PLoS Biol.* 3:e159. doi: 10.1371/journal.pbio.0030159

Ishizuka, T., Kakuda, M., Araki, R., and Yawo, H. (2006). Kinetic evaluation of photosensitivity in genetically engineered neurons expressing green algae light-gated channels. *Neurosci. Res.* 54, 85–94. doi: 10.1016/j.neures.2005.10.009

Karalis, N., Dejean, C., Chaudun, F., Khoder, S., Rozeske, R. R., Wurtz, H., et al. (2016). 4-Hz oscillations synchronize prefrontal-amygdala circuits during fear behavior. *Nat. Neurosci.* 19, 605–612. doi: 10.1038/nn.4251

Keeley, S., Fenton, A. A., and Rinzel, J. (2017). Modeling fast and slow gamma oscillations with interneurons of different subtype. *J. Neurophysiol.* 117, 950–965. doi: 10.1152/jn.00490.2016

Kepecs, A., and Fishell, G. (2014). Interneuron cell types are fit to function. *Nature* 505, 318–326. doi: 10.1038/nature12983

Kim, H., Ahrlund-Richter, S., Wang, X., Deisseroth, K., and Carlen, M. (2016). Prefrontal parvalbumin neurons in control of attention. *Cell* 164, 208–218. doi: 10.1016/j.cell.2015.11.038

Klausberger, T., Magill, P. J., Marton, L. F., Roberts, J. D., Cobden, P. M., Buzsaki, G., et al. (2003). Brain-state- and cell-type-specific firing of hippocampal interneurons in vivo. *Nature* 421, 844–848. doi: 10.1038/nature01374

Klausberger, T., and Somogyi, P. (2008). Neuronal diversity and temporal dynamics: the unity of hippocampal circuit operations. *Science* 321, 53–57. doi: 10.1126/science.1149381

Kuki, T., Fujihara, K., Miwa, H., Tamamaki, N., Yanagawa, Y., and Mushiake, H. (2015). Contribution of parvalbumin and somatostatin-expressing GABAergic neurons to slow oscillations and the balance in beta-gamma oscillations across cortical layers. *Front. Neural. Circuits* 9:6. doi: 10.3389/fncir.2015.00006

Kvitsiani, D., Ranade, S., Hangya, B., Taniguchi, H., Huang, J. Z., and Kepecs, A. (2013). Distinct behavioural and network correlates of two interneuron types in prefrontal cortex. *Nature* 498, 363–366. doi: 10.1038/nature12176

Lee, A. T., Gee, S. M., Vogt, D., Patel, T., Rubenstein, J. L., and Sohal, V. S. (2014). Pyramidal neurons in prefrontal cortex receive subtype-specific forms of excitation and inhibition. *Neuron* 81, 61–68. doi: 10.1016/j.neuron.2013.10.031

Lin, L., Chen, G., Xie, K., Zaia, K. A., Zhang, S., and Tsien, J. Z. (2006). Large-scale neural ensemble recording in the brains of freely behaving mice. *J. Neurosci. Methods* 155, 28–38. doi: 10.1016/j.jneumeth.2005.12.032

Madisen, L., Mao, T., Koch, H., Zhuo, J. M., Berenyi, A., Fujisawa, S., et al. (2012). A toolbox of Cre-dependent optogenetic transgenic mice for light-induced activation and silencing. *Nat. Neurosci.* 15, 793–802. doi: 10.1038/nn.3078

Miller, E. K. (2000). The prefrontal cortex and cognitive control. *Nat. Rev. Neurosci.* 1, 59–65. doi: 10.1038/35036228

Pfeffer, C. K., Xue, M., He, M., Huang, Z. J., and Scanziani, M. (2013). Inhibition of inhibition in visual cortex: the logic of connections between molecularly distinct interneurons. *Nat. Neurosci.* 16, 1068–1076. doi: 10.1038/nn.3446

Puig, M. V., Ushimaru, M., and Kawaguchi, Y. (2008). Two distinct activity patterns of fast-spiking interneurons during neocortical UP states. *Proc. Natl. Acad. Sci. U S A.* 105, 8428–8433. doi: 10.1073/pnas.0712219105

Salkoff, D. B., Zagha, E., Yuzgec, O., and McCormick, D. A. (2015). Synaptic mechanisms of tight spike synchrony at gamma frequency in cerebral cortex. *J. Neurosci.* 35, 10236–10251. doi: 10.1523/JNEUROSCI.0828-15.2015

Scheffer-Teixeira, R., Belchior, H., Leao, R. N., Ribeiro, S., and Tort, A. B. (2013). On high-frequency field oscillations (>100 Hz) and the spectral leakage of spiking activity. *J. Neurosci.* 33, 1535–1539. doi: 10.1523/JNEUROSCI.4217-12.2013

Siapas, A. G., Lubenov, E. V., and Wilson, M. A. (2005). Prefrontal phase locking to hippocampal theta oscillations. *Neuron* 46, 141–151. doi: 10.1016/j.neuron.2005.02.028

Stark, E., Roux, L., Eichler, R., Senzai, Y., Royer, S., and Buzsaki, G. (2014). Pyramidal cell-interneuron interactions underlie hippocampal ripple oscillations. *Neuron* 83, 467–480. doi: 10.1016/j.neuron.2014.06.023

Tamura, M., Spellman, T. J., Rosen, A. M., Gogos, J. A., and Gordon, J. A. (2017). Hippocampal-prefrontal theta-gamma coupling during performance of a spatial working memory task. *Nat. Commun.* 8:2182. doi: 10.1038/s41467-017-02108-2109

Tarvainen, M. P., Hilturien, J. K., Ranta-Aho, P. O., and Karjalainen, P. A. (2004). Estimation of nonstationary EEG with Kalman smoother approach: an application to event-related synchronization (ERS). *IEEE Trans. Biomed. Eng.* 51, 516–524. doi: 10.1109/Tbme.2003.821029

Tort, A. B., Scheffer-Teixeira, R., Souza, B. C., Draguhn, A., and Brankack, J. (2013). Theta-associated high-frequency oscillations (110-160Hz) in the hippocampus and neocortex. *Prog. Neurobiol.* 100, 1–14. doi: 10.1016/j.pneurobio.2012.09.002

Tremblay, R., Lee, S., and Rudy, B. (2016). GABAergic interneurons in the neocortex: from cellular properties to circuits. *Neuron* 91, 260–292. doi: 10.1016/j.neuron.2016.06.033

Vinck, M., Battaglia, F. P., Womelsdorf, T., and Pennartz, C. (2012). Improved measures of phase-coupling between spikes and the Local Field Potential. *J. Comput. Neurosci.* 33, 53–75. doi: 10.1007/s10827-011-0374-374

Vinck, M., van Wingerden, M., Womelsdorf, T., Fries, P., and Pennartz, C. M. A. (2010). The pairwise phase consistency: a bias-free measure of rhythmic neuronal synchronization. *Neuroimage* 51, 112–122. doi: 10.1016/j.neuroimage.2010.01.073

Ward, L. M. (2003). Synchronous neural oscillations and cognitive processes. *Trends Cogn. Sci.* 7, 553–559. doi: 10.1016/j.tics.2003.10.012

Xu, Q., Cobos, I., De La Cruz, E., Rubenstein, J. L., and Anderson, S. A. (2004). Origins of cortical interneuron subtypes. *J. Neurosci.* 24, 2612–2622. doi: 10.1523/JNEUROSCI.5667-03.2004

Xue, M., Atallah, B. V., and Scanziani, M. (2014). Equalizing excitation-inhibition ratios across visual cortical neurons. *Nature* 511, 596–600. doi: 10.1038/nature13321

Yizhar, O., Fenno, L. E., Prigge, M., Schneider, F., Davidson, T. J., O'Shea, D. J., et al. (2011). Neocortical excitation/inhibition balance in information processing and social dysfunction. *Nature* 477, 171–178. doi: 10.1038/nature10360

Ylinen, A., Bragin, A., Nadasdy, Z., Jando, G., Szabo, I., Sik, A., et al. (1995). Sharp wave-associated high-frequency oscillation (200 Hz) in the intact hippocampus: network and intracellular mechanisms. *J. Neurosci.* 15(1 Pt 1), 30–46.

Zeisel, A., Munoz-Manchado, A. B., Codeluppi, S., Lonnerberg, P., La Manno, G., Jureus, A., et al. (2015). Brain structure. Cell types in the mouse cortex and hippocampus revealed by single-cell RNA-seq. *Science* 347, 1138–1142. doi: 10.1126/science.aaa1934

Zhang, L., Chen, G., Niu, R., Wei, W., Ma, X., Xu, J., et al. (2012). Hippocampal theta-driving cells revealed by granger causality. *Hippocampus* 22, 1781–1793. doi: 10.1002/hipo.22012

Conflict of Interest: The authors declare that the research was conducted in the absence of any commercial or financial relationships that could be construed as a potential conflict of interest.

frontiers in Cellular Neuroscience

REVIEW
published: 17 December 2020
doi: 10.3389/fncel.2020.611732

Prefrontal Disinhibition in Social Fear: A Vital Action of Somatostatin Interneurons

Jun Wang[1,2], *Yuanyuan Tian*[1,2], *Ling-Hui Zeng*[3] *and Han Xu*[1,2,3]*

[1]*Department of Neurobiology and Department of Neurology of the Second Affiliated Hospital, Zhejiang University School of Medicine, Hangzhou, China,* [2]*NHC and CAMS Key Laboratory of Medical Neurobiology, MOE Frontier Science Center for Brain Research and Brain-Machine Integration, School of Brain Science and Brain Medicine, Zhejiang University, Hangzhou, China,* [3]*Department of Pharmacology, School of Medicine, Zhejiang University City College, Hangzhou, China*

Social fear and avoidance of social partners and social situations represent the core behavioral symptom of Social Anxiety Disorder (SAD), a prevalent psychiatric disorder worldwide. The pathological mechanism of SAD remains elusive and there are no specific and satisfactory therapeutic options currently available. With the development of appropriate animal models, growing studies start to unravel neuronal circuit mechanisms underlying social fear, and underscore a fundamental role of the prefrontal cortex (PFC). Prefrontal cortical functions are implemented by a finely wired microcircuit composed of excitatory principal neurons (PNs) and diverse subtypes of inhibitory interneurons (INs). Disinhibition, defined as a break in inhibition *via* interactions between IN subtypes that enhances the output of excitatory PNs, has recently been discovered to serve as an efficient strategy in cortical information processing. Here, we review the rodent animal models of social fear, the prefrontal IN diversity, and their circuits with a particular emphasis on a novel disinhibitory microcircuit mediated by somatostatin-expressing INs in gating social fear behavior. The INs subtype distinct and microcircuit-based mechanism advances our understanding of the etiology of social fear and sheds light on developing future treatment of neuropsychiatric disorders associated with social fear.

Keywords: social anxiety disorder, social fear, interneuron, disinhibition, prefrontal cortex

OPEN ACCESS

Edited by:
Miao He,
Fudan University, China

Reviewed by:
Chaoran Ren,
Jinan University, China
Yiran Gu,
East China Normal University, China

***Correspondence:**
Han Xu
xuhan2014@zju.edu.cn

Specialty section:
This article was submitted to Non-Neuronal Cells, a section of the journal Frontiers in Cellular Neuroscience

Received: *30 September 2020*
Accepted: *27 November 2020*
Published: *17 December 2020*

Citation:
Wang J, Tian Y, Zeng L-H and Xu H (2020) Prefrontal Disinhibition in Social Fear: A Vital Action of Somatostatin Interneurons. Front. Cell. Neurosci. 14:611732. doi: 10.3389/fncel.2020.611732

INTRODUCTION

The fear response to an imminent threat is an adaptive behavior and is essential to avoid danger in the environment for animals and humans. However, persistent and unnecessary fear response represents a maladaptive behavior evident in a large number of psychiatric diseases such as posttraumatic stress disorder (PTSD) and anxiety disorders (Buff et al., 2016; Nees et al., 2018). Intense and persistent fear and avoidance of social situations represent the core behavioral symptom of social anxiety disorder (SAD), a prevalent psychiatric disorder worldwide (Kessler et al., 2005a,b; Stein and Stein, 2008; Leichsenring and Leweke, 2017). Social fear makes even the simplest daily task challenging and distressful and literally disconnects individuals afflicted from others and society. Unfortunately, there are no satisfactory therapeutic options currently available (Stein and Stein, 2008; Dos Santos et al., 2019). The pathological mechanism underlying SAD is undetermined partly due to a lack of specific animal models (Toth et al., 2012, 2013; Toth and Neumann, 2013). Recently, thanks to the effort of several groups of researchers, a couple of experimental paradigms have been

developed to induce social fear in rodents. Importantly, these paradigms reliably induce robust behavioral changes recapitulating core behavioral symptoms of SAD in humans, without affecting non-social behaviors such as locomotion, general anxiety, and depressive-like behaviors (Toth et al., 2012; Toth and Neumann, 2013; Franklin et al., 2017; Xu et al., 2019). Notably, by using these rodent animal models, neuroscientists start to dissect the neuronal circuit substrates underlying social fear (Franklin et al., 2017; Xu et al., 2019).

Accumulating evidence from human functional brain imaging studies suggests that the prefrontal cortex (PFC) contributes essentially to the processes of social fear responses (Buff et al., 2016; Kawashima et al., 2016). The PFC is composed of a majority of principal neurons (PNs) and a minority of inhibitory interneurons (INs) which exhibit remarkable diversity in morphology, physiological properties, immunohistochemical characteristics, and connectivity (Kawaguchi and Kubota, 1997; Rudy et al., 2011; Xu et al., 2013; Hattori et al., 2017). Different subtypes of INs could effectively control cortical network activity *via* feedforward, feedback inhibition, and disinhibition (Xu et al., 2013, 2019; Tremblay et al., 2016). Both human and animal studies found that an exquisite balance between excitation and inhibition plays a fundamental role in cortical functions (Rubenstein and Merzenich, 2003; Yizhar et al., 2011; Sohal and Rubenstein, 2019). Moreover, the exact activity patterns of specific prefrontal IN subtypes and their precise microcircuit mechanism in fear-related behaviors including social fear start to emerge (Xu et al., 2019; Cummings and Clem, 2020).

In this review, we will first briefly introduce SAD and summarize major attempts in developing proper experimental paradigms to induce social fear in rodents. Then, we will discuss studies in the exploration of pathological mechanisms underlying social fear by using these rodent animal models. Given the complexity and multidimensional nature of social fear behavior, we will focus our discussion on the brain region of PFC. In specific, we will discuss prefrontal IN diversity and their microcircuits in the context of social fear regulation. Particularly, we will highlight a newly discovered disinhibitory microcircuit in the PFC *via* interactions between subtypes of INs. We suggest that prefrontal disinhibition mediated by somatostatin-expressing (SST^+) INs represents an essential circuit mechanism in the regulation of social fear behavior.

SOCIAL FEAR AND ANIMAL MODELS OF SOCIAL FEAR

SAD, also known as social phobia, is one of the most frequent psychiatric illness, with a worldwide lifetime prevalence of up to 13% (Kessler et al., 2005a,b; Stein and Stein, 2008; Leichsenring and Leweke, 2017), and is more prevalent in adolescents than in adults (Stein and Stein, 2008; Leichsenring and Leweke, 2017). SAD is essentially characterized by persistent avoidance, anxiety, or fear of social or performance situations (Stein and Stein, 2008; Leichsenring and Leweke, 2017). Indeed, social fear and social avoidance is the core behavioral symptom of SAD in clinical diagnosis. In addition to SAD, social fear or avoidance of social situations is also commonly observed in many other neuropsychiatric disorders, such as autism, schizophrenia, and depression (Jones et al., 2017). Social fear leads to low self-esteem and disconnects individuals from others and society to a varying degree and can cause devastating consequences on the individuals' daily life. Besides, it also causes high social and medical costs to the families afflicted and the society (American Psychiatric Publishing, 2013). Current treatments involve psychotherapy, pharmacotherapy, or a combination of both. These treatment options are effective for some individuals suffering from the disorder. However, the problem is that only partial remission of symptoms can be achieved and the recurrence rate after discontinuation of treatments is high (Blanco et al., 2002). What is even worse, for up to 30–40% of patients, these exiting treatments do not work (Blanco et al., 2002; Leichsenring and Leweke, 2017). Essentially, a deeper understanding of the pathological mechanisms underlying SAD is urgently needed.

Animal models offer valuable tools for understanding the biological mechanisms involved and finding more effective therapeutic targets for many diseases. However, it has not been successful in developing appropriate animal models for SAD. It has been shown that social fear and social avoidance could be reliably induced with several experimental paradigms, including social conflict (Huhman, 2006), foot shock (Haller and Bakos, 2002), social isolation (Hermes et al., 2011), and maternal separation (Niwa et al., 2011; for review, Toth and Neumann, 2013). Unfortunately, none of these paradigms produced behavioral outcomes that are specified in the social domain. Instead, other phenotypical changes were also evident in these experimental animal models, such as alterations in general anxiety, locomotor functions, as well as depressive-like behaviors (Toth and Neumann, 2013). Therefore, more specific animal models with no confounding factors are required to probe the underlying substrates of social fear. Such animal models are also useful for screening drugs for psychiatric disorders associated with social fear.

To develop rodent models of social fear with more specificity, a couple of elegant studies have recently been conducted by making use of either social fear conditioning (SFC) or sub-chronic social defeat (**Figure 1**). The SFC paradigm was first introduced by Toth et al. (2012, 2013), which is based on the principle of operant fear conditioning by paring a conspecific social investigation with physical punishment (an electric foot shock). On the conditioning day, the experimental mouse was allowed to acclimate to the conditioning chamber with a floor consisting of a stainless-steel grid that delivers electric foot shocks and an empty wire mesh cage placed near a wall of the chamber. Then an unfamiliar conspecific mouse with matched gender was introduced to the wire mesh cage as a social stimulus. The experimental mouse was allowed to freely investigate the stimulus mouse before conditioning, and then an electric foot shock was manually delivered to the conditioned mouse each time when it approached and investigated the social stimulus mouse. After the conditioning, the conditioned mouse showed a dramatic reduction in the time of social investigation to unfamiliar conspecific mouse and other aversive responses toward the stimulus mouse.

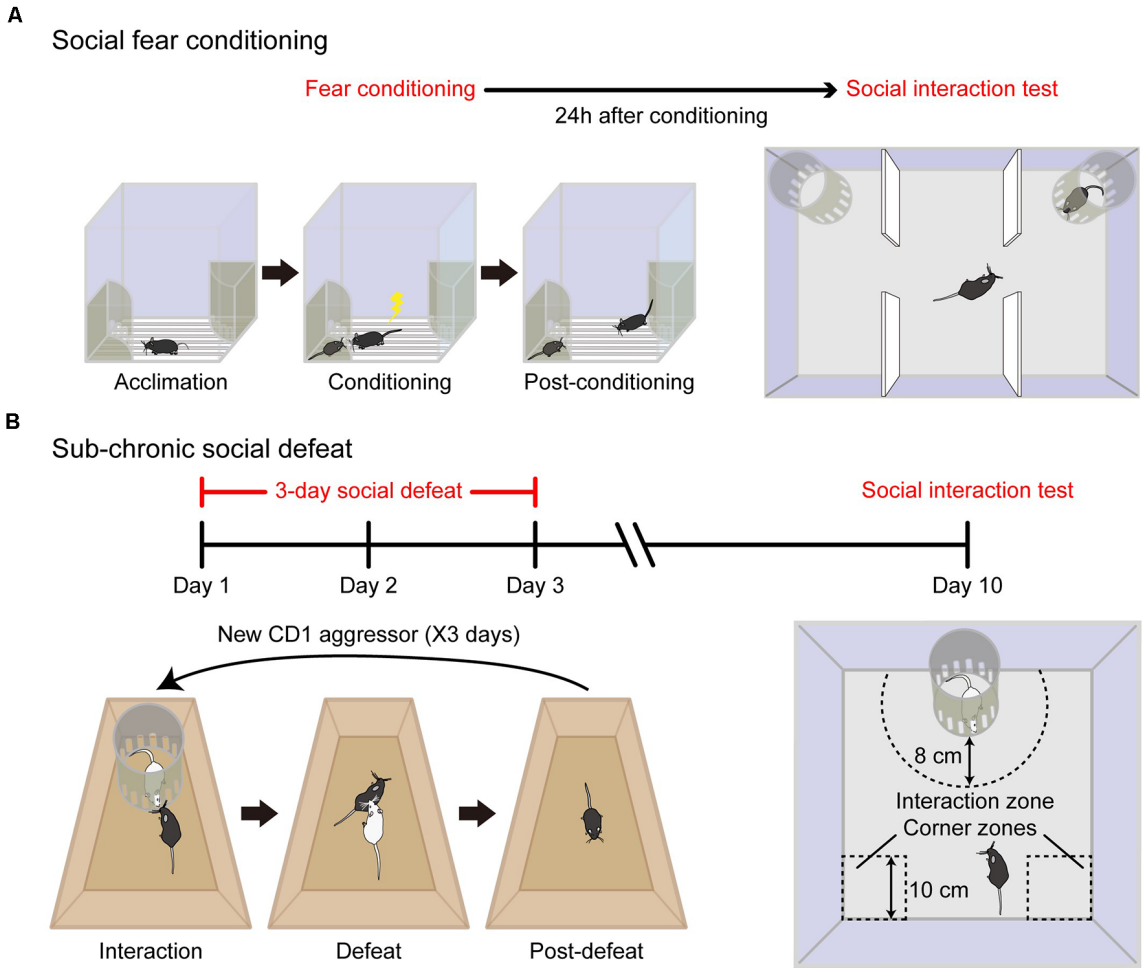

FIGURE 1 | Specific animal models of social fear. **(A)** Schematic diagram of the social fear conditioning (SFC) paradigm. The experimental mouse was first allowed to acclimate to the conditioning chamber (Acclimation) and then a stimulus mouse was introduced to one of the stimulus cages placed on opposing corners of the conditioning chamber. During the conditioning session, the experimental mouse was allowed to freely interact with the stimulus mouse, while a foot shock was delivered each time when it approached and investigated the stimulus mouse (Conditioning). After conditioning, the procedure was extended to a longer duration to reinforce behavioral adaption (Post-conditioning). Adapted from Xu et al. (2019). **(B)** Schematic diagram of sub-chronic social defeat paradigm. For three consecutive days, an unfamiliar aggressive male CD1 intruder mouse (white color) was introduced to the home cage of singly-housed adult C57BL/6J male mice (black color). The intruder was confined within a Plexiglas stimulus cage (10 cm in diameter) for the first 5 min (interaction) and then was allowed to attack the experimental mouse for 10 min (defeat) and withdraw immediately after social confrontations (post-defeat). After 1 week recovery, the expression of social fear to an unfamiliar CD1 mouse was detected in an open field. Social avoidance was assessed by relative time spent in the interaction zone to corner zones.

These behavioral changes reflect the successful induction of social fear in the conditioned mouse. In contrast to previous paradigms, the social fear mouse induced by the SFC paradigm showed no alterations in locomotion, general anxiety, or depressive-like behavior. Therefore, SFC is a reliable paradigm to induce social fear in mice with good specificity (Toth et al., 2012).

In a more recent study by us (Xu et al., 2019), we adopted the conditioning paradigm pioneered by Toth et al. (2012) and made several significant improvements. First, to ensure consistency of conditioning criteria and to reduce the behavioral variation among conditioned subjects, social contacts were monitored, and electric foot shocks were delivered automatically with a computerized conditioning unit equipped with a video tracking system. Second, to ensure fear acquisition specifically to the stimulus mouse but not to the cage, two identical cages were placed at each of two opposing corners of the conditioning unit with one containing a stimulus mouse and the other remaining empty during the conditioning procedure. Third, to reinforce behavioral adaptation of the conditioned mouse, the conditioning procedure was extended to a longer duration (20 min) although the experimental mice usually did not investigate stimulus mice and thus did not get foot shocks any longer after 5 min. Moreover, we employed C57BL/6J mice for the SFC paradigm instead of CD1 mice or rats by Toth et al. (2012, 2013) and therefore extended the application of this conditioning paradigm to a more broadly used species. This extension is important for

future studies aimed to elucidate the etiology of social fear given that a large number of genetic resources and tools are readily available for C57BL/6J mouse lines. Consistent with the findings reported by Toth et al. (2012), the conditioned mice spent significantly less time with the stimulus mouse in a three-chamber social interaction test and exhibited significantly fewer approach times to social stimulus in a social preference-avoidance test. Besides, conditioned mice approached the stimulus mouse in a stretched posture and at a slow speed, two behavioral indicators of an elevated fear state in rodents that were absent in unconditioned control animals. Therefore, our modified conditioning paradigm is robust and reliable. Importantly, conditioned mice behaved normally in response to a novel object and exhibited no alterations in locomotion, general anxiety, and depressive-like behaviors, validating the specificity of behavioral changes in the social domain.

We also compared another social fear model that is induced by social defeat (Xu et al., 2019), which is adapted from a previous study conducted by Franklin et al. (2017). Unlike the SFC that relies on an artificial punishment (electric foot shock), social defeat happens in an experimental setting comparable to the mouse's natural environment, that is, exposure to an aggressor. Repeated social defeat is widely employed as a standardized protocol to induce depressive-like behaviors in C57BL/6J mice (Golden et al., 2011). However, there are several significant differences in using social defeat to induce social fear. First, the duration of social defeat is shorter to establish a social fear mouse model than that for a depressive mouse model. The experimental C57BL/6J mice are exposed to agonistic social confrontations with an aggressive CD1 mouse for three consecutive days (Xu et al., 2019) for the social fear mouse model (so it is called sub-chronic social defeat) compared to a couple of weeks for depression (chronic social defeat). Second, to induce social fear an aggressive CD1 mouse is introduced into the home cage of experimental C57BL/6J mice and withdrawn immediately after social confrontations. In contrast, to induce depression the C57BL/6J mouse was living in a shared home cage with a CD1 mouse separated by a clear perforated divider (Golden et al., 2011). In this manner, the defeated mouse is subjected to continuous psychological stress from sensory interaction with the aggressor for the entire modeling period which facilitates its behavioral adaptions. As a consequence, after chronic social defeat, some mice exhibit specific depressive-like behaviors (termed "susceptible") and the others have no change (termed "resilient"; Golden et al., 2011). In comparison, the mice subjected to sub-chronic social defeat showed a reduction in social investigations without alterations in locomotion, general anxiety, and depressive-like behaviors (Xu et al., 2019). Note that, for the SFC paradigm, the conditioned mouse develops a tight association between social stimulus and foot shock after SFC, and the animal shows social fear behavior to the stimulus mouse. Similarly, after sub-chronic defeat, the defeated mouse shows submission to the aggressive intruder. Despite the behavioral similarity of these two animal models, it is still an open question whether these defensive behaviors share the same neural circuits or not.

FUNCTIONS OF THE PREFRONTAL CORTEX IN SOCIAL FEAR

Recent functional brain imaging studies have identified abnormal activities in several brain regions of patients with SAD (Zhu et al., 2017; Doruyter et al., 2018). These brain regions largely belong to the limbic system including the amygdala (Kraus et al., 2018; Figel et al., 2019; Frick et al., 2020), bed nucleus of the stria terminalis (BNST; Figel et al., 2019), and PFC (Buff et al., 2016; Kawashima et al., 2016; Frick et al., 2020). In particular, both near-infrared spectroscopy (Kawashima et al., 2016) and functional magnetic resonance imaging (fMRI) studies (Buff et al., 2016) revealed that hyperactivity of PFC is tightly linked to excessive and long-lasting fear states in patients with SAD. In human, the PFC is mainly composed of four subregions, namely, orbitofrontal cortex (OFC), dorsolateral PFC, ventrolateral PFC, and mPFC (Ko, 2017), which have an important role in the processing of complicated cognitive and executive behaviors (e.g., social behaviors; Amodio and Frith, 2006) as well as emotion (Etkin et al., 2011). Although it is still controversial, emerging evidence suggests that it is anatomically comparable and functional homologous between human and rodent PFC structures (Dalley et al., 2004). The PFC regions in rodents can be categorized into three major subregions: the dorsal part of the medial PFC (dmPFC), ventral part of the medial PFC (vmPFC), and lateral OFC (lOFC; Kamigaki, 2019). Notably, it is clear now that mPFC is closely linked to fear-related behaviors in rodents, albeit with divergent functions of distinct subregions (Amodio and Frith, 2006).

The prelimbic (PrL) PFC neurons have been believed to encode sustained fear response in classic auditory fear conditioning (Burgos-Robles et al., 2009). It has long been demonstrated by *in vivo* unit recording that neurons in the amygdala elicit potentiated tone responses that correlate with the acquisition of conditioned fear (Quirk et al., 1995; Paré and Collins, 2000), while these neuronal activities last only a few hundred milliseconds and cannot be responsible for sustained fear responses in the auditory fear conditioning paradigm that last tens of seconds, suggesting the long-lasting fear responses should be stored in other brain structures. Using multichannel electrophysiological recordings in behaving rats, Burgos-Robles et al. (2009) revealed that sustained hyperactivity of the PrL neurons in response to the conditioned tone is correlated with freezing behavior suggesting that PrL neurons integrate inputs from the amygdala and other brain structures that form a top-down control of fear (Etkin et al., 2011) and contribute to the sustained fear expression. In support of this hypothesis, Karalis et al. (2016) found that the freezing response elicited by conditioned tone temporally coincided with sustained synchrony of 4-Hz oscillations in prefrontal-amygdala circuits. Contrary to the PrL, substantial evidence indicates that infralimbic (IL) sub-divisions of the mPFC is necessary for the extinction of conditioned fear (Quirk et al., 2006; Wang et al., 2018). Besides, collective evidence supports that OFC, another sub-division of the mPFC, also plays a crucial role in the regulation of

conditioned fear (Sarlitto et al., 2018) and fear extinction (Rodriguez-Romaguera et al., 2015; Chang et al., 2018; Hsieh and Chang, 2020). However, in contrast to IL, activation of OFC negatively impaired extinction outcome (Rodriguez-Romaguera et al., 2015; Chang et al., 2018; Hsieh and Chang, 2020).

Despite a large amount of evidence supporting the essential function of PFC in conditioned auditory fear, its role in social fear is much less understood. By c-fos staining, our study found that after exposure to a conspecific mouse, the number of c-fos positive cells was increased in PrL but not in IL of mice with conditioned social fear, indicating a tight link between PrL neuronal activity and social fear expression (Xu et al., 2019). Further, pharmacological inhibition of mPFC with GABAa receptor agonist muscimol dramatically reduces social avoidance in mice with social fear elicited by either SFC or social defeat. As a high-order cerebral cortex, mPFC influences sociability by its projection to several brain areas, including the amygdala, hippocampus, and brainstem (Goodson, 2005). Interestingly, social defeat weakens neural functional connectivity between mPFC and periaqueductal gray (PAG), and selective chemogenetic inhibition of mPFC-PAG projection increases social avoidance (Franklin et al., 2017). Moreover, it has been clarified that layer 5 mPFC projection neurons inhibit excitatory inputs to glutamatergic neurons in PAG *via* presynaptic neuromodulatory mechanisms, and selective inhibition of these PAG neurons reduces social avoidance (Franklin et al., 2017). These observations provide mechanistic insight regarding the prefrontal modulation of social fear by a specific prefrontal projection to PAG.

CORTICAL INs AND MICROCIRCUIT

In the adult neocortex, the complex circuitry functions rely on a delicate balance between excitation and inhibition (Xu et al., 2013, 2019). Although neocortical INs represent a minority of total cortical neurons (10–20% in rodents; Kamigaki, 2019; Xu et al., 2019), they exhibit remarkable diversity in morphology, physiological properties, immunohistochemical characteristics, and connectivity (Kawaguchi and Kubota, 1997; Rudy et al., 2011; Xu et al., 2013; Hattori et al., 2017). Recent evidence suggests that neocortical INs can be divided into non-overlapping subgroups that expressing three different biomarkers: parvalbumin (PV, account for ∼40% of total INs), the neuropeptide somatostatin (SST, account for ∼30% of total INs), and the ionotropic serotonin receptor 5HT3a (5HT3aR, account for ∼30% of total Ins; Rudy et al., 2011; Tremblay et al., 2016). Within 5HT3aR-expressing INs, ∼40% of neurons also expressing vasoactive intestinal peptide (VIP), and the remaining are non-VIP INs (Rudy et al., 2011; Tremblay et al., 2016), which are the third-largest subtype of INs in the neocortex. In addition to PV, SST, and VIP, other biomarkers are often used to label cortical INs, including neuropeptides cholecystokinin (CCK), neuropeptide Y (NPY), and calcium-binding proteins calbindin (CB). However, these markers are expressed in overlapping populations of INs (Tremblay et al., 2016). The heterogeneity of INs is believed to facilitate their ability to perform complex operations.

INs actively gate information flow and sculpt network dynamics in a subtype-specific manner. PV^+ and SST^+ INs mainly target the perisomatic and distal dendritic regions of postsynaptic excitatory neurons, respectively (Hattori et al., 2017). By contrast to PV^+ and SST^+ INs, VIP^+ INs mostly disinhibit excitatory neurons through inhibition of PV^+ and SST^+ INs (Tremblay et al., 2016). The PV INs can be further divided into fast-spiking (FS) basket and chandelier cells according to their morphology. Chandelier cells, also known as axo-axonic neurons due to their synaptic terminals specifically target the axon initial segment of PNs. In contrast, basket cells mostly target the soma and proximal dendrites of PNs and other INs. SST^+ INs also constitute a diverse group and can be divided into Martinotti and non-Martinotti cells based on their different morphology (Tremblay et al., 2016). In the somatosensory cortex, Martinotti cells are mostly located in superficial (layer 2/3, L2/3) and deep (L5/6) layers, while non-Martinotti cells are mainly located in L4. Intriguingly, these two subtypes of SST^+ INs also differ in terms of connectivity. In comparison to L2/3 Martinotti cells that predominantly target PNs, L4 non-Martinotti cells predominantly target local PV^+ INs and disinhibit PNs (Xu et al., 2013).

Due to their distinct membrane properties and subcellular targeting on postsynaptic cells, it is suggested that distinct subtypes of INs contribute differentially to different cortical rhythmic oscillations. PV^+ INs have fast kinetics of membrane property and inhibit local PNs at short latency. Also, PV^+ INs target soma and perisomatic compartments of PNs which are essential subcellular regions to generate spikes, and therefore control the spiking output of PNs (Abbas et al., 2018). The nearby neural assemblies fire co-occurring spikes during the intervals of PV firing and follow the cycle of PV^+ INs' inhibitory inputs, which in turn leads to coherent oscillation in the local network with a high-frequency band (i.e., gamma oscillation; Cardin et al., 2009; Kamigaki, 2019). In contrast, SST^+ INs have slow kinetics of membrane property and target distal dendrites, which can summate and integrate excitatory inputs of postsynaptic cells over a long time scale (Kamigaki, 2019), and maybe suitable for controlling long-range synchrony between neocortex and the sub-cortical or cortical afferents (Abbas et al., 2018). Although synchronized oscillations, particularly in the gamma band, are thought to facilitate information transfer within and across brain areas, their underlying mechanisms, as well as exact roles, remain a matter of debate (Veit et al., 2017). For example, Chen et al. (2017) showed that suppression of SST^+ INs reduces both the spontaneous and visually induced enhancement of low-frequency band (beta) oscillation in the primary visual cortex (V1). In contrast, suppression of PV^+ INs reduces oscillations in a broad frequency range (beta and gamma), suggesting that although PV^+ INs are thought to generate cortical gamma oscillation (Cardin et al., 2009), they also strongly modulate low-frequency band activity. Consistently, another study conducted by Veit et al. (2017) also demonstrated that context-dependent visually induced low-gamma activity in the V1 also requires SST^+ INs.

OPTOGENETICS AND CHEMOGENETICS HIGHLIGHT CELL-TYPE SPECIFIC ROLE OF INs IN SOCIAL FEAR

Although subtypes of cortical INs based on the expression of a single molecular marker may oversimplify the diversity of neural network organization (Kamigaki, 2019), this classification provides important opportunities to dissect cell-type-specific functions by recent innovative genetic tools. Optogenetics and chemogenetics are two of the most frequently used genetic techniques to specifically manipulate neuronal activity (Biselli et al., 2019). Optogenetics uses light-sensitive ion channels expressed in targeted cells allowing for neuronal depolarization or hyperpolarization with light illumination (Boyden et al., 2005), while chemogenetics uses designer receptors exclusively activated by designer drugs (DREADDs) expressed in targeted cells (Armbruster et al., 2007). The stimulatory DREADD hM3Dq (a modified human M3 muscarinic receptor) and the Gi-coupled hM4Di DREADD (a modified human M4 muscarinic receptor) have low affinity for the native ligand acetylcholine, but a high affinity for the synthetic ligand clozapine-N-oxide (CNO). Intraperitoneally or intracranial CNO administration causes a downstream signaling cascade leading to either increased firing (for hM3Dq) or silencing (for hM4Di) of the targeted neurons, allowing for prolonged neuronal excitation or inhibition. Although CNO has been widely used as a ligand to activate muscarinic-based DREADDs, sluggish kinetics and metabolic liabilities have also existed. Notedly, a new high-affinity and selective agonist deschloroclozapine (DCZ) can also combine muscarinic-based DREADDs with utility in both mice and nonhuman primates for a variety of applications (Nagai et al., 2020). Except for muscarinic-based DREADD, other types of DREADDs were also developed for chemogenetic manipulations. For example, kappa opioid receptor (KOR)-based DREADD is activated by Salvinorin B (SalB) allowing for inhibition of neuronal activity. Thus, co-expression of KOR- and M3-DREADDs allows remotely bidirectional modulation of activities of the same set of neurons with different ligands (Vardy et al., 2015).

Advances in tools for modulating or monitoring neuronal activity with cell-type specificity have expanded our understanding of the role of prefrontal INs in regulating social behaviors and dysfunctions. The development of genetically encoded calcium indicators, such as GCaMP (Chen et al., 2013), allows researchers to detect calcium transient in an individual neuron or a population of neurons (Ferguson and Gao, 2018). For example, by using fiber photometry to detect the overall activity of a distinct neuronal population, Selimbeyoglu et al. (2017) revealed that the activity of mPFC PV^+ INs is increased in wild-type mice during social interactions with a conspecific compared to interactions with a novel object; however, in a genetic mouse model of autism, this difference was disappeared. Furthermore, either optogenetically increasing the activity of PV^+ INs or decreasing the activity of excitatory PNs in the mPFC rescues social impairment in this autism mouse model (Yizhar et al., 2011). Together, these findings suggest that elevated prefrontal cellular balance of excitation and inhibition (E/I balance) causes a profound impairment in social behaviors, and that compensation of mPFC inhibition can rescue social deficits. Similarly, Courtin et al. (2014) demonstrated that fear expression in conditioned auditory fear is causally linked to the phasic inhibition of mPFC PV^+ INs.

One extremely useful technique termed "optogenetic tagging," which combines optogenetics with electrophysiological recording has been developed for *in vivo* identification of different neuronal subtypes at a single unit level (Zhao et al., 2011). This method is especially powerful for recording genetically identified subtypes of cortical GABAergic INs (Roux et al., 2014). Using this approach, we found that a majority of mPFC PV^+ INs decrease their firing rate upon social confrontation in social fear-conditioned mice, whereas most PV^+ INs maintain their activity in unconditioned mice (Xu et al., 2019). The activity of another two types of mPFC INs, SST^+, and VIP^+ INs was also monitored by fiber photometry in freely moving mice. It was found that the activity of SST^+ INs is dramatically increased in social fear expression indicated by an increase in fluorescent signals when the mouse started each risk assessment behavior to approach a stimulus mouse. In contrast to SST^+ INs, the activity of VIP^+ INs is not altered during social fear expression (Xu et al., 2019). These observations clarified a significant association between the activities of distinct subtypes of mPFC INs with social fear expression. To further determine the causal relationship between mPFC INs activities and social fear expression, we employed a chemogenetic approach. After expression of hM3D on PV^+ INs in the mPFC of social fear-conditioned mice, the social fear behavior is reduced upon CNO administration to activate those PV^+ INs. Conversely, chemogenetic inactivation of mPFC SST^+ INs also reduced social fear expression (Xu et al., 2019). These findings demonstrate that neuronal activities of dmPFC INs were potently modified by aversive social experience and that the hyperactivity of mPFC SST^+ INs and hypoactivity of PV^+ INs are critical mechanisms of social fear.

SST^+ INs MEDIATED DISINHIBITION IN SOCIAL FEAR

Besides feedforward inhibition and feedback inhibition, there is the third main type of "archetype circuit motifs" in the neural network, namely disinhibition (Letzkus et al., 2015; Tremblay et al., 2016; Möhler and Rudolph, 2017). Disinhibition is the removal of inhibition produced by one type of INs as a result of inhibitory action by another type of INs, and consequently enhances the activity of excitatory output neurons. It was firstly found in the hippocampus that a subpopulation of INs selectively innervates other GABAergic neurons, and this subpopulation includes calretinin-positive (CR^+) INs (Gulyás et al., 1996) and VIP^+ INs (Hajos et al., 1996). Such findings were then extended to the neocortex, where CR^+ INs often preferentially target other CR^+ INs and CB^+ INs in L2/3 (Defelipe et al., 1999; Gonchar and Burkhalter, 1999; Caputi et al., 2009). Growing studies using slice recordings revealed that VIP^+ INs have preferential connections with SST^+ INs in diverse neocortices (Lee et al., 2013;

Pfeffer et al., 2013; Pi et al., 2013). The VIP to SST disinhibitory connection is likely a general principle in the superficial layers of the neocortex (Tremblay et al., 2016). Furthermore, in L4 of the primary somatosensory cortex SST^+ INs preferentially target PV^+ INs, although their connection probability and synaptic strength are larger for PNs in the superficial layers (Xu et al., 2013). It seems that neocortical disinhibition of excitatory cells could be as powerful as direct inhibition (Tremblay et al., 2016).

All of the above observations were demonstrated in brain slices, it is critical to uncover whether this disinhibitory circuit operates *in vivo*, in particular under behavioral conditions. Here, we summarized well-known disinhibitory circuits in the literature, in particular for those with determined behavioral outcomes (**Table 1**). Recently, a couple of studies demonstrated that prefrontal SST^+ INs mediated disinhibition also plays a critical role in the control of fear-related behaviors in rodents. In one of our recent studies, three lines of observations support that it is SST^+ INs that inhibited PV^+ INs during social fear expression (**Figure 2**; Xu et al., 2019). First, there was a robust enhancement of the neuronal activity of SST^+ INs when the conditioned mouse approached the stimulus mouse, meanwhile, the activity of PV^+ INs was largely suppressed. Second, after chemogenetical inactivation of SST^+ INs, the activity reduction of PV^+ INs was significantly suppressed during the social approach. Third, the inactivation of SST^+ INs also decreased social fear behaviors in conditioned mice.

Consistently, using the auditory fear conditioning paradigm, an elegant study conducted by Cummings and Clem (2020) revealed that synaptic transmission, as well as auditory cue-evoked activity of prefrontal SST+ INs, are potentiated following cued fear learning. Besides, adopting diverse transgenic mice to independently tag SST^+ INs and PV^+ INs, they also provide direct electrophysiological evidence to show SST^+ INs-evoked disinhibition in brain slices. The ratio of SST^+ INs elicited monosynaptic inhibition in PV^+ INs vs. surrounding PNs is strikingly increased in foot shock paired mice compared with that in the unpaired controls (Cummings and Clem, 2020), suggesting that fear conditioning shifts SST^+ INs to preferentially

TABLE 1 | Disinhibitory circuits and their physiological functions.

Disinhibitory circuit	Brain region	Physiological function	Reference
L1 INs-L2/3 VIP- PNs	V1	Sharpening orientation by sound	Ibrahim et al. (2016)
VIP-SST-PNs	V1	Enhancement of visual response by locomotion/top-down modulation	Fu et al. (2014) and Zhang et al. (2014)
CR-L2/3 CR/CB-PNs	V1/neocortex	NA	Defelipe et al. (1999), Gonchar and Burkhalter (1999) and Caputi et al. (2009)
VIP-SST-PNs; SST-PV-PNs; VIP-PV-PNs	Visual cortex	NA	Pfeffer et al. (2013) and Karnani et al. (2016)
VIP-SST-PNs	Auditory cortex	Auditory discrimination	Pi et al. (2013)
L1 INs-L2/3 PV-PNs	Auditory cortex	Auditory associative fear learning	Letzkus et al. (2011, 2015)
VIP-SST-PNs	S1	Enhancement of sensory processing by motor activity	Lee et al. (2013)
VIP-SST-PNs	S1	Intracortical LTP	Williams and Holtmaat (2019)
VIP-PV-PNs	S1	NA	Dávid et al. (2007)
L4 SST-PV- PNs	S1	NA	Xu et al. (2013)
L4 INs-L2/3 PV-L2/3 PNs	S1	NA	Gainey et al. (2018)
SST-PV- PNs	mPFC	Fear-related behaviors	Xu et al. (2019) and Cummings and Clem (2020)
SST-PV- PNs	mPFC	Spatial working memory	Kim et al. (2016)
SST-PV- PNs	Piriform cortex	NA	Sturgill and Isaacson (2015) and Large et al. (2016)
VIP/CR-unknown-PNs	Hippocampal CA1	Spatial Learning	Pardi et al. (2019) and Turi et al. (2019)
VIP/CR-O/A INs-PNs	Hippocampal CA1	NA	Gulyás et al. (1996), Hajos et al. (1996), Chamberland and Topolnik (2012), Tyan et al. (2014) and Pelkey et al. (2017)
VIP-PV-PNs	Hippocampal CA3	Spatial learning; novel object recognition	Donato et al. (2013)
PV-SST-PNs	BLA	Fear learning	Wolff et al. (2014) and Letzkus et al. (2015)
VIP-PV/SST-PNs	BLA	Auditory associative fear learning	Krabbe et al. (2019)
CeL SST-CeL PKC-δ-CeM output neurons	CeA	Fear responses	Ciocchi et al. (2010), Haubensak et al. (2010) and Li et al. (2013)
SST-CRF-output neurons; CRF-SST-output neurons	CeA	Selection of active and passive fear responses	Fadok et al. (2017)
Unknown INs-granule cells-mitral cells	Olfactory bulb	Odor discrimination	Nunes and Kuner (2015)
NAcLat D1 MSNs-VTA INs-DA	VTA	Reward-related behavior	Yang et al. (2018)
CEA INs-vlPAG INs-vlPAG glutamatergic neurons	PAG	Motor response of freezing	Tovote et al. (2016)

BLA, basolateral amygdala; CB, calcium-binding proteins calbindin; CeA, central amygdala; CeM, medial part of central amygdala; CeL, lateral part of central amygdala; CR, calretinin; CRF, corticotropin-releasing factor; D1, D1-type DA receptors; DA, dopamine; LTP, long term potentiation; MSNs, medium spiny neurons; NAcLat, nucleus accumbens lateral shell; O/A, hippocampal CA1 stratum oriens/alveus; PAG, periaqueductal gray region; PKC-δ, protein kinase C-δ; PNs, principle neurons; V1, primary visual cortex; S1, primary somatosensory barrel cortex; vlPAG, ventrolateral periaqueductal gray region; VTA, ventral tegmental area.

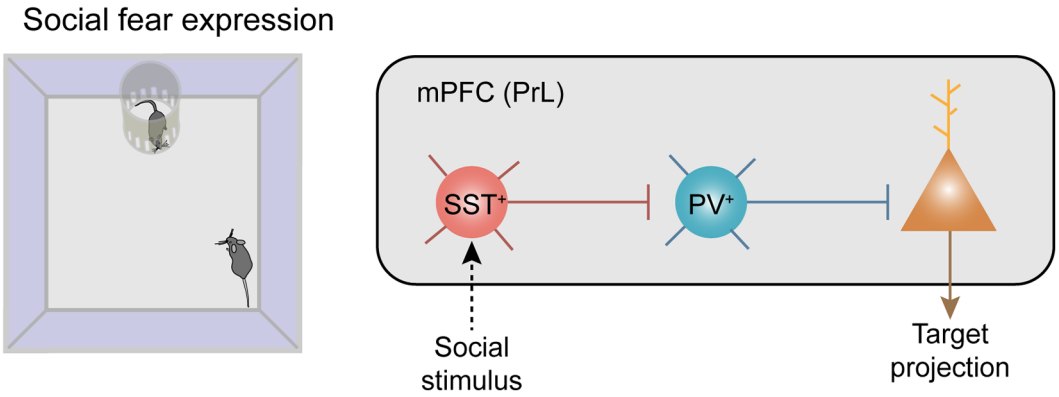

FIGURE 2 | Recruitment of neocortical disinhibitory microcircuits in fear-related behaviors. Disinhibitory connectivity in the medial prefrontal cortex (mPFC) during social fear expression. Left: the behavioral paradigm of the social fear expression. Right: social stimuli recruit SST$^+$ inhibitory interneurons (INs) which strongly inhibit PV$^+$ INs and trigger disinhibition of the projecting principal neurons (PNs) in the mPFC.

inhibit PV$^+$ INs and thereby produces disinhibition of PNs. This SST$^+$ INs-mediated disinhibition is also reflected in behavioral tests. For instance, concurrent optogenetic activation of SST$^+$ INs and PV$^+$ INs abolished the fear-promoting effect of SST$^+$ INs (Cummings and Clem, 2020), implying that this potent disinhibitory control is important for fear expression. Additionally, it was previously found that in the auditory cortex a disinhibitory microcircuit mediated by L1 INs, which robustly inhibit L2/3 PV$^+$ INs and produce disinhibition of projecting PNs, plays a critical role in auditory fear learning (Letzkus et al., 2015).

It is known that distinct GABAergic neuronal populations in the mPFC receive differential long-range inputs from subcortical regions (Sun et al., 2019). In particular, SST$^+$ INs in the mPFC receive more cholinergic inputs compared with PV$^+$ or VIP$^+$ INs, implying that acetylcholine release may preferentially drive SST$^+$ INs (Sun et al., 2019). Using channelrhodopsin-assisted patching in awake mice, Muñoz et al. (2017) revealed that cholinergic modulation of SST$^+$ INs in the somatosensory cortex provides a major excitatory drive to these neurons during whisking. Interestingly, Letzkus et al. (2011) found that in the auditory cortex an aversive stimulus (i.e., a foot shock) strongly recruits cholinergic afferents from the basal forebrain. Taken together, it is likely that acetylcholine release during fear expression could potentially recruit the SST$^+$ INs-mediated disinhibitory microcircuit to reinforce mPFC output to drive social fear expression (Xu et al., 2019).

It is also important to determine downstream targets of the disinhibitory circuit mediated by SST$^+$ INs for top-down behavioral controls in social fear. Anatomically, the PNs in the mPFC send their axons to multiple cortical and subcortical brain regions that are involved in the regulation of fear expression. Besides PAG that has been shown in the regulation of social fear (Franklin et al., 2017), other downstream brain regions such as the amygdala (Ciocchi et al., 2010; Wolff et al., 2014), paraventricular nucleus of the thalamus (PVT; Do-Monte et al., 2015; Penzo et al., 2015) are also possible targets since they are well known for various forms of fear regulation. Indeed, by c-fos staining, Cummings and Clem (2020) found that following optogenetic activation of prefrontal SST$^+$ INs at 24 h after fear conditioning, a couple of remote downstream targets are identified, including BLA, PVT, lateral habenula, ventrolateral PAG and dorsomedial hypothalamus, suggesting that these brain regions are probably involved in this fear recruitment of SST$^+$ INs-mediated disinhibition. Although PNs in the neocortex compose major output projections, GABAergic projections from the neocortex to subcortical regions have also been characterized recently (Lee et al., 2014). It was found that a subpopulation of PV$^+$ FS INs in the mPFC projects to the nucleus accumbens (NAc) which release GABA, and activation of this projection elicits avoidance behavior in a real-time place preference task, suggesting that this projection is involved in aversive signaling (Lee et al., 2014). However, this projection is not likely involved in the expression of conditioned social fear since the firing activities of PV$^+$ INs are indeed suppressed but not enhanced during social fear expression. Nevertheless, the exact brain networks downstream of mPFC outputs in control of social fear are to be dissected in future studies.

TARGETING SST$^+$ INs TO CURE SOCIAL FEAR

The aforementioned potent disinhibitory microcircuit in the mPFC opens a new possibility by targeting SST$^+$ INs to alleviate social fear behaviors. A couple of studies demonstrated that manipulation of prefrontal SST$^+$ INs can alter animals' defensive behaviors to fear response. For instance, we showed that chemogenetic inhibition of dmPFC SST$^+$ INs causes a direct reduction of social fear (Xu et al., 2019). Consistently, Cummings and Clem (2020) showed that optogenetic inhibition of SST$^+$ INs in the dmPFC markedly reduces freezing in mice 24 h after cue-foot shock pairing. On the other hand, optogenetic activation of SST$^+$ INs *de nova* increases freezing in the absence of auditory cues. These observations suggest that inactivation of SST$^+$ INs in the dmPFC could serve as an effective treatment option to mitigate fear responses.

The majority of antipsychotic drugs applied in the clinic to treat neuropsychiatric disorders have side effects due to their nonspecific actions outside the targeted brain regions. Besides, electric deep brain stimulation (DBS) or transcranial magnetic stimulation lacks cell-type specificity. A better understanding of brain node and network connectivity as well as advanced approaches like optogenetics and chemogenetics that can specifically manipulate targeted neuronal circuits could therefore be useful and of value to optimize therapeutic outcomes, although the invasiveness of these approaches limits their application in human beings (Jiang et al., 2017). Hopefully, progress in engineering will allow a new strategy of optogenetics-based DBS (Ramirez-Zamora et al., 2019) to selectively inhibit SST^+ INs in the dmPFC with a high spatiotemporal resolution for future therapeutic purposes to treat social fear. For instance, using a potent fast red-shifted opsin ChRmine neuronal activations could be achieved by direct photostimulation above the surface of the intact skull (Chen et al., 2020). To avoid cranial surgery for viral delivery, systemic viral delivery of ChRmine was achieved to target dorsal raphe serotonergic neurons using engineered AAV to cross the blood-brain barrier, and activation of these neurons by transcranial light can promote social preference in a three-chamber test (Chen et al., 2020). Hence, a surgery-free and temporally-precise control of specific neural populations in animals is already doable. Currently, non-invasive optogenetics for neural manipulation at a depth of centimeters is not available for stimulating deep brain regions in humans (Chen and McHugh, 2020). However, from a translational point of view, it is likely feasible to target prefrontal SST^+ INs given the fact that the cerebral cortex is the outmost structure of our brain.

CONCLUDING REMARKS AND PERSPECTIVE

Focused on mainly animal studies, we have reviewed recent research advances in social fear. We have presented evidence that both SFC and sub-chronic social defeat in mice can induce core behavioral symptoms of SAD without alterations in locomotion, general anxiety, and depressive-like behaviors. A cell-type-specific alteration in neuronal activities of mPFC neurons represents an important mechanism underlying social fear. Further, a potent disinhibitory control of surrounding PNs by prefrontal SST^+ INs plays a causal role in gating social fear behavior. In the future, identification of upstream inputs to the mPFC and also the exact downstream targets of the mPFC will help to draw a more complete picture regarding the circuit mechanism underlying social fear.

Generally, social-behavioral decisions depend on the dynamic integration of sensory information and the animal's internal states (for review, see Chen and Hong, 2018). Correspondingly, for social fear expression, animals need to constantly combine both spatial and temporal sensory information with high-order memory representations originally acquired during fear conditioning. Integrating all this information with constantly changing internal states, animals eventually make a final decision and display appropriate defensive behaviors. The exact contribution of SST^+ INs and the SST^+ INs-mediated disinhibitory circuitry in each of these processes is another important question to be addressed.

Current evidence suggests that prefrontal SST^+ INs exert a potent disinhibitory control over PNs during fear-related behaviors that are not necessarily specific in the social domain. Interestingly, it is recently reported that prefrontal SST^+ INs are involved in discriminating the affective states of conspecifics in mice (Scheggia et al., 2020). Therefore, it is still possible that there exists a subpopulation of SST^+ INs and their network are somehow wired specifically for processing social related information due to their distinct sensory inputs. Future studies using *in vivo* two-photo calcium imaging or microendoscope will be helpful to address this issue.

AUTHOR CONTRIBUTIONS

JW, YT, L-HZ and HX made a direct contribution to the work and approved it for publication. All authors contributed to the article and approved the submitted version.

FUNDING

This study was supported by grants from the National Natural Science Foundation of China (32071005, 31471025, and 91432110) to HX and JW (31900729); the National Key R&D Program of China (2016YFA0501000); the Zhejiang Provincial Natural Science Foundation of China (LR17H090002); the Chinese Ministry of Education Project 111 Program (B13026); and the Non-profit Central Research Institute Fund of Chinese Academy of Medical Sciences (2017PT31038 and 2018PT31041) to HX. This study was also supported by the Fundamental Research Funds for the Central Universities.

REFERENCES

Abbas, A. I., Sundiang, M. J. M., Henoch, B., Morton, M. P., Bolkan, S. S., Park, A. J., et al. (2018). Somatostatin interneurons facilitate hippocampal-prefrontal synchrony and prefrontal spatial encoding. *Neuron* 100, 926.e3–939.e3. doi: 10.1016/j.neuron.2018.09.029

Amodio, D. M., and Frith, C. D. (2006). Meeting of minds: the medial frontal cortex and social cognition. *Nat. Rev. Neurosci.* 7, 268–277. doi: 10.1038/nrn1884

Armbruster, B. N., Li, X., Pausch, M. H., Herlitze, S., and Roth, B. L. (2007). Evolving the lock to fit the key to create a family of G protein-coupled receptors potently activated by an inert ligand. *Proc. Natl. Acad. Sci. U S A* 104, 5163–5168. doi: 10.1073/pnas.0700293104

American Psychiatric Publishing. (2013). *Diagnostic and Statistical Manual of Mental Disorders (DSM-5)*. Arlington: American Psychiatric Publishing .

Biselli, T., Lange, S. S., Sablottny, L., Steffen, J., and Walther, A. (2019). Optogenetic and chemogenetic insights into the neurocircuitry of depression-like behaviour: a systematic review. *Eur. J. Neurosci.* doi: 10.1111/ejn.14603. [Epub ahead of print].

Blanco, C., Antia, S. X., and Liebowitz, M. R. (2002). Pharmacotherapy of social anxiety disorder. *Biol. Psychiatry* 51, 109–120. doi: 10.1016/s0006-3223(01)01294-x

Boyden, E. S., Zhang, F., Bamberg, E., Nagel, G., and Deisseroth, K. (2005). Millisecond-timescale, genetically targeted optical control of neural activity. *Nat. Neurosci.* 8, 1263–1268. doi: 10.1038/nn1525

Buff, C., Brinkmann, L., Neumeister, P., Feldker, K., Heitmann, C., Gathmann, B., et al. (2016). Specifically altered brain responses to threat in generalized anxiety disorder relative to social anxiety disorder and panic disorder. *Neuroimage Clin.* 12, 698–706. doi: 10.1016/j.nicl.2016.09.023

Burgos-Robles, A., Vidal-Gonzalez, I., and Quirk, G. J. (2009). Sustained conditioned responses in prelimbic prefrontal neurons are correlated with fear expression and extinction failure. *J. Neurosci.* 29, 8474–8482. doi: 10.1523/JNEUROSCI.0378-09.2009

Caputi, A., Rozov, A., Blatow, M., and Monyer, H. (2009). Two calretinin-positive GABAergic cell types in layer 2/3 of the mouse neocortex provide different forms of inhibition. *Cereb. Cortex* 19, 1345–1359. doi: 10.1093/cercor/bhn175

Cardin, J. A., Carlén, M., Meletis, K., Knoblich, U., Zhang, F., Deisseroth, K., et al. (2009). Driving fast-spiking cells induces gamma rhythm and controls sensory responses. *Nature* 459, 663–667. doi: 10.1038/nature08002

Chang, Y.-H., Liu, S.-W., and Chang, C.-H. (2018). Pharmacological activation of the lateral orbitofrontal cortex on regulation of learned fear and extinction. *Neurobiol. Learn. Mem.* 148, 30–37. doi: 10.1016/j.nlm.2017.12.011

Chamberland, S., and Topolnik, L. (2012). Inhibitory control of hippocampal inhibitory neurons. *Front. Neurosci.* 6:165. doi: 10.3389/fnins.2012.00165

Chen, R., Gore, F., Nguyen, Q. A., Ramakrishnan, C., Patel, S., Kim, S. H., et al. (2020). Deep brain optogenetics without intracranial surgery. *Nat. Biotechnol.* doi: 10.1038/s41587-020-0679-9 [Epub ahead of print].

Chen, P., and Hong, W. (2018). Neural circuit mechanisms of social behavior. *Neuron* 98, 16–30. doi: 10.1016/j.neuron.2018.02.026

Chen, S., and McHugh, T. J. (2020). Further-reaching optogenetics. *Nat. Biomed. Eng.* 4, 1028–1029. doi: 10.1038/s41551-020-00648-y

Chen, T.-W., Wardill, T.-J., Sun, Y., Pulver, S. R., Renninger, S. L., Baohan, A., et al. (2013). Ultrasensitive fluorescent proteins for imaging neuronal activity. *Nature* 499, 295–300. doi: 10.1038/nature12354

Chen, G., Zhang, Y., Li, X., Zhao, X., Ye, Q., Lin, Y., et al. (2017). Distinct inhibitory circuits orchestrate cortical beta and gamma band oscillations. *Neuron* 96, 1403.e6–1418.e6. doi: 10.1016/j.neuron.2017.11.033

Ciocchi, S., Herry, C., Grenier, F., Wolff, S. B., Letzkus, J. J., Vlachos, I., et al. (2010). Encoding of conditioned fear in central amygdala inhibitory circuits. *Nature* 468, 277–282. doi: 10.1038/nature09559

Courtin, J., Chaudun, F., Rozeske, R. R., Karalis, N., Gonzalez-Campo, C., Wurtz, H., et al. (2014). Prefrontal parvalbumin interneurons shape neuronal activity to drive fear expression. *Nature* 505, 92–96. doi: 10.1038/nature12755

Cummings, K. A., and Clem, R. L. (2020). Prefrontal somatostatin interneurons encode fear memory. *Nat. Neurosci.* 23, 61–74. doi: 10.1038/s41593-019-0552-7

Dalley, J. W., Cardinal, R. N., and Robbins, T. W. (2004). Prefrontal executive and cognitive functions in rodents: neural and neurochemical substrates. *Neurosci. Biobehav. Rev.* 28, 771–784. doi: 10.1016/j.neubiorev.2004.09.006

Dávid, C., Schleicher, A., Zuschratter, W., and Staiger, J. F. (2007). The innervation of parvalbumin-containing interneurons by VIP-immunopositive interneurons in the primary somatosensory cortex of the adult rat. *Eur. J. Neurosci.* 25, 2329–2340. doi: 10.1111/j.1460-9568.2007.05496.x

Defelipe, J., González-Albo, M. C., Del Río, M. R., and Elston, G. N. (1999). Distribution and patterns of connectivity of interneurons containing calbindin, calretinin, and parvalbumin in visual areas of the occipital and temporal lobes of the macaque monkey. *J. Comp. Neurol.* 412, 515–526. doi: 10.1002/(sici)1096-9861(19990927)412:3<515::aid-cne10>3.0.co;2-1

Do-Monte, F. H., Quinones-Laracuente, K., and Quirk, G. J. (2015). A temporal shift in the circuits mediating retrieval of fear memory. *Nature* 519, 460–463. doi: 10.1038/nature14030

Donato, F., Rompani, S. B., and Caroni, P. (2013). Parvalbumin-expressing basket-cell network plasticity induced by experience regulates adult learning. *Nature* 504, 272–276. doi: 10.1038/nature12866

Doruyter, A. G., Dupont, P., Stein, D. J., Lochner, C., and Warwick, J. M. (2018). Nuclear neuroimaging in social anxiety disorder: a review. *J. Nucl. Med.* 59, 1794–1800. doi: 10.2967/jnumed.118.212795

Dos Santos, R. G., de Lima Osório, F., Martin-Santos, R., Zuardi, A. W., Hallak, J. E. C., and Crippa, J. A. S. (2019). Modulation of the endocannabinoid and oxytocinergic systems as a potential treatment approach for social anxiety disorder. *CNS Drugs* 33, 1031–1038. doi: 10.1007/s40263-019-00669-5

Etkin, A., Egner, T., and Kalisch, R. (2011). Emotional processing in anterior cingulate and medial prefrontal cortex. *Trends Cogn. Sci.* 15, 85–93. doi: 10.1016/j.tics.2010.11.004

Fadok, J. P., Krabbe, S., Markovic, M., Courtin, J., Xu, C., Massi, L., et al. (2017). A competitive inhibitory circuit for selection of active and passive fear responses. *Nature* 542, 96–100. doi: 10.1038/nature21047

Ferguson, B. R., and Gao, W.-J. (2018). PV interneurons: critical regulators of E/I balance for prefrontal cortex-dependent behavior and psychiatric disorders. *Front. Neural Circuits* 12:37. doi: 10.3389/fncir.2018.00037

Figel, B., Brinkmann, L., Buff, C., Heitmann, C. Y., Hofmann, D., Bruchmann, M., et al. (2019). Phasic amygdala and BNST activation during the anticipation of temporally unpredictable social observation in social anxiety disorder patients. *Neuroimage Clin.* 22:101735. doi: 10.1016/j.nicl.2019.101735

Franklin, T. B., Silva, B. A., Perova, Z., Marrone, L., Masferrer, M. E., Zhan, Y., et al. (2017). Prefrontal cortical control of a brainstem social behavior circuit. *Nat. Neurosci.* 20, 260–270. doi: 10.1038/nn.4470

Frick, A., Engman, J., Alaie, I., Bjorkstrand, J., Gingnell, M., Larsson, E. M., et al. (2020). Neuroimaging, genetic, clinical, and demographic predictors of treatment response in patients with social anxiety disorder. *J. Affect. Disord.* 261, 230–237. doi: 10.1016/j.jad.2019.10.027

Fu, Y., Tucciarone, J. M., Espinosa, J. S., Sheng, N., Darcy, D. P., Nicoll, R. A., et al. (2014). A cortical circuit for gain control by behavioral state. *Cell* 156, 1139–1152. doi: 10.1016/j.cell.2014.01.050

Gainey, M. A., Aman, J. W., and Feldman, D. E. (2018). Rapid disinhibition by adjustment of PV intrinsic excitability during whisker map plasticity in mouse S1. *J. Neurosci.* 38, 4749–4761. doi: 10.1523/JNEUROSCI.3628-17.2018

Golden, S. A., Covington, H. E. III., Berton, O., and Russo, S. J. (2011). A standardized protocol for repeated social defeat stress in mice. *Nat. Protoc.* 6, 1183–1191. doi: 10.1038/nprot.2011.361

Gonchar, Y., and Burkhalter, A. (1999). Connectivity of GABAergic calretinin-immunoreactive neurons in rat primary visual cortex. *Cereb. Cortex* 9, 683–696. doi: 10.1093/cercor/9.7.683

Goodson, J. L. (2005). The vertebrate social behavior network: evolutionary themes and variations. *Horm. Behav.* 48, 11–22. doi: 10.1016/j.yhbeh.2005.02.003

Gulyás, A. I., Hájos, N., and Freund, T. F. (1996). Interneurons containing calretinin are specialized to control other interneurons in the rat hippocampus. *J. Neurosci.* 16, 3397–3411. doi: 10.1523/JNEUROSCI.16-10-03397.1996

Hajos, N., Acsady, L., and Freund, T. F. (1996). Target selectivity and neurochemical characteristics of VIP-immunoreactive interneurons in the rat dentate gyrus. *Eur. J. Neurosci.* 8, 1415–1431. doi: 10.1111/j.1460-9568.1996.tb01604.x

Haller, J., and Bakos, N. (2002). Stress-induced social avoidance: a new model of stress-induced anxiety? *Physiol. Behav.* 77, 327–332. doi: 10.1016/s0031-9384(02)00860-0

Hattori, R., Kuchibhotla, K. V., Froemke, R. C., and Komiyama, T. (2017). Functions and dysfunctions of neocortical inhibitory neuron subtypes. *Nat. Neurosci.* 20, 1199–1208. doi: 10.1038/nn.4619

Haubensak, W., Kunwar, P. S., Cai, H., Ciocchi, S., Wall, N. R., Ponnusamy, R., et al. (2010). Genetic dissection of an amygdala microcircuit that gates conditioned fear. *Nature* 468, 270–276. doi: 10.1038/nature09553

Hermes, G., Li, N., Duman, C., and Duman, R. (2011). Post-weaning chronic social isolation produces profound behavioral dysregulation with decreases in prefrontal cortex synaptic-associated protein expression in female rats. *Physiol. Behav.* 104, 354–359. doi: 10.1016/j.physbeh.2010.12.019

Hsieh, H.-T., and Chang, C.-H. (2020). Activation of medial orbitofrontal cortex abolishes fear extinction and interferes with fear expression in rats. *Neurobiol. Learn. Mem.* 169:107170. doi: 10.1016/j.nlm.2020.107170

Huhman, K. L. (2006). Social conflict models: can they inform us about human psychopathology? *Horm. Behav.* 50, 640–646. doi: 10.1016/j.yhbeh.2006.06.022

Ibrahim, L. A., Mesik, L., Ji, X. Y., Fang, Q., Li, H. F., Li, Y. T., et al. (2016). Cross-modality sharpening of visual cortical processing through layer-1-mediated inhibition and disinhibition. *Neuron* 89, 1031–1045. doi: 10.1016/j.neuron.2016.01.027

Jiang, J., Cui, H., and Rahmouni, K. (2017). Optogenetics and pharmacogenetics: principles and applications. *Am. J. Physiol. Regul. Integr. Comp. Physiol.* 313, R633–R645. doi: 10.1152/ajpregu.00091.2017

Jones, C., Barrera, I., Brothers, S., Ring, R., and Wahlestedt, C. (2017). Oxytocin and social functioning. *Dialogues Clin. Neurosci.* 19, 193–201. doi: 10.31887/DCNS.2017.19.2/cjones

Kamigaki, T. (2019). Prefrontal circuit organization for executive control. *Neurosci. Res.* 140, 23–36. doi: 10.1016/j.neures.2018.08.017

Karalis, N., Dejean, C., Chaudun, F., Khoder, S., Rozeske, R. R., Wurtz, H., et al. (2016). 4-Hz oscillations synchronize prefrontal-amygdala circuits during fear behavior. *Nat. Neurosci.* 19, 605–612. doi: 10.1038/nn.4251

Karnani, M. M., Jackson, J., Ayzenshtat, I., Hamzehei Sichani, A., Manoocheri, K., Kim, S., et al. (2016). Opening holes in the blanket of inhibition: localized lateral disinhibition by VIP interneurons. *J. Neurosci.* 36, 3471–3480. doi: 10.1523/JNEUROSCI.3646-15.2016

Kawaguchi, Y., and Kubota, Y. (1997). GABAergic cell subtypes and their synaptic connections in rat frontal cortex. *Cereb. Cortex* 7, 476–486. doi: 10.1093/cercor/7.6.476

Kawashima, C., Tanaka, Y., Inoue, A., Nakanishi, M., Okamoto, K., Maruyama, Y., et al. (2016). Hyperfunction of left lateral prefrontal cortex and automatic thoughts in social anxiety disorder: a near-infrared spectroscopy study. *J. Affect. Disord.* 206, 256–260. doi: 10.1016/j.jad.2016.07.028

Kessler, R. C., Berglund, P., Demler, O., Jin, R., Merikangas, K. R., and Walters, E. E. (2005a). Lifetime prevalence and age-of-onset distributions of DSM-IV disorders in the National Comorbidity Survey Replication. *Arch. Gen. Psychiatry* 62, 593–602. doi: 10.1001/archpsyc.62.6.593

Kessler, R. C., Chiu, W. T., Demler, O., Merikangas, K. R., and Walters, E. E. (2005b). Prevalence, severity, and comorbidity of 12-month DSM-IV disorders in the National Comorbidity Survey Replication. *Arch. Gen. Psychiatry* 62, 617–627. doi: 10.1001/archpsyc.62.6.617

Kim, D., Jeong, H., Lee, J., Ghim, J. W., Her, E. S., Lee, S. H., et al. (2016). Distinct roles of parvalbumin- and somatostatin-expressing interneurons in working memory. *Neuron* 92, 902–915. doi: 10.1016/j.neuron.2016.09.023

Ko, J. (2017). Neuroanatomical substrates of rodent social behavior: the medial prefrontal cortex and its projection patterns. *Front. Neural Circuits* 11:41. doi: 10.3389/fncir.2017.00041

Krabbe, S., Paradiso, E., d'Aquin, S., Bitterman, Y., Courtin, J., Xu, C., et al. (2019). Adaptive disinhibitory gating by VIP interneurons permits associative learning. *Nat. Neurosci.* 22, 1834–1843. doi: 10.1038/s41593-019-0508-y

Kraus, J., Frick, A., Fischer, H., Howner, K., Fredrikson, M., and Furmark, T. (2018). Amygdala reactivity and connectivity during social and non-social aversive stimulation in social anxiety disorder. *Psychiatry Res. Neuroimaging* 280, 56–61. doi: 10.1016/j.pscychresns.2018.08.012

Large, A. M., Kunz, N. A., Mielo, S. L., and Oswald, A. M. (2016). Inhibition by somatostatin interneurons in olfactory cortex. *Front. Neural Circuits* 10:62. doi: 10.3389/fncir.2016.00062

Lee, S., Kruglikov, I., Huang, Z. J., Fishell, G., and Rudy, B. (2013). A disinhibitory circuit mediates motor integration in the somatosensory cortex. *Nat. Neurosci.* 16, 1662–1670. doi: 10.1038/nn.3544

Lee, A. T., Vogt, D., Rubenstein, J. L., and Sohal, V. S. (2014). A class of GABAergic neurons in the prefrontal cortex sends long-range projections to the nucleus accumbens and elicits acute avoidance behavior. *J. Neurosci.* 34, 11519–11525. doi: 10.1523/JNEUROSCI.1157-14.2014

Leichsenring, F., and Leweke, F. (2017). Social anxiety disorder. *N. Engl. J. Med.* 376, 2255–2264. doi: 10.1056/NEJMcp1614701

Letzkus, J. J., Wolff, S. B., and Lüthi, A. (2015). Disinhibition, a circuit mechanism for associative learning and memory. *Neuron* 88, 264–276. doi: 10.1016/j.neuron.2015.09.024

Letzkus, J. J., Wolff, S. B., Meyer, E. M., Tovote, P., Courtin, J., Herry, C., et al. (2011). A disinhibitory microcircuit for associative fear learning in the auditory cortex. *Nature* 480, 331–335. doi: 10.1038/nature10674

Li, H., Penzo, M. A., Taniguchi, H., Kopec, C. D., Huang, Z. J., and Li, B. (2013). Experience-dependent modification of a central amygdala fear circuit. *Nat Neurosci* 16, 332–339. doi: 10.1038/nn.3322

Möhler, H., and Rudolph, U. (2017). Disinhibition, an emerging pharmacology of learning and memory. *F1000Res.* 6:F1000. doi: 10.12688/f1000research.9947.1

Muñoz, W., Tremblay, R., Levenstein, D., and Rudy, B. (2017). Layer-specific modulation of neocortical dendritic inhibition during active wakefulness. *Science* 355, 954–959. doi: 10.1126/science.aag2599

Nagai, Y., Miyakawa, N., Takuwa, H., Hori, Y., Oyama, K., Ji, B., et al. (2020). Deschloroclozapine, a potent and selective chemogenetic actuator enables rapid neuronal and behavioral modulations in mice and monkeys. *Nat. Neurosci.* 23, 1157–1167. doi: 10.1038/s41593-020-0661-3

Nees, F., Witt, S. H., and Flor, H. (2018). Neurogenetic approaches to stress and fear in humans as pathophysiological mechanisms for posttraumatic stress disorder. *Biol. Psychiatry* 83, 810–820. doi: 10.1016/j.biopsych.2017.12.015

Niwa, M., Matsumoto, Y., Mouri, A., Ozaki, N., and Nabeshima, T. (2011). Vulnerability in early life to changes in the rearing environment plays a crucial role in the aetiopathology of psychiatric disorders. *Int. J. Neuropsychopharmacol.* 14, 459–477. doi: 10.1017/S1461145710001239

Nunes, D., and Kuner, T. (2015). Disinhibition of olfactory bulb granule cells accelerates odour discrimination in mice. *Nat. Commun.* 6:8950. doi: 10.1038/ncomms9950

Pardi, M. B., Abs, E., and Letzkus, J. J. (2019). Disinhibition goes spatial. *Neuron* 101, 994–996. doi: 10.1016/j.neuron.2019.03.006

Paré, D., and Collins, D. R. (2000). Neuronal correlates of fear in the lateral amygdala: multiple extracellular recordings in conscious cats. *J. Neurosci.* 20, 2701–2710. doi: 10.1523/JNEUROSCI.20-07-02701.2000

Pelkey, K. A., Chittajallu, R., Craig, M. T., Tricoire, L., Wester, J. C., and McBain, C. J. (2017). Hippocampal GABAergic inhibitory interneurons. *Physiol. Rev.* 97, 1619–1747. doi: 10.1152/physrev.00007.2017

Penzo, M. A., Robert, V., Tucciarone, J., De Bundel, D., Wang, M., Van Aelst, L., et al. (2015). The paraventricular thalamus controls a central amygdala fear circuit. *Nature* 519, 455–459. doi: 10.1038/nature13978

Pfeffer, C. K., Xue, M., He, M., Huang, Z. J., and Scanziani, M. (2013). Inhibition of inhibition in visual cortex: the logic of connections between molecularly distinct interneurons. *Nat. Neurosci.* 16, 1068–1076. doi: 10.1038/nn.3446

Pi, H.-J., Hangya, B., Kvitsiani, D., Sanders, J. I., Huang, Z. J., and Kepecs, A. (2013). Cortical interneurons that specialize in disinhibitory control. *Nature* 503, 521–524. doi: 10.1038/nature12676

Quirk, G. J., Garcia, R., and González-Lima, F. (2006). Prefrontal mechanisms in extinction of conditioned fear. *Biol. Psychiatry* 60, 337–343. doi: 10.1016/j.biopsych.2006.03.010

Quirk, G. J., Repa, C., and LeDoux, J. E. (1995). Fear conditioning enhances short-latency auditory responses of lateral amygdala neurons: parallel recordings in the freely behaving rat. *Neuron* 15, 1029–1039. doi: 10.1016/0896-6273(95)90092-6

Ramirez-Zamora, A., Giordano, J., Boyden, E. S., Gradinaru, V., Gunduz, A., Starr, P. A., et al. (2019). Proceedings of the sixth deep brain stimulation think tank modulation of brain networks and application of advanced neuroimaging, neurophysiology, and optogenetics. *Front. Neurosci.* 13:936. doi: 10.3389/fnins.2019.00936

Rodriguez-Romaguera, J., Do-Monte, F. H., Tanimura, Y., Quirk, G. J., and Haber, S. N. (2015). Enhancement of fear extinction with deep brain stimulation: evidence for medial orbitofrontal involvement. *Neuropsychopharmacology* 40, 1726–1733. doi: 10.1038/npp.2015.20

Roux, L., Stark, E., Sjulson, L., and Buzsaki, G. (2014). *in vivo* optogenetic identification and manipulation of GABAergic interneuron subtypes. *Curr. Opin. Neurobiol.* 26, 88–95. doi: 10.1016/j.conb.2013.12.013

Rubenstein, J. L., and Merzenich, M. M. (2003). Model of autism: increased ratio of excitation/inhibition in key neural systems. *Genes Brain Behav.* 2, 255–267. doi: 10.1034/j.1601-183x.2003.00037.x

Rudy, B., Fishell, G., Lee, S., and Hjerling-Leffler, J. (2011). Three groups of interneurons account for nearly 100% of neocortical GABAergic neurons. *Dev. Neurobiol.* 71, 45–61. doi: 10.1002/dneu.20853

Sarlitto, M. C., Foilb, A. R., and Christianson, J. P. (2018). Inactivation of the ventrolateral orbitofrontal cortex impairs flexible use of safety signals. *Neuroscience* 379, 350–358. doi: 10.1016/j.neuroscience.2018.03.037

Scheggia, D., Managò, F., Maltese, F., Bruni, S., Nigro, M., Dautan, D., et al. (2020). Somatostatin interneurons in the prefrontal cortex control affective state discrimination in mice. *Nat. Neurosci.* 23, 47–60. doi: 10.1038/s41593-019-0551-8

Selimbeyoglu, A., Kim, C. K., Inoue, M., Lee, S. Y., Hong, A. S. O., Kauvar, I., et al. (2017). Modulation of prefrontal cortex excitation/inhibition balance rescues social behavior in CNTNAP2-deficient mice. *Sci. Transl. Med.* 9:eaah6733. doi: 10.1126/scitranslmed.aah6733

Sohal, V. S., and Rubenstein, J. L. R. (2019). Excitation-inhibition balance as a framework for investigating mechanisms in neuropsychiatric disorders. *Mol. Psychiatry* 24, 1248–1257. doi: 10.1038/s41380-019-0426-0

Stein, M. B., and Stein, D. J. (2008). Social anxiety disorder. *Lancet* 371, 1115–1125. doi: 10.1016/S0140-6736(08)60488-2

Sturgill, J. F., and Isaacson, J. S. (2015). Somatostatin cells regulate sensory response fidelity *via* subtractive inhibition in olfactory cortex. *Nat. Neurosci.* 18, 531–535. doi: 10.1038/nn.3971

Sun, Q., Li, X., Ren, M., Zhao, M., Zhong, Q., Ren, Y., et al. (2019). A whole-brain map of long-range inputs to GABAergic interneurons in the mouse medial prefrontal cortex. *Nat. Neurosci.* 22, 1357–1370. doi: 10.1038/s41593-019-0429-9

Toth, I., and Neumann, I. D. (2013). Animal models of social avoidance and social fear. *Cell Tissue Res.* 354, 107–118. doi: 10.1007/s00441-013-1636-4

Toth, I., Neumann, I. D., and Slattery, D. A. (2012). Social fear conditioning: a novel and specific animal model to study social anxiety disorder. *Neuropsychopharmacology* 37, 1433–1443. doi: 10.1038/npp.2011.329

Toth, I., Neumann, I. D., and Slattery, D. A. (2013). Social fear conditioning as an animal model of social anxiety disorder. *Curr. Protoc. Neurosci.* Chapter 9:Unit 9.42. doi: 10.1002/0471142301.ns0942s63

Tovote, P., Esposito, M. S., Botta, P., Chaudun, F., Fadok, J. P., Markovic, M., et al. (2016). Midbrain circuits for defensive behaviour. *Nature* 534, 206–212. doi: 10.1038/nature17996

Tremblay, R., Lee, S., and Rudy, B. (2016). GABAergic interneurons in the neocortex: from cellular properties to circuits. *Neuron* 91, 260–292. doi: 10.1016/j.neuron.2016.06.033

Turi, G. F., Li, W. K., Chavlis, S., Pandi, I., O'Hare, J., Priestley, J. B., et al. (2019). Vasoactive intestinal polypeptide-expressing interneurons in the hippocampus support goal-oriented spatial learning. *Neuron* 101, 1150.e8–1165.e8. doi: 10.1016/j.neuron.2019.01.009

Tyan, L., Chamberland, S., Magnin, E., Camire, O., Francavilla, R., David, L. S., et al. (2014). Dendritic inhibition provided by interneuron-specific cells controls the firing rate and timing of the hippocampal feedback inhibitory circuitry. *J. Neurosci.* 34, 4534–4547. doi: 10.1523/JNEUROSCI.3813-13.2014

Vardy, E., Robinson, J. E., Li, C., Olsen, R. H. J., DiBerto, J. F., Giguere, P. M., et al. (2015). A new DREADD facilitates the multiplexed chemogenetic interrogation of behavior. *Neuron* 86, 936–946. doi: 10.1016/j.neuron.2015.03.065

Veit, J., Hakim, R., Jadi, M. P., Sejnowski, T. J., and Adesnik, H. (2017). Cortical gamma band synchronization through somatostatin interneurons. *Nat. Neurosci.* 20, 951–959. doi: 10.1038/nn.4562

Wang, Q., Wang, Q., Song, X.-L., Jiang, Q., Wu, Y.-J., Li, Y., et al. (2018). Fear extinction requires ASIC1a-dependent regulation of hippocampal-prefrontal correlates. *Sci. Adv.* 4:eaau3075. doi: 10.1126/sciadv.aau3075

Williams, L. E., and Holtmaat, A. (2019). Higher-order thalamocortical inputs gate synaptic long-term potentiation *via* disinhibition. *Neuron* 101, 91.e4–102.e4. doi: 10.1016/j.neuron.2018.10.049

Wolff, S. B., Gründemann, J., Tovote, P., Krabbe, S., Jacobson, G. A., Muller, C., et al. (2014). Amygdala interneuron subtypes control fear learning through disinhibition. *Nature* 509, 453–458. doi: 10.1038/nature13258

Xu, H., Jeong, H.-Y., Tremblay, R., and Rudy, B. (2013). Neocortical somatostatin-expressing GABAergic interneurons disinhibit the thalamorecipient layer 4. *Neuron* 77, 155–167. doi: 10.1016/j.neuron.2012.11.004

Xu, H., Liu, L., Tian, Y., Wang, J., Li, J., Zheng, J., et al. (2019). A disinhibitory microcircuit mediates conditioned social fear in the prefrontal cortex. *Neuron* 102, 668.e5–682.e5. doi: 10.1016/j.neuron.2019.02.026

Yang, H., de Jong, J. W., Tak, Y., Peck, J., Bateup, H. S., and Lammel, S. (2018). Nucleus accumbens subnuclei regulate motivated behavior *via* direct inhibition and disinhibition of VTA dopamine subpopulations. *Neuron* 97, 434.e4–449.e4. doi: 10.1016/j.neuron.2017.12.022

Yizhar, O., Fenno, L. E., Prigge, M., Schneider, F., Davidson, T. J., O'Shea, D. J., et al. (2011). Neocortical excitation/inhibition balance in information processing and social dysfunction. *Nature* 477, 171–178. doi: 10.1038/nature10360

Zhang, S., Xu, M., Kamigaki, T., Hoang Do, J. P., Chang, W. C., Jenvay, S., et al. (2014). Selective attention. Long-range and local circuits for top-down modulation of visual cortex processing. *Science* 345, 660–665. doi: 10.1126/science.1254126

Zhao, S., Ting, J. T., Atallah, H. E., Qiu, L., Tan, J., Gloss, B., et al. (2011). Cell type-specific channelrhodopsin-2 transgenic mice for optogenetic dissection of neural circuitry function. *Nat. Methods* 8, 745–752. doi: 10.1038/nmeth.1668

Zhu, H., Qiu, C., Meng, Y., Yuan, M., Zhang, Y., Ren, Z., et al. (2017). Altered topological properties of brain networks in social anxiety disorder: a resting-state functional MRI study. *Sci. Rep.* 7:43089. doi: 10.1038/srep43089

Conflict of Interest: The authors declare that the research was conducted in the absence of any commercial or financial relationships that could be construed as a potential conflict of interest.

frontiers in Genetics

ORIGINAL RESEARCH
published: 17 December 2020
doi: 10.3389/fgene.2020.551065

Integration of Transcriptome Resequencing and Quantitative Proteomics Analyses of Collagenase VII-Induced Intracerebral Hemorrhage in Mice

Fang Cao[1†], Yu Guo[2†], Qiang Zhang[1], Yinchun Fan[1], Qian Liu[1], Jiancheng Song[1], Hua Zhong[3] and Shengtao Yao[1]**

[1] Department of Cerebrovascular Disease, Affiliated Hospital of Zunyi Medical University, Zunyi, China, [2] Department of Radiology, Daping Hospital, Army Medical University, Chongqing, China, [3] College of Life Sciences, Wuhan University, Wuhan, China

OPEN ACCESS

Edited by:
Giordano Lippi,
The Scripps Research Institute,
United States

Reviewed by:
Bradley Pearce Ander,
UC Davis Medical Center,
United States
Miao He,
Fudan University, China

***Correspondence:**
Hua Zhong
zhonghua0103@whu.edu.cn
Shengtao Yao
YST@zmu.edu.cn

[†] These authors have contributed equally to this work

Specialty section:
This article was submitted to Neurogenomics, a section of the journal Frontiers in Genetics

Received: 11 April 2020
Accepted: 20 November 2020
Published: 17 December 2020

Citation:
Cao F, Guo Y, Zhang Q, Fan Y, Liu Q, Song J, Zhong H and Yao S (2020) Integration of Transcriptome Resequencing and Quantitative Proteomics Analyses of Collagenase VII-Induced Intracerebral Hemorrhage in Mice. Front. Genet. 11:551065. doi: 10.3389/fgene.2020.551065

Objective: Intracerebral hemorrhage (ICH) is a subtype of stroke with high mortality and morbidity rates. Our aim was to comprehensively analyze transcriptome and proteome in an experimental ICH model.

Methods: All mice were divided into ICH model (n = 3) and sham groups (n = 3). ICH was induced by collagenase VII. The ipsilateral hemisphere was used for whole transcriptome and proteomics resequencing. After preprocessing, differentially expressed lncRNAs (DElncRNAs), mRNAs (DEmRNAs), miRNAs (DEmiRNAs), and DEproteins between ICH and sham groups were identified. Functional enrichment analysis was performed using the clusterProfiler package, followed by protein–protein interaction (PPI) analysis. After that, the Pearson correlation coefficient between DEmRNAs and DElncRNAs or between DEmRNAs and DEproteins was calculated. DElncRNAs with similar functions were analyzed by the GOSemSim package. After prediction of DEmiRNA–DEmRNA and DElncRNA–DEmiRNA relationships, a competing endogenous RNA (ceRNA) network was constructed. Several DEmRNAs and DElncRNAs were validated in ipsilateral hemisphere tissues of the ICH model and control groups using RT-qPCR and western blot.

Results: Between the ICH and sham groups, 31 DElncRNAs, 367 DEmRNAs, 35 DEmiRNAs, and 96 DEproteins were identified. DEmRNAs were mainly enriched in inflammation, such as cytokine–cytokine receptor interaction, IL-17, and TNF signaling pathways. A PPI network of DEmRNAs was constructed and hub genes were identified, such as IL6 (degree = 59), TNF (degree = 44), and CXCR2 (degree = 39). 24 DElncRNAs with similar functions were identified, including 15 up- and 9 down-regulated lncRNAs.

After integration of DEmiRNA–DEmRNA and DElncRNA–DEmiRNA relationships, we constructed a ceRNA network, composed of 71 DEmRNAs, 17 DEmiRNAs, and 12 DElncRNAs. RT-qPCR and western blot results confirmed that C3, Fga, and Slc4a1 proteins were more lowly expressed and Penk was more highly expressed in ICH than control groups, which could become potential markers for ICH.

Conclusion: Our findings identified ICH-related DE-RNAs and proteins and potential molecular mechanisms of ICH by transcriptome resequencing and quantitative proteomic analyses.

Keywords: intracerebral hemorrhage, transcriptome resequencing, proteomic analyses, inflammation, competing endogenous RNA, protein–protein interactions

INTRODUCTION

Strokes are divided into either ischemic stroke or ICH. ICH accounts for about 15% to 20% of all stroke cases, characterized by hematoma expansion and inflammation. ICH patients have a mortality rate of up to 40% in the first month. The mortality and disability rates of ICH patients is much higher than that of ischemic stroke patients (Fang et al., 2013). Although efforts have been made to reduce ICH and post-ICH complications, the clinical outcomes have been suboptimal. About 20% of ICH survival patients suffer from neurological dysfunction (Duan et al., 2016). However, effective treatment options for ICH are still lacking, and few studies provide evidence to guide ICH treatment (Jia et al., 2018). ICH patients' poor prognosis is closely related to the complicated pathogenesis of ICH. A previous study has shown that targeting ICH-related molecules could be a promising therapeutic strategy (Liu et al., 2019). Thus, it is urgent to explore and understand the molecular mechanisms of ICH.

Non-coding RNAs (ncRNAs), such as lncRNA and miRNA, exhibit important biological functions (Beermann et al., 2016; Matsui and Corey, 2017). ncRNAs could affect the expression of target genes. lncRNA, a non-coding RNA larger than 200 nucleotides, has been reported to play an important role in the pathophysiology of ICH (Zhang and Wang, 2019). Furthermore, lncRNA as a sponge of miRNA can indirectly regulate the expression of downstream messenger RNA (mRNA), which is described as ceRNA (Park et al., 2018). The interactions between genes or proteins are involved in the pathogenesis of diseases. The functions of mRNA, miRNA, lncRNA, and proteins in ICH remains largely unknown.

Herein, this study comprehensively analyzed the transcriptome and proteome of ICH based on collagenase VII-induced ICH mouse models, which could provide an insight into ICH-related DE-RNAs, proteins, and potential molecular mechanisms.

Abbreviations: ICH, intracerebral hemorrhage; DElncRNAs, differentially expressed lncRNAs (DElncRNAs); DEmRNAs, differentially expressed mRNAs; DEmiRNAs, differentially expressed miRNAs; DEproteins, differentially expressed proteins; PPI, protein–protein interaction; ceRNA, competing endogenous RNA; ncRNAs, non-coding RNAs; GO, gene ontology; KEGG, Kyoto Encyclopedia of Genes and Genomes (KEGG); CC, cellular component; MF, molecular function; BP, biological process.

MATERIALS AND METHODS

Animals

Male C57BL/6 mice (age: 10–12 weeks; weight: 22–25 g) were purchased from the Animal Institute of the Third Military Medical University. All mice were fed under a 12 h light/dark cycle in a temperature-controlled and specific pathogen-free environment. All animal experiments conformed to the animal experiment manual approved by the Animal Ethics Committee of Zunyi Medical University. All experiments were performed and reported according to the Animal Research: Reporting *in vivo* Experiments (ARRIVE) guidelines.

ICH Mouse Model

The collagenase VII-induced ICH model was established as previously reported (Xie et al., 2016). All mice were randomly divided into ICH model group (n = 3) and sham operation (n = 3). All mice were anesthetized by intraperitoneal injection of pentobarbital sodium and placed on a brain stereotaxic apparatus (RWD, China) in the ventricumbent position. A previously reported coordinate point (coordinates: 0.2 mm anterior, 2.3 mm lateral, and 3.5 mm depth to bregma) was utilized to inject 1 μL bacterial collagenase (0.0375 units per 1 μL, type VII-S; Sigma-Aldrich, United States) into the striatum at a rate of approximately 0.1 μL/min using a microinjection pump (Longer, TJ-2A/L0107-2A, China). After that, the needle was kept at the injection point for 5 min to prevent liquid backflow. The microsyringe was removed slowly and the cranial pinhole was closed with bone wax. The incisions in the skin were sutured. The sham operation group was injected with an equivalent volume of PBS only, and the other operations were the same.

Mice Hemisphere Harvest

In this study, all mice were scanned by a Bruker 7T MRI (70/20) system (BrukerBiospin, Billerica, MA, United States) (Cao et al., 2016). After the rotarod test pre- and post-CCI, mice were anesthetized with gas mixture (induction: 5% isoflurane with 1 L/min O_2, maintenance: 1% isoflurane with 1 L/min O_2), mounted in a Bruker animal bed, and their body temperature was maintained at 37°C with respiratory rate continuously monitored. T2-weighted images were acquired using RARE (TR = 4000, TE = 45, RARE factor 8, 0.5 mm, FOV 2.5 cm,

256 × 256). Images were analyzed using Bruker ParaVision 6.0 software. The lesion volumes were determined as pixels that had T2 values higher than the mean plus two standard deviations of the value in the homologous contralesional region. The model was confirmed to be successfully constructed before euthanizing at 24 h after ICH injury or sham injury, and the whole brain was divided into two halves, as described in a previous study (Cao et al., 2016). The ipsilateral hemisphere was used for whole transcriptome resequencing by Novaseq 6000 (Illumina, United States) and whole proteomics resequencing that were analyzed on an Orbitrap Fusion Lumos Tribrid mass spectrometer (Thermo Scientific, United States).

Whole Transcriptome Resequencing Analysis

Total RNA was extracted from tissues using TRIzol reagent (Invitrogen, United States). Standard denaturing gel electrophoresis was used to assess RNA integrity. Extracted RNA was transcribed into cDNA. Mouse reference genome and annotation information were downloaded using Ensembl Genome Browser [version: GRCm38.p6 (GCA_000001635.8)]. An index of the reference genome was created via hisat2. The transcriptome sequencing double-end data were firstly cleaned using Trim Galore. Trim Galore can automatically identify and remove the 3′ end adapter. In this way, the transcriptome data were quantified after obtaining clean data from raw data. Two separate library preparations were used for the long and small RNAs. The ribosomal depletion was utilized for library preparations of the long RNAs. Furthermore, small RNA-seq cDNA library preparation was performed for the small RNAs.

The quantification of the RNA (including lncRNA and mRNA) transcriptome was performed using hisat2. The parameters were defaulted. The alignment rates were as follows: M1: 96.65% overall alignment rate, M2: 96.61% overall alignment rate, M3: 96.63% overall alignment rate, M7: 96.47% overall alignment rate, M8: 96.86% overall alignment rate, and M9: 96.52% overall alignment rate. Among them, M1-3 represented three ICH mouse models and M7-9 represented three sham operation mice. After sorting the mapping results by samtools, featureCounts was used to quantify. The quantitative results of the RNA transcriptome data were obtained for further analysis.

The miRNA transcriptome was quantified using miRDeep2. All mouse miRNA sequence data were downloaded as alignment references and as annotated files from the miRBase database (version: 22) (Griffiths-Jones et al., 2006). Trim Galore was used to remove the adapters in the raw data, and then cutadapt was used to screen sequences with a sequence length of 18–25. The above result was used as a clean read for subsequent alignment analysis. Redundant sequences were removed by miRDeep2 and unique reads were obtained. Based on mouse miRNA data in the miRBase database, quantification of miRNA transcriptome data was presented.

Differential Expression Analysis

Differential expression analysis was performed by the likelihood ratio test method of the edgeR package (Robinson et al., 2010). After deletion of genes with a lower abundance and normalization by TMM, DElncRNAs, DEmRNAs, and DEmiRNAs between the ICH and sham groups were identified, and the threshold was set to FDR (adjusted p-value) < 0.05 and $\log2|\text{ fold change (FC)}| > 1.5$. Finally, the results were visualized as volcano plots and heat maps.

Functional Enrichment Analysis

Functional enrichment analysis was performed using the clusterProfiler package, including GO and KEGG pathway (Yu et al., 2012). GO contains cellular component (GO-CC), molecular function (GO-MF), and biological process (GO-BP). P-value < 0.05 after correction was considered significantly enriched.

PPI

DEmRNAs were imported into the STRING database for PPI analysis. The combined score > 0.7 was set as the threshold. The PPI network was constructed using the Cytoscape. CytoNCA plug-in of Cytoscape was used to calculate degree centrality, betweenness centrality, and closeness centrality. Nodes with high scores were considered as hub genes.

Correlation Analysis of lncRNAs and mRNAs

For the DEmRNAs and DElncRNAs obtained, the correlation between lncRNA and mRNA was calculated using the Pearson correlation coefficient. P-value was corrected by the BH method and corrected p-value < 0.01 indicated that there could be a significant correlation between lncRNA and mRNA. The lncRNA–mRNA network was drawn through the Cytoscape.

lncRNA Functional Similarity Analysis

To explore potential functions of DElncRNAs, functional enrichment analysis of target genes of DElncRNAs was performed. The semantic similarity between GO-BP terms enriched by target genes of DElncRNAs was quantified using the Resnik method and Wang method provided by GOSemSim package, which was used to measure the functional similarity between DElncRNAs (Wang et al., 2007; Yu et al., 2010).

miRNA–mRNA Prediction and ceRNA Network Construction

For the obtained DEmiRNAs, miRNA-target prediction was performed by miRWalk, Microt4, miRanda, mirbridge, miRDB, miRMap, miRNAMap, Pictar2, PITA RNA22, RNAhybrid, and Targetscan databases on miRWalk 2.0 platform. Prediction results supported by over seven databases were considered reliable miRNA–mRNA relationships.

After obtaining the sequence of the DElncRNAs from the reference genome and the sequence of the DEmiRNAs from the miRBase database, the miRanda tool (parameters: -sc 120, -en -20) was used to predict whether there was a binding site between miRNA and lncRNA. If there were more than five binding sites, it was considered that there was a regulatory relationship between miRNA and lncRNA.

After integration of DEmiRNA–DEmRNA and DElncRNA–DEmiRNA relationships, a lncRNA–miRNA–mRNA ceRNA network was constructed.

Proteomic Analysis

Tissues were lysed using RIPA lysis (Beyotime, Beijing, China). After centrifugation, the supernatant was collected. DEproteins were analyzed based on proteome resequencing analysis results, with the threshold of q-value < 0.05 and $|\log2FC| > 0.5$. Functional enrichment analysis of these proteins was performed using the clusterProfiler package. Furthermore, a PPI network was conducted to predict the interactions between DEproteins.

mRNA–Protein Correlation Analysis

Venn analysis was performed on DEmRNAs from transcriptome data and DEproteins from proteomic analysis. Pearson correlation coefficient was calculated to analyze the correlation between DEmRNAs and DEproteins.

Real-Time Quantitative Polymerase Chain Reaction (RT-qPCR)

Total RNA was extracted from tissues by Trizol (Invitrogen, United States). The extracted RNA was reverse transcribed into cDNA in the following reaction procedures: 37°C for 60 min, 85°C for 5 min, and 4°C for 5 min. cDNA was amplified by SYBR Green PCR kit (#K0223; Thermo, Waltham, MA, United States) through the following procedures: 40 circles of 95°C for 10 min, 95°C for 15 s, 60°C for 1 min, 95°C for 15 s, and 60°C for 15 s. Primer sequences were as follows: Fga: 5′-GCG GCAGATGAGAATGGAG-3′ (forward), 5′-GTTCCCAGGACG CCAATAC-3′ (reverse); C3: 5′-TGGGAGAAGTTCGGCATA GAG-3′ (forward), 5′-GGTTGTTGAAGGCAGCATAGG-3′ (reverse); 5′-AGCACCAACAATGACGAAG-3′ (forward), 5′-TT CAGAACCGCATAAAGCC-3′ (reverse); Slc4a1: 5′-CAGGA CTACCCACTACAAC-3′ (forward), 5′-CCACCAGGACCATT ATCAG-3′ (reverse); GAPDH: 5′-CTGCCCAGAACATCAT CC-3′ (forward), 5′-CTCAGATGCCTGCTTCAC-3′ (reverse). The relative expression levels were quantified with the $2^{-\Delta\Delta Ct}$ method.

Western Blot

Protein was extracted from tissues via RIPA (Beyotime, Beijing, China). The protein concentration was assessed by BCA kit (Beyotime). Then, protein samples were separated through SDS-PAGE, which was transferred onto PVDF membrane. The membrane was blocked by 0.5% skimmed milk for 2 h at room temperature, followed by incubation with primary antibodies against Protein Penk (1:1000; ab150346; Abcam, United States), C3 (1:1000; ab181147; Abcam), Fga (1:2000; ab108616; Abcam), Slc4a1 (1:1000; ab196798; Abcam), and β-actin (1:200; ab115777; Abcam) at 4°C overnight, and secondary antibodies (1:5000; ab7090) at room temperature for 2 h. Protein blots were analyzed through the Western Lighting Ultra (Thermo).

Statistical Analysis

Statistical analyses were performed by R 3.6.3 and GraphPad 7.0. Data from experiments were presented as mean ± standard deviation. Paired student's t-test was used for comparisons between the two groups. $P < 0.05$ was considered statistically significant.

RESULTS

Identification of DElncRNAs and DEmRNAs for ICH

In this study, we conducted ICH mouse models, and all the ICH mouse models were confirmed by the T2-weighted images from a Bruker 7T MRI (70/20) system (BrukerBiospin, Billerica, MA, United States) before use (**Supplementary Figure S1**). The ipsilateral hemisphere tissues of ICH model and sham groups were used for whole transcriptome resequencing analyses. Raw data were pre-processed and lowly expressed lncRNAs or mRNAs were removed (**Figures 1A,B**). Then, filtered data were normalized by TMM methods (**Figures 1C,D**). Before differential expression analysis, we performed PCA analysis. In **Figure 1E**, the PCA analysis results of the two dimensions (ICH and sham groups) showed that the interpretation of the data by the two dimensions exceeded 50% (32.8% + 27%). Beginning with comp. 2, the scree plot began to flatten, indicating that the two dimensions could well explain the characteristics of the data (**Figure 1F**). The above results suggested that there were obvious differences in the characteristics between the two groups of data. Thus, differential expression analysis results would be reliable. Differential expression analysis was performed using the edgeR package. As depicted in the volcano plot, there were 318 up- and 84 down-regulated RNAs between ICH groups and sham groups (**Figure 1G**). Among them, 31 DElncRNAs were identified, including 11 up- and 20 down-regulated lncRNAs (**Figure 1H**). Furthermore, there were 367 DEmRNAs between the ICH groups and sham groups, including 306 up- and 64 down-regulated mRNAs (**Figure 1I**). These DElncRNAs and DEmRNAs can accurately distinguish the two group samples into two clusters, indicating that the results of the differential expression analysis were reliable.

Functional Enrichment Analysis and PPI Network of DEmRNAs

To explore potential functions of DEmRNAs, GO and KEGG functional enrichment analyses were performed. The top ten enrichment results were shown in **Figure 2A**. For GO enrichment analysis results, we found that these DEmRNAs were mainly enriched in inflammation responses, such as leukocyte, neutrophil, granulocyte, cytokine, and so on. As for KEGG pathway results, these DEmRNAs were also mainly enriched in immune-related pathways, including cytokine–cytokine receptor interaction, viral protein interaction with cytokine and cytokine receptor, IL-17 signaling pathway, TNF signaling pathway, complement and coagulation cascades, neuroactive ligand–receptor interaction, JAK-STAT signaling pathway, and chemokine signaling pathway.

A PPI network of DEmRNAs was constructed for ICH. There were 184 nodes, including 151 up- and 33 down-related genes

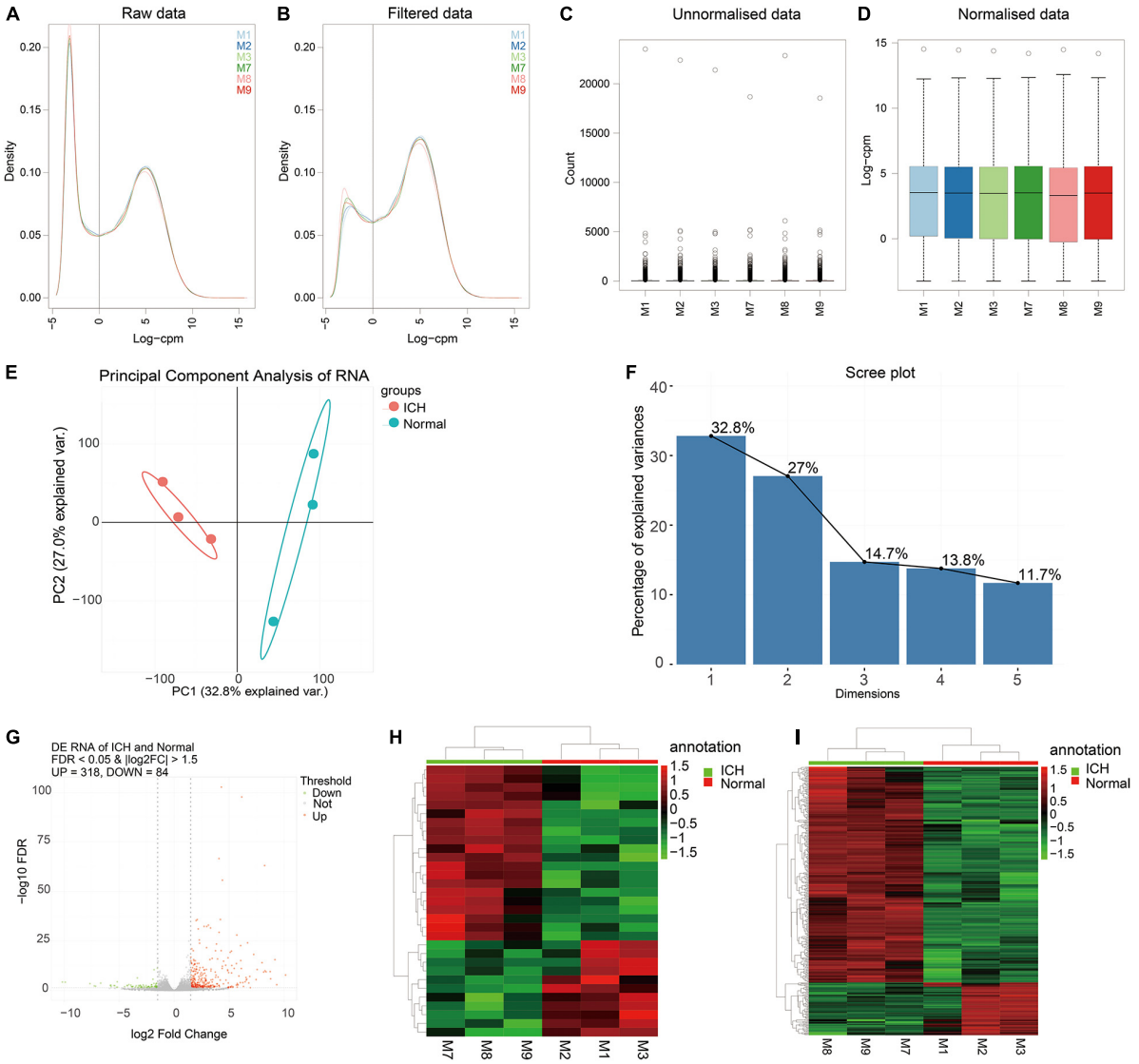

FIGURE 1 | Identification of DElncRNAs and DEmRNAs for ICH. **(A,B)** The data density distribution curve before or after removing low-expressed lncRNAs or mRNAs. **(C,D)** The box plot showing the unnormalized data or normalized data by TMM. **(E)** PCA analysis of RNA transcriptome. **(F)** Scree plot of RNA transcriptome. **(G)** Volcano plot showing 318 up- and 84 down-regulated RNAs between ICH groups and sham groups. **(H)** Hierarchical clustering showing the differential expression patterns of DElncRNAs between ICH and sham groups. **(I)** Hierarchical clustering showing all DEmRNAs between ICH and sham groups. M1-3 represents three ICH mouse models and M7-9 represent three sham operation mice. Red indicates up-regulation and green indicates down-regulation.

(**Figure 2B**). The top ten nodes with the highest degree were as follows: IL6 (degree = 59), TNF (degree = 44), CXCR2 (degree = 39), CXCL1 (degree = 39), CXCL2 (degree = 39), C3 (degree = 36), FPR2 (degree = 36), CXCXL10 (degree = 35), C5AR1 (degree = 32), and IL1b (degree = 30). These genes could play a critical role in the PPI network.

Co-expression Analysis of DElncRNAs and DEmRNAs

The correlation analysis of DElncRNAs and DEmRNAs was performed by calculating the Pearson correlation coefficients. In this study, the corrected p-value < 0.01 indicated that DElncRNAs were significantly correlated with DEmRNAs. The co-expression analysis results of DElncRNAs and DEmRNAs were listed in **Table 1**.

Functional Similarity Analysis of DElncRNAs

Gene ontology and KEGG enrichment analyses of DElncRNAs were performed based on co-expressed DEmRNAs. Based on GO-BP results, we analyzed the functional similarity of these DElncRNAs by Gosemsim. As shown in **Figure 2C**, there were 24 DElncRNAs with similar functions, including 15 up- and 9 down-regulated lncRNAs. The thicker the line between

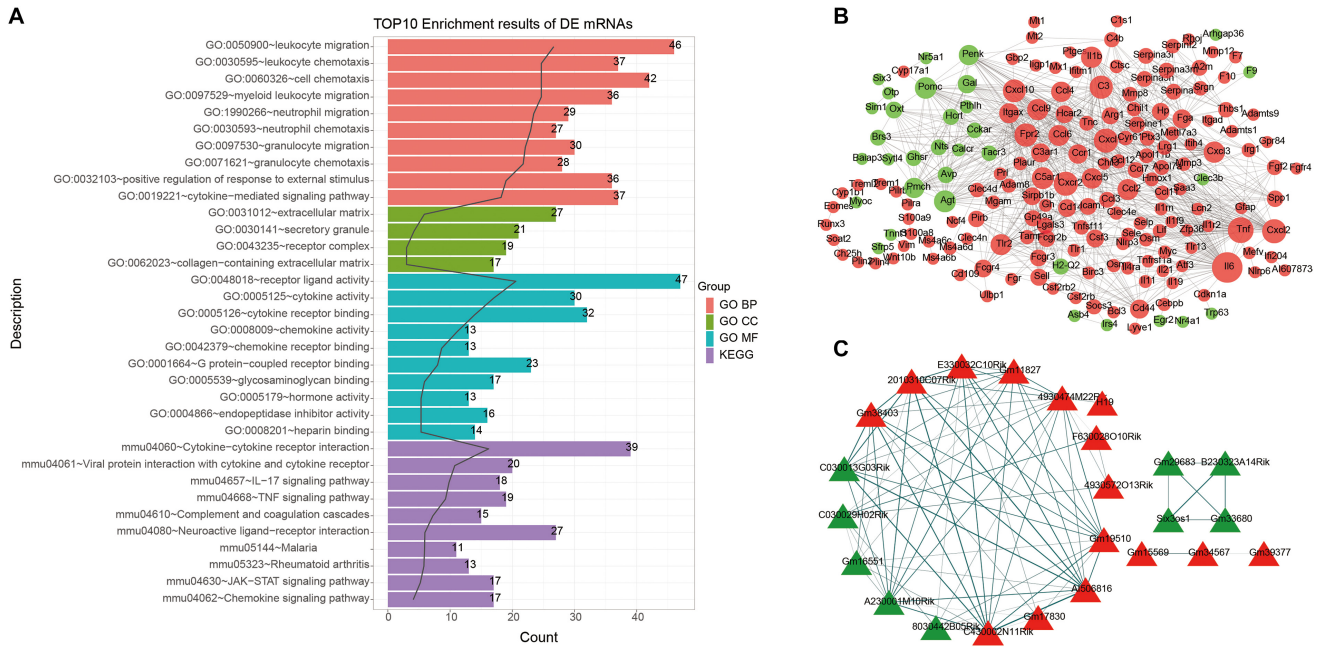

FIGURE 2 | Functional enrichment analysis and PPI network of DEmRNAs. **(A)** The top 10 functional enrichment analysis results based on DEmRNAs. **(B)** A PPI network. The larger the circle, the greater the degree. **(C)** Functional similarity analysis of DElncRNAs. Red represents up-regulation and green represents down-regulation. The thickness of the line indicates the degree of functional similarity.

the two DElncRNAs, the more similar the function between the two DElncRNAs.

Identification of DEmiRNAs for ICH

We further analyzed miRNA transcriptome for ICH. By data preprocessing, lowly expressed miRNAs were removed (**Figures 3A,B**). Then, the filtered data were normalized by TMM methods (**Figures 3C,D**). As shown in the PCA analysis results, the interpretation of the data by the two dimensions exceeded 50% (32.2% + 20.6%) in **Figure 3E**. Furthermore, from comp.2, the scree plot began to flatten, indicating that the two dimensions can well explain the characteristics of the data (**Figure 3F**).

After PCA, we performed differential expression analysis. The results showed that there were 25 up- and 10 down-regulated miRNAs between the ICH and sham groups (**Figure 3G**). As depicted in the hierarchical clustering analysis results, these DEmiRNAs could obviously distinguish the ICH group from the sham group (**Figure 3H**).

TABLE 1 | Co-expression analysis results of DElncRNAs and DEmRNAs.

DElncRNAs	Number of co-expressed DEmRNAs	DElncRNAs	Number of co-expressed DEmRNAs
2010310C07Rik	205	Gm15569	70
AI506816	175	Gm39377	68
Gm19510	175	8030442B05Rik	65
C430002N11Rik	172	Gm16551	64
4930474M22Rik	149	Gm33100	64
E330032C10Rik	140	F630028O10Rik	54
A230001M10Rik	129	A730006G06Rik	49
Gm38403	115	Gm17830	48
C030013G03Rik	113	B230323A14Rik	47
Gm11827	113	Gm33680	42
H19	96	Gm29683	41
A530001N23Rik	94	Six3os1	37
4930572O13Rik	81	E230016K23Rik	36
C030029H02Rik	72	A330076C08Rik	15
Gm34567	71	AU023762	15

Construction of a ceRNA Network for ICH

The DEmiRNA–DEmRNA relationships were predicted using the miRWalk, Microt4, miRanda, mirbridge, miRDB, miRMap, miRNAMap, Pictar2, PITA RNA22, RNAhybrid, and Targetscan databases on miRWalk 2.0 platform. DEmiRNA–mRNA relationships supported by over seven databases were used for the construction of a ceRNA network. Furthermore, relationships between DElncRNAs and DEmiRNAs were predicted by the miRanda tool. In this study, if there were more than five binding sites, DElncRNA–DEmiRNA interactions were identified for further analysis. After integration of DEmiRNA–DEmRNA and DElncRNA–DEmiRNA relationships, we constructed a lncRNA–miRNA–mRNA ceRNA network (**Figure 4**). In the ceRNA network, there were 71 DEmRNAs, 17 DEmiRNAs, and 12 DElncRNAs. Furthermore, there were 78 DElncRNA–DEmiRNA relationships (**Supplementary Table S1**) and 119 DEmiRNA–DEmRNA relationships (**Supplementary Table S2**).

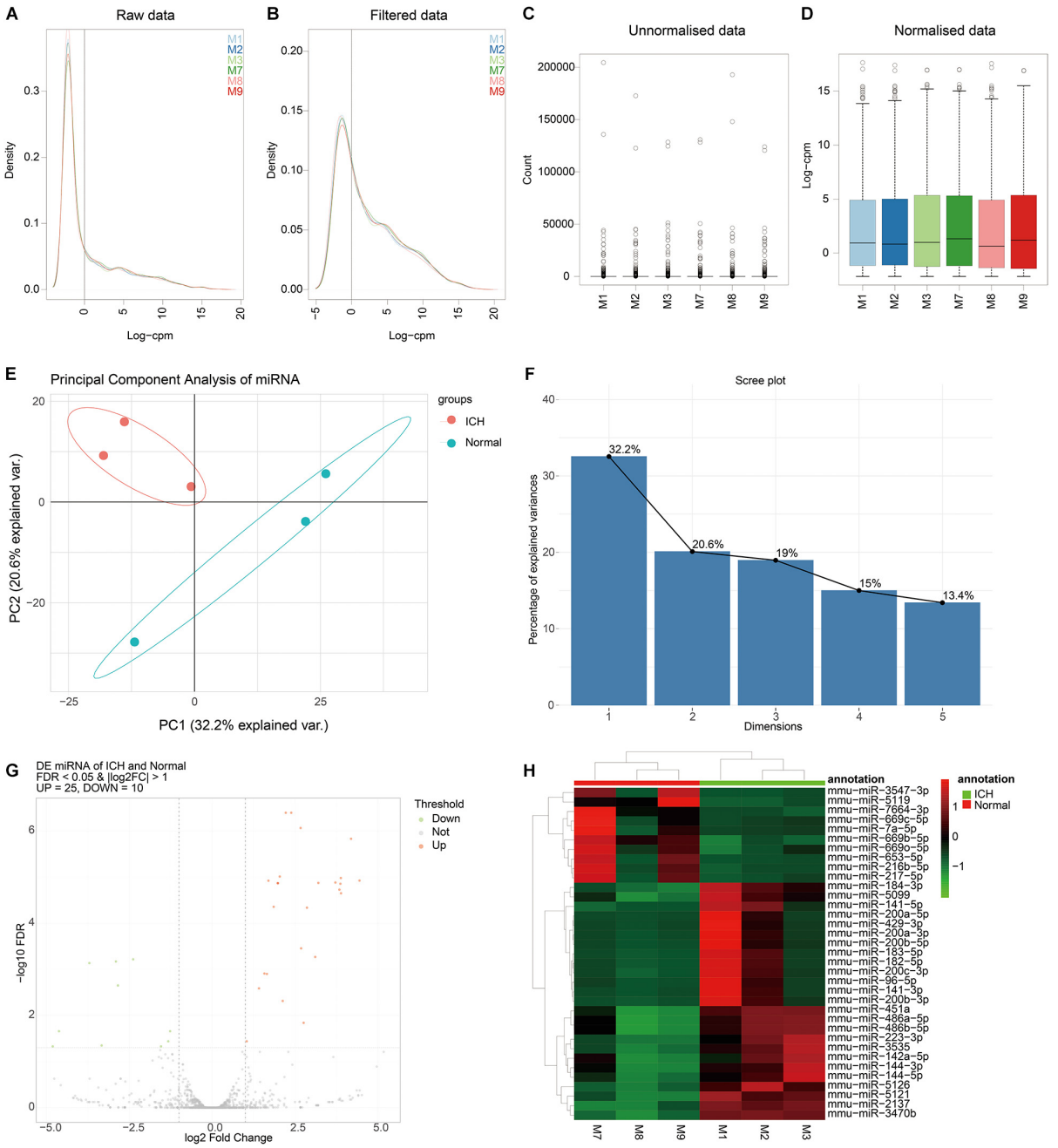

FIGURE 3 | Identification of DEmiRNAs for ICH. **(A,B)** The data density distribution curve before or after removing low-expressed miRNAs. **(C,D)** The box plot showing the unnormalized or normalized data. **(E)** PCA results of miRNAs. **(F)** Scree plot of PCA. **(G)** Volcano plot showing DEmiRNAs between ICH and sham groups. **(H)** Hierarchical clustering analysis results depicting the expression patterns of DEmiRNAs between ICH and sham groups. M1-3 represents three ICH mouse models and M7-9 represent three sham operation mice. Red indicates up-regulated miRNAs and green indicates down-regulated miRNAs.

The larger the node, the larger the degree, the more important the role of the node in the network.

Identification of DEproteins for ICH and Functional Enrichment Analysis

The whole proteomics resequencing of ICH model and sham groups was performed. Ninety six DEproteins were identified between ICH and sham groups. Hierarchical clustering analysis results suggested that these DEproteins could obviously distinguish ICH samples from sham samples (**Figure 5A** and **Supplementary Table S3**). To explore protein–protein interactions, we constructed a PPI network based on these DEproteins. In the PPI network, there were 58 nodes, including 15 highly expressed and 43 lowly expressed proteins (**Figure 5B**).

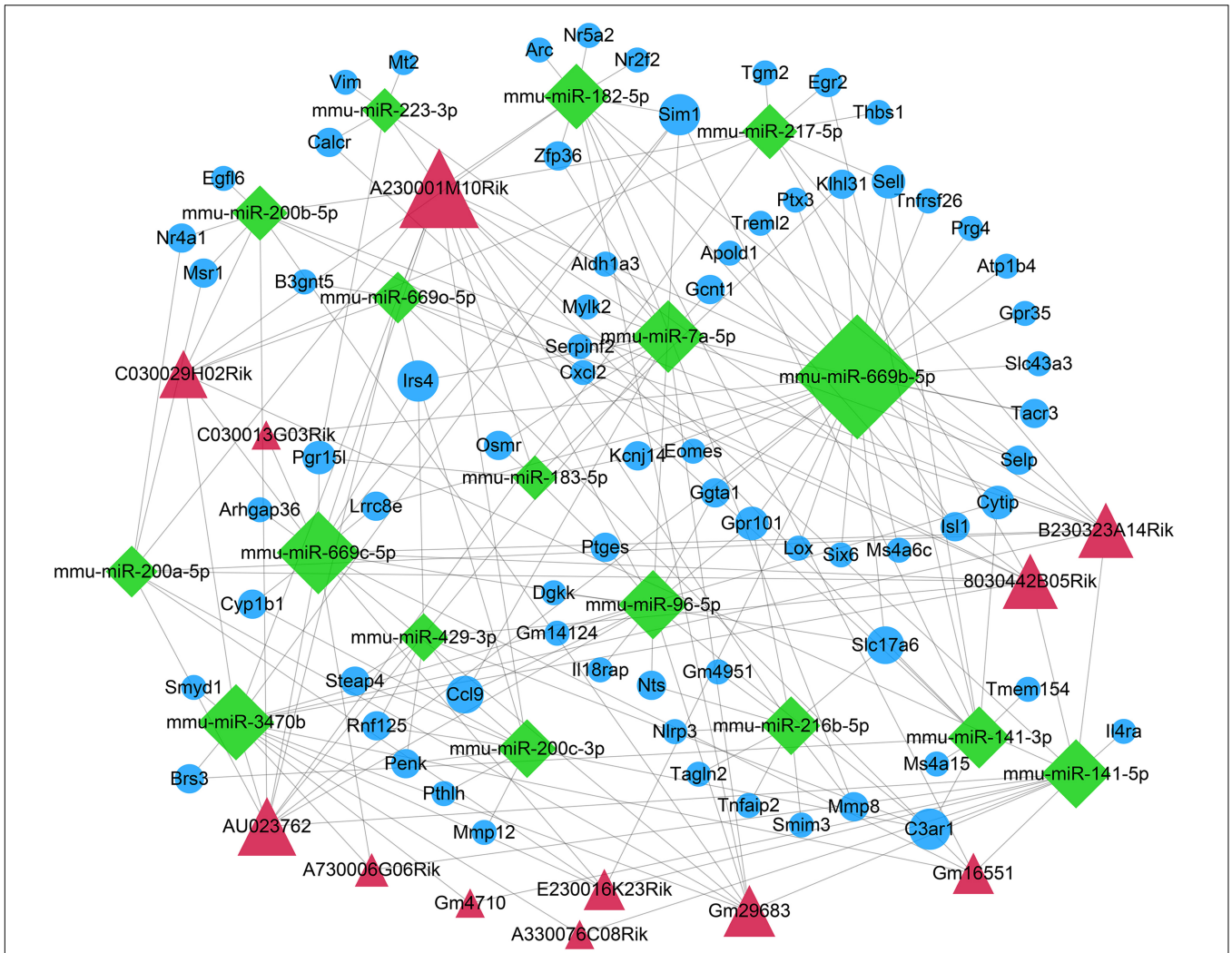

FIGURE 4 | Construction of a ceRNA network for ICH. The red triangle represents the DElncRNAs, the green diamond represents DEmiRNAs, and the blue circle represents mRNAs. The node size indicates the degree.

The top ten nodes with the highest degree were as follows: Alb (degree = 31), Fga (degree = 26), Fgg (degree = 26), Apoa1 (degree = 26), Ahsg (degree = 25), Fn1 (degree = 24), Apoa2 (degree = 23), Kng1 (degree = 23), C3 (degree = 23), and Plg (degree = 21). These nodes could play important roles in the PPI network. We further explored the functions of these proteins. The top ten GO-BP enrichment analysis results were shown in **Figure 5C**, such as B cell mediated immunity, blood coagulation and hemostasis, and so on. As for GO-CC, these proteins were mainly enriched in extracellular regions, extracellular region parts and extracellular space (**Figure 5D**). Furthermore, these DEproteins were significantly associated with molecular function regulators, enzyme regulator activity, and signaling receptor binding (**Figure 5E**). KEGG enrichment analysis results showed that these DEproteins were mainly enriched in complement and coagulation cascades, pertussis, and staphylococcus aureus infection (**Figure 5F**). Thus, these proteins could be involved in various key biological processes and pathways.

mRNA–Protein Correlation Analysis

Venn analysis showed the intersections between DEmRNAs and DEproteins. We found that Fga, Hp, C3, Apod, Serpinf2, Penk, Serpina3n, and Slc4a1 were differentially expressed in ICH compared to sham groups at the mRNA and protein levels (**Figure 6A**). Pearson correlation analysis results show that there were high correlations between several DEmRNAs and DEproteins, indicating that there could be mutual regulatory relationships between these RNAs and proteins (**Figure 6B**). However, several DEproteins did not correlate with DEmRNAs, indicating that the two could have regulatory relationships for ICH.

Validation of DEmRNAs and DEproteins for ICH

DEmRNAs and DEproteins were validated in ipsilateral hemisphere tissues of ICH model and control groups using

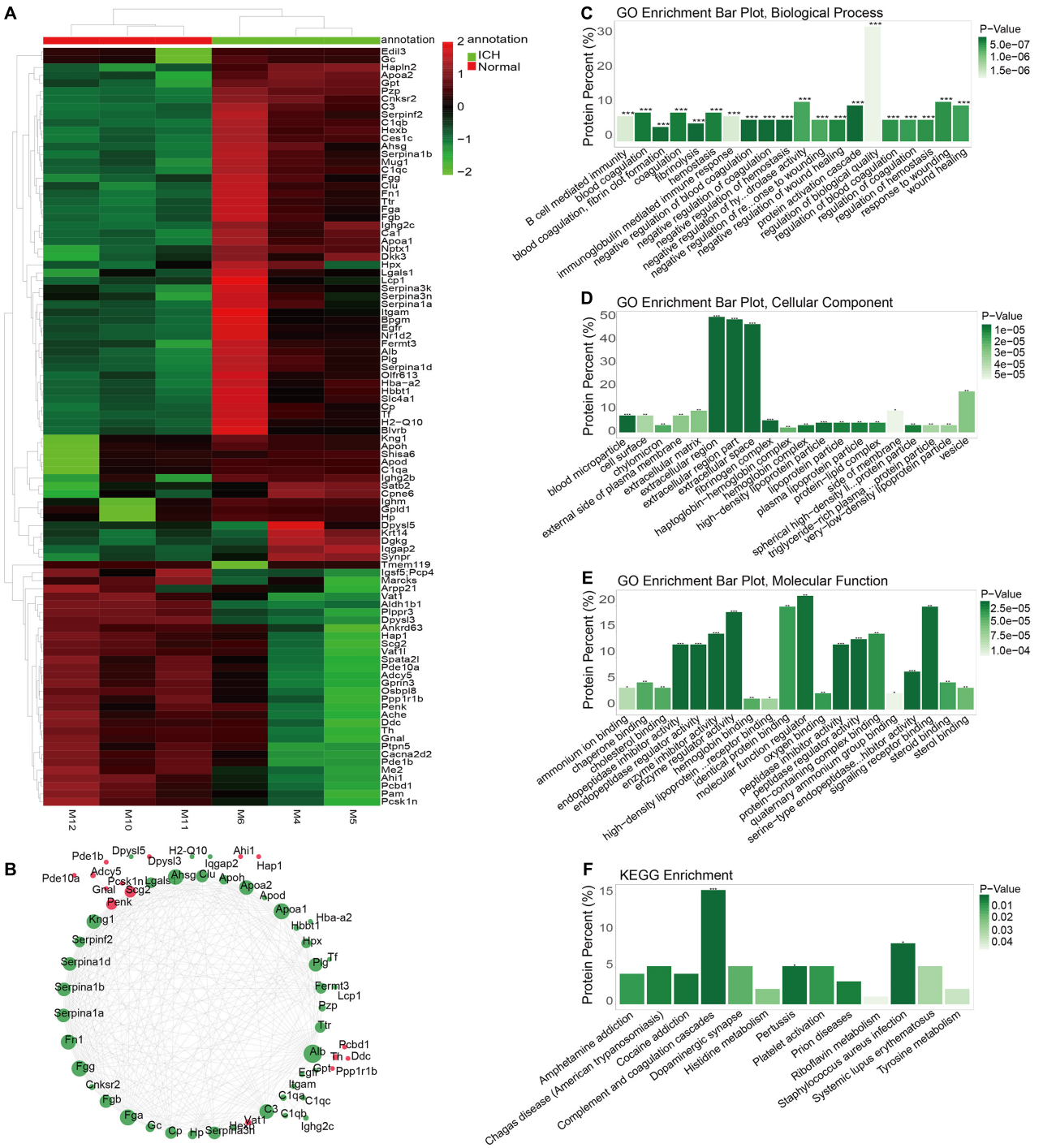

FIGURE 5 | Identification of DEproteins for ICH and functional enrichment analysis. **(A)** Hierarchical clustering analysis results showing the expression patterns of 96 DEproteins between ICH and sham groups. M1-3 represents three ICH mouse models and M7-9 represent three sham operation mice. **(B)** Construction of a PPI network. Red represents up-regulation and green represents down-regulation. The circle size indicates the degree of the node in the PPI network. **(C)** GO-BP enrichment analysis results. **(D)** GO-CC enrichment analysis results. **(E)** GO-MF enrichment analysis results. **(F)** KEGG pathway enrichment analysis results. $^{*}p < 0.05$; $^{**}p < 0.01$; $^{***}p < 0.001$.

RT-qPCR and western blot. Our RT-qPCR confirmed that Fga ($p < 0.0001$; **Figure 7A**), C3 ($p < 0.0001$; **Figure 7B**), Penk ($p = 0.0025$; **Figure 7C**), and Slc4a1 ($p = 0.0020$; **Figure 7D**) were differentially expressed between ICH and control groups. Among them, Fga, C3, and Slc4a1 mRNAs were markedly down-regulated in ICH than controls. Furthermore, we examined the

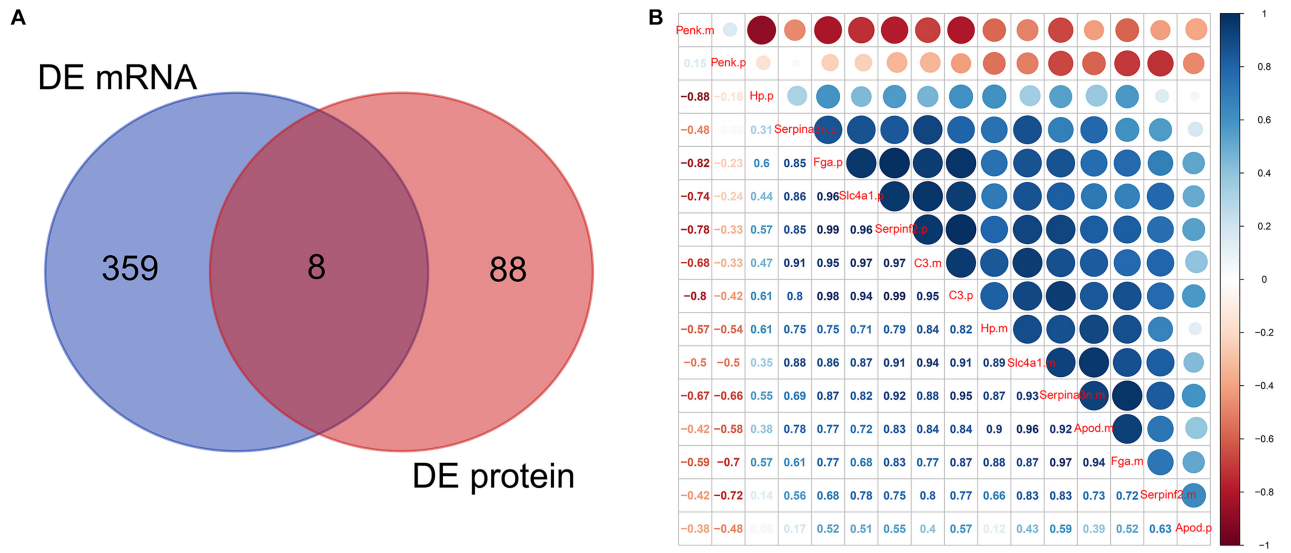

FIGURE 6 | mRNA–protein correlation analysis. **(A)** Venn analysis of DEmRNAs and DEproteins. **(B)** Pearson correlation analysis results showing the correlation between DEmRNAs and DEproteins.

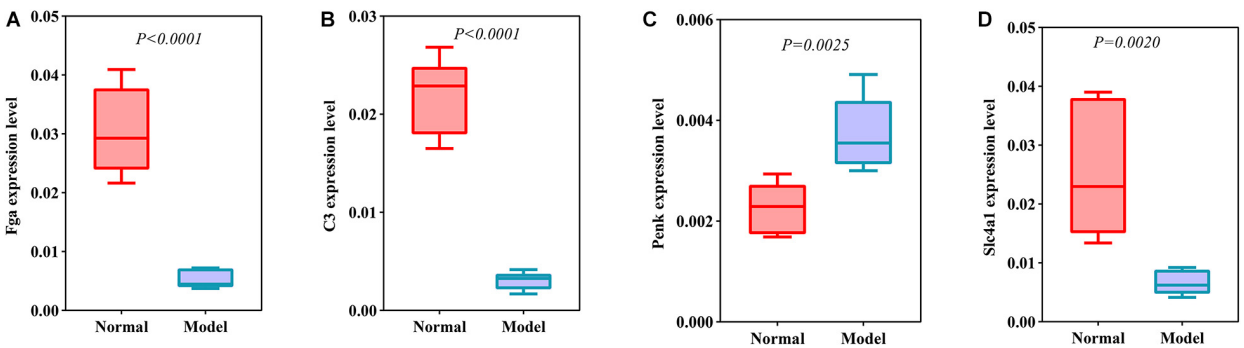

FIGURE 7 | Validation of DEmRNAs in ipsilateral hemisphere tissues of ICH model and control groups using RT-qPCR. **(A)** Fga; **(B)** C3; **(C)** Penk; **(D)** Slc4a1.

expression of Fga, C3, Penk, and Slc4a1 proteins in ipsilateral hemisphere tissues by western blot (**Figure 8A**). Consistently, the data showed that C3 ($p = 0.0001$; **Figure 8B**), Fga ($p = 0.0015$; **Figure 8C**), and Slc4a1 ($p < 0.0001$; **Figure 8D**) proteins were lowly expressed in ICH compared to control groups. Penk ($p = 0.0004$; **Figure 8E**) exhibited higher expression levels in the ICH model group than the control group.

DISCUSSION

Currently, research on the treatment of ICH mainly focuses on the clinical aspects of therapeutic intervention, however, the molecular mechanism of ICH is still unclear (Yin et al., 2017). Therefore, the identification of therapeutic targets for ICH can improve the treatment strategies for ICH. In this study, we conducted a collagenase VII-induced ICH model. The whole transcriptome resequencing analysis was performed between ICH model and sham groups. Increasing evidence has confirmed that lncRNA is involved in brain function and neurological diseases (Jia et al., 2018; Zhang and Wang, 2019; Zhang et al., 2019). However, the expression characteristics of lncRNA after ICH remain to be elucidated. In this study, we analyzed the expression patterns of lncRNAs between collagenase VII-induced ICH mouse model and sham operation mice. After preprocessing, we identified 31 DElncRNAs in the ICH model compared to sham group, including 11 up- and 20 down-regulated lncRNAs. Furthermore, 367 DEmRNAs were obtained between ICH and sham groups, including 306 up- and 64 down-regulated mRNAs. These DElncRNAs and DEmRNAs can obviously distinguish ICH from sham operation groups, which could be involved in the pathological processes of ICH.

We further explored the potential functions of DEmRNAs by GO and KEGG functional enrichment analyses. We found that these DEmRNAs were mainly enriched in inflammation responses. It has been confirmed that inflammation plays an important role in the brain injury after ICH (Zhou et al., 2014). Furthermore, the mechanism of ICH is closely related to the

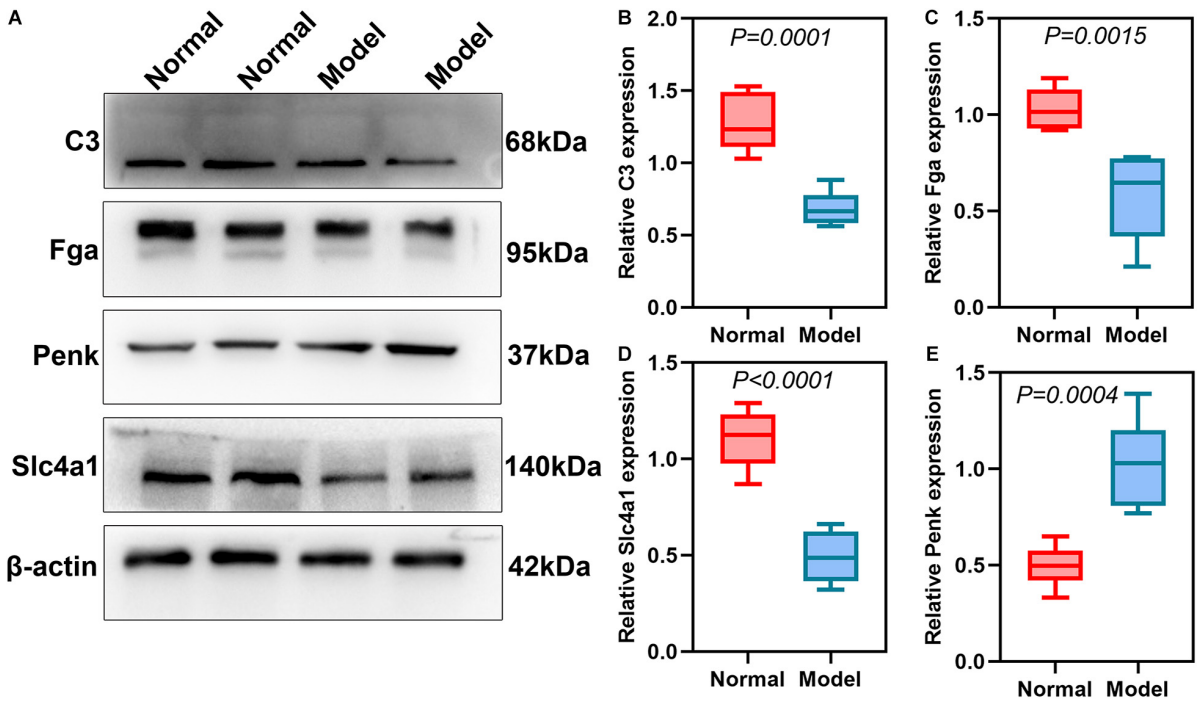

FIGURE 8 | Validation of DEproteins in ipsilateral hemisphere tissues of ICH model and control groups using RT-qPCR. **(A)** Representative images of western blot results. **(B)** C3; **(C)** Fga; **(D)** Slc4a1; **(E)** Penk.

infiltration of inflammatory cells (Lan et al., 2019). However, few effective treatments have been found so far. Our GO enrichment analysis results showed that these DEmRNAs were in association with leukocytes, neutrophils, granulocytes, and so on. It has been confirmed that acute leukocytosis responds to ICH (Morotti et al., 2016). Neutrophil infiltration as a therapeutic target can aggravate brain damage after ICH (Zhao et al., 2017). A clinical study has reported that the neutrophil-to-lymphocyte ratio can predict acute ICH up to 3 months in advance (Lattanzi et al., 2016). Moreover, granulocyte colony-stimulating factor can alleviate neurological function and angiogenesis in ICH rat model (Liang et al., 2018). KEGG pathway results showed that these DEmRNAs were also mainly enriched in immune-related pathways such as IL-17, TNF, and JAK-STAT signaling pathways. Pro-inflammatory cytokines IL-17 and TNF-α are elevated in the serum of patients with neurodegenerative diseases, including ICH (Yang and Shao, 2016; Chaudhry et al., 2017). A previous study has reported that osteopontin could attenuate inflammatory response by JAK2/STAT1 in ICH hyperglycemic rat models (Gong et al., 2018). Based on previous findings, after the onset of ICH, cytokines released by various inflammatory cells are involved in secondary brain damage caused by ICH. There are many potential genes in the pathological processes of ICH. Thus, these DEmRNAs might participate in inflammation after ICH, which could be considered as potential therapeutic targets.

It is critical to explore the interactions between DEmRNAs and understand their biological significance. In our study, we constructed a PPI network based on DEmRNAs for ICH, including 151 up- and 33 down-related genes. The nodes with the highest degree could become potential hub genes, including IL6, TNF, CXCR2, CXCL1, CXCL2, C3, FPR2, CXCXL10, C5AR1, and IL1b. Most of them are inflammatory cytokines, suggesting that immunity plays an important role in the pathological processes of ICH. Pearson correlation analysis was used to explore correlation DElncRNAs and DEmRNAs. The functions of DElncRNAs were predicted by functional enrichment analysis based on their co-expressed DEmRNAs. Furthermore, we found that 24 DElncRNAs could possess similar functions by Gosemsim, including 15 up- and 9 down-regulated lncRNAs. In line with a previous study, lncRNA H19 is up-regulated in the ICH model compared to controls (Kim et al., 2019). These DElncRNAs require further exploration.

We further analyzed miRNA transcriptome for ICH and identified 25 up- and 10 down-regulated miRNAs between ICH and sham groups. These DEmiRNAs had a significant difference between the ICH group and sham group. lncRNA can respond to miRNAs with specific miRNA response elements in the 3′UTR region, and then represses the expression of miRNA targets (Tay et al., 2014). In our study, we predicted the DElncRNA–DEmiRNA and DEmiRNA–DEmRNA relationship pairs. After integration of DEmiRNA–DEmRNA and DElncRNA–DEmiRNA relationships, we constructed a lncRNA–miRNA–mRNA ceRNA network. The regulatory mechanism of the ceRNA network in ICH remains unknown (Dou et al., 2020). Our findings proposed the ceRNA network of ICH that deepened the understanding of molecular mechanisms of ICH.

In this study, 96 DEproteins were identified between ICH and sham groups. As depicted in the PPI network, Alb, Fga,

Fgg, Apoa1, Ahsg, Fn1, Apoa2, Kng1, C3, and Plg could become potential hub proteins, which could play important roles in ICH. These DEproteins were significantly associated with B cell mediated immunity, blood coagulation, and hemostasis, indicating that these DEproteins could be involved in ICH. Our results showed that Fga, Hp, C3, Apod, Serpinf2, Penk, Serpina3n, and Slc4a1 were differentially expressed in ICH at the mRNA and protein levels. A clinical study found that FGA Thr312Ala polymorphism could affect the risk of ICH in Polish participants (Jagiella et al., 2014). A study has confirmed that C3 is in association with the risk of ICH (Jiang et al., 2015). Furthermore, it can cause brain injury induced by ICH (Yang et al., 2006). After validation using RT-qPCR and western blot, our study confirmed that C3, Fga, and Slc4a1 were lowly expressed and Penk was highly expressed in ICH compared to control groups. These markers could be involved in the progression of ICH. More experiments should be presented to validate their biological functions in ICH.

CONCLUSION

In this study, we constructed an ICH model. By comprehensively analyzing transcriptome resequencing and quantitative proteomic analyses, we identified ICH-related DE-RNAs and proteins and potential molecular mechanisms of ICH, which are worthy of further exploration.

DATA AVAILABILITY STATEMENT

The original contributions presented in the study are included in the article/**Supplementary Material**, further inquiries can be directed to the corresponding author/s.

ETHICS STATEMENT

The animal study was reviewed and approved by Animal Ethics Committee of Zunyi Medical University.

AUTHOR CONTRIBUTIONS

SY and FC conducted, conceived of, and designed the experiments, and wrote the manuscript. YG did the MRI scan. HZ and QZ analyzed the data. YF, JS, and QL built the models. All authors read and approved the final manuscript.

FUNDING

This research was funded by the National Natural Science Foundation of China (NSFC: 81660211 and 81960230), Outstanding Youth Foundation of Zunyi medical university (2018-07), and the Department of Science and Technology of Guizhou Province [2020]1Y318

ACKNOWLEDGMENTS

We thank the assistance and support from the Department of Biochemistry and Molecular Biology of Zunyi Medical University, the Guizhou Key Laboratory of Anesthesia and Organ Protection, and the Key Laboratory of Basic Pharmacology of Ministry of Education and Joint International Research Laboratory of Ethnomedicine of Ministry of Education.

SUPPLEMENTARY MATERIAL

The Supplementary Material for this article can be found online at: https://www.frontiersin.org/articles/10.3389/fgene.2020.551065/full#supplementary-material

Supplementary Figure 1 | T2-weighted images of ICH mouse models.

Supplementary Table 1 | Seventy eight DElncRNA–DEmiRNA relationships in the ceRNA network.

Supplementary Table 2 | One hundred and nineteen DEmiRNA–DEmRNA relationships in the ceRNA network.

Supplementary Table 3 | Ninety six DEproteins between ICH and sham groups.

REFERENCES

Beermann, J., Piccoli, M. T., Viereck, J., and Thum, T. (2016). Non-coding RNAs in development and disease: background, mechanisms, and therapeutic approaches. *Physiol. Rev.* 96, 1297–1325. doi: 10.1152/physrev.00041.2015

Cao, F., Jiang, Y., Wu, Y., Zhong, J., Liu, J., Qin, X., et al. (2016). Apolipoprotein E-Mimetic COG1410 reduces acute vasogenic edema following traumatic brain injury. *J. Neurotrauma* 33, 175–182. doi: 10.1089/neu.2015.3887

Chaudhry, S. R., Guresir, E., Vatter, H., Kinfe, T. M., Dietrich, D., Lamprecht, A., et al. (2017). Aneurysmal subarachnoid hemorrhage lead to systemic upregulation of IL-23/IL-17 inflammatory axis. *Cytokine* 97, 96–103. doi: 10.1016/j.cyto.2017.05.025

Dou, Z., Yu, Q., Wang, G., Wu, S., Reis, C., Ruan, W., et al. (2020). Circular RNA expression profiles alter significantly after intracerebral hemorrhage in rats. *Brain Res.* 1726:146490. doi: 10.1016/j.brainres.2019.146490

Duan, X., Wen, Z., Shen, H., Shen, M., and Chen, G. (2016). Intracerebral hemorrhage, oxidative stress, and antioxidant therapy. *Oxid. Med. Cell Longev.* 2016:1203285. doi: 10.1155/2016/1203285

Fang, H., Wang, P. F., Zhou, Y., Wang, Y. C., and Yang, Q. W. (2013). Toll-like receptor 4 signaling in intracerebral hemorrhage-induced inflammation and injury. *J. Neuroinflammat.* 10:27. doi: 10.1186/1742-2094-10-27

Gong, L., Manaenko, A., Fan, R., Huang, L., Enkhjargal, B., McBride, D., et al. (2018). Osteopontin attenuates inflammation via JAK2/STAT1 pathway in hyperglycemic rats after intracerebral hemorrhage. *Neuropharmacology* 138, 160–169. doi: 10.1016/j.neuropharm.2018.06.009

Griffiths-Jones, S., Grocock, R. J., van Dongen, S., Bateman, A., and Enright, A. J. (2006). miRBase: microRNA sequences, targets and gene nomenclature. *Nucleic Acids Res.* 34, D140–D144. doi: 10.1093/nar/gkj112

Jagiella, J., Dardiotis, E., Gasowski, J., Pera, J., Dziedzic, T., Klimkowicz-Mrowiec, A., et al. (2014). The FGA Thr312Ala polymorphism and risk of intracerebral haemorrhage in polish and greek populations. *Neurol. Neurochir. Pol.* 48, 105–110. doi: 10.1016/j.pjnns.2013.12.004

Jia, J., Zhang, M., Li, Q., Zhou, Q., and Jiang, Y. (2018). Long noncoding ribonucleic acid NKILA induces the endoplasmic reticulum stress/autophagy pathway and inhibits the nuclear factor-k-gene binding pathway in rats after intracerebral hemorrhage. *J. Cell Physiol.* 233, 8839–8849. doi: 10.1002/jcp.26798

Jiang, Y., Ma, J., Li, H., Liu, Y., and You, C. (2015). Effect of apolipoprotein C3 genetic polymorphisms on serum lipid levels and the risk of intracerebral hemorrhage. *Lipids Health Dis.* 14:48. doi: 10.1186/s12944-015-0047-49

Kim, J. M., Moon, J., Yu, J. S., Park, D. K., Lee, S. T., Jung, K. H., et al. (2019). Altered long noncoding RNA profile after intracerebral hemorrhage. *Ann. Clin. Transl. Neurol.* 6, 2014–2025. doi: 10.1002/acn3.50894

Lan, X., Han, X., Liu, X., and Wang, J. (2019). Inflammatory responses after intracerebral hemorrhage: from cellular function to therapeutic targets. *J. Cereb. Blood Flow Metab.* 39, 184–186. doi: 10.1177/0271678x18805675

Lattanzi, S., Cagnetti, C., Provinciali, L., and Silvestrini, M. (2016). Neutrophil-to-Lymphocyte ratio predicts the outcome of acute intracerebral hemorrhage. *Stroke* 47, 1654–1657. doi: 10.1161/strokeaha.116.013627

Liang, S. D., Ma, L. Q., Gao, Z. Y., Zhuang, Y. Y., and Zhao, Y. Z. (2018). Granulocyte colony-stimulating factor improves neurological function and angiogenesis in intracerebral hemorrhage rats. *Eur. Rev. Med. Pharmacol. Sci.* 22, 2005–2014. doi: 10.26355/eurrev_201804_14729

Liu, Z., Zhang, R., Chen, X., Yao, P., Yan, T., Liu, W., et al. (2019). Identification of hub genes and small-molecule compounds related to intracerebral hemorrhage with bioinformatics analysis. *PeerJ* 7:e7782. doi: 10.7717/peerj.7782

Matsui, M., and Corey, D. R. (2017). Non-coding RNAs as drug targets. *Nat. Rev. Drug Discov.* 16, 167–179. doi: 10.1038/nrd.2016.117

Morotti, A., Phuah, C. L., Anderson, C. D., Jessel, M. J., Schwab, K., Ayres, A. M., et al. (2016). Leukocyte count and intracerebral hemorrhage expansion. *Stroke* 47, 1473–1478. doi: 10.1161/strokeaha.116.013176

Park, H. J., Ji, P., Kim, S., Xia, Z., Rodriguez, B., Li, L., et al. (2018). 3' UTR shortening represses tumor-suppressor genes in trans by disrupting ceRNA crosstalk. *Nat. Genet.* 50, 783–789. doi: 10.1038/s41588-018-0118-118

Robinson, M. D., McCarthy, D. J., and Smyth, G. K. (2010). edgeR: a Bioconductor package for differential expression analysis of digital gene expression data. *Bioinformatics* 26, 139–140. doi: 10.1093/bioinformatics/btp616

Tay, Y., Rinn, J., and Pandolfi, P. P. (2014). The multilayered complexity of ceRNA crosstalk and competition. *Nature* 505, 344–352. doi: 10.1038/nature12986

Wang, J. Z., Du, Z., Payattakool, R., Yu, P. S., and Chen, C. F. (2007). A new method to measure the semantic similarity of GO terms. *Bioinformatics* 23, 1274–1281. doi: 10.1093/bioinformatics/btm087

Xie, J., Wang, B., Wang, L., Dong, F., Bai, G., and Liu, Y. (2016). Intracerebral and intravenous transplantation represents a favorable approach for application of human umbilical cord mesenchymal stromal cells in intracerebral hemorrhage rats. *Med. Sci. Monit.* 22, 3552–3561. doi: 10.12659/msm.900512

Yang, G., and Shao, G. F. (2016). Elevated serum IL-11, TNF alpha, and VEGF expressions contribute to the pathophysiology of hypertensive intracerebral hemorrhage (HICH). *Neurol. Sci.* 37, 1253–1259. doi: 10.1007/s10072-016-2576-z

Yang, S., Nakamura, T., Hua, Y., Keep, R. F., Younger, J. G., He, Y., et al. (2006). The role of complement C3 in intracerebral hemorrhage-induced brain injury. *J. Cereb. Blood. Flow Metab.* 26, 1490–1495. doi: 10.1038/sj.jcbfm.9600305

Yin, Y., Ge, H., Zhang, J. H., and Feng, H. (2017). Targeting vascular neural network in intracerebral hemorrhage. *Curr. Pharm. Des.* 23, 2197–2205. doi: 10.2174/1381612822666161027122821

Yu, G., Li, F., Qin, Y., Bo, X., Wu, Y., and Wang, S. (2010). GOSemSim: an R package for measuring semantic similarity among GO terms and gene products. *Bioinformatics* 26, 976–978. doi: 10.1093/bioinformatics/btq064

Yu, G., Wang, L. G., Han, Y., and He, Q. Y. (2012). clusterProfiler: an R package for comparing biological themes among gene clusters. *Omics* 16, 284–287. doi: 10.1089/omi.2011.0118

Zhang, J., Dong, B., Hao, J., Yi, S., Cai, W., and Luo, Z. (2019). LncRNA Snhg3 contributes to dysfunction of cerebral microvascular cells in intracerebral hemorrhage rats by activating the TWEAK/Fn14/STAT3 pathway. *Life Sci.* 237:116929. doi: 10.1016/j.lfs.2019.116929

Zhang, L., and Wang, H. (2019). Long Non-coding RNA in CNS Injuries: a new target for therapeutic intervention. *Mol. Ther. Nucleic Acids* 17, 754–766. doi: 10.1016/j.omtn.2019.07.013

Zhao, X., Ting, S. M., Liu, C. H., Sun, G., Kruzel, M., Roy-O'Reilly, M., et al. (2017). Neutrophil polarization by IL-27 as a therapeutic target for intracerebral hemorrhage. *Nat. Commun.* 8:602. doi: 10.1038/s41467-017-00770-777

Zhou, Y., Wang, Y., Wang, J., Anne Stetler, R., and Yang, Q. W. (2014). Inflammation in intracerebral hemorrhage: from mechanisms to clinical translation. *Prog. Neurobiol.* 115, 25–44. doi: 10.1016/j.pneurobio.2013.11.003

Conflict of Interest: The authors declare that the research was conducted in the absence of any commercial or financial relationships that could be construed as a potential conflict of interest.

frontiers in Cellular Neuroscience

MINI REVIEW
published: 10 February 2021
doi: 10.3389/fncel.2021.628010

D1R- and D2R-Medium-Sized Spiny Neurons Diversity: Insights Into Striatal Vulnerability to Huntington's Disease Mutation

*Guendalina Bergonzoni, Jessica Döring and Marta Biagioli**

NeuroEpigenetics Laboratory, Department of Cellular, Computational and Integrative Biology (CIBIO), University of Trento, Trento, Italy

Huntington's disease (HD) is a devastating neurodegenerative disorder caused by an aberrant expansion of the CAG tract within the exon 1 of the *HD* gene, *HTT*. HD progressively impairs motor and cognitive capabilities, leading to a total loss of autonomy and ultimate death. Currently, no cure or effective treatment is available to halt the disease. Although the *HTT* gene is ubiquitously expressed, the striatum appears to be the most susceptible district to the HD mutation with Medium-sized Spiny Neurons (MSNs) (D1R and D2R) representing 95% of the striatal neuronal population. Why are striatal MSNs so vulnerable to the HD mutation? Particularly, why do D1R- and D2R-MSNs display different susceptibility to HD? Here, we highlight significant differences between D1R- and D2R-MSNs subpopulations, such as morphology, electrophysiology, transcriptomic, functionality, and localization in the striatum. We discuss possible reasons for their selective degeneration in the context of HD. Our review suggests that a better understanding of cell type-specific gene expression dysregulation within the striatum might reveal new paths to therapeutic intervention or prevention to ameliorate HD patients' life expectancy.

Keywords: Huntington's disease, neurodegeneration, striatum, medium-sized spiny neurons, selective vulnerability, D1R, D2R

OPEN ACCESS

Edited by:
Giordano Lippi, The Scripps Research Institute, United States

Reviewed by:
Emmanuel Valjent, Centre National de la Recherche Scientifique (CNRS), France
Laurie Galvan, INSERM U1084 Laboratoire de Neurosciences Expérimentales et Cliniques, France

***Correspondence:**
Marta Biagioli
marta.biagioli@unitn.it

Specialty section:
This article was submitted to Cellular Neurophysiology, a section of the journal Frontiers in Cellular Neuroscience

Received: *10 November 2020*
Accepted: *20 January 2021*
Published: *10 February 2021*

Citation:
Bergonzoni G, Döring J and Biagioli M (2021) D1R- and D2R-Medium-Sized Spiny Neurons Diversity: Insights Into Striatal Vulnerability to Huntington's Disease Mutation. Front. Cell. Neurosci. 15:628010. doi: 10.3389/fncel.2021.628010

HUNTINGTON'S DISEASE: GENETIC, CLINIC, AND PATHOLOGIC CHARACTERISTICS

Huntington's disease (HD) is a rare, progressive, neurodegenerative disorder characterized by devastating motor, cognitive, and psychiatric symptoms. The monogenic, autosomal dominant disease is caused by a CAG repeat expansion in exon 1 of the HD gene (*HTT*), encoding for the huntingtin protein (MacDonald et al., 1993). The worldwide prevalence of HD is estimated to be 2.71 per 100,000 individuals (Pringsheim et al., 2012) and the average age of onset is between 30 and 50 years (Roos, 2010). So far, no treatments are available to block or slow-down the HD pathologic process, albeit mutant huntingtin lowering strategies are currently tested in clinical trials as promising therapeutic (Hoffmann-La Roche, 2020; Wave Life Sciences Ltd, 2020).

Although mutant huntingtin protein is ubiquitously expressed in all human districts, the brain, wherein the striatum, is the primary deteriorating region in HD (Saudou and Humbert, 2016; Ghosh and Tabrizi, 2018). Most striatal functions are mediated by inhibitory Medium-sized

Spiny Neurons (MSNs), which comprise 95% of neurons in this area with the remaining being interneurons. There are two subtypes of MSNs differentiable by the expression of the D1 and D2 dopamine families' receptors, constituting the direct and indirect pathways, respectively (Lanciego et al., 2012). The dorsal striatum (neostriatum) is the input module to the cortico-basal ganglia-thalamo-cortical loop (CBGTC), a neuronal circuit necessary for voluntary movement control. In the direct pathway, glutamatergic cortical terminals activate dopamine receptor 1 (D1R)-expressing MSNs, which exert their inhibitory effect on the globus pallidus internal segment (GPi) (*Entopeduncular nucleus*, in rodents). Inhibitory neurons in this area, project to the ventral anterior/lateral motor thalamus. Thus, the stimulation of D1R-MSNs has a net excitatory effect on the motor thalamus, allowing the final switch of the motor cortex and the stimulation of skeletal muscles. On the other hand, in the indirect pathway, dopamine receptor 2 (D2R)-expressing, inhibitory MSNs are also stimulated by glutamate release of cortical terminals. D2R neurons connect to the GP through an indirect loop, such that, they first project to and inhibit the globus pallidus external segment (GPe). These neurons firstly connect to the subthalamic nucleus exciting the area through glutamate release. Finally, the excitation of inhibitory GPi neurons produces motor thalamus repression (Alexander et al., 1986; Bolam et al., 2000). Dysfunction and death of striatal MSNs are the main causes for the motor disorders associated with HD (Ghosh and Tabrizi, 2018). In this review, we provide an overview of key pathological pathways leading to striatal degeneration. Furthermore, we describe general characteristics and physiological differences between D1R- and D2R-MSNs and highlight distinct morphological and functional alterations of MSNs during the disease. Our review emphasizes the importance of understanding cell-type specific physiological differences contributing to striatal vulnerability which may provide insights toward new avenues of therapeutic intervention.

PATHOGENIC MECHANISMS OF THE HD MUTATION IN STRIATAL DISTRICTS

Altered Cellular and Molecular Pathways

Because of unavailability of pre-symptomatic HD brain tissues, the reasons behind selective striatal vulnerability in HD were mostly investigated using animal models. In fact, the basal ganglia and, particularly, the cortico-striatal motor circuitry, appears to be conserved in mouse, minipig, and primates (Vodicka et al., 2005; Stephenson-Jones et al., 2011; Balsters et al., 2020). Thus, genetically engineered models, bearing normal or pathological CAG repeat lengths, have revealed important pathogenic mechanisms of the HD mutation (Menalled, 2005; Lerner et al., 2012; Peng et al., 2016; **Table 1** and **Figures 1A,B**). Nevertheless, several salient features of human HD pathology–such as overt striatal atrophy, cortical degeneration, and onset of choreic movements–failed to fully replicate in animal models of the disease (Rubinsztein, 2002).

Huntington's disease *post-mortem* brains revealed that MSNs exhibit altered morphology, with proliferative changes–recurving and branching of dendrites and increased number and size of spines–since early stages of the disease. Degenerative alterations–truncation of the dendritic arborization and loss of spines–are characteristics of severe grades (Ferrante et al., 1991; **Figure 1A**). MSNs of 3 months old R6/2 N-terminal transgenic line–which overexpress human mutant *HTT* exon 1 (Mangiarini et al., 1996)- and of 20–26 months old Hdh^{Q140} knock-in mice–with the endogenous mouse *Htt* gene engineered to express a longer polyglutamine tract (Menalled et al., 2003)- do present similar decreased spine density and size of dendritic arborization (Klapstein et al., 2001; Lerner et al., 2012; **Figure 1B**).

Other studies in *post-mortem* brains also highlighted mutant huntingtin aggregates within neuronal MSNs nuclei (DiFiglia et al., 1997; Rüb et al., 2016; **Figure 1A**). Similarly, mutant huntingtin diffuse nuclear localization could be visualized at earlier ages (3 months) in MSNs of zQ175 knock-in mouse models (Menalled et al., 2012), while clear nuclear inclusions can be spotted only at later stages (8–12 months old) (Carty et al., 2015; **Figure 1B**).

Most observations point toward toxic gain-of-function for the pathogenic mechanisms. However, some data suggest that a loss-of-function mechanism should not be completely ruled out (Borrell-Pagès et al., 2006). Specifically, mutant huntingtin impairs the brain-derived neurotrophic factor-tropomyosin-related kinase receptor type B (BDNF-TrkB) signaling in striatal neurons (**Table 1**). This deficiency plays a pivotal role in dysfunction and death of MSNs and may represent a therapeutic target for HD treatment. Accordingly, several studies examined whether increasing levels of BDNF may be a viable strategy (Baydyuk and Xu, 2014). R6/2 mice, perfused with BDNF at 4 and 13 weeks of age showed less severe neurological dysfunction (Giampà et al., 2013), and significantly reduced motor coordination impairment (Giralt et al., 2011). However, the administration of citalopram, an antidepressant believed to increase BDNF levels, failed to improve motor and psychiatric symptoms in HD patients (Beglinger et al., 2014).

Recently, a significant increase in reactive oxygen species (ROS) production was described in the striatum of HD patients (Kumar and Ratan, 2016). ROS, produced by excitotoxicity or mitochondrial dysfunction, are important mediators of cell death (Gu et al., 1996; Browne et al., 1997). Coherently, mutant huntingtin seems to interfere with mitochondrial functioning (**Table 1**). Lymphoblasts from HD patients present mitochondrial fragmentation and cristae alterations (Costa et al., 2010), while cortical specimens from grade 3–4 HD patients display downregulation of complexes II, III, and IV of the oxidative phosphorylation (OXPHOS) pathway (Tabrizi et al., 2000; Shirendeb et al., 2011; Liot et al., 2017; **Figure 1A**). Energy metabolism alterations were also detected in R6/2 transgenic mice (Tabrizi et al., 2000), in Hdh^{Q111} knock-in models with decreased cAMP levels in the striatum at 10 weeks of age (Gines et al., 2003; Mochel et al., 2012) and, finally, precursor cells from striatal primordia of knock-in mice (Trettel et al., 2000) show significantly reduced respiration and ATP production (**Figure 1B**). Thus, considering that striatal neurons require higher amounts of ATP to maintain their hyperpolarized resting membrane potential (Hammond, 2015), it is conceivable that they might result more sensitive to mitochondrial dysfunction.

TABLE 1 | Pathogenic mechanisms correlated with striatal degeneration in Huntington's Disease.

Altered Mechanism*	Cellular and molecular phenotype*	References
BDNF-TrkB[1] signaling[a]	Decreased BDNF synthesis and transport	Zuccato et al., 2003; Gauthier et al., 2004
Glutamate reuptake[b]	Glutamate excitotoxicity: decreased expression of, NMDA, AMPA, kainate, and excitatory amino acid transporter 2	Cha, 2007; Rebec, 2018
ROS[2] production[b]	Increased: reduced expression of dopamine receptor D2R, nitric oxide synthase, and glutamate transporter GLT1	Cha, 2007; Kumar and Ratan, 2016
Mitochondrial functioning	Dysfunction: altered calcium homeostasis[c,d], reduced ATP synthesize[e], impaired mitochondrial trafficking[e], mitochondrial fragmentation, and crestae alterations[d] Dysregulation of electron transport chain genes[b,c] and consequent alteration in OXPHOS[3] complexes[b]	Panov et al., 2002; Seong et al., 2005; Costa et al., 2010; Li et al., 2010; Shirendeb et al., 2011; Liot et al., 2017
Gene expression[a,b,d,e,f]	Downregulated genes: neurotransmitter receptors, neurotransmitters, intracellular signaling molecules, and cytoskeletal/structural proteins Transcriptional changes also observed in glial cells	Luthi-Carter et al., 2000; Hodges et al., 2006; Cha, 2007; Tang et al., 2011; Ament et al., 2017
miRNA[4] biogenesis and expression[d]	miRNA and miRNA biogenesis-related molecules are upregulated at earlier stages and downregulated at later stages of HD	Johnson et al., 2008; Packer et al., 2008; Lee S.T. et al., 2011
Alternative splicing	Aberrant: dysregulated *TRANS*-splicing factors (PTBP1, SRSF6)[b]. Mutant *HTT* mRNA sequesters spliceosome components, dysregulating splicing, and causing toxicity[g]	Sathasivam et al., 2013; Lin et al., 2016; Schilling et al., 2019
Epigenetics	Preferentially closed chromatin state and transcriptional repression: reduced histone acetylation, increased histone methylation[e,f], decreased AcH3 levels, decreased number of genes bound by AcH3[f], increased H3K27me3 and decreased H3K4me3[e]	Ferrante et al., 2003; Stack et al., 2007; Luthi-Carter et al., 2010; Seong et al., 2010; McFarland et al., 2012; Biagioli et al., 2015; Hervás-Corpión, 2018; Pearl et al., 2020
Dopamine signaling[b]	Altered dopamine signaling has been associated with behavioral alterations observed in HD. Dopamine levels are increased at early stage and decreased at later stage	Chen et al., 2013; Koch and Raymond, 2019
Somatic CAG instability[b]	Increased in striatum and cerebral cortex	Telenius et al., 1994; Swami et al., 2009
Electrophysiology[d]	Changes in the balance of excitatory and inhibitory inputs to the direct and indirect pathway MSNs	Galvan et al., 2012

**Abbreviations are indicated with superscript numbers, models used in the studies with superscript letters.*
[1] *Brain-derived neurotrophic factor-tropomyosin-related kinase receptor type B.*
[2] *Reactive oxygen species.*
[3] *Oxidative phosphorylation.*
[4] *MicroRNA.*
[a] *Knock-in mouse cell line (endogenous mouse Htt gene engineered to express a longer polyglutamine tract).*
[b] *HD patients.*
[c] *HD patients' lymphoblastoid.*
[d] *Full-length mouse model (overexpression of full-length mutant huntingtin).*
[e] *Knock-in mouse model.*
[f] *R6/2 N-terminal mouse model (overexpression of human mutant HTT exon 1).*
[g] *Cell-line overexpressing mutant huntingtin.*

Initial studies on HD mouse models and later on HD *post-mortem* striatum revealed that mutant huntingtin causes transcriptional dysregulation of signaling pathways, neuronal, gliosis, and neuroinflammatory genes. Moreover, studies on Hdh^{Q111} knock-in models also demonstrated that transcriptional alterations can already be detected at 9 weeks of age (Cha, 2000; Luthi-Carter et al., 2000; Hodges et al., 2006; Ament et al., 2017; **Table 1**). Interestingly, striatal transcriptional changes are among the earliest detectable phenotypes in HD mouse models (Langfelder et al., 2016; Ament et al., 2017, 2018), which conform with HD patients (Seredenina and Luthi-Carter, 2012; Labadorf et al., 2015; **Figures 1A,B**).

Transcriptional dysregulation of synaptic proteins, such as complexin 2, dynamin, and PACSIN 1, correlates with neuronal morphological changes and reduction in the number of axonal fibers in early-stage HD patients (DiProspero et al., 2004; Han et al., 2010; **Figure 1A**). Furthermore, altered microRNA biogenesis and expression was reported in HD *post-mortem* tissues and in YAC128 murine models of full-length mutant huntingtin overexpression (Johnson et al., 2008; Packer et al., 2008; Lee S.T. et al., 2011; **Table 1**). Notably, mutant huntingtin can directly or indirectly compromise the epigenetic status of brain cells (**Table 1**), at least in part explaining the observed transcriptional dysregulation (Stack et al., 2007; Seong et al., 2010; McFarland et al., 2012; Biagioli et al., 2015; Hervás-Corpión, 2018; Pearl et al., 2020).

Recent RNAseq analysis of HD patients' motor cortex revealed that mutant huntingtin interferes with RNA processing and induces aberrant alternative splicing (**Table 1**), affecting the expression levels of *TRANS*-splicing factors and/or trapping specific RNA binding proteins (Sathasivam et al., 2013; Lin et al., 2016; Schilling et al., 2019).

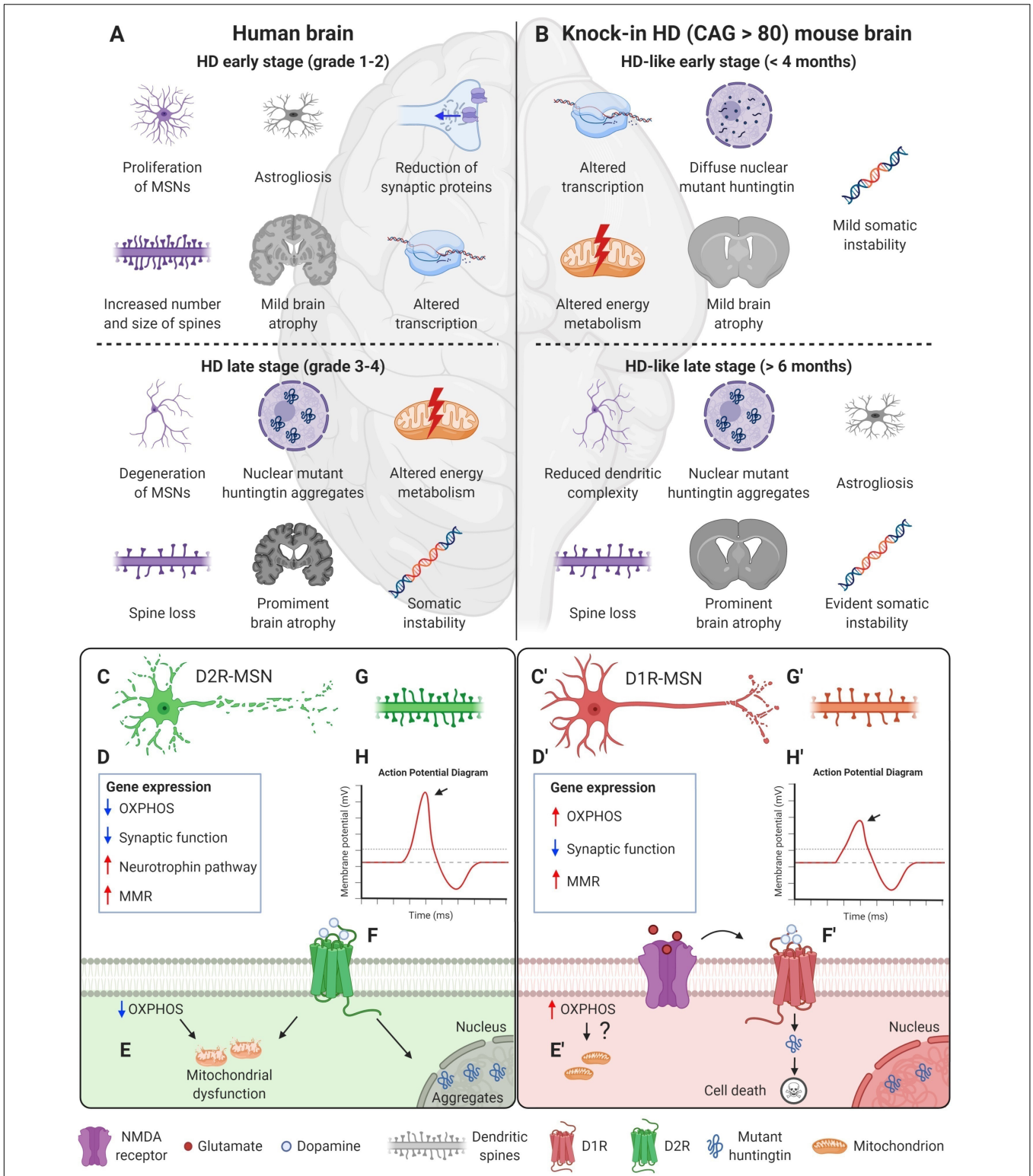

FIGURE 1 | HD profoundly alters the striatum and MSNs in both patients and mouse models, upper panel. **(A)** Schematic representation of HD patient brain. At the early stage of the disease (grade 1–2), patients already manifest mild brain atrophy and astrogliosis (Ross and Tabrizi, 2011; Rüb et al., 2016). MSNs undergo proliferative expansion and show increased number and size of spines (Ferrante et al., 1991). At the molecular level, a reduction of synaptic proteins and alterations in gene transcription are detected (DiProspero et al., 2004; Hodges et al., 2006). These changes continue during advanced stages (grade 3–4), when brain atrophy becomes prominent (Rüb et al., 2016). MSNs undergo degenerative changes and spine loss, and mutant huntingtin aggregates can be detected within nuclei

(Continued)

FIGURE 1 | Continued
(Ferrante et al., 1991; DiFiglia et al., 1997; Rüb et al., 2016). Altered energy metabolism and somatic instability of the CAG tract are detected (Gines et al., 2003; Swami et al., 2009; Liot et al., 2017). **(B)** Knock-in HD mouse models (CAG > 80) faithfully recapitulate the human HD mutation and mimic several aspects of the human condition. At early age (<4 months), mice show mild brain atrophy (Peng et al., 2016) and diffuse accumulation of mutant huntingtin within MSNs nuclei (Carty et al., 2015). At the molecular level, energy metabolism and transcription are altered (Gines et al., 2003; Mochel et al., 2012; Ament et al., 2017). Somatic instability is already detectable at this stage (Pinto et al., 2013). At later stages (>6 months), brain atrophy becomes more prominent and astrogliosis could be detected (Menalled, 2005; Lerner et al., 2012; Peng et al., 2016). MSNs show reduced dendritic complexity and spine loss, and nuclear mutant huntingtin aggregates inclusions (Lerner et al., 2012; Carty et al., 2015). The molecular alterations proceed and somatic instability becomes particularly evident (Lee J.M. et al., 2011). Specific pathways and phenotypes developed by D1R- and D2R-MSNs upon expression of mutant huntingtin, lower panel. **(C,C′)** Striatopallidal neurons (D2R-MSNs) are affected earlier than striatonigral ones (D1R-MSNs) by HD mutation (Sapp et al., 1995). **(D,D′)** Gene expression profiling on R6/2 mice revealed that neurotrophin pathway is specifically upregulated in D2R-MSNs, while mismatch repair (MMR) and synaptic functioning pathways seem to be altered in both MSNs subpopulations (Lee et al., 2020). **(E)** In both R6/2 and zQ175 mice, oxidative phosphorylation (OXPHOS) downregulation observed in D2R cells contribute to mitochondrial dysfunction (Lee et al., 2020), while **(E′)** OXPHOS genes are upregulated in D1R cells, possibly suggesting a homeostatic response (Lee et al., 2020). **(F)** In mice and rat striatal cell cultures overexpressing mutant huntingtin, D2R stimulation enhances mutant huntingtin aggregation and mitochondrial dysfunction (Charvin et al., 2005; Benchoua et al., 2008). **(F′)** In *Hdh*^{Q111} models, dopamine and glutamate synergistically enhance MSNs sensitivity to mutant huntingtin toxicity through D1R activation (Paoletti et al., 2008). **(G,G′)** In 12 months old zQ175 KI mice, D1R neurons show proliferative expansion of the dendritic arborization and a significant reduction in the density of thin spines, while D2R neurons do not show significant differences (Goodliffe et al., 2018). **(H,H′)** In the same model, only D1R neurons exhibit reduced rheobase and action potential amplitude (arrows). Figure created with BioRender.com.

Dopaminergic Signaling

Dopaminergic inputs from the *substantia nigra* are crucial for proper signaling of striatal MSNs in the basal ganglia circuit. Indeed, *substantia nigra pars compacta* (SNc) modulates the direct and indirect pathways by releasing dopamine, which has an excitatory effect on D1R and an inhibitory one on D2R. Consequently, dopamine excites the direct pathways and inhibits the indirect pathway, producing an overall stimulation of the motor activity (Leisman et al., 2013).

Studies on HD patients suggest that early stages of the disease are characterized by an increase in dopamine levels, contributing to choreiform symptoms. This might be due to the inhibitory effect of MSNs projecting to the SNc, which, in early stages, may produce hyperactivation of this pathway. Conversely, as disease progresses, dopamine levels decrease–possibly because of dopaminergic nigrostriatal terminals loss–accounting for the late akinetic stage (Chen et al., 2013; Koch and Raymond, 2019; **Table 1**). Accordingly, studies on both patients and mouse models confirmed an increase in dopamine release and tyrosine hydroxylase levels in early HD, followed by a reduction of the same parameters in advanced disease conditions (Koch and Raymond, 2019).

Within striatal MSNs, a modulatory mechanism between dopamine and glutamate was observed. On one hand, dopamine binding to D1R stimulates surface expression of NMDA and AMPA receptors, resulting in an increased responsiveness of D1R-MSNs to glutamate release. On the other hand, dopamine binding to D2R decreases surface AMPA receptors, reducing their glutamate excitability (Surmeier et al., 2007). Interestingly, both in patients and murine models, glutamate signaling follows the same pattern of dopamine alterations, being increased during HD early stages and decreased at advanced stages (Chen et al., 2013), thus suggesting a cross-talk between these two neurotransmitters.

Somatic CAG Instability

The expanded CAG repeat in the mutant huntingtin gene is unstable, undergoing progressive length increases over time and resulting in somatic mosaicism in selective human body districts (**Table 1**). Specifically, it is possible that high level of somatic CAG instability in the striatum and cerebral cortex (Telenius et al., 1994; Swami et al., 2009; Lee J.M. et al., 2011) contributes to HD pathology (**Figures 1A,B**). Knock-out of DNA mismatch repair (MMR) proteins in *Hdh*^{Q111} knock-in mice showed that Msh2/3/6, Mlh1, and Mlh3 are modifiers of somatic CAG instability (Wheeler, 2003; Dragileva et al., 2009; Pinto et al., 2013). Importantly, genome-wide association analysis of a cohort of 9,000 HD patients confirmed MMR genes and specifically *MLH1* as crucial HD genetic modifiers (Lee et al., 2015, 2019).

D1R- VERSUS D2R-MSNs: GENERAL CHARACTERISTICS AND PHYSIOLOGICAL DIFFERENCES

Medium-sized spiny neurons are characterized by a small to medium cellular body size (10–15 μm in diameter) and a radially oriented large dendritic tree covered by spines. Upon dopamine binding, D1R activates adenylyl cyclase (AC) signaling, leading to an excitatory effect, whereas D2R represses AC through Gi-protein signaling, resulting in inhibition (Lanciego et al., 2012). Striatopallidal (D2R) and striatonigral (D1R) neurons exhibit a random distribution in the murine rostral, dorsal striatum. However, a regionalization is observed in the caudal part, near the GPe, which comprises almost exclusively D1R-MSNs (Gangarossa et al., 2013). It is well accepted that D2R-MSNs are affected earlier than D1R-MSNs (Sapp et al., 1995; **Figures 1C,C′**) and, accordingly, GPe-targeting MSNs show substantial loss in patients at early stages of the disease (Albin et al., 1992). The lack of inhibition of the GPe by D2R-MSNs results in an excessive activation of the pallidal neurons, leading to choreiform movements observed in HD (Hedreen and Folstein, 1995). Nevertheless, in the latest stages, GPi-targeting MSNs of the direct pathway undergo marked decline, resulting in akinetic movements and rigidity (Deng et al., 2004; Lanciego et al., 2012).

Morphologically, striatonigral neurons show more primary dendrites and a more extended arborization than

striatopallidal ones. Experimental simulation suggested that different dendritic areas may contribute to the divergent electrophysiological properties. Indeed, experiments performed on brain slices from D1R and D2R-EGFP BAC transgenic mice demonstrated that D1R neurons display a more hyperpolarized resting membrane potential and a greater rheobase (Gertler et al., 2008).

Accordingly, recent experiments using *Drd1a*-td Tomato mice revealed an increased intrinsic excitability for D2R-MSNs compared to D1R-MSNs. This might be due to the different rheobase, which is decreased in D2R neurons (Willett et al., 2019). Previous studies, however, pointed to a differential role of M1 muscarinic receptors activation, which downregulates Kir channel currents in striatopallidal MSNs, but not in striatonigral ones (Shen et al., 2007).

Considering that increased release of glutamate might contribute to MSNs degeneration (DiFiglia, 1990; Cepeda et al., 2007), it is noteworthy that D2R-MSNs receive more cortical inputs, mainly from pyramidal neurons (Francelle et al., 2014). Moreover, cortical axons making synapses with D2R-MSNs are larger in size, compared with the ones from D1R neurons (Lei, 2004). Altogether, these characteristics expose them to higher excitotoxicity, possibly reflecting on their greater susceptibility to cell death (**Table 1**). D2R-, but not D1R-, MSNs can form the protein complex with β-arrestin2, Akt, and protein phosphatase 2A (PP2A), which, in turn, reduces the phosphorylation of glycogen synthase kinase-3 (GSK3) (Harrison et al., 2013). GSK3 plays crucial roles in neuronal function, synapse formation, and neurite outgrowth (Beaulieu et al., 2004, 2005). Since both Rhes and Akt have been demonstrated to interact with and modulate mutant huntingtin toxicity, the Akt/β-Arrestin 2PP2A/GSK3 pathway may represent an additional mediator of D2R specific selective vulnerability (Colin et al., 2005; Lee et al., 2014).

Furthermore, TrkB is unequally expressed in striatal MSNs, with higher level in D2R-MSNs (Baydyuk and Xu, 2014). Thus, the aberrant BDNF-TrkB signaling caused by mutant huntingtin might have stronger effects in these cells (**Table 1**). Analysis of mouse striatum using single cell RNA sequencing (scRNA-seq) unveiled additional transcriptional differences between D1R- and D2R-MSNs. Further complexity emerged following the discovery of region-specific molecular markers for dorsal D2R neurons (Puighermanal et al., 2020), the identification of discrete subgroups of D1R and D2R neurons (Gokce et al., 2016) and of a possible third subtype of MSNs, which may have unique characteristics (Gokce et al., 2016). The existence of a third subpopulation of MSNs was also reported by Saunders et al. (2018), who observed a cluster of neurons in the striatum of C57BL6/N, co-expressing *Drd1* and *Adora2a*, named as "eccentric" MSNs. It is still premature to point to a clear connection between these physiological differences and the unequal cellular vulnerability to HD of the two MSNs subpopulations. Nevertheless, evaluation and integration of these single-cell analyses with other molecular aspects, such as alternative splicing, somatic mosaicism, and epigenetics differences between MSNs subtypes (**Table 1**), will be instrumental to understand the molecular mechanisms impinging on different vulnerability of D1R- and D2R-MSNs.

DO D1R- AND D2R-MSNs DIFFERENTIALLY RESPOND TO THE HD MUTATION?

Recent studies on HD patients described rostro-caudal and dorso-ventral degenerative gradients. Specifically, the caudal striatum displayed greater neuronal death compared to the rostral part, while the dorsal-medial area seemed to degenerate faster compared to the ventral-lateral striatum (Morigaki and Goto, 2017). Although the contribution of MSNs' physiological regionalization to selective vulnerability in HD is not fully dissected, some unequal distribution of the subclasses (Gangarossa et al., 2013) and subgroups (Gokce et al., 2016; Puighermanal et al., 2020) of MSNs might play a role.

To dissect why D1R- and D2R-MSNs are differentially affected by HD, Lee et al. (2020) highlighted thousands dysregulated protein-coding genes implicated in OXPHOS, synaptic functioning and circadian entrainment by using translating ribosome affinity purification and snRNA-seq of D1R and D2R neurons of HD patients and mouse models (R6/2 and zQ175DN, a knock-in zQ175 line without neomycin cassette) (Franich et al., 2019). Strikingly, downregulation of OXPHOS and upregulation of neurotrophin pathway genes in D2R neurons indicated a cell-type specific response to the disease (**Figure 1D**). Notably, Lee et al. (2020) demonstrated that OXPHOS genes downregulation causes mitochondrial dysfunction (**Figure 1E**) and mitochondrial RNA release in the cytosol, which, in turn, activates protein kinase R and cellular toxicity through the interferon pathways. Coherently, it was shown previously that D2R contributes to mutant huntingtin aggregation and mitochondrial impairment (Charvin et al., 2005, 2008; Benchoua et al., 2008; **Figure 1F**). Moreover, the upregulation of MMR genes, implicated in somatic instability of the CAG tract (**Table 1**), in both D1R- and D2R-MSNs supported a possible predisposing feature for selective degeneration (**Figures 1D,D′**). However, additional studies will be needed to correlate these findings with HD progression and MSNs vulnerability (Lee et al., 2020).

On the other hand, analysis on YAC128 and BACHD mouse models demonstrated that glutamate transmission was increased in D1R neurons at early disease and decreased in both D1R and D2R cells at advanced stages (André et al., 2011). Since a modulatory mechanism between dopamine and glutamate was observed within healthy striatal MSNs (Surmeier et al., 2007), dopamine and glutamate might synergistically enhance sensitivity to mutant huntingtin toxicity through D1R but not D2R activation (Paoletti et al., 2008; **Figure 1F′**). Similarly, in a different study using 12 months old zQ175 knock-in models, striatonigral neurons showed more prominent morphological and electrophysiological changes than striatopallidal ones (Goodliffe et al., 2018; **Figures 1G′,H′**). While this view is in contrast with the well-established hypothesis that D2R neurons are selectively damaged in early stages of HD, nonetheless,

these findings might highlight the presence of a compensatory mechanism in D1R neurons. It is interesting to note that, in the knock-in mouse model zQ175DN, Lee et al. (2020) reported an increased expression for OXPHOS genes in D1R neurons (**Figure 1D′**), which, indeed, may support the activation of a transcriptional protective response in this subclass of MSNs.

CONCLUSION AND PERSPECTIVE

In conclusion, our review provides a general overview into key pathological pathways leading to neuronal cell death of striatal MSNs in HD. We specifically focus on differences between D1R- and D2R-MSNs, underpinning sensitizing or protective features that might determine diverse responses to the same mutation. From initial studies, a combination of cell-type specific and non-specific reactions seem to be activated in HD, sensitizing D2R-MSNs to cell death. However, the application of single cell techniques, such as, but not limited to, scRNA-seq, is nowadays pioneering a new field of discussion, addressing the contribution of each single cell type (neuronal or glial) to HD striatal vulnerability. Specifically, other cell clusters in the striatum, such as striatal interneurons and astroglia, seem to respond to the HD mutation with some altered genes and pathways as in D1R and D2R, while microglia, oligodendrocytes, and oligodendrocytes precursors seem to be less responsive (Lee et al., 2020). The role of astrocytes in HD has been previously proposed, since mutant huntingtin downregulates the expression of the glial glutamine transporter GLT-1, exacerbating neuronal excitotoxicity. Similarly, specific mutant huntingtin expression in astrocytes prompts motor function deficits, weight loss, and age-dependent neurological phenotypes in transgenic mouse models (Bradford et al., 2009, 2010). Previous studies have provided evidence that activated microglia and reactive astrocytes might contribute to human HD pathology, perpetuating inflammation (Palpagama et al., 2019). However, still debatable is the attribution of beneficial vs. detrimental effects to activated microglia and astrocytes. Moreover, the highly heterogeneous class of striatal interneurons, generally thought to be spared in HD (Cicchetti et al., 2000), still displays selective degeneration in presence of the HD mutation, with documented loss of only parvalbumin-positive interneurons (Cicchetti et al., 2000; Reiner and Deng, 2018). Therefore, a better understanding of the neuroinflammatory environment, but also a detailed clarification of the interneurons population in the HD brain is needed. Moreover, analysis of chromatin, genome-architecture, and spatial distribution will assist in the elucidation of single cell characteristics. This will offer a new angle of interpretation to selective vulnerability to HD and will possibly pave the way to new avenues of therapeutic intervention.

AUTHOR CONTRIBUTIONS

GB made substantial contributions to conception, design of the work, and writing of the manuscript. JD assisted with drafting and critical reading of the text. MB conceived, supervised the project, and wrote the paper. All authors contributed to the article and approved the submitted version.

FUNDING

This work was supported by the University of Trento, the HDSA Human Biology Project and the EHDN 1041 to MB. MB was a recipient of a Marie SkłodowskaŰCurie reintegration fellowship (The European Union's Horizon 2020 Research and Innovation Program) under the grant agreement No. 706567.

REFERENCES

Albin, R. L., Reiner, A., Anderson, K. D., Dure, L. S., Handelin, B., Balfour, R., et al. (1992). Preferential loss of striato-external pallidal projection neurons in presymptomatic Huntington's disease. *Ann. Neurol.* 31, 425–430. doi: 10.1002/ana.410310412

Alexander, G. E., DeLong, M. R., and Strick, P. L. (1986). Parallel organization of functionally segregated circuits linking basal ganglia and cortex. *Annu. Rev. Neurosci.* 9, 357–381. doi: 10.1146/annurev.ne.09.030186.002041

Ament, S. A., Pearl, J. R., Cantle, J. P., Bragg, R. M., Skene, P. J., Coffey, S. R., et al. (2018). Transcriptional regulatory networks underlying gene expression changes in Huntington's disease. *Mol. Syst. Biol.* 14:e7435. doi: 10.15252/msb.20167435

Ament, S. A., Pearl, J. R., Grindeland, A., St Claire, J., Earls, J. C., Kovalenko, M., et al. (2017). High resolution time-course mapping of early transcriptomic, molecular and cellular phenotypes in Huntington's disease CAG knock-in mice across multiple genetic backgrounds. *Hum. Mol. Genet.* 26, 913–922. doi: 10.1093/hmg/ddx006

André, V. M., Cepeda, C., Fisher, Y. E., Huynh, M., Bardakjian, N., Singh, S., et al. (2011). Differential electrophysiological changes in striatal output neurons in Huntington's disease. *J. Neurosci.* 31, 1170–1182. doi: 10.1523/JNEUROSCI.3539-10.2011

Balsters, J. H., Zerbi, V., Sallet, J., Wenderoth, N., and Mars, R. B. (2020). Primate homologs of mouse cortico- striatal circuits. *elife* 9:e53680.

Baydyuk, M., and Xu, B. (2014). BDNF signaling and survival of striatal neurons. *Front. Cell. Neurosci.* 8:254. doi: 10.3389/fncel.2014.00254

Beaulieu, J.-M., Sotnikova, T. D., Marion, S., Lefkowitz, R. J., Gainetdinov, R. R., and Caron, M. G. (2005). An Akt/β-Arrestin 2/PP2A signaling complex mediates dopaminergic neurotransmission and behavior. *Cell* 122, 261–273. doi: 10.1016/j.cell.2005.05.012

Beaulieu, J.-M., Sotnikova, T. D., Yao, W. D., Kockeritz, L., Woodgett, J. R., Gainetdinov, R. R., et al. (2004). Lithium antagonizes dopamine-dependent behaviors mediated by an AKT/glycogen synthase kinase 3 signaling cascade. *Proc. Natl. Acad. Sci.U.S.A.* 101, 5099–5104. doi: 10.1073/pnas.0307921101

Beglinger, L. J., Adams, W. H., Langbehn, D., Fiedorowicz, J. G., Jorge, R., Biglan, K., et al. (2014). Results of the citalopram to enhance cognition in Huntington disease trial: citalopram in HD. *Mov. Dis.* 29, 401–405. doi: 10.1002/mds.25750

Benchoua, A., Trioulier, Y., Diguet, E., Malgorn, C., Gaillard, M. C., Dufour, N., et al. (2008). Dopamine determines the vulnerability of striatal neurons to the N-terminal fragment of mutant huntingtin through the regulation of mitochondrial complex II. *Hum. Mol. Genet.* 17, 1446–1456. doi: 10.1093/hmg/ddn033

Biagioli, M., Ferrari, F., Mendenhall, E. M., Zhang, Y., Erdin, S., Vijayvargia, R., et al. (2015). *Htt* CAG repeat expansion confers pleiotropic gains of mutant huntingtin function in chromatin regulation. *Hum. Mol. Genet.* 24, 2442–2457. doi: 10.1093/hmg/ddv006

Bolam, J. P., Hanley, J. J., Booth, P. A., and Bevan, M. D. (2000). Synaptic organisation of the basal ganglia. *J. Anat.* 196 (Pt 4), 527–542. doi: 10.1046/j.1469-7580.2000.19640527.x

Borrell-Pagès, M., Zala, D., Humbert, S., and Saudou, F. (2006). Huntington's disease: from huntingtin function and dysfunction to therapeutic strategies. *Cell. Mol. Life Sci.* 63, 2642–2660. doi: 10.1007/s00018-006-6242-0

Bradford, J., Shin, J. Y., Roberts, M., Wang, C. E., Li, X. J., and Li, S. (2009). Expression of mutant huntingtin in mouse brain astrocytes causes age-dependent neurological symptoms. *Proc. Natl. Acad. Sci.U.S.A.* 106, 22480–22485. doi: 10.1073/pnas.0911503106

Bradford, J., Shin, J. Y., Roberts, M., Wang, C. E., Sheng, G., Li, S., et al. (2010). Mutant huntingtin in glial cells exacerbates neurological symptoms of huntington disease mice. *J. Biol. Chem.* 285, 10653–10661. doi: 10.1074/jbc.M109.083287

Browne, S. E., Bowling, A. C., MacGarvey, U., Baik, M. J., Berger, S. C., Muqit, M. M., et al. (1997). Oxidative damage and metabolic dysfunction in Huntington's disease: selective vulnerability of the basal ganglia. *Ann. Neurol.* 41, 646–653. doi: 10.1002/ana.410410514

Carty, N., Berson, N., Tillack, K., Thiede, C., Scholz, D., Kottig, K., et al. (2015). Characterization of HTT inclusion size, location, and timing in the zQ175 mouse model of Huntington's disease: an in vivo high-content imaging study. *PLoS One* 10:e0123527. doi: 10.1371/journal.pone.0123527

Cepeda, C., Wu, N., André, V. M., Cummings, D. M., and Levine, M. S. (2007). The corticostriatal pathway in Huntington's disease. *Prog. Neurobiol.* 81, 253–271. doi: 10.1016/j.pneurobio.2006.11.001

Cha, J.-H. J. (2000). Transcriptional dysregulation in Huntington's disease. *Trends Neurosci.* 23, 387–392.

Cha, J.-H. J. (2007). Transcriptional signatures in Huntington's disease. *Prog. Neurobiol.* 83, 228–248.

Charvin, D., Roze, E., Perrin, V., Deyts, C., Betuing, S., Pagès, C., et al. (2008). Haloperidol protects striatal neurons from dysfunction induced by mutated huntingtin in vivo. *Neurobiol. Dis.* 29, 22–29. doi: 10.1016/j.nbd.2007.07.028

Charvin, D., Vanhoutte, P., Pagès, C., Borrelli, E., and Caboche, J. (2005). Unraveling a role for dopamine in Huntington's disease: the dual role of reactive oxygen species and D2 receptor stimulation. *Proc. Natl. Acad. Sci.U.S.A.* 102, 12218–12223. doi: 10.1073/pnas.0502698102

Chen, J. Y., Wang, E. A., Cepeda, C., and Levine, M. S. (2013). Dopamine imbalance in Huntington's disease: a mechanism for the lack of behavioral flexibility. *Front. Neurosci.* 7:114. doi: 10.3389/fnins.2013.00114

Cicchetti, F., Prensa, L., Wu, Y., and Parent, A. (2000). Chemical anatomy of striatal interneurons in normal individuals and in patients with Huntington's disease. *Brain Res. Brain Res. Rev.* 34, 80–101. doi: 10.1016/s0165-0173(00)00039-4

Colin, E., Régulier, E., Perrin, V., Dürr, A., Brice, A., Aebischer, P., et al. (2005). Akt is altered in an animal model of Huntington's disease and in patients. *Eur. J. Neurosci.* 21, 1478–1488. doi: 10.1111/j.1460-9568.2005.03985.x

Costa, V., Giacomello, M., Hudec, R., Lopreiato, R., Ermak, G., Lim, D., et al. (2010). Mitochondrial fission and cristae disruption increase the response of cell models of Huntington's disease to apoptotic stimuli. *EMBO Mol. Med.* 2, 490–503. doi: 10.1002/emmm.201000102

Deng, Y. P., Albin, R. L., Penney, J. B., Young, A. B., Anderson, K. D., and Reiner, A. (2004). Differential loss of striatal projection systems in Huntington's disease: a quantitative immunohistochemical study. *J. Chem. Neuroanatomy* 27, 143–164. doi: 10.1016/j.jchemneu.2004.02.005

DiFiglia, M. (1990). Excitotoxic injury of the neostriatum: a model for Huntington's disease. *Trends Neurosci.* 13, 286–289. doi: 10.1016/0166-2236(90)90111-M

DiFiglia, M., Sapp, E., Chase, K. O., Davies, S. W., Bates, G. P., Vonsattel, J. P., et al. (1997). Aggregation of huntingtin in neuronal intranuclear inclusions and dystrophic neurites in brain. *Science (New York N.Y.)* 277, 1990–1993. doi: 10.1126/science.277.5334.1990

DiProspero, N. A., Chen, E. Y., Charles, V., Plomann, M., Kordower, J. H., and Tagle, D. A. (2004). Early changes in Huntington's disease patient brains involve alterations in cytoskeletal and synaptic elements. *J. Neurocytol.* 33, 517–533. doi: 10.1007/s11068-004-0514-8

Dragileva, E., Hendricks, A., Teed, A., Gillis, T., Lopez, E. T., Friedberg, E. C., et al. (2009). Intergenerational and striatal CAG repeat instability in Huntington's disease knock-in mice involve different DNA repair genes. *Neurobiol. Dis.* 33, 37–47. doi: 10.1016/j.nbd.2008.09.014

Ferrante, R. J., Kowall, N. W., and Richardson, E. P. (1991). Proliferative and degenerative changes in striatal spiny neurons in huntington's disease: a combined study using the section-golgi method and calbindin D28k lmmunocytochemistry. *J. Neurosci.* 11, 3877–3887.

Ferrante, R. J., Kubilus, J. K., Lee, J., Ryu, H., Beesen, A., Zucker, B., et al. (2003). Histone deacetylase inhibition by sodium butyrate chemotherapy ameliorates the neurodegenerative phenotype in Huntington's disease mice. *J. Neurosci.* 23, 9418–9427.

Francelle, L., Galvan, L., and Brouillet, E. (2014). Possible involvement of self-defense mechanisms in the preferential vulnerability of the striatum in Huntington's disease. *Front. Cell. Neurosci.* 8:295. doi: 10.3389/fncel.2014.00295

Franich, N. R., Hickey, M. A., Zhu, C., Osborne, G. F., Ali, N., Chu, T., et al. (2019). Phenotype onset in Huntington's disease knock-in mice is correlated with the incomplete splicing of the mutant huntingtin gene. *J. Neurosci. Res.* 97, 1590–1605. doi: 10.1002/jnr.24493

Galvan, L., André, V. M., Wang, E. A., Cepeda, C., and Levine, M. S. (2012). Functional differences between direct and indirect striatal output pathways in huntington's Disease. *J. Huntingtons Dis.* 1, 17–25. doi: 10.3233/JHD-2012-120009

Gangarossa, G., Espallergues, J., Mailly, P., De Bundel, D., de Kerchove d'Exaerde, A., Hervé, D., et al. (2013). Spatial distribution of D1R- and D2R-expressing medium-sized spiny neurons differs along the rostro-caudal axis of the mouse dorsal striatum. *Front. Neural Circ.* 7:124. doi: 10.3389/fncir.2013.00124

Gauthier, L. R., Charrin, B. C., Borrell-Pagès, M., Dompierre, J. P., Rangone, H., Cordelières, F. P., et al. (2004). Huntingtin controls neurotrophic support and survival of neurons by enhancing BDNF vesicular transport along microtubules. *Cell* 118, 127–138. doi: 10.1016/j.cell.2004.06.018

Gertler, T. S., Chan, C. S., and Surmeier, D. J. (2008). Dichotomous anatomical properties of adult striatal medium spiny neurons. *J. Neurosci.* 28, 10814–10824. doi: 10.1523/JNEUROSCI.2660-08.2008

Ghosh, R., and Tabrizi, S. J. (2018). "Huntington disease," in *Handbook of Clinical Neurology*, eds D. H. Geschwind, H. L. Paulson, and C. Klein (Amsterdam: Elsevier), 255–278. doi: 10.1016/B978-0-444-63233-3.00017-8

Giampà, C., Montagna, E., Dato, C., Melone, M. A., Bernardi, G., and Fusco, F. R. (2013). Systemic delivery of recombinant brain derived neurotrophic factor (BDNF) in the R6/2 mouse model of Huntington's disease. *PLoS One* 8:e64037. doi: 10.1371/journal.pone.0064037

Gines, S., Seong, I. S., Fossale, E., Ivanova, E., Trettel, F., Gusella, J. F., et al. (2003). Specific progressive cAMP reduction implicates energy deficit in presymptomatic Huntington's disease knock-in mice. *Hum. Mol. Genet.* 12, 497–508. doi: 10.1093/hmg/ddg046

Giralt, A., Carretón, O., Lao-Peregrin, C., Martín, E. D., and Alberch, J. (2011). Conditional BDNF release under pathological conditions improves Huntington's disease pathology by delaying neuronal dysfunction. *Mol. Neurodegen.* 6:71. doi: 10.1186/1750-1326-6-71

Gokce, O., Stanley, G. M., Treutlein, B., Neff, N. F., Camp, J. G., Malenka, R. C., et al. (2016). Cellular taxonomy of the mouse striatum as revealed by single-cell RNA-Seq. *Cell Rep.* 16, 1126–1137. doi: 10.1016/j.celrep.2016.06.059

Goodliffe, J. W., Song, H., Rubakovic, A., Chang, W., Medalla, M., Weaver, C. M., et al. (2018). Differential changes to D1 and D2 medium spiny neurons in the 12-month-old Q175+/- mouse model of Huntington's Disease. *PLoS One* 13:e0200626. doi: 10.1371/journal.pone.0200626

Gu, M., Gash, M. T., Mann, V. M., Javoy-Agid, F., Cooper, J. M., and Schapira, A. H. (1996). Mitochondrial defect in Huntington's disease caudate nucleus. *Ann. Neurol.* 39, 385–389. doi: 10.1002/ana.410390317

Hammond, C. (2015). *Cellular and Molecular Neurophysiology*, 4th Edn. Amsterdam: Elsevier Ltd.

Han, I., You, Y., Kordower, J. H., Brady, S. T., and Morfini, G. A. (2010). Differential vulnerability of neurons in Huntington's disease: the role of cell type-specific features. *J. Neurochem.* 113, 1073–1091. doi: 10.1111/j.1471-4159.2010.06672.x

Harrison, L. M., Muller, S. H., and Spano, D. (2013). Effects of the ras homolog rhes on Akt/Protein kinase B and glycogen synthase kinase 3 phosphorylation in striatum. *Neuroscience* 236C, 21–30. doi: 10.1016/j.neuroscience.2012.12.062

Hedreen, J. C., and Folstein, S. E. (1995). Early loss of neostriatal striosome neurons in Huntington's disease. *J. Neuropathol. Exp. Neurol.* 54, 105–120. doi: 10.1097/00005072-199501000-00013

Hervás-Corpión, I. (2018). Early alteration of epigenetic-related transcription in Huntington's disease mouse models. *Sci. Rep.* 8:9925.

Hodges, A., Strand, A. D., Aragaki, A. K., Kuhn, A., Sengstag, T., Hughes, G., et al. (2006). Regional and cellular gene expression changes in human Huntington's disease brain. *Hum. Mol. Genet.* 15, 965–977. doi: 10.1093/hmg/ddl013

Hoffmann-La Roche (2020). *A Randomized, Multicenter, Double-Blind, Placebo-Controlled, Phase III Clinical Study to Evaluate the Efficacy and Safety of Intrathecally Administered RO7234292 (RG6042) in Patients With Manifest Huntington's Disease*. Clinical trial registration NCT03761849. clinicaltrials.gov. Available online at: https://clinicaltrials.gov/ct2/show/NCT03761849 (accessed October 12, 2020).

Johnson, R., Zuccato, C., Belyaev, N. D., Guest, D. J., Cattaneo, E., Buckley, N. J., et al. (2008). A microRNA-based gene dysregulation pathway in Huntington's disease. *Neurobiol. Dis.* 29, 438–445. doi: 10.1016/j.nbd.2007.11.001

Klapstein, G. J., Fisher, R. S., Zanjani, H., Cepeda, C., Jokel, E. S., Chesselet, M. F., et al. (2001). Electrophysiological and morphological changes in striatal spiny neurons in R6/2 Huntington's disease transgenic mice. *J. Neurophysiol.* 86, 2667–2677. doi: 10.1152/jn.2001.86.6.2667

Koch, E. T., and Raymond, L. A. (2019). Dysfunctional striatal dopamine signaling in Huntington's disease. *J. Neurosci. Res.* 97, 1636–1654. doi: 10.1002/jnr.24495

Kumar, A., and Ratan, R. R. (2016). Oxidative stress and Huntington's disease: the good, the bad, and the ugly. *J. Huntingtons Dis.* 5, 217–237. doi: 10.3233/JHD-160205

Labadorf, A., Hoss, A. G., Lagomarsino, V., Latourelle, J. C., Hadzi, T. C., Bregu, J., et al. (2015). RNA sequence analysis of human huntington disease brain reveals an extensive increase in inflammatory and developmental gene expression. *PloS One* 10:e0143563. doi: 10.1371/journal.pone.0143563

Lanciego, J. L., Luquin, N., and Obeso, J. A. (2012). Functional neuroanatomy of the basal ganglia. *Cold Spring Harb. Perspect. Med.* 2:a009621. doi: 10.1101/cshperspect.a009621

Langfelder, P., Cantle, J. P., Chatzopoulou, D., Wang, N., Gao, F., Al-Ramahi, I., et al. (2016). Integrated genomics and proteomics define huntingtin CAG length–dependent networks in mice. *Nat. Neurosci.* 19, 623–633. doi: 10.1038/nn.4256

Lee, H., Fenster, R. J., Pineda, S. S., Gibbs, W. S., Mohammadi, S., Davila-Velderrain, J., et al. (2020). Cell type-specific transcriptomics reveals that mutant huntingtin leads to mitochondrial RNA release and neuronal innate immune activation. *Neuron* 107, 891–908.e8. doi: 10.1016/j.neuron.2020.06.021

Lee, J. H., Sowada, M. J., Boudreau, R. L., Aerts, A. M., Thedens, D. R., Nopoulos, P., et al. (2014). Rhes suppression enhances disease phenotypes in Huntington's disease mice. *J. Huntingtons Dis.* 3, 65–71. doi: 10.3233/JHD-140094

Lee, J.-M., Correia, K., Loupe, J., Kim, K.-H., Barker, D., Hong, E. P., et al. (2019). CAG repeat not polyglutamine length determines timing of Huntington's disease onset. *Cell* 178, 887-900.e14. doi: 10.1016/j.cell.2019.06.036

Lee, J.-M., Pinto, R. M., Gillis, T., St Claire, J. C., and Wheeler, V. C. (2011). Quantification of age-dependent somatic CAG repeat instability in Hdh CAG knock-in mice reveals different expansion dynamics in striatum and liver. *PLoS One* 6:e23647. doi: 10.1371/journal.pone.0023647

Lee, J.-M., Wheeler, V. C., Chao, M. J., Vonsattel, J. P. G., Pinto, R. M., Lucente, D., et al. (2015). Identification of genetic factors that modify clinical onset of Huntington's disease. *Cell* 162, 516–526. doi: 10.1016/j.cell.2015.07.003

Lee, S.-T., Chu, K., Im, W. S., Yoon, H. J., Im, J. Y., Park, J. E., et al. (2011). Altered microRNA regulation in Huntington's disease models. *Exp. Neurol.* 227, 172–179. doi: 10.1016/j.expneurol.2010.10.012

Lei, W. (2004). Evidence for differential cortical input to direct pathway versus indirect pathway striatal projection neurons in rats. *J. Neurosci.* 24, 8289–8299. doi: 10.1523/JNEUROSCI.1990-04.2004

Leisman, G., Melillo, R., and Carrick, F. R. (2013). "Clinical motor and cognitive neurobehavioral relationships in the basal ganglia," in *Basal Ganglia – An Integrative View*, ed. E. Franz (Rijeka: InTech), 1–30. doi: 10.5772/55227

Lerner, R. P., Trejo Martinez Ldel, C., Zhu, C., Chesselet, M. F., and Hickey, M. A. (2012). Striatal atrophy and dendritic alterations in a knock-in mouse model of Huntington's disease. *Brain Res. Bull.* 87, 571–578. doi: 10.1016/j.brainresbull.2012.01.012

Li, X.-J., Orr, A. L., and Li, S. (2010). Impaired mitochondrial trafficking in Huntington's disease. *Biochim. Biophys. Acta BBA Mol. Basis Dis.* 1802, 62–65. doi: 10.1016/j.bbadis.2009.06.008

Lin, L., Park, J. W., Ramachandran, S., Zhang, Y., Tseng, Y. T., Shen, S., et al. (2016). Transcriptome sequencing reveals aberrant alternative splicing in Huntington's disease. *Hum. Mol. Genet.* 25, 3454–3466. doi: 10.1093/hmg/ddw187

Liot, G., Valette, J., Pépin, J., Flament, J., and Brouillet, E. (2017). Energy defects in Huntington's disease: why "in vivo" evidence matters'. *Biochem. Biophys. Res. Commun.* 483, 1084–1095. doi: 10.1016/j.bbrc.2016.09.065

Luthi-Carter, R., Strand, A., Peters, N. L., Solano, S. M., Hollingsworth, Z. R., Menon, A. S., et al. (2000). Decreased expression of striatal signaling genes in a mouse model of Huntington's disease. *Hum. Mol. Genet.* 9, 1259–1271. doi: 10.1093/hmg/9.9.1259

Luthi-Carter, R., Taylor, D. M., Pallos, J., Lambert, E., Amore, A., Parker, A., et al. (2010). SIRT2 inhibition achieves neuroprotection by decreasing sterol biosynthesis. *Proc. Natl. Acad. Sci.U.S.A.* 107, 7927–7932. doi: 10.1073/pnas.1002924107

MacDonald, M. E., Ambrose, C. M., Duyao, M. P., Myers, R. H., Lin, C., Srinidhi, L., et al. (1993). A novel gene containing a trinucleotide repeat that is expanded and unstable on Huntington's disease chromosomes. *Cell* 72, 971–983. doi: 10.1016/0092-8674(93)90585-E

Mangiarini, L., Sathasivam, K., Seller, M., Cozens, B., Harper, A., Hetherington, C., et al. (1996). Exon 1 of the HD gene with an expanded CAG repeat is sufficient to cause a progressive neurological phenotype in transgenic mice. *Cell* 87, 493–506. doi: 10.1016/S0092-8674(00)81369-0

McFarland, K. N., Das, S., Sun, T. T., Leyfer, D., Xia, E., Sangrey, G. R., et al. (2012). Genome-wide histone acetylation is altered in a transgenic mouse model of Huntington's disease. *PLoS One* 7:e41423. doi: 10.1371/journal.pone.0041423

Menalled, L. B. (2005). Knock-in mouse models of Huntington's disease. *NeuroRX* 2, 465–470. doi: 10.1602/neurorx.2.3.465

Menalled, L. B., Kudwa, A. E., Miller, S., Fitzpatrick, J., Watson-Johnson, J., Keating, N., et al. (2012). Comprehensive behavioral and molecular characterization of a new knock-in mouse model of Huntington's disease: zQ175'. *PLoS One* 7:e49838. doi: 10.1371/journal.pone.0049838

Menalled, L. B., Sison, J. D., Dragatsis, I., Zeitlin, S., and Chesselet, M. F. (2003). Time course of early motor and neuropathological anomalies in a knock-in mouse model of Huntington's disease with 140 CAG repeats. *J. Comp. Neurol.* 465, 11–26. doi: 10.1002/cne.10776

Mochel, F., Durant, B., Meng, X., O'Callaghan, J., Yu, H., Brouillet, E., et al. (2012). Early alterations of brain cellular energy homeostasis in huntington disease models. *J. Biol. Chem.* 287, 1361–1370. doi: 10.1074/jbc.M111.309849

Morigaki, R., and Goto, S. (2017). Striatal vulnerability in huntington's disease: neuroprotection versus neurotoxicity. *Brain Sci.* 7:63. doi: 10.3390/brainsci7060063

Packer, A. N., Xing, Y., Harper, S. Q., Jones, L., and Davidson, B. L. (2008). The bifunctional microRNA miR-9/miR-9* regulates REST and CoREST and is downregulated in Huntington's disease. *J. Neurosci.* 28, 14341–14346. doi: 10.1523/JNEUROSCI.2390-08.2008

Palpagama, T. H., Waldvogel, H. J., Faull, R. L. M., and Kwakowsky, A. (2019). The role of microglia and astrocytes in huntington's disease. *Front. Mol. Neurosci.* 12:258. doi: 10.3389/fnmol.2019.00258

Panov, A. V., Gutekunst, C. A., Leavitt, B. R., Hayden, M. R., Burke, J. R., Strittmatter, W. J., et al. (2002). Early mitochondrial calcium defects in Huntington's disease are a direct effect of polyglutamines. *Nat. Neurosci.* 5, 731–736. doi: 10.1038/nn884

Paoletti, P., Vila, I., Rifé, M., Lizcano, J. M., Alberch, J., and Ginés, S. (2008). Dopaminergic and glutamatergic signaling crosstalk in huntington's disease neurodegeneration: the role of p25/Cyclin-dependent kinase 5. *J. Neurosci.* 28, 10090–10101. doi: 10.1523/JNEUROSCI.3237-08.2008

Pearl, J. R., Shetty, A. C., Cantle, J. P., Bergey, D. E., Bragg, R. M., Coffey, S. R., et al. (2020). Altered huntingtin-chromatin interactions predict transcriptional and epigenetic changes in Huntington's disease. *bioRixv* [preprint] doi: 10.1101/2020.06.04.132571

Peng, Q., Wu, B., Jiang, M., Jin, J., Hou, Z., Zheng, J., et al. (2016). Characterization of behavioral, neuropathological, brain metabolic and key molecular changes in zQ175 knock-in mouse model of huntington's disease. *PLoS One* 11:e0148839. doi: 10.1371/journal.pone.0148839

Pinto, R. M., Dragileva, E., Kirby, A., Lloret, A., Lopez, E., St Claire, J., et al. (2013). Mismatch repair genes Mlh1 and Mlh3 modify CAG instability in huntington's disease mice: genome-wide and candidate approaches. *PLoS Genet.* 9:e1003930. doi: 10.1371/journal.pgen.1003930

Pringsheim, T., Wiltshire, K., Day, L., Dykeman, J., Steeves, T., and Jette, N. (2012). The incidence and prevalence of Huntington's disease: a systematic review and meta-analysis. *Mov. Disord.* 27, 1083–1091. doi: 10.1002/mds.25075

Puighermanal, E., Castell, L., Esteve-Codina, A., Melser, S., Kaganovsky, K., and Zussy, C. (2020). Functional and molecular heterogeneity of D2R neurons along dorsal ventral axis in the striatum. *Nat. Commun.* 11:1957. doi: 10.1038/s41467-020-15716-9

Rebec, G. V. (2018). Corticostriatal network dysfunction in Huntington's disease: deficits in neural processing, glutamate transport, and ascorbate release. *CNS Neurosci. Ther.* 24, 281–291. doi: 10.1111/cns.12828

Reiner, A., and Deng, Y.-P. (2018). Disrupted striatal neuron inputs and outputs in Huntington's disease. *CNS Neurosci. Ther.* 24, 250–280. doi: 10.1111/cns.12844

Roos, R. A. C. (2010). Huntington's disease: a clinical review. *Orphanet J. Rare Dis.* 5:40. doi: 10.1186/1750-1172-5-40

Ross, C. A., and Tabrizi, S. J. (2011). Huntington's disease: from molecular pathogenesis to clinical treatment. *Lancet Neurol.* 10, 83–98. doi: 10.1016/S1474-4422(10)70245-3

Rüb, U., Seidel, K., Heinsen, H., Vonsattel, J. P., den Dunnen, W. F., and Korf, H. W. (2016). Huntington's disease (HD): the neuropathology of a multisystem neurodegenerative disorder of the human brain. *Brain Pathol. (Zurich Switzerland)* 26, 726–740. doi: 10.1111/bpa.12426

Rubinsztein, D. C. (2002). Lessons from animal models of Huntington's disease. *Trends Genet.* 18, 202–209. doi: 10.1016/S0168-9525(01)02625-7

Sapp, E., Ge, P., Aizawa, H., Bird, E., Penney, J., Young, A. B., et al. (1995). Evidence for a preferential loss of enkephalin immunoreactivity in the external globus pallidus in low grade Huntington's disease using high resolution image analysis. *Neuroscience* 64, 397–404. doi: 10.1016/0306-4522(94)00427-7

Sathasivam, K., Neueder, A., Gipson, T. A., Landles, C., Benjamin, A. C., Bondulich, M. K., et al. (2013). Aberrant splicing of *HTT* generates the pathogenic exon 1 protein in Huntington disease'. *Proc. Natl. Acad. Sci.U.S.A.* 110, 2366–2370. doi: 10.1073/pnas.1221891110

Saudou, F., and Humbert, S. (2016). The biology of huntingtin. *Neuron* 89, 910–926. doi: 10.1016/j.neuron.2016.02.003

Saunders, A., Macosko, E. Z., Wysoker, A., Goldman, M., Krienen, F. M., de Rivera, H., et al. (2018). Molecular diversity and specializations among the cells of the adult mouse brain. *Cell* 174, 1015–1030.e16. doi: 10.1016/j.cell.2018.07.028

Schilling, J., Broemer, M., Atanassov, I., Duernberger, Y., Vorberg, I., Dieterich, C., et al. (2019). Deregulated splicing is a major mechanism of RNA-Induced toxicity in Huntington's disease. *J. Mol. Biol.* 431, 1869–1877. doi: 10.1016/j.jmb.2019.01.034

Seong, I. S., Ivanova, E., Lee, J. M., Choo, Y. S., Fossale, E., Anderson, M., et al. (2005). HD CAG repeat implicates a dominant property of huntingtin in mitochondrial energy metabolism. *Hum. Mol. Genet.* 14, 2871–2880. doi: 10.1093/hmg/ddi319

Seong, I. S., Woda, J. M., Song, J. J., Lloret, A., Abeyrathne, P. D., Woo, C. J., et al. (2010). Huntingtin facilitates polycomb repressive complex 2. *Hum. Mol. Genet.* 19, 573–583. doi: 10.1093/hmg/ddp524

Seredenina, T., and Luthi-Carter, R. (2012). What have we learned from gene expression profiles in Huntington's disease?. *Neurobiol. Dis.* 45, 83–98. doi: 10.1016/j.nbd.2011.07.001

Shen, W., Tian, X., Day, M., Ulrich, S., Tkatch, T., Nathanson, N. M., et al. (2007). Cholinergic modulation of Kir2 channels selectively elevates dendritic excitability in striatopallidal neurons. *Nat. Neurosci.* 10, 1458–1466. doi: 10.1038/nn1972

Shirendeb, U., Reddy, A. P., Manczak, M., Calkins, M. J., Mao, P., Tagle, D. A., et al. (2011). Abnormal mitochondrial dynamics, mitochondrial loss and mutant huntingtin oligomers in Huntington's disease: implications for selective neuronal damage. *Hum. Mol. Genet.* 20, 1438–1455. doi: 10.1093/hmg/ddr024

Stack, E. C., Del Signore, S. J., Luthi-Carter, R., Soh, B. Y., Goldstein, D. R., Matson, S., et al. (2007). Modulation of nucleosome dynamics in Huntington's disease. *Hum. Mol. Genet.* 16, 1164–1175. doi: 10.1093/hmg/ddm064

Stephenson-Jones, M., Samuelsson, E., Ericsson, J., Robertson, B., and Grillner, S. (2011). Evolutionary conservation of the basal ganglia as a common vertebrate mechanism for action selection. *Curr. Biol.* 21, 1081–1091. doi: 10.1016/j.cub.2011.05.001

Surmeier, D. J., Ding, J., Day, M., Wang, Z., and Shen, W. (2007). D1 and D2 dopamine-receptor modulation of striatal glutamatergic signaling in striatal medium spiny neurons. *Trends Neurosci.* 30, 228–235. doi: 10.1016/j.tins.2007.03.008

Swami, M., Hendricks, A. E., Gillis, T., Massood, T., Mysore, J., and Myers, R. H. (2009). Somatic expansion of the Huntington's disease CAG repeat in the brain is associated with an earlier age of disease onset. *Hum. Mol. Genet.* 18, 3039–3047. doi: 10.1093/hmg/ddp242

Tabrizi, S. J., Workman, J., Hart, P. E., Mangiarini, L., Mahal, A., Bates, G., et al. (2000). Mitochondrial dysfunction and free radical damage in the Huntington R6/2 transgenic mouse. *Ann. Neurol.* 47, 80–86.

Tang, B., Seredenina, T., Coppola, G., Kuhn, A., Geschwind, D. H., Luthi-Carter, R., et al. (2011). Gene expression profiling of R6/2 transgenic mice with different CAG repeat lengths reveals genes associated with disease onset and progression in Huntington's disease. *Neurobiol. Dis.* 42, 459–467. doi: 10.1016/j.nbd.2011.02.008

Telenius, H., Kremer, B., Goldberg, Y. P., Theilmann, J., Andrew, S. E., Zeisler, J., et al. (1994). Somatic and gonadal mosaicism of the Huntington disease gene CAG repeat in brain and sperm. *Nat. Genet.* 6, 409–414. doi: 10.1038/ng0494-409

Trettel, F., Rigamonti, D., Hilditch-Maguire, P., Wheeler, V. C., Sharp, A. H., Persichetti, F., et al. (2000). Dominant phenotypes produced by the HD mutation in ST*Hdh*(Q111) striatal cells. *Hum. Mol. Genet.* 9, 2799–2809. doi: 10.1093/hmg/9.19.2799

Vodicka, P., Smetana, K. Jr., Dvoránková, B., Emerick, T., Xu, Y. Z., Ourednik, J., et al. (2005). The miniature pig as an animal model in biomedical research. *Ann. N. Y. Acad. Sci.* 1049, 161–171. doi: 10.1196/annals.1334.015

Wave Life Sciences Ltd (2020). *A Multicenter, Randomized, Double-blind, Placebo-controlled, Phase 1b/2a Study of WVE-120101 Administered Intrathecally in Patients With Huntington's Disease*. Clinical trial registration NCT03225833. clinicaltrials.gov. Available online at: https://clinicaltrials.gov/ct2/show/NCT03225833 (accessed October 12, 2020).

Wheeler, V. C. (2003). Mismatch repair gene Msh2 modifies the timing of early disease in HdhQ111 striatum. *Hum. Mol. Genet.* 12, 273–281. doi: 10.1093/hmg/ddg056

Willett, J. A., Cao, J., Dorris, D. M., Johnson, A. G., Ginnari, L. A., and Meitzen, J. (2019). Electrophysiological properties of medium spiny neuron subtypes in the caudate-putamen of prepubertal male and female *Drd1a* -tdTomato line 6 BAC transgenic mice. *Eneuro* 6, ENEURO.0016-19.2019.

Zuccato, C., Tartari, M., Crotti, A., Goffredo, D., Valenza, M., Conti, L., et al. (2003). Huntingtin interacts with REST/NRSF to modulate the transcription of NRSE-controlled neuronal genes. *Nat. Genet.* 35, 76–83. doi: 10.1038/ng1219

Conflict of Interest: The authors declare that the research was conducted in the absence of any commercial or financial relationships that could be construed as a potential conflict of interest.

frontiers in Cellular Neuroscience

REVIEW
published: 12 March 2021
doi: 10.3389/fncel.2021.627291

Pericytes Across the Lifetime in the Central Nervous System

*Hannah C. Bennett and Yongsoo Kim**

Department of Neural and Behavioral Sciences, Penn State University, Hershey, PA, United States

The pericyte is a perivascular cell type that encapsulates the microvasculature of the brain and spinal cord. Pericytes play a crucial role in the development and maintenance of the blood-brain barrier (BBB) and have a multitude of important functions in the brain. Recent evidence indicates that pericyte impairment has been implicated in neurovascular pathology associated with various human diseases such as diabetes mellitus, Alzheimer's disease (AD), and stroke. Although the pericyte is essential for normal brain function, knowledge about its developmental trajectory and anatomical distribution is limited. This review article summarizes the scientific community's current understanding of pericytes' regional heterogeneity in the brain and their changes during major life stages. More specifically, this review article focuses on pericyte differentiation and migration during brain development, regional population differences in the adult brain, and changes during normal and pathological aging. Most of what is known about pericytes come from studies of the cerebral cortex and hippocampus. Therefore, we highlight the need to expand our understanding of pericyte distribution and function in the whole brain to better delineate this cell type's role in the normal brain and pathological conditions.

Keywords: pericyte, brain, development, aging, blood brain barrier, regional heterogeneity, mouse

OPEN ACCESS

Edited by:
Miao He,
Fudan University, China

Reviewed by:
Berislav Zlokovic,
University of Southern California, United States
Xiaoqun Wang,
Chinese Academy of Sciences, China
Brad A. Sutherland,
University of Tasmania, Australia

****Correspondence:***
Yongsoo Kim
yuk17@psu.edu

Specialty section:
This article was submitted to Non-Neuronal Cells, a section of the journal Frontiers in Cellular Neuroscience

Received: *09 November 2020*
Accepted: *23 February 2021*
Published: *12 March 2021*

Citation:
Bennett HC and Kim Y (2021) Pericytes Across the Lifetime in the Central Nervous System. Front. Cell. Neurosci. 15:627291. doi: 10.3389/fncel.2021.627291

INTRODUCTION

Pericytes are a mural cell type that are highly abundant in the microvasculature in the central nervous system (CNS). These cells are tightly associated with the brain's blood vessels and form one of the major components of the blood-brain barrier (BBB). The BBB, which forms during the embryonic and early postnatal period of development in mice, is comprised of endothelial cells, pericytes, and their shared basement membrane, as well as astrocytic endfeet (Ballabh et al., 2004). In humans, the development of the BBB corresponds to preterm infant development, or up to 32 weeks' gestation (Semple et al., 2013). The BBB is crucial for regulating substances transported between the vessel lumen and the brain parenchyma and provides the nutrients, water, and oxygen required

Abbreviations: aminopeptidase N, CD13; CNS, central nervous system; BBB, blood-brain barrier; PDGFRβ, platelet-derived growth factor receptor β; PDGF-β, platelet-derived growth factor β; NG2, neural glial antigen 2; vSMC, vascular smooth muscle cell; VEGF, vascular endothelial growth factor; VEGFR1, vascular endothelial growth factor receptor 1; TGFβ, transforming growth factor β; FoxF2, forkhead box F2; Mfsd2a, endothelial major facilitator superfamily domain-containing 2a; postnatal day #, P#; embryonic day #, E#; AD, Alzheimer's disease; APP, amyloid precursor protein; Amyloid β, Aβ; LRP1, low-density receptor-related protein 1; APOE4, apolipoprotein E4; sPDGFRβ, soluble PDGFRβ.

for proper brain function (Ballabh et al., 2004). Pericytes, in particular, form lock and socket junctions with endothelial cells and contribute significantly to the maintenance of the BBB (Gökçinar-Yagci et al., 2015). Various markers have been used to label pericytes, such as platelet-derived growth factor receptor β (PDGFRβ), neural glial antigen 2 (NG2), desmin, and aminopeptidase N (CD13; Birbrair, 2019; Brown et al., 2019). However, these markers are also expressed in other cell types, posing challenges in clearly labeling pericytes (Bondjers et al., 2006; Attwell et al., 2016). Moreover, pericytes have additional functions pertaining to toxin clearance, cytokine and chemokine production, as well as capillary blood flow regulation (Bell et al., 2010; Kamouchi et al., 2011; Gökçinar-Yagci et al., 2015; Sweeney et al., 2016; Trost et al., 2016; Brown et al., 2019). Several excellent reviews have recently summarized current evidence relating to the importance of pericytes, as well as their identification and versatile functions (Sims, 2000; Bergers and Song, 2005; Bell et al., 2010; Kamouchi et al., 2011; Gökçinar-Yagci et al., 2015; Attwell et al., 2016; Trost et al., 2016; Yamazaki and Mukouyama, 2018; Brown et al., 2019; Coelho-Santos and Shih, 2020). By analyzing the topics of embryonic and postnatal pericyte development, differences in brain regional vulnerability, as well as BBB and pericyte changes in normal and pathological aging, this review seeks to not only provide an integrated view of current knowledge but also emphasizes the need to further study pericyte populations across multiple brain regions to better delineate their roles in human disease.

EMBRYONIC PERICYTE DEVELOPMENT AND MIGRATION

BBB development, particularly that involves pericyte differentiation and migration, begins embryonically for both humans and rodents (Armulik et al., 2005). Most of what is known regarding CNS pericyte development is gleaned primarily from rodent studies in the brain and the retina. Although spinal cord pericyte development is also crucial for neurovascular development, potential differences between brain and spinal cord pericytes are largely understudied and both populations are presumed to be similar (Bartanusz et al., 2011; Picoli et al., 2019). CNS pericytes are thought to be primarily derived from the neural crest and mesenchymal cell lineages (Prazeres et al., 2018). However, a subset of the embryonic CNS pericyte population may arise from other sources, such as blood-borne macrophages (Yamamoto et al., 2017). At approximately embryonic day 10 (E10) of mouse development, there are hematopoietic lineage cells ($CD31^+F4/80^+$) containing well-known macrophage markers in the avascular region near the developing midbrain (Yamamoto et al., 2017). This particular subset of macrophages was tracked to the subventricular vascular plexus, within which they differentiated into cells expressing classic pericyte markers, including NG2, PDGFRβ, and desmin, and wrapped around the growing microvasculature (Yamamoto et al., 2017). Thus, the lineage of pericytes in the brain, and the CNS in general, may be heterogeneous (**Figure 1A**). Although the source of this cell type may vary, several studies have investigated the coordinated and essential roles of pericytes in the development of the neurovascular system (Armulik et al., 2005, 2011; Bergers and Song, 2005; Nakagomi et al., 2015).

Vascularization of the mouse brain is thought to begin at approximately E9.5 based on studies of the hindbrain, forebrain, and retina (Armulik et al., 2005, 2011; Paredes et al., 2018). In the spinal cord, vascularization begins slightly earlier, and current understanding of this process as well as differences between the BBB and blood spinal cord barrier have recently been reviewed (Bartanusz et al., 2011; Paredes et al., 2018; Picoli et al., 2019). Endothelial growth is largely driven by vascular endothelial growth factor (VEGF) signaling with the majority of mural cell precursors arising from the neural crest at around E10.5 (Armulik et al., 2005; Paredes et al., 2018). PDGFRβ is a receptor for the primary signaling growth factor for pericytes and is crucial for the migration and survival of these cells (Sweeney et al., 2016). PDGFRβ can be activated by both PDGF-B and PDGF-D isoforms, for which the ligand PDGF-B is primarily produced by endothelial cells (Sweeney et al., 2016). From E11.5 through E14, PDGF-B signaling plays an important role at all levels of the developing vasculature to help drive pericyte migration (Hellström et al., 2001). By E18.5 this expression is limited to capillaries, which then become a major site of pericyte cell density (Hellström et al., 2001). Also, there are several other pathways associated with the migration of these cells. For example, endothelial-derived transforming growth factor β (TGFβ) signaling and downstream components, such as Alk5/SMAD2/3, have been shown to play a role in the differentiation of pericytes, as well as the formation of the classic peg and socket junctions between pericytes and endothelial cells (Dave et al., 2018). The associated Alk5/Timp3 pathway in pericytes contributes to endothelial morphogenesis and regulation of basement membrane formation during embryonic development (Dave et al., 2018). TGFβ is also known to drive the incorporation of vascular smooth muscle cells (vSMCs) into larger arteries and venules (Allinson et al., 2012). Also, angiopoietin 1-Tie2 signaling mediates intercommunication between developing endothelium and pericytes (Teichert et al., 2017). More recently, precursor neural crest cells expressing PDGFRβ, described above, have also been shown to express forkhead box F2 (FoxF2; Reyahi et al., 2015). These cells are thought to comprise the precursors of mural cell types, including both pericytes and vSMCs (Armulik et al., 2005). FoxF2 is a factor that drives the development of mesenchymal cells of the gut, but it is also expressed by neural crest cells in brain development (Reyahi et al., 2015). The loss of FoxF2 perturbs the vascular system and BBB development by reducing TGFβ/Smad2/3 signaling as well as PDGFRβ expression (Reyahi et al., 2015). This indicates that FoxF2 plays a major role in the regulation of pericyte development as it has an impact on pathways essential for pericyte growth, differentiation, and survival. Additionally, molecules such as Gpr124, Zo-1, Notch, and others have also been implicated in pericyte and vascular development (Armulik et al., 2011; Wang et al., 2014; Yamazaki and Mukouyama, 2018; Zaitoun et al., 2019). Many of these signaling pathways associated with pericyte development are summarized in **Figure 1B**. Despite such a short developmental period, the BBB becomes functional by age

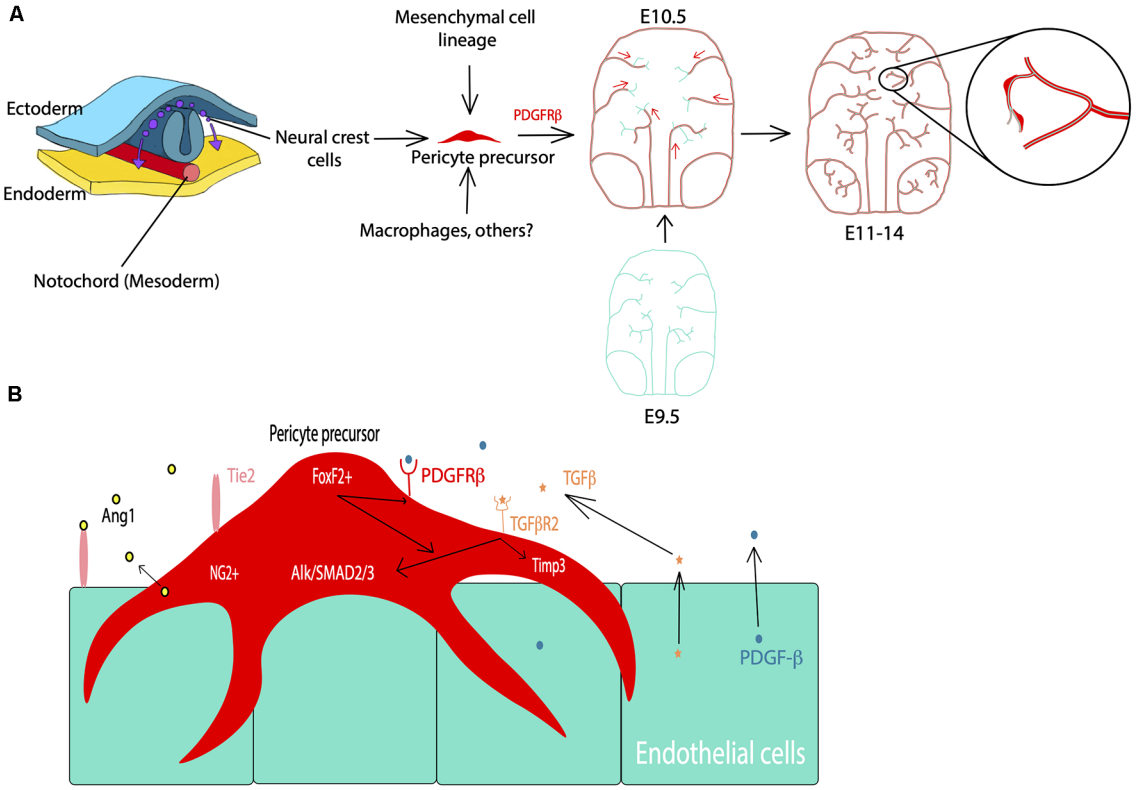

FIGURE 1 | Pericyte development during the embryonic period. **(A)** Cell lineage of pericytes including neural crest cells, mesenchymal cells, and macrophages. PDGFRβ signaling facilitates pericyte migration during embryonic development starting at E10.5 in mice. Cyan: endothelial cells, Red: pericytes. **(B)** Examples of the major players in pericyte-endothelial interactions during embryonic development such as PDGFRβ signaling for pericyte development and migration, TGFβ signaling, Alk/SMAD2/3 and Timp3 signaling for pericyte-endothelial junctions and basement membrane formation, and FoxF2 for mediating PDGFRβ and TGFβ signaling during development.

E15.5 in mice and E17 in rats due to highly regulated pericyte-endothelial interactions (Daneman et al., 2010; Ben-Zvi et al., 2014). Although this structure is considered to be functional, its development is not quite finished at birth (Obermeier et al., 2013). In essence, pericytes play crucial roles in early vascular development, particularly by influencing the formation of the BBB and endothelial growth which are essential for proper neurovascular development.

POSTNATAL PERICYTE DEVELOPMENT

Following embryonic developmental migration and formation of the BBB, the microvasculature begins to mature in the early postnatal period in rodents (**Figure 2**), corresponding to the late gestational period in humans. After birth, endothelial cells show sharp proliferation to expand the vascular network which peaks at postnatal day 10 (P10) and drops by P25 (Harb et al., 2013). This is particularly apparent in the gray matter where the vascular density doubles by P20 and has a much higher pericyte density than the white matter (Zeller et al., 1996). Similarly, vascular branching increases around P10 and appears more similar to the adult brain by P25 (Harb et al., 2013). Alternatively, pericyte proliferation begins to decline in the postnatal period, while pericyte coverage of the vasculature continues to expand (Harb et al., 2013). Although pericyte proliferation is not as pronounced, pericyte coverage and vessel stability continue to mature during this period (Harb et al., 2013). By P1 in the mouse brain, pericytes have transitioned to partial coverage resembling that of adult pericyte morphology (Daneman et al., 2010; Obermeier et al., 2013). Additionally, pericyte expression of certain factors is crucial for proper development during this period. For example, loss of the pericyte-derived RBPJ transcription factor results in increased BBB permeability, excess TGFβ activation, cavernous malformations, and impaired vascular integrity (Diéguez-Hurtado et al., 2019). Finally, pericytes themselves are not mature until the postnatal period, as they do not begin to express CD13 until around P6 (Jung et al., 2018).

The BBB undergoes further maturation in the early postnatal period through the further attachment of astrocytic endfeet, with regulation and maintenance provided by pericytes and endothelial cells (Ma et al., 2012). Many of the factors that initiate the formation of vascular development *in utero* continue to refine these processes during the early postnatal period. For example, pericyte-expressed Tie2 plays an instrumental role in retinal angiogenesis, as Tie2 deletion delays postnatal angiogenesis

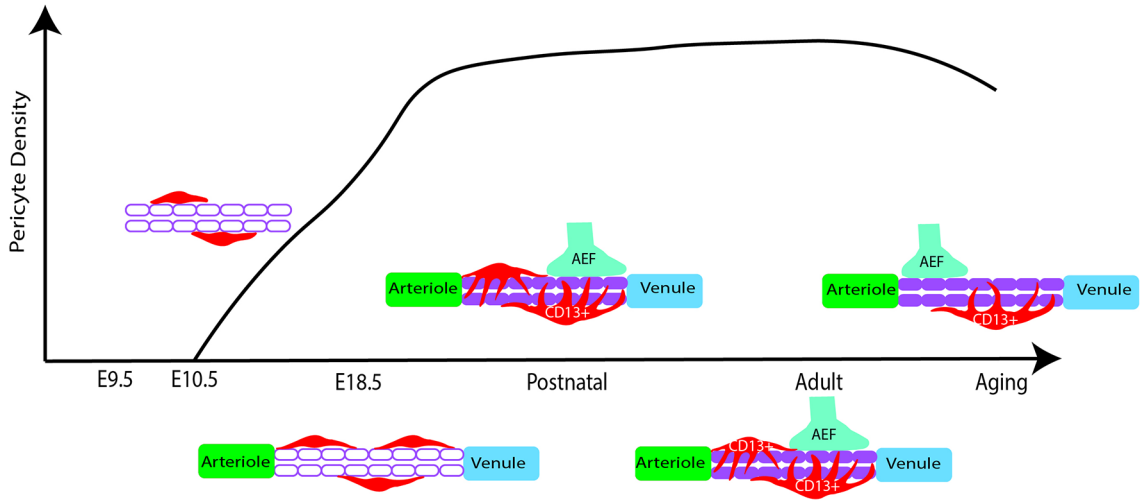

FIGURE 2 | Pericyte density changes from early embryonic development to aging in mice. At E10.5 pericyte precursors are present and begin to migrate and develop along the developing vasculature. In late embryonic development, there is increased proliferation of pericytes, showing a higher density of cells in the capillaries. During early postnatal development, proliferation subsides while increased pericyte coverage of capillaries contributes to vessel stability. Pericytes also appear more similar to adult morphology. Astrocytic end feet (AEF) properly attach and contribute to brain barrier (BBB) maturation during this period. In adulthood, the population density is rather stable while there are differences by brain region. Finally, possible pericyte loss during aging. Red: pericyte, Purple: microvessel.

and confers a migratory pericyte phenotype (Teichert et al., 2017). Additionally, PDGF-B/PDGFRβ signaling continues to promote pericyte survival and coverage of the microvasculature (Lindahl et al., 1997; Nikolakopoulou et al., 2017). There is also evidence to suggest pericytes regulate and guide postnatal endothelial expansion. This is particularly evident in the restriction of VEGF-induced endothelial sprouting, through the pericyte expression of VEGF receptor 1 (Darden et al., 2019). When VEGFR1 is specifically knocked out in pericytes there is an enlargement of vessels and associated angiogenic defects (Darden et al., 2019). Moreover, pericytes further facilitate endothelial function and BBB integrity through regulation of a key BBB regulator called endothelial major facilitator superfamily domain-containing 2a (Mfsd2a) expression, which serves to suppress transcytosis in these cells (Ben-Zvi et al., 2014). Loss of this BBB-specific protein serves to perturb tight junctions and increase endothelial transcytosis (Ben-Zvi et al., 2014). The above is only a snapshot of this concerted effort to develop and mature the BBB but also provides context for the important role pericytes play in this process. However, there are still gaps in our knowledge of these vascular developmental processes, and how this relates to neurodevelopmental disorders. For example, what is an underlying mechanism to regulate pericyte density in the early postnatal period? Do pericytes undergo a pruning stage of postnatal development that is similar to endothelial cells and neurons? How might disturbed processes in vascular development relate to neurodevelopmental disorders? Although there is much more to investigate, this vascular growth trajectory is important for understanding how the brain develops and how this development progresses in parallel with neuronal development. For further reading, the development of cerebrovascular structure and the neurogliovascular unit during the postnatal period was recently summarized in several excellent reviews (Paredes et al., 2018; Coelho-Santos and Shih, 2020).

REGIONAL DIFFERENCES OF THE PERICYTE AND ASSOCIATED VULNERABILITY IN THE ADULT CNS

Pericytes are present in most regions of the adult CNS and yet the distribution of this cell population and its associated characteristics are a major area of exploration. Although several studies have utilized *in vivo* 2-photon imaging and immunohistochemical methods to study these cells during development, aging, and disease pathology, very few studies have described pericyte population differences across brain regions of the adult mouse CNS, let alone in humans. However, pericyte populations are likely to be variable across different tissues and organs (Sims, 2000). Studies of wild-type mice demonstrate that pericyte density is decreased in the spinal cord compared to the brain, with regional variations between spinal cord levels (Winkler et al., 2012). Major challenges associated with investigating pericyte population variability, particularly in the brain, include a lack of specific cellular markers for pericytes, controversy in the field about pericyte classification, and technological limitations in quantitative cell type brain mapping (Sims, 2000; Attwell et al., 2016; Yamamoto et al., 2017). The use of transgenic PDGFRβ-Cre and NG2-Cre mouse lines has helped to demonstrate that pericytes are generally present throughout the whole mouse brain (Hartmann et al., 2015). Additionally, pericyte distribution differs by cortical layer within the cerebral cortex, indicating that these cells may not be uniformly located along the vasculature (Hartmann et al., 2015). The morphology of these cells can vary as well (Sims, 2000;

Hartmann et al., 2015; Berthiaume et al., 2018). For example, pericytes within the cerebral cortex can accommodate several morphologies, including the classical *en passant* or helical pericyte, as well as mesh pericytes which are more difficult to visually distinguish from vSMCs (Hartmann et al., 2015). Moreover, pericyte subtypes with different morphologies cover different vascular territories (Grant et al., 2019). These different pericyte morphologies and the terms used to categorize them have been recently described (Berthiaume et al., 2018). The phenotypic and molecular differences between pericytes and other mural cells have been further explored thanks to advances in single-cell RNA sequencing (Vanlandewijck et al., 2018; Zeisel et al., 2018). There seems to be a continuum in the transitions between different types of mural cells across the vasculature, in which the transition from arteriolar vSMCs to pericytes can occur between neighboring cells (Vanlandewijck et al., 2018; Grant et al., 2019). Additionally, transcriptional differences exist between arteriolar- and venule-associated vSMCs, as well as pericytes. However, there appears to be a lack of transcriptional heterogeneity within the pericyte population itself (Vanlandewijck et al., 2018).

Of course, it is necessary to note that this uniformity also depends on the definition of the pericyte that is used, which remains intensely debated in the field (Attwell et al., 2016). For example, the inclusion of smooth muscle actin-expressing contractile PDGFRβ+ cells located within the arteriolar branches of the capillary bed as pericytes may expand the transcriptional diversity of this cell population (Hall et al., 2014; Attwell et al., 2016). Additionally, another transcriptomic study indicates that there are three pericyte subtypes with type 1 being the most numerous throughout the brain while type 3 pericytes are more similar to vascular smooth muscle cells, as per their respective expression profiles (Zeisel et al., 2018). To complicate things further, studies continue to demonstrate that pericytes, even capillary pericytes, may also have vasomotor functions to regulate cerebral blood flow and neurovascular coupling (Alarcon-Martinez et al., 2020; Nelson et al., 2020). Recently, a pericyte-specific mouse model was developed using a double promoter method to exclusively label pericytes and to highlight the catastrophic effects of pericyte ablation (Nikolakopoulou et al., 2019). This new animal model will help to further delineate the complicated categorization of pericytes in the future. Additional comprehensive transcriptomic and cell-type mapping studies can also help to develop a more well-rounded definition of the pericyte by uncovering specific characteristics of this intriguing and rather unique cell population.

Pericytes have heterogeneous vulnerability across regions of the CNS in pathological conditions as well. For example, a study using $Pdgfr\beta^{F7/F7}$ mice, a model of pericyte deficiency, showed that there are regional differences in pericyte loss, capillary length reductions, and BBB breakdown (Nikolakopoulou et al., 2017). Importantly, these losses occurred much earlier and more significantly in the somatosensory cortex and hippocampus, while the thalamus and striatum were less affected (Nikolakopoulou et al., 2017). Although vSMCs also express PDGFRβ, these populations appeared to be less affected at time points in which pericyte loss was already present (Nikolakopoulou et al., 2017). This could indicate that there is a difference in the vulnerability of cortical vs. subcortical pericyte populations. The use of a similar mouse model of pericyte deficiency showed that there is also BBB permeability heterogeneity by region upon pericyte loss (Villaseñor et al., 2017). In this study, there was increased BBB permeability, measured by both Evan's blue dye and IgG leakage, in the areas of the cortex, striatum, and hippocampus, while areas such as the cerebellum and midbrain were less prominent (Villaseñor et al., 2017). Importantly, this difference was not due to differences in local pericyte coverage or changes in tight junction integrity (Villaseñor et al., 2017). The reasons behind this regional difference in permeability following significant pericyte loss should be further explored. Many of the above findings are summarized in **Figure 3**. Also, pericytes appear to be more susceptible to ischemic injury compared to endothelial cells in both the gray and white matter of rat neocortical and cerebellar brain slices, respectively (Hall et al., 2014). This susceptibility is not limited to the brain, as pericytes in the spinal cord are also quite heterogeneous and implicated in several pathologies (Bartanusz et al., 2011; Almeida et al., 2018; Picoli et al., 2019). In fact, in studies of Amyotrophic Lateral Sclerosis (ALS), there is evidence of pericyte dysfunction and loss in particular regions of the spinal cord such as the ventral horn (Winkler et al., 2013; Yamadera et al., 2015). Moreover, pericytes have been a focus of study in spinal cord injury due to their role as a potential therapeutic target and pericyte Glast-expressing subtype involvement in scar formation in response to injury (Almeida et al., 2018; Picoli et al., 2019). Differences in cell lineage and normal behaviors associated with these spinal cord pericyte subtypes would be invaluable to expanding the field's understanding of this population. Summarization of this pericyte heterogeneity in the spinal cord is also shown in **Figure 3**. This CNS pericyte vulnerability and evidence of cell loss suggest that there are cell-specific and regional differences in terms of microvascular vulnerability to injury or disease. However, several questions about CNS pericyte populations remain. How do pericyte morphology, function, and regional vulnerability differ if the population seems to be transcriptionally uniform? Are there fewer pericytes in circumventricular organs, as would be expected given the known "leakiness" of these brain regions (Wilhelm et al., 2016)? How do spinal cord pericytes differ from brain pericytes in terms of their cell lineage? One thing is certain, further studies are required to better understand pericyte and mural cell populations in general.

BBB AND PERICYTE CHANGES IN NORMAL AGING

Given the apparent evidence for pericyte vulnerability, it is possible that aging may influence the BBB and pericyte population changes. Aging itself is rather complex and further complicated by diseases that seem to be inextricably linked to the aging process in humans. Some of these pathologies include dementia, a vast array of cerebrovascular diseases, endocrine diseases, and autoimmune disorders. Not only does aging affect the body systemically, but it also has implications

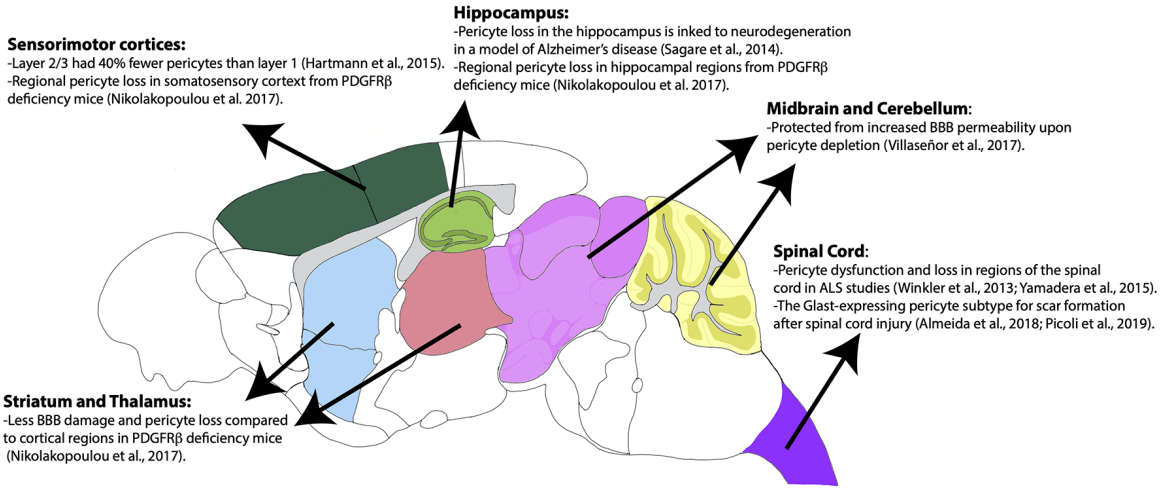

FIGURE 3 | Regional heterogeneity of pericyte distribution and vulnerabilities. Brain regions are color-coded according to the Allen Mouse Brain Atlas. Brain regions with heterogenous distribution and vulnerability are highlighted.

within the brain. Aging is known to have a multitude of effects on neuronal and glial cells, including DNA damage, morphological changes, activation of inflammatory cascades, and impairments in function, which have been recently reviewed (Knox, 1982; Peters et al., 1991; Palmer and Ousman, 2018; Valles et al., 2019). Studies also indicate that aging may contribute to changes in the neurovasculature and the BBB (Li et al., 2019). This is often linked to the consistent finding of chronic inflammation that develops during aging, typically referred to as immunoaging (Fjell et al., 2014; Palmer and Ousman, 2018; Valles et al., 2019). For example, in C57 mice aged 24 months, there is increased BBB permeability and elevated neurovascular inflammation in hippocampal and cortical regions when compared to young controls (Jansson et al., 2014; Duan et al., 2018). Furthermore, changes in inflammatory molecule expression during normal aging lead to loss of tight junction integrity and increased BBB leakiness (Jansson et al., 2014; Duan et al., 2018). The findings of this study support previous work in humans showing that healthy participants greater than 60 years of age had increased BBB permeability (Farrall and Wardlaw, 2009). Additionally, an MRI study found that even individuals without cognitive impairment had age-dependent decreases in BBB integrity in the hippocampus, particularly the dentate gyrus and CA1 region, while other cortical and subcortical regions were less affected (Montagne et al., 2015). Evidence of these age-related neurovascular changes in humans is particularly striking, especially when considering that this may be occurring in normal aging. Finally, a notable study showed that even aside from BBB leakiness, there is an age-related shift in transcytosis at the BBB, involving a decrease in receptor-mediated transport, which can heavily influence brain homeostasis (Yang et al., 2020). This study also suggested that this age-related change in transcytosis may be influenced by pericyte loss (Yang et al., 2020). Needless to say, the impacts of aging on the BBB are likely to be due to changes in its components.

There is also evidence to suggest that aging is also associated with changes in CNS pericyte populations themselves, as well as their functions and interactions with other cell types. Even in the absence of pathological states, aging in mice is associated with pericyte dysfunction (Peters et al., 1991; Hughes et al., 2006; Elahy et al., 2015). Various studies indicate that during aging, pericytes may have impaired interactions with endothelial cells (Armulik et al., 2005; Hughes et al., 2006; Elahy et al., 2015). Moreover, aging-related pericyte dysfunction has been associated with mitochondrial, migratory, and phenotypic changes (Armulik et al., 2011; Erdö et al., 2017; Jackson et al., 2017; Yamazaki and Mukouyama, 2018). For example, studies have noted ultrastructural changes in these cells, such as lipofuscin inclusions, changes in mitochondrial size, increased smooth muscle expression, and overall changes to pericyte structure and morphology (Knox, 1982; Bar, 1985; Peters et al., 1991; Hughes et al., 2006; Elahy et al., 2015). A more severe change in neurovascular function is pericyte loss, which has previously been suggested to occur in normal aging (Peters et al., 1991; Farrall and Wardlaw, 2009). Pericyte loss is well known to have detrimental effects on BBB permeability, which could also explain compromised neurovascular regulation demonstrated in previous aging studies (Bell and Zlokovic, 2009; Bell et al., 2010; Elahy et al., 2015). Additionally, pericyte loss impacts the microcirculation within the brain, leading to oxidative stress and hypoxia in these oxygen-starved areas (Bell et al., 2010). However, pericyte loss upon aging remains controversial, as pericyte populations appeared to be similar when compared in 2-month-old and 22-month-old mice, according to a recent transcriptomic study (Ximerakis et al., 2019). Of course, it is important to keep in mind that this study does not account for potential subtypes or regional differences in this cell population. Therefore, it will be necessary to resolve this controversy to better distinguish changes in normal aging from those that occur in pathological processes.

TABLE 1 | Pericyte involvement in human diseases.

System	Disease	Associated regions	References
Neurological	Epilepsy	Temporal lobe (most commonly)	Sweeney et al. (2018b)
	Spinal cord injury	The spinal cord, CNS	Bartanusz et al. (2011), Almeida et al. (2018), Sweeney et al. (2018b) and Picoli et al. (2019)
Neurodegenerative	Alzheimer's disease	Hippocampus, entorhinal cortex, basal forebrain	Girouard and Iadecola (2006), Zlokovic (2008), Bell and Zlokovic (2009), Armulik et al. (2011), Winkler et al. (2011), Baloyannis and Baloyannis (2012), Rosenberg (2014), Di Marco et al. (2015), Lane-Donovan and Herz (2017), Newcombe et al. (2018), Sweeney et al. (2018a), Lendahl et al. (2019), Nation et al. (2019) and Montagne et al. (2020)
	Vascular dementia	Commonly vascular regions of the middle cerebral artery	Montagne et al. (2020), Moretti and Caruso (2020) and Uemura et al. (2020)
	Parkinson's disease	Substantia nigra pars compacta	Erdö et al. (2017), Sweeney et al. (2018b) and Li et al. (2019)
	Traumatic brain injury/traumatic encephalopathy	Frontal lobe regions	Dore-Duffy et al. (2000) and Main et al. (2018)
Cardiovascular	Diabetes mellitus, DM Retinopathy	Retina	Pfister et al. (2008), Persidsky et al. (2016), Laredo et al. (2019) and Rhea and Banks (2019), Liu et al. (2020)
	Hypertension	The vascular territory of the middle cerebral artery	Knox (1982), Girouard and Iadecola (2006) and Hirunpattarasilp et al. (2019)
	Small vessel disease	Microvasculature	Hogan and Feeney (1963), Neurology Working Group of the Cohorts for Heart and Aging Research in Genomic Epidemiology (CHARGE) Consortium, the Stroke Genetics Network (SiGN) and the International Stroke Genetics Consortium (ISGC) (2016) and Moretti and Caruso (2020)
	Stroke, Ischemia	Several CNS regions	Girouard and Iadecola (2006), Lucke-Wold et al. (2014), Neurology Working Group of the Cohorts for Heart and Aging Research in Genomic Epidemiology (CHARGE) Consortium, the Stroke Genetics Network (SiGN) and the International Stroke Genetics Consortium (ISGC) (2016) and Hu et al. (2017)
Immunological	(ALS)	Spinal cord	Zlokovic (2008) and Winkler et al. (2011)
	Multiple sclerosis (MS)	White matter tracts of the brain	Ortiz et al. (2014)
	General neuroinflammation	Blood-brain barrier (BBB)	Jansson et al. (2014), Persidsky et al. (2016), Rustenhoven et al. (2017) and Newcombe et al. (2018)
CNS Infection	Viral: HIV, CMV	BBB	Nakagawa et al. (2012) and Bertrand et al. (2019)
	Bacterial infections	BBB	Guijarro-Muñoz et al. (2014)
Cancer of the CNS	Glioblastoma/Glioma	BBB, midline cortical regions	Liebner et al. (2018) and Valdor et al. (2019)

BBB AND PERICYTE DYSFUNCTION IN PATHOLOGICAL AGING

Pathological states, particularly neurodegenerative diseases, have increased damage to the cerebral microvasculature and pericytes. Notably, increased BBB permeability and inflammation have been demonstrated in human patients with Alzheimer's disease (AD) and AD mouse models (Bell and Zlokovic, 2009; Halliday et al., 2016; Kisler et al., 2017; Brown et al., 2019). Given that these changes are also present in normal aging, it is likely that these pathological processes further compromise neurovascular function. For example, in the amyloid precursor protein (APP) overexpression mouse model of AD, pericyte loss accelerated Amyloid β (Aβ) pathology and neurodegeneration with deteriorated memory performance (Sagare et al., 2013). Several studies have further demonstrated that pericyte deficiency is associated with neurodegeneration in both the gray and white matter of the brain (Bell et al., 2010; Montagne et al., 2018; Nikolakopoulou et al., 2019). Moreover, pericytes express pleiotrophin which is a neurotrophic growth factor that is crucial for neuronal health (Nikolakopoulou et al., 2019). This suggests that pericytes' roles may expand

beyond BBB functions to directly contribute to neuronal health in the brain. Furthermore, this provides evidence that vascular and pericyte dysfunction occurs before neurons begin to show evidence of damage and cell loss. Additionally, Aβ oligomers have been shown to signal to pericytes, thereby causing capillary constriction (Nortley et al., 2019). This demonstrates a crucial link between the toxic accumulation of cellular byproducts and associated neurovascular dysfunction. Moreover, pericytes are known to clear Aβ through receptor-mediated endocytosis, involving the low-density receptor-related protein 1 (LRP1), which is an important protein in Aβ homeostasis at the BBB (Shibata et al., 2000; Ma et al., 2018). Clearly, pericytes are instrumental in the regulation of Aβ accumulation and may provide a key link in the pathophysiology of AD.

Importantly, apolipoprotein E4 (APOE4), which is a major susceptibility factor for the development of AD has also been linked to BBB dysfunction and injury to pericytes in both AD models and in human carriers (Lane-Donovan and Herz, 2017; Uddin et al., 2019; Montagne et al., 2020). For instance, APOE4 is linked to BBB breakdown through the activation of a proinflammatory cascade in pericytes through upregulation of the cyclophilin A-mediated nuclear factor κB-matrix metalloproteinase-9 pathway (Bell et al., 2012; Halliday et al., 2016). This not only helps to clarify the role of pericytes in neuroinflammatory states but could also relate to the inflammatory processes that are classically associated with AD pathology. Recently, APOE4 carriers were shown to have increased evidence of pericyte injury, measured by soluble PDGFRβ (sPDGFRβ), which was predictive of cognitive decline independent of Aβ and pTau status (Sagare et al., 2015; Sweeney et al., 2015; Nation et al., 2019; Montagne et al., 2020). Moreover, a new method for detecting sPDGFRβ in both the plasma and cerebrospinal fluid can be clinically useful for identifying pericyte injury in neurovascular diseases (Sweeney et al., 2020). These studies further support that pericytes have an important role in neurodegenerative disease and spark additional questions relating to the role of pericytes in AD. Furthermore, pericyte loss has long been associated with diabetic retinopathy and diabetes mellitus is known to be a major risk factor for the development of AD (Pfister et al., 2008, 2010; Hayden, 2019). It is not surprising to think that neurovascular dysfunction likely serves as a unifying factor in the development of these disease processes. It would be intriguing to know whether the sPDGFRβ marker for pericyte injury could also be identified in other diseases associated with neurovascular dysfunction, such as diabetes, and how this could serve clinically to potentially identify patients with higher risk of cognitive decline. However, pericytes are not only implicated in AD, as evidence relating to pericyte involvement in various human diseases has recently been described in several excellent reviews (**Table 1**).

CONCLUSION

The pericyte population of the brain is not static during our lifetime. These cells arise from heterogeneous sources and undergo significant cell proliferation and migration throughout embryonic development. Unlike other cell types, they have slowed proliferation in early postnatal stages, while also reaching their processes extensively across the microvasculature. Finally, in adulthood pericytes show varying morphologies and characteristics, and yet, this cell population is transcriptionally similar across the board. Moreover, mounting evidence continues to demonstrate the importance of these cells during the lifespan and in all regions of the mammalian brain. Pericytes are also becoming increasingly recognized for their potential roles in the pathophysiology of various human diseases, particularly those impacted by the aging process. With each new study, these mural cells become more intriguing and unique. To better understand this cell population and the brain vasculature as a whole, research cannot only be restricted to particular regions as this does not encompass the systemic impact of the brain vasculature.

AUTHOR CONTRIBUTIONS

HB and YK conceptualized the manuscript. HB wrote the initial manuscript draft and figures. YK handled the funding and critically revised the manuscript. All authors contributed to the article and approved the submitted version.

FUNDING

This publication was made possible by an NIH Blueprint for Neuroscience Research, NIH grant R01NS108407 to YK. Its contents are solely the responsibility of the authors and do not necessarily represent the views of the funding agency.

ACKNOWLEDGMENTS

We thank Rebecca Betty for her assistance in editing the manuscript.

REFERENCES

Alarcon-Martinez, L., Villafranca-Baughman, D., Quintero, H., Kacerovsky, J. B., Dotigny, F., Murai, K. K., et al. (2020). Interpericyte tunnelling nanotubes regulate neurovascular coupling. *Nature* 585, 91–95. doi: 10.1038/s41586-020-2589-x

Allinson, K. R., Lee, H. S., Fruttiger, M., McCarty, J. H., McCarty, J., and Arthur, H. M. (2012). Endothelial expression of TGFβ type II receptor is required to maintain vascular integrity during postnatal development of the central nervous system. *PLoS One* 7:e39336. doi: 10.1371/journal.pone.0039336

Almeida, V. M., Paiva, A. E., Sena, I. F. G., Mintz, A., Magno, L. A. V., and Birbrair, A. (2018). Pericytes make spinal cord breathless after injury. *Neuroscientist* 24, 440–447. doi: 10.1177/1073858417731522

Armulik, A., Abramsson, A., and Betsholtz, C. (2005). Endothelial/pericyte interactions. *Circ. Res.* 97, 512–523. doi: 10.1161/01.RES.0000182903.16652.d7

Armulik, A., Genové, G., and Betsholtz, C. (2011). Pericytes: developmental, physiological, and pathological perspectives, problems, and promises. *Dev. Cell* 21, 193–215. doi: 10.1016/j.devcel.2011.07.001

Attwell, D., Mishra, A., Hall, C. N., O'Farrell, F. M., and Dalkara, T. (2016). What is a pericyte? *J. Cereb. Blood Flow Metab.* 36, 451–455. doi: 10.1177/0271678X15610340

Ballabh, P., Braun, A., and Nedergaard, M. (2004). The blood-brain barrier: an overview: structure, regulation, and clinical implications. *Neurobiol. Dis.* 16, 1–13. doi: 10.1016/j.nbd.2003.12.016

Baloyannis, S. J., and Baloyannis, I. S. (2012). The vascular factor in Alzheimer's disease: a study in Golgi technique and electron microscopy. *J. Neurol. Sci.* 322, 117–121. doi: 10.1016/j.jns.2012.07.010

Bar, T. (1985). Morphometric aspects of aging in central nervous system capillaries. *Atti della Fondazione Giorgio Ronchi*, 40, 471.

Bartanusz, V., Jezova, D., Alajajian, B., and Digicaylioglu, M. (2011). The blood-spinal cord barrier: morphology and clinical implications. *Ann. Neurol.* 70, 194–206. doi: 10.1002/ana.22421

Bell, R. D., Winkler, E. A., Sagare, A. P., Singh, I., LaRue, B., Deane, R., et al. (2010). Pericytes control key neurovascular functions and neuronal phenotype in the adult brain and during brain aging. *Neuron* 68, 409–427. doi: 10.1016/j.neuron.2010.09.043

Bell, R. D., Winkler, E. A., Singh, I., Sagare, A. P., Deane, R., Wu, Z., et al. (2012). Apolipoprotein E controls cerebrovascular integrity *via* cyclophilin A. *Nature* 485, 512–516. doi: 10.1038/nature11087

Bell, R. D., and Zlokovic, B. V. (2009). Neurovascular mechanisms and blood-brain barrier disorder in Alzheimer's disease. *Acta Neuropathol.* 118, 103–113. doi: 10.1007/s00401-009-0522-3

Ben-Zvi, A., Lacoste, B., Kur, E., Andreone, B. J., Mayshar, Y., Yan, H., et al. (2014). Mfsd2a is critical for the formation and function of the blood-brain barrier. *Nature* 509, 507–511. doi: 10.1038/nature13324

Bergers, G., and Song, S. (2005). The role of pericytes in blood-vessel formation and maintenance. *Neuro Oncol.* 7, 452–464. doi: 10.1215/S1152851705000232

Berthiaume, A. A., Hartmann, D. A., Majesky, M. W., Bhat, N. R., and Shih, A. Y. (2018). Pericyte structural remodeling in cerebrovascular health and homeostasis. *Front. Aging Neurosci.* 10:210. doi: 10.3389/fnagi.2018.00210

Bertrand, L., Cho, H. J., and Toborek, M. (2019). Blood-brain barrier pericytes as a target for HIV-1 infection. *Brain* 142, 502–511. doi: 10.1093/brain/awy339

Birbrair, A. (Ed.). (2019). *Pericyte Biology in Disease.* Switzerland: Springer International Publishing. doi: 10.1007/978-3-030-16908-4

Bondjers, C., He, L., Takemoto, M., Norlin, J., Asker, N., Hellström, M., et al. (2006). Microarray analysis of blood microvessels from PDGF-B and PDGF-Rβ mutant mice identifies novel markers for brain pericytes. *FASEB J.* 20, 1703–1705. doi: 10.1096/fj.05-4944fje

Brown, L. S., Foster, C. G., Courtney, J.-M., King, N. E., Howells, D. W., and Sutherland, B. A. (2019). Pericytes and neurovascular function in the healthy and diseased brain. *Front. Cell. Neurosci.* 13:282. doi: 10.3389/fncel.2019.00282

Coelho-Santos, V., and Shih, A. Y. (2020). Postnatal development of cerebrovascular structure and the neurogliovascular unit. *Wiley Interdiscip. Rev. Dev. Biol.* 9:e363. doi: 10.1002/wdev.363

Daneman, R., Zhou, L., Kebede, A. A., and Barres, B. A. (2010). Pericytes are required for blood-brain barrier integrity during embryogenesis. *Nature* 468, 562–566. doi: 10.1038/nature09513

Darden, J., Payne, L. B., Zhao, H., and Chappell, J. C. (2019). Excess vascular endothelial growth factor-A disrupts pericyte recruitment during blood vessel formation. *Angiogenesis* 22, 167–183. doi: 10.1007/s10456-018-9648-z

Dave, J. M., Mirabella, T., Weatherbee, S. D., and Greif, D. M. (2018). Pericyte ALK5/TIMP3 axis contributes to endothelial morphogenesis in the developing brain. *Dev. Cell* 44, 665.e6–678.e6. doi: 10.1016/j.devcel.2018.01.018

Di Marco, L. Y., Venneri, A., Farkas, E., Evans, P. C., Marzo, A., and Frangi, A. F. (2015). Vascular dysfunction in the pathogenesis of Alzheimer's disease-A review of endothelium-mediated mechanisms and ensuing vicious circles. *Neurobiol. Dis.* 82, 593–606. doi: 10.1016/j.nbd.2015.08.014

Diéguez-Hurtado, R., Kato, K., Giaimo, B. D., Nieminen-Kelhä, M., Arf, H., Ferrante, F., et al. (2019). Loss of the transcription factor RBPJ induces disease-promoting properties in brain pericytes. *Nat. Commun.* 10:2817. doi: 10.1038/s41467-019-10643-w

Dore-Duffy, P., Owen, C., Balabanov, R., Murphy, S., Beaumont, T., and Rafols, J. A. (2000). Pericyte migration from the vascular wall in response to traumatic brain injury. *Microvasc. Res.* 60, 55–69. doi: 10.1006/mvre.2000.2244

Duan, L., Zhang, X.-D., Miao, W.-Y., Sun, Y.-J., Xiong, G., Wu, Q., et al. (2018). PDGFRβ cells rapidly relay inflammatory signal from the circulatory system to neurons *via* chemokine CCL2. *Neuron* 100, 183.e8–200.e8. doi: 10.1016/j.neuron.2018.08.030

Elahy, M., Jackaman, C., Mamo, J. C., Lam, V., Dhaliwal, S. S., Giles, C., et al. (2015). Blood-brain barrier dysfunction developed during normal aging is associated with inflammation and loss of tight junctions but not with leukocyte recruitment. *Immun. Ageing* 12:2. doi: 10.1186/s12979-015-0029-9

Erdö, F., Denes, L., and de Lange, E. (2017). Age-associated physiological and pathological changes at the blood-brain barrier: a review. *J. Cereb. Blood Flow Metab.* 37, 4–24. doi: 10.1177/0271678X16679420

Farrall, A. J., and Wardlaw, J. M. (2009). Blood-brain barrier: ageing and microvascular disease—systematic review and meta-analysis. *Neurobiol. Aging* 30, 337–352. doi: 10.1016/j.neurobiolaging.2007.07.015

Fjell, A. M., McEvoy, L., Holland, D., Dale, A. M., and Walhovd, K. B. (2014). What is normal in normal aging? Effects of aging, amyloid and Alzheimer's disease on the cerebral cortex and the hippocampus. *Prog. Neurobiol.* 117, 20–40. doi: 10.1016/j.pneurobio.2014.02.004

Girouard, H., and Iadecola, C. (2006). Neurovascular coupling in the normal brain and in hypertension, stroke, and Alzheimer disease. *J. Appl. Physiol.* 100, 328–335. doi: 10.1152/japplphysiol.00966.2005

Gökçinar-Yagci, B., Uçkan-Çetinkaya, D., and Çelebi-Saltik, B. (2015). Pericytes: properties, functions and applications in tissue engineering. *Stem Cell Rev. Rep.* 11, 549–559. doi: 10.1007/s12015-015-9590-z

Grant, R. I., Hartmann, D. A., Underly, R. G., Berthiaume, A.-A., Bhat, N. R., and Shih, A. Y. (2019). Organizational hierarchy and structural diversity of microvascular pericytes in adult mouse cortex. *J. Cereb. Blood Flow Metab.* 39, 411–425. doi: 10.1177/0271678X17732229

Guijarro-Muñoz, I., Compte, M., Álvarez-Cienfuegos, A., Álvarez-Vallina, L., and Sanz, L. (2014). Lipopolysaccharide activates Toll-like receptor 4 (TLR4)-mediated NF-κB signaling pathway and proinflammatory response in human pericytes. *J. Biol. Chem.* 289, 2457–2468. doi: 10.1074/jbc.M113.521161

Hall, C. N., Reynell, C., Gesslein, B., Hamilton, N. B., Mishra, A., Sutherland, B. A., et al. (2014). Capillary pericytes regulate cerebral blood flow in health and disease. *Nature* 508, 55–60. doi: 10.1038/nature13165

Halliday, M. R., Rege, S. V., Ma, Q., Zhao, Z., Miller, C. A., Winkler, E. A., et al. (2016). Accelerated pericyte degeneration and blood-brain barrier breakdown in apolipoprotein E4 carriers with Alzheimer's disease. *J. Cereb. Blood Flow Metab.* 36, 216–227. doi: 10.1038/jcbfm.2015.44

Harb, R., Whiteus, C., Freitas, C., and Grutzendler, J. (2013). *in vivo* imaging of cerebral microvascular plasticity from birth to death. *J. Cereb. Blood Flow Metab.* 33, 146–156. doi: 10.1038/jcbfm.2012.152

Hartmann, D. A., Underly, R. G., Grant, R. I., Watson, A. N., Lindner, V., and Shih, A. Y. (2015). Pericyte structure and distribution in the cerebral cortex revealed by high-resolution imaging of transgenic mice. *Neurophotonics* 2:041402. doi: 10.1117/1.NPh.2.4.041402

Hayden, . (2019). Type 2 diabetes mellitus increases the risk of late-onset Alzheimer's disease: ultrastructural remodeling of the neurovascular unit and diabetic gliopathy. *Brain Sci.* 9:262. doi: 10.3390/brainsci9100262

Hellström, M., Gerhardt, H., Kalén, M., Li, X., Eriksson, U., Wolburg, H., et al. (2001). Lack of pericytes leads to endothelial hyperplasia and abnormal vascular morphogenesis. *J. Cell Biol.* 153, 543–553. doi: 10.1083/jcb.153.3.543

Hirunpattarasilp, C., Attwell, D., and Freitas, F. (2019). The role of pericytes in brain disorders: from the periphery to the brain. *J. Neurochem.* 150, 648–665. doi: 10.1111/jnc.14725

Hogan, M. J., and Feeney, L. (1963). The ultrastructure of the retinal vessels: II. The small vessels. *J. Ultrastruct. Res.* 9, 29–46. doi: 10.1016/s0022-5320(63)80034-9

Hu, X., De Silva, T. M., Chen, J., and Faraci, F. M. (2017). Cerebral vascular disease and neurovascular injury in ischemic stroke. *Circ. Res.* 120, 449–471. doi: 10.1161/CIRCRESAHA.116.308427

Hughes, S., Gardiner, T., Hu, P., Baxter, L., Rosinova, E., and Chan-Ling, T. (2006). Altered pericyte-endothelial relations in the rat retina during aging: implications for vessel stability. *Neurobiol. Aging* 27, 1838–1847. doi: 10.1016/j.neurobiolaging.2005.10.021

Jackson, S., ElAli, A., Virgintino, D., and Gilbert, M. R. (2017). Blood-brain barrier pericyte importance in malignant gliomas: what we can learn from stroke and Alzheimer's disease. *Neuro Oncol.* 19, 1173–1182. doi: 10.1093/neuonc/nox058

Jansson, D., Rustenhoven, J., Feng, S., Hurley, D., Oldfield, R. L., Bergin, P. S., et al. (2014). A role for human brain pericytes in neuroinflammation. *J. Neuroinflammation* 11:104. doi: 10.1186/1742-2094-11-104

Jung, B., Arnold, T. D., Raschperger, E., Gaengel, K., and Betsholtz, C. (2018). Visualization of vascular mural cells in developing brain using genetically labeled transgenic reporter mice. *J. Cereb. Blood Flow Metab.* 38, 456–468. doi: 10.1177/0271678X17697720

Kamouchi, M., Ago, T., and Kitazono, T. (2011). Brain pericytes: emerging concepts and functional roles in brain homeostasis. *Cell. Mol. Neurobiol.* 31, 175–193. doi: 10.1007/s10571-010-9605-x

Kisler, K., Nelson, A. R., Rege, S. V., Ramanathan, A., Wang, Y., Ahuja, A., et al. (2017). Pericyte degeneration leads to neurovascular uncoupling and limits oxygen supply to brain. *Nat. Neurosci.* 20, 406–416. doi: 10.1038/nn.4489

Knox, C. A. (1982). Effects of aging and chronic arterial hypertension on the cell populations in the neocortex and archicortex of the rat. *Acta Neuropathol.* 56, 139–145. doi: 10.1007/BF00690585

Lane-Donovan, C., and Herz, J. (2017). ApoE, ApoE receptors, and the synapse in Alzheimer's disease. *Trends Endocrinol. Metab.* 28, 273–284. doi: 10.1016/j.tem.2016.12.001

Laredo, F., Plebanski, J., and Tedeschi, A. (2019). Pericytes: problems and promises for CNS repair. *Front. Cell. Neurosci.* 13:546. doi: 10.3389/fncel.2019.00546

Lendahl, U., Nilsson, P., and Betsholtz, C. (2019). Emerging links between cerebrovascular and neurodegenerative diseases-a special role for pericytes. *EMBO Rep.* 20:e48070. doi: 10.15252/embr.201948070

Li, Y., Xie, L., Huang, T., Zhang, Y., Zhou, J., Qi, B., et al. (2019). Aging neurovascular unit and potential role of DNA Damage and repair in combating vascular and neurodegenerative disorders. *Front. Neurosci.* 13:778. doi: 10.3389/fnins.2019.00778

Liebner, S., Dijkhuizen, R. M., Reiss, Y., Plate, K. H., Agalliu, D., and Constantin, G. (2018). Functional morphology of the blood-brain barrier in health and disease. *Acta Neuropathol.* 135, 311–336. doi: 10.1007/s00401-018-1815-1

Lindahl, P., Johansson, B. R., Levéen, P., and Betsholtz, C. (1997). Pericyte loss and microaneurysm formation in PDGF-B-deficient mice. *Science* 277, 242–245. doi: 10.1126/science.277.5323.242

Liu, Q., Yang, Y., and Fan, X. (2020). Microvascular pericytes in brain-associated vascular disease. *Biomed. Pharmacother.* 121:109633. doi: 10.1016/j.biopha.2019.109633

Lucke-Wold, B. P., Logsdon, A. F., Turner, R. C., Rosen, C. L., and Huber, J. D. (2014). Aging, the metabolic syndrome, and ischemic stroke: redefining the approach for studying the blood-brain barrier in a complex neurological disease. *Adv Pharmacol.* 71, 411–449. doi: 10.1016/bs.apha.2014.07.001

Ma, Q., Zhao, Z., Sagare, A. P., Wu, Y., Wang, M., Owens, N. C., et al. (2018). Blood-brain barrier-associated pericytes internalize and clear aggregated amyloid-β42 by LRP1-dependent apolipoprotein E isoform-specific mechanism. *Mol. Neurodegener.* 13:57. doi: 10.1186/s13024-018-0286-0

Ma, S., Kwon, H. J., and Huang, Z. (2012). A functional requirement for astroglia in promoting blood vessel development in the early postnatal brain. *PLoS One* 7:e48001. doi: 10.1371/journal.pone.0048001

Main, B. S., Villapol, S., Sloley, S. S., Barton, D. J., Parsadanian, M., Agbaegbu, C., et al. (2018). Apolipoprotein E4 impairs spontaneous blood brain barrier repair following traumatic brain injury. *Mol. Neurodegener.* 13:17. doi: 10.1186/s13024-018-0249-5

Montagne, A., Barnes, S. R., Sweeney, M. D., Halliday, M. R., Sagare, A. P., Zhao, Z., et al. (2015). Blood-brain barrier breakdown in the aging human hippocampus. *Neuron* 85, 296–302. doi: 10.1016/j.neuron.2014.12.032

Montagne, A., Nation, D. A., Sagare, A. P., Barisano, G., Sweeney, M. D., Chakhoyan, A., et al. (2020). APOE4 leads to blood-brain barrier dysfunction predicting cognitive decline. *Nature* 581, 71–76. doi: 10.1038/s41586-020-2247-3

Montagne, A., Nikolakopoulou, A. M., Zhao, Z., Sagare, A. P., Si, G., Lazic, D., et al. (2018). Pericyte degeneration causes white matter dysfunction in the mouse central nervous system. *Nat. Med.* 24, 326–337. doi: 10.1038/nm.4482

Moretti, R., and Caruso, P. (2020). Small vessel disease-related dementia: an invalid neurovascular coupling? *Int. J. Mol. Sci.* 21:1095. doi: 10.3390/ijms21031095

Nakagawa, S., Castro, V., and Toborek, M. (2012). Infection of human pericytes by HIV-1 disrupts the integrity of the blood-brain barrier. *J. Cell. Mol. Med.* 16, 2950–2957. doi: 10.1111/j.1582-4934.2012.01622.x

Nakagomi, T., Nakano-Doi, A., Kawamura, M., and Matsuyama, T. (2015). Do vascular pericytes contribute to neurovasculogenesis in the central nervous system as multipotent vascular stem cells? *Stem Cells Dev.* 24, 1730–1739. doi: 10.1089/scd.2015.0039

Nation, D. A., Sweeney, M. D., Montagne, A., Sagare, A. P., D'Orazio, L. M., Pachicano, M., et al. (2019). Blood-brain barrier breakdown is an early biomarker of human cognitive dysfunction. *Nat. Med.* 25, 270–276. doi: 10.1038/s41591-018-0297-y

Nelson, A. R., Sagare, M. A., Wang, Y., Kisler, K., Zhao, Z., and Zlokovic, B. V. (2020). Channelrhodopsin excitation contracts brain pericytes and reduces blood flow in the aging mouse brain *in vivo*. *Front. Aging Neurosci.* 12:108. doi: 10.3389/fnagi.2020.00108

Neurology Working Group of the Cohorts for Heart and Aging Research in Genomic Epidemiology (CHARGE) Consortium, the Stroke Genetics Network (SiGN) and the International Stroke Genetics Consortium (ISGC). (2016). Identification of additional risk loci for stroke and small vessel disease: a meta-analysis of genome-wide association studies. *Lancet Neurol.* 15, 695–707. doi: 10.1016/S1474-4422(16)00102-2

Newcombe, E. A., Camats-Perna, J., Silva, M. L., Valmas, N., Huat, T. J., and Medeiros, R. (2018). Inflammation: the link between comorbidities, genetics, and Alzheimer's disease. *J. Neuroinflammation* 15:276. doi: 10.1186/s12974-018-1313-3

Nikolakopoulou, A. M., Montagne, A., Kisler, K., Dai, Z., Wang, Y., Huuskonen, M. T., et al. (2019). Pericyte loss leads to circulatory failure and pleiotrophin depletion causing neuron loss. *Nat. Neurosci.* 22, 1089–1098. doi: 10.1038/s41593-019-0434-z

Nikolakopoulou, A. M., Zhao, Z., Montagne, A., and Zlokovic, B. V. (2017). Regional early and progressive loss of brain pericytes but not vascular smooth muscle cells in adult mice with disrupted platelet-derived growth factor receptor-β signaling. *PLoS One* 12:e0176225. doi: 10.1371/journal.pone.0176225

Nortley, R., Korte, N., Izquierdo, P., Hirunpattarasilp, C., Mishra, A., Jaunmuktane, Z., et al. (2019). Amyloid β oligomers constrict human capillaries in Alzheimer's disease *via* signaling to pericytes. *Science* 365:eaav9518. doi: 10.1126/science.aav9518

Obermeier, B., Daneman, R., and Ransohoff, R. M. (2013). Development, maintenance and disruption of the blood-brain barrier. *Nat. Med.* 19, 1584–1596. doi: 10.1038/nm.3407

Ortiz, G. G., Pacheco-Moisés, F. P., Macías-Islas, M. Á., Flores-Alvarado, L. J., Mireles-Ramírez, M. A., González-Renovato, E. D., et al. (2014). Role of the blood-brain barrier in multiple sclerosis. *Arch. Med. Res.* 45, 687–697. doi: 10.1016/j.arcmed.2014.11.013

Palmer, A. L., and Ousman, S. S. (2018). Astrocytes and aging. *Front. Aging Neurosci.* 10, 337–337. doi: 10.3389/fnagi.2018.00337

Paredes, I., Himmels, P., and Ruiz de Almodóvar, C. (2018). Neurovascular communication during CNS development. *Dev. cell* 45, 10–32. doi: 10.1016/j.devcel.2018.01.023

Persidsky, Y., Hill, J., Zhang, M., Dykstra, H., Winfield, M., Reichenbach, N. L., et al. (2016). Dysfunction of brain pericytes in chronic neuroinflammation. *J. Cereb. Blood Flow Metab.* 36, 794–807. doi: 10.1177/0271678X15606149

Peters, A., Josephson, K., and Vincent, S. L. (1991). Effects of aging on the neuroglial cells and pericytes within area 17 of the rhesus monkey cerebral cortex. *Anat. Rec.* 229, 384–398. doi: 10.1002/ar.1092290311

Pfister, F., Feng, Y., Hagen, F. V., Hoffmann, S., Molema, G., Hillebrands, J. L., et al. (2008). Pericyte migration: a novel mechanism of pericyte loss in experimental diabetic retinopathy. *Diabetes* 57, 2495–2502. doi: 10.2337/db08-0325

Pfister, F., Lin, J., and Hammes, H.-P. (2010). "Pericyte loss in the diabetic retina," in *Experimental Approaches to Diabetic Retinopathy*, eds H.-P. Hammes and M. Porta (Basel: Karger), 61–78. doi: 10.1159/000262662

Picoli, C. C., Coimbra-Campos, L. M. C., Guerra, D. A. P., Silva, W. N., Prazeres, P. H. D. M., Costa, A. C., et al. (2019). Pericytes act as key players in spinal cord injury. *Am. J. Pathol.* 189, 1327–1337. doi: 10.1016/j.ajpath.2019.03.008

Prazeres, P. H. D. M., Almeida, V. M., Lousado, L., Andreotti, J. P., Paiva, A. E., Santos, G. S. P., et al. (2018). Macrophages generate pericytes in the developing brain. *Cell. Mol. Neurobiol.* 38, 777–782. doi: 10.1007/s10571-017-0549-2

Reyahi, A., Nik, A. M., Ghiami, M., Gritli-Linde, A., Pontén, F., Johansson, B. R., et al. (2015). Foxf2 is required for brain pericyte differentiation and development and maintenance of the blood-brain barrier. *Dev. Cell* 34, 19–32. doi: 10.1016/j.devcel.2015.05.008

Rhea, E. M., and Banks, W. A. (2019). Role of the blood-brain barrier in central nervous system insulin resistance. *Front. Neurosci.* 13:521. doi: 10.3389/fnins.2019.00521

Rosenberg, G. A. (2014). Blood-brain barrier permeability in aging and Alzheimer's disease. *J. Prev. Alzheimers Dis.* 1, 138–139. doi: 10.14283/jpad.2014.25

Rustenhoven, J., Jansson, D., Smyth, L. C., and Dragunow, M. (2017). Brain pericytes as mediators of neuroinflammation. *Trends Pharmacol. Sci.* 38, 291–304. doi: 10.1016/j.tips.2016.12.001

Sagare, A. P., Bell, R. D., Zhao, Z., Ma, Q., Winkler, E. A., Ramanathan, A., et al. (2013). Pericyte loss influences Alzheimer-like neurodegeneration in mice. *Nat. Commun.* 4:2932. doi: 10.1038/ncomms3932

Sagare, A. P., Sweeney, M. D., Makshanoff, J., and Zlokovic, B. V. (2015). Shedding of soluble platelet-derived growth factor receptor-β from human brain pericytes. *Neurosci. Lett.* 607, 97–101. doi: 10.1016/j.neulet.2015.09.025

Semple, B. D., Blomgren, K., Gimlin, K., Ferriero, D. M., and Noble-Haeusslein, L. J. (2013). Brain development in rodents and humans: identifying benchmarks of maturation and vulnerability to injury across species. *Prog. Neurobiol.* 106–107, 1–16. doi: 10.1016/j.pneurobio.2013.04.001

Shibata, M., Yamada, S., Kumar, S. R., Calero, M., Bading, J., Frangione, B., et al. (2000). Clearance of Alzheimer's amyloid-β(1–40) peptide from brain by LDL receptor-related protein-1 at the blood-brain barrier. *J. Clin. Invest.* 106, 1489–1499. doi: 10.1172/JCI10498

Sims, D. E. (2000). Diversity within pericytes. *Clin. Exp. Pharmacol. Physiol.* 27, 842–846. doi: 10.1046/j.1440-1681.2000.03343.x

Sweeney, M. D., Ayyadurai, S., and Zlokovic, B. V. (2016). Pericytes of the neurovascular unit: key functions and signaling pathways. *Nat. Neurosci.* 19, 771–783. doi: 10.1038/nn.4288

Sweeney, M. D., Sagare, A. P., and Zlokovic, B. V. (2015). Cerebrospinal fluid biomarkers of neurovascular dysfunction in mild dementia and Alzheimer's disease. *J. Cereb. Blood Flow Metab.* 35, 1055–1068. doi: 10.1038/jcbfm.2015.76

Sweeney, M. D., Sagare, A. P., and Zlokovic, B. V. (2018a). Blood-brain barrier breakdown in Alzheimer disease and other neurodegenerative disorders. *Nat. Rev. Neurol.* 14, 133–150. doi: 10.1038/nrneurol.2017.188

Sweeney, M. D., Zhao, Z., Montagne, A., Nelson, A. R., and Zlokovic, B. V. (2018b). Blood-brain barrier: from physiology to disease and back. *Physiol. Rev.* 99, 21–78. doi: 10.1152/physrev.00050.2017

Sweeney, M. D., Sagare, A. P., Pachicano, M., Harrington, M. G., Joe, E., Chui, H. C., et al. (2020). A novel sensitive assay for detection of a biomarker of pericyte injury in cerebrospinal fluid. *Alzheimers Dement.* 16, 821–830. doi: 10.1002/alz.12061

Teichert, M., Milde, L., Holm, A., Stanicek, L., Gengenbacher, N., Savant, S., et al. (2017). Pericyte-expressed Tie2 controls angiogenesis and vessel maturation. *Nat. Commun.* 8:16106. doi: 10.1038/ncomms16106

Trost, A., Lange, S., Schroedl, F., Bruckner, D., Motloch, K. A., Bogner, B., et al. (2016). Brain and retinal pericytes: origin, function and role. *Front. Cell. Neurosci.* 10:20. doi: 10.3389/fncel.2016.00020

Uddin, M. S., Kabir, M. T., Al Mamun, A., Abdel-Daim, M. M., Barreto, G. E., and Ashraf, G. M. (2019). APOE and Alzheimer's disease: evidence mounts that targeting APOE4 may combat Alzheimer's pathogenesis. *Mol. Neurobiol.* 56, 2450–2465. doi: 10.1007/s12035-018-1237-z

Uemura, M. T., Maki, T., Ihara, M., Lee, V. M. Y., and Trojanowski, J. Q. (2020). Brain microvascular pericytes in vascular cognitive impairment and dementia. *Front. Aging Neurosci.* 12:80. doi: 10.3389/fnagi.2020.00080

Valdor, R., García-Bernal, D., Riquelme, D., Martinez, C. M., Moraleda, J. M., Cuervo, A. M., et al. (2019). Glioblastoma ablates pericytes antitumor immune function through aberrant up-regulation of chaperone-mediated autophagy. *Proc. Natl. Acad. Sci. U S A* 116, 20655–20665. doi: 10.1073/pnas.1903542116

Valles, S. L., Iradi, A., Aldasoro, M., Vila, J. M., Aldasoro, C., de la Torre, J., et al. (2019). Function of glia in aging and the brain diseases. *Int. J. Med. Sci.* 16, 1473–1479. doi: 10.7150/ijms.37769

Vanlandewijck, M., He, L., Mäe, M. A., Andrae, J., Ando, K., Del Gaudio, F., et al. (2018). A molecular atlas of cell types and zonation in the brain vasculature. *Nature* 554, 475–480. doi: 10.1038/nature25739

Villaseñor, R., Kuennecke, B., Ozmen, L., Ammann, M., Kugler, C., Grüninger, F., et al. (2017). Region-specific permeability of the blood-brain barrier upon pericyte loss. *J. Cereb. Blood Flow Metab.* 37, 3683–3694. doi: 10.1177/0271678X17697340

Wang, Y., Pan, L., Moens, C. B., and Appel, B. (2014). Notch3 establishes brain vascular integrity by regulating pericyte number. *Development* 141, 307–317. doi: 10.1242/dev.096107

Wilhelm, I., Nyúl-Tóth, Á., Suciu, M., Hermenean, A., and Krizbai, I. A. (2016). Heterogeneity of the blood-brain barrier. *Tissue Barriers* 4:e1143544. doi: 10.1080/21688370.2016.1143544

Winkler, E. A., Bell, R. D., and Zlokovic, B. V. (2011). Central nervous system pericytes in health and disease. *Nat. Neurosci.* 14, 1398–1405. doi: 10.1038/nn.2946

Winkler, E. A., Sengillo, J. D., Bell, R. D., Wang, J., and Zlokovic, B. V. (2012). Blood-spinal cord barrier pericyte reductions contribute to increased capillary permeability. *J. Cereb. Blood Flow Metab.* 32, 1841–1852. doi: 10.1038/jcbfm.2012.113

Winkler, E. A., Sengillo, J. D., Sullivan, J. S., Henkel, J. S., Appel, S. H., and Zlokovic, B. V. (2013). Blood-spinal cord barrier breakdown and pericyte reductions in amyotrophic lateral sclerosis. *Acta Neuropathol.* 125, 111–120. doi: 10.1007/s00401-012-1039-8

Ximerakis, M., Lipnick, S. L., Innes, B. T., Simmons, S. K., Adiconis, X., Dionne, D., et al. (2019). Single-cell transcriptomic profiling of the aging mouse brain. *Nat. Neurosci.* 22, 1696–1708. doi: 10.1038/s41593-019-0491-3

Yamadera, M., Fujimura, H., Inoue, K., Toyooka, K., Mori, C., Hirano, H., et al. (2015). Microvascular disturbance with decreased pericyte coverage is prominent in the ventral horn of patients with amyotrophic lateral sclerosis. *Amyotroph. Lateral Scler. Frontotemporal Degener.* 16, 393–401. doi: 10.3109/21678421.2015.1011663

Yamamoto, S., Muramatsu, M., Azuma, E., Ikutani, M., Nagai, Y., Sagara, H., et al. (2017). A subset of cerebrovascular pericytes originates from mature macrophages in the very early phase of vascular development in CNS. *Sci. Rep.* 7:3855. doi: 10.1038/s41598-017-03994-1

Yamazaki, T., and Mukouyama, Y. (2018). Tissue specific origin, development, and pathological perspectives of pericytes. *Front. Cardiovasc. Med.* 5:78. doi: 10.3389/fcvm.2018.00078

Yang, A. C., Stevens, M. Y., Chen, M. B., Lee, D. P., Stähli, D., Gate, D., et al. (2020). Physiological blood-brain transport is impaired with age by a shift in transcytosis. *Nature* 583, 425–430. doi: 10.1038/s41586-020-2453-z

Zaitoun, I. S., Wintheiser, C. M., Jamali, N., Wang, S., Suscha, A., Darjatmoko, S. R., et al. (2019). Bcl-2 expression in pericytes and astrocytes impacts vascular development and homeostasis. *Sci. Rep.* 9:9700. doi: 10.1038/s41598-019-45915-4

Zeisel, A., Hochgerner, H., Lönnerberg, P., Johnsson, A., Memic, F., van der Zwan, J., et al. (2018). Molecular architecture of the mouse nervous system. *Cell* 174, 999.e22–1014.e22. doi: 10.1016/j.cell.2018.06.021

Zeller, K., Vogel, J., and Kuschinsky, W. (1996). Postnatal distribution of Glut1 glucose transporter and relative capillary density in blood-brain barrier structures and circumventricular organs during development. *Dev. Brain Res.* 91, 200–208. doi: 10.1016/0165-3806(95)00177-8

Zlokovic, B. V. (2008). The blood-brain barrier in health and chronic neurodegenerative disorders. *Neuron* 57, 178–201. doi: 10.1016/j.neuron.2008.01.003

Conflict of Interest: The authors declare that the research was conducted in the absence of any commercial or financial relationships that could be construed as a potential conflict of interest.

frontiers in Cellular Neuroscience

ORIGINAL RESEARCH
published: 22 March 2021
doi: 10.3389/fncel.2021.624826

Single Cell Transcriptome Data Analysis Defines the Heterogeneity of Peripheral Nerve Cells in Homeostasis and Regeneration

Bing Chen[1], Matthew C. Banton[2], Lolita Singh[3], David B. Parkinson[3] and Xin-peng Dun[3,4]*

[1] Department of Neurology, The Affiliated Huai'an No. 1 People's Hospital of Nanjing Medical University, Huai'an, China, [2] Faculty of Health, School of Biomedical Science, University of Plymouth, Plymouth, United Kingdom, [3] Faculty of Health, Peninsula Medical School, University of Plymouth, Plymouth, United Kingdom, [4] School of Pharmacy, Hubei University of Science and Technology, Xianning, China

The advances in single-cell RNA sequencing technologies and the development of bioinformatics pipelines enable us to more accurately define the heterogeneity of cell types in a selected tissue. In this report, we re-analyzed recently published single-cell RNA sequencing data sets and provide a rationale to redefine the heterogeneity of cells in both intact and injured mouse peripheral nerves. Our analysis showed that, in both intact and injured peripheral nerves, cells could be functionally classified into four categories: Schwann cells, nerve fibroblasts, immune cells, and cells associated with blood vessels. Nerve fibroblasts could be sub-clustered into epineurial, perineurial, and endoneurial fibroblasts. Identified immune cell clusters include macrophages, mast cells, natural killer cells, T and B lymphocytes as well as an unreported cluster of neutrophils. Cells associated with blood vessels include endothelial cells, vascular smooth muscle cells, and pericytes. We show that endothelial cells in the intact mouse sciatic nerve have three sub-types: epineurial, endoneurial, and lymphatic endothelial cells. Analysis of cell type-specific gene changes revealed that Schwann cells and endoneurial fibroblasts are the two most important cell types promoting peripheral nerve regeneration. Analysis of communication between these cells identified potential signals for early blood vessel regeneration, neutrophil recruitment of macrophages, and macrophages activating Schwann cells. Through this analysis, we also report appropriate marker genes for future single cell transcriptome data analysis to identify cell types in intact and injured peripheral nerves. The findings from our analysis could facilitate a better understanding of cell biology of peripheral nerves in homeostasis, regeneration, and disease.

Keywords: peripheral nerve, injury, cell type identification, marker genes, cell-cell communication, scRNA-seq analysis

OPEN ACCESS

Edited by:
Miao He,
Fudan University, China

Reviewed by:
Ying Zhu,
Fudan University, China
Sheng Yi,
Nantong University, China

****Correspondence:***
Bing Chen
chenbing2007@163.com

Specialty section:
This article was submitted to Cellular Neuropathology, a section of the journal Frontiers in Cellular Neuroscience

Received: *11 November 2020*
Accepted: *26 February 2021*
Published: *22 March 2021*

Citation:
Chen B, Banton MC, Singh L, Parkinson DB and Dun X (2021) Single Cell Transcriptome Data Analysis Defines the Heterogeneity of Peripheral Nerve Cells in Homeostasis and Regeneration. Front. Cell. Neurosci. 15:624826. doi: 10.3389/fncel.2021.624826

INTRODUCTION

Our nervous system comprises of two parts: the central nervous system (CNS) and the peripheral nervous systems (PNS). The CNS is the part of the nervous system consisting primarily of the brain and spinal cord. The brain is encased in the skull and the spinal cord is protected by the vertebrae. Outside of the brain and spinal cord is the PNS,

which due to the lack of protection, is prone to damage from traumatic injuries. It is not until the PNS is damaged that the huge consequences become clear. These injuries often lead to the development of neuropathic pain and life-long loss of both motor and sensory function. The injuries not only greatly compromise the quality of life of affected individuals but also impose a great financial burden on the healthcare system (Deumens et al., 2010).

In contrast to CNS injury, the PNS has a stunning ability to regenerate following injury. This remarkable regenerative ability is achieved by the rapid activation of an intrinsic regeneration program in damaged neurons and through a permissive environment created by supporting cells in the distal nerve stump such as Schwann cells, nerve fibroblasts, endothelial cells and infiltrated immune cells (Chandran et al., 2016; Jessen and Mirsky, 2016; Renthal et al., 2020). Thus, identifying all the cell types in a healthy peripheral nerve and studying the cell type changes following injury could facilitate our understanding of key cellular and molecular mechanisms regulating peripheral nerve regeneration. Previous studies frequently use methods such as immunohistochemistry, *in situ* hybridization, electron microscopy and transgenic mice expressing fluorescent proteins to identify cell types in the peripheral nerves (Mallon et al., 2002; Stierli et al., 2018; Ydens et al., 2020). However, usually a combination of these approaches are required in order to identify most of the cell types present, and cells with low abundance are much harder to identify with these techniques (Stierli et al., 2018).

The advance of single-cell RNA sequencing (scRNA-seq) technologies and the development of bioinformatics pipelines not only enable us to define the heterogeneity of cell types in a selected tissue but also allow us to study a cell-specific gene expression profile (Chen et al., 2019b). Single-cell RNA sequencing technologies have been widely used in different research fields to reveal complex and rare cell populations, to track the trajectories of distinct cell lineages, and to study the gene expression profiles of selected cell types (Hwang et al., 2018). However, this technique has only recently been applied to study the cell types and gene expression profiles of intact and injured mouse peripheral nerves (Carr et al., 2019; Toma et al., 2020; Wolbert et al., 2020). In this report, we re-analyzed recently published single-cell RNA sequencing data sets and provide our rationale to define the heterogeneity of cells in intact and injured peripheral nerves. We compared the changes of cell type composition and gene expression patterns between intact and injured sciatic nerve with our analysis, and revealed cell-cell communications in intact and injured sciatic nerve. We also provide suggested markers for future single cell transcriptome data analysis for the identification of cell types in intact and injured peripheral nerves. The findings from our analysis will, we hope, facilitate a better understanding of peripheral nerve cell biology in homeostasis, regeneration and disease.

METHODS

Computational Analysis of Single-Cell RNA Sequencing Data Sets

scRNA-seq data set GSE142541 for intact mouse sciatic nerve and the brachial nerve plexus (Wolbert et al., 2020), data set GSE147285 for intact mouse sciatic nerve and post-injury day 3 distal nerve (Toma et al., 2020), and data set GSE120678 for post-injury day 9 distal nerve (Carr et al., 2019) were downloaded from the NCBI GEO database. Data sets were analyzed using the Seurat v.3.2.1 (https://satijalab.org/seurat/) and sctransform v.0.3 R packages using R v.4.0.2. Quality control plots of number of features, counts and percentage mitochondrial content per cell were plotted for each data set and used to determine filtering conditions. For the quality control of intact mouse sciatic nerve data set GSE42541, cells were filtered using the following conditions: number of features per cell 200–2,000 and percent mitochondrial DNA content per cell <8%. For the quality control of intact mouse sciatic nerve data set GSE147285, filtering conditions were: number of features per cell 200–6,000 and percent mitochondrial DNA content per cell <8%. For the quality control of post-injury day 3 nerve data set, cells were filtered using the following conditions: number of features per cell 200–6,000 and percent mitochondrial DNA content per cell <6%. For the quality control of post-injury day 9 nerve data set, cells were filtered using the following conditions: number of features per cell 200–4,000 and percent mitochondrial DNA content per cell <8%.

Filtered cell data were normalized, variable genes identified and data scaled using SCTransform, a recently published highly effective method for removing technical artifacts from scRNAseq data while retaining biological heterogeneity (Hafemeister and Satija, 2019). The dimensionality of the dataset was determined using elbow plots to identify the appropriate number of principal components used for clustering. Cell clustering was performed using the FindNeighbors and FindCluster functions in Seurat. Differentially expressed genes (DEG) were identified using the FindAllMarkers Seurat function using the Wilcoxon rank sum test for genes with a minimum 0.25 log fold change between clusters and expressed in at least 10% of cells between clusters, unless otherwise stated. To annotate the clusters, genes differentially expressed in a one vs. all cluster comparison were queried for known expression in a literature search and gene expression plotted. Integration of data sets was performed using Seurat (v.3.2.1) using the SCTransform normalized data and PrepSCTIntegration function. DEG between conditions within each cluster were identified using the FindMarkers function using the same argument values as the FindAllMarkers Seurat function described above. Cell clustering was visualized using t-distributed stochastic neighbor embedding (tSNE) using the FeaturePlot function in Seurat. t-SNE gene expression overlays, violin plots, dot plots and heatmaps for cell type specific marker genes were also plotted using Seurat specific functions.

Marker Genes for the Identification of Cell Clusters

Cell clusters were identified based on the use of the following established marker genes for cell types of mouse sciatic nerves (Evrard et al., 2018; Zhao et al., 2018; Carr et al., 2019; Renthal et al., 2020; Toma et al., 2020; Wolbert et al., 2020; Xie et al., 2020; Ydens et al., 2020). Egfl7, Ecscr, Pecam1/Cd31, Tie1, Emcn, Cdh5, and Esam for endothelial cells. Sox17, Spock2, and Rgcc for epineurial endothelial cells, Lrg1 and Icam1 for endoneurial endothelial cells. Lyve1, Mmrn1, Flt4, and Prox1 for lymphatic

endothelial cells. Des, Tpm2, Myh11, Acta2, Mylk, Myom1, and Myocd for vascular smooth muscle (VSM) cells. Rgs5, Kcnj8, and Pdgfrb for pericytes. Sox10, Plp1, and S100b for Schwann cells. Cdh2 and L1cam for non-myelinating Schwann cells. Mbp, Mpz, Mag, and Egr2 for myelinating Schwann cells. Dcn, Mfap5, Serpinf1, and Gsn for fibroblasts. Sfrp2, Dpt, Pcolce2, Adamts5, Pi16, Sfrp4, Prrx1, Comp, and Ly6c1 for epineurial fibroblasts. Cldn1/claudin-1, Lypd2, Ntn4, Msln, Ntng1, Slc2a1/Glut1, and Mpzl2 for perineurial cells. Sox9, Osr2, Wif1, Abca9, Cdkn2a, Cdkn2b, and Plxdc1 for endoneurial fibroblasts. Dlk1, Mest, Cilp, Tnc, Plagl1, and Ptn for differentiating fibroblasts. Pdgfra, Thy1, and Cd34 for mesenchymal cells. Ptprc/CD45 and Cd52 as general marker for immune cells. Aif1/Iba1, Cd68, Mrc1/Cd206, and Adgre1/F4/80 for macrophages. Retnla and Clec10a for epineurial macrophages. Ccl6, Fcgr3, Cx3cr1, Csf1r, Cd300a, and Clec4e for monocytes. S100a8, S100a9, Cxcr2, and Cxcl2 for neutrophils. Cma1, Mcpt4, Mcpt1, and Kit for mast cells. Cd3g, Cxcr6, Trac, and Cd3e for T cells. Nkg7, Klrk1, and Ncr1 for natural killer (NK) cells. Bank1, Cbfa2t3, Taok3, Ms4a1, Cd19, and Cd79a for B cells (Evrard et al., 2018; Zhao et al., 2018; Carr et al., 2019; Renthal et al., 2020; Toma et al., 2020; Wolbert et al., 2020; Xie et al., 2020; Ydens et al., 2020).

Peripheral Nerve Surgery

Two-month-old C57BL/6J and PLP-GFP mice were used in the study, Schwann cells are labeled with GFP in PLP-GFP mice (Mallon et al., 2002; Dun et al., 2019). All work involving animals was carried out according to Home Office regulation under the UK Animals Scientific Procedures Act 1986. Ethical approval for all experiments was granted by Plymouth University Animal Welfare and Ethical Review Board. Mice were housed in a controlled laboratory environment (temperature 22 ± 2°C, humidity 50–60%, 12-h light/dark cycle), and fed with standard rodent diet and water added *ad libitum*. For sciatic nerve transection injury, six male mice were anesthetized with isoflurane, the right sciatic nerve was exposed and transected at approximately 0.5 cm proximal to the nerve trifurcation site and no re-anastamosis of the severed nerve was performed. Overlying muscle was sutured and the skin was closed with an Autoclip applier. Mice undergoing surgery were given appropriate post-operative analgesia, 0.05% bupivacaine solution, topically applied above the muscle suture before applying surgical clips. Meloxicam (5 mg/kg) injections were given just before recovery from anesthetic. Mice undergoing surgery were given nesting material and cage enrichment to minimize the risk of autotomy. Animals under surgery were monitored daily. At day 3 and day 7 post surgery, animals were euthanased humanely using carbon dioxide in accordance with UK Home Office regulations.

Edu Labeling and Cell Proliferation Assay

Proliferation was measured using the Click-iT™ EdU kit (Thermo Fisher Scientific). At 7 days post injury, a stock solution containing 2 mg of EdU (Invitrogen; cat.no C1033) was administered to each mouse via intraperitoneal injection (total volume 200 μL in PBS) and mice were sacrificed 3 h later. Sciatic nerves were collected and fixed in 4% paraformaldehyde/PBS overnight. Next day, nerves were washed 3 times with PBS and then cryopreserved in 30% sucrose/PBS overnight. Subsequently, nerves were embedded in OCT medium and sectioned longitudinally on a cryostat at a thickness of 10 μm. Sections were permeabilised with 0.25% Triton X-100 plus 1% bovine serum albumin (BSA) in PBS for 45 min and then blocked with blocking buffer (3% BSA plus 0.05% Triton X-100 in PBS) for 1 h at room temperature. Sections of the sciatic nerve were then incubated with the EdU Click-iT reaction cocktail (Invitrogen; cat.no C1033) for 30 min at room temperature followed by three PBS washing steps for 10 min each. Sections or cells were incubated with S100 primary antibodies (1:500 diluted in blocking buffer) overnight at 4°C. The next day, sections were washed with PBS (3 × 10 min) and then incubated with secondary antibody plus Hoechst dye (1:500 diluted in blocking buffer) for 1 h at room temperature. Finally, sections were washed with PBS (3 × 10 min) and mounted with Citifluor (Agar Scientific, R1320) for imaging with a LeicaSPE confocal microscope.

Immunohistochemistry

Sciatic nerve were dissected out and fixed 5 h in 4% paraformaldehyde (in PBS, PH7.2) at 4°C. Nerves were then washed in PBS (3 × 10 min) and dehydrated in 30% sucrose (in PBS) overnight at 4°C. Subsequently, nerves were embedded in OCT medium and sectioned on a cryostat at a thickness of 12 μm. Sections were permeabilised with 0.25% Triton X-100 plus 1% bovine serum albumin (BSA) in PBS for 45 min and then blocked with blocking buffer (3% BSA plus 0.05% Triton X-100 in PBS) for 1 h at room temperature. Sections were incubated with Ki67 (Abcam, ab15580), S100 (Dako, Z0311), Csf3r (Thermofisher, BS-2574R), Spock2 (Thermofisher, BS-11966R), Rgcc (Thermofisher, BS-9079R), Lrg1 (Invitrogen, PA5-96832) primary antibody (1:100 diluted in blocking buffer) overnight at 4°C. The next day, sections were washed with PBS (3 × 10 min) and then incubated with donkey anti-rabbit secondary antibody conjugated with Alexa Fluor 488 or 568 (1:300 diluted in blocking buffer) for 1 h at room temperature. Hoechst dye (1:500) was also added into secondary antibody solution in order to label cell nuclei. Finally, sections were washed with PBS (3 × 10 min) and mounted with Citifluor (Agar Scientific, R1320) for imaging with a LeicaSPE confocal microscope.

Identifying Ligand-Receptor Interactions Between the Cell Clusters in Intact and Injured Nerves

Cell-cell communication between Seurat identified clusters was analyzed using CellPhoneDB (https://www.cellphonedb.org) (Efremova et al., 2020) using the SCTransform normalized gene counts. Mouse HGNC symbols for genes present in the CellPhoneDB database were converted to human orthologs using the R package biobtreeR (Gur, 2019). CellPhoneDB was run using 1,000 statistical iterations and a threshold of at least 10% of cells expressing a gene in a cluster was used.

RESULTS

Computational Analysis of scRNA-seq Data Sets

To generate an unbiased cellular map of the peripheral nerve in homeostasis and regeneration at single cell resolution, we analyzed the data sets GSE147285 and GSE120678 with the R-package Seurat v3.2.1 in R v.4.0.2. Data were filtered prior to normalization and dimensional reduction by principal component analysis. This resulted in a total of 1936 cells with 14,993 features for the intact mouse sciatic nerve, a total of 2,231 cells with 16,888 features for the nerves at 3 days post-injury, and a total of 3,894 cells with 16,937 features for the nerves at 9 days post-injury. Cell transcriptomes were then normalized using SCTransform. This method is effective at normalizing scRNAseq data and allows potentially a higher number of principal components to be used for downstream analysis and clustering (Hafemeister and Satija, 2019). Principal component (PC) analysis and clustering was then undertaken using highly variable genes. Previously, Carr et al. assigned the lowest resolution at 0.4 for conservative analysis of all three datasets (Carr et al., 2019). We found that resolution 0.4 could distinguish distinct cell types in both post-injury day 3 and day 9 nerve samples (**Figures 2**, **3**), as defined by established marker genes. However, the cell cluster of lymphatic endothelial cells, which has been reported by Wolbert et al. recently (Wolbert et al., 2020), was not labeled in intact nerves with a resolution of 0.4. We therefore increased the clustering resolution to 0.75 in order to effectively separate the cluster of lymphatic endothelial cells from other cell clusters. The increase of resolution to 0.75 also divided the epineurial fibroblast cluster into three sub-clusters (cluster 2, 6, 7 in **Figure 1A**). Our analysis resulted in 14 cell clusters in intact nerves (**Figure 1A**), 11 cell clusters in post-injury day 3 nerves (**Figure 2A**) and 13 cell clusters in post-injury day 9 nerves (**Figure 3A**). Differentially expressed genes (DEGs) for each cell cluster were identified through the analysis (**Supplementary Tables 1–3**).

To determine the identity of each cell cluster, we examined the expression of well-known cell type specific marker genes in cells of both intact and injured peripheral nerves (Carr et al., 2019; Toma et al., 2020; Wolbert et al., 2020). t-SNE gene expression overlays, heatmaps and dot plots were used to visualize the expression of the cell type marker genes in each cluster. In agreement with previous findings analyzing cell types in both intact and injured mouse sciatic nerve (Carr et al., 2019; Toma et al., 2020; Wolbert et al., 2020), our approach identified similar cell clusters in both intact and injured nerves (**Figures 1–3**). Based upon the cell function in peripheral nerve homeostasis and regeneration, we classified them as four categories of cells: Schwann cells, nerve fibroblasts, immune cells and cells associated with blood supply to the nerve. However, our analysis shows four sub-clusters of endothelial cells in the intact nerve (cluster 3, 4, 5, and 13 in **Figure 1A**), and in addition we identified a cluster of neutrophils in injured nerves (cluster 9 in **Figures 2A**, **3A**), which have not been reported in previous analyses (Carr et al., 2019; Toma et al., 2020; Wolbert et al., 2020).

Identifying Epineurial and Endoneurial Endothelial Cells in Intact Mouse Sciatic Nerve

In the intact nerve, in addition to the lymphatic EC cluster (cluster 13, **Figure 1A**) identified by marker genes for lymphatic ECs such as Lyve1, Mmrn1, Prox1, and Flt4 (**Supplementary Figure 1**) (Engelbrecht et al., 2020; Fujimoto et al., 2020; Wolbert et al., 2020), our analysis shows three distinct sub-clusters of blood vessel ECs in the intact nerve not described in the previous studies (cluster 3, 4, and 5, **Figure 1A**). All three new EC sub-clusters express classic EC marker genes such as Pecam1/Cd31, Tie1, and Emcn (**Supplementary Figure 2**) (Zhao et al., 2018; Carr et al., 2019; Kalluri et al., 2019; Toma et al., 2020; Wolbert et al., 2020). Previous studies using scRNA-seq to analyse endothelial cell profiles of specific structures of the blood supply system such as the aorta, the hematopoietic niche, the lymph nodes and the heart, often resulted in the identification of 2–4 sub-clusters of endothelial cells. These studies showed that it can be very difficult to name individual sub-clusters of EC cells because of overlapping expression patterns of key endothelial cell genes (Kenswil et al., 2018; Feng et al., 2019; Kalluri et al., 2019; Engelbrecht et al., 2020; Fujimoto et al., 2020).

It has been proposed that ECs of the blood vessels show remarkable heterogeneity and their phenotypes vary in time and space, differ in structure and function, and change in health and disease (Aird, 2012); this might explain why the EC sub-types can be difficult to identify in scRNA-seq studies. To name the subtype of ECs in cluster 3, 4 and 5, we searched DEGs (**Supplementary Table 1**) that was identified during cell clustering analysis in order to find unique DEGs for cluster 3, 4, and 5 respectively. This analysis revealed that Slco1a4, Slc39a8, Prom1, Spock2, Mfsd2a, Maoa, Slc39a10, and Slc7a5 are unique DEGs for cluster 3 ($p \leq 3.56008242907399E-123$). Rbp7, Gpihbp1, Btnl9, and Rgcc are unique DEGs for cluster 4 ($p \leq 5.82149130420303E-45$). Selp, Lrg1, Darc, Tmem252, Sele, Rasa4, Rnd1, Ptgs1, 2200002D01Rik, Cysltr1, Icam1, Tes, Pgm5, and Cd14 are unique DEGs for cluster 5 ($p \leq 4.27728189243353E-59$) (**Figure 4A**). Next, we used bulk mRNA sequencing data sets GSE109074 (Gokbuget et al., 2018) and GSE108231 (Norrmen et al., 2018) to determine the expression level of above DEGs in the intact mouse sciatic nerve in order to select appropriate marker genes for *in vivo* validation by immunostaining. Bulk mRNA sequencing data sets analysis showed that Spock2, Slc7a5, Mfsd2a, Maoa, Slc39a10, Slco1a4, and Rgcc are highly expressed in the intact mouse sciatic nerve (**Figures 4C,D**). We therefore chose Spock2 for cluster 3 and Rgcc for cluster 4 to validate their *in vivo* expression in ECs by immunostaining (**Figure 4B**). All the unique DEGs for cluster 5 are weakly expressed in the intact mouse sciatic nerve (**Figures 4C,D**). Lrg1 has been shown to promote new blood vessel growth by modulating Tgfβ signaling in endothelial cells (Wang et al., 2013). We chose Lrg1 for cluster 5 to do *in vivo* staining based on the availability of a good Lrg1 antibody (**Figure 4B**). Interestingly, most unique DEGs for cluster 3 and cluster 4 were down-regulated following injury while most unique DEGs for cluster 5 were up-regulated in response to

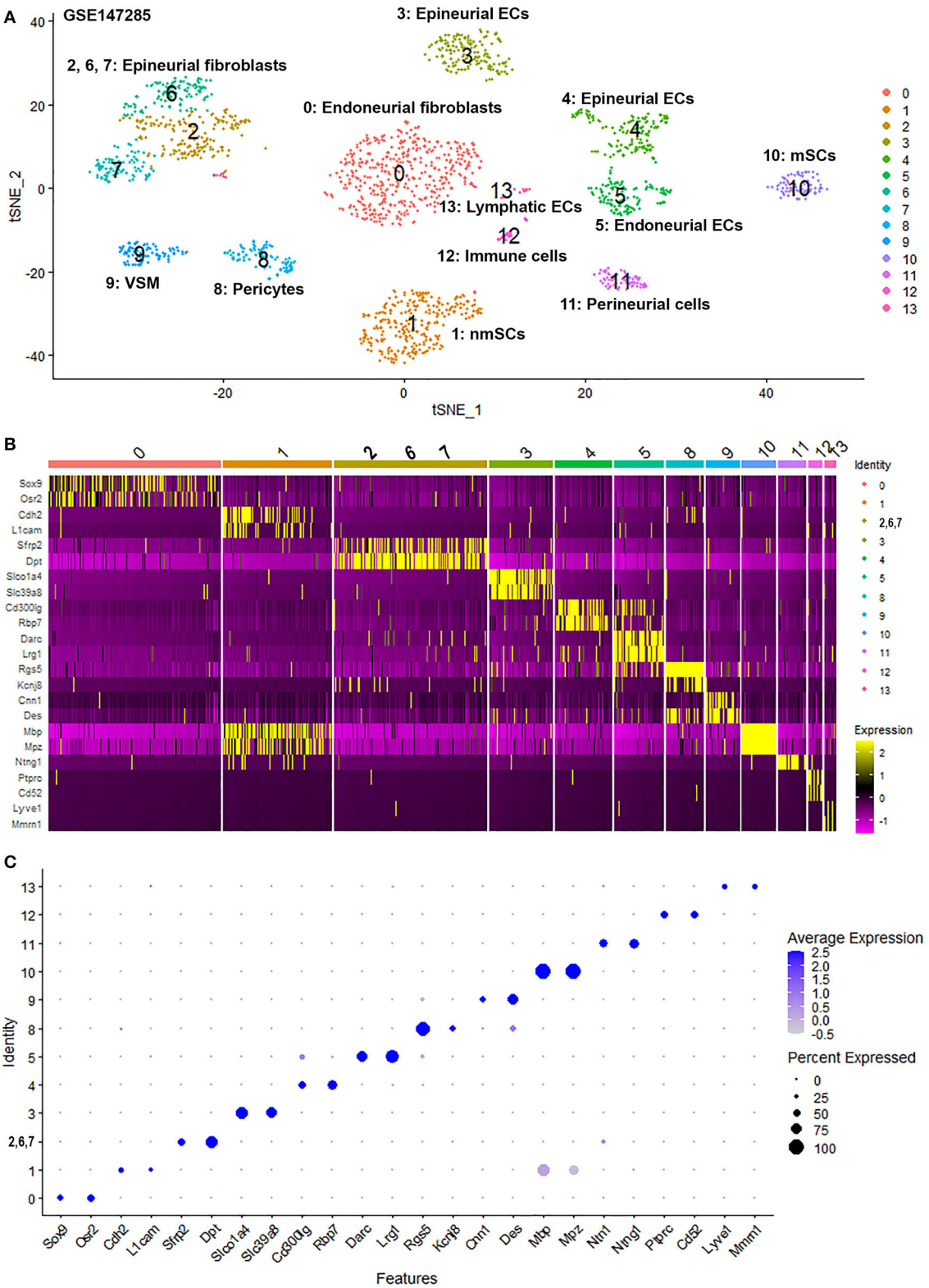

FIGURE 1 | Single cell transcriptomics (GSE147285) defines cellular phenotypes in intact mouse sciatic nerve. **(A)** tSNE visualization of cell clusters in intact mouse sciatic nerve. 0: Endoneurial fibroblasts; 1: Non-myelinating Schwann cells (nmSCs); 2, 6, 7: Epineurial fibroblasts; 3, 4: Epineurial endothelial cells; 5: Endoneurial endothelial cells; 8: Pericytes; 9: Vascular smooth muscle (VSM) cells; 10: Myelinating Schwann cells (mSCs); 11: Perineurial cells; 12: Immune cells (resident macrophages, mast cells, T/NK cells); 13: Lymphatic endothelial cells. **(B)** Heat map of selected marker genes for each cell cluster, cluster 2, 6, and 7 has been merged. **(C)** Dot plot of selected marker genes for each cell cluster, cluster 2, 6, and 7 has been merged.

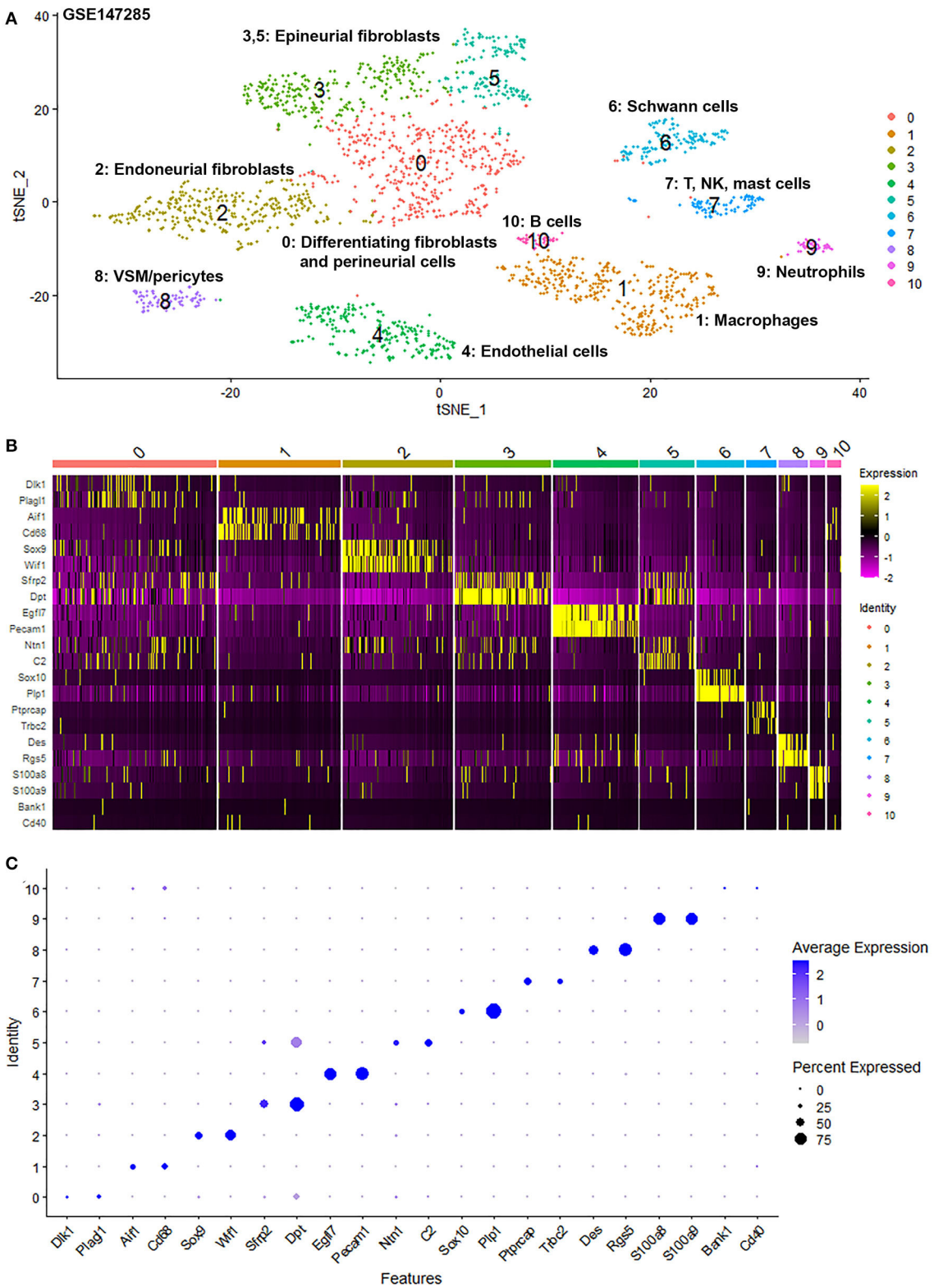

FIGURE 2 | Single cell transcriptomics (GSE147285) defines cellular phenotypes in day 3 post-injury distal mouse sciatic nerve. **(A)** tSNE visualization of cell clusters in day 3 post-injury distal mouse sciatic nerve. 0: Differentiating fibroblasts and perineurial cells; 1: Macrophages; 2: Endoneurial fibroblasts; 3 and 5: Epineurial fibroblasts; 4: Endothelial cells; 6: Schwann cells; 7: T, NK and mast cells; 8: VSM/pericytes; 9: Neutrophils; 10: B cells. **(B)** Heat map of selected marker genes for each cell cluster. **(C)** Dot plot of selected marker genes for each cell cluster.

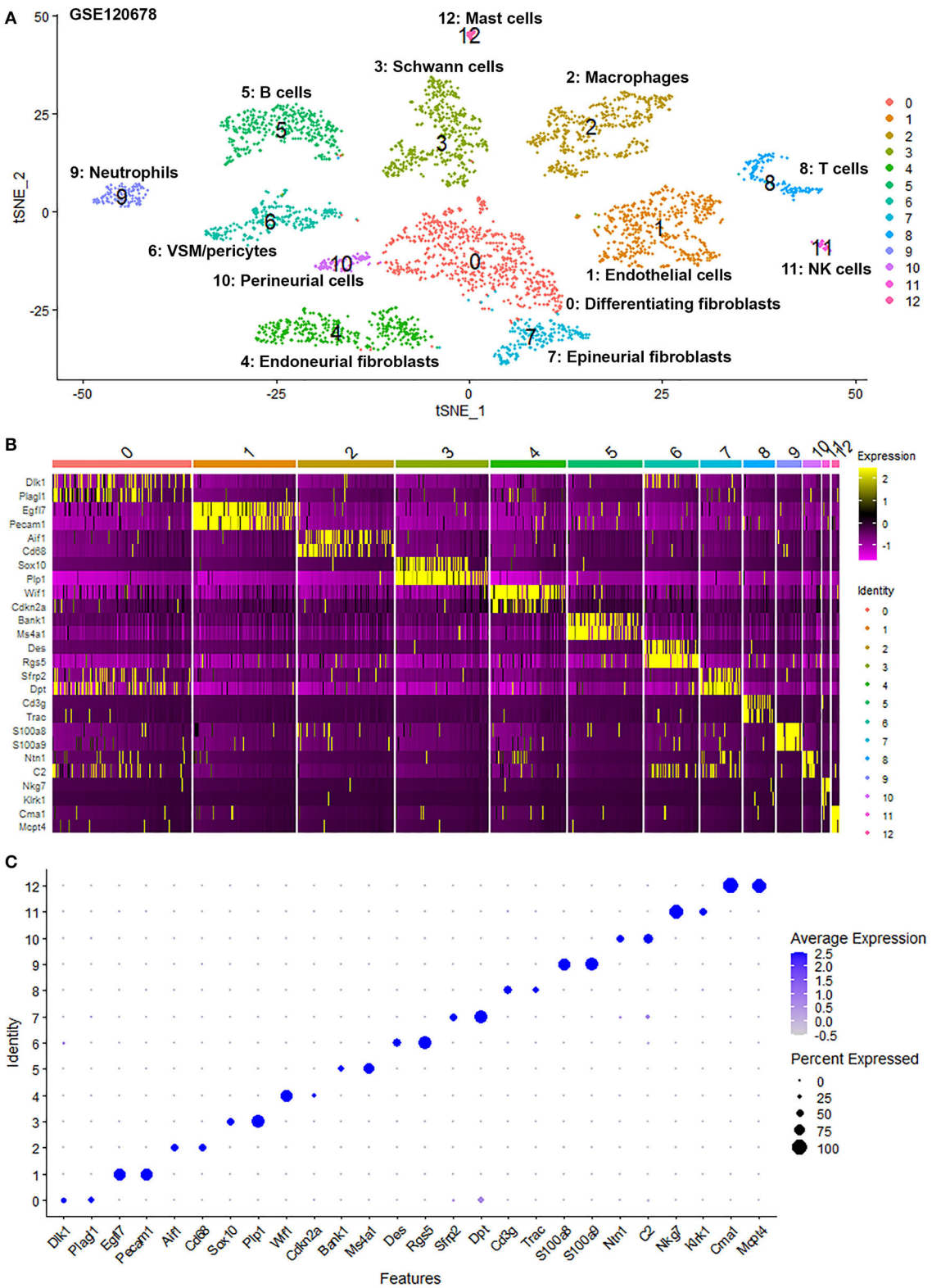

FIGURE 3 | Single cell transcriptomics (GSE120678) defines cellular phenotypes in day 9 post-injury distal mouse sciatic nerve. **(A)** tSNE visualization of cell clusters in day 9 post-injury distal mouse sciatic nerve. 0: Differentiating fibroblasts; 1: Endothelial cells; 2: Macrophages; 3: Schwann cells; 4: Endoneurial fibroblasts; 5: B cells; 6: VSM/pericytes; 7: Epineurial fibroblasts; 8: T cells; 9: Neutrophils; 10: Perineurial cells; 11: NK cells; 12: Mast cells. **(B)** Heat map of selected marker genes for each cell cluster. **(C)** Dot plot of selected marker genes for each cell cluster.

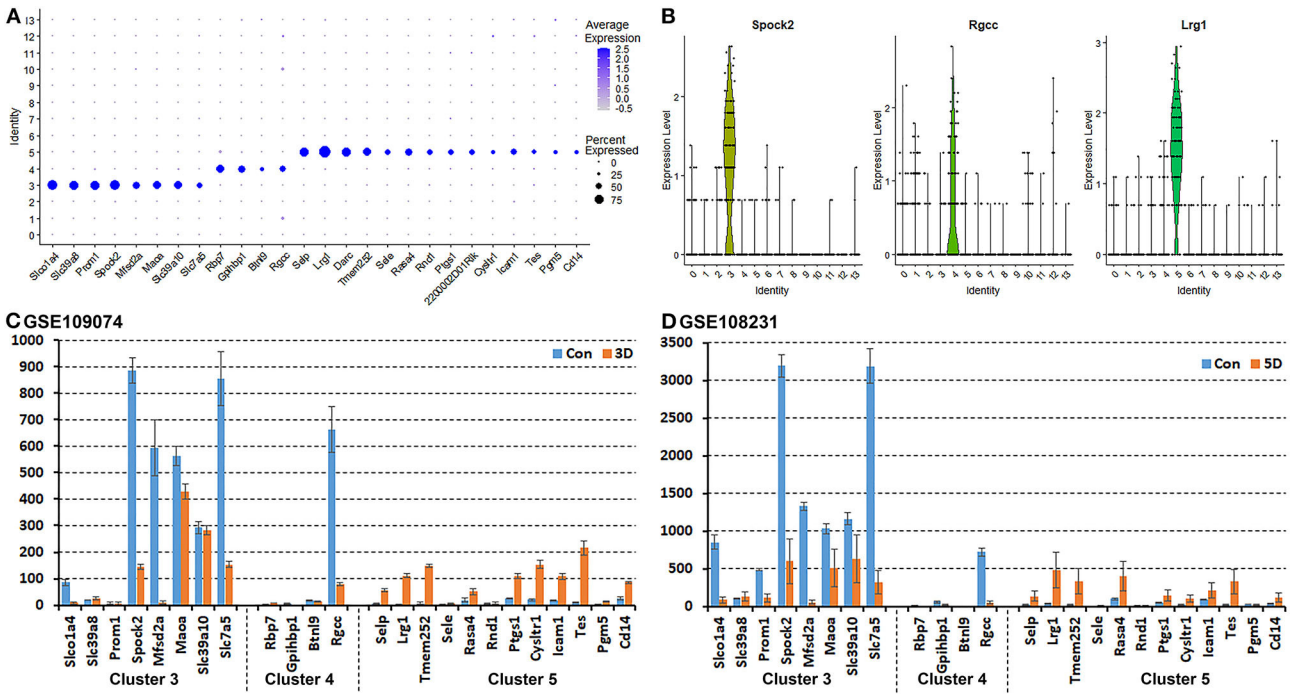

FIGURE 4 | Identification of DEGs unique to cluster 3, 4, and 5 in the intact mouse sciatic nerve. **(A)** Dot plot showing unique DEGs for cluster 3, 4, and 5 in the intact sciatic nerve. **(B)** Violin plot showing Spock2 expression in cluster 3, Rgcc in cluster 4 and Lrg1 in cluster 5 ECs in the intact sciatic nerve. **(C)** mRNA count showing the expression level of unique DEGs for cluster 3, 4, and 5 in intact sciatic nerve and in the distal nerve at day 3 post crush injury. **(D)** mRNA count showing the expression level of unique DEGs for cluster 3, 4, and 5 in intact sciatic nerve and in the distal nerve at day 5 post crush injury.

injury (**Figures 4C,D**). This might explain why all ECs have been placed into just one cluster in both day 3 post injury (cluster 4 in **Figure 2A**) and day 9 post injury (cluster 1 in **Figure 3A**) because they lose their sub-cluster identity following injury.

All cells in cluster 3, 4, and 5 express the classic EC marker gene Pecam1/Cd31 (**Supplementary Figure 2**). We then double stained CD31 with Spock2, Rgcc or Lrg1 to reveal the difference of their expression pattern in intact mouse sciatic nerve. Control sections without adding primary antibodies only showed weak background staining (**Figures 5A–D**). Staining Spock2 and Rgcc showed that both Spock2 and Rgcc are strongly expressed in ECs of large diameter blood vessels outside the epineurium (**Figures 5E–L**, indicated by arrows). The expression of both Spock2 and Rgcc are hardly detectable in ECs of endoneurium (**Figures 5E–L**, indicated by arrowheads). In contrast, Lrg1 is expressed in ECs of endoneurium (**Figures 5M–P**, indicated by arrows). In the intact sciatic nerve, Spock2 is only expressed in ECs outside the epineurium (**Figures 5E–H**), however, both Rgcc and Lrg1 also show strong expression as round dots inside the endoneurium which is, the typical morphology of peripheral axons (**Figures 5I–P**). According to the expression pattern of Spock2, Rgcc, and Lrg1 in the intact mouse sciatic nerve, we named cluster 3 and cluster 4 as epineurial ECs, and named cluster 5 as endoneurial ECs (**Figure 1A**).

To confirm our finding that ECs in the intact mouse peripheral nerves could be grouped into epineurial, endoneurial and lymphatic sub-types, we further analyzed another scRNA-seq data set GSE142541 generated to analyse cell types in the intact mouse sciatic nerve and the brachial nerve plexus (Wolbert et al., 2020). This data set contains more cells but lower number of genes per cell compared to data set GSE147285. Cells were filtered using the following conditions: number of features per cell 200–2,000 and percent mitochondrial DNA content per cell < 8%. This resulted in a total of 5,188 samples with 15,057 features. In contrast to the data set GSE147285, our analysis for GSE142541 only show three EC sub-clusters (cluster 2, 20 and 24 in **Figure 6A**), possibly due to the lower number of genes per cell. Using the above marker genes, we identify cluster 2 as epineurial ECs, cluster 20 as endoneurial ECs, and cluster 24 as lymphatic ECs (**Figure 6A**). Examining DEGs for both cluster 3 and 4 of data set GSE147285 showed that they are also expressed epineurial EC cluster genes found in the GSE142541 data set (cluster 2) (**Supplementary Table 4**) such as Sox17 and Spock2 (**Figure 6B**). This data set analysis further confirmed our finding from immunostaining that cluster 3 and 4 in data set GSE147285 are epineurial ECs (**Figure 1A**). Lrg1 remains a DEG for endoneurial ECs (**Figure 6C**), and Lyve1 remains a DEG for lymphatic ECs (**Figure 6D**). The GSE142541 data set contains cells from the brachial nerve plexus in addition to cells from sciatic nerves (Wolbert et al., 2020). Thus, analyzing this data set showed that ECs in the mouse peripheral nerves could be grouped into lymphatic, endoneurial and epineurial sub-types by scRNA data analysis.

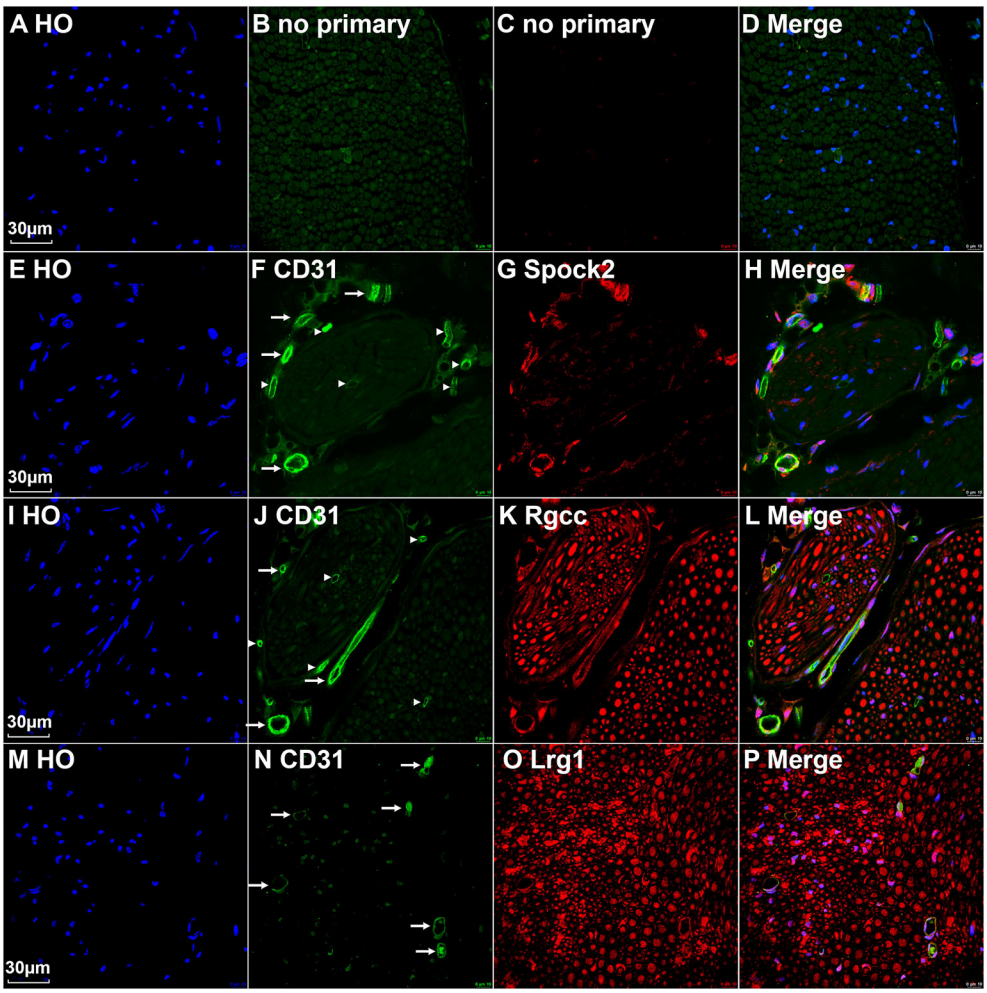

FIGURE 5 | Identify epineurial and endoneurial endothelial cells in intact mouse sciatic nerve by immunostaining. **(A–D)** Control slides staining without adding primary antibodies in the blocking buffer. **(E–H)** Double staining CD31 with Spock2 showing that Spock2 is strongly expressed in ECs of large diameter blood vessels outside the epineurium (indicated by arrows). Arrowheads show no expression. **(I–L)** Double staining CD31 with Rgcc showing that Rgcc is strongly expressed in ECs of large diameter blood vessels outside the epineurium (indicated by arrows). Arrowheads show no expression. Rgcc is also strongly expressed in axons inside the endoneurium. **(M–P)** Double staining CD31 with Lrg1 showing that Lrg1 is expressed in ECs of endoneurium (indicated by arrows). Lrg1 is also strongly expressed in axons inside the endoneurium. Scale bars in **(A)**, **(E)**, **(I)**, and **(M)** 30 μm.

Identifying Endoneurial Fibroblasts and Perineurial Cells in Data Set GSE142541

Due to endoneurial fibroblasts expressing Ngfr (Stierli et al., 2018), in the paper by Wolbert et al., 2020, they named a cluster of endoneurial fibroblasts as nmSCs in their analysis, therefore suggested Smoc2 and Apod, which are also expressed in this mis-labeled cluster, as marker genes for nmSCs (Wolbert et al., 2020). By re-analysis the data set GSE142541, we identified cluster 0, 3, 4 and 12 as endoneurial fibroblasts (**Figure 6A**) as they express marker genes for endoneurial fibroblasts such as Sox9, Osr2, Pdgfra, Cd34, Abca9, Cdkn2a, Cdkn2b, and Plxdc1 (**Figures 7A,B**, **Supplementary Table 4**). They also express high levels of Smoc2 and Apod (**Figures 7C,D**). Instead, we identify myelinating Schwann cells (mSC) as cluster 17 and nmSCs as cluster 5 (**Figure 6A**). Cluster 25 express high levels of Cldn1, Lypd2, Ntng1, Slc2a1, and Itgb4 (**Figures 7E–G**), and we identified cluster 25 as perineurial cells (**Figure 6A**), which previously have been named as a novel cluster of endothelial cells (Wolbert et al., 2020). Because of the high number of cells for this data set, immune cells could be clustered into B cells (cluster 13 in **Figure 6A**), epineurial macrophages (cluster 15 in **Figure 6A**), endoneurial macrophages (cluster 16 in **Figure 6A**), T cells (cluster 14, 19 and 21 in **Figure 6A**) and NK cells (cluster 22 in **Figure 6A**).

Identifying the Cluster of Neutrophils in Injured Nerves

Neutrophils are the early inflammatory cells infiltrating the injury site and the distal nerve for debris clearance (Lindborg et al., 2017). Previous studies have shown that the number of

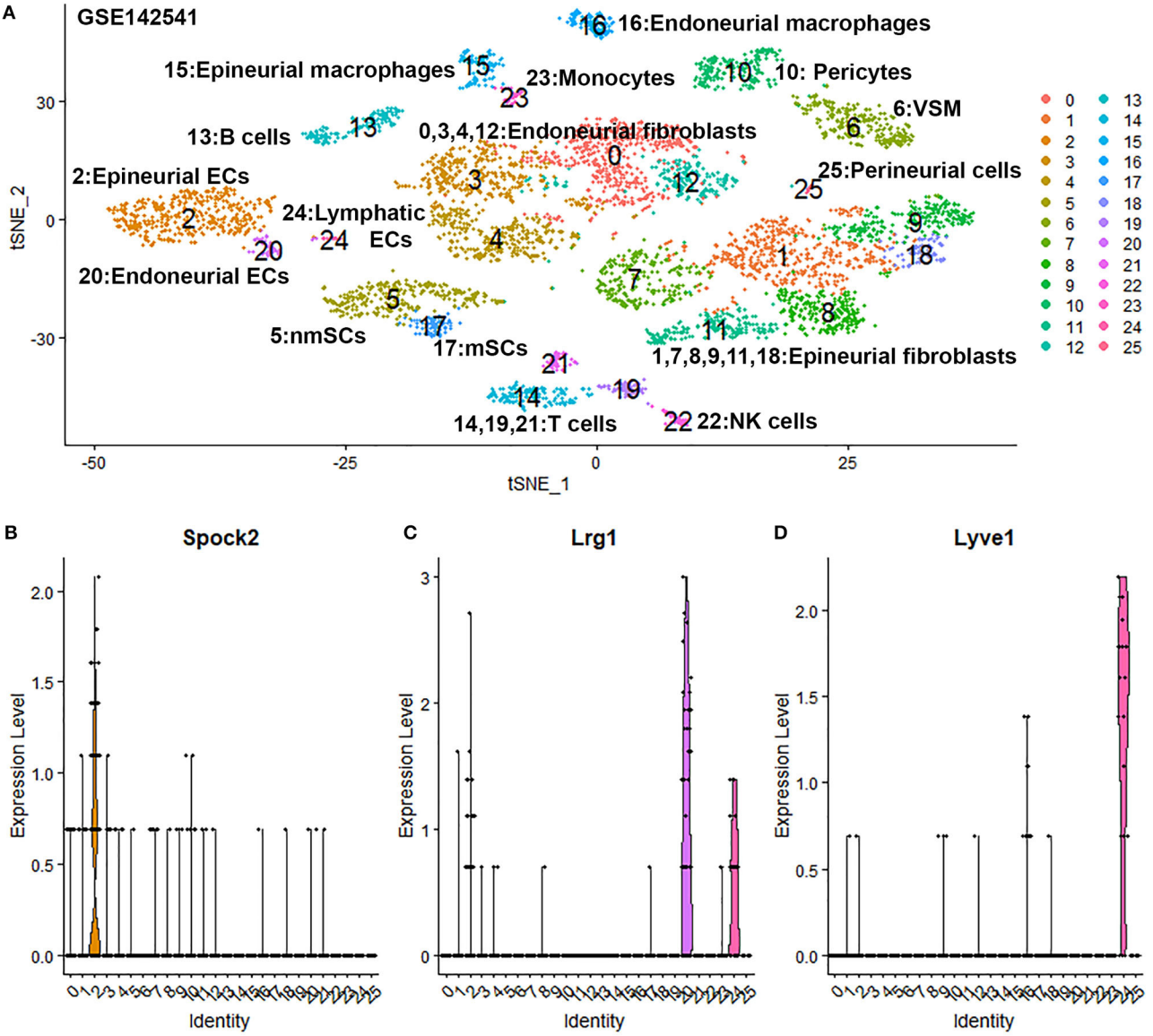

FIGURE 6 | Single cell transcriptomics (GSE142541) defines cellular phenotypes in intact mouse sciatic nerve and the brachial nerve plexus. **(A)** tSNE visualization of 26 cell clusters in intact mouse sciatic nerve at resolution 1.35. **(B)** Violin plot showing Spock2 expression in the epineurial EC cluster (cluster 2). **(C)** Violin plot showing Lrg1 expression in the endoneurial EC cluster (cluster 20). **(D)** Violin plot showing Lyve1 expression in the lymphatic EC cluster (cluster 24).

neutrophils increases rapidly after injury and can be detected at just 8 h after injury with a peak at 24 h post-injury (Perkins and Tracey, 2000; Barrette et al., 2008; Lindborg et al., 2017). However, the cluster of neutrophils was not identified in Carr et al. and Toma et al.'s reports because their studies focused on the cell population of fibroblasts (Carr et al., 2019; Toma et al., 2020). Recently scRNA-seq data analysis in other tissues showed that S100a8, S100a9, Cxcr2, and Cxcl2 are effective marker genes to identify neutrophils (Evrard et al., 2018; Xie et al., 2020). We tested these marker genes in the injured mouse sciatic nerve and identified cluster 9 in both post-injury day 3 and post-injury day 9 nerves as neutrophils (**Figures 2A**, **3A**, **8A–H**). Examining the DEGs for nerves at day 3 post injury (**Supplementary Table 2**) revealed that top 10 suggested marker genes for cluster 9 are Cxcr2, Trem1, S100a9, Il1b, S100a8, Trem3, Clec4e, Nlrp3, Il1r2, and Csf3r (all p vablues≤1.06160807720519E-79).

The Csf3r gene encodes the colony-stimulating factor 3 receptor that is critical for differentiation and proliferation of neutrophils (Maxson and Tyner, 2017). Mutation of Csf3r activates the receptor and promotes neutrophil proliferation, leading to chronic neutrophilic leukemia (Duployez et al., 2019). We then select Csf3r as a marker to validate its expression on neutrophils using immunostaining on mouse distal sciatic nerve sections at day 3 post injury. Staining for Csf3r on distal

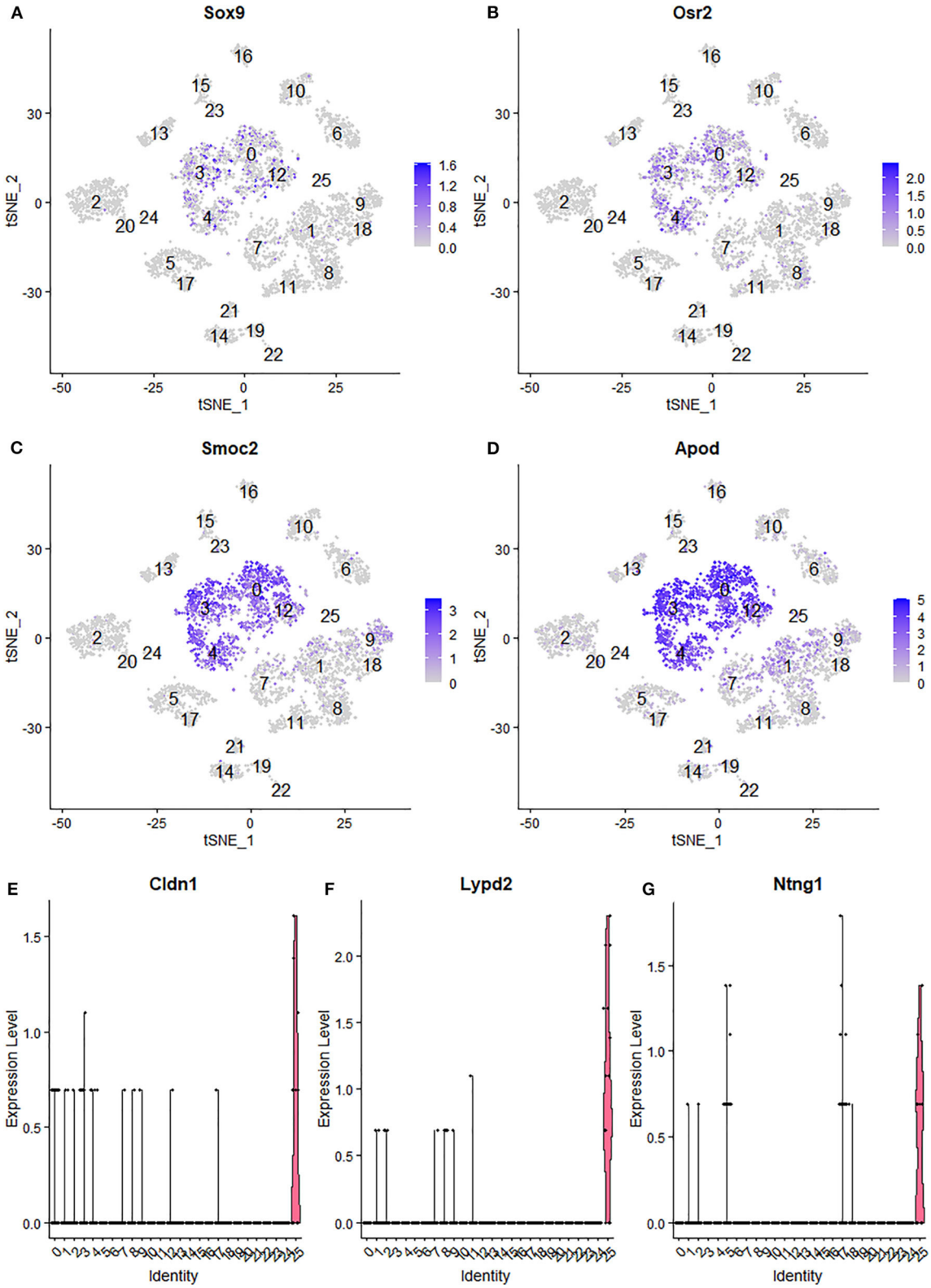

FIGURE 7 | Identifying endoneurial fibroblasts and perineurial cells in data set GSE142541. **(A,B)** tSNE plot showing Sox9 and Osr2 expression in endoneurial fibroblasts (cluster 0, 3, 4, and 12). **(C,D)** tSNE plot showing Smoc2 and Apod expression in endoneurial fibroblasts. **(E,F)** Violinplot showing Cldn1, Lypd2, and Ntng1 expression in perineurial cells (cluster 25).

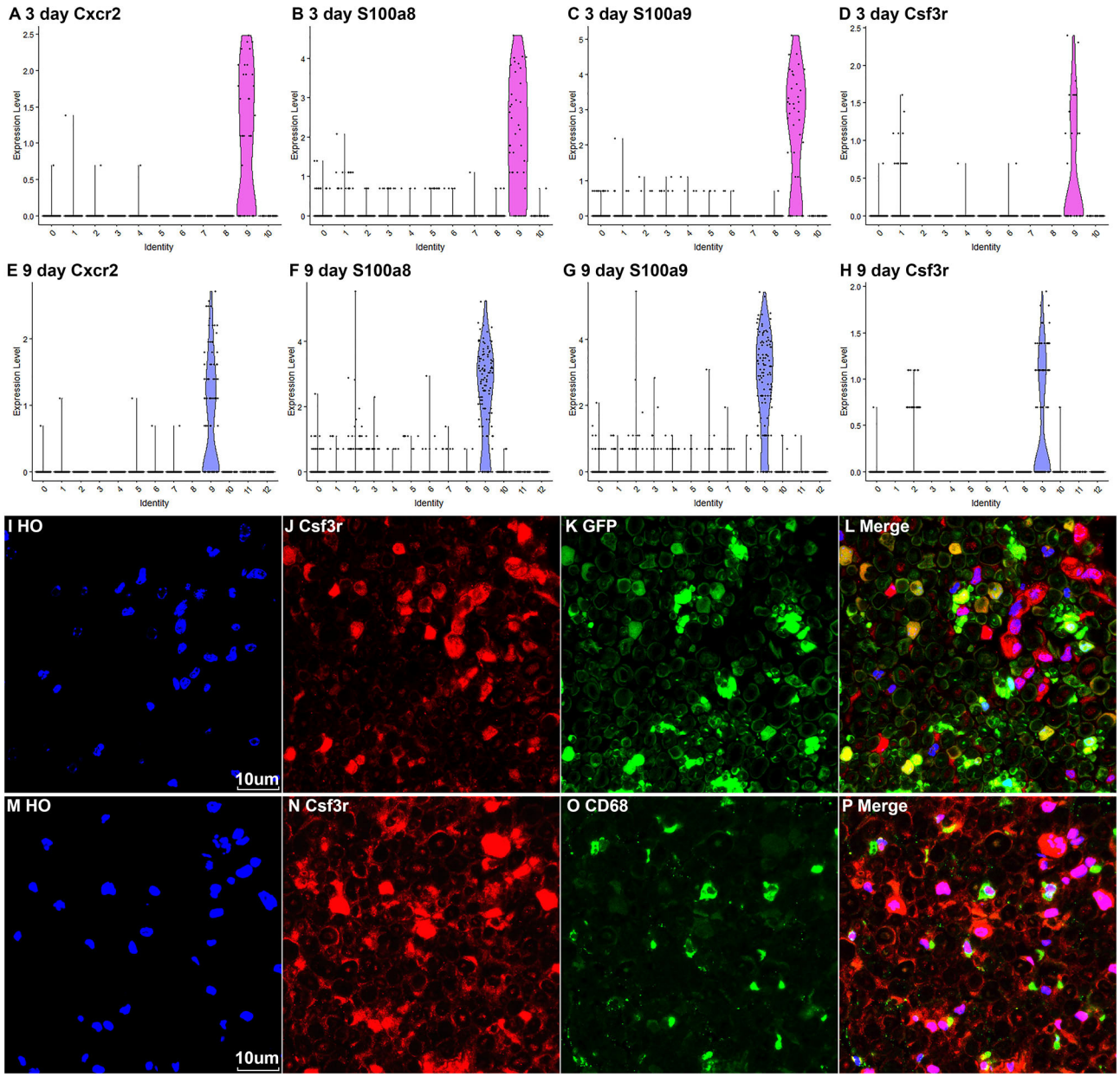

FIGURE 8 | Marker genes for identifying the cluster of neutrophils in injured nerves. **(A–D)** Violin plot of selected marker genes Cxcr2, S100a8, S100a9, and Csf3r for neutrophils at day 3 post-injury. **(E–H)** Violin plot of selected marker genes Cxcr2, S100a8, S100a9, and Csf3r for neutrophils at day 9 post-injury. **(I–L)** Csf3r staining showing neutrophils in the distal nerve of PLP-GFP mice at day 3 post injury. **(M–P)** Csf3r and Cd68 double staining showing neutrophils in the distal nerve of C57BL/6 mice at day 3 post injury. Scales bars in **(I)** and **(M)** 10 μm.

nerve sections from PLP-GFP mice at day 3 post injury showed that Csf3r is expressed by large cells localized between GFP positive Schwann cells (**Figures 8I–L**). Double staing Csf3r with a marophage marker CD68 indiated that Csf3r is expressed on a diffrenct cell population from macrophages in the distal nerve (**Figures 8M–P**). In particularly, Csf3r positive cells exhibit segmented nuclei with three to five distinct lobes connected by thin filaments (**Figures 8I,M**), this is a key feature of mature neutrophils (Hermann and Gunzer, 2019). Thus, the Csf3r immunostating confirms that Csf3r is a reliable marker gene to identify neutrophils in the distal nerve stump.

Proliferating Cells in the Distal Nerve Stump Following Injury

Cells proliferate in the distal nerve stump following peripheral nerve injury, we then identify proliferating cells in the distal nerve stump using well characterize marker genes Mki67/Ki67, Top2a, Prc1, and Ccna2 for proliferating cells (Stierli et al.,

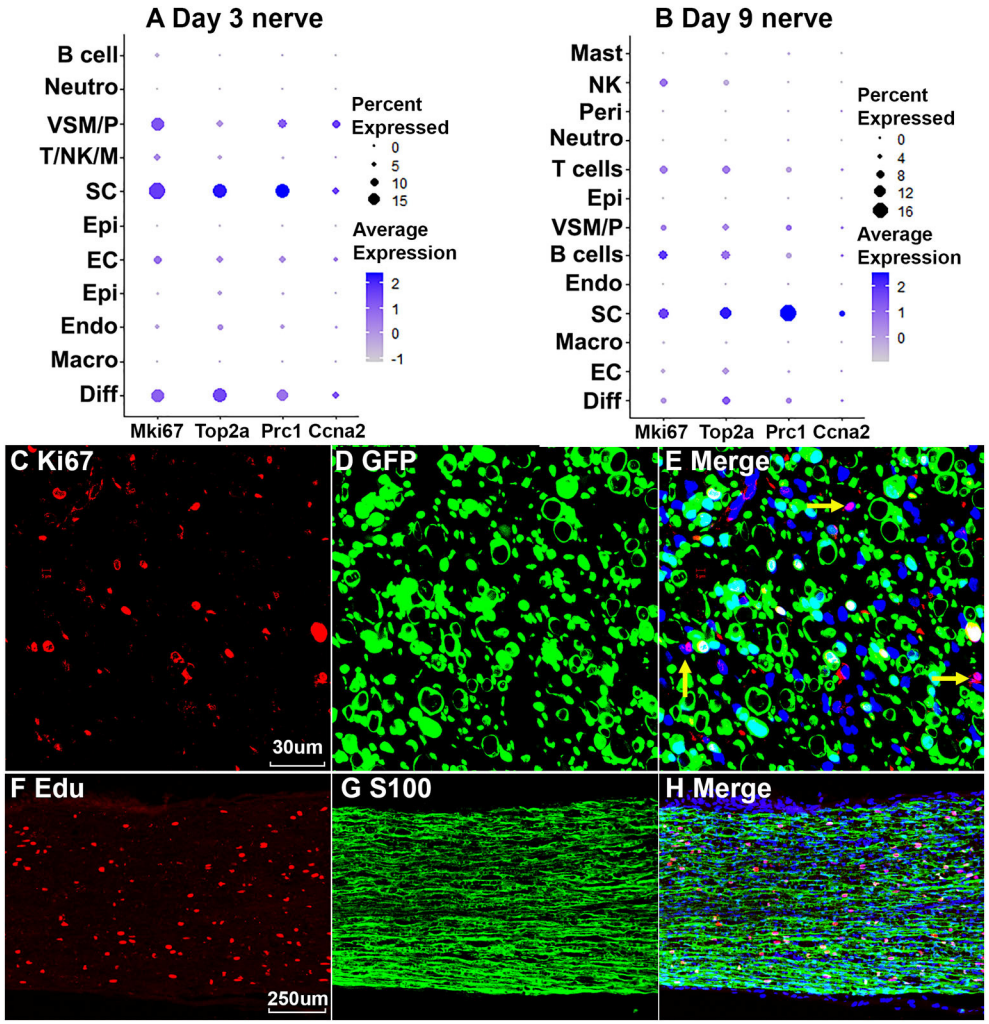

FIGURE 9 | Proliferating cells in the injured peripheral nerves. **(A)** Marker genes Mki67, Top2a, Prc1, and Ccna2 identify Schwann cells as the most proliferative cells in the distal nerve at day 3 post injury. **(B)** Mki67, Top2a, Prc1, and Ccna2 identify Schwann cells as the most proliferative cells in the distal nerve at day 9 post injury. **(C–E)** Mki67/Ki67 staining showing Schwann cells (GFP positive) are the most proliferative cells in the distal nerve at day 7 post injury in PLP-GFP mice. Yellow arrows in **(E)** show proliferation of non-Schwann cells (GFP negative). **(F–H)** EdU labeling showing that Schwann cells (S100 positive) are the most proliferative cells in the distal nerve at day 7 post injury in C57 mice. Scales bar in **(C)** 30, in **(F)** 250 μm.

2018; Carr et al., 2019; Dun et al., 2019; Toma et al., 2020; Wolbert et al., 2020). At day 3 post injury, Mki67/Ki67, Top2a, Prc1, and Ccna2 marker genes identify Schwann cells as the most proliferative cells in the distal nerve stump (**Figure 9A**). Fibroblasts, vascular smooth muscle (VSM) cells and pericytes are also highly proliferative in the distal nerve stump at day 3 post injury (**Figure 8A**). ECs proliferate as well at day 3 post injury but with much lower percentage of cells proliferating (**Figure 9A**). At day 3 post injury, 19.85% Schwann cells, 15.76% fibroblasts, 15.29% VSM and pericytes, and 7.87% ECs express Mki67/Ki67 (**Figure 9A**). At day 9 post injury, Schwann cells remain the most proliferative cells in the distal nerve stump (**Figure 9B**). In contrast to day 3 post injury, infiltrated B cells, T cells and NK cells at day 9 post injury are more proliferative than other cell types except Schwann cells (**Figure 9B**). At day 9 post injury, 11.34% Schwann cells, 9.42% B cells, 7.93% T cells and 7.89% NK cells express Mki67/Ki67 (**Figure 9A**). Having identified Schwann cells as the most proliferative cells in the distal nerve stump, we performed Ki67 staining in PLP-GFP mice as well as EdU and S100b double labeling in C57BL/6J mice to reveal proliferating cells in the distal nerve stump at day 7 post injury. Both Ki67 staining (**Figures 9C–E**) and EdU labeling (**Figures 9F–H**) results confirm that Schwann cells are the most proliferative cells in the injured mouse sciatic nerve.

Changes in the Molecular Profile of Each Cell Type Following Peripheral Nerve Injury

Gene expression changes following peripheral nerve injury have been extensively studied by microarray analysis and bulk mRNA sequencing (Arthur-Farraj et al., 2012, 2017; Fontana et al., 2012;

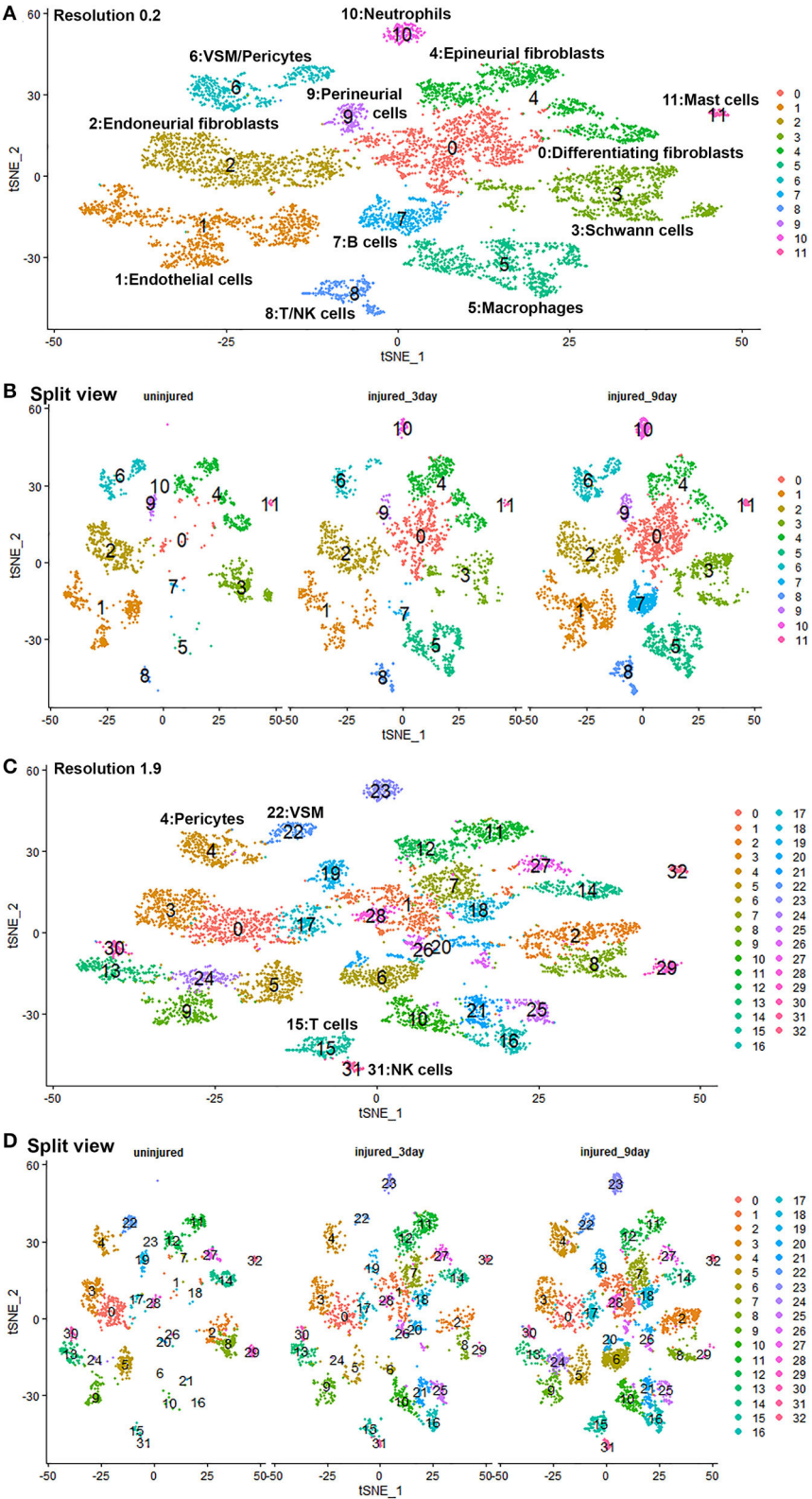

FIGURE 10 | GSE147285 and GSE120678 data sets integrated analysis for intact sciatic nerve and sciatic nerves at day 3 and day 9 post injury. **(A)** tSNE visualization of cell clusters for integrated analysis at resolution 0.2. NK cells were not separated from T cells, and pericytes were not separated from VSM at resolution 0.2. **(B)** Split view of cell clusters at resolution 0.2 for intact sciatic nerve and sciatic nerves at day 3 and day 9 post injury. **(C)** tSNE visualization of cell clusters for integrated analysis at resolution 1.9. NK cells (cluster 31) were separated from T cells (cluster 15), and pericytes (cluster 4) were separated from VSM (cluster 22). **(D)** Split view of cell clusters at resolution 1.9 for intact sciatic nerve and sciatic nerves at day 3 and day 9 post-injury.

TABLE 1 | Cell type specific gene up- and down-regulation.

Cell types	Intact vs 3D injury		Intact vs 9D injury		3D injury vs 9D injury		Total changes
	Up	Down	Up	Down	Up	Down	
Differentiating fibroblasts	300	15	120	34	75	480	1,024
Endothelial cells	176	93	121	269	28	187	874
Endoneurial fibroblasts	1,533	153	719	191	72	521	3,189
Schwann cells	2,045	117	66	658	1,529	172	4,587
Epineurial fibroblasts	100	69	21	53	11	76	330
Macrophages	27	0	25	0	30	77	159
B cells	1	1	17	215	12	192	438
Perineurial cells	14	2	4	4	1	3	28
Pericytes	109	19	0	0	0	0	128
VSM	11	0	0	0	0	0	11

Jessen and Mirsky, 2016; Clements et al., 2017; Gokbuget et al., 2018; Norrmen et al., 2018; Stratton et al., 2018; Tomlinson et al., 2018; Boissonnas et al., 2020; Ydens et al., 2020). However, cell type specific gene expression changes have not been studied. We therefore performed integrated analysis for intact sciatic nerve and sciatic nerves at day 3 and day 9 post injury, followed by a detailed analysis of cell type specific differential gene expression between intact and injured nerves. Only data set GSE147285 for the intact nerves was used for this analysis because our analysis showed that GSE142541 data set contains much lower numbers of genes per cell compared to data sets GSE147285 and data set GSE120678.

Quality control filtering was the same as described for the individual data sets. After integration of the three data sets there were 8061 cells with 37,607 genes. The three datasets are well-integrated according to the t-SNE plots while some differences between the cell populations in each condition are apparent (**Figure 10**). To compare gene expression changes for the main cell types, a lower clustering resolution (0.2) was used to avoid sub-clusters forming in each cell type. Using a low clustering resolution, NK cells were not separated from T cells, and pericytes were not separated from VSM, but the other cell types clustered appropriately (**Figures 10A,B**). We then increased the clustering resolution (1.9) in order to separate the NK cells from T cells (**Figures 10C,D**) and pericytes from VSM cells (**Figures 10C,D**). Subsequently, we compared differential gene expression between intact and injured nerves for T cells, NK cells, pericytes and VSM at resolution 1.9, and compared cell type specific differential gene expression between intact and injured nerves for other cell types at resolution 0.2. This analysis identified genes significantly up-regulated and down-regulation in Schwann cells, fibroblasts, endothelial cells, B cells, macrophages VSM and pericytes (**Table 1**, **Supplementary Table 5**).

Schwann cells have the highest number of significant DEG and endoneurial fibroblasts have second highest number, supporting the view that Schwann cells and endoneurial fibroblasts are the two most important cell types promoting peripheral nerve regeneration. Our analysis showed that there were no significant gene up- or down regulation in mast cells, neutrophils, T cells and NK cells. One possible reason is the low number or lack of these immune cells in the intact nerve would impede this analysis. Another possibility is that these immune cells are recruited to the distal nerve stump to execute their function and the distal nerve environment does not significantly regulate their gene expression.

Cell-Cell Communication in Intact and Injured Nerves

Another great advantage of analyzing scRNA-seq data is that cell-cell communication can be revealed in order to further understand physiological processes. Bioinformatic tools for cell-cell communication analysis have been developed such as CellPhoneDB (Efremova et al., 2020) and Celltalker (Cillo et al., 2020). Previously, Toma et al. analyzed cells of the distal nerve stump communicating with regenerating neurons during peripheral nerve regeneration (Toma et al., 2020). Here we report our analysis of cell-cell communication in the nerve trunk using CellPhoneDB with the cell clusters identified in intact nerves and cell clusters identified in the distal nerve at day 3 and day 9 post-injury.

CellPhoneDB ranks interactions based on the proportion of potentially interacting receptor ligand pairs with significant *p*-values across the cell clusters. In total, we identified 298 significant ligand-receptor interactions in intact nerves (**Figure 11A**). The largest number of interactions occur between epineurial fibroblasts, perineurial cells and endoneurial fibroblasts in the intact nerve. Subcluster 2 and 7 of epineurial fibroblasts have the highest number of potential ligand-receptor interactions (**Figure 11B**). Myelinating Schwann cells are known to become quiescent in adult nerves (Tikoo et al., 2000; Stierli et al., 2018) and our CellPhoneDB analysis also revealed that myelinating Schwann cells have the lowest number of ligand-receptor interactions compared with any other cell types in the intact nerve (**Figure 11B**). All significant ligand-receptor interactions in intact nerves were shown in **Supplementary Table 6**.

In total, we identified 213 significant ligand-receptor interactions in the distal nerve at day 3 post-injury (**Figure 11C**).

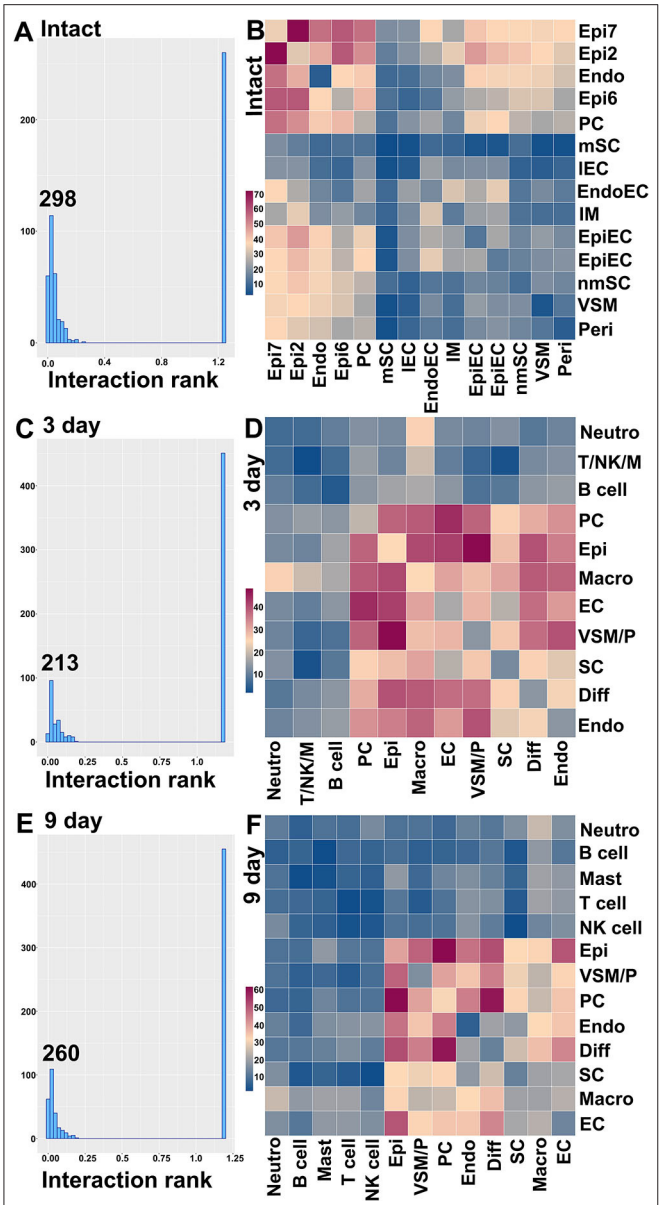

FIGURE 11 | Ligand-receptor interactions between the cell clusters in intact and injuried nerves. **(A)** Distribution of CellphoneDB interaction rank for intact nerves. 298 significant ligand-receptor interactions were identified. **(B)** Heatmap of number of ligand-receptor interactions between the cell clusters in intact nerves. **(C)** Distribution of CellphoneDB interaction rank for the distal nerve at day 3 post-injury. Two hundred and thirteen significant ligand-receptor interactions were identified. **(D)** Heatmap of number of ligand-receptor interactions between the cell cluters in the distal nerve at day 3 post-injury. **(E)** Distribution of CellphoneDB interaction rank for the distal nerve at day 9 post-injury. Two hundred and sixty significant ligand-receptor interactions were identified. **(F)** Heatmap of number of ligand-receptor interactions between the cell clusters in the distal nerve at day 9 post-injury. Endo, Endoneurial fibroblasts; PC, Perineurial cells; Epi, Epineurial fibroblasts; SC, Schwann cells; nmSC, non-myelinating Schwann cells; mSC, Myelinating Schwann cells; EC, Endothelial cells; EpiEC, Epineurial endothelial cells; EndoEC, Endoneurial endothelial cells; IEC, Lymphatic endothelial cells; Peri, Pericytes; VSM, Vascular smooth muscle cells; VSM/P, Vascular smooth muscle cells and Pericytes. IM, Immune cells. Neutro, Neutrophils; Macro, Macrophages; T/NK/M, T, NK and mast cells.

The most significant interactions occur between fibroblasts, macrophages, Schwann cells and cells associated with the blood supply system (**Figure 11D**). Epineurial fibroblasts and perineurial cells have the highest number of ligand-receptor interactions with cells associated with the blood supply system at day 3 post-injury such as Vegfa-Ephb2, Vegfa-Flt1, and Vegfa-Nrp interactions between epineurial fibroblasts and endothelial cells (**Supplementary Table 7**). This is the key stage of blood vessel regeneration following peripheral nerve injury (Cattin et al., 2015), indicating that signals from epineurial fibroblasts and perineurial cells may contribute significantly to early blood vessel regeneration. In contrast to the intact nerves, Schwann cells in the distal nerve increase the number of interactions with fibroblasts, macrophages and cells associated with the blood supply system (**Figure 11D**). At day 3 post-injury, Schwann cells have the highest number of interactions with macrophages. Among identified ligands, Tnfα, Il1β, Csf1, and Tgfβ1 are important signals secreted by macrophages to interact with Schwann cells (**Supplementary Table 7**), indicating that cytokines secreted by macrophages could be important signals to activate Schwann cells at this stage of Wallerian degeneration. At day 3 post-injury, neutrophils potentially also strongly communicate with macrophages (**Figure 11D**). Examination of ligands revealed that Tnfα, Il1β, Ccl3, and Ccl4 are important signals secreted by neutrophils to activate resident macrophages or attract monocytes from the circulating blood (**Supplementary Table 7**). T cells, B cells, NK cells and mast cells have a low number of interactions with other cell types compared to fibroblasts, macrophages, Schwann cells and cells associated with the blood supply system. All significant ligand-receptor interactions in the distal nerve at day 3 post-injury are shown in **Supplementary Table 7**.

In total, we identified 260 significant ligand-receptor interactions in the distal nerve at day 9 post-injury (**Figure 11E**). At day 9 post-injury, the most significant interactions occur between subgroups of fibroblasts. The highest number of interactions happened between epineurial fibroblasts with perineurial cells, and perineurial cells with differentiating fibroblasts (**Figure 11F**). Examining the ligand-receptors pairs showed that Collagen-Integrin, Ephrin-Eph and Fgf-Fgfr interactions are the most important signaling pathways between the subgroups of fibroblasts (**Supplementary Table 8**). Neutrophils, T cells, B cells, NK cells and mast cells have a low number of interactions with other cell types at day 9 post-injury. All significant ligand-receptor interactions in the distal nerve at day 9 post-injury are shown in **Supplementary Table 8**.

DISCUSSION

scRNA-seq allows the cellular composition of complex tissues to be defined in an unbiased fashion (Haque et al., 2017; Hwang et al., 2018). Carr et al. reported the first use of scRNA-seq on the transected mouse sciatic nerve at day 9 post-injury with a focus on studying the function of mesenchymal cells in peripheral nerve regeneration (Carr et al., 2019). One year later, the same group, Toma et al., reported their combined scRNA-seq data at

both day 3 and day 9 post-injury for transected mouse sciatic nerve focussing on the study of secreted signals in the distal nerve stump (Toma et al., 2020). In the same year, Wolbert et al. also reported their scRNA-seq data analysis for intact mouse sciatic nerve and the brachial nerve plexus (Wolbert et al., 2020). However, differences exist for the analysis of these three available scRNA-seq data sets in terms of identified cell clusters and suitable marker genes for cell cluster identification. Wolbert et al. (2020) identified the lymphatic endothelial cell cluster that had not been reported by Carr et al. (2019) and Toma et al. (2020). Wolbert et al. (2020) reported a novel endothelial cell cluster in the intact nerve, which shares a similar gene expression profile to perineurial cells as identified by Carr et al. (2019) and Toma et al. (2020). Furthermore, endoneurial fibroblasts were named as nmSCs in Wolbert et al.'s analysis due to endoneurial fibroblasts expressing Ngfr, and therefore they suggested marker genes for endoneurial fibroblasts as marker genes for nmSC, for example Somc2 and Apod (Wolbert et al., 2020). Moreover, neutrophils, a previously well-characterized cell population in the injured nerves by both immunostaining and flow cytometry (Cattin et al., 2015; Lindborg et al., 2017), had not previously been identified in these scRNA-seq data analyses (Carr et al., 2019; Toma et al., 2020). Therefore, we re-analyzed these data sets and provided our rationale for the identification of cell clusters in both intact and injured mouse scitic nerve.

The intact nerve trunk contains both myelinating Schwann cells (mSCs) and non-myelinating Schwann cells (nmSCs). mSCs wrap around and insulate large diameter axons of motor and sensory neurons, forming a myelin sheath, which allows conduction of rapid action potentials. nmSCs ensheath several small diameter axons forming Remak bundles. In adult nerves, mSCs and nmSCs can be easily distinguished by their morphology or myelin protein immunostaining. In our scRNA-seq data analysis, mSCs (cluster 10, **Figure 1A**) and nmSCs (cluster 1, **Figure 1A**) could be easily separated into two distinct clusters in intact nerves. However, injury to a peripheral nerve results in both mSCs and nmSCs in the distal nerve stump being rapidly reprogramed into a repair cell phenotype (Jessen and Mirsky, 2016, 2019). The clearance of myelin proteins, the cell morphology change and the down-regulation of classic mSC and nmSC markers make it difficult to distinguish the mSC and nmSC lineage in the distal nerve stump. This might explain why in our analysis, all Schwann cells (SC) cluster into one group, indicating that both mSCs and nmSCs dedifferentiate into more similar phenotypes in the distal nerve following peripheral nerve injury.

S100b has been frequently used as an immunostaining marker to label Schwann cells in both intact and injured nerves. Ngfr/p75 labeling is more frequently used to label Schwann cells in the injured nerves. However, a study has indicated that endoneurial fibroblasts, which makes up 12.5% of the cells within an intact peripheral nerve, also express Ngfr/p75 (Stierli et al., 2018). Recent scRNA-seq data analysis has used Ngfr/p75, S100b, Erbb3, and Sox10 to identify Schwann cell clusters in intact and injured nerves (Carr et al., 2019; Toma et al., 2020; Wolbert et al., 2020). We first tested these markers but found that S100b is not an ideal marker in scRNA-seq data analysis to identify SCs in injured nerves although it can be used as a marker to identify both mSCs and nmSCs clusters in intact nerve (**Supplementary Figure 7**). In contrast, Ngfr is not a suitable marker to identify both mSCs and nmSCs in intact nerves while Erbb3 is not the best marker to identify mSC in intact nerves (**Supplementary Figure 7**). Through our analysis, we show that Sox10 and Plp1 are more suitable marker genes in scRNA-seq data analysis to identify Schwann cell clusters in both intact and injured nerves (**Supplementary Figure 8**). Sox10 is a transcription factor required to specify the Schwann cell lineage (Finzsch et al., 2010). Although Proteolipid protein 1 (PLP1) is a form of myelin proteolipid protein (PLP), transgenic mice expressing green fluorescence protein under the PLP promoter labels both mSCs and nmSCs in intact nerves as well as all SCs in the injured nerves (Mallon et al., 2002; Chen et al., 2019a; Dun et al., 2019). For identifying mSCs in intact nerves, Mbp, Mpz, Mag and Egr2 are all good marker genes (**Supplementary Figure 8**). Testing marker genes used for identifying nmSCs in the intact nerve, we found that Cdh2 and L1cam are good marker genes (**Supplementary Figure 8**). Previously, Wolbert et al. have suggested Smoc2 and Apod as nmSC markers (Wolbert et al., 2020). We also analyzed their data set, our analysis indicated that the cluster of endoneurial fibroblasts has been named as nmSCs due to endoneurial fibroblasts expressing Ngfr/p75 (**Supplementary Figure 7**). In agreement with Carr et al's. findings (Carr et al., 2019), we showed that Smoc2 and Apod have their highest expression in endoneurial fibroblasts (**Supplementary Figure 9**).

Fibroblasts are another important cell type in peripheral nerves; they are the most abundant cells in the endoneurium, perineurium and epineurium and provide structural support, regional separation and protection of nerve fibers from damage (Parrinello et al., 2010; Stierli et al., 2018; Carr et al., 2019; Diaz-Flores et al., 2020). They have mesenchymal cell properties and play an important role in nerve repair following injury (Parrinello et al., 2010; Carr et al., 2019). We tested marker genes for fibroblasts reported in previous mouse sciatic nerve scRNA-seq studies including: Sfrp4, Pi16, Dpt, Gsn, Col1a1, Col1a2, Col3a1, Col14a1, Clec3b, Cygb, Prrx1, and Aebp1 (Carr et al., 2019; Diaz-Flores et al., 2020; Toma et al., 2020; Wolbert et al., 2020). We found that some of these genes are not fibroblast-specific and that while some of them were fibroblast specific, they only label one sub-population of epineurial, perineurial or endoneurial fibroblasts. Particularly, most of the genes show up-regulation in other cells types in response to injury. We therefore screened DEGs and revealed that Mfap5 and Serpinf1 are better marker genes to identify fibroblast clusters in both intact and injured nerve (**Supplementary Figure 10**). Studies have shown that microfibrillar-associated protein 5 (Mfap5), is a fibroblast derived factor, which can promote tumor cell epithelial-mesenchymal transition, migration and metastasis (Valenzi et al., 2019; Chen et al., 2020). Examination of gene expression in mesenchymal cells of the lung by single-cell analysis also found that lung fibroblasts express high levels of Mfap5 (Valenzi et al., 2019). Serpinf1 encodes the pigment epithelium-derived factor (PEDF) and is secreted by fibroblasts. Homozygous mutations in Serpinf1 cause deficiency of PEDF, which leads to osteogenesis imperfecta (Al-Jallad et al., 2014). Similar to the function of Mfap5, loss

of PEDF in cancer cells is associated with poor prognosis and metastasis (Nwani et al., 2016). Using these analyses, we identified that cell cluster 0, 2, 6, 7 and 11 in intact nerve are fibroblasts (**Figure 1A**), cell cluster 0, 2, 3, and 5 in post-injury day 3 nerves are fibroblasts (**Figure 2A**), and cell cluster 0, 4, 7, and 10 in post-injury day 9 nerves are fibroblasts (**Figure 3A**).

According to the anatomical location, peripheral nerve fibroblasts could be divided into endoneurial, perineurial and epineurial fibroblasts (Osawa and Ide, 1986; Pina-Oviedo and Ortiz-Hidalgo, 2008). Endoneurial fibroblasts are spindle-shaped cells with long processes making contact with other cell types in the endoneurium, they are present between nerve fibers and compose 12.5% of all endoneurial cells (Stierli et al., 2018; Carr et al., 2019; Diaz-Flores et al., 2020). Endoneurial fibroblasts have also been named as tactocytes (Stierli et al., 2018), endoneurial mesenchymal cells (Carr et al., 2019) and endoneurial telocytes (Diaz-Flores et al., 2020). They express marker genes Sox9 and Osr2, they also up-regulate Wif1 in response to nerve injury (Carr et al., 2019; Toma et al., 2020). Using these reported marker genes together with DEGs in our analysis (**Supplementary Tables 1–3**), we found that Sox9, Osr2, Wif1, Abca9, Cdkn2a, Cdkn2b, and Plxdc1 are all good marker genes for the identification of endoneurial fibroblasts (**Supplementary Figure 11**). Our analysis revealed that cluster 0 in intact nerves, cluster 2 in nerves at 3 days post-injury and cluster 4 in nerves at 9 days post-injury are all endoneurial fibroblasts (**Figures 1–3**).

Axons targeting the same anatomical location within the nerve are bundled together into fascicles by a protective sheath known as the perineurium (Pina-Oviedo and Ortiz-Hidalgo, 2008). Fibroblasts in the perineurium have long been named as perineurial cells (Strauss and Cohen, 1981; Theaker and Fletcher, 1989; Inokuchi et al., 1991; Schroder et al., 1993; Weis et al., 1994; Kucenas, 2015). Perineurial cells are the first cell type to migrate into the nerve bridge following peripheral nerve transection injury and form a perineurial tube to control the trajectory and migration of other cells (Schroder et al., 1993; Weis et al., 1994; Min et al., 2020). Perineurial cells express marker genes such as Slc2a1/Glut1, Lypd2, Sfrp5, Ntn4, Msln, Ntng1, the tight junction genes Tjp1/ZO-1, the desmosome protein Perp, and integrins Itgb4 and Itga6 (Theaker and Fletcher, 1989; Kucenas, 2015; Carr et al., 2019; Toma et al., 2020; Wolbert et al., 2020). We used these marker genes (**Supplementary Figure 11**) and identify perineurial cells in intact nerve (cluster 11) as well as post-injury day 9 (cluster 10) nerves (**Figures 1A**, **3A**). However, perineurial cells were clustered into the cluster of differentiating fibroblasts for nerves at 3 days post-injury due to the low number of perineurial cells (**Figure 2A**). We also performed the integrated data analysis and perineurial cells could be visualized as an individual cluster at day 3 post injury with integrated data analysis (**Figure 10B**). Our analysis showed that that perineurial cells also share some gene signatures with endothelial cells such as Moxd1, Ntng1, Lypd2, Krt19, and Dleu7 (**Supplementary Tables 1–3**), which resulted in perineurial cells being identified as an additional cluster of endothelial cells in a recently reported scRNA-seq data analysis (Wolbert et al., 2020).

The epineurium is the outermost layer of connective tissue surrounding and protecting nerve fibers. It contains not only fibroblasts but also immune cells, adipocytes and blood vessel associated cells (Osawa and Ide, 1986). Epineurial fibroblasts highly express Sfrp2, Adamts5, Pcolce2, Clec3b, Pi16, Ly6c1, Dpt, Dpp4, Gsn, Comp, and Sfrp4 (Carr et al., 2019; Toma et al., 2020; Wolbert et al., 2020). Using these marker genes, we identify cluster 2, 6, and 7 as epineurial fibroblasts in intact nerves, cluster 3 and 5 as epineurial fibroblasts in post-injury day 3 nerves, and cluster 7 as epineurial fibroblasts in post-injury day 9 nerves (**Supplementary Figure 10**). We used a resolution of 0.75 for cell clustering in the intact nerves in order to label the cell cluster of lymphatic endothelial cells. This has resulted in the separation of epineurial fibroblasts into three sub-clusters in intact nerves. Similar to cluster 0 of endoneurial fibroblasts in intact nerves, cluster 2 and cluster 7 epineurial fibroblasts express high levels of Pdgfr2 (**Supplementary Figure 3**) which is a mesenchymal cell marker for epi- and endoneurial mesenchymal-like fibroblasts (Carr et al., 2019). Indeed, in Pdgfra-EGFP mice, epineurial sheaths contain 60.5 ± 6.0% GFP positive mesenchymal cells (Carr et al., 2019; Toma et al., 2020). In response to injury, fibroblasts in the distal nerve undergo differentiation and differentiating nerve fibroblasts could be identified using differentiating marker genes Dlk1, Mest, Cilp, Tnc, Plagl1, and Ptn (Carr et al., 2019; Toma et al., 2020). Using these marker genes, we identified the largest fibroblast cluster (cluster 0) in both post-injury day 3 and post-injury day 9 nerves as differentiating fibroblasts (**Supplementary Figure 4**).

We use Ptprc/CD45 and Cd52 as general marker genes to identify immune cells in intact and injured nerves (Carr et al., 2019; Wolbert et al., 2020; Ydens et al., 2020). The number of immune cells in the intact nerve is low in data set GSE147285 and all immune cells have been clustered into one cluster (cluster 12, **Figure 1**) as revealed by Ptprc/CD45 and Cd52 expression (**Figure 1A** and **Supplementary Figure 5**). Due to the high number of cells in data set GSE142541 (Wolbert et al., 2020), immune cells could be clustered to B cells (cluster 13 in **Figure 6A**), epineurial macrophages (cluster 15 in **Figure 6A**), endoneurial macrophages (cluster 16 in **Figure 6A**), T cells (cluster 14, 19 and 21 in **Figure 6A**) and NK cells (cluster 22 in **Figure 6A**). Previous studies have shown that resident macrophages are the major immune cells in the intact nerve and compose 8–9% cells of the intact mouse sciatic nerve (Stierli et al., 2018; Amann and Prinz, 2020). However, this analysis revealed that the intact mouse peripheral nerves also contain a large number of T cells. In the intact nerve, macrophage express genes Aif1/Iba1, Cd68, and Mrc1/Cd206 (**Supplementary Figure 12**) and these marker genes label two sub-cluster of macrophages (cluster 15 and 16 in **Figure 4A**). Macrophages in cluster 15 express Retnla and Clec10a and they are epineurial macrophages (Ydens et al., 2020). Thus, macrophages in cluster 16 are resident macrophages.

Following peripheral nerve injury, a large number of immune cells infiltrate the distal nerve (Gaudet et al., 2011). Ptprc/CD45 and Cd52 label four clusters of cells (cluster 1, 7, 9, and 10) in post-injury day 3 nerves, and label six cell clusters (cluster 2, 5, 8, 9, 11, and 12) in post-injury day 9 nerves (**Supplementary Figure 5**). Immune cells can be divided into myeloid cell lineages and the lymphoid cell lineage. Myeloid

cells include macrophages, neutrophils and mast cells, and can be identified with myeloid marker genes Lyz2, Ccl6, and Lyz1 (Carr et al., 2019; Amann and Prinz, 2020; Kolter et al., 2020; Toma et al., 2020; Wolbert et al., 2020; Ydens et al., 2020). Lymphoid cells include B cells, T cells and NK cells, they can be identified with lymphoid marker genes Ptprcap and Trbc2 (Carr et al., 2019; Toma et al., 2020; Wolbert et al., 2020; Ydens et al., 2020). These markers genes were initially used to distinguish myeloid cells from lymphoid cells in the immune cell clusters (**Supplementary Figure 13**).

Peripheral nerve injury results in rapid resident macrophage activation and infiltration of a large number of bone marrow derived macrophages into the distal nerve (Dun et al., 2019; Zigmond and Echevarria, 2019; Kolter et al., 2020). Currently, there are no clear markers to distinguish activated resident macrophages from infiltrated macrophages in injured nerves (Amann and Prinz, 2020; Kolter et al., 2020). A recent publication using both Csf1r-ECFP and Cx3cr1-EGFP mice demonstrated that resident macrophages have distinct function and morphological difference from recruited macrophages (Boissonnas et al., 2020). Macrophages in the distal nerve could be identified with macrophage marker genes Aif1/Iba1, Cd68, and Mrc1/Cd206. These marker genes label cluster 1 in day 3 post-injury nerves and cluster 2 in day 9 post-injury nerves (**Supplementary Figure 12**).

We used marker genes Cma1, Mcpt4, Mcpt1, and Kit to identify mast cells as suggested in recent scRNA-seq data analysis in mouse sciatic nerve samples (Carr et al., 2019; Toma et al., 2020; Wolbert et al., 2020). In our analysis, mast cells clustered together with all immune cells (cluster 12, **Figure 1A**) in intact nerve and were also clustered with T/NK cells (cluster 7, **Figure 2A**) in day 3 post-injury nerves. However, t-SNE visualization analysis revealed that mast cells form distinct sub-clusters (indicated by a red circle in **Supplementary Figure 14**) both in intact nerves and day 3 post-injury nerves although increasing the clustering resolution in our analysis we were unable to further separate them as an individual cluster. The low abundance of mast cells in intact and day 3 post-injury nerves could be the reason that they grouped into a single cluster with other immune cells as mast cells clustered separately (cluster 12, **Figure 1A**) in day 9 post-injury nerves when more mast cells were apparently present (**Supplementary Figure 14**).

T cells could be identified by marker genes Cd3e, Cd3g, Cxcr6, and Trac, and NK cells could be identified by marker genes Ncr1, Nkg7, and Klrk1 (**Supplementary Figure 15**). In day 3 post-injury nerves, T cells and NK cells are found in the same cluster (cluster 7, **Figure 2A**), but T cells and NK cells cluster separately in day 9 post-injury nerves (cluster 8 for T cells and cluster 11 for NK cells, **Figure 3A**). Recently, Wolbert et al. showed that B cells could be identified in intact mouse sciatic nerves using marker genes such as Bank1, Ms4a1, Cd19, Cd40, and Cd79a (Wolbert et al., 2020). There is a significant number of B cells in 3 day post-injury nerves and they have been grouped into cluster 10 (**Figure 2A** and **Supplementary Figure 16**). There are even more B cells in day 9 post-injury nerves (cluster 5, **Figure 3A**), indicating a rapid infiltration of B cells into the distal nerve between day 3 and day 9 following injury.

Classic gene markers used in scRNA-seq data analysis to identify ECs include Pecam1/Cd31, Tie1, and Emcn (Zhao et al., 2018; Carr et al., 2019; Kalluri et al., 2019; Toma et al., 2020; Wolbert et al., 2020). We used these markers to identify ECs, which are found in clusters 3, 4 and 5 in intact nerves, cluster 4 in 3 day post-injury nerves, and cluster 1 in 9 day post-injury nerves (**Supplementary Figure 5**). Recently, Wolbert et al. also identified lymphatic ECs in the intact nerves in their scRNA-seq data analysis using lymphatic EC marker genes Lyve1 and Prox1 (Wolbert et al., 2020). Other scRNA-seq data analysis have shown that lymphatic ECs have distinct gene expression profiles including the expression of Lyve1, Mmrn1, Prox1, and Flt4 (Engelbrecht et al., 2020; Fujimoto et al., 2020). Therefore, we used these marker genes to identify the cluster containing lymphatic ECs. Our analysis showed that Lyve1, Mmrn1, and Flt4 are suitable marker genes to identify the lymphatic EC cluster in intact nerves (**Supplementary Figure 1**). However, all four distinct EC clusters in the intact nerves have been clustered into just one EC cluster in day 3 and day 9 post-injury nerves (**Figures 2A**, **3A**, **Supplementary Figure 17**).

Our analysis confirmed that there are three distinct EC subgroups in the intact mouse sciatic nerve: epineurial, endoneurial and lymphatic ECs. However, classic EC markers such as Pecam1/Cd31, Tie1 and Emcn were unable to identify lymphatic ECs (**Supplementary Figure 2**). In this study, we investigated if there were better marker genes that could label all the ECs in mouse sciatic nerve. Our investigation revealed that Cdh5, another common marker gene for ECs, could label all four EC clusters but Cdh5 could also label perineurial cells in both intact and injured nerves (**Supplementary Figure 17**). Further analysis indicates that Egfl7 and Ecscr are the better marker genes to identify all types of ECs in mouse sciatic nerve for scRNA-seq data analysis (**Supplementary Figure 17**). EGFL7 is a highly conserved angiogenic factor in vertebrates. Unlike most secreted angiogenic signaling molecules such as vascular endothelial growth factor and fibroblast growth factor-2, which are mainly expressed by non-endothelial cell types, EGFL7 is almost exclusively expressed and secreted by endothelial cells, it binds to components of the extracellular matrix and acts as a chemoattractant for endothelial cells (Nichol and Stuhlmann, 2012). EGFL7 also regulates the collective migration of endothelial cells and controls their spatial distribution (Schmidt et al., 2007). EGFL7 expression is highest when the endothelium is in an active and proliferating state (Nichol and Stuhlmann, 2012). In contrast, ECSCR is an endothelial cell-specific chemotaxis receptor selectively expressed by endothelial cells; it plays roles in endothelial cell migration, proliferation and promotes angiogenesis (Verma et al., 2010; Kilari et al., 2013). The high expression of EGFL7 and ECSCR in mouse sciatic nerve indicates that EGFL7 and ECSCR could play important roles in peripheral nerve vascular homeostasis and regeneration following injury.

In conclusion, we re-analyzed recently published single-cell RNA sequencing data sets and generated a cellular

composition map of the peripheral nerve in homeostasis and regeneration. We identified each cell type using marker genes reported from the literature (Carr et al., 2019; Toma et al., 2020; Wolbert et al., 2020). In addition, DEGs between clusters were used to established suitable marker genes for future single cell transcriptomic analyses for the identification of cell types in intact and injured peripheral nerves. Our analysis also revealed three sub-groups of endothelial cells in the intact nerve and identified the neutrophil cluster in injured nerves, which were not reported in previous studies (Carr et al., 2019; Toma et al., 2020; Wolbert et al., 2020). Identification of these cell clusters will enable us to further study their distinct gene expression profiles for each cell type and the signals that mediate cell-cell communication in intact and injured peripheral nerves. The findings from our analysis could facilitate a better understanding of the cell biology of peripheral nerves in homeostasis, regeneration and disease.

DATA AVAILABILITY STATEMENT

The original contributions presented in the study are included in the article/supplementary material, further inquiries can be directed to the corresponding author/s.

AUTHOR CONTRIBUTIONS

XD designed the research. MB, BC, and XD performed scRNA-seq data analysis. LS performed immunostaining. BC, DP, and XD wrote the paper. All authors contributed to the article and approved the submitted version.

SUPPLEMENTARY MATERIAL

The Supplementary Material for this article can be found online at: https://www.frontiersin.org/articles/10.3389/fncel.2021.624826/full#supplementary-material

REFERENCES

Aird, W. C. (2012). Endothelial cell heterogeneity. *Cold Spring Harb Perspect Med.* 2:a006429. doi: 10.1101/cshperspect.a006429

Al-Jallad, H., Palomo, T., Moffatt, P., Roughley, P., Glorieux, F. H., and Rauch, F. (2014). Normal bone density and fat mass in heterozygous SERPINF1 mutation carriers. *J. Clin. Endocrinol. Metab.* 99, E2446–2450. doi: 10.1210/jc.2014-2505

Amann, L., and Prinz, M. (2020). The origin, fate and function of macrophages in the peripheral nervous system - an update. *Int. Immunol.* 32, 709–717. doi: 10.1093/intimm/dxaa030

Arthur-Farraj, P. J., Latouche, M., Wilton, D. K., Quintes, S., Chabrol, E., Banerjee, A., et al. (2012). c-Jun reprograms Schwann cells of injured nerves to generate a repair cell essential for regeneration. *Neuron* 75, 633–647. doi: 10.1016/j.neuron.2012.06.021

Arthur-Farraj, P. J., Morgan, C. C., Adamowicz, M., Gomez-Sanchez, J. A., Fazal, S. V., Beucher, A., et al. (2017). Changes in the coding and non-coding transcriptome and DNA methylome that define the schwann cell repair phenotype after nerve injury. *Cell Rep.* 20, 2719–2734. doi: 10.1016/j.celrep.2017.08.064

Barrette, B., Hebert, M. A., Filali, M., Lafortune, K., Vallieres, N., Gowing, G., et al. (2008). Requirement of myeloid cells for axon regeneration. *J. Neurosci.* 28, 9363–9376. doi: 10.1523/JNEUROSCI.1447-08.2008

Boissonnas, A., Louboutin, F., Laviron, M., Loyher, P. L., Reboussin, E., Barthelemy, S., et al. (2020). Imaging resident and recruited macrophage contribution to Wallerian degeneration. *J. Exp. Med.* 217:e20200471. doi: 10.1084/jem.20200471

Carr, M. J., Toma, J. S., Johnston, A. P. W., Steadman, P. E., Yuzwa, S. A., Mahmud, N., et al. (2019). Mesenchymal precursor cells in adult nerves contribute to mammalian tissue repair and regeneration. *Cell Stem Cell.* 24, 240-256 e249. doi: 10.1016/j.stem.2018.10.024

Cattin, A. L., Burden, J. J., Van Emmenis, L., Mackenzie, F. E., Hoving, J. J., Garcia Calavia, N., et al. (2015). Macrophage-induced blood vessels guide schwann cell-mediated regeneration of peripheral nerves. *Cell.* 162, 1127–1139. doi: 10.1016/j.cell.2015.07.021

Chandran, V., Coppola, G., Nawabi, H., Omura, T., Versano, R., Huebner, E. A., et al. (2016). A systems-level analysis of the peripheral nerve intrinsic axonal growth program. *Neuron* 89, 956–970. doi: 10.1016/j.neuron.2016.01.034

Chen, B., Chen, Q., Parkinson, D. B., and Dun, X. P. (2019a). Analysis of schwann cell migration and axon regeneration following nerve injury in the sciatic nerve bridge. *Front. Mol. Neurosci.* 12:308. doi: 10.3389/fnmol.2019.00308

Chen, G., Ning, B., and Shi, T. (2019b). Single-Cell RNA-seq technologies and related computational data analysis. *Front Genet.* 10:317. doi: 10.3389/fgene.2019.00317

Chen, Z., Yan, X., Li, K., Ling, Y., and Kang, H. (2020). Stromal fibroblast-derived MFAP5 promotes the invasion and migration of breast cancer cells via Notch1/slug signaling. *Clin. Transl. Oncol.* 22, 522–531. doi: 10.1007/s12094-019-02156-1

Cillo, A. R., Kurten, C. H. L., Tabib, T., Qi, Z., Onkar, S., Wang, T., et al. (2020). Immune landscape of viral- and carcinogen-driven head and neck cancer. *Immunity* 52, 183-199 e189. doi: 10.1016/j.immuni.2019.11.014

Clements, M. P., Byrne, E., Camarillo Guerrero, L. F., Cattin, A. L., Zakka, L., Ashraf, A., et al. (2017). The wound microenvironment reprograms schwann cells to invasive mesenchymal-like cells to drive peripheral nerve regeneration. *Neuron* 96, 98–114 e117. doi: 10.1016/j.neuron.2017.09.008

Deumens, R., Bozkurt, A., Meek, M. F., Marcus, M. A., Joosten, E. A., Weis, J., et al. (2010). Repairing injured peripheral nerves: bridging the gap. *Prog, Neurobiol.* 92, 245–276. doi: 10.1016/j.pneurobio.2010.10.002

Diaz-Flores, L., Gutierrez, R., Garcia, M. P., Gayoso, S., Gutierrez, E., Diaz-Flores, L. Jr., et al. (2020). Telocytes in the normal and pathological peripheral nervous system. *Int. J. Mol. Sci.* 21:4320. doi: 10.3390/ijms21124320

Dun, X. P., Carr, L., Woodley, P. K., Barry, R. W., Drake, L. K., Mindos, T., et al. (2019). Macrophage-Derived Slit3 controls cell migration and axon pathfinding in the peripheral nerve bridge. *Cell Rep.* 26, 1458–1472 e1454. doi: 10.1016/j.celrep.2018.12.081

Duployez, N., Willekens, C., Plo, I., Marceau-Renaut, A., de Botton, S., Fenwarth, L., et al. (2019). Inherited transmission of the CSF3R T618I mutational hotspot in familial chronic neutrophilic leukemia. *Blood* 134, 2414–2416. doi: 10.1182/blood.2019003206

Efremova, M., Vento-Tormo, M., Teichmann, S. A., and Vento-Tormo, R. (2020). CellPhoneDB: inferring cell-cell communication from combined expression of multi-subunit ligand-receptor complexes. *Nat. Protoc.* 15, 1484–1506. doi: 10.1038/s41596-020-0292-x

Engelbrecht, E., Levesque, M. V., He, L., Vanlandewijck, M., Nitzsche, A., Niazi, H., et al. (2020). Sphingosine 1-phosphate-regulated transcriptomes in heterogenous arterial and lymphatic endothelium of the aorta. *Elife* 9:e52690. doi: 10.7554/eLife.52690

Evrard, M., Kwok, I. W. H., Chong, S. Z., Teng, K. W. W., Becht, E., Chen, J., et al. (2018). Developmental analysis of bone marrow neutrophils reveals populations specialized in expansion, trafficking, and effector functions. *Immunity* 48, 364–379 e368. doi: 10.1016/j.immuni.2018.02.002

Feng, W., Chen, L., Nguyen, P. K., Wu, S. M., and Li, G. (2019). Single cell analysis of endothelial cells identified organ-specific molecular signatures and heart-specific cell populations and molecular features. *Front. Cardiovasc. Med.* 6:165. doi: 10.3389/fcvm.2019.00165

Finzsch, M., Schreiner, S., Kichko, T., Reeh, P., Tamm, E. R., Bosl, M. R., et al. (2010). Sox10 is required for Schwann cell identity and progression

beyond the immature Schwann cell stage. *J. Cell Biol.* 189, 701–712. doi: 10.1083/jcb.200912142

Fontana, X., Hristova, M., Da Costa, C., Patodia, S., Thei, L., Makwana, M., et al. (2012). c-Jun in Schwann cells promotes axonal regeneration and motoneuron survival via paracrine signaling. *J. Cell Biol.* 198, 127–141. doi: 10.1083/jcb.201205025

Fujimoto, N., He, Y., D'Addio, M., Tacconi, C., Detmar, M., and Dieterich, L. C. (2020). Single-cell mapping reveals new markers and functions of lymphatic endothelial cells in lymph nodes. *PLoS Biol.* 18:e3000704. doi: 10.1371/journal.pbio.3000704

Gaudet, A. D., Popovich, P. G., and Ramer, M. S. (2011). Wallerian degeneration: gaining perspective on inflammatory events after peripheral nerve injury. *J. Neuroinflammation.* 8:110. doi: 10.1186/1742-2094-8-110

Gokbuget, D., Pereira, J. A., Opitz, L., Christe, D., Kessler, T., Marchais, A., et al. (2018). The miRNA biogenesis pathway prevents inappropriate expression of injury response genes in developing and adult Schwann cells. *Glia.* 66, 2632–2644. doi: 10.1002/glia.23516

Gur, T. (2019). Biobtree: a tool to search, map and visualize bioinformatics identifiers and special keywords. *F1000Res* 8:145. doi: 10.12688/f1000research.17927.4

Hafemeister, C., and Satija, R. (2019). Normalization and variance stabilization of single-cell RNA-seq data using regularized negative binomial regression. *Genome Biol.* 20:296. doi: 10.1186/s13059-019-1874-1

Haque, A., Engel, J., Teichmann, S. A., and Lonnberg, T. (2017). A practical guide to single-cell RNA-sequencing for biomedical research and clinical applications. *Genome Med.* 9:75. doi: 10.1186/s13073-017-0467-4

Hermann, D. M., and Gunzer, M. (2019). Polymorphonuclear neutrophils play a decisive role for brain injury and neurological recovery poststroke. *Stroke* 50, e40–e41. doi: 10.1161/STROKEAHA.118.021564

Hwang, B., Lee, J. H., and Bang, D. (2018). Single-cell RNA sequencing technologies and bioinformatics pipelines. *Exp. Mol. Med.* 50:96. doi: 10.1038/s12276-018-0071-8

Inokuchi, T., Yokoyama, R., Higashi, R., Takahashi, Y., and Miyajima, S. (1991). Ultrastructure of the perineurial cell of the sciatic nerve in rats–a transmission and scanning electron microscopic study. *Kurume Med. J.* 38, 221–232.

Jessen, K. R., and Mirsky, R. (2016). The repair Schwann cell and its function in regenerating nerves. *J Physiol.* 594, 3521–3531. doi: 10.1113/JP270874

Jessen, K. R., and Mirsky, R. (2019). The success and failure of the schwann cell response to nerve injury. *Front. Cell Neurosci.* 13:33. doi: 10.3389/fncel.2019.00033

Kalluri, A. S., Vellarikkal, S. K., Edelman, E. R., Nguyen, L., Subramanian, A., Ellinor, P. T., et al. (2019). Single-cell analysis of the normal mouse aorta reveals functionally distinct endothelial cell populations. *Circulation* 140, 147–163. doi: 10.1161/CIRCULATIONAHA.118.038362

Kenswil, K. J. G., Jaramillo, A. C., Ping, Z., Chen, S., Hoogenboezem, R. M., Mylona, M. A., et al. (2018). Characterization of endothelial cells associated with hematopoietic niche formation in humans identifies IL-33 as an anabolic factor. *Cell Rep.* 22, 666–678. doi: 10.1016/j.celrep.2017.12.070

Kilari, S., Remadevi, I., Zhao, B., Pan, J., Miao, R., Ramchandran, R., et al. (2013). Endothelial cell-specific chemotaxis receptor (ECSCR) enhances vascular endothelial growth factor (VEGF) receptor-2/kinase insert domain receptor (KDR) activation and promotes proteolysis of internalized KDR. *J Biol Chem.* 288, 10265–10274. doi: 10.1074/jbc.M112.413542

Kolter, J., Kierdorf, K., and Henneke, P. (2020). Origin and Differentiation of Nerve-Associated Macrophages. *J Immunol.* 204, 271–279. doi: 10.4049/jimmunol.1901077

Kucenas, S. (2015). Perineurial glia. *Cold Spring Harb Perspect Biol.* 7:a020511. doi: 10.1101/cshperspect.a020511

Lindborg, J. A., Mack, M., and Zigmond, R. E. (2017). Neutrophils are critical for myelin removal in a peripheral nerve injury model of wallerian degeneration. *J. Neurosci.* 37, 10258–10277. doi: 10.1523/JNEUROSCI.2085-17.2017

Mallon, B. S., Shick, H. E., Kidd, G. J., and Macklin, W. B. (2002). Proteolipid promoter activity distinguishes two populations of NG2-positive cells throughout neonatal cortical development. *J Neurosci.* 22, 876–885. doi: 10.1523/JNEUROSCI.22-03-00876.2002

Maxson, J. E., and Tyner, J. W. (2017). Genomics of chronic neutrophilic leukemia. *Blood* 129, 715–722. doi: 10.1182/blood-2016-10-695981

Min, Q., Parkinson, D. B., and Dun, X. P. (2020). Migrating Schwann cells direct axon regeneration within the peripheral nerve bridge. *Glia*. 69, 235–254. doi: 10.1002/glia.23892

Nichol, D., and Stuhlmann, H. (2012). EGFL7: a unique angiogenic signaling factor in vascular development and disease. *Blood* 119, 1345–1352. doi: 10.1182/blood-2011-10-322446

Norrmen, C., Figlia, G., Pfistner, P., Pereira, J. A., Bachofner, S., and Suter, U. (2018). mTORC1 is transiently reactivated in injured nerves to promote c-jun elevation and schwann cell dedifferentiation. *J. Neurosci.* 38, 4811–4828. doi: 10.1523/JNEUROSCI.3619-17.2018

Nwani, N. G., Deguiz, M. L., Jimenez, B., Vinokour, E., Dubrovskyi, O., Ugolkov, A., et al. (2016). Melanoma cells block PEDF production in fibroblasts to induce the tumor-promoting phenotype of cancer-associated fibroblasts. *Cancer Res.* 76, 2265–2276. doi: 10.1158/0008-5472.CAN-15-2468

Osawa, T., and Ide, C. (1986). Changes in thickness of collagen fibrils in the endo- and epineurium of the mouse sciatic nerve during development. *Acta Anat. (Basel).* 125, 245–251. doi: 10.1159/000146171

Parrinello, S., Napoli, I., Ribeiro, S., Wingfield Digby, P., Fedorova, M., Parkinson, D. B., et al. (2010). EphB signaling directs peripheral nerve regeneration through Sox2-dependent Schwann cell sorting. *Cell.*- 143, 145–155. doi: 10.1016/j.cell.2010.08.039

Perkins, N. M., and Tracey, D. J. (2000). Hyperalgesia due to nerve injury: role of neutrophils. *Neuroscience* 101, 745–757. doi: 10.1016/s0306-4522(00)00396-1

Pina-Oviedo, S., and Ortiz-Hidalgo, C. (2008). The normal and neoplastic perineurium: a review. *Adv. Anat. Pathol.* 15, 147–164. doi: 10.1097/PAP.0b013e31816f8519

Renthal, W., Tochitsky, I., Yang, L., Cheng, Y. C., Li, E., Kawaguchi, R., et al. (2020). Transcriptional reprogramming of distinct peripheral sensory neuron subtypes after axonal injury. *Neuron*. 108, 128–144. doi: 10.1016/j.neuron.2020.07.026

Schmidt, M., Paes, K., De Maziere, A., Smyczek, T., Yang, S., Gray, A., et al. (2007). EGFL7 regulates the collective migration of endothelial cells by restricting their spatial distribution. *Development* 134, 2913–2923. doi: 10.1242/dev.002576

Schroder, J. M., May, R., and Weis, J. (1993). Perineurial cells are the first to traverse gaps of peripheral nerves in silicone tubes. *Clin. Neurol. Neurosurg.* 95 (Suppl.), S78–83.

Stierli, S., Napoli, I., White, I. J., Cattin, A. L., Cabrejos, A. M., Calavia, N. G., et al. (2018). The regulation of the homeostasis and regeneration of peripheral nerve is distinct from the CNS and independent of a stem cell population. *Development*. 145:dev170316. doi: 10.1242/dev.170316

Stratton, J. A., Holmes, A., Rosin, N. L., Sinha, S., Vohra, M., Burma, N. E., et al. (2018). Macrophages regulate schwann cell maturation after nerve injury. *Cell Rep.* 24, 2561–2572 e2566. doi: 10.1016/j.celrep.2018.08.004

Strauss, M., and Cohen, C. (1981). Perineurial invasion of the facial nerve: a case report with extension from cutaneous squamous cell carcinoma. *Otolaryngol Head Neck Surg.* 89, 831–835. doi: 10.1177/019459988108900526

Theaker, J. M., and Fletcher, C. D. (1989). Epithelial membrane antigen expression by the perineurial cell: further studies of peripheral nerve lesions. *Histopathology* 14, 581–592.

Tikoo, R., Zanazzi, G., Shiffman, D., Salzer, J., and Chao, M. V. (2000). Cell cycle control of Schwann cell proliferation: role of cyclin-dependent kinase-2. *J. Neurosci.* 20, 4627–4634. doi: 10.1523/JNEUROSCI.20-12-04627.2000

Toma, J. S., Karamboulas, K., Carr, M. J., Kolaj, A., Yuzwa, S. A., Mahmud, N., et al. (2020). Peripheral nerve single-cell analysis identifies mesenchymal ligands that promote axonal growth. *eNeuro* 7. doi: 10.1523/ENEURO.0066-20.2020

Tomlinson, J. E., Zygelyte, E., Grenier, J. K., Edwards, M. G., and Cheetham, J. (2018). Temporal changes in macrophage phenotype after peripheral nerve injury. *J. Neuroinfl.* 15, 185. doi: 10.1186/s12974-018-1219-0

Valenzi, E., Bulik, M., Tabib, T., Morse, C., Sembrat, J., Trejo Bittar, H., et al. (2019). Single-cell analysis reveals fibroblast heterogeneity and myofibroblasts in systemic sclerosis-associated interstitial lung disease. *Ann. Rheum. Dis.* 78, 1379–1387. doi: 10.1136/annrheumdis-2018-214865

Verma, A., Bhattacharya, R., Remadevi, I., Li, K., Pramanik, K., Samant, G. V., et al. (2010). Endothelial cell-specific chemotaxis receptor (ecscr) promotes angioblast migration during vasculogenesis and enhances VEGF

receptor sensitivity. *Blood* 115, 4614–4622. doi: 10.1182/blood-2009-10-248856

Wang, X., Abraham, S., McKenzie, J. A. G., Jeffs, N., Swire, M., Tripathi, V. B., et al. (2013). LRG1 promotes angiogenesis by modulating endothelial TGF-beta signalling. *Nature* 499, 306–311. doi: 10.1038/nature12345

Weis, J., May, R., and Schroder, J. M. (1994). Fine structural and immunohistochemical identification of perineurial cells connecting proximal and distal stumps of transected peripheral nerves at early stages of regeneration in silicone tubes. *Acta Neuropathol.* 88, 159–165.

Wolbert, J., Li, X., Heming, M., Mausberg, A. K., Akkermann, D., Frydrychowicz, C., et al. (2020). Redefining the heterogeneity of peripheral nerve cells in health and autoimmunity. *Proc. Natl. Acad. Sci. U.S.A.* 117, 9466–9476. doi: 10.1073/pnas.1912139117

Xie, X., Shi, Q., Wu, P., Zhang, X., Kambara, H., Su, J., et al. (2020). Single-cell transcriptome profiling reveals neutrophil heterogeneity in homeostasis and infection. *Nat. Immunol.* 21, 1119–1133. doi: 10.1038/s41590-020-0736-z

Ydens, E., Amann, L., Asselbergh, B., Scott, C. L., Martens, L., Sichien, D., et al. (2020). Profiling peripheral nerve macrophages reveals two macrophage subsets with distinct localization, transcriptome and response to injury. *Nat. Neurosci.* 23, 676–689. doi: 10.1038/s41593-020-0618-6

Zhao, Q., Eichten, A., Parveen, A., Adler, C., Huang, Y., Wang, W., et al. (2018). Single-cell transcriptome analyses reveal endothelial cell heterogeneity in tumors and changes following antiangiogenic treatment. *Cancer Res.* 78, 2370–2382. doi: 10.1158/0008-5472.CAN-17-2728

Zigmond, R. E., and Echevarria, F. D. (2019). Macrophage biology in the peripheral nervous system after injury. *Prog. Neurobiol.* 173, 102–121. doi: 10.1016/j.pneurobio.2018.12.001

Conflict of Interest: The authors declare that the research was conducted in the absence of any commercial or financial relationships that could be construed as a potential conflict of interest.

frontiers in Cellular Neuroscience

ORIGINAL RESEARCH
published: 14 April 2021
doi: 10.3389/fncel.2021.648570

Single-Cell Multiomic Approaches Reveal Diverse Labeling of the Nervous System by Common Cre-Drivers

Rachel A. Keuls[1,2,3,4] *and Ronald J. Parchem*[1,2,3,4]*

[1]*Development, Disease Models & Therapeutics Graduate Program, Baylor College of Medicine, Houston, TX, United States,* [2]*Center for Cell and Gene Therapy, Stem Cells and Regenerative Medicine Center, Baylor College of Medicine, Houston, TX, United States,* [3]*Department of Molecular and Cellular Biology, Baylor College of Medicine, Houston, TX, United States,* [4]*Department of Neuroscience, Baylor College of Medicine, Houston, TX, United States*

Neural crest development involves a series of dynamic, carefully coordinated events that result in human disease when not properly orchestrated. Cranial neural crest cells acquire unique multipotent developmental potential upon specification to generate a broad variety of cell types. Studies of early mammalian neural crest and nervous system development often use the Cre-loxP system to lineage trace and mark cells for further investigation. Here, we carefully profile the activity of two common neural crest Cre-drivers at the end of neurulation in mice. RNA sequencing of labeled cells at E9.5 reveals that Wnt1-Cre2 marks cells with neuronal characteristics consistent with neuroepithelial expression, whereas Sox10-Cre predominantly labels the migratory neural crest. We used single-cell mRNA and single-cell ATAC sequencing to profile the expression of *Wnt1* and *Sox10* and identify transcription factors that may regulate the expression of Wnt1-Cre2 in the neuroepithelium and Sox10-Cre in the migratory neural crest. Our data identify cellular heterogeneity during cranial neural crest development and identify specific populations labeled by two Cre-drivers in the developing nervous system.

Keywords: single-cell mRNA sequencing, single-cell ATAC sequencing, cranial neural crest, neural tube, Wnt1-Cre2, Sox10-Cre, cell diversity

OPEN ACCESS

Edited by:
Jiangteng Lu,
Shanghai Jiao Tong University, China

Reviewed by:
Ying Zhu,
Fudan University, China
Zhiyong Liu,
Chinese Academy of Sciences (CAS), China

***Correspondence:**
Ronald J. Parchem
ronald.parchem@bcm.edu

Specialty section:
This article was submitted to Cellular Neurophysiology, a section of the journal Frontiers in Cellular Neuroscience

Received: *31 December 2020*
Accepted: *15 March 2021*
Published: *14 April 2021*

Citation:
Keuls RA and Parchem RJ (2021) Single-Cell Multiomic Approaches Reveal Diverse Labeling of the Nervous System by Common Cre-Drivers. Front. Cell. Neurosci. 15:648570. doi: 10.3389/fncel.2021.648570

INTRODUCTION

Neural crest cells are a unique population of multipotent progenitors that have the developmental potential to give rise to a variety of diverse cell types, including peripheral neurons, glia, cranial bone and cartilage, and melanocytes. Neural crest cells arise during a very dynamic stage of early development at the end of gastrulation, beginning with neural plate border formation, followed by the specification of neural crest progenitors, epithelial-to-mesenchymal transition (EMT), migration, and finally, terminal differentiation. The dynamic developmental trajectory of the neural crest has contributed to the difficulty of studying these cells *in vivo*.

Early studies in chicken, frog, and fish uncovered key gene regulatory networks (GRNs) and core transcription factor families important for the sequential stages of neural crest development. Several transcription factor families are conserved among neural crest specification genes, such as *Pax3/7*, *AP2*, and *SoxE* factors (e.g., *Sox9* and *Sox10*). Mutations in these factors cause severe, life-threatening disorders that usually manifest in infants and young children, such as neuroblastoma (Pasterls et al., 1993; Shakhova et al., 2012; Shirley et al., 2012; Weiss et al., 2012), skeletal dysplasia (campomelic dysplasia), and abnormalities of the jaw and palate, which compromise the airways at birth (Houston et al., 1983; Shinwell et al., 1988; Kwok et al., 1995; Mansour et al., 1995; Sock et al., 2003; Herman and Siegel, 2012).

Despite the severe phenotypes that are characteristic of neural crest-related defects, far less is known about mammalian neural crest development compared to the avian, fish, and amphibian models used in the foundational studies that constitute much of the current knowledge of neural crest development. The extent to which mechanisms uncovered using the classical models translate to mammalian models is unclear. Indeed, the neural crest-specific ablation of factors identified in other animal models as being critical for EMT did not affect the early stages of mouse neural crest development (Brault et al., 2001; Hari et al., 2002; Jia et al., 2007; Büchmann-Møller et al., 2009). It is not clear whether this failure to identify genes critical to early neural crest development reflects true species-specific differences or technical limitations of the available tools to study neural crest (Barriga et al., 2015).

Two of the most commonly used Cre-drivers for neural crest studies are Wnt1-Cre (Danielian et al., 1998; Lewis et al., 2013) and Sox10-Cre (Stine et al., 2009). The utility of Sox10-Cre is that it has a high specificity for labeling migratory neural crest cells and neural crest-derived structures. The Sox10-Cre transgenic mouse strain, designated as the S4F:Cre mouse, contains a *Sox10* distal enhancer MCS4 and a *c-Fos* minimal promoter followed by the Cre-recombinase coding sequence. At E9.5, Sox10-Cre induced recombination in the migratory neural crest, the otic placode, and the dorsal root ganglia of the pharyngeal arches, with little evidence of recombination in the dorsal neural tube (Stine et al., 2009). While the specificity to migratory neural crest is a great advantage to this Cre-driver, one drawback is that Sox10-Cre cannot be used for studies of the premigratory neural crest.

Wnt1-Cre is a well-established Cre-driver with over 50 citations that are frequently used to study multiple aspects of early brain and premigratory neural crest development in mice (Danielian et al., 1998; The Jackson Laboratory, 2020). The Wnt1-Cre transgene contains a Wnt1 promoter followed by the Cre-recombinase coding region, the Wnt1 coding region, and the 3' Wnt1 enhancer. This transgenic mouse line is accepted as a robust way to label approximately 96% of neural crest cells, including both premigratory and migratory cells (Hari et al., 2012). However, Wnt1-Cre has been reported to be expressed in cell types other than the neural crest, including cells of the midbrain, which results in ectopic activation of Wnt signaling and disrupted midbrain development. This led to the development of the Wnt1-Cre2 transgene, which labels neural crest similarly to the first version of Wnt1-Cre (Lewis et al., 2013) without ectopic activation of Wnt signaling. The Wnt1-Cre2 transgene consists of the Wnt1 promoter region followed by the Cre-recombinase coding region and the 3' Wnt1 enhancer. Thus, Wnt1-Cre2 lacks the coding sequence for Wnt1 to avoid ectopic activation of Wnt signaling. However, the recombination achieved with Wnt1-Cre2 has not been thoroughly investigated using single-cell transcriptomic approaches and the importance to do so increases as more studies use Wnt1-Cre2 to harvest early neural crest cells (Lumb et al., 2017; Soldatov et al., 2019).

In the present study, we carefully profile the recombination of the ROSA26$^{Tomato/+}$ Cre-reporter (Ai9; Luche et al., 2007) achieved *in vivo* with both Wnt1-Cre2 (Lewis et al., 2013) and Sox10-Cre (Stine et al., 2009) in the cranial region of mouse embryos at E9.5. In addition to efficient labeling of neural crest, we reveal expression of both Wnt1-Cre2 and Sox10-Cre in other cell types and therefore identify differences in the transcriptomes of cells harvested using either Cre. To study endogenous expression, we used single-cell transcriptomics to demonstrate that *Wnt1* and *Sox10* are expressed in different subpopulations of the neural crest at E9.5. Furthermore, we use single-cell ATAC sequencing to analyze chromatin structure and identify accessible motifs containing predicted binding sites for transcription factors, which may regulate the expression of *Wnt1* and *Sox10* in the neural tube and neural crest. Our combined *in vivo* and multiomics approach reveals the coordination of gene expression and chromatin accessibility contributing to the cellular diversity of early central and peripheral nervous system development.

MATERIALS AND METHODS

Immunofluorescence

Mouse embryos were dissected in phosphate-buffered saline, pH 7.4 (PBS), fixed in 3.7% formaldehyde overnight at 4°C, and washed in PBS containing 0.1% Triton (PT). Embryos were stored at −30°C in methanol and were rehydrated at the time of use in PT. Embryos were cryopreserved using a sucrose gradient of 10%, 20% then 30% w/v sucrose in PT, followed by 1:1 30% sucrose:OCT Compound (Fisher Scientific 23730571) and 100% OCT. Embryos were flash-frozen in OCT for cryosectioning using dry ice and 100% ethanol bath and were stored at −80°C until sectioning. Cryo-sectioning was performed at 10 um and slides were stored at −80°C until staining. Sections on slides were washed with PT and blocking was performed at room temperature for 1 h in 5% Gibco normal goat serum (16210064) and 1% bovine serum albumin (Fisher Scientific BP1600100). Primary antibodies were diluted in blocking solution and applied to tissue overnight at 4°C [Sox9 (EMD Millipore AB5535; 1:1,000) Pax3 (DSHB PAX3; 1:100)]. Secondary antibodies (AlexaFluor) diluted in blocking buffer (1:500) were applied for 1.5 h at room temperature. Sections were mounted with Fluoromount G (Fisher Scientific OB10001). Images of the cross-sections were taken on Zeiss LSM780 or LSM 980. Wholemount embryos were imaged on

Leica M165FC dissecting microscope with a Leica DFC 3000G camera or Zeiss LSM780.

Embryo Dissociation and Cell Sorting

Wnt1-Cre2 (Lewis et al., 2013) or Sox10-Cre (Stine et al., 2009) mice were crossed with ROSA26$^{Tomato/+}$ mice (Luche et al., 2007) to lineage trace neural crest cells at E9.5. Mouse embryos were decapitated anterior to the otic placode. The cranial region was enzymatically dissociated with papain at room temperature combined with gentle pipetting until a single-cell suspension was achieved. An equal volume of FBS was used to quench the enzyme. The single-cell suspension was filtered, spun at 300 g for 5 min, and resuspended in PBS with 1% BSA. Samples were filtered and fluorescent cells were sorted on a BD FACSAria III instrument with a 70-μm nozzle into a 1.5 ml Eppendorf tube that contained Trizol-LS (Thermo Fisher Scientific, 10296028).

Bulk RNA Isolation, Library Preparation, and Sequencing

Total RNA was extracted from cells using RNeasy Micro Kit (QIAGEN 74004). For mRNA sequencing cDNA synthesis was performed using SMART-Seq Ultra Low Input RNA Kit for Sequencing (Takara 634889) from approximately 500 pg of total RNA. cDNA was validated using the High Sensitivity NGS Fragment Analysis Kit (Agilent formerly AATI DNF-474-0500) on a 12-Capillary Fragment Analyzer. Quantification was determined using the Quant-iT dsDNA Assay Kit, high sensitivity (Thermo Fisher Q33120), and 100 pg of cDNA was tagmented and ligated using the Nextera XT DNA Library Kit (Illumina FC-131-1024) at $\frac{1}{2}$ volumes to produce sequencing libraries. The resulting libraries were validated using the High Sensitivity NGS Fragment Analysis Kit on a 12-Capillary Fragment Analyzer and quantified using the Quant-iT dsDNA Assay Kit, high sensitivity. Equal concentrations of libraries were pooled, denatured, diluted, and subjected to paired-end sequencing using the Mid Output v2.5 kit (Illumina FC-404-2001) on a NextSeq550 following the manufacturer's instructions.

Bulk RNA-Sequencing Bioinformatic Analysis

Sequencing files from each flow cell lane were downloaded and the resulting FASTQ files were merged. Quality control was performed using fastQC (v0.10.1). Reads were mapped to the mouse genome mm10 assembly using STAR (v2.5.0a). In R (v3.5.2), gene count matrices were built with Bioconductor packages Rsamtools (v2.0.0) and GenomicFeatures (v1.32.2). mRNA-sequencing datasets were annotated with UCSC transcripts downloaded from Illumina iGenomes in GTF file format. We determined reads per million (RPM) using GenomicAlignments (v1.16.0). Principal component analysis (PCA) was performed using an rlog transformed gene expression matrix of global gene expression >1 for each region. DESeq2 (v1.20.0) was used for differential gene expression analysis and read count normalization. Expression heat maps were generated using ComplexHeatmap (v2.0.0). Biological Process GO analyses were determined using Enrichr and visualized using ggplot.

Single-Cell Sample Preparation and Bioinformatic Analysis

Wildtype mouse embryos were decapitated at the otic placode and the cranial region was enzymatically dissociated with papain at room temperature combined with gentle pipetting until a single-cell suspension was achieved. At which time the dissociation was quenched with an equal volume of FBS. The single-cell suspension was filtered (Falcon 352235), spun at 300 g for 5 min, and resuspended in DMEM with 10% FBS. For single-cell ATAC sequencing, nuclei were isolated by resuspending cell pellet in lysis buffer (10 mM Tris-Cl pH 7.4, 10 mM NaCl, 3 mM $MgCl_2$, 0.1% Tween-20, 0.01% Nonidet P40, 0.01% Digitonin, 1% BSA). Lysis was diluted with wash buffer (10 mM Tris-Cl pH 7.4, 10 mM NaCl, 3 mM $MgCl_2$, 0.1% Tween-20, 1% BSA, 0.1% Tween-20) and nuclei were pelleted by spinning at 500 g for 5 min. Nuclei were then washed, pelleted, and resuspended in nuclei buffer (10× Genomics 2000153). Nuclei count and quality were assessed on a hemocytometer using 0.4% Trypan blue to stain nuclei. GEM generation was performed on a 10× Chromium Controller Instrument on Chromium Next GEM Chip G for mRNA (10× Genomics 1000120) and Next GEM Chromium Chip H for ATAC (10× Genomics 1000161). Libraries were subsequently prepped using Chromium Next GEM Single Cell 3' Library Kit v3.1 for mRNA (10× Genomics 1000158) and Chromium Next GEM Single Cell ATAC Library Kit v1.1 for ATAC (10× Genomics 1000163). Chromium Single Index Kit T Set A (10× Genomics 1000213) was used to index mRNA libraries and i7 Multiplex Kit N Set A (10× Genomics 1000084) was used to index ATAC libraries. Libraries were validated using the High Sensitivity NGS Fragment Analysis Kit on a 12-Capillary Fragment Analyzer and quantified using the Quant-iT dsDNA Assay Kit, high sensitivity. Equal concentrations of libraries were pooled, denatured, diluted, and subjected to paired-end sequencing using the Mid Output v2.5 kit (Illumina FC-404-2001) on a NextSeq550 following the manufacturer's instructions. At E9.5 16,949, cells were sequenced from a C57BL/6 wildtype mouse embryo (128, 243, 041 reads; an average of 7,566 reads per cell). Single-cell mRNA Raw bcl files were downloaded using Illumina's BaseSpaceCLI version 0.10.7 and were converted to fastq files using 10× Genomics Cell Ranger mkfastq and were aligned to the mm10 genome using 10× Genomics Cell Ranger count. Data were subsequently log normalized and clustered using five statistically significant principal components in Seurat version 3.1.5 (Butler et al., 2018). Mitochondrial genes and cells with <200 UMI and >2,500 UMIs were filtered out. Cell populations were identified for single-cell mRNA data as in previous studies (Pijuan-Sala et al., 2019) and cell markers are provided in **Supplementary Table 1**. Single-cell ATAC raw bcl files were downloaded using Illumina's BaseSpaceCLI version 0.10.7 and were converted to fastq files using 10× Genomics Cell Ranger ATAC mkfastq (version 1.1.0) and were aligned to the mm10 genome using 10× Genomics Cell Ranger ATAC count. Peaks were unified, quantified, and visualized in Seurat and Signac (version 0.2). Single-cell

ATAC data was overlayed with cell populations from annotated single-cell mRNA similar to previous studies (Stuart et al., 2019, 2020 preprint and motifs were called within 2 kb of the loci of interest by Homer. Enrichr was used for gene ontology analyses.

RNAScope

RNAScope was performed using the Multiplex Fluorescent Reagent Kit v2 (ACD Bio 323100). Embryos were dissected, fixed, cryopreserved, and cryosectioned as above. Slides were stored at −80°C until use and were brought to room temperature. Tissue sections were re-fixed for 15 min at room temperature and subsequently dehydrated in 50% ethanol, followed by 70% and 100% ethanol. Hydrogen peroxide was applied to tissue sections for 10 min at room temperature and antigen retrieval was performed for 5 min at >99°C in a Black and Decker HS800 steamer. Sections were subsequently washed in distilled water, dehydrated in 100% ethanol, dried at room temperature, and subsequently treated with RNAScope Protease III for 30 min at 40°C. Mm-Wnt1-C2 RNAScope 2.5 LS Probe (ACD Bio 4011098-C2) was diluted 1:10 with Mm-Sox10 RNAScope 2.5 LS Probe (ACD Bio 435938) and the probe mixture was hybridized at 40°C for 2 h. Signal was amplified with RNAScope Multiplex FL v2 AMP1-3 for 30 min each at 40°C. Sox10 signal was developed by incubating tissue sections for 15 min at 40°C in RNAScope Multiplex FL v2 hP-C1 and Opal 570 [Perkin Elmer FP1488A (diluted 1:2,000 in TSA buffer)] was applied for 30 min at 40°C. HRP blocker was applied for 15 min at 40°C and Wnt1 signal was subsequently developed by incubating tissue sections for 15 min at 40°C in RNAScope Multiplex FL v2 hP-C2 and Opal 690 [Perkin Elmer FP1497A (diluted 1:500 in TSA buffer)] was applied for 30 min at 40°C. Images were taken on a Zeiss LSM 980.

Animal Work

All research and animal care procedures were approved by the Baylor College of Medicine Institutional Animal Care and Use Committee and housed in the Association for Assessment and Accreditation of Laboratory Animal Care-approved animal facility at Baylor College of Medicine. All strains were maintained on the C57BL/6 background. Adult genotyping was performed by lysing 1–2 mm ear clippings in 75 μl 25 mM NaOH 0.2 mM EDTA at 98°C for 1 h and neutralized with 75 μl 40 mM Tris-Cl, pH 5.5. Embryo genotyping was performed by digesting yolk sac tissue overnight in lysis buffer [50 mM Tris-HCl (pH 8.0), 10 mM EDTA, 100 mM NaCl, 0.1% SDS, and 5 mg/ml proteinase K]. Cell debris was removed and an equal amount of isopropanol was used to precipitate DNA at −30°C for 1 h. DNA was pelleted by a 30 min centrifugation, washed with 70% ethanol, and resuspended in water. PCR for all alleles was performed using 40 cycles 95 °C for 20 s and touch-down annealing at 64°C, 62°C, 60°C, 58°C, followed by 40 s extension at 72°C. All PCR primers and expected band sizes are in **Table 1**.

RESULTS

Wnt1-Cre2 and Sox10-Cre Label the Neural Crest and the Neural Tube

To compare the expression of the most common Cre-drivers used to label neural crest, we crossed both Wnt1-Cre2 (Lewis et al., 2013) and Sox10-Cre (Stine et al., 2009) with ROSA26$^{Tomato/+}$ [Gt(ROSA)26Sor$^{tm9(CAG-tdTomato)Hz}$; Luche et al., 2007] and harvested embryos at E9.5, the time at which neural crest cells are delaminating and migrating into cranial structures such as the frontonasal process and pharyngeal arches (**Supplementary Figure 1A**). Analysis of wholemount embryos revealed that recombination from Wnt1-Cre2 was more widespread throughout the neural tube as compared to Sox10-Cre, which was largely localized to the neural crest in the frontonasal process and pharyngeal arches (**Figures 1A,B**, **Supplementary Figure 1A**).

To more carefully analyze and compare the cell populations labeled from each Cre-driver, we used immunofluorescence (IF) for the neural crest marker SOX9 in transverse cross-sections of the cranial region in E9.5 embryos labeled with Sox10-Cre or Wnt1-Cre2. Recombination with Sox10-Cre resulted in robust neural crest labeling (**Figure 1A**). Interestingly, we found Tomato-positive cells scattered within the anterior neural tube and to a lesser extent in more posterior sections, where the labeled cells were more restricted to the ventral neuroepithelium (**Figure 1A**). Labeling with Wnt1-Cre2 revealed nearly ubiquitous Tomato expression within SOX9-positive neural crest as well as throughout the neuroepithelium just anterior to the mid/hindbrain boundary including a low level of scattered labeling within the neuroepithelium of the forebrain (**Figure 1B**). When we analyzed the co-localization of the SOX9-positive neural crest, we found that both Cre-drivers labeled greater than 90% of SOX9-positive cells in each section (**Figure 1C**). We found that 50–60% of the non-neural ectoderm within each section was Tomato-positive using Wnt1-Cre2 whereas less than 20% of the non-neural ectoderm per section was Tomato-positive using Sox10-Cre, consistent with a lateral

TABLE 1 | PCR primers and expected band sizes.

Genotyping primer	Sequence	Expected band sizes
Tomato forward	CACTTGCTCTCCCAAAGTCG	550 bp wildtype and 300 bp mutant
Wildtype reverse	TAGTCTAACTCGCGACACTG	
Tomato reverse	GTTATGTAACGCGGAACTCC	
Cre 26	CCT GGA AAA TGC TTC TGT CCG	300 bp Gabra control and 400 bp Cre
Cre 36	CAG GGT GTT ATA AGC AAT CCC	
Gabra 12	CAA TGG TAG GCT CAC TCT GGG AGA TGA TA	
Gabra 70	AAC ACA CAC TGG CAG GAC TGG CTA GG	

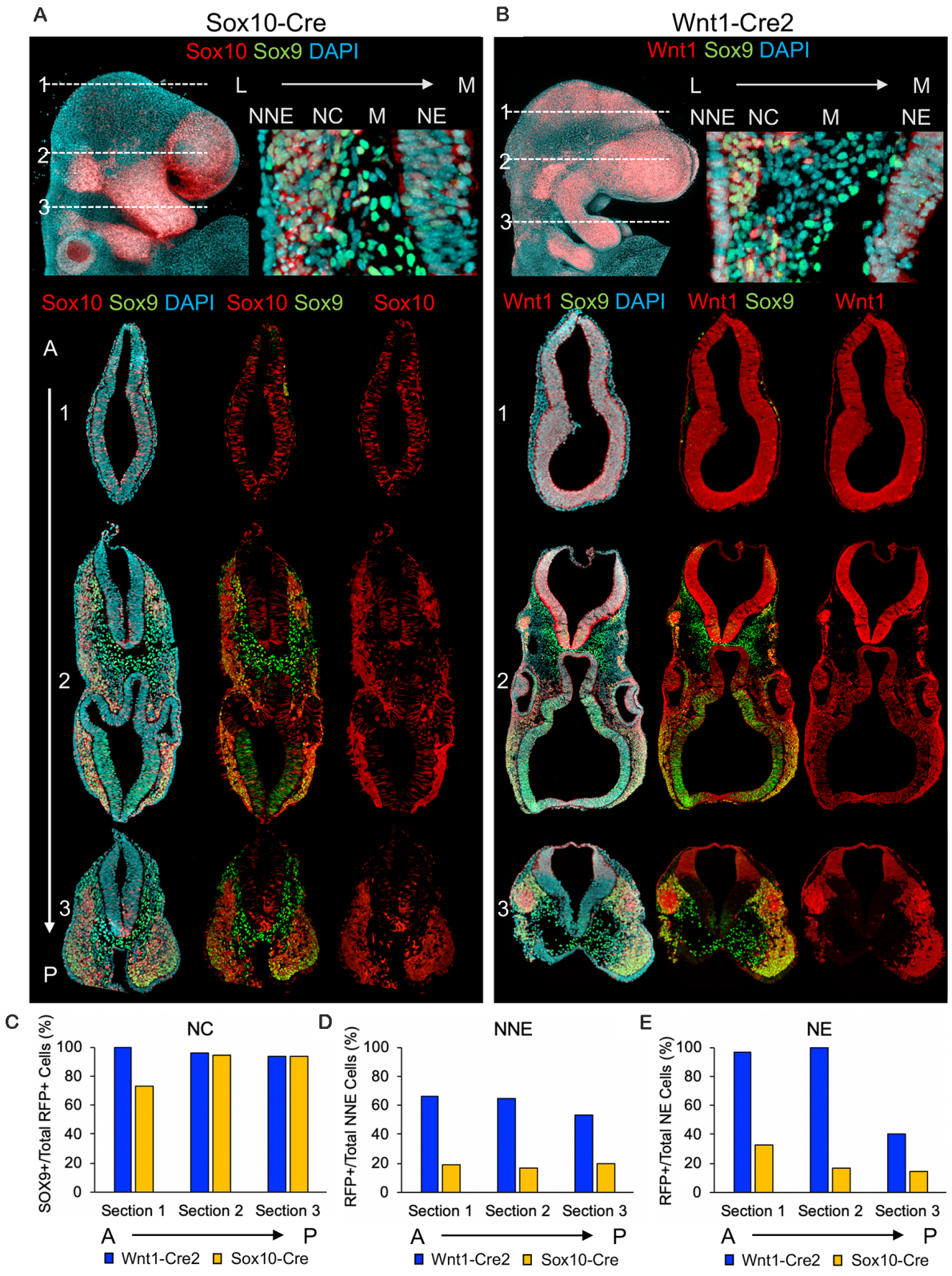

FIGURE 1 | Wnt1-Cre2 and Sox10-Cre label neural crest and cells of the neural tube. **(A)** Wholemount and sequential transverse cross-sections of embryos in which ROSA26$^{Tomato/+}$ embryos were recombined using Sox10-Cre and **(B)** Wnt1-Cre. Axial positions of transverse cross-sections are noted for each Cre-driver. **(C)** Quantification of neural crest, **(D)** non-neural ectoderm and **(E)** neuroepithelial labeling obtained from Sox10-Cre and Wnt1-Cre.

source of Wnt signaling during neural plate border formation (**Figure 1D**). In each section, Wnt1-Cre2 labeled 100% of neuroepithelial cells anterior to the mid/hindbrain boundary while Sox10-Cre labeled less than 30% of neural tube cells in each section (**Figure 1E**).

Although recombination by Wnt1-Cre2 in the neuroepithelium allows for the labeling of premigratory neural crest, it also limits the ability to isolate a pure population of neural crest cells. This also applies to studies using Wnt1-Cre2 to delete a gene of interest within the neural crest, as the use of Wnt1-Cre2 would cause deletion in the mid-and hindbrain region. These results are in agreement with previous findings that Wnt1-Cre2 labels cell types other than neural crest. For example, recombination has been observed in the pharyngeal arch and frontonasal process epithelial cells (Lewis et al., 2013). Analysis of wholemount embryos from Lewis et al. (2013) also suggests recombination in neuroepithelial cells anterior to the mid/hindbrain boundary. Additionally, we observed some scattered recombination driven by Sox10-Cre in the anterior neural tube, suggesting Sox10-Cre also marks cell types other than migratory neural crest.

Cells Harvested Using Wnt1-Cre2 Have a Neuroepithelial Gene Signature Compared to Cells Harvested Using Sox10-Cre

To identify changes in gene expression that may result from the differential labeling of cells between Wnt1-Cre2 and Sox10-Cre, we crossed both Wnt1-Cre2 and Sox10-Cre with ROSA26$^{Tomato/+}$. Tomato-positive cells were isolated from the cranial region using fluorescence-activated cell sorting (FACS), and we analyzed their transcriptomes using mRNA sequencing (**Supplementary Figures 2A,B**). A principal component analysis was used to compare samples harvested with each Cre-driver and found that samples clustered together based on the Cre-driver used to harvest them (**Figures 1A,B**). Differential expression analysis was used to compare transcriptomes of cells harvested with Wnt1-Cre2 to cells harvested with Sox10-Cre. We found more upregulated genes as compared to downregulated genes, consistent with a broader labeling when using Wnt1-Cre2 as compared to Sox10-Cre (**Figure 2C**). We predicted that genes upregulated in our comparison were those enriched in Wnt1-Cre2 that confer a more neuroepithelial identity while the downregulated genes are enriched in Sox10-Cre and would provide a more migratory neural crest-like identity. Indeed, gene ontology (GO) analysis of the upregulated genes enriched in cells harvested with Wnt1-Cre2 revealed predicted functions such as neuronal differentiation and planar cell polarity, consistent with neuroepithelial labeling, as these cells will go on to differentiate into neurons of the central nervous system. GO analysis of the downregulated genes revealed predicted function in the positive regulation of cell migration and negative regulation of cell adhesion consistent with a migratory neural crest identity (**Figure 2D**). The expression of neural crest specification genes such as *Sox9*, *Pax3*, and *Ets1* was greater in cells harvested at E9.5 using Sox10-Cre as compared to those harvested using Wnt1-Cre2. Similarly, expression of EMT genes such as *FoxD3*, *Snai2*, and *Sox5* was more enriched in cells harvested at E9.5 using Sox10-Cre. Neuronal genes such as *Atoh1*, *Fgf15*, and *Olig2*, were more highly expressed in cells labeled by Wnt1-Cre2 (**Figure 2E**). These results are consistent with Wnt1-Cre2 broadly labeling cells of the neural tube near the mid-hindbrain boundary while

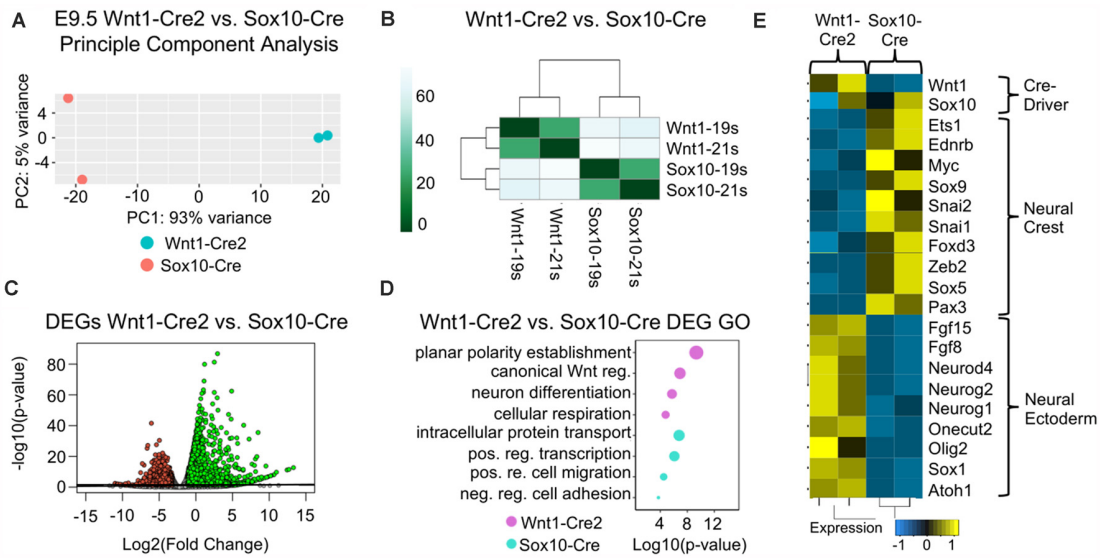

FIGURE 2 | Cells harvested using Wnt1-Cre2 have a neuroepithelial gene signature compared to cells harvested using Sox10-Cre. **(A)** Principal component analysis (PCA) plot and **(B)** heatmap normalized counts per million reads (CPM) showing that samples group together by Cre-driver. **(C)** Volcano plot of the significantly up- and downregulated genes obtained from comparing Wnt1-Cre2 to Sox10-Cre. **(D)** Gene ontology (GO) analysis of the significant differentially expressed genes. Categories were ordered by −log10(*p*-value) and dot size represents −log10(*p*-value). **(E)** Heatmap of normalized CPM values for neural crest and neuronal genes from cells harvested with Wnt1-Cre2 or Sox10-Cre.

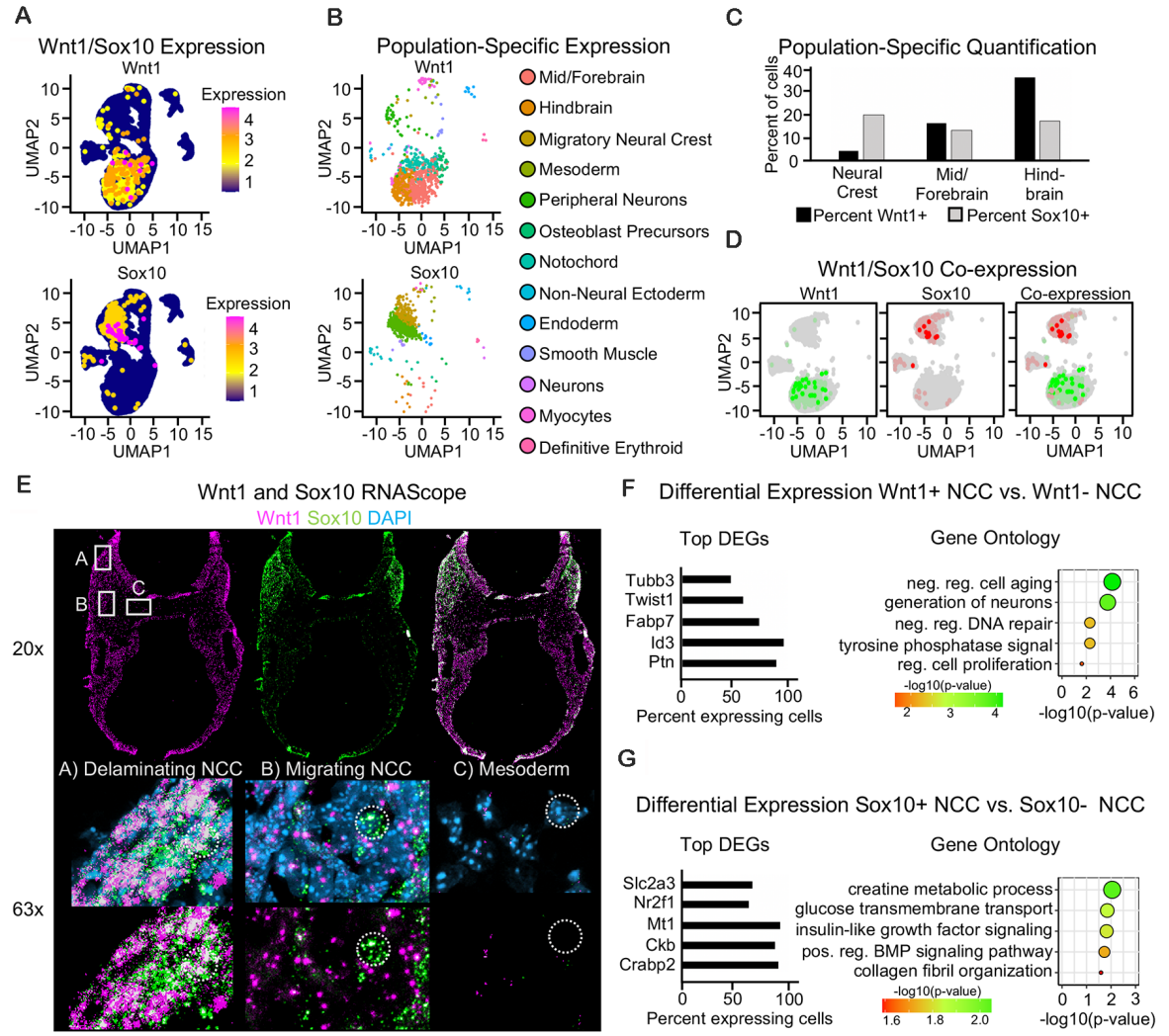

FIGURE 3 | Single-cell sequencing reveals little co-expression of Wnt1 and Sox10 in E9.5 neural crest cells. **(A)** UMAP plot showing expression of *Wnt1* and *Sox10* in cells of the E9.5 cranial region. **(B)** UMAP plot with *Wnt1*- and *Sox10*-expressing cells colored by cell population. **(C)** Bar plot of the percent of cells within the neural tube and neural crest expressing *Wnt1* or *Sox10*. **(D)** Blended UMAP plot showing little co-expression of *Wnt1* and *Sox10*. **(E)** Images of RNAScope for *Sox10* and *Wnt1* in E9.5 transverse cross-section through the cranial region showing co-localization in the delaminating neural crest, minimal co-localization in the migratory neural crest, and minimal expression of both *Wnt1* and *Sox10* in cells of the mesoderm. The location of the 63× image is noted within the 20× image. **(F)** Bar plot of differentially expressed genes and GO analysis of *Wnt1*-positive cells and **(G)** *Sox10*-positive cells. Categories were ordered by −log10(*p*-value) and dot size represents −log10(*p*-value).

the labeling achieved with Sox10-Cre is more restricted to migratory neural crest.

Single-Cell Sequencing Reveals Little Co-expression of Wnt1 and Sox10 in E9.5 Neural Crest Cells

To further interrogate cell populations expressing *Wnt1* and *Sox10*, we used single-cell mRNA sequencing of the cranial region from an E9.5 mouse embryo (**Supplementary Figures 3A–D**). When we mapped the expression of *Wnt1*, we found that the majority of *Wnt1*-positive cells were found in the mid-, fore- and hindbrain (**Figures 3A,B**). The majority of *Sox10*-positive cells were found in migratory neural crest and peripheral neuron populations (**Figures 3A,B**). Indeed, Sox10-Cre has been shown to label the dorsal root ganglia (Stine et al., 2009). Similar to our results from lineage tracing, quantification of the number and percent of cells in each population of the neuroepithelium and the neural crest revealed that *Wnt1* is expressed in more cells of the mid/forebrain and the hindbrain neuroepithelium as compared to *Sox10* at E9.5. Indeed, *Sox10* was expressed in more neural crest cells as compared to *Wnt1* (**Figure 3C**). When we interrogated the co-expression of *Sox10* and *Wnt1* in the neural crest, interestingly, we found very few co-expressing cells (**Figure 3D**). Fluorescent RNAScope for *Wnt1* and *Sox10* confirmed the expression of *Wnt1* in both the neural tube and neural crest

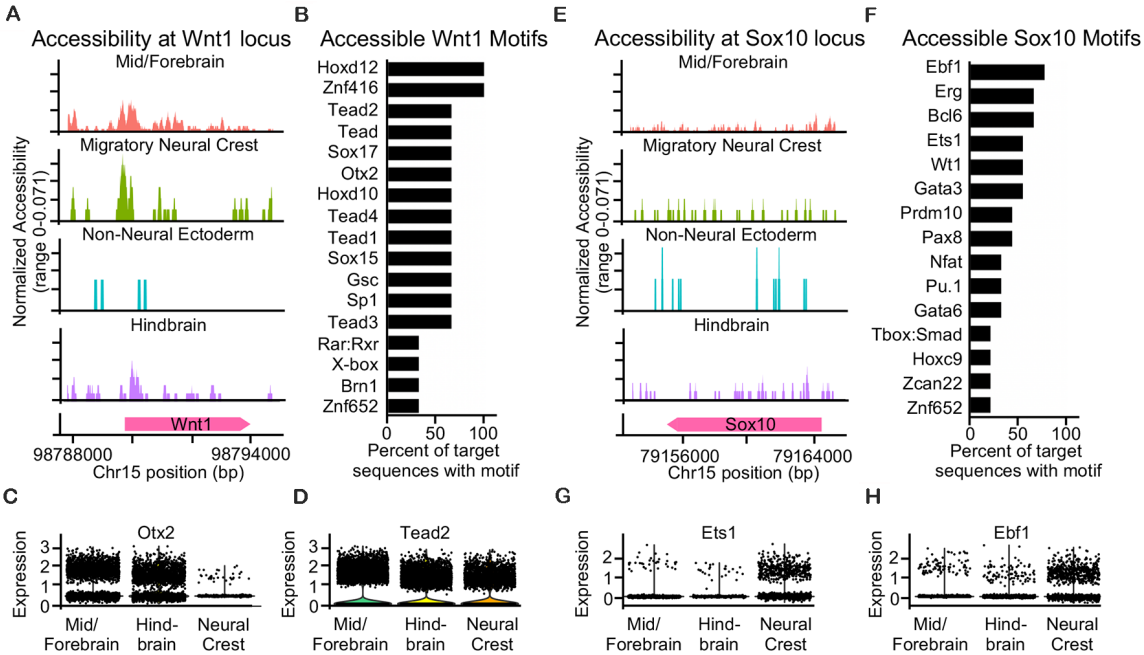

FIGURE 4 | Single-cell ATAC sequencing reveals accessible motifs near Wnt1 in the neuroepithelium and Sox10 in neural crest. **(A)** Coverage plot of accessibility at the *Wnt1* locus in ectoderm-derived cell populations. **(B)** Bar plot of accessible motifs at the *Wnt1* locus. **(C)** Dot plot showing expression of *Otx2* and **(D)** *Tead2* transcription factors with accessible predicted motifs at the *Wnt1* locus. **(E)** Coverage plot of accessibility at the *Sox10* locus in ectoderm-derived cell populations. **(F)** Bar plot of accessible motifs at the *Sox10* locus. **(G)** Dot plot showing expression of *Ets1* and **(H)** *Ebf1* transcription factors with accessible predicted motifs at the *Sox10* locus.

and expression of *Sox10* specifically in the neural crest. Similar to single-cell sequencing, RNAScope similarly revealed minimal co-expression of *Wnt1* and *Sox10*, except in delaminating neural crest cells. Delaminating neural crest immediately adjacent to the neural tube expressed both *Wnt1* and *Sox10* consistent with homogeneity of neural crest undergoing EMT (**Figure 3E**). Differential expression analysis was used to identify the genes enriched in the *Wnt1*-expressing neural crest as compared to the *Sox10*-expressing neural crest and found each population had a unique gene signature (**Figures 3F,G**). Genes enriched in *Wnt1*-positive neural crest were involved in neuron formation, regulation of cell proliferation, and DNA repair regulation (**Figure 3F**). Genes enriched in *Sox10*-positive neural crest were involved in glucose transport, BMP signaling, and collagen fibril organization (**Figure 3G**). Taken together, these findings support a distinct gene signature of *Wnt1*- and *Sox10*-expressing neural crest at E9.5.

Single-Cell ATAC Sequencing Reveals Accessible Motifs Near Wnt1 in the Neuroepithelium and Sox10 in the Neural Crest

Since we found distinct gene signatures of *Wnt1*- and *Sox10*-expressing neural crest and broad labeling of the neuroepithelium when we used Wnt1-Cre2, we performed single-cell ATAC sequencing of the cranial region from an E9.5 mouse embryo to identify and compare accessible transcription factor motifs near the transcriptional start sites at the *Wnt1* and *Sox10* gene loci. We hypothesized that accessible regions of chromatin near the *Wnt1* locus may contain motifs for factors expressed in both the neural tube and neural crest while accessible regions of chromatin near the *Sox10* locus may contain motifs for factors expressed specifically in the migratory neural crest. Chromatin structure around the *Wnt1* locus was largely accessible in cells of the mid/forebrain, possibly contributing to the labeling of the neuroepithelium that we observed with Wnt1-Cre2 (**Figure 4A**). In the migratory neural crest and the hindbrain, chromatin at the *Wnt1* locus is accessible at the transcriptional start site as well as specific regions upstream. Accessible regions upstream of the *Wnt1* locus are similar between the migratory neural crest and the hindbrain which may suggest that these regulatory regions enable the labeling of both the premigratory and migratory neural crest. Chromatin structure around the *Wnt1* locus in cells of the non-neural ectoderm was largely closed. However, we found that some cells of the non-neural ectoderm were labeled when we crossed Wnt1-Cre2 with ROSA26$^{Tomato/+}$. These findings suggest that cells of the non-neural ectoderm may transiently express *Wnt1* earlier in development, possibly during the division of the non-neural, neural, and neural plate border domains of the epithelium (**Figure 4A**). Motifs present in the accessible regions near the *Wnt1* locus included *Hoxd12*, *Tead2*, *Sox17*, *Znf416*, and *Otx2* (**Figure 4B**, **Supplementary Figure 4A**). Of these transcription factors, we found that *Tead2* was robustly expressed

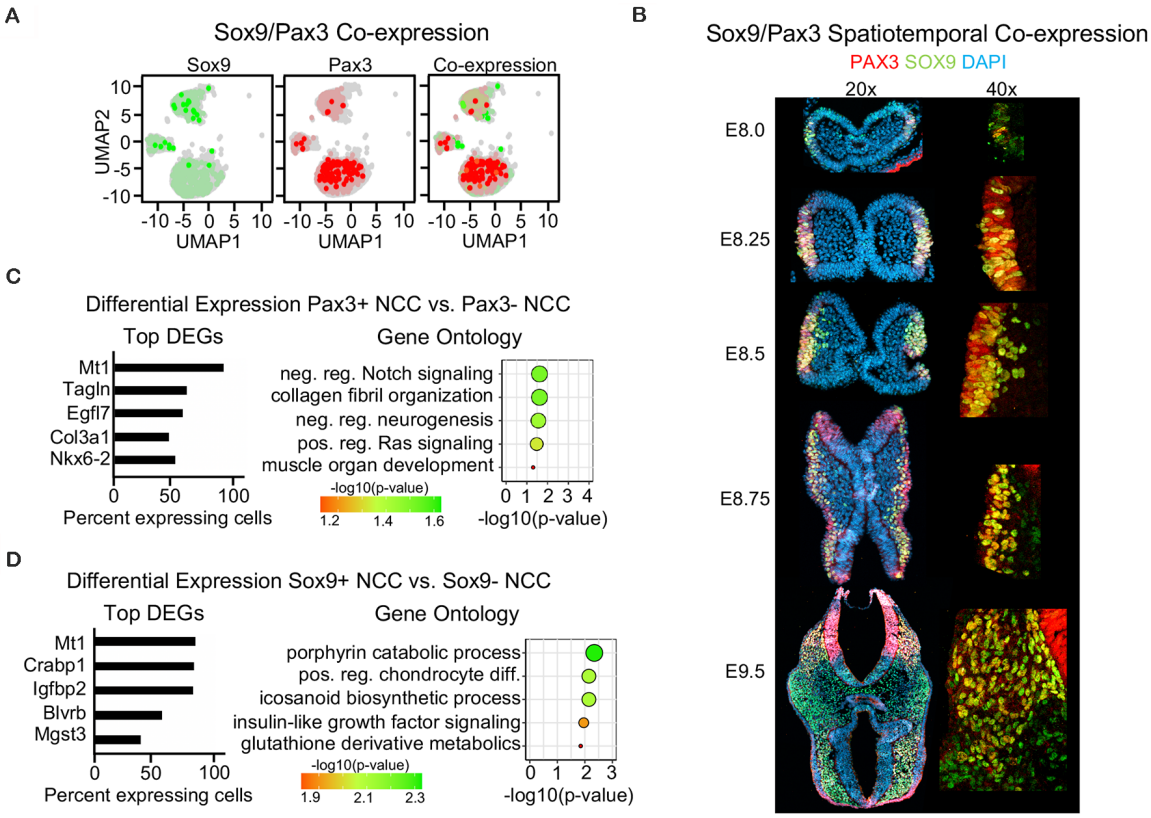

FIGURE 5 | Single-cell sequencing reveals little co-expression of Sox9 and Pax3 in E9.5 neural crest cells. **(A)** Blended UMAP plot showing little co-expression of *Sox9* and *Pax3*. **(B)** Immunofluorescence of transverse mouse embryo sections for PAX3 and SOX9 from E8.0 to E9.5. **(C)** Bar plot of differentially expressed genes and GO analysis of *Pax3*-positive cells and **(D)** *Sox9*-positive cells at E9.5.

in both the neural crest and neuroepithelium and *Otx2* was more highly expressed in the neuroepithelium compared to the neural crest (**Figures 4C,D**). Indeed, *Otx2* has been suggested as a specification factor in premigratory neural crest (Finkelstein and Perrimon, 1991; LeDouarin et al., 1999; Williams et al., 2019), and our results suggest that *Otx2* expression may decline in the late migratory neural crest. These findings suggest that broad expression of *Wnt1* could be due to transcriptional activation by transcription factors expressed in both the neural crest and neural tube.

We found the chromatin structure around *Sox10* was slightly less accessible as compared to *Wnt1* at E9.5 (**Figures 4A,E**). Chromatin around the *Sox10* locus was largely inaccessible in the non-neural ectoderm and was accessible similarly within the migratory neural crest, mid/forebrain, and hindbrain (**Figure 4E**). The accessible regions of chromatin around the *Sox10* locus contained motifs for transcription factors such as *Ebf1, Erg, Bcl6, Ets1*, and *Wt1* (**Figures 4F**, **Supplementary Figure 4B**). Of the transcription factors predicted to bind at the accessible regions near the *Sox10* locus, we found that *Ebf1* and *Ets1* were most highly expressed and enriched in the neural crest with little expression in either the mid/forebrain or hindbrain populations (**Figures 4G,H**). Our analysis of motifs present in the accessible regions of chromatin upstream of *Wnt1* reveals transcriptional control by factors expressed in both the neuroepithelium and neural crest, while motifs present in the accessible regions of chromatin upstream of *Sox10* reveal transcriptional control by factors expressed exclusively in the neural crest.

Single-Cell Sequencing Reveals Little Co-expression of Sox9 and Pax3 in E9.5 Neural Crest Cells

Since we found that *Wnt1* and *Sox10* were largely not co-expressed within neural crest cells at E9.5, we analyzed co-expression of canonical neural crest markers *Pax3* and *Sox9*. Surprisingly, we found that *Pax3* and *Sox9* were similarly not co-expressed at E9.5 (**Figure 5A**, **Supplementary Figures 5A,B**). Moreover, IF staining for PAX3 and SOX9 during neural crest development revealed little co-expression at the earliest stages of formation between E8.0 to E8.25, suggesting that early neural crests are heterogeneous in mice (**Figure 4B**, **Supplementary Figure 4B**). In migratory neural crest at E8.5 and E8.75, the co-expression of PAX3 and SOX9 increased, consistent with previous studies (Soldatov et al., 2019). However, at E9.5, PAX3 and SOX9 are largely not co-expressed except for a few delaminating crests located near the dorsal neural tube

consistent with the divergence of neural crest populations as they begin to commit to a terminal fate (**Figure 5B**). Differential expression between the *Pax3*- or *Sox9*-positive neural crest and non-expressing cells revealed a unique gene signature (**Figures 5C,D**). Genes enriched in *Pax3*-positive neural crest are involved in Ras and Notch signaling and neural crest terminal differentiation (**Figure 5C**). Genes enriched in *Sox9*-positive neural crest are involved in chondrocyte differentiation as well as porphyrin, icosanoid, and glutathione metabolic processes (**Figure 5D**). However, we did identify *Mt1* as a gene enriched in both *Pax3*-positive and *Sox9*-positive neural crest. *Mt1* is an antioxidant gene activated by the redox sensing transcription factor *Nrf1* (Ohtsuji et al., 2008). Differential expression analyses suggest that *Pax3*- and *Sox9*-positive cells may differ in their terminal differentiation capacity and use of specific metabolic processes, yet remain similarly enriched for genes involved in metabolism. Taken together, our findings identify different types of nervous system cells captured by commonly used Cre-drivers, identify transcription factors that may contribute to the labeling obtained in the neural tube by Wnt1-Cre2, and highlight the heterogeneity of E9.5 neural crest cells.

DISCUSSION

We use multiple approaches to shed light on the extent of labeling from common neural crest Cre-drivers and demonstrate the importance of carefully profiling recombination. We find using IF of transverse serial cross-sections that Wnt1-Cre2 ubiquitously labels the neural tube near the mid/hindbrain boundary at E9.5 resulting in a neuronal-like gene signature from cells isolated using FACS as compared to cells harvested with Sox10-Cre. Previously, Wnt1-Cre2 was profiled in E8.5 and E9.5 wholemount embryos and transverse section through the E9.5 pharyngeal arch to show that labeling of the neural crest with Wnt1-Cre2 was similar to that of the original Wnt1-Cre2 (Lewis et al., 2013). Our results expand on the understanding of labeling by Wnt1-Cre2 by analyzing serial cross-sections along the anterior/posterior axis at E9.5. While Wnt1-Cre2 corrects for the ectopic activation of Wnt signaling and associated phenotypes, Wnt1-Cre2 robustly labels cells of the neural tube, which may be a limitation for studies that require neural crest specificity. The labeling of the neuroepithelium by Wnt1-Cre2 and the endogenous expression of *Wnt1* in the neuroepithelium at E9.5 does allow for the continual labeling of the premigratory neural crest. However, the labeling of premigratory neural crest by Wnt1-Cre2 may not accurately target the process of neural crest formation as previous studies have found that recombination by Wnt1-Cre2 may occur too late to allow for early neural crest studies (Brault et al., 2001; Hari et al., 2002; Jia et al., 2007; Büchmann-Møller et al., 2009). Our work profiling the recombination of Wnt1-Cre2 and Sox10-Cre focuses on E9.5 neural crest populations. Future studies may be aimed at profiling the recombination of Wnt1-Cre2 during neural crest formation. It will be important to determine how Wnt1-Cre2 labels cells at the earliest stages of neural crest development. For example, it remains to be determined whether premigratory cells possess an ectomesenchymal vs. neural fate bias and whether both fates are comparably captured by Wnt1-Cre2 in mice. Furthermore, it has been shown that *Wnt1* expression declines in neural crest as they delaminate from the neural tube (Zervas et al., 2004; Kléber et al., 2005; Rabadán et al., 2016; Bhattacharya et al., 2018; Hutchins and Bronner, 2018). We similarly found robust *Wnt1* expression in neuroepithelial cells compared to neural crest and little co-expression of *Wnt1* and *Sox10* in migratory neural crest at E9.5. This may reflect the downregulation of *Wnt1* after the neural crest migrates away from the neural tube or the possibility that *Wnt1* and *Sox10* label different neural crest cell populations or derivatives.

We identified predicted motifs of transcription factors that may promote the expression of *Wnt1* in both the neural tube and neural crest. We identified predicted motifs for *Otx2* and *Tead2* in the accessible regions of chromatin around the *Wnt1* locus and both of these factors are expressed in the neural tube. *Otx2* expression parallels that of *Wnt1*; *Otx2* was expressed in more cells of the neural tube than neural crest at E9.5. Furthermore, *Otx2* has been suggested to be an early mammalian neural crest transcription factor and have a role in the neural specification (Finkelstein and Perrimon, 1991; LeDouarin et al., 1999; Williams et al., 2019). *Otx2* expression may decline in more mature neural crest cells. *Tead2* is known to interact with an enhancer element to regulate the expression of *Pax3*, a factor that is also expressed in both the neural crest and the dorsal neural tube. Similar to the labeling achieved with Wnt1-Cre2, we find *Tead2* is expressed in both neural crest cells and cells of the neural tube. We also identified predicted motifs of transcription factors that may promote the expression of *Sox10* specifically in the neural crest. We found that accessible regions of chromatin around the *Sox10* locus at E9.5 contain motifs for *Ets1* and *Ebf1*. *Ets1* is a canonical cranial neural crest specification transcription factor (Barembaum and Bronner, 2013). *Ebf1* has been identified as a neural crest migration transcription factor (Simões-Costa et al., 2014). Our multiomics approach enables the identification of accessible motifs which may promote expression of *Wnt1* in both migratory neural crest and neural tube, as well as endow specificity of *Sox10* to migratory neural crest. However, with our approach, single-cell ATAC data was obtained from one embryo and overlayed with single-cell mRNA data from a second embryo and future studies may benefit from newer technologies where both types of libraries can be constructed from the same cell.

Our findings reveal cellular heterogeneity that should be taken into account when selecting a Cre-driver for labeling the nervous system in mice. The heterogeneity of neural crest has long been a question of interest as these cells must maintain the multipotent differentiation potential to form various derivatives during migration. The degree to which migratory neural crests are a homogeneous cell population that will subsequently diverge vs. heterogeneous populations that exist immediately after delamination from the neural tube remains to be determined. Heterogeneity of neural crest cells was evident *via* immunofluorescence for canonical neural crest transcription factors SOX9 and PAX3 at most stages of neural crest development. However, we did find considerable SOX9 and PAX3 co-expression during delamination, similar to *Wnt1* and

Sox10 co-expression, and a recent study which found that neural crest cells are similar during EMT and then subsequently diverge into various lineages (Soldatov et al., 2019). Studies in chick revealed subpopulations of the neural crest that largely do not co-express neural crest transcription factors consistent with our findings (Roellig et al., 2017). Regardless of the transcription factors expressed in each subpopulation of neural crest, our analysis revealed that neural crest subpopulations are similarly metabolically active, consistent with previous studies (Bhattacharya et al., 2020; Keuls et al., 2020). Taken together, our findings uncover unique aspects of cellular diversity amongst early cranial neural crest and identify specific populations of cells targeted by Wnt1-Cre2 and Sox10-Cre during early neural development in mice.

DATA AVAILABILITY STATEMENT

The datasets presented in this study can be found in online repositories. Raw and processed single-cell mRNA and single-cell ATAC data can be found under GEO SuperSeries GSE167456. Bulk mRNA sequencing data can be found on the GEO database under GSE137227.

ETHICS STATEMENT

The animal study was reviewed and approved by Baylor College of Medicine Institutional Animal Care and Use Committee.

AUTHOR CONTRIBUTIONS

RAK contributed to **Figures 1–5** and **Supplementary Figures 1–5**, writing/editing of the manuscript, and conceptualizing the project. RJP contributed to editing the manuscript. All authors contributed to the article and approved the submitted version.

FUNDING

This research was supported by funds from CPRIT, the V Foundation, Andrew McDonough B+ Foundation, and the National Institutes of Health (NIH; R01-HD099252 and R01-HD098131). This project was supported by the Single-cell Genomics Core and by the Cytometry and Cell Sorting Core (CPRIT-RP180672, NIH P30 CA125123, and S10 RR024574) at Baylor College of Medicine. RJP is a CPRIT Scholar in Cancer Research (RR150106) and a V Scholar in Cancer Research (V Foundation).

ACKNOWLEDGMENTS

We would like to thank Xuemei Wang for technical assistance, Dr. Ross Poche for sharing mice, and Dr. Richard Finnell for feedback on the manuscript.

SUPPLEMENTARY MATERIAL

The Supplementary Material for this article can be found online at: https://www.frontiersin.org/articles/10.3389/fncel.2021.648570/full#supplementary-material.

SUPPLEMENTARY FIGURE 1 | Wnt1-Cre2 and Sox10-Cre label the neural crest and the neural tube. Whole-mount images of Wnt1-Cre2 and Sox10-Cre were used to lineage trace neural crest.

SUPPLEMENTARY FIGURE 2 | Cells harvested using Wnt1-Cre2 have a neuroepithelial gene signature compared to cells harvested using Sox10-Cre. **(A)** Violin and **(B)** density plot showing that the expression values for all samples used in the analysis are comparable.

SUPPLEMENTARY FIGURE 3 | Single-cell sequencing reveals little co-expression of Wnt1 and Sox10 in E9.5 neural crest cells. **(A)** Violin plot and **(B)** scatter plot showing the count of RNA transcripts and mapped features for each cell. **(C)** Jackstraw plot showing the significance of 20 principal components. **(D)** Elbow plot showing the standard deviation of 20 principal components. **(E)** RNAScope for Wnt1 and Sox10 in transverse cranial cross-sections at 63× and corresponding co-localization scatter plot showing the minimal overlap of *Wnt1* and *Sox10*.

SUPPLEMENTARY FIGURE 4 | Single-cell ATAC sequencing reveals accessible motifs near Wnt1 in the neuroepithelium and Sox10 in neural crest. **(A)** Bar plot showing the significance of predicted motifs present in the accessible regions of chromatin at the *Wnt1* and **(B)** *Sox10* loci.

SUPPLEMENTARY FIGURE 5 | Single-cell sequencing reveals little co-expression of Sox9 and Pax3 in E9.5 neural crest cells. **(A)** Bar plot quantifying the co-expression of PAX3 and SOX9. **(B)** Immunofluorescence of transverse mouse embryo cross-sections for PAX3 and SOX9 from E8.0 to E9.5.

REFERENCES

Barembaum, M., and Bronner, M. E. (2013). Identification and dissection of a key enhancer mediating cranial neural crest specific expression of transcription factor, Ets-1. *Dev. Biol.* 382, 567–575. doi: 10.1016/j.ydbio.2013.08.009

Barriga, E. H., Trainor, P. A., Bronner, M., and Mayor, R. (2015). Animal models for studying neural crest development: is the mouse different? *Development* 142, 1555–1560. doi: 10.1242/dev.121590

Bhattacharya, D., Azambuja, A. P., and Simoes-Costa, M. (2020). Metabolic reprogramming promotes neural crest migration *via* Yap/Tead signaling. *Dev. Cell* 53, 199–211. doi: 10.1016/j.devcel.2020.03.005

Bhattacharya, D., Rothstein, M., Azambuja, A. P., and Simoes-Costa, M. (2018). Control of neural crest multipotency by Wnt signaling and the Lin28/*let-7* axis. *eLife* 7:e40556. doi: 10.7554/eLife.40556

Brault, V., Moore, R., Kutsch, S., Ishibashi, M., Rowitch, D. H., McMahon, A. P., et al. (2001). Inactivation of the (β)-catenin gene by Wnt1-Cre-mediated deletion results in dramatic brain malformation and failure of craniofacial development. *Development* 128, 1253–1264.

Büchmann-Møller, S., Miescher, I., John, N., Krishnan, J., Deng, C. X., and Sommer, L. (2009). Multiple lineage-specific roles of Smad4 during neural crest development. *Dev. Biol.* 330, 329–338. doi: 10.1016/j.ydbio.2009.04.001

Butler, A., Hoffman, P., Smibert, P., Papalexi, E., and Satija, R. (2018). Integrating single-cell transcriptomic data across different conditions, technologies, and species. *Nat. Biotechnol.* 36, 411–420. doi: 10.1038/nbt.4096

Danielian, P. S., Muccino, D., Rowitch, D. H., Michael, S. K., and McMahon, A. P. (1998). Modification of gene activity in mouse embryos *in utero* by a

tamoxifen-inducible form of Cre recombinase. *Curr. Biol.* 8, 1323–1326. doi: 10.1016/s0960-9822(07)00562-3

Finkelstein, R., and Perrimon, N. (1991). The molecular genetics of head development in *Drosophila melanogaster*. *Development* 112, 899–912.

Hari, L., Brault, V., Kléber, M., Lee, H. Y., Ille, F., Leimeroth, R., et al. (2002). Lineage-specific requirements of β-catenin in neural crest development. *J. Cell Biol.* 159, 867–880. doi: 10.1083/jcb.200209039

Hari, L., Miescher, I., Shakhova, O., Suter, U., Chin, L., Taketo, M., et al. (2012). Temporal control of neural crest lineage generation by Wnt/β-catenin signaling. *Development* 139, 2107–2117. doi: 10.1242/dev.073064

Herman, T. E., and Siegel, M. J. (2012). Acampomelic campomelic dysplasia in genetic male without sex reversal. *J. Perinatol.* 32, 75–77. doi: 10.1038/jp.2011.92

Houston, C. S., Opitz, J. M., Spranger, J. W., Macpherson, R. I., Reed, M. H., Gilbert, E. F., et al. (1983). The campomelic syndrome: review, report of 17 cases, and follow-up on the currently 17-year-old boy first reported by Maroteaux et al., in 1971. *Am. J. Med. Genet.* 15, 3–28. doi: 10.1002/ajmg.1320150103

Hutchins, E. J., and Bronner, M. E. (2018). Draxin acts as a molecular rheostat of canonical Wnt signaling to control cranial neural crest EMT. *J. Cell Biol.* 217, 3683–3697. doi: 10.1083/jcb.201709149

Jia, Q., McDill, B. W., Li, S. Z., Deng, C., Chang, C. P., and Chen, F. (2007). Smad signaling in the neural crest regulates cardiac outflow tract remodeling through cell autonomous and non-cell autonomous effects. *Dev. Biol.* 311, 172–184. doi: 10.1016/j.ydbio.2007.08.044

Keuls, R. A., Kojima, K., Lozzi, B., Steele, J. W., Chen, Q., Gross, S. S., et al. (2020). MiR-302 regulates glycolysis to control cell-cycle during neural tube closure. *Int. J. Mol. Sci.* 21:7534. doi: 10.3390/ijms21207534

Kléber, M., Lee, H. Y., Wurdak, H., Buchstaller, J., Riccomagno, M. M., Ittner, L. M., et al. (2005). Neural crest stem cell maintenance by combinatorial Wnt and BMP signaling. *J. Cell Biol.* 169, 309–320. doi: 10.1083/jcb.200411095

Kwok, C., Weller, P. A., Guioli, S., Foster, J. W., Mansour, S., Zuffardi, O., et al. (1995). Mutations in SOX9, the gene responsible for campomelic dysplasia and autosomal sex reversal. *Am. J. Hum. Genet.* 57, 1028–1036.

LeDouarin, N., LeDouarin, N. M., and Kalcheim, C. (1999). *The Neural Crest (No. 36)*. New York, NY: Cambridge University Press.

Lewis, A. E., Vasudevan, H. N., O'Neill, A. K., Soriano, P., and Bush, J. O. (2013). The widely used Wnt1-Cre transgene causes developmental phenotypes by ectopic activation of Wnt signaling. *Dev. Biol.* 379, 229–234. doi: 10.1016/j.ydbio.2013.04.026

Luche, H., Weber, O., Nageswara Rao, T., Blum, C., and Fehling, H. J. (2007). Faithful activation of an extra-bright red fluorescent protein in "knock-in" Cre-reporter mice ideally suited for lineage tracing studies. *Eur. J. Immunol.* 37, 43–53. doi: 10.1002/eji.200636745

Lumb, R., Buckberry, S., Secker, G., Lawrence, D., and Schwarz, Q. (2017). Transcriptome profiling reveals expression signatures of cranial neural crest cells arising from different axial levels. *BMC Dev. Biol.* 17:5. doi: 10.1186/s12861-017-0147-z

Mansour, S., Hall, C. M., Pembrey, M. E., and Young, I. D. (1995). A clinical and genetic study of campomelic dysplasia. *J. Med. Genet.* 32, 415–420. doi: 10.1136/jmg.32.6.415

Ohtsuji, M., Katsuoka, F., Kobayashi, A., Aburatani, H., Hayes, J. D., and Yamamoto, M. (2008). Nrf1 and Nrf2 play distinct roles in activation of antioxidant response element-dependent genes. *J. Biol. Chem.* 283, 33554–33562. doi: 10.1074/jbc.M804597200

Pasterls, N. G., Trask, B. J., Sheldon, S., and Gorskl, J. L. (1993). Discordant phenotype of two overlapping deletions involving the PAX3 gene in chromosome 2q35. *Hum. Mol. Genet.* 2, 953–959. doi: 10.1093/hmg/2.7.953

Pijuan-Sala, B., Griffiths, J. A., Guibentif, C., Hiscock, T. W., Jawaid, W., Calero-Nieto, F. J., et al. (2019). A single-cell molecular map of mouse gastrulation and early organogenesis. *Nature* 566, 490–495. doi: 10.1038/s41586-019-0933-9

Rabadán, M. A., Herrera, A., Fanlo, L., Usieto, S., Carmona-Fontaine, C., Barriga, E. H., et al. (2016). Delamination of neural crest cells requires transient and reversible Wnt inhibition mediated by Dact1/2. *Development* 143, 2194–2205. doi: 10.1016/j.jinf.2021.01.030

Roellig, D., Tan-Cabugao, J., Esaian, S., and Bronner, M. E. (2017). Dynamic transcriptional signature and cell fate analysis reveals plasticity of individual neural plate border cells. *eLife* 6:e21620. doi: 10.7554/eLife.21620

Shakhova, O., Zingg, D., Schaefer, S. M., Hari, L., Civenni, G., Blunschi, J., et al. (2012). Sox10 promotes the formation and maintenance of giant congenital naevi and melanoma. *Nat. Cell Biol.* 14, 882–890. doi: 10.1038/ncb2535

Shinwell, E. S., Hengerer, A. S., and Kendig, J. W. (1988). A third case of bronchoscopic diagnosis of tracheobronchomalacia in campomelic dysplasia. *Pediatr. Pulmonol.* 4, 192–192. doi: 10.1002/ppul.1950040313

Shirley, S. H., Greene, V. R., Duncan, L. M., Cabala, C. A. T., Grimm, E. A., and Kusewitt, D. F. (2012). Slug expression during melanoma progression. *Am. J. Pathol.* 180, 2479–2489. doi: 10.1016/j.ajpath.2012.02.014

Simões-Costa, M., Tan-Cabugao, J., Antoshechkin, I., Sauka-Spengler, T., and Bronner, M. E. (2014). Transcriptome analysis reveals novel players in the cranial neural crest gene regulatory network. *Genome Res.* 24, 281–290. doi: 10.1101/gr.161182.113

Sock, E., Pagon, R. A., Keymolen, K., Lissens, W., Wegner, M., and Scherer, G. (2003). Loss of DNA-dependent dimerization of the transcription factor SOX9 as a cause for campomelic dysplasia. *Hum. Mol. Genet.* 12, 1439–1447. doi: 10.1093/hmg/ddg158

Soldatov, R., Kaucka, M., Kastriti, M. E., Petersen, J., Chontorotzea, T., Englmaier, L., et al. (2019). Spatiotemporal structure of cell fate decisions in murine neural crest. *Science* 364:eaas9536. doi: 10.1126/science.aas9536

Stine, Z. E., Huynh, J. L., Loftus, S. K., Gorkin, D. U., Salmasi, A. H., Novak, T., et al. (2009). Oligodendroglial and pan-neural crest expression of Cre recombinase directed by Sox10 enhancer. *Genesis* 47, 765–770. doi: 10.1002/dvg.20559

Stuart, T., Butler, A., Hoffman, P., Hafemeister, C., Papalexi, E., Mauck, W. M. III., et al. (2019). Comprehensive integration of single-cell data. *Cell* 177, 1888–1902. doi: 10.1016/j.cell.2019.05.031

Stuart, T., Srivastava, A., Lareau, C., and Satija, R. (2020). Multimodal single-cell chromatin analysis with Signac. *bioRxiv* [Preprint]. doi: 10.1126/science.abc3172

The Jackson Laboratory. (2020). *The Jackson Laboratory*. Available online at: https://www.jax.org/strain/022137. Accessed December 31, 2020.

Weiss, M. B., Abel, E. V., Mayberry, M. M., Basile, K. J., Berger, A. C., and Aplin, A. E. (2012). TWIST1 is an ERK1/2 effector that promotes invasion and regulates MMP-1 expression in human melanoma cells. *Cancer Res.* 72, 6382–6392. doi: 10.1158/0008-5472.CAN-12-1033

Williams, R. M., Candido-Ferreira, I., Repapi, E., Gavriouchkina, D., Senanayake, U., Ling, I. T., et al. (2019). Reconstruction of the global neural crest gene regulatory network *in vivo*. *Dev. Cell* 51, 255.e7–276.e7. doi: 10.1016/j.devcel.2019.10.003

Zervas, M., Millet, S., Ahn, S., and Joyner, A. L. (2004). Cell behaviors and genetic lineages of the mesencephalon and rhombomere 1. *Neuron* 43, 345–357. doi: 10.1016/j.neuron.2004.07.010

Conflict of Interest: The authors declare that the research was conducted in the absence of any commercial or financial relationships that could be construed as a potential conflict of interest.

frontiers in Neuroscience

ORIGINAL RESEARCH
published: 20 April 2021
doi: 10.3389/fnins.2021.639527

Cell-Type-Specific Gene Modules Related to the Regional Homogeneity of Spontaneous Brain Activity and Their Associations With Common Brain Disorders

*Junlin Shen[1†], Bingbing Yang[1†], Zhonghua Xie[2], Heng Wu[3], Zhanye Zheng[4], Jianhua Wang[4], Ping Wang[5], Peng Zhang[6,7,8], Wei Li[6,7,8], Zhaoxiang Ye[6,7,8] and Chunshui Yu[1]**

[1] Department of Radiology and Tianjin Key Laboratory of Functional Imaging, Tianjin Medical University General Hospital, Tianjin, China, [2] Department of Mathematics, School of Science, Tianjin University of Science and Technology, Tianjin, China, [3] Tianjin Key Laboratory of Lung Cancer Metastasis and Tumor Microenvironment, Tianjin Lung Cancer Institute, Tianjin Medical University General Hospital, Tianjin, China, [4] Department of Pharmacology, School of Basic Medical Science, Tianjin Medical University, Tianjin, China, [5] School of Medical Imaging and Tianjin Key Laboratory of Functional Imaging, Tianjin Medical University, Tianjin, China, [6] Department of Radiology, National Clinical Research Center for Cancer, Tianjin Medical University Cancer Institute and Hospital, Tianjin, China, [7] Key Laboratory of Cancer Prevention and Therapy, Tianjin, China, [8] Tianjin's Clinical Research Center for Cancer, Tianjin, China

Mapping gene expression profiles to neuroimaging phenotypes in the same anatomical space provides opportunities to discover molecular substrates for human brain functional properties. Here, we aimed to identify cell-type-specific gene modules associated with the regional homogeneity (ReHo) of spontaneous brain activity and their associations with brain disorders. Fourteen gene modules were consistently associated with ReHo in the three datasets, five of which showed cell-type-specific expression (one neuron-endothelial module, one neuron module, one astrocyte module and two microglial modules) in two independent cell series of the human cerebral cortex. The neuron-endothelial module was mainly enriched for transporter complexes, the neuron module for the synaptic membrane, the astrocyte module for amino acid metabolism, and microglial modules for leukocyte activation and ribose phosphate biosynthesis. In enrichment analyses of cell-type-specific modules for 10 common brain disorders, only the microglial module was significantly enriched for genes obtained from genome-wide association studies of multiple sclerosis (MS) and Alzheimer's disease (AD). The ReHo of spontaneous brain activity is associated with the gene expression profiles of neurons, astrocytes, microglia and endothelial cells. The microglia-related genes associated with MS and AD may provide possible molecular substrates for ReHo abnormality in both brain disorders.

Keywords: gene expression, Allen Human Brain Atlas, cell type, regional homogeneity, fMRI

OPEN ACCESS

Edited by:
Giordano Lippi, The Scripps Research Institute, United States

Reviewed by:
Marta Olah, Columbia University Irving Medical Center, United States
Thomas W. Mühleisen, Research Centre Jülich, Germany

***Correspondence:**
Chunshui Yu
chunshuiyu@tmu.edu.cn

[†] These authors have contributed equally to this work

Specialty section:
This article was submitted to Neurogenomics, a section of the journal Frontiers in Neuroscience

Received: *09 December 2020*
Accepted: *25 March 2021*
Published: *20 April 2021*

Citation:
Shen J, Yang B, Xie Z, Wu H, Zheng Z, Wang J, Wang P, Zhang P, Li W, Ye Z and Yu C (2021) Cell-Type-Specific Gene Modules Related to the Regional Homogeneity of Spontaneous Brain Activity and Their Associations With Common Brain Disorders. Front. Neurosci. 15:639527. doi: 10.3389/fnins.2021.639527

INTRODUCTION

Resting-state functional magnetic resonance imaging (rs-fMRI) has been widely used to assess spontaneous brain activity, which records the blood oxygen level-dependent (BOLD) fluctuations during rest. Regional homogeneity (ReHo) is a measure reflecting the degree of local synchronization that occurs over the course of the rs-fMRI, that is, the similarity of the fluctuation of BOLD signals of a given voxel with those of its nearest neighbors (Zang et al., 2004; Zuo et al., 2013), which is measured by Kendall's coefficient of concordance (KCC). Abnormal ReHo may be associated with pathological changes in the brain caused by specific neuropsychitric diseases (He et al., 2007; Wu et al., 2009; You et al., 2011). We were particularly interested in this measure for three reasons: (a) as a data-driven method, ReHo does not require an *a priori* hypothesis, which is appropriate for exploratory analysis; (b) the test-retest reliability of ReHo is well established. With a popular acquisition and preprocessing pipeline, ReHo has been demonstrated to be a highly robust and reliable index for mapping the local activity of the human functional connectome (Zuo et al., 2013; Zuo and Xing, 2014); and (c) ReHo has been used to identify brain functional abnormalities in many brain disorders, such as Alzheimer's disease (AD) (He et al., 2007; Zhang et al., 2012), Parkinson's disease (PD) (Zeng et al., 2017; Liu et al., 2019), epilepsy (EP) (Zeng et al., 2013, 2015), stroke (Liu et al., 2014; Zhao et al., 2018), multiple sclerosis (MS) (Dogonowski et al., 2013; Wu et al., 2016), bipolar disorder (BP) (Yao et al., 2018; Liu et al., 2020), major depressive disorder (MDD) (Guo et al., 2011; Sun et al., 2018), schizophrenia (SCZ) (Xu et al., 2015; Wang et al., 2018), autism spectrum disorders (ASD) (Paakki et al., 2010; Shukla et al., 2010), and attention deficit hyperactivity disorder (ADHD) (Cao et al., 2006; Wang et al., 2013). Although candidate gene studies in healthy and diseased populations have indicated the genetic bases of ReHo (Yu et al., 2014; Zheng et al., 2017; Gou et al., 2018; Shang et al., 2019), the molecular substrates underlying the ReHo of spontaneous brain activity remain elusive.

Genome-wide association studies (GWASs) of neuroimaging phenotypes suggest that resting-state brain functional phenotypes derived from both fMRI (Elliott et al., 2018) and electroencephalogram (Jawinski et al., 2019) are heritable, although the latter did not find genome-wide significant hit due to small sample size (n = 1877). These studies provide the basis for further linking gene expression with resting-state brain functional phenotypes, such as ReHo. Allen Human Brain Atlas (AHBA) provides a new approach for linking gene expression to neuroimaging phenotypes without stringent requirements for sample size (Fornito et al., 2019). By projecting gene expression data from postmortem human brains and neuroimaging data from living human brains to the same standard space, spatial correlation analysis between gene expression and neuroimaging measurement across brain regions or tissue samples can identify genes associated with neuroimaging phenotypes (Fornito et al., 2019). With this approach, several studies have provided new molecular insights into the neuroimaging phenotypes of both healthy and diseased brains (Hawrylycz et al., 2015; Rittman et al., 2016; Romme et al., 2017; Romero-Garcia et al., 2018; Morgan et al., 2019). However, none of these studies have investigated the association between gene expression and ReHo.

In humans, there are more than 20,000 genes, thousands of which have unknown functions. Gene-wise spatial correlations with neuroimaging phenotypes may face challenges not only in correcting multiple comparisons but also in interpreting significant genes with unknown functions. Weighted gene coexpression network analysis (WGCNA) has been proposed to cluster more than 20,000 genes into several dozen gene modules based on the similarity of their spatial expression patterns (Langfelder and Horvath, 2008). Using a module eigengene (ME) to represent the gene expression profile of each module, one can identify gene modules associated with neuroimaging phenotypes by analyzing spatial correlations between ME expression and neuroimaging phenotypes across brain regions, through which the numbers of comparisons are greatly reduced. Regarding the interpretability of significant gene modules, the functions of each module (generally consisting of hundreds of genes) can be investigated through a variety of enrichment analyses. For example, with the RNA-seq data of various types of purified human neocortical cells, one can identify the cell type in which a gene module shows specific expression (Xu et al., 2014). One can also investigate the enrichment of a certain module for biological processes, molecular functions and cellular components (Ashburner et al., 2000). Moreover, one can identify genes shared by neuroimaging phenotypes and brain disorders through enrichment analyses of phenotype-related genes for GWAS results of neuropsychiatric diseases (Gandal et al., 2018). These analyses may provide valuable insight into the molecular mechanisms underlying the neuroimaging abnormalities observed in these disorders.

In this exploratory study, we aimed to clarify the following questions: (a) which gene modules show consistent spatial correlations between gene expression and ReHo across neocortical regions; (b) which ReHo-related gene modules are specifically enriched in particular types of cells in the cerebral cortex; (c) what biological processes, molecular functions and cellular components are associated with these cell-type-specific modules; and (d) which cell-type-specific ReHo-related gene modules are related to common brain disorders. A schematic summary of the study design is shown in **Figure 1**.

MATERIALS AND METHODS

Participants

After excluding participants with any neuropsychiatric illnesses, contraindications for MRI examination, or imaging artifacts, 1101 right-handed healthy young Chinese Han participants (509 males and 592 females; mean age: 24 years, ranging from 18 to 30 years) were recruited from Tianjin Medical University General Hospital (discovery sample: n = 409, 161 males and 248 females; mean age: 24 years, ranging from 18 to 30 years) and Cancer Hospital (replication sample 1: n = 692, 348 males and 344 females; mean age: 24 years, ranging from 18 to 30 years). The study protocol was approved by the Medical Research Ethics Committee of Tianjin Medical University, and written informed

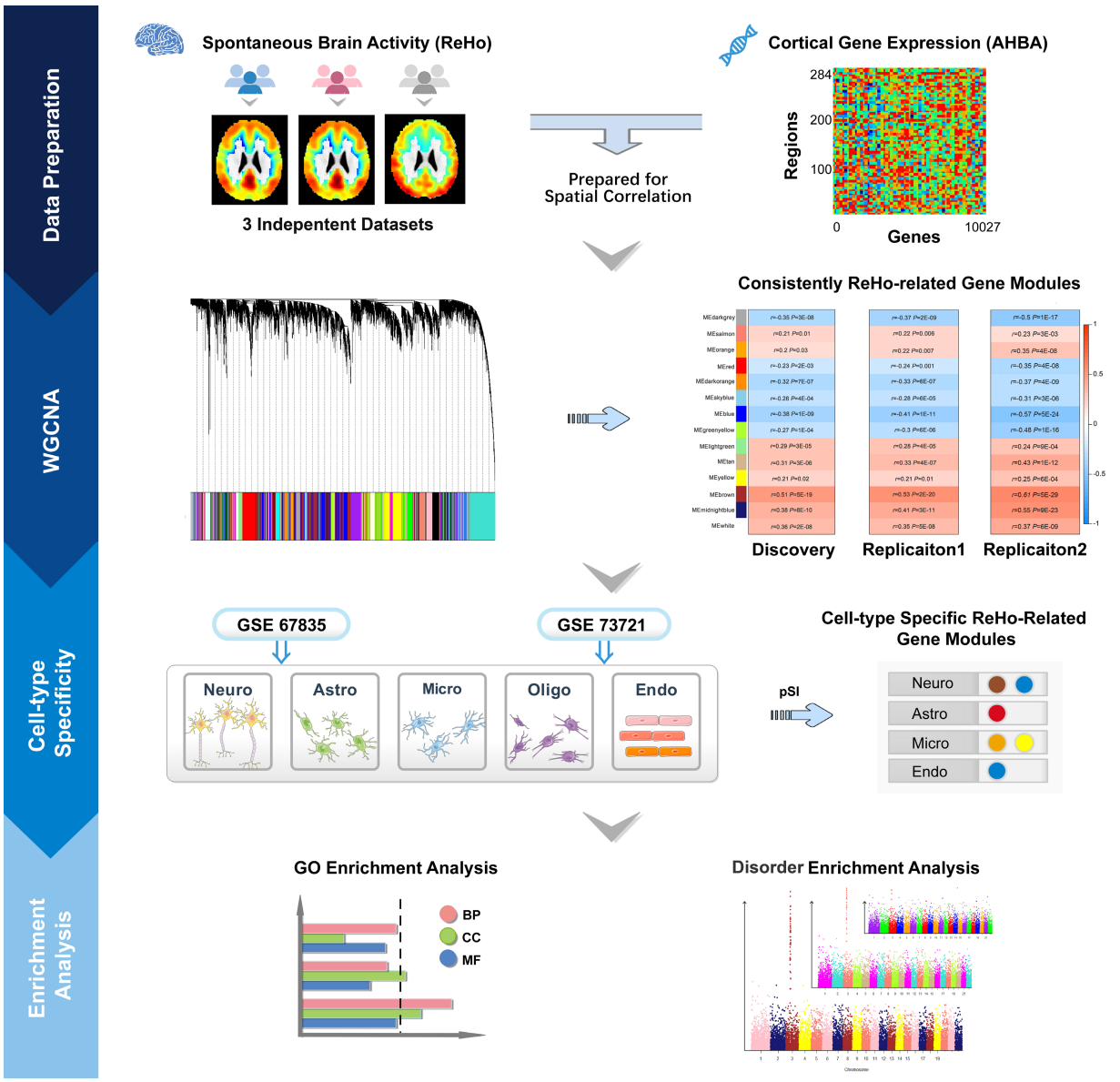

FIGURE 1 | Schematic summary of the study design. This study comprised data preparation, WGCNA, cell-type-specific analysis and enrichment analysis. During data preparation, three mean ReHo maps were obtained from three independent datasets, and a cortical gene transcription matrix was constructed from AHBA. Both ReHo maps and the transcription matrix were assigned to neocortical regions from the HCP Atlas. WGCNA was used to cluster individual genes into gene modules, and spatial correlation was then performed between the ReHo maps and the gene expression profile of each gene module. The significantly correlated gene modules common to the three datasets were considered ReHo-related gene modules. Cell-type-specific analysis was performed for each ReHo-related gene module based on the transcriptomic profiles of neurons, astrocytes, oligodendrocytes, microglia, and endothelial cells from the GSE73721 and GSE67835 series, and the modules that were consistently related to a specific type of neocortical cells in both series were included in the following enrichment analysis. Finally, the identified cell-type-specific modules were annotated by GO and brain disorder enrichment analysis to identify the functions of these modules and to establish their relationships with brain disorders. GO, Gene Ontology; GSE, gene series expression; HCP, Human Connectome Project; ReHo, regional homogeneity; WGCNA, weighted gene coexpression network analysis.

consent was obtained from each participant. To generalize our findings to participants of other ethnicities, the data of 600 healthy young non-Chinese adults (replication sample 2: 297 males and 303 females; mean age: 29 years, ranging from 22 to 36 years) were obtained from the Human Connectome Project (HCP) (Van Essen et al., 2013) (**Supplementary Table 1**).

MRI Data Acquisition

In Tianjin Medical University General Hospital and Cancer Hospital, MRI data were acquired by using Discovery MR750 3.0-Tesla MR scanners (General Electric, Milwaukee, WI, United States) with the same parameters. Tight but comfortable foam padding was used to minimize head motion, and earplugs

were used to reduce scanner noise. The rs-fMRI data were acquired using the Gradient-Echo Single-Shot Echo-Planar Imaging (GRE-SS-EPI) sequence with the following parameters: repetition time (TR)/echo time (TE) = 2000/30 ms; field of view (FOV) = 220 mm × 220 mm; matrix = 64 × 64; flip angle (FA) = 90°; slice thickness = 3 mm; gap = 1 mm; 36 interleaved transverse slices; and 180 volumes. All subjects were instructed to keep their eyes closed, relax, move as little as possible, think of nothing in particular, and stay awake during fMRI scans. Sagittal 3D T1-weighted images were acquired by brain volume sequence (TR/TE = 8.16/3.18 ms; inversion time = 450 ms; FA = 12°; FOV = 256 mm × 256 mm; matrix = 256 × 256; slice thickness = 1 mm, no gap; 188 slices). The HCP MRI data were collected by a customized 3.0-Tesla MR scanner. The rs-fMRI data were acquired by the GRE-SS-EPI sequence (TR/TE = 720/33.1 ms; FOV = 208 mm × 180 mm; matrix = 104 × 90; FA = 52°; slice thickness = 2 mm, no gap; 72 transverse slices; and 1200 volumes), and the 3D-T1-weighted images were acquired by the magnetization prepared rapid acquisition gradient echo sequence (TR/TE = 2400/2.14 ms; inversion time = 1000 ms; FA = 8°; FOV = 224 mm × 224 mm; matrix = 320 × 320; slice thickness = 0.7 mm, no gap; 260 sagittal slices).

MRI Data Preprocessing

All fMRI data were preprocessed with the same procedures. The first 5 volumes were discarded to allow signals to reach equilibrium and to ensure that the participants had adapted to scanning noise. The remaining volumes were corrected for intra-volume temporal differences using sinc-interpolation. Inter-volume head motion was then corrected using rigid-body transformations. After removing non-brain tissues from functional and structural images, functional images were co-registered to corresponding structural images using the boundary-based registration method. Structural images were spatially normalized to the Montreal Neurological Institute (MNI) space, and functional images were normalized to the MNI space using the transformation parameters derived from structural image normalization and were resampled to 3-mm isotropic voxels. Several sources of variance were regressed out from the functional images, including the frame-wise displacement (volume-to-volume changes in head position), linear drift, Friston's 24 head motion parameter, and signals from the white matter and ventricles.

Individual-Level zReHo Calculation for Each Voxel

For each gray matter voxel of each subject, ReHo was defined as the KCC of spontaneous brain activity between this voxel and its nearest 26 neighboring voxels (Zang et al., 2004). To improve the normality and reliability of this measure across subjects, a zReHo values was calculated for each voxel by subtracting the mean ReHo values and dividing it by the standard deviation of all gray matter voxels (Zuo et al., 2013). The resulting zReHo map of each subject was spatially smoothed with an 8 mm × 8 mm × 8 mm full width at half-maximum Gaussian kernel.

Group-Level zReHo Calculation for Each Brain Region

For each of the three groups (one discovery group and two replication groups), the corresponding zReHo map was calculated by voxel-wised one-sample *t*-test using SPM8[1] within the gray matter mask, and the mean zReHo maps of each of the three groups were also calculated and are provided in **Supplementary Figure 1**. Brain regions of interest were defined based on the HCP Atlas (HCP's multi-modal parcelation version 1.0, HCP_MMP1.0), which divides the human cerebral cortex into 360 non-overlapping regions (Glasser et al., 2016). In each group, we calculated the mean zReHo for each region by averaging the zReHo values of all voxels of that region in the corresponding zReHo map. Thus, we obtained the mean zReHo values for each of the 360 cerebral cortical regions in each of the three groups.

Gene Expression Data Processing

The AHBA provided six donated postmortem brains with 3702 densely sampled expression data of more than 20,000 genes detected by 58,692 probes. To avoid biases from gross gene expression dissimilarities between brain regions, we excluded 1998 samples from subcortical nuclei, brainstem and cerebellum, and kept 1704 cerebral cortical samples. We followed a standardized pipeline proposed for AHBA data processing to link gene expression and neuroimaging phenotypes (Arnatkevic Iute et al., 2019). Specifically, the Re-Annotator toolkit v1.0 was used to update probe-to-gene annotations with the up-to-date gene symbol ID and name (Arloth et al., 2015), and the resulting 45,821 probes (20,232 genes) were used for further processing. After intensity-based filtering, 31,977 probes (15,746 genes) with expression values exceeding the background in at least 50% of the samples were preserved. After probe selection, 10,027 probes showing the highest correlation with RNA-seq gene expression were preserved to represent the expression of the corresponding 10,027 genes. The 10,027 genes exhibited relatively high reproducible expression patterns across brain structures between donors, indicating that they are suitable for investigating correlations between expression data from postmortem donors and neuroimaging data from living humans. For each AHBA brain, each tissue sample was assigned to the nearest neocortical region of the HCP Atlas with a recommended distance threshold of less than 2 mm (Arnatkevic Iute et al., 2019). In addition, samples that were assigned to a hemisphere that differed from the annotations provided with their MNI coordinates were excluded. After sample assignment, 820 out of 1704 cortical tissue samples were matched to brain regions in the HCP Atlas (**Supplementary Table 2**). For each brain region with more than one tissue sample, the mean gene expression values of these samples was defined as the expression values of the gene in that region. Due to the lack of any matched tissue samples, 76 regions were excluded from further analysis. Thus, we obtained the expression values of each gene in each of the 284 regions. Scaled robust sigmoid normalization was applied

[1] http://www.fil.ion.ucl.ac.uk/spm

to remove donor-specific variability in gene expression (Fulcher et al., 2013). Finally, a gene transcription matrix of 284 × 10,027 regions × genes was constructed. The code for implementing the AHBA gene expression data processing steps can be downloaded from https://github.com/BMHLab/AHBAprocessing.

Calculation of Gene Modules

Based on the gene transcription matrix of 284 × 10,027 regions × genes, WGCNA was used to identify gene modules and a gene module was defined as a set of genes with similar expression profile across brain regions (n = 284). For each brain region (n = 284), we performed principal component analysis (PCA) of the expression profiles of genes of each module (n = 30) and defined the first component as the module eigengene (ME) to represent the gene expression profile of this module. Specifically, according to the criterion of approximate scale-free topology (fit index = 0.9), a soft thresholding power of 7 was chosen to transform the correlation matrix into an adjacency matrix. Then, the topological similarity of gene expression was calculated using the adjacency matrix. A hierarchical clustering algorithm was used to generate a hierarchical clustering tree (dendrogram) of genes. Gene modules with similar expression profiles were obtained with dynamic tree-cutting with the following parameters: a minimum module size of 50 genes; a deep split of 2; and a height threshold of 0.1. The ME, representing the expression profile of a module, was defined as the first principal component of each module. Finally, we obtained ME values of each gene module (n = 30) of each brain region (n = 284) from AHBA data.

Identification of ReHo-Related Gene Modules

Based on the ME values of the 30 modules × 284 brain regions and zReHo values of the same 284 brain regions, spatial correlation was performed between ME and zReHo across these brain regions for each of the 30 modules, respectively. Since brain regions have different ME values of the same gene module, we have considered the transcriptional variation of each gene module between brain regions. However, the spatial correlation was performed between gene expression and ReHo data derived from different individuals, only genes with similar expression profiles across individuals can be identified by this approach. Because the ME of all 30 gene modules deviated from a normal distribution (**Supplementary Table 3**), the ReHo-related gene modules were identified by the spatial Spearman correlation between the ME of each module and zReHo across the 284 neocortical regions. The same Bonferroni method was used to correct for multiple comparisons ($P_c < 0.05$, equal to an uncorrected $P < 0.05/30 = 0.0017$) in both the discovery and the two replication samples. The criterion for replication was defined as statistically significant in both the discovery and the two replication samples.

Cell-Type-Specific Analysis

We performed cell-type-specific analysis for each ReHo-related gene module. The GSE73721 and GSE67835 series from normal adult human neocortices include the transcriptomic profiles of purified neurons, astrocytes, oligodendrocytes, microglia, and endothelial cells (Darmanis et al., 2015; Zhang et al., 2016). RNA-seq data of the two series were separately processed using the following steps: (a) sequencing files downloaded from the Sequence Read Archive (SRA) database[2] were converted to Fastq files; (b) Prinseq v0.20.4 (Schmieder and Edwards, 2011), FASTQC v0.11.8[3], Trim Galore v0.6.4_dev[4] and Cutadapt v2.7 (Martin, 2011) were used to trim and filter reads and to identify and remove adaptors; (c) reads were aligned to the hg38 genome with STAR v2.7.3a (Dobin et al., 2013) and converted to counts using HTSeq v0.11.2 (Anders et al., 2015); (d) reads per kilobase per million (RPKM) values were calculated following the EdgeR pipeline v3.30.3 (Robinson et al., 2010; McCarthy et al., 2012); and (e) the averaged RPKM values of each neocortical cell type were used in the specificity index (SI) analysis to determine the specific neocortical cell type for which the Reho-related modules were enriched using pSI v1.1[5]. Specifically, RPKM values from one neocortical cell type were compared to those of the other cell types across genes. For each comparison between cell types, the genes were ranked from the highest to the lowest fold changes. The SI for each gene was calculated as the average rank across all comparisons. A P-values was assigned to each SI values via permutation testing, resulting in a pSI values, representing how likely it was that a gene was specifically expressed in a given cell type relative to other cortical cells. A pSI threshold of 0.05 was used to generate a cell-type-enriched gene list. Fisher's exact test was used to evaluate the significance of the overlap between the candidate gene list in the module and the cell-type-specific genes as the background list. The Bonferroni method was used to correct for multiple comparisons (5 cell types and 14 ReHo-related modules) ($P_c < 0.05$, uncorrected $P < 0.05/5/14 = 7.14 \times 10^{-4}$).

Gene Ontology Enrichment Analysis

To characterize the possible biological processes, molecular functions and cellular components of each ReHo-related cell-type-specific gene module, GO enrichment analysis was performed with WebGestalt v2019[6] using Fisher's exact test with FDR correction ($q_c < 0.05$) (Liao et al., 2019).

Enrichment Analysis for Common Brain Disorders

Associations between ReHo-related cell-type-specific gene modules and common brain disorders were identified with MAGMA v1.07b, a software for gene analysis and generalized gene-set analysis of GWAS data (de Leeuw et al., 2015). The single nucleotide polymorphism (SNP) P-values of the GWAS summary statistics of common brain disorders (AD, PD, EP, Stroke, MS, BD, MDD, SCZ, ADHD and ASD) were obtained from previous studies (Pankratz et al., 2012; Beecham et al., 2013;

[2]https://www.ncbi.nlm.nih.gov/sra

[3]https://www.bioinformatics.babraham.ac.uk/projects/fastqc/

[4]https://www.bioinformatics.babraham.ac.uk/projects/trim_galore/

[5]http://genetics.wustl.edu/jdlab/psi_package/

[6]http://www.webgestalt.org/option.php

Ripke et al., 2013; Autism Spectrum Disorders Working Group of The Psychiatric Genomics Consortium, 2017; International League Against Epilepsy Consortium on Complex Epilepsies, 2018; Malik et al., 2018; Martin et al., 2018; Pardinas et al., 2018; International Multiple Sclerosis Genetics Consortium, 2019; Jansen et al., 2019; Kunkle et al., 2019; Stahl et al., 2019; **Supplementary Table 4**). The European panel of the 1000 Genomes phase 3 data were used as reference dataset to account for linkage disequilibrium (LD) between SNPs. The SNP locations in the data were determined in reference to human genome build 37 or 36. MAGMA-based enrichment basically consists of two steps: gene analysis and gene-set analysis.

The gene analysis followed a multiple linear principal component regression model to project the SNP *P* values matrix for a gene onto its principal components, which were used as predictors for the brain disorders in the linear regression model to calculate a gene *P* values. The gene *P* values was then converted to *Z* values to improve normality, which reflects the correlation strength of each gene with each brain disorder. In addition, a gene-gene correlation matrix was calculated to account for the dependency between genes in the following gene-set analysis.

In the gene-set analysis, each gene set consisted of the genes of each ReHo-related cell-type-specific module and represented as binary indicator variables, coded 1 for disease-related genes in that gene module and 0 otherwise. General linear regression analysis was performed at the gene level to test whether genes in the module were more strongly associated with brain diseases than genes outside the module while correcting for gene size, gene density and the minor allele count. Then, the gene-set *P* values were obtained and subjected to Bonferroni correction (the number of comparisons corresponding to the ReHo-related cell-type-specific gene modules) to assess the enrichment of the GWAS signal for each gene module. Moreover, the gene *P* values of the significant enrichment module were also subjected to Bonferroni correction (accounting for the total number of genes in the module) to identify the significant genes within each module for brain disorders.

RESULTS

ReHo-Related Gene Modules

Based on the similarity of gene expression across brain regions, WGCNA divided the 10,027 genes into 30 non-overlapping gene modules (**Supplementary Figure 2**). Spatial correlations identified 14 significant ReHo-related gene modules across neocortical samples in the discovery sample of 409 Chinese subjects. In a replication sample of 692 Chinese subjects, 15 significant ReHo-related gene modules were identified across the neocortical samples, and 14 of these modules were identical to those in the discovery cohort. Furthermore, in another replication sample of 600 non-Chinese people, 14 out of the 20 gene modules were repeated. Thus, the 14 gene modules common to the three cohorts were considered as candidate ReHo-related gene modules (**Figure 2** and **Supplementary Table 5**).

Cell-Type Specificity of ReHo-Related Gene Modules

In all 14 modules, only five ReHo-related gene modules showed consistent enrichment for a specific type of neocortical cells in both the GSE73721 and GSE67835 series, and these modules were deemed cell-type-specific modules. Specifically, the genes of the blue module were enriched in neurons and endothelial cells ($P_c = 6.31 \times 10^{-9}$ in GSE73721, and $P_c = 7.73 \times 10^{-4}$ in GSE67835 for neuron; $P_c = 1.18 \times 10^{-2}$ in GSE73721, and $P_c = 1.87 \times 10^{-2}$ in GSE67835 for endothelial cell); the genes of the brown module were enriched in neurons ($P_c = 2.17 \times 10^{-20}$ in GSE73721, and $P_c = 1.35 \times 10^{-3}$ in GSE67835); the genes of the red module were enriched in astrocytes ($P_c = 6.02 \times 10^{-219}$ in GSE73721, $P_c = 1.29 \times 10^{-68}$ in GSE67835); and the genes of the dark orange and yellow modules were enriched in microglia ($P_c = 8.44 \times 10^{-105}$ in GSE73721, $P_c = 5.43 \times 10^{-102}$ in GSE67835 for the dark orange module; $P_c = 8.22 \times 10^{-3}$ in GSE73721, $P_c = 1.17 \times 10^{-2}$ in GSE67835 for the yellow module) (**Figure 3** and **Supplementary Table 6**). However, none of these modules showed significant specific expression in oligodendrocytes in either series. The ME values of the brown and yellow modules showed a positive correlation with zReHo values across neocortical regions ($r = 0.51$, $P_c = 5 \times 10^{-19}$ for brown module; $r = 0.21$, $P_c = 0.02$ for yellow module); however, the ME values of the blue, red and dark orange modules showed negative correlations with zReho values across neocortical regions ($r = -0.38$, $P_c = 1 \times 10^{-9}$ for blue module; $r = -0.23$, $P_c = 2 \times 10^{-3}$ for red module; $r = -0.32$, $P_c = 7 \times 10^{-7}$ for dark orange module) in both the discovery sample (**Figure 4**) and the two replication samples (**Supplementary Figures 3, 4**).

Among the top hit genes obtained from GWAS of resting-state fMRI phenotypes, *INPP5A* in blue module that has been associated with resting-state activity of the prefrontal cortex in the UK Biobank paper (Elliott et al., 2018) was also associated with zReHo, a measure of resting-state brain activity.

GO Enrichment for Cell-Type-Specific ReHo-Related Gene Modules

The genes of brown module (neuron-endothelial module) were significantly enriched for transporter complexes ($q_c = 1.3 \times 10^{-3}$) and transcription factor activity ($q_c = 7.3 \times 10^{-3}$) (**Figure 5A**). The genes of blue module (neuron module) were associated with signal release ($q_c = 1.8 \times 10^{-2}$), the synaptic membrane ($q_c = 5.9 \times 10^{-3}$) and passive transmembrane transporter activity ($q_c = 4.1 \times 10^{-2}$) (**Figure 5B**). The genes of red module (astrocyte module) were enriched for cellular amino acid metabolic processes ($q_c = 1 \times 10^{-4}$), the extracellular matrix ($q_c = 1.2 \times 10^{-2}$) and sulfur compound binding ($q_c = 3 \times 10^{-4}$) (**Figure 5C**). The genes of dark orange module (microglial module) were associated with leukocyte activation involved in inflammatory response ($q_c = 1.0 \times 10^{-13}$), major histocompatibility complex (MHC) protein complexes ($q_c = 5.6 \times 10^{-9}$) and antigen binding ($q_c = 2.3 \times 10^{-3}$) (**Figure 5D**). The genes of yellow module (microglial module) were associated with ribose phosphate biosynthetic processes ($q_c = 2.2 \times 10^{-4}$) and the mitochondrial

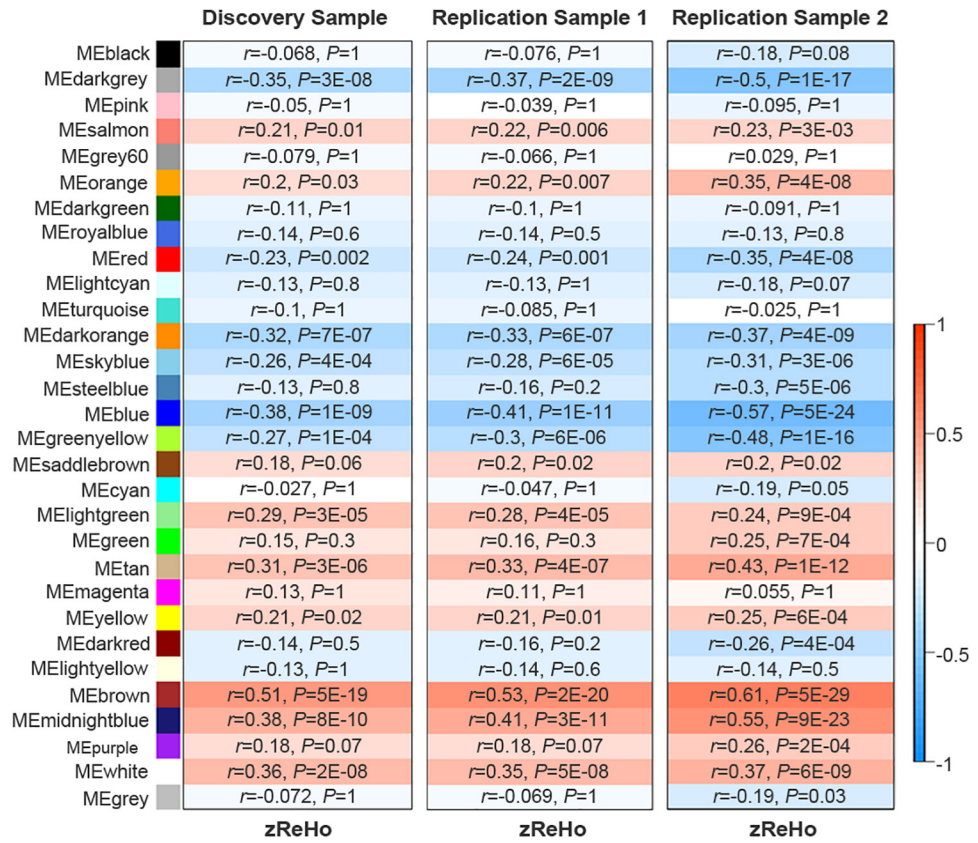

FIGURE 2 | Identification of ReHo-related gene modules. The original 30 modules in the discovery sample and the two replication samples. Color bar denotes correlation coefficients between ME and zReHo. Warm color represents positive correlations and cold color represents negative correlations with correlation coefficients and Bonferroni-corrected *P* values listed for each module. ME, module eigengene; zReHo, z transformed regional homogeneity.

inner membrane ($q_c = 3.2 \times 10^{-3}$) (**Figure 5E**). Other significantly enriched GO terms of the five cell-type-specific modules are listed in **Supplementary Table 7**.

Brain Disorder Enrichment for Cell-Type-Specific ReHo-Related Gene Modules

Since ReHo abnormalities have been reported in brain disorders, enrichment was applied to investigate whether these cell-type-specific ReHo-related gene modules are associated with genetic susceptibility for common brain disorders. Among the 10 common brain disorders considered herein, only the microglial module was significantly enriched for multiple sclerosis and Alzheimer's disease (MAGMA gene-set P_c values of 8.26×10^{-3} and 1.88×10^{-4}, respectively, accounting for the 5 cell-type-specific modules) (**Figure 6A** and **Supplementary Table 8**). The other two GWAS summary statistics of multiple sclerosis and Alzheimer's disease with different sample sizes from previous analysis were further tested to validate our findings. After Bonferroni correction for 5 cell-type-specific modules, the microglial module again exhibited significant associations with multiple sclerosis and Alzheimer's disease (MAGMA gene-set P_c values of 3.12×10^{-2} and 1.78×10^{-3}, respectively) (**Figure 6B** and **Supplementary Table 8**).

The comparison of MAGMA gene *P* values against a Bonferroni-corrected threshold of $0.05/94 = 5.32 \times 10^{-4}$ in the microglial module revealed that the significant genes associated with MS were interferon gamma-inducible protein 30 (*IFI30*), regulator of G-protein signaling 1 (*RGS1*), and cluster of differentiation 86 (*CD86*) in both MS GWAS summaries. Comparison against a threshold of $0.05/101 = 4.95 \times 10^{-4}$ in the microglial module revealed that the significant genes associated with AD were membrane spanning 4-domains A4A (*MS4A4A*), human leukocyte antigen-DR alpha (*HLA-DRA*), triggering receptor expressed on myeloid cells 2 (*TREM2*), human leukocyte antigen-DR beta 5 (*HLA-DRB5*) and cluster of differentiation 33 (*CD33*) in both AD GWAS summaries (**Supplementary Table 9**).

DISCUSSION

This study identified five cell-type-specific gene modules associated with ReHo. The neuron-endothelial module was enriched for transporter complexes, the neuron module for the synaptic membrane, the astrocyte module for amino acid

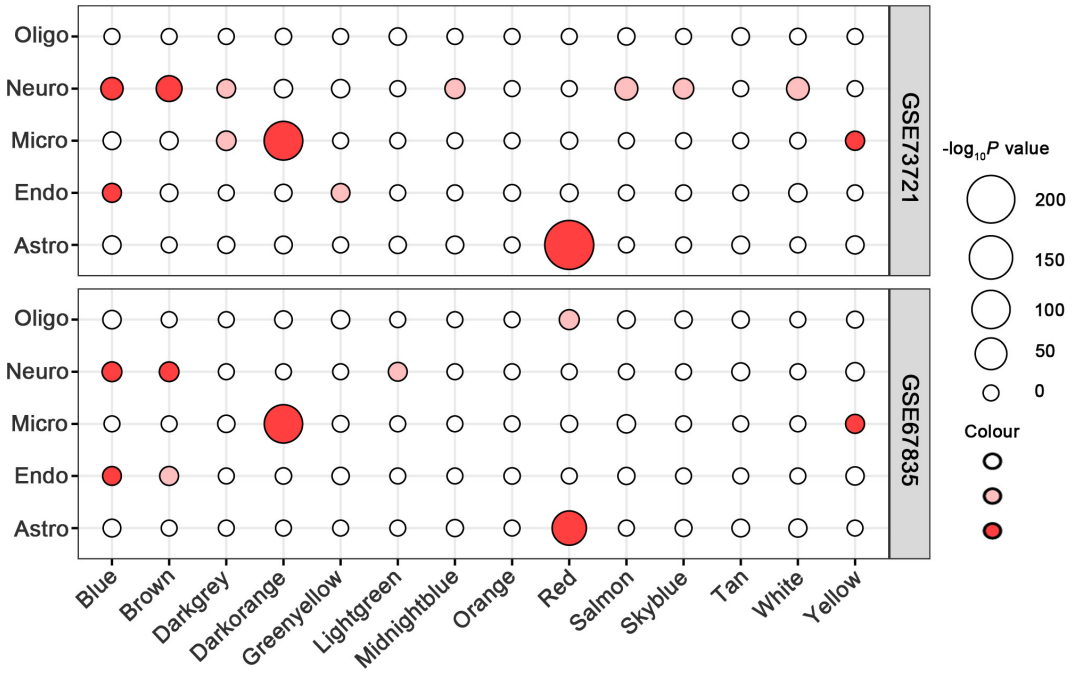

FIGURE 3 | Cell-type-specific analyses for ReHo-related modules in the GSE73721 and GSE67835 series. The size of a given circle corresponds to the cell-type-specific enrichment -$\log_{10}$ Bonferroni-corrected *P*-values for each module. Solid red indicates significant enrichment in both series, faint red indicates significant enrichment in only one series, and white indicates non-significant in neither series. GSE, gene series expression; ReHo, regional homogeneity.

metabolism, and the microglial modules for leukocyte activation and ribose phosphate anabolism, indicating that neurons, astrocytes, microglia and endothelial cells are all associated with the ReHo of spontaneous brain activity. We also found that the ReHo-related microglial module was enriched for MS and AD, indicating that the molecular pathology of microglial cells is a possible mechanism underlying ReHo abnormalities in both diseases.

Regional homogeneity is a measure of the local synchronization of BOLD signals among neighboring voxels (Zang et al., 2004), and the BOLD signal is a reflection of neurovascular coupling linking neural firing to cerebral blood flow changes to accommodate changing energy demands during brain activity (Metea and Newman, 2006). Neurovascular coupling depends on the structure and function of the neurovascular unit consisting of neurons, astrocytes and vessel endothelial cells. The associations between ReHo and gene expression in the neuron, astrocyte and neuron-endothelial modules are consistent with the neurovascular coupling theory of BOLD signals. In this study, we identified two sets of genes significantly expressed in neurons that exert different modulatory effects on the ReHo of spontaneous brain activity. The higher expression of the brown module related to transporter complexes and ligand-activated transcription factor activity corresponds to higher ReHo; however, the higher expression of the blue module related to the formation of the synaptic membrane, signal release, and passive transmembrane transporter activity corresponds to lower ReHo. These findings indicate that the ReHo of spontaneous brain activity may be modulated by neuron-related genes with different functions. In addition, the endothelial component in the blue module may also account for this difference. Astrocytes coordinate information exchange between neurons and vessels and act as a hub for neurovascular coupling (Filosa et al., 2016). We found that an astrocyte module enriched for extracellular matrix formation, sulfur compound binding, and amino acid metabolic processes was associated with ReHo, indicating that it is not only gene expression in neurons but also expression in astrocytes that may play an important role in modulating the ReHo of spontaneous brain activity.

A novel finding of this study was the association between microglia-related genes and the ReHo of spontaneous brain activity. Microglia in the central nervous system are responsible for regulating the immune response involving antigen presentation, debris phagocytosis and cytokine production (Sasaki, 2017). The significant enrichment of the dark orange module for the MHC, antigen binding and leukocyte activation was consistent with the immune inflammatory role of microglia. The yellow module was also specifically expressed in microglia but with different modulatory effects in ReHo compared with the dark orange module. The enrichment of ribose phosphate biosynthetic processes and the mitochondrial inner membrane observed for the yellow module may indicate that genes in this module may participate in adenosine triphosphate synthesis in mitochondria for energy supplementation to microglia. Interindividual and interregional variations in microglia-related gene expression will influence the function of microglia, resulting in individual and regional differences in the production of cytokines and the removal of free radicals (Kaur et al., 2017).

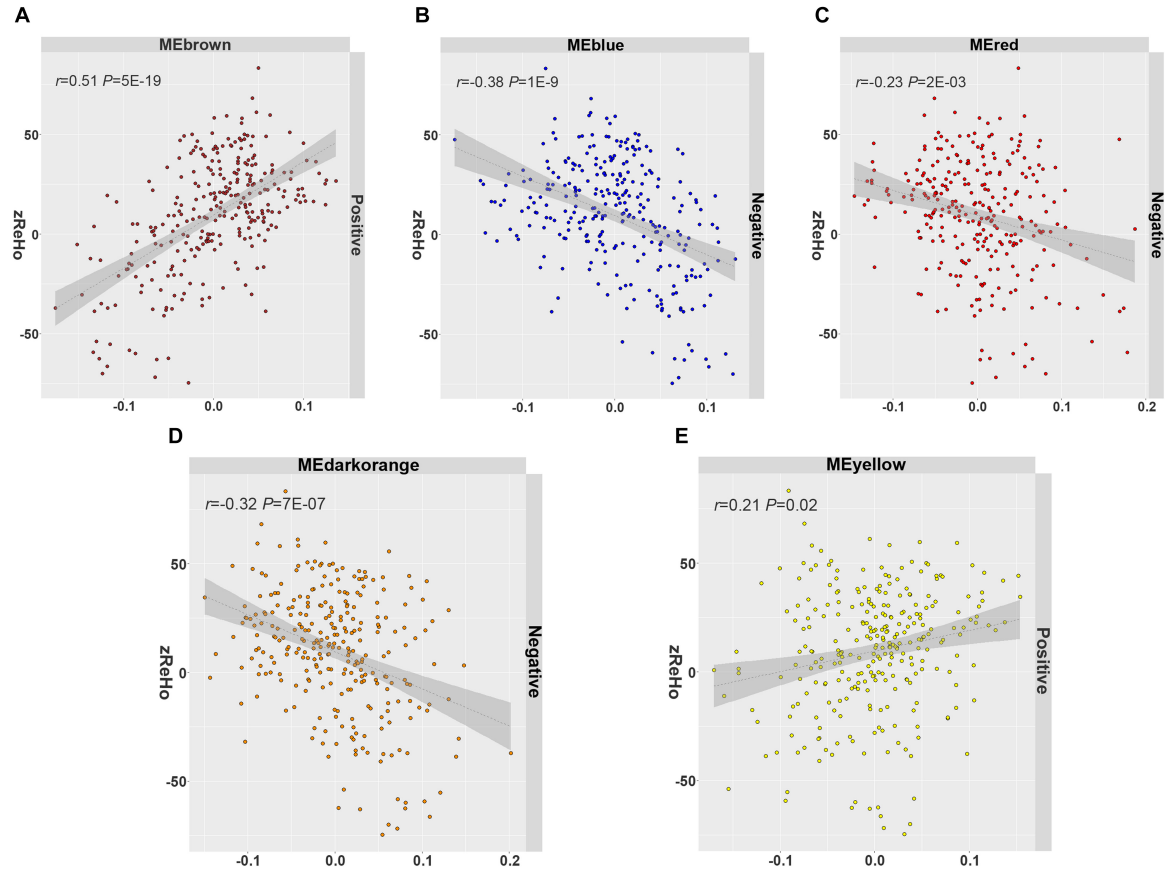

FIGURE 4 | The spatial correlation between the ME and zReHo of each cell-type-specific module with the correlation coefficient and Bonferroni-corrected *P* values. **(A)** Brown module, **(B)** blue module, **(C)** red module, **(D)** dark orange module, **(E)** yellow module in the discovery sample. ME, module eigengene; zReHo, z transformed regional homogeneity.

Both cytokines and free radicals influence components of the neurovascular unit and, thus, ReHo.

In the enrichment analysis for common brain disorders, one significant result was the enrichment of the microglial module for multiple sclerosis, which was consistent with previous findings of microglial abnormalities in multiple sclerosis (Voet et al., 2019). In early active multiple sclerosis, microglia predominantly display a proinflammatory phenotype and express molecules involved in oxidative injury, phagocytosis, T cell stimulation, antigen presentation, and iron metabolism (Zrzavy et al., 2017). In addition to the active lesions, a similar microglial activation pattern was observed for the gene expression of different surface markers at the site of lesion expansion in chronic MS lesions (Frischer et al., 2009; Zrzavy et al., 2017). Furthermore, microglial modules (clusters of activated microglia) are observed in the white matter in the shadow of plaques in MS patients, which are deemed pre-active MS lesions (Ramaglia et al., 2012; Singh et al., 2013). PET using 18-kDa translocator protein (TSPO)-binding radioligands can detect MS-related pathology at the molecular level *in vivo*. Increased TSPO binding is observed in scattered areas related to demyelinating lesions in relapsing-remitting MS patients, which further supports neuroinflammation and neuronal injury involving activated microglia for MS (Airas et al., 2015). In the dark orange microglial module, three genes associated with MS were identified in both GWAS datasets. *IFI30* plays a crucial role in MHC class II-restricted antigen processing, and its expression is greatly enhanced on microglia in active demyelinating lesions of multiple sclerosis (Maric et al., 2001; Satoh et al., 2008). Previous studies have shown the expression of *CD86* in microglia within brain lesions in multiple sclerosis (Windhagen et al., 1995). Moreover, the expression of *CD86* is influenced by local variants correlated with disease susceptibility in the pathogenesis of multiple sclerosis (Smets et al., 2018). Regulators of G-protein signaling (RGS) proteins, especially *RGS1*, play a key role in the negative regulation of G-protein-coupled receptor signaling (Neves et al., 2002). There is a growing body of literature that suggests that *RGS1* is expressed in microglia (Atwood et al., 2011). *RGS1* presents a close relationship with neuroinflammation by responding to diverse chemokines (Balashov et al., 1999) and was recently designated as an MS susceptibility locus by the International Multiple Sclerosis Genetics Consortium (International Multiple Sclerosis Genetics Consortium, 2010).

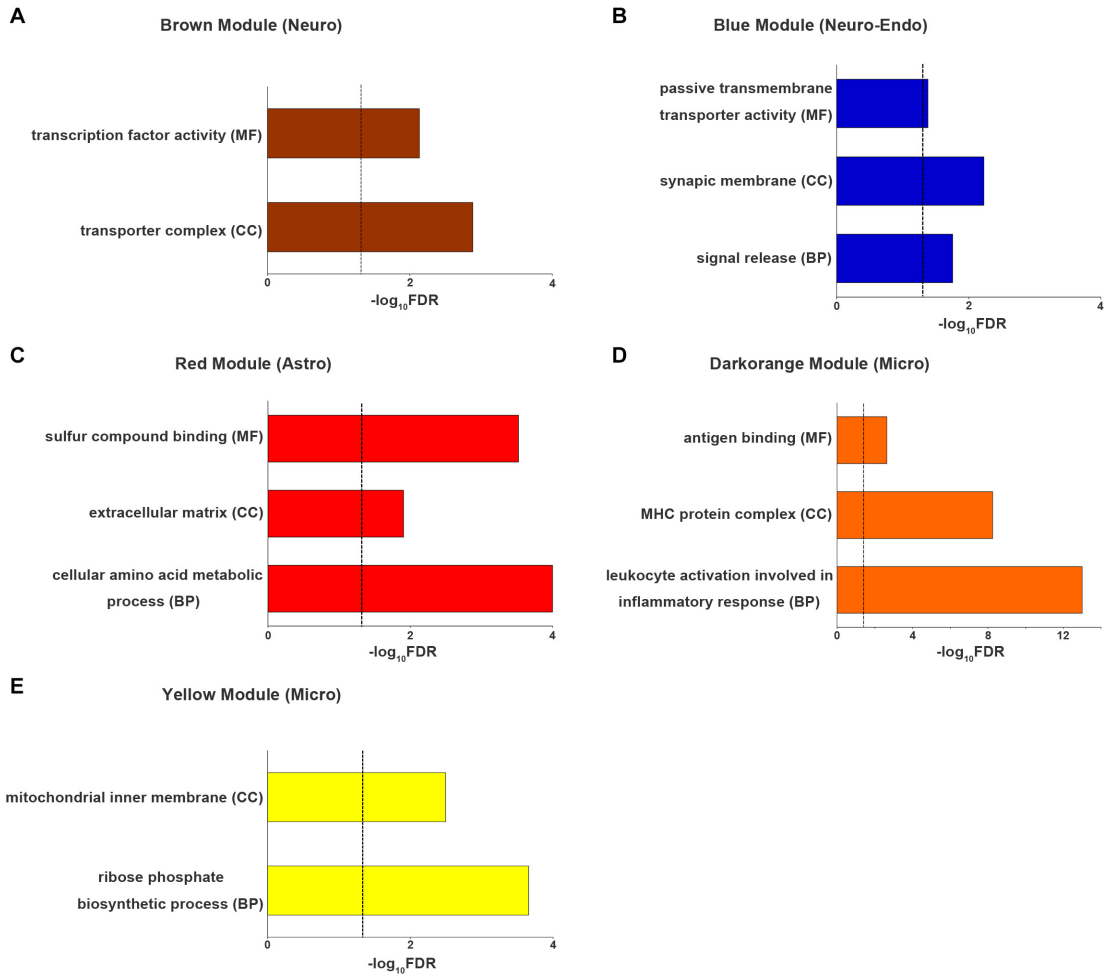

FIGURE 5 | The top enriched Gene Ontology terms for each cell-type-specific module. **(A)** neuron (brown) module, **(B)** neuron-endo (blue) module, **(C)** astrocyte (red) module and **(D,E)** microglia (darkorange and yellow) modules. The dashed line indicates the FDR-corrected threshold. Astro, astrocytoma; BP, biological process; CC, cellular component; Endo, endothelium; Micro, microglia; FDR, the corrected *P* values with the false discovery rate method; MF, molecular function; Neuro, neuron; Oligo, oligodendrocyte.

Our enrichment analysis also provided further evidence that the dark orange microglial module was associated with genetic susceptibility for AD (Hansen et al., 2018). In addition to the characteristic histopathological findings of extracellular amyloid-β (Aβ) plaques and intracellular neurofibrillary tangles (NFTs), the cumulative evidence supports microglia-mediated neuroinflammation as a major contributor to the neurodegenerative processes and cognitive deficits observed in AD (Heneka et al., 2015). Histopathological studies showing activated microglia surrounding Aβ plaques and NFTs suggest a relationship between neuroinflammation and AD pathology (Rozemuller et al., 1992; Sheffield et al., 2000). Neuroinflammation in AD is recognized as a 'double-edged sword' in which microglia exhibit both neuroprotective and neurotoxic effects (Hansen et al., 2018). In the initial phase of AD, moderate activation of microglia exerts an anti-inflammatory function, promoting Aβ clearance and eliminating reactive oxygen and nitrogen species (ROS/RNS) (Ahmad et al., 2019). With the progression of AD, overactivated microglia secrete proinflammatory mediators and upregulate oxidative stress, which may exacerbate Aβ deposition and NFT formation, ultimately leading to progressive neuronal and synaptic damage (Ahmad et al., 2019). By using TSPO to reflect microglial activation, PET imaging allows the visualization and quantification of AD-related neuroinflammatory changes *in vivo* (Varley et al., 2015). Despite conflicting results, it is generally accepted that increased TSPO radioligand binding occurs across brain regions and is correlated with tau aggregation and amyloid deposition (Dani et al., 2018; Edison et al., 2018), which further supports the microglia-mediated neuroinflammation hypothesis for AD. In the dark orange microglial module, a total of five genes associated with AD were identified in both GWAS datasets, most of which were established AD-susceptibility genes (Naj et al., 2011; Guerreiro et al., 2013; Lambert et al., 2013). *MS4A4A* is a member of the *MS4A* gene family and is highly expressed on the plasma membrane in microglia in the brain;

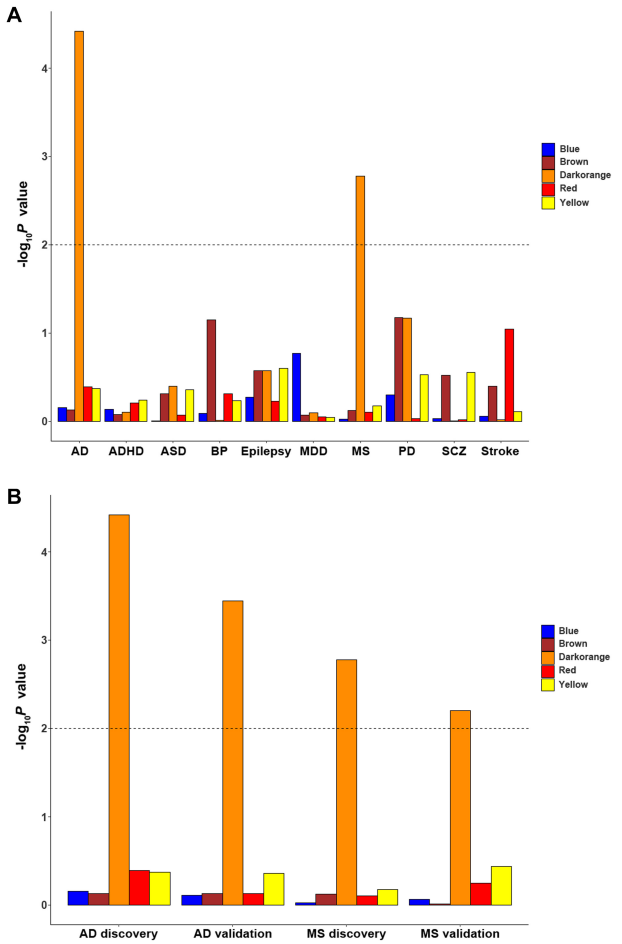

FIGURE 6 | The enrichment of cell-type-specific modules in ten common brain disorders. **(A)** The significant finding is that the microglial module is significantly enriched for MS and AD. **(B)** The discovery and replication enrichment for MS and AD. The dashed line indicates the Bonferroni-corrected threshold for 5 cell-type-specific modules. AD, Alzheimer's disease; ADHD, attention deficit hyperactivity disorder; ASD, autism spectrum disorders; BP, bipolar disorder; EP, epilepsy; MDD, major depressive disorder; MS, multiple sclerosis; SCZ, schizophrenia; PD, Parkinson's disease.

its functions are still poorly understood, but possible roles in protein trafficking and clathrin-dependent endocytosis have been indicated (Cruse et al., 2015). Previous evidence suggested that the expression of *MS4A4A* was increased in the brain tissue of autopsied AD patients (Allen et al., 2012). *TREM2* lies in a cluster of *TREM* family genes and is uniquely expressed on the surface of microglia in the brain (Gao et al., 2017). Mounting evidence indicates that *TREM2* may modulate AD-related neuropathology by suppressing the inflammatory response, increasing Aβ phagocytosis, ameliorating tau pathology and promoting neuronal survival, thus contributing to neuroimmune homeostasis (Yeh et al., 2017). The *HLA-DRA* and *HLA-DRB5* genes are members of MHC class II, a highly polymorphic region involved in the immune response and histocompatibility; both of these genes are predominantly expressed by microglia in the brain and might play a role in susceptibility to AD (Zhang et al., 2015; Villegas-Llerena et al., 2016; Yokoyama et al., 2016). *CD33* belongs to the sialic acid-binding immunoglobulin-like lectin (Siglec) family and is a myeloid cell receptor that is mainly expressed by microglia in the brain (Jiang et al., 2014). The expression of *CD33* is elevated in AD patients' brains, where it is thought to impair Aβ clearance via immunoreactive microglia (Bradshaw et al., 2013; Griciuc et al., 2013).

There are several limitations to our study. First, there are currently no AD and MS patients for whom both gene expression data and ReHo data are available, which prevents us from establishing a causal link between the expression of microglia-related genes and ReHo abnormalities in these two brain disorders. Further replication in patients with MS and AD may provide us with a more complete understanding of the effects of the ReHo-related microglial module on both disorders. Second, for each gray matter voxel of each subject, ReHo is a measure of the temporal coherence of the fluctuation of the mean BOLD signals of this voxel with its nearest 26 neighboring voxels. For each time point, the hemodynamic signal of each voxel is the mean signal of this voxel during a period of TR. Although we cannot exclude the effect of the overlapping signals on ReHo, the similar results derived from fMRI data with different scan parameters (discovery sample and replication sample 1: TR = 2000 ms, voxel size = 3.4 × 3.4 × 3.0 mm with 1 mm gap; replication sample 2: TR = 720 ms, voxel size = 2.0 × 2.0 × 2.0 mm without gap) indicate a relatively small effect of the overlapping signals on ReHo. Third, the zReHo values of neocortical regions used for spatial correlation analysis were derived from the group-level zReHo map, which may loss the information of individual variation. The best way to establish the connection between ReHo and gene expression in a given brain region is to observe their correlation in a large number of individuals with both gene expression data of this region and brain fMRI data to calculate ReHo of this region. However, no such large-scale data are available so far, even for a single brain region. An alternative but suboptimal way is to investigate the spatial correlation between ReHo and gene expression across brain regions in a single subject. Although ReHo values of many brain regions can be easily obtained from fMRI data, gene expression data of many brain regions are available only in a few datasets, such as the AHBA provided six donated postmortem brains with 3702 densely sampled expression data of more than 20,000 genes detected by 58,692 probes. An ideal strategy is to investigate the spatial correlation between ReHo and gene expression derived from the same AHBA subject; however, the fMRI data were not acquired in the AHBA data. Based on the fact that the expression patterns of some genes across brain structures are conserved between individuals (Hawrylycz et al., 2015), several pioneer studies have studied the spatial correlations between the gene expression of postmortem AHBA brains and neuroimaging measures of living human brains and found reasonable associations between gene expression and brain imaging phenotypes (Rittman et al., 2016; Romme et al., 2017; Romero-Garcia et al., 2018; Morgan et al., 2019). In this study, we found that the microglial module was selectively enriched for multiple sclerosis and Alzheimer's disease rather than other

brain disorders, which are well consistent with previous findings (Hansen et al., 2018; Voet et al., 2019). In summary, although the spatial correlation analysis is not the best way to investigate the correlation between ReHo and gene expression, it can still provide useful information about the association of gene expression with ReHo.

Although transcription-neuroimaging spatial correlation analysis identified 14 gene modules that were significantly associated with ReHo in both Chinese and non-Chinese samples, more gene modules (n = 20) were associated with ReHo in non-Chinese than in Chinese (n = 14 for the discovery sample and n = 15 for the replication sample 1). The reasons for this discrepancy between different ethnic populations are complex and are so far known to include (1) the ethnic difference in the association between gene expression and ReHo; (2) the difference in ethnic consistency since three of the six AHBA donors are American Caucasian, but none of them are Chinese; and (3) the differences in spatial and temporal resolutions between the two populations, which may influence the resulting ReHo values.

CONCLUSION

In conclusion, this transcription-neuroimaging association study revealed that the ReHo of spontaneous brain activity was related to gene expression in cell-type-specific modules of neurons, astrocytes, microglia and epithelial cells, indicating a complex cellular architecture of ReHo. Moreover, we linked gene expression in the microglial module to MS and AD, which may provide possible molecular substrates for ReHo abnormalities in both brain disorders.

DATA AVAILABILITY STATEMENT

The original contributions presented in the study are included in the article/**Supplementary Material**, further inquiries can be directed to the corresponding author/s.

ETHICS STATEMENT

The studies involving human participants were reviewed and approved by Medical Research Ethics Committee of Tianjin Medical University. The patients/participants provided their written informed consent to participate in this study. Written informed consent was obtained from the individual(s) for the publication of any potentially identifiable images or data included in this article.

AUTHOR CONTRIBUTIONS

JS and CY conceived of the idea. BY, PZ, WL, and ZY analyzed the fMRI data. ZX, HW, ZZ, JW, and PW analyzed the transcription data. JS, BY, and CY wrote the initial draft. All authors agreed with the final version of the manuscript.

FUNDING

This work was supported by the National Key Research and Development Program of China (2018YFC1314300), the National Natural Science Foundation of China (81601476 and 81701676), and the Tianjin Key Technology R&D Program (17ZXMFSY00090).

SUPPLEMENTARY MATERIAL

The Supplementary Material for this article can be found online at: https://www.frontiersin.org/articles/10.3389/fnins.2021.639527/full#supplementary-material

Supplementary Figure 1 | The mean zReHo maps of discovery sample **(A)**, replication sample 1 **(B)** and replication sample 2 **(C)**.

Supplementary Figure 2 | The cluster dendrogram and 30 gene modules clustered following weighted gene coexpression network analysis.

Supplementary Figure 3 | The spatial correlation between ME and zReHo of each cell-type-specific module with correlation coefficient and Bonferroni-corrected *P* values in replication sample 1. **(A)** Brown module, **(B)** blue module, **(C)** red module, **(D)** dark orange module, **(E)** yellow module. ME, module eigengene; zReHo, z transformed regional homogeneity.

Supplementary Figure 4 | The spatial correlation between ME and zReHo of each cell-type-specific module with correlation coefficient and Bonferroni-corrected *P* values in replication sample 2. **(A)** Brown module, **(B)** blue module, **(C)** red module, **(D)** dark orange module, **(E)** yellow module. ME, module eigengene; zReHo, z transformed regional homogeneity.

Supplementary Figure 5 | The group-level zReHo of three cohorts mapping on cortical surface of the HCP Atlas. **(A)** discovery sample, **(B)** replication sample 1, **(C)** replication sample 2. HCP, Human Connectome Project; L, left hemisphere; R, right hemisphere; zReHo, z transformed regional homogeneity.

Supplementary Figure 6 | The ME values of cell-type-specific modules mapping on cortical surface of the HCP Atlas. **(A)** ME brown, **(B)** ME blue, **(C)** ME red, **(D)** ME darkorange, **(E)** ME yellow. HCP, Human Connectome Project; L, left hemisphere; ME, module eigengene; R, right hemisphere.

Supplementary Table 1 | The 820 neocortical sample coordinates with the corresponding HCP brain regions. HCP, Human Connectome Project; MNI, Montreal Neurological Institute; Parcel Index, parcelation index.

Supplementary Table 2 | The normality test results of ME for all modules across neocortical regions. Note: The Kolmogorov-Smirnov test was applied to check the normality of ME for modules across neocortical regions. ME, module eigengene.

Supplementary Table 3 | The GWAS datasets of common brain disorders involved in this study. GWAS, genome-wide association studies; IGAP, International Genomics of Alzheimer's Project; ILAE, International League Against Epilepsy; IMSGC, International Multiple Sclerosis Genetics Consortium; MEGASTROKE, International Stroke Genetics Consortium; PGC, Psychiatric Genomics Consortium; iPSYCH, Integrative Psychiatric Research Consortium.

Supplementary Table 4 | The significant ReHo-related modules in the discovery sample and replication samples. Note: the significant modules common to the three samples are labeled with bold font. *r*, correlation coefficients between ME and zReHo; *Pc*, Bonferroni-corrected *P* values; ReHo, regional homogeneity.

Supplementary Table 5 | The results of cell-type-specific enrichment analysis in two GSE samples. The significant cell-type-specific ReHo-related modules in both GSE samples are labeled with bold font. Astro, astrocytoma; Endo, endothelium; GSE, gene series expression; Micro, microglia; Neuro, neuron; Oligo, oligodendrocyte; *Pc*, Bonferroni-corrected *P* values; ReHo, regional homogeneity.

Supplementary Table 6 | The significant GO terms in ReHo-related cell-type-specific modules. BP, biological process; CC, cellular component; FDR, the corrected *P* values with the false discovery rate method; GO, gene ontology; MF, molecular function; ReHo, regional homogeneity.

Supplementary Table 7 | The enrichment results for 10 common brain disorders in this study. The significant modules enriched for brain disorders are labeled with bold font. AD, Alzheimer's disease; ADHD, attention deficit hyperactivity disorder; ASD, autism spectrum disorder; BP, bipolar disorder; IGAP, International Genomics of Alzheimer's Project; ILAE, International League Against Epilepsy; IMSGC, International Multiple Sclerosis Genetics Consortium; iPSYCH, Integrative Psychiatric Research Consortium; MDD, major depressive disorder; MEGASTROKE, International Stroke Genetics Consortium; MS, multiple Sclerosis; PD, Parkinson's disease; PGC, Psychiatric Genomics Consortium; *Pc*, Bonferroni-corrected *P* values; SCZ, schizophrenia.

Supplementary Table 8 | The MAGMA gene level analysis results in the microglial module for AD and MS. The significant genes common to both discovery and replication GWAS datasets are labeled with bold font. AD, Alzheimer's disease; IGAP, International Genomics of Alzheimer's Project; IMSGC, International Multiple Sclerosis Genetics Consortium; MAGMA, multi-marker analysis of genomic annotation; MS, multiple sclerosis.

REFERENCES

Ahmad, M. H., Fatima, M., and Mondal, A. C. (2019). Influence of microglia and astrocyte activation in the neuroinflammatory pathogenesis of Alzheimer's disease: rational insights for the therapeutic approaches. *J. Clin. Neurosci.* 59, 6–11. doi: 10.1016/j.jocn.2018.10.034

Airas, L., Rissanen, E., and Rinne, J. O. (2015). Imaging neuroinflammation in multiple sclerosis using TSPO-PET. *Clin. Transl. Imaging* 3, 461–473. doi: 10.1007/s40336-015-0147-6

Allen, M., Zou, F., Chai, H. S., Younkin, C. S., Crook, J., Pankratz, V. S., et al. (2012). Novel late-onset Alzheimer disease loci variants associate with brain gene expression. *Neurology* 79, 221–228. doi: 10.1212/WNL.0b013e3182605801

Anders, S., Pyl, P. T., and Huber, W. (2015). HTSeq–a Python framework to work with high-throughput sequencing data. *Bioinformatics* 31, 166–169. doi: 10.1093/bioinformatics/btu638

Arloth, J., Bader, D. M., Roh, S., and Altmann, A. (2015). Re-annotator: annotation pipeline for microarray probe sequences. *PLoS One* 10:e0139516. doi: 10.1371/journal.pone.0139516

Arnatkevic Iute, A., Fulcher, B. D., and Fornito, A. (2019). A practical guide to linking brain-wide gene expression and neuroimaging data. *Neuroimage* 189, 353–367. doi: 10.1016/j.neuroimage.2019.01.011

Ashburner, M., Ball, C. A., Blake, J. A., Botstein, D., Butler, H., Cherry, J. M., et al. (2000). Gene ontology: tool for the unification of biology. The gene ontology Consortium. *Nat. Genet.* 25, 25–29. doi: 10.1038/75556

Atwood, B. K., Lopez, J., Wager-Miller, J., Mackie, K., and Straiker, A. (2011). Expression of G protein-coupled receptors and related proteins in HEK293, AtT20, BV2, and N18 cell lines as revealed by microarray analysis. *BMC Genomics* 12:14. doi: 10.1186/1471-2164-12-14

Autism Spectrum Disorders Working Group of The Psychiatric Genomics Consortium, (2017). Meta-analysis of GWAS of over 16,000 individuals with autism spectrum disorder highlights a novel locus at 10q24.32 and a significant overlap with schizophrenia. *Mol. Autism* 8:21. doi: 10.1186/s13229-017-0137-9

Balashov, K. E., Rottman, J. B., Weiner, H. L., and Hancock, W. W. (1999). CCR5(+) and CXCR3(+) T cells are increased in multiple sclerosis and their ligands MIP-1alpha and IP-10 are expressed in demyelinating brain lesions. *Proc. Natl. Acad. Sci. U.S.A.* 96, 6873–6878. doi: 10.1073/pnas.96.12.6873

Beecham, A. H., Patsopoulos, N. A., Xifara, D. K., Davis, M. F., Kemppinen, A., Cotsapas, C., et al. (2013). Analysis of immune-related loci identifies 48 new susceptibility variants for multiple sclerosis. *Nat. Genet.* 45, 1353–1360. doi: 10.1038/ng.2770

Bradshaw, E. M., Chibnik, L. B., Keenan, B. T., Ottoboni, L., Raj, T., Tang, A., et al. (2013). CD33 Alzheimer's disease locus: altered monocyte function and amyloid biology. *Nat. Neurosci.* 16, 848–850. doi: 10.1038/nn.3435

Cao, Q., Zang, Y., Sun, L., Sui, M., Long, X., Zou, Q., et al. (2006). Abnormal neural activity in children with attention deficit hyperactivity disorder: a resting-state functional magnetic resonance imaging study. *Neuroreport* 17, 1033–1036. doi: 10.1097/01.wnr.0000224769.92454.5d

Cruse, G., Beaven, M. A., Music, S. C., Bradding, P., Gilfillan, A. M., and Metcalfe, D. D. (2015). The CD20 homologue MS4A4 directs trafficking of KIT toward clathrin-independent endocytosis pathways and thus regulates receptor signaling and recycling. *Mol. Biol. Cell* 26, 1711–1727. doi: 10.1091/mbc.E14-07-1221

Dani, M., Wood, M., Mizoguchi, R., Fan, Z., Walker, Z., Morgan, R., et al. (2018). Microglial activation correlates in vivo with both tau and amyloid in Alzheimer's disease. *Brain* 141, 2740–2754. doi: 10.1093/brain/awy188

Darmanis, S., Sloan, S. A., Zhang, Y., Enge, M., Caneda, C., Shuer, L. M., et al. (2015). A survey of human brain transcriptome diversity at the single cell level. *Proc. Natl. Acad. Sci. U.S.A.* 112, 7285–7290. doi: 10.1073/pnas.1507125112

de Leeuw, C. A., Mooij, J. M., Heskes, T., and Posthuma, D. (2015). MAGMA: generalized gene-set analysis of GWAS data. *PLoS Comput. Biol.* 11:e1004219. doi: 10.1371/journal.pcbi.1004219

Dobin, A., Davis, C. A., Schlesinger, F., Drenkow, J., Zaleski, C., Jha, S., et al. (2013). STAR: ultrafast universal RNA-seq aligner. *Bioinformatics* 29, 15–21. doi: 10.1093/bioinformatics/bts635

Dogonowski, A. M., Andersen, K. W., Madsen, K. H., Sørensen, P. S., Paulson, O. B., Blinkenberg, M., et al. (2013). Multiple sclerosis impairs regional functional connectivity in the cerebellum. *Neuroimage Clin.* 4, 130–138. doi: 10.1016/j.nicl.2013.11.005

Edison, P., Donat, C. K., and Sastre, M. (2018). In vivo imaging of glial activation in Alzheimer's disease. *Front. Neurol.* 9:625. doi: 10.3389/fneur.2018.00625

Elliott, L. T., Sharp, K., Alfaro-Almagro, F., Shi, S., Miller, K. L., Douaud, G., et al. (2018). Genome-wide association studies of brain imaging phenotypes in UK Biobank. *Nature* 562, 210–216. doi: 10.1038/s41586-018-0571-7

Filosa, J. A., Morrison, H. W., Iddings, J. A., Du, W., and Kim, K. J. (2016). Beyond neurovascular coupling, role of astrocytes in the regulation of vascular tone. *Neuroscience* 323, 96–109. doi: 10.1016/j.neuroscience.2015.03.064

Fornito, A., Arnatkeviciute, A., and Fulcher, B. D. (2019). Bridging the gap between connectome and transcriptome. *Trends Cogn. Sci.* 23, 34–50. doi: 10.1016/j.tics.2018.10.005

Frischer, J. M., Bramow, S., Dal-Bianco, A., Lucchinetti, C. F., Rauschka, H., Schmidbauer, M., et al. (2009). The relation between inflammation and neurodegeneration in multiple sclerosis brains. *Brain* 132, 1175–1189. doi: 10.1093/brain/awp070

Fulcher, B. D., Little, M. A., and Jones, N. S. (2013). Highly comparative time-series analysis: the empirical structure of time series and their methods. *J. R. Soc. Interface* 10:20130048. doi: 10.1098/rsif.2013.0048

Gandal, M. J., Haney, J. R., Parikshak, N. N., Leppa, V., Ramaswami, G., Hartl, C., et al. (2018). Shared molecular neuropathology across major psychiatric disorders parallels polygenic overlap. *Science* 359, 693–697. doi: 10.1126/science.aad6469

Gao, L., Jiang, T., Yao, X., Yu, L., Yang, X., and Li, Y. (2017). TREM2 and the progression of Alzheimer's disease. *Curr. Neurovasc. Res.* 14, 177–183. doi: 10.2174/1567202614666170404165201

Glasser, M. F., Coalson, T. S., Robinson, E. C., Hacker, C. D., Harwell, J., Yacoub, E., et al. (2016). A multi-modal parcellation of human cerebral cortex. *Nature* 536, 171–178. doi: 10.1038/nature18933

Gou, N., Liu, Z., Palaniyappan, L., Li, M., Pan, Y., Chen, X., et al. (2018). Effects of DISC1 polymorphisms on resting-state spontaneous neuronal activity in the early-stage of schizophrenia. *Front. Psychiatry* 9:137. doi: 10.3389/fpsyt.2018.00137

Griciuc, A., Serrano-Pozo, A., Parrado, A. R., Lesinski, A. N., Asselin, C. N., Mullin, K., et al. (2013). Alzheimer's disease risk gene CD33 inhibits microglial uptake of amyloid beta. *Neuron* 78, 631–643. doi: 10.1016/j.neuron.2013.04.014

Guerreiro, R., Wojtas, A., Bras, J., Carrasquillo, M., Rogaeva, E., Majounie, E., et al. (2013). TREM2 variants in Alzheimer's disease. *N. Engl. J. Med.* 368, 117–127. doi: 10.1056/NEJMoa1211851

Guo, W. B., Liu, F., Xue, Z. M., Yu, Y., Ma, C. Q., Tan, C. L., et al. (2011). Abnormal neural activities in first-episode, treatment-naive, short-illness-duration, and

treatment-response patients with major depressive disorder: a resting-state fMRI study. *J. Affect. Disord.* 135, 326–331. doi: 10.1016/j.jad.2011.06.048

Hansen, D. V., Hanson, J. E., and Sheng, M. (2018). Microglia in Alzheimer's disease. *J. Cell Biol.* 217, 459–472. doi: 10.1083/jcb.201709069

Hawrylycz, M., Miller, J. A., Menon, V., Feng, D., Dolbeare, T., Guillozet-Bongaarts, A. L., et al. (2015). Canonical genetic signatures of the adult human brain. *Nat. Neurosci.* 18, 1832–1844. doi: 10.1038/nn.4171

He, Y., Wang, L., Zang, Y., Tian, L., Zhang, X., Li, K., et al. (2007). Regional coherence changes in the early stages of Alzheimer's disease: a combined structural and resting-state functional MRI study. *Neuroimage* 35, 488–500. doi: 10.1016/j.neuroimage.2006.11.042

Heneka, M. T., Carson, M. J., El Khoury, J., Landreth, G. E., Brosseron, F., Feinstein, D. L., et al. (2015). Neuroinflammation in Alzheimer's disease. *Lancet Neurol.* 14, 388–405. doi: 10.1016/S1474-4422(15)70016-5

International League Against Epilepsy Consortium on Complex Epilepsies, (2018). Genome-wide mega-analysis identifies 16 loci and highlights diverse biological mechanisms in the common epilepsies. *Nat. Commun.* 9:5269. doi: 10.1038/s41467-018-07524-z

International Multiple Sclerosis Genetics Consortium, (2010). IL12A, MPHOSPH9/CDK2AP1 and RGS1 are novel multiple sclerosis susceptibility loci. *Genes Immun.* 11, 397–405. doi: 10.1038/gene.2010.28

International Multiple Sclerosis Genetics Consortium, (2019). Multiple sclerosis genomic map implicates peripheral immune cells and microglia in susceptibility. *Science* 365:eaav7188. doi: 10.1126/science.aav7188

Jansen, I. E., Savage, J. E., Watanabe, K., Bryois, J., Williams, D. M., Steinberg, S., et al. (2019). Genome-wide meta-analysis identifies new loci and functional pathways influencing Alzheimer's disease risk. *Nat. Genet.* 51, 404–413. doi: 10.1038/s41588-018-0311-9

Jawinski, P., Kirsten, H., Sander, C., Spada, J., Ulke, C., Huang, J., et al. (2019). Human brain arousal in the resting state: a genome-wide association study. *Mol. Psychiatry* 24, 1599–1609. doi: 10.1038/s41380-018-0052-2

Jiang, T., Yu, J. T., Hu, N., Tan, M. S., Zhu, X. C., and Tan, L. (2014). CD33 in Alzheimer's disease. *Mol. Neurobiol.* 49, 529–535. doi: 10.1007/s12035-013-8536-1

Kaur, C., Rathnasamy, G., and Ling, E. A. (2017). Biology of microglia in the developing brain. *J. Neuropathol. Exp. Neurol.* 76, 736–753. doi: 10.1093/jnen/nlx056

Kunkle, B. W., Grenier-Boley, B., Sims, R., Bis, J. C., Damotte, V., Naj, A. C., et al. (2019). Genetic meta-analysis of diagnosed Alzheimer's disease identifies new risk loci and implicates Abeta, tau, immunity and lipid processing. *Nat. Genet.* 51, 414–430. doi: 10.1038/s41588-019-0358-2

Lambert, J. C., Ibrahim-Verbaas, C. A., Harold, D., Naj, A. C., Sims, R., Bellenguez, C., et al. (2013). Meta-analysis of 74,046 individuals identifies 11 new susceptibility loci for Alzheimer's disease. *Nat. Genet.* 45, 1452–1458. doi: 10.1038/ng.2802

Langfelder, P., and Horvath, S. (2008). WGCNA: an R package for weighted correlation network analysis. *BMC Bioinformatics* 9:559. doi: 10.1186/1471-2105-9-559

Liao, Y., Wang, J., Jaehnig, E. J., Shi, Z., and Zhang, B. (2019). WebGestalt 2019: gene set analysis toolkit with revamped UIs and APIs. *Nucleic Acids Res.* 47, W199–W205. doi: 10.1093/nar/gkz401

Liu, J., Qin, W., Wang, H., Zhang, J., Xue, R., Zhang, X., et al. (2014). Altered spontaneous activity in the default-mode network and cognitive decline in chronic subcortical stroke. *J. Neurol. Sci.* 347, 193–198. doi: 10.1016/j.jns.2014.08.049

Liu, P., Li, Q., Zhang, A., Liu, Z., Sun, N., Yang, C., et al. (2020). Similar and different regional homogeneity changes between bipolar disorder and unipolar depression: a resting-state fMRI study. *Neuropsychiatr. Dis. Treat.* 16, 1087–1093. doi: 10.2147/NDT.S249489

Liu, Y., Li, M., Chen, H., Wei, X., Hu, G., Yu, S., et al. (2019). Alterations of regional homogeneity in Parkinson's disease patients with freezing of gait: a resting-state fMRI study. *Front. Aging Neurosci.* 11:276. doi: 10.3389/fnagi.2019.00276

Malik, R., Chauhan, G., Traylor, M., Sargurupremraj, M., Okada, Y., Mishra, A., et al. (2018). Multiancestry genome-wide association study of 520,000 subjects identifies 32 loci associated with stroke and stroke subtypes. *Nat. Genet.* 50, 524–537. doi: 10.1038/s41588-018-0058-3

Maric, M., Arunachalam, B., Phan, U. T., Dong, C., Garrett, W. S., Cannon, K. S., et al. (2001). Defective antigen processing in GILT-free mice. *Science* 294, 1361–1365. doi: 10.1126/science.1065500

Martin, J., Walters, R. K., Demontis, D., Mattheisen, M., Lee, S. H., Robinson, E., et al. (2018). A genetic investigation of sex bias in the prevalence of attention-deficit/hyperactivity disorder. *Biol. Psychiatry* 83, 1044–1053. doi: 10.1016/j.biopsych.2017.11.026

Martin, M. (2011). Cutadapt removes adapter sequences from high-throughput sequencing reads. *EMBnet. J.* 17, 10–12. doi: 10.14806/ej.17.1.200

McCarthy, D. J., Chen, Y., and Smyth, G. K. (2012). Differential expression analysis of multifactor RNA-Seq experiments with respect to biological variation. *Nucleic Acids Res.* 40, 4288–4297. doi: 10.1093/nar/gks042

Metea, M. R., and Newman, E. A. (2006). Glial cells dilate and constrict blood vessels: a mechanism of neurovascular coupling. *J. Neurosci.* 26, 2862–2870. doi: 10.1523/JNEUROSCI.4048-05.2006

Morgan, S. E., Seidlitz, J., Whitaker, K. J., Romero-Garcia, R., Clifton, N. E., Scarpazza, C., et al. (2019). Cortical patterning of abnormal morphometric similarity in psychosis is associated with brain expression of schizophrenia-related genes. *Proc. Natl. Acad. Sci. U.S.A.* 116, 9604–9609. doi: 10.1073/pnas.1820754116

Naj, A. C., Jun, G., Beecham, G. W., Wang, L. S., Vardarajan, B. N., Buros, J., et al. (2011). Common variants at MS4A4/MS4A6E, CD2AP, CD33 and EPHA1 are associated with late-onset Alzheimer's disease. *Nat. Genet.* 43, 436–441. doi: 10.1038/ng.801

Neves, S. R., Ram, P. T., and Iyengar, R. (2002). G protein pathways. *Science* 296, 1636–1639. doi: 10.1126/science.1071550

Paakki, J. J., Rahko, J., Long, X., Moilanen, I., Tervonen, O., Nikkinen, J., et al. (2010). Alterations in regional homogeneity of resting-state brain activity in autism spectrum disorders. *Brain Res.* 1321, 169–179. doi: 10.1016/j.brainres.2009.12.081

Pankratz, N., Beecham, G. W., Destefano, A. L., Dawson, T. M., Doheny, K. F., Factor, S. A., et al. (2012). Meta-analysis of Parkinson's disease: identification of a novel locus, RIT2. *Ann. Neurol.* 71, 370–384. doi: 10.1002/ana.22687

Pardinas, A. F., Holmans, P., Pocklington, A. J., Escott-Price, V., Ripke, S., Carrera, N., et al. (2018). Common schizophrenia alleles are enriched in mutation-intolerant genes and in regions under strong background selection. *Nat. Genet.* 50, 381–389. doi: 10.1038/s41588-018-0059-2

Ramaglia, V., Hughes, T. R., Donev, R. M., Ruseva, M. M., Wu, X., Huitinga, I., et al. (2012). C3-dependent mechanism of microglial priming relevant to multiple sclerosis. *Proc. Natl. Acad. Sci. U.S.A.* 109, 965–970. doi: 10.1073/pnas.1111924109

Ripke, S., Wray, N. R., Lewis, C. M., Hamilton, S. P., Weissman, M. M., Breen, G., et al. (2013). A mega-analysis of genome-wide association studies for major depressive disorder. *Mol. Psychiatry* 18, 497–511. doi: 10.1038/mp.2012.21

Rittman, T., Rubinov, M., Vertes, P. E., Patel, A. X., Ginestet, C. E., Ghosh, B. C. P., et al. (2016). Regional expression of the MAPT gene is associated with loss of hubs in brain networks and cognitive impairment in Parkinson disease and progressive supranuclear palsy. *Neurobiol. Aging* 48, 153–160. doi: 10.1016/j.neurobiolaging.2016.09.001

Robinson, M. D., McCarthy, D. J., and Smyth, G. K. (2010). edgeR: a bioconductor package for differential expression analysis of digital gene expression data. *Bioinformatics* 26, 139–140. doi: 10.1093/bioinformatics/btp616

Romero-Garcia, R., Whitaker, K. J., Vasa, F., Seidlitz, J., Shinn, M., Fonagy, P., et al. (2018). Structural covariance networks are coupled to expression of genes enriched in supragranular layers of the human cortex. *Neuroimage* 171, 256–267. doi: 10.1016/j.neuroimage.2017.12.060

Romme, I. A., De Reus, M. A., Ophoff, R. A., Kahn, R. S., and Van Den Heuvel, M. P. (2017). Connectome disconnectivity and cortical gene expression in patients with schizophrenia. *Biol. Psychiatry* 81, 495–502. doi: 10.1016/j.biopsych.2016.07.012

Rozemuller, J. M., Van Der Valk, P., and Eikelenboom, P. (1992). Activated microglia and cerebral amyloid deposits in Alzheimer's disease. *Res. Immunol.* 143, 646–649. doi: 10.1016/0923-2494(92)80050-u

Sasaki, A. (2017). Microglia and brain macrophages: an update. *Neuropathology* 37, 452–464. doi: 10.1111/neup.12354

Satoh, J., Obayashi, S., Misawa, T., Tabunoki, H., Yamamura, T., Arima, K., et al. (2008). Neuromyelitis optica/Devic's disease: gene expression profiling of brain lesions. *Neuropathology* 28, 561–576. doi: 10.1111/j.1440-1789.2008.00915.x

Schmieder, R., and Edwards, R. (2011). Quality control and preprocessing of metagenomic datasets. *Bioinformatics* 27, 863–864. doi: 10.1093/bioinformatics/btr026

Shang, C. Y., Lin, H. Y., and Gau, S. S. (2019). The norepinephrine transporter gene modulates intrinsic brain activity, visual memory, and visual attention in children with attention-deficit/hyperactivity disorder. *Mol. Psychiatry* [Epub ahead of print]. doi: 10.1038/s41380-019-0545-7

Sheffield, L. G., Marquis, J. G., and Berman, N. E. (2000). Regional distribution of cortical microglia parallels that of neurofibrillary tangles in Alzheimer's disease. *Neurosci. Lett.* 285, 165–168. doi: 10.1016/s0304-3940(00)01037-5

Shukla, D. K., Keehn, B., and Muller, R. A. (2010). Regional homogeneity of fMRI time series in autism spectrum disorders. *Neurosci. Lett.* 476, 46–51. doi: 10.1016/j.neulet.2010.03.080

Singh, S., Metz, I., Amor, S., Van Der Valk, P., Stadelmann, C., and Bruck, W. (2013). Microglial nodules in early multiple sclerosis white matter are associated with degenerating axons. *Acta Neuropathol.* 125, 595–608. doi: 10.1007/s00401-013-1082-0

Smets, I., Fiddes, B., Garcia-Perez, J. E., He, D., Mallants, K., Liao, W., et al. (2018). Multiple sclerosis risk variants alter expression of co-stimulatory genes in B cells. *Brain* 141, 786–796. doi: 10.1093/brain/awx372

Stahl, E. A., Breen, G., Forstner, A. J., Mcquillin, A., Ripke, S., Trubetskoy, V., et al. (2019). Genome-wide association study identifies 30 loci associated with bipolar disorder. *Nat. Genet.* 51, 793–803. doi: 10.1038/s41588-019-0397-8

Sun, H., Luo, L., Yuan, X., Zhang, L., He, Y., Yao, S., et al. (2018). Regional homogeneity and functional connectivity patterns in major depressive disorder, cognitive vulnerability to depression and healthy subjects. *J. Affect. Disord.* 235, 229–235. doi: 10.1016/j.jad.2018.04.061

Van Essen, D. C., Smith, S. M., Barch, D. M., Behrens, T. E., Yacoub, E., and Ugurbil, K. (2013). The WU-minn human connectome project: an overview. *Neuroimage* 80, 62–79. doi: 10.1016/j.neuroimage.2013.05.041

Varley, J., Brooks, D. J., and Edison, P. (2015). Imaging neuroinflammation in Alzheimer's disease and other dementias: recent advances and future directions. *Alzheimers Dement.* 11, 1110–1120. doi: 10.1016/j.jalz.2014.08.105

Villegas-Llerena, C., Phillips, A., Garcia-Reitboeck, P., Hardy, J., and Pocock, J. M. (2016). Microglial genes regulating neuroinflammation in the progression of Alzheimer's disease. *Curr. Opin. Neurobiol.* 36, 74–81. doi: 10.1016/j.conb.2015.10.004

Voet, S., Prinz, M., and Van Loo, G. (2019). Microglia in central nervous system inflammation and multiple sclerosis pathology. *Trends Mol. Med.* 25, 112–123. doi: 10.1016/j.molmed.2018.11.005

Wang, S., Zhang, Y., Lv, L., Wu, R., Fan, X., Zhao, J., et al. (2018). Abnormal regional homogeneity as a potential imaging biomarker for adolescent-onset schizophrenia: a resting-state fMRI study and support vector machine analysis. *Schizophr. Res.* 192, 179–184. doi: 10.1016/j.schres.2017.05.038

Wang, X., Jiao, Y., Tang, T., Wang, H., and Lu, Z. (2013). Altered regional homogeneity patterns in adults with attention-deficit hyperactivity disorder. *Eur. J. Radiol.* 82, 1552–1557. doi: 10.1016/j.ejrad.2013.04.009

Windhagen, A., Newcombe, J., Dangond, F., Strand, C., Woodroofe, M. N., Cuzner, M. L., et al. (1995). Expression of costimulatory molecules B7-1 (CD80), B7-2 (CD86), and interleukin 12 cytokine in multiple sclerosis lesions. *J. Exp. Med.* 182, 1985–1996. doi: 10.1084/jem.182.6.1985

Wu, L., Zhang, Y., Zhou, F., Gao, L., He, L., Zeng, X., et al. (2016). Altered intra- and interregional synchronization in relapsing-remitting multiple sclerosis: a resting-state fMRI study. *Neuropsychiatr. Dis. Treat.* 12, 853–862. doi: 10.2147/NDT.S98962

Wu, T., Long, X., Zang, Y., Wang, L., Hallett, M., Li, K., et al. (2009). Regional homogeneity changes in patients with Parkinson's disease. *Hum. Brain Mapp.* 30, 1502–1510. doi: 10.1002/hbm.20622

Xu, X., Wells, A. B., O'brien, D. R., Nehorai, A., and Dougherty, J. D. (2014). Cell type-specific expression analysis to identify putative cellular mechanisms for neurogenetic disorders. *J. Neurosci.* 34, 1420–1431. doi: 10.1523/JNEUROSCI.4488-13.2014

Xu, Y., Zhuo, C., Qin, W., Zhu, J., and Yu, C. (2015). Altered spontaneous brain activity in schizophrenia: a meta-analysis and a large-sample Study. *Biomed. Res. Int.* 2015:204628. doi: 10.1155/2015/204628

Yao, X., Yin, Z., Liu, F., Wei, S., Zhou, Y., Jiang, X., et al. (2018). Shared and distinct regional homogeneity changes in bipolar and unipolar depression. *Neurosci. Lett.* 673, 28–32. doi: 10.1016/j.neulet.2018.02.033

Yeh, F. L., Hansen, D. V., and Sheng, M. (2017). TREM2, microglia, and neurodegenerative diseases. *Trends Mol. Med.* 23, 512–533. doi: 10.1016/j.molmed.2017.03.008

Yokoyama, J. S., Wang, Y., Schork, A. J., Thompson, W. K., Karch, C. M., Cruchaga, C., et al. (2016). Association between genetic traits for immune-mediated diseases and Alzheimer disease. *JAMA Neurol.* 73, 691–697. doi: 10.1001/jamaneurol.2016.0150

You, H., Wang, J., Wang, H., Zang, Y. F., Zheng, F. L., Meng, C. L., et al. (2011). Altered regional homogeneity in motor cortices in patients with multiple system atrophy. *Neurosci. Lett.* 502, 18–23. doi: 10.1016/j.neulet.2011.07.015

Yu, R., Gollub, R. L., Vangel, M., Kaptchuk, T., Smoller, J. W., and Kong, J. (2014). Placebo analgesia and reward processing: integrating genetics, personality, and intrinsic brain activity. *Hum. Brain Mapp.* 35, 4583–4593. doi: 10.1002/hbm.22496

Zang, Y., Jiang, T., Lu, Y., He, Y., and Tian, L. (2004). Regional homogeneity approach to fMRI data analysis. *Neuroimage* 22, 394–400. doi: 10.1016/j.neuroimage.2003.12.030

Zeng, H., Pizarro, R., Nair, V. A., La, C., and Prabhakaran, V. (2013). Alterations in regional homogeneity of resting-state brain activity in mesial temporal lobe epilepsy. *Epilepsia* 54, 658–666. doi: 10.1111/epi.12066

Zeng, H., Ramos, C. G., Nair, V. A., Hu, Y., Liao, J., La, C., et al. (2015). Regional homogeneity (ReHo) changes in new onset versus chronic benign epilepsy of childhood with centrotemporal spikes (BECTS): a resting state fMRI study. *Epilepsy Res.* 116, 79–85. doi: 10.1016/j.eplepsyres.2015.06.017

Zeng, Q., Guan, X., Lun, J. C. F., Shen, Z., Guo, T., Xuan, M., et al. (2017). Longitudinal alterations of local spontaneous brain activity in Parkinson's disease. *Neurosci. Bull.* 33, 501–509. doi: 10.1007/s12264-017-0171-9

Zhang, Y., Sloan, S. A., Clarke, L. E., Caneda, C., Plaza, C. A., Blumenthal, P. D., et al. (2016). Purification and characterization of progenitor and mature human astrocytes reveals transcriptional and functional differences with mouse. *Neuron* 89, 37–53. doi: 10.1016/j.neuron.2015.11.013

Zhang, Z., Liu, Y., Jiang, T., Zhou, B., An, N., Dai, H., et al. (2012). Altered spontaneous activity in Alzheimer's disease and mild cognitive impairment revealed by regional homogeneity. *Neuroimage* 59, 1429–1440. doi: 10.1016/j.neuroimage.2011.08.049

Zhang, Z. G., Li, Y., Ng, C. T., and Song, Y. Q. (2015). Inflammation in Alzheimer's disease and molecular genetics: recent update. *Arch. Immunol. Ther. Exp.* 63, 333–344. doi: 10.1007/s00005-015-0351-0

Zhao, Z., Tang, C., Yin, D., Wu, J., Gong, J., Sun, L., et al. (2018). Frequency-specific alterations of regional homogeneity in subcortical stroke patients with different outcomes in hand function. *Hum. Brain Mapp.* 39, 4373–4384. doi: 10.1002/hbm.24277

Zheng, L. J., Su, Y. Y., Wang, Y. F., Zhong, J., Liang, X., Zheng, G., et al. (2017). Altered spontaneous brain activity pattern in cognitively normal young adults carrying mutations of APP, presenilin-1/2 and APOE epsilon4. *Eur. J. Radiol.* 95, 18–23. doi: 10.1016/j.ejrad.2017.07.006

Zrzavy, T., Hametner, S., Wimmer, I., Butovsky, O., Weiner, H. L., and Lassmann, H. (2017). Loss of 'homeostatic' microglia and patterns of their activation in active multiple sclerosis. *Brain* 140, 1900–1913. doi: 10.1093/brain/awx113

Zuo, X. N., and Xing, X. X. (2014). Test-retest reliabilities of resting-state FMRI measurements in human brain functional connectomics: a systems neuroscience perspective. *Neurosci. Biobehav. Rev.* 45, 100–118. doi: 10.1016/j.neubiorev.2014.05.009

Zuo, X. N., Xu, T., Jiang, L., Yang, Z., Cao, X. Y., He, Y., et al. (2013). Toward reliable characterization of functional homogeneity in the human brain: preprocessing, scan duration, imaging resolution and computational space. *Neuroimage* 65, 374–386. doi: 10.1016/j.neuroimage.2012.10.017

Conflict of Interest: The authors declare that the research was conducted in the absence of any commercial or financial relationships that could be construed as a potential conflict of interest.

frontiers in Molecular Neuroscience

REVIEW
published: 29 April 2021
doi: 10.3389/fnmol.2021.646072

MicroRNAs Instruct and Maintain Cell Type Diversity in the Nervous System

*Norjin Zolboot[1], Jessica X. Du[1,2], Federico Zampa[1] and Giordano Lippi[1]**

[1] The Scripps Research Institute, La Jolla, CA, United States, [2] Department of Neurosciences, University of California, San Diego, San Diego, CA, United States

Characterizing the diverse cell types that make up the nervous system is essential for understanding how the nervous system is structured and ultimately how it functions. The astonishing range of cellular diversity found in the nervous system emerges from a small pool of neural progenitor cells. These progenitors and their neuronal progeny proceed through sequential gene expression programs to produce different cell lineages and acquire distinct cell fates. These gene expression programs must be tightly regulated in order for the cells to achieve and maintain the proper differentiated state, remain functional throughout life, and avoid cell death. Disruption of developmental programs is associated with a wide range of abnormalities in brain structure and function, further indicating that elucidating their contribution to cellular diversity will be key to understanding brain health. A growing body of evidence suggests that tight regulation of developmental genes requires post-transcriptional regulation of the transcriptome by microRNAs (miRNAs). miRNAs are small non-coding RNAs that function by binding to mRNA targets containing complementary sequences and repressing their translation into protein, thereby providing a layer of precise spatial and temporal control over gene expression. Moreover, the expression profiles and targets of miRNAs show great specificity for distinct cell types, brain regions and developmental stages, suggesting that they are an important parameter of cell type identity. Here, we provide an overview of miRNAs that are critically involved in establishing neural cell identities, focusing on how miRNA-mediated regulation of gene expression modulates neural progenitor expansion, cell fate determination, cell migration, neuronal and glial subtype specification, and finally cell maintenance and survival.

Keywords: microRNA, cell type, CNS – central nervous system, neural progenitor, cell fate, neuron, glia, cell diversity

OPEN ACCESS

Edited by:
Guilherme Lucas,
University of São Paulo, Brazil

Reviewed by:
Eva Maria Jimenez-Mateos,
Trinity College Dublin, Ireland
Davide De Pietri Tonelli,
Italian Institute of Technology (IIT), Italy

***Correspondence:**
Giordano Lippi
glippi@scripps.edu

Received: *24 December 2020*
Accepted: *30 March 2021*
Published: *29 April 2021*

Citation:
Zolboot N, Du JX, Zampa F and Lippi G (2021) MicroRNAs Instruct and Maintain Cell Type Diversity in the Nervous System. Front. Mol. Neurosci. 14:646072. doi: 10.3389/fnmol.2021.646072

INTRODUCTION

Understanding the biological basis of the vast cellular diversity found in the nervous system remains a high priority for neuroscience research. Recent advances in single-cell transcriptomics have enabled the exploration of neural cell diversity with increasing spatial and temporal resolution, generating unprecedented quantitative and comprehensive datasets characterizing the transcriptomes, morphology and electrophysiology of neuronal subtypes (Zeisel et al., 2015, 2018;

Shekhar et al., 2016; Tasic et al., 2016, 2018; Saunders et al., 2018; Gouwens et al., 2019). Moreover, combining single-cell RNA sequencing with techniques such as patch-clamp has allowed scientists to establish direct correspondence between transcriptomic, morphological and physiological datasets leading to a more integrative and multimodal approach of classifying cell types (Cadwell et al., 2016; Fuzik et al., 2016; Földy et al., 2016; Scala et al., 2019; Gouwens et al., 2020). However, the molecular mechanisms that instruct the emergence of cell diversity remain elusive.

There is increasing evidence that microRNAs (miRNAs) can act as key regulators of cellular identity. miRNAs are non-coding RNAs that function as post-transcriptional repressors of mRNA expression. A distinctive feature of miRNAs is that evolution has favored a continual expansion in the miRNA repertoire with increasing number of distinct cell types in an organism (i.e., biological complexity) across metazoans. This is in clear contrast to protein-coding genes, whose number show no correlation to biological complexity. Once miRNAs are added to metazoan genomes and integrated into gene regulatory networks, they are strongly conserved in primary sequence and rarely secondarily lost (Heimberg et al., 2008; Kosik, 2009; Liu et al., 2013). These features strongly suggest that cellular diversity might arise from increasingly sophisticated regulation of gene expression by non-coding RNAs, and in particular by miRNAs.

The expression patterns of miRNAs in the brain show an impressive specificity for distinct developmental stages, brain regions and cell types. A single miRNA is capable of regulating hundreds of different targets and these targets can also vary according to specific cell types and developmental stages (He et al., 2012; Jovičić et al., 2013; Nowakowski et al., 2018). This suggests that the brain utilizes differential miRNA expression and target regulation to establish and maintain cellular diversity. Indeed, during the development of a cell type, miRNAs are known to sharpen developmental stage transitions by repressing residual transcripts specific to the previous stage. Once the cells have achieved a mature differentiation state, miRNAs confer robustness to the developmental decision by reducing fluctuations in gene expression and restricting protein levels within a range of values that maintain cell identity (Ebert and Sharp, 2012).

The dynamic expression patterns of miRNAs, their ability to facilitate developmental transitions and fine-tune protein levels, their conservation as well as their evolutionary expansion with increasing biological complexity all make miRNAs well-suited to instruct and maintain the astonishing cellular diversity found in the nervous system. In this review, we discuss current evidence supporting critical roles for miRNAs in determining cell identity across their developmental trajectory. We describe miRNAs and their targets that are critical throughout neural development from neurulation to neural progenitor expansion, fate determination, neuronal and glial subtype specification, and finally maintenance and survival of these cell types. Furthermore, we also discuss how miRNAs regulate migration, lamination, morphology, and functional connectivity of neurons and glia, all aspects that are integral to cellular identity. A summary of the miRNAs and targets involved in all of these processes are listed in **Table 1**.

NEUROGENESIS AND NEURONAL FATE

Developmental programs generate distinct cell types as opposed to continuous diversity by making distinct lineage decisions, which sequentially narrow the range of possible forms and functions. Early lineage decisions, including those that affect progenitor cells, have enormous power over the developmental trajectories a newly born cell can follow. Progenitor state, which is known to change over developmental time and in response to signaling, sets daughter cells along the path to a neuronal fate or glial fate, biases them to specify into early-born or late-born cell types, and determines their responsiveness to extrinsic maturation cues (Telley and Jabaudon, 2018). In this section, we review how miRNAs affect early stages of cell identity by controlling multiple aspects of progenitor development, from expansion and maintenance of the stem cell population to the production of a range of neuronal subtypes in several different progenitor niches.

Proliferative Progenitors

It is common to interrogate the overall function of miRNAs by examining phenotypes induced by removal of all miRNAs. Mature, functional miRNAs are processed from precursor miRNAs by the endonuclease activity of the enzyme DICER. Thus, DICER knockout prevents miRNA biogenesis and eventually results in functional ablation of the vast majority of miRNAs (Davis and Hata, 2009). While global miRNA ablation is embryonic lethal (Bernstein et al., 2003), conditional and inducible DICER knockouts have provided much insight on the roles miRNAs play in different cell types at each stage of development. Recent reports suggest that well-known miRNA biogenesis enzymes participate in regulatory mechanisms independent of miRNA function, for example by cleaving other classes of RNAs or even regulating DNA repair (Pong and Gullerova, 2018). Thus, DICER knockout studies reflect a ceiling effect, including the effects of removing almost all miRNAs as well as miRNA-independent functions of DICER. Probing the mechanisms of developmental gene regulation at finer resolution will necessarily require disentangling phenotypes and consideration of non-canonical functions of miRNA biogenesis enzymes, but these experiments serve as a starting point for investigating specific miRNA functions, as illustrated by the next few examples.

A study examining miRNA ablation via DICER knockout in Emx1-expressing cortical cells and progenitors found no defect in proliferation or neurogenesis, only defects in later differentiation and survival (de Pietri Tonelli et al., 2008). However, miRNAs may persist long after DICER knockout begins, meaning that this manipulation may not effectively probe miRNA function in early progenitors. miRNA ablation at an earlier timepoint—using Rx-Cre-driven conditional knockout of DICER, which starts at E7.5—caused overt structural defects in the neuroepithelium by disrupting adherens junctions and inducing hyperproliferation of radial glial cells (Fernández et al., 2020). Part of the above phenotype seem to be mediated by miR-302a-d, a member of a miRNA family highly implicated in regulating cell cycle in

TABLE 1 | Summary of the most important miRNAs that instruct the identity of multiple cell types in the nervous system.

CELL type	Developmental processes	miRNA	Known targets	References
Neural progenitors	Proliferation	let-7, miR-125, miR-9, miR-137	lin-28	Rybak et al., 2008
		let-7, miR-9, miR-137	Nr2e1	Zhao et al., 2009
	Proliferation, cell cycle	miR-2115	Orc4	Nowakowski et al., 2018
		miR-302a-d		Parchem et al., 2015
	Proliferation, differentiation	miR-20a, miR-20b, miR-23a	CyclinD1	Ghosh et al., 2014
		miR-934		Prodromidou et al., 2020
		miR-486a/b-5p		Dori et al., 2020
	Neuronal differentiation	miR-124, miR-9	REST, BAF complexes	Yoo et al., 2011; Lee et al., 2018
		miR-124	Ptbp1	Makeyev et al., 2007
Intermediate progenitors	Differentiation	miR-92b	Tbr2	Nowakowski et al., 2013
Retinal progenitors	Neurogenesis, differentiation	let-7, miR-125, miR-9	Prtg, Lin28b	La Torre et al., 2013
Olfactory progenitor cells	Neurogenesis, survival	miR-200a-c, miR-429, miR-141	Mash1	Choi et al., 2008
Adult neurogenic progenitors	Proliferation, progenitor identity	miR-184, miR-34a	Numbl	Shen et al., 2002; Fineberg et al., 2012
	Neuronal differentiation	miR-124	Sox9	Cheng et al., 2009
Cortical pyramidal neurons	Laminar identity	miR-128, let-7b, miR-9		Shu et al., 2019
	Migration	mi-129-3p/5p	Fmr1	Wu et al., 2019
		miR-396-3p, miR-496, miR-543	Cdh2	Rago et al., 2014
	Dendritic outgrowth	miR-101	Slc12a2, Ank2, Kif1a	Lippi et al., 2016
		miR-9		Giusti et al., 2014
Adult-born hippocampal neurons	Migration	miR-19	Rapgef2	Han et al., 2016
	Dendritic outgrowth	miR-132, miR-212		Vo et al., 2005; Magill et al., 2010
		miR-19		Han et al., 2016
Cajal–Retzius cell	Differentiation	miR-9	Foxg1	Shibata et al., 2011
Corticospinal motor neurons	Differentiation, axon growth	miR-409-3p	LMO4	Diaz et al., 2020
Dopamine neurons	Differentiation, survival	miR-133b	Pitx3	Kim et al., 2007
		miR-200c	Zeb2	Yang et al., 2018
Spinal motor neurons	Differentiation, survival	miR-218	Kcnh1	Thiebes et al., 2015; Reichenstein et al., 2019
Dorsal root ganglion neurons	Axon growth	miR-132	Ras1	Hancock et al., 2014
Retinal ganglion cells	Axon growth	miR-182	Cfl1	Bellon et al., 2017
Retinal photoreceptors	Differentiation, morphology	miR-183/96/182 cluster		Busskamp et al., 2014
Olfactory interneurons	Migration, dendritic outgrowth	miR-125		Åkerblom et al., 2014
Olfactory dopamine neurons	Differentiation	miR-7a	Pax6	de Chevigny et al., 2012
Mechanosensory neurons	Subtype specification	miR-183/96/182 cluster	Shox2, Cacna2d1/2	Peng et al., 2018
Microglia	Activation state	miR-128, miR-124	Cebpa	Yang et al., 2017
Oligodendrocytes	Differentiation	miR-219, miR-338	Sox6, Hes5, Zfp238	Dugas et al., 2010; Zhao et al., 2010
		miR-7a	Pax6, NeuroD4	Zhao et al., 2012
		miR-23	LmnB1	Lin and Fu, 2009
	Survival	miR-17/92 cluster	Pten	Budde et al., 2010
Schwann cells	Differentiation, proliferation	miR-34a	Notch1, Ccnd1	Viader et al., 2011
		miR-140	Egr2	Viader et al., 2011
Astrocytes	Differentiation, proliferation	miR-31	lin-28	Meares et al., 2018
		miR-125b		Pogue et al., 2010

For each cell type, the developmental processes and the relevant miRNAs are listed. In addition, known targets of those miRNAs and the main references are indicated (e.g., in human neural progenitors, the timing and duration of the cell cycle is regulated by the great ape-specific miR-2115 through the repression of the DNA replication regulator ORC4).

embryonic stem cells. miR-302a-d is essential to successful brain development in mammals. Knockout of this single miRNA caused profound dysregulation of early neural progenitors: increased proliferation, decreased apoptosis, and premature differentiation of progeny neurons (**Figure 1**, top-left). Ultimately, over-expansion of neural progenitors thickened the neuroepithelium, preventing closure of the neural tube and leading to embryonic lethality (Parchem et al., 2015). Recently, an intriguing hypothesis has been put forward, suggesting that primate-specific miRNAs selectively affect this process.

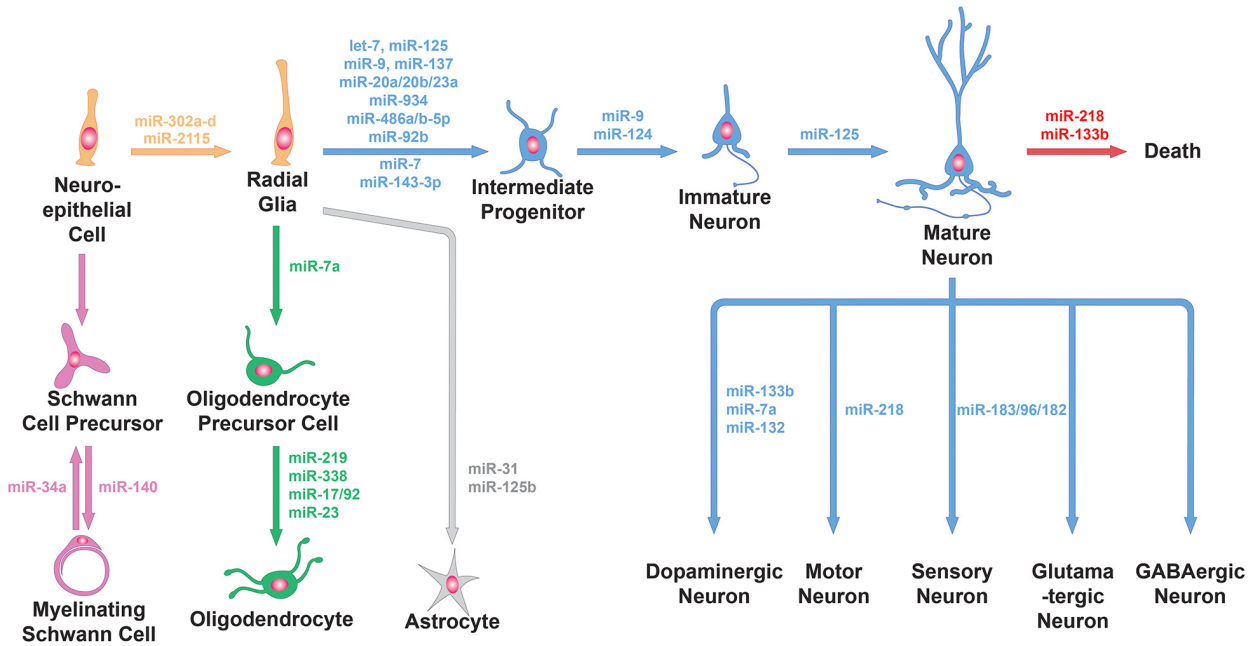

FIGURE 1 | miRNA functions in neural cell lineage. miRNAs are involved in the generation of progenitors from neuroepithelial cells, the differentiation of progenitor cells into neuronal or glial cells, the further specialization of neuronal cells and glial cells into specific subtypes and neuronal survival. Specific examples of miRNAs involved in these processes (e.g., miR-9 and miR-124 for neuronal differentiation, miR-31 for astrocyte differentiation, miR-218 for the specification and survival of motor neurons and miR-34a for Schwann cell dedifferentiation) are shown here.

Timing and duration of the cell cycle in radial glia progenitors is regulated by the great ape-specific miR-2115 through repression of the DNA replication regulator ORC4 (**Figure 1**, top-left). This interaction could provide insight on the evolution of progenitor expansion mechanisms in human brain development (Nowakowski et al., 2018).

While studying the roles of these miRNAs, it is important to remember that miRNAs function in complex networks with their targets, other miRNAs, and other non-coding RNAs. For example, one or multiple miRNAs may target multiple aspects of a cellular pathway or biological process in order to cooperatively regulate neuronal progenitors. This allows miRNAs to substantially boost the magnitude of repression and fine tune the timing of regulation in response to several intersecting cues. In addition, miRNAs and their targets may form regulatory loops for controlling the timing of critical transitions and strongly reinforcing fate decisions. The lin-28 gene supports pluripotency in proliferating stem cells, where it is highly expressed, and simultaneously suppresses the production of mature let-7 and miR-125 (Rybak et al., 2008). When lin-28 expression begins to fall as the cells differentiate, let-7 and miR-125 escape repression and further repress lin-28 translation, forming an auto-regulatory loop that quickly changes gene expression to reinforce the fate decision. Let-7 has also been shown in cancer cell lines to repress multiple other factors involved in proliferation (Johnson et al., 2007; Dong et al., 2010), and in neurons cooperates with miR-9 and miR-137 to repress TLX, again inhibiting progenitor proliferation by downregulating Wnt signaling (Zhao et al., 2009; Sun et al., 2011). Biogenesis of miR-9 and miR-137 is repressed by TLX in unique positive feedback loops. Thus, miRNAs such as let-7 illustrate the complex molecular circuitry required to regulate progenitor proliferation and fate decisions with temporal precision.

MicroRNA regulation of the progenitor pool is the first step required for proper development of the brain architecture and thus foundational to maintaining proper developmental trajectories. Below, we discuss the following stages that are necessary to setting up the cell diversity in the brain.

Cortical and Subcortical Neurogenesis

Neuronal fate appears as progenitors switch from expanding the progenitor pool to producing terminally differentiated neurons or neurogenic progenitors with restricted potency. miRNAs are crucial regulators of these processes. For example, cyclin D1, a key component of cell cycle regulation that affects the balance between progenitor proliferation and neuronal differentiation, both regulates and is regulated by miR-20a, miR-20b, and miR-23a, forming a regulatory loop controlling the transition to neurogenesis and differentiation (Ghosh et al., 2014). Other miRNAs are necessary for progenitor proliferation. miR-486a/b-5p is downregulated as progenitors transition from self-replenishing proliferation to neurogenesis; ectopic expression in radial glia prolongs the proliferative stage, leading to over-expansion of the progenitor pool at the expense of neuron number (Dori et al., 2020). Experiments in human induced pluripotent stem cells (iPSCs) have identified the primate-specific miR-934 as

another potential regulator of this transition, with miR-934 activity during neural induction of stem cells correlating to neurogenesis and decreased numbers of proliferative progenitors (Prodromidou et al., 2020).

Adult neurogenesis requires miRNAs to do the opposite: stably maintain progenitor fate to allow proliferation throughout life. Adult stem cells undergo asymmetric divisions to repopulate the stem cell pool while producing more differentiated progenitors, fated to produce differentiated neurons. miR-184 and miR-34a upregulate Notch signaling in the daughter cell fated for neuronal differentiation by targeting the Notch repressor Numbl (Shen et al., 2002; Fineberg et al., 2012). Meanwhile, this pathway is not active in the other daughter cell, which maintains its stem cell identity and tightly controls further proliferation. Thus, miRNAs play critical roles in controlling progenitor fate, whether that means transitioning to terminal differentiation during development or maintaining stem cell identity in adulthood.

The function of a miRNA can vary depending on the progenitor population, co-expressed factors, and developmental timepoint. miR-9 provides an illustrating example of this complexity. miR-9 overexpression at E11.5, at the start of neurogenesis, increased differentiation of progenitors and caused overproduction of Cajal-Retzius cells, one of the earliest cortical cell types produced and a key director of cortical lamination (Shibata et al., 2008). This stems from dysregulation of Foxg1, a transcription factor thought to promote proliferation and suppress early differentiation, in the cortical hem. However, by E16.5 Foxg1 seems to escape the repressive influence of miR-9; *in vitro* experiments suggest that this is mediated by co-expression of Foxg1 and Elavl2, an RNA binding protein that may block miR-9 from targeting Foxg1's 3′UTR. At these ages, miR-9 seems to decrease cortical progenitor proliferation by repressing other transcription factors such as Pax6, Meis2, and Nr2e1 (Shibata et al., 2011). At the midbrain-hindbrain boundary (MHB), miR-9 expression is repressed in progenitors of since these cells must resist differentiation in order to signal in cell fate decisions in surrounding areas. Ectopic miR-9 expression caused these progenitors to become neurogenic and lose MHB markers (Leucht et al., 2008). miRNA function is modified by changes in the cell type-specific and developmentally regulated network of co-expressed factors, allowing more nuanced control of progenitor and neuronal fate.

During these progenitor transitions, miRNAs may also be regulated by other non-coding RNAs, which can sequester miRNAs at repeated miRNA binding sites—so-called 'miRNA sponges'—thus blocking their function on target mRNAs. miR-7 and the stem cell-expressed lncRNA Cyrano form an autoregulatory loop, with miR-7 overexpression in zebrafish zygotes causing defects in early brain development that are rescued by expression of a miR-7-insensitive mutant Cyrano (Smith et al., 2017; Sarangdhar et al., 2018). Meanwhile Cyrano represses miR-7 by triggering target-directed miRNA degradation, which occurs when miRNAs bind sites with high complementarity extending beyond the seed region into the 3′ region (Han et al., 2020). The primate long non-coding RNA (lncRNA) LncND binds miR-143-3p to prevent repression of Notch signaling and promote proliferation (Rani et al., 2016). Ectopic expression of LncND in mouse embryos during early cortical development significantly increased the population of radial glia and decreased numbers of more differentiated intermediate progenitors (IPs). The human circRNA CDR1as sequesters miR-7; both miR-7 knockdown and exogenous CDR1as expression lead zebrafish to exhibit underdeveloped midbrains (Memczak et al., 2013). The complex loops and network relationships miRNAs form with other classes of ncRNAs contributes to finely tuned control of neurogenesis and potential species-specific mechanisms of brain development.

Neurogenic progenitors can also transition through progenitor subtypes and gradually undergo multipotency restriction. Cortical progenitors—radial glia—divide to generate IPs, which increase the neurogenic capacity of the progenitor pool. miRNAs seem to negatively regulate IP production, in particular through repression of the IP marker Tbr2 by miR-92b (Nowakowski et al., 2013; **Figure 1**, top-left). And when miRNAs are ablated in Emx1-expressing differentiated progenitors, these cells fail to switch from producing deep layer neurons to upper layer neurons (Saurat et al., 2013). By controlling subtypes within the progenitor pool, miRNAs help fine-tune their potencies so that multiple neuron types are produced sequentially and in the correct proportions.

During cortical neurogenesis, progenitors transition from a proliferative state—required for expanding and maintaining the progenitor pool—to a neurogenic state, where they must produce the correct numbers of neurons and lay the foundation for neuronal diversity. The principles of progenitor regulation by miRNAs may also be illustrated in systems outside the cortex, as described briefly in the following section.

Neurogenesis in the Retina and Olfactory Bulb

Lineage relationships and neuronal diversity are relatively well-characterized in the retina and olfactory bulb. These systems provide additional examples of how miRNAs regulate progenitors to ensure that precise numbers and types of neurons are produced. miRNA ablation in retinal progenitors starting at E10.5 caused overproduction of early-born cell types (ganglion and horizontal cells) and failure to produce late-born cell types. These progenitors did not express late progenitor markers, reflecting a defect in progenitor developmental trajectory that ultimately disrupted neurogenesis (Georgi and Reh, 2010). This effect seems to be largely mediated by let-7, miR-125, and miR-9 repression of Prtg and Lin28b (La Torre et al., 2013). In the olfactory system, olfactory progenitor cells (OPCs) rely on a network of several basic helix-loop-helix (bHLH) transcription factors to generate olfactory sensory neurons representing a huge repertoire of olfactory receptors. miRNA ablation in OPCs downregulated key players such as Mash1, inhibited neurogenesis, and induced apoptosis of progenitors, all of which decreased the pool of sensory neurons. These defects were recapitulated by blocking the miR-200 family of five miRNAs (Choi et al., 2008). These

examples show that miRNAs also play key roles regulating neurogenesis in the central nervous system beyond the cortex, sometimes utilizing common mechanisms observed in cortical neurogenesis.

After neurogenesis creates populations of immature neurons, more mechanisms involving miRNAs activate to reinforce neuronal fate and set up the molecular machinery underlying neuronal function.

Determination of Neuronal Fate

As neurogenesis is underway, newly born neurons undergo further changes to embrace their neuronal fate, becoming post-mitotic and activating neuronal global gene expression programs. Neuronal fate determination relies heavily on the expression of miR-9 and miR-124, two of the most abundant and highly enriched miRNAs in neurons (**Figure 1**, top-left). Experiments in differentiating stem cells *in vitro* showed that manipulating these miRNAs changes the proportions of cells differentiating into neurons versus glia (Krichevsky et al., 2006). Ectopic expression of these miRNAs supports conversion of cultured fibroblasts into neurons, including development of neuron-like morphology, marker expression, and electrophysiological responses (Yoo et al., 2011). Neuronal fate determination involves global gene expression programs, so miR-9 and miR-124 must exert huge control over the transcriptional and regulatory landscape of cells. Both miRNAs repress specific subunits of the BAF chromatin-remodeling complex to induce epigenetic changes as part of a previously characterized, evolutionarily conserved neuronal development program (Yoo et al., 2011). They have also been suggested to cooperatively repress the REST transcription repressor complex to promote neuronal transcription programs and suppress the transition to gliogenesis (Krichevsky et al., 2006; Lee et al., 2018). Neurons use alternative splicing extensively to generate essential neuron-specific proteins and to target proteins to unique cellular compartments. PTBP1, a protein known to hinder neuron-specific alternative splicing, is repressed by miR-124 during early development to switch from general to neuron-specific alternative splicing programs, thus promoting neuronal differentiation (Makeyev et al., 2007). Adult neurogenesis in the subventricular zone (SVZ) produces olfactory bulb interneurons; differentiation of these cells from progenitors into neurons is also dependent on miR-124, which may target the stem cell maintenance gene Sox9 (Cheng et al., 2009).

Newly born neurons engage dramatic changes in gene expression and gene regulation to transform themselves from the progeny of stem-like progenitor cells into terminally differentiated neurons. miR-9 and miR-124 are key players in this process, working cooperatively to regulate influential transcriptional and post-transcriptional modifiers. Specification of neuronal fate then sets the stage for further differentiation into finer neuronal subtypes.

Specification of Neuronal Subtypes

MicroRNAs reinforce additional fate decisions that allow neurons to differentiate into subtypes with distinct molecular characteristics. Among cortical PNs, corticospinal motor neurons (CSMNs) of layer V and callosal projection neurons (CPNs) of layers II/III and V form the corticospinal tract and corpus callosum, two main white matter tracts that are unique to placental mammals and that contribute to the functional and cell type complexity of these brains. miR-409-3p suppresses CPN fate in favor of CSMN development by downregulating LMO4, a transcription factor known to promote CPN areal identity. Layer V CSMN and CPN are born from the same progenitors and initially all express LMO4, so miR-409-3p is thought to mediate divergence of these two cell types (Diaz et al., 2020). Meanwhile, cortical inhibitory interneurons are born in several progenitor zones distant from the cortex and specify into different subtypes depending on which progenitor population they derived from. The medial ganglionic eminence (MGE) produces the cortical interneuron subtypes marked by expression of somatostatin (SST) or parvalbumin (PV). After miRNA ablation in all MGE cells, these interneurons failed to express SST or PV, indicating that miRNAs are necessary for interneuron subtype fate determination (Tuncdemir et al., 2015). While many of the miRNA-regulated molecular pathways regulating interneuron specification must still be characterized, it is clear that miRNAs are crucial for proper subtype specification.

There is also evidence that miRNAs help specify neuronal subtypes outside of the cortex. Olfactory sensory neurons produced by progenitors lacking DICER failed to express mature marker genes and olfactory receptors, indicating a differentiation defect in addition to decreased neurogenesis (Choi et al., 2008). The fate determination of spinal motor neurons (MNs) is also regulated by miRNAs. Generic spinal MN identity is established by cooperative binding of the LIM complex comprising ISL1 and LHX3 to MN-specific enhancers, thereby inducing the expression of a battery of MN genes that induce functional hallmarks of MNs, while suppressing key interneuron genes. The LIM complex highly and directly upregulates miR-218 at the onset of MN differentiation. miR-218 is specifically expressed in MNs throughout spinal cord development and is necessary for establishing MN fate while suppressing interneuron fate both *in vitro* and *in vivo* (Thiebes et al., 2015; **Figure 1**, bottom-right). miR-218 is also critical for mature MN maintenance and function, which we will discuss below. For a more detailed discussion on the role of miRNAs in the neurogenesis of spinal MNs we refer the readers to this review (Chen and Chen, 2019).

Together, these studies show that miRNAs coordinate progenitor proliferation and identity, neurogenesis, and adoption of neuronal fate. In doing so, they play critical roles in laying the groundwork for functional differentiation into neuronal subtypes and development of brain regions. We will now explore how miRNAs continue to guide cell type specification in postmitotic neurons by regulating migration and lamination, development of morphology and connectivity, and molecular identity.

MIGRATION AND LAMINATION

Neuronal progenitors reside in bounded niches of the developing brain; to build other brain regions, they come in contact with

neurons from other lineages, and form functional circuits, neurons must move out of progenitor zones after neurogenesis. Migration of newly born neurons must be precisely coordinated with other developmental processes, since migratory routes vary depending on cell identity and have been shown to influence morphological and functional development (Lim et al., 2018). For populations such as neural crest cells, it is known that migration along stereotyped routes helps resolve subtype identity, perhaps by bringing cells in contact with sequences of environmental signals (Soldatov et al., 2019). Lamination, the process of arranging cells in layers such as the six layers of cortex, relies on migration routes that specify final laminar positions. Cells in different layers may come from different lineages or birthdates, express distinct markers, form different connections and projections, and take on different microcircuit roles, meaning that lamination is closely tied up with cell identity. Defects in migration and lamination, as in the case of Type I lissencephaly, can induce additional phenotypes in morphology and firing properties (Ekins et al., 2020). Thus, migration, though a transient part of a neuron's development, is a lasting influence on neuronal subtype diversity.

MicroRNA-mediated control of neuronal development includes migration and decisions made along the migratory path. In the cortex, DICER ablation in MGE-derived GABAergic interneurons induces a migration defect in addition to defects in mature marker expression. Interneurons must migrate tangentially from progenitor zones to reach and disperse throughout the cortex, after which they switch to radial migration and enter the cortical layers. Without miRNAs, many of these cells fail to enter the superficial migratory streams, causing a reduction in the number of interneurons reaching the cortex. These interneurons also show a defect in radially migrating into the cortical plate, contributing to reduced interneurons number across the cortical layers (Tuncdemir et al., 2015). However, the roles of specific miRNAs in this phenotype is still under investigation.

Meanwhile, excitatory pyramidal neurons (PNs) migrate radially from the ventricular progenitor zones. The combinatorial expression levels of miR-128, miR-9, and let-7b in radial glia modulate the lamination of the PNs they produce, including the proportions of cells that migrate into each layer. While miR-128 and let-7b seem to encode deep- and upper-layer identity in a dose-dependent manner, miR-9 specifically promotes development of layer V identity (Shu et al., 2019). Since the position of these cells in specific cortical layers is key to their function in stereotyped cortical microcircuits, this manipulation affects development of cortical cell types. Expression of miR-129-3p and miR-129-5p also controls migration across different PN identities. Upregulating or suppressing expression of these miRNAs causes PNs to fail to reach or overshoot their target layers, respectively, without affecting the expression of layer-specific marker genes. This effect is mediated by miR-129 repression of Fmr1, a gene associated with neurodevelopmental disorders. Cells overexpressing miR-129 were less likely to adopt a bipolar morphology, a key step preceding radial migration (Wu et al., 2019). Thus, miRNAs are able to control neuronal migration in coordination with layer identity, a key aspect of cortical cell type.

In some cases, we know that miRNAs directly regulate the molecular mechanisms of migration. Neurons follow fibers extended by radial glia across the cortical plate to climb into the cortical layers; they interact with these fibers through N-cadherin on the cell membrane. The miR-379/410 cluster regulates the expression of N-cadherin in both cortical progenitors and neurons. Simultaneously manipulating the expression of three miRNAs in this cluster—miR-396-3p, miR-496, and miR-543—reversibly controls the rate of migration out of the ventricular zone. Interestingly, overexpression of these miRNAs individually did not affect N-cadherin expression or induce a migration phenotype, but overexpressing pairs of miRNAs can bias neurons to migrate into the deep or upper layers (Rago et al., 2014). Elucidating the cooperative relationships between these miRNAs may further illustrate the complexity of miRNA network function in developing neurons. Meanwhile, altered miR-19 expression is associated with neurodevelopmental defects (Celli et al., 2003; Hemmat et al., 2014), suggesting that this miRNA plays an important role in neuronal development. While the mechanisms underlying the function of miR-19 in early development remain unclear, one study has found that miR-19 promotes migration of adult-born neurons born in the dentate gyrus, thus affecting their final position within the granule cell layer. miR-19 represses Rapgef2, a Rap1 and Rap2 activator known to influence cell adhesion and migration (Han et al., 2016).

MicroRNA control of migration, whether through affecting large programs coordinating layer identity or by directly affecting the molecular migration machinery, is an important contributor to the developmental trajectory of a cell. Laminar positioning then contributes to how a neuron integrates into circuits and takes on mature functions. Next, we continue along this developmental trajectory by examining miRNA functions in morphological and functional development.

MORPHOLOGY AND FUNCTIONAL CONNECTIVITY

Neuronal morphology was historically the main way of categorizing cells and remains a key indicator of cell type and function. For example, parvalbumin (PV)-expressing interneurons share fast-spiking electrophysiological characteristics and of course expression of PV, but can be categorized further into basket cells, chandelier cells, and translaminar cells by their morphologies, which reflect diverging connectivity and circuit functions. By regulating the growth and elaboration of neuronal compartments, miRNAs control the development of cell type-specific characteristics.

Cell and Neurite Morphology

MicroRNA function can have drastic effects on neurite outgrowth, and hence affect the function of individual cell types. This is evidenced by experiments where DICER was knocked out in postmitotic cortical pyramidal neurons. Loss of

miRNAs caused dramatic reductions in soma size and neurite growth, which compounded into decreased brain size (Hong et al., 2013). miRNA ablation via knockout of Dgcr8, another component of the canonical miRNA biogenesis pathway, also in postmitotic pyramidal neurons revealed additional phenotypes in inhibitory synapse development: reduced PV interneuron abundance, reduced inhibitory synapse formation, and reduced IPSC amplitude and frequency (Hsu et al., 2012). DICER knockout in D1R-expressing striatal neurons also reduced cell size, leading to smaller brain size and profound defects in movement and behavior (Cuellar et al., 2008). Postnatal DICER knockout in cerebellar Purkinje cells caused gradual dendritic degeneration and spine loss, with eventual cell death and tissue degeneration (Schaefer et al., 2007). These dramatic phenotypes—from the neuronal level all the way to gross brain structure—suggest that miRNAs are crucial for multiple aspects of morphological development in neurons.

In addition, specific mechanisms mediated by individual miRNAs have been shown to regulate specific morphological characteristics such as dendritic outgrowth and maturation. miR-101 regulates dendrite development and scales overall network excitability through multiple parallel mechanisms. NKCC1 is a chloride channel that is downregulated as part of the GABA switch, when neuronal responses to GABA switch from excitation to inhibition. In this study blocking miR-101 repression of NKCC1 impaired neuronal functional maturation and increased spontaneous activity, which in turn increased dendritic growth and excitatory synapses. Derepression of other miR-101 targets, namely Ank2 and Kif1a, caused further hyperexcitability by producing and stabilizing more excitatory synapses (Lippi et al., 2016). miR-9 has key roles in neuronal fate determination; later in development, its repression of the REST complex also acts to increase dendritic length and complexity (Giusti et al., 2014). miR-132 and miR-212, contained in the same locus, have been shown to promote dendrite growth *in vitro* and in adult-born hippocampal neurons (Vo et al., 2005; Magill et al., 2010). In conjunction to its role in migration, miR-19 also regulates the development of mature morphology in adult-born hippocampal neurons. miR-19 overexpression led to decreased dendritic length and dendritic branching and prevented spines from becoming mature mushroom spines. Since miR-19 expression is high only in progenitor cells and turns off as neurons differentiate, it may control neuronal specification programs such as morphological maturation (Han et al., 2016).

Morphological development, including aspects of cell size, neurite growth, and spine formation, requires miRNA function. Elaboration of axons and dendrites must be coordinated with processes such as axon pathfinding, formation of specific synaptic connections, and circuit wiring, which will be explored in the following section.

Functional Connectivity and Circuit Integration

Developing synaptic connections and integrating into circuits is fundamental to the functional maturation of any neuron. The arborization and targeting of dendrites and axons is specific to each cell type and carefully regulated during brain development. DICER knockout in dorsal root ganglion (DRG) neurons reduced axon growth *in vivo* and thus significantly reduced innervation of peripheral tissues. Inhibition of miR-132 phenocopies miRNA ablation *in vitro*. This effect has been suggested to be mediated by miR-132 repression of Rasa1, a Ras GTPase-activating protein known to respond to guidance cues, locally in axons (Hancock et al., 2014). Axon extension and targeting is critical to the functional development of retinal ganglion cells (RGCs), which must, in zebrafish, extend axons to the correct regions of the optic tectum. miR-182 regulates this process by repressing translation of Cfl1, part of the signaling cascade that responds to axon guidance cue Slit2 (Bellon et al., 2017). miR-409-3p promotes specification of CSMN fate over other projection neuron fates, and this includes the specific axon targeting of CSMNs. Overexpression of miR-409-3p caused more cells to not only express CSMN markers, but also to extend axons to the internal capsule, functionally joining the corticospinal tract (Diaz et al., 2020).

Olfactory interneurons provide a case where a specific miRNA has been shown to control the trajectory of a cell's functional development, in a way that specifies distinct trajectories for developmentally- and adult-born neurons. The olfactory bulb contains interneurons born during early development in the olfactory bulb, and interneurons born during adulthood from subventricular adult progenitors. Early-born interneurons mature and integrate into circuits rapidly, while adult-born interneurons first migrate to the olfactory bulb and then slowly integrate into existing olfactory circuitry over several weeks. They form two distinct cell types, with different lineages, physiological characteristics, morphology, and roles in odor discrimination. miR-125 is expressed in only in the adult-born population, and inhibition of miR-125 leads to increased dendritic arborization in the olfactory bulb and abnormally early functional integration. This was assayed by quantifying *Fos* expression in 1-week-old interneurons following exposure to various odor stimuli. Thus miR-125 seems to control the timing of functional development in adult-born interneurons (Åkerblom et al., 2014; **Figure 1**, top-right).

In the cortex, perturbations in specification of one cell type can disrupt circuit formation, leading to additional abnormalities in other cell types and network-level defects. Cortical VIP-expressing interneurons disinhibit PNs by axonal targeting of other cortical interneurons. They play a key role in regulating network activity of cortical circuits, so disruption of VIP interneurons can negatively affect proper cortical function and development. VIP interneurons with postmitotic DICER ablation initially followed a normal developmental trajectory but exhibited progressive cell death in adulthood. Mature VIP interneurons also showed altered electrophysiological characteristics and deficits in synaptic inputs, leading to increased PN excitability and overall cortical activity (Qiu et al., 2020). These findings suggest that miRNAs are indispensable for maintaining the normal function of VIP interneurons, which have far-reaching effects on cortical circuit development and overall network function.

We have now seen that miRNAs guide newly born neurons through a complex series of developmental processes, including migration, morphological elaboration, and circuit integration. Next, we will examine how miRNAs interact with the transcriptomic environment of cells on unique developmental trajectories to resolve them into distinct cell types.

NEURONAL SUBTYPE DETERMINATION AND FUNCTION

In addition to their role in neural progenitor identity, cell fate determination and various developmental processes, miRNAs contribute to the diversity of cell types found in the nervous system. Not only do miRNAs exhibit developmental stage-specific expression patterns, but they also have distinct cell-type specific expression patterns. Indeed, miRNA expression profiles vary greatly across neurons and glial cell types including astrocytes, oligodendrocytes and microglia (Jovičić et al., 2013). Furthermore, from an unbiased screen in mouse, He et al. (2012) discovered that hundreds of miRNAs are enriched in different neuronal subtypes, such as cerebellar Purkinje neurons, cortical glutamatergic neurons, GABAergic INs, and even in different subtypes of INs. These findings strongly suggest an important role for miRNAs in neural cell type specification and maintenance. The identity of different neuronal and glial cell types is determined by combinatorial expression of transcription factors. Post-transcriptional regulation of their expression by miRNAs acts a network-level control mechanism that serves as a critical tuner of precise and robust identities. Below, we describe the specific miRNAs and their transcription factor targets involved in the determination of different neuronal subtypes such as dopaminergic (DA) neurons, spinal MNs and various sensory neurons.

Dopaminergic Neurons

During development, transcription factors are known to operate in feedforward and feedback loops with miRNAs to reinforce lineage commitment. These are often negative feedback loops involving a cell type-specific miRNA, where the miRNA represses the transcription factor that induced its expression to prevent reverting to the previous developmental stage (Ebert and Sharp, 2012). For instance, miR-133b is specifically expressed in and regulates the maturation and function of midbrain DA neurons within a negative feedback loop that includes the transcription factor PITX3 (**Figure 1**, bottom-right). In this feedback loop, PITX3 specifically induces transcription of miR-133b, and miR-133b positively regulates dopaminergic neuron numbers in mouse primary midbrain cultures by downregulating PITX3 (Kim et al., 2007). In another example, a negative feedback loop involving the transcription factor ZEB2 and miR-200c was shown to control the expression and function of several key genes of midbrain DA neuron development (Yang et al., 2018; **Figure 1**, bottom-right). Among these genes was *Nr4a2*, which encodes for a transcription factor required for the generation of midbrain DA neurons. NR4A2 is also a known target of miR-132 (Yang et al., 2012; **Figure 1**, bottom-right). These examples highlight the specific miRNA/transcription factor loops involved in midbrain DA neuron differentiation.

The differentiation of olfactory bulb DA neurons is also under the regulation of a miRNA/transcription factor interaction. The transcription factor PAX6 is an important determinant of DA neurons in the olfactory bulb. In the postnatal and adult mouse forebrain, several olfactory bulb neuron subtypes are generated from a mosaic of neural stem cells that are spatially organized along the lateral ventricle. Olfactory bulb DA neurons are mainly generated from progenitors localized to the dorsal region of the ventricle. The mRNA of PAX6 is transcribed widely along the ventricular walls, but PAX6 protein expression is restricted to the dorsal region. This dorsal restriction was found to be a result of inhibition of PAX6 protein expression by miR-7a. Furthermore, *in vivo* inhibition of miR-7a in PAX6-negative regions of the lateral wall induces PAX6 protein expression and increased DA neuron number in the olfactory bulb (de Chevigny et al., 2012). Regulation of PAX6 by miRNAs has also been implicated in activity-dependent neurotransmitter switching between DA and GABA in developing *Xenopus* olfactory bulb interneurons in response to kinship odorants (Dulcis et al., 2017). This study found that miR-375 and miR-200b facilitate the switch between dopaminergic and GABAergic interneurons by targeting PAX6 and BCL11B, respectively. These findings highlight how regulation by miRNAs can alter neuronal identity.

Motor Neurons

In addition to the differentiation of DA neurons in the midbrain and olfactory bulb, miRNAs have also been proven indispensable for the proper function of postnatal spinal MNs. In particular, a miRNA that is necessary to establish MN fate, miR-218, is also necessary for mature MNs (**Figure 1**, bottom-right). Mutant mice lacking miR-218 exhibit neuromuscular junction defects, MN hyperexcitability, and progressive MN cell loss (Amin et al., 2015). The relevance of miR-218 in proper function of MNs was further established with the discovery that miR-218 is downregulated in human amyotrophic lateral sclerosis (ALS). In this study the authors identified the potassium channel KV10.1 as a novel miR-218 target that regulates neuronal activity. From sequencing thousands of ALS genomes, they also identified six rare miR-218-2 gene variants that failed to regulate neuronal activity due to reduced processing by DICER, further highlighting the importance of miR-218 in MNs (Reichenstein et al., 2019).

Sensory Neurons

Sensory neurons provide another set of examples, where cell type-specific miRNAs and their transcription factor targets interact to regulate neuronal subtype determination. The miR-183/96/182 cluster is highly expressed in sensory neurons and plays a role in regulating the molecular and functional identities of multiple different subtypes. Myelinated (A-fiber type) low-threshold mechanoreceptors (LTMRs) terminate peripherally in the skin and participate in touch sensation. There are three types of myelinated LTMRs: Aδ LTMRs, Aβ rapidly adapting LTMRs and Aβ slowly adapting (Aβ SA) LTMRs. Conditional loss of the miR-183/96/182 cluster in mice leads to a failure to

extinguish expression of the transcription factor SHOX2 during development and an increase in the proportion of Aδ LTMRs at the expense of Aβ SA-LTMRs. Conversely, overexpression of the miR-183/96/182 cluster that represses SHOX2 expression, or loss of SHOX2, both increase the Aβ SA-LTMR population at the expense of Aδ LTMRs (Peng et al., 2018; **Figure 1**, bottom-right). Furthermore, the miR-183/96/182 cluster was shown to regulate the function of Aδ LTMRs by scaling acute noxious mechanical sensitivity by regulating CACNA2D1 and 2 and modulating neuronal excitability (Peng et al., 2017). The miR-183/96/182 cluster is also particularly important in photoreceptors, where it is highly expressed with peak levels in the adult retina. Cone-specific loss of miRNAs led to reduced expression of cone-specific genes and gradual degeneration of the outer segments, resulting in photoreceptors with reduced light responses (**Figure 1**, bottom-right). Re-expression of miR-183 and miR-182 prevented these phenotypes. The miR-183/96/182 cluster was also necessary and sufficient for the formation of inner segments, connecting cilia and short outer segments, as well as light responses in stem-cell-derived retinal cultures (Busskamp et al., 2014). The studies discussed above demonstrate the critical role of the miR-183/96/182 cluster in not only sensory neuron subtype determination but for their proper function. In addition, miRNAs were also found necessary for the retinal pigmented epithelium (RPE), which plays key supportive roles in photoreceptor development and function. Without miRNAs, RPE cells developed abnormal cellular morphology, underwent de-pigmentation, and showed defects in enzyme production, all of which contributed to non-cell-autonomous defects in photoreceptor differentiation (Ohana et al., 2015). In summary, in this section we have described how specific miRNAs can determine and maintain the identity of a wide variety of neuronal subtypes, through mechanisms that target a lineage's unique transcriptome. Next, we discuss how miRNAs regulate various aspects of glial cell identity.

GLIAL SUBTYPE DETERMINATION, MORPHOLOGY AND FUNCTION

In recent years, numerous studies have demonstrated the importance of miRNAs in the development of various glial cell lineages such as Schwann cells (SCs) in the peripheral nervous system (PNS) and astrocytes, oligodendrocytes and microglia in the CNS. Below we summarize the critical miRNAs and their targets that regulate the differentiation, morphology, and function of these four glial subtypes.

Microglia

Microglia are the resident macrophages of the CNS that represent the first line of immune defense in the brain and spinal cord. They originate from early yolk sac myeloid progenitors and infiltrate the brain during early development. In their steady state, microglia mainly function to maintain brain homeostasis and upon injury or infection microglia transform to an activated state. Emerging evidence continue to show that microglia are in fact a multifunctional housekeeping cell type that contributes to many aspects of brain development such as neural circuit wiring, neuronal survival, synaptogenesis, synaptic transmission and myelination (Thion and Garel, 2020; Cserép et al., 2021). Microglia-specific DICER ablation during embryonic development results in spontaneous microglial activation and accumulation of DNA damage (Varol et al., 2017). Consistent with this finding, there are numerous miRNAs known to inhibit microglia activation, which are described in detail here (Guo et al., 2019). Microglia are usually activated into two polarized states, termed the classical "M1" phenotype that releases destructive pro-inflammatory mediators and the alternative "M2" phenotype, which produces protective factors. Two neuronal enriched miRNAs, miR-128 and miR-124 is known to regulate microglia polarization. In a spinal cord injury (SCI) mouse model, miR-128 was downregulated in microglial cells and overexpression of miR-128 promoted viability of microglia and increased the expression levels of M2 phenotypic markers (Yang et al., 2017). miR-124 was also found to promote M2-like polarization by increasing the expression levels of M2 markers and decreasing M1 markers expression after injury (Hamzei Taj et al., 2016). It was further demonstrated that in a steady state, miR-124 can directly target C/EBP-α, a master transcription factor involved in differentiation of myeloid cells and its downstream target PU.1 and promote microglia quiescence (Ponomarev et al., 2011). Thus, miRNAs are critical for mediating microglial activation and polarization.

Oligodendrocytes

Oligodendrocytes are a unique glial cell type in the CNS that synthesizes multilamellar myelin membranes which ensheath axons. Myelination electrically insulates axons to promote rapid, energy-efficient action potential propagation and is thus crucial for the development and function of the CNS. Two independent studies demonstrated that DICER ablation in oligodendrocyte precursor cells (OPCs) disrupts proper CNS myelination and delays oligodendrocyte differentiation (Dugas et al., 2010; Zhao et al., 2010). These studies identified miR-219 and miR-338 as oligodendrocyte-specific miRNAs and showed that overexpression of these miRNAs is sufficient to promote oligodendrocyte differentiation. miR-219 and miR-338 function in part by directly repressing negative regulators of oligodendrocyte differentiation SOX6, HES5, and ZFP238 (**Figure 1**, bottom-left). miR-7a is also highly enriched in OPCs, overexpression of which in NPCs or embryonic mouse cortex promoted oligodendrocyte generation. Blocking miR-7a function instead resulted reduction in oligodendrocyte number and an expansion of neuronal populations. miR-7a may exert these functions by directly targeting proneuronal transcription factors including PAX6 and NEUROD4 (Zhao et al., 2012; **Figure 1**, bottom-left). Finally, miR-23 has been shown to promote oligodendrocyte differentiation by downregulating Lamin 1B, a crucial determinant of oligodendrocyte maturation and myelin formation, whose overexpression was shown to suppress oligodendrocyte-specific genes (Lin and Fu, 2009; **Figure 1**, bottom-left). These studies together demonstrate the crucial role of miRNAs in promoting oligodendrocyte differentiation.

Schwann Cells

Schwann cells are the principal glial cells in the PNS, where they play essential roles in the development, maintenance, function and regeneration of peripheral nerves. SCs can be categorized into two major classes - myelinating and nonmyelinating SCs. Myelinating SCs provide the myelin ensheathment of all large-diameter peripheral axons, while nonmyelinating SCs typically associate with smaller axons. Several studies have shown that DICER ablation in SCs fully arrests their differentiation and ability to myelinate. Gene expression analyses from these studies revealed drastic downregulation of promyelinating transcription factors KROX20 (Pereira et al., 2010) and EGR2 (Yun et al., 2010) and upregulation of myelination inhibitors NOTCH1 and HES1 (Pereira et al., 2010). Yun et al. (2010) also showed that DICER-ablated SCs maintained expression of genes characterizing the undifferentiated SC state, such as *Sox2, Jun, and Ccnd1,* providing some basis for the arrested differentiation of SCs. Further experiments will be required to determine the specific miRNAs and their targets that regulate SC differentiation and function (Bremer et al., 2010). Following axonal loss, SCs have the striking ability to dedifferentiate to an immature-like state, proliferate transiently, and help support axonal regeneration. As peripheral axons regenerate, SCs re-differentiate to form new myelin sheaths, helping to restore peripheral nerve function (Jessen and Mirsky, 2016). A miRNA profiling study in SCs following nerve injury found that most SC miRNAs were downregulated in response to injury, facilitating the de-differentiation process, which involves large-scale changes in gene expression. Shortly after axonal regrowth these expression levels of these SC miRNAs were restored. Most of these injury-regulated miRNAs were computationally predicted to target positive regulators of SC dedifferentiation and proliferation that must be repressed for proper SC re-differentiation to occur. In particular, the authors found that miR-34a targets NOTCH1 and CCND1, and miR-140 targets EGR2 to modulate dedifferentiation/proliferation and remyelination, respectively (Viader et al., 2011; **Figure 1**, bottom-left). Altogether these studies indicate that miRNAs are critical for facilitating SC differentiation and maintaining the differentiated state of mature SCs.

Astrocytes

Astrocytes are the most abundant cell type in the CNS and are crucial regulators of neuronal development, function and connectivity. Thus, it is not surprising that astrocyte-specific DICER ablation results in drastic phenotypes across multiple regions in the brain. These phenotypes range from deficits in dendritic spine development in cortical and hippocampal neurons (Sun et al., 2019) to major behavioral phenotypes such as ataxia, seizures and ultimately premature death (Tao et al., 2011). The cerebellum was found to be particularly susceptible to insults caused by astrocytic DICER ablation, largely due to dysfunction of Bergmann glia (BG), specialized astrocytes that serve as scaffolds during early postnatal cerebellar development. DICER-ablated BG exhibited thickened, swollen processes preceding cerebellar degeneration and ataxia, suggesting that miRNAs have a direct role in the morphology and function of BG (Tao et al., 2011). A different study showed that, in addition to morphological defects, embryonic DICER ablation in astrocytes results in decreased expression of BG markers and an intrinsic blockage of Notch signaling. Notch signaling is crucial for the maintenance of BG during postnatal cerebellar development. Furthermore, the authors found that miR-9 is required for proper Notch1 signaling in early postnatal BG (Kuang et al., 2012). Recent studies have implicated more miRNAs in astrocyte development and function. miR-31, a miRNA enriched in differentiated astrocytes, is required for terminal astrocyte differentiation as the loss of miR−31 impairs differentiation and prevents astrocyte maturation *in vitro* (**Figure 1**, bottom-left). This function is mediated in part by miR-31 targeting of LIN28, a stem cell factor implicated in neural progenitor cells (Meares et al., 2018). Another *in vitro* study showed that miR-125b positively regulates astrogliogenesis and promotes astrocyte proliferation (Pogue et al., 2010; **Figure 1**, bottom-left). Finally, a FMRP-dependent miRNA-mediated mechanism has been shown to alter developmental astroglial mGluR5 signaling, which is important for mediating developmental astroglia to neuron communication. Selective loss of FMRP in mouse and human astroglia *in vivo* was shown to upregulate a brain-enriched miRNA, miR-128-3p, which in turn suppressed developmental expression of astroglial mGluR5. mGluR5 expression was not altered in FMRP-deficient neurons, highlighting an astroglia-specific mechanism (Men et al., 2020). These studies demonstrate the crucial role of miRNAs in of astrocyte differentiation, morphology and function. Overall, we have outlined how miRNAs are critically involved in various developmental processes of distinct glial subtypes found in the nervous system.

CELL MAINTENANCE AND SURVIVAL

Seeing as miRNAs are necessary for developing the characteristics of cell type—including laminar position, morphology, connectivity, and molecular markers—it is not surprising that they also play key roles in maintaining these cell types. Differentiated neurons must tightly regulate gene expression to remain functional throughout life and avoid cell death. Continual miRNA regulation buffers potentially harmful changes in gene expression and stabilizes a cell's identity over its lifetime. Decreased miRNA function, by allowing harmful changes in identity and gene expression networks, may contribute to neurodegeneration. Recent studies have also suggested that many miRNAs repress pro-apoptotic genes, such that miRNA misexpression or gain-of-function mutations may provide cancerous cells with a mechanism of escaping apoptosis, making miRNA dysfunction a potential "second hit" during oncogenesis (Bejarano et al., 2021). The following examples will highlight degenerative phenotypes caused by miRNA dysfunction in the brain, in glial cells, and in other CNS neurons, such as those of the spinal cord.

Reduced miRNA function caused by hemizygous DICER knockout in adult DA neurons reduced levels of DA and other molecules in DA metabolic pathways, while complete DICER knockout led to severe DA neuron death, especially in the substantia nigra (Chmielarz et al., 2017). Dysfunction and progressive loss of DA neurons underlies Parkinson's

disease (PD), leading some to hypothesize that age-related decline in miRNA function may contribute to PD pathology. miRNA biogenesis has been observed to decline with age, and pharmacological stimulation of miRNA biogenesis improved DA neuron survival after cellular stress. Downregulation of midbrain-enriched miRNAs, such as miR-133b, may contribute to the selective vulnerability of DA neurons (Kim et al., 2007; **Figure 1**, top-right). miRNA ablation in cerebellar Purkinje cells eventually leads to cell death following morphological degeneration (Schaefer et al., 2007), and MGE-derived GABAergic interneurons also show increased apoptosis after DICER knockout (Tuncdemir et al., 2015). A specific subtype of interneurons, VIP interneurons were also found to exhibit progressive cell death with postmitotic DICER knockout (Qiu et al., 2020).

During development, oligodendrocytes are greatly overproduced and only by competing for limiting amounts of target-derived growth factors is their number adjusted according to the number and length of the axons requiring myelination. The miR-17/92 cluster was shown to regulate this culling process of oligodendrocytes by promoting their proliferation through activation of the Akt signaling pathway (Budde et al., 2010). Postnatal ablation of DICER in microglia found that absence of miRNAs does not induce spontaneous activation or morphological abnormalities but results in reduced microglia number, highlighting a role for miRNAs in microglia survival during adulthood (Varol et al., 2017).

Without miR-218-1 and miR-218-2, spinal MNs are born in normal numbers but fail to innervate muscles and die off in large numbers before birth (Amin et al., 2015; **Figure 1**, top-right). Proprioceptive DRG neurons express PV late in development, meaning that conditional DICER knockout driven PV expression ablates miRNAs in only more mature cells. These mutant mice initially develop normally, with normal proprioceptive DRG neuron number and function, but show progressive proprioceptive DRG neuron loss and locomotor defects by P30. Cell death is preceded by disruption of cell identity, as evidenced by downregulation of proprioceptor-enriched genes, upregulation of markers for other cell types, and decreased responsiveness to vibration (O'Toole et al., 2017). DICER knockout in mature, postmitotic rod photoreceptors lead to outer segment disorganization in adult mice, followed by robust retinal degeneration and eventual loss of visual function. Interestingly, these mice did not exhibit significant defects in either phototransduction or the visual cycle prior to retinal degeneration, suggesting that miRNAs in rods primarily function to support their survival (Sundermeier et al., 2014).

In addition to developmental establishment of cellular diversity, miRNA function throughout life is necessary to maintenance of cell identity and health. Dysfunction of miRNA networks can induce degenerative phenotypes and may contribute to the mechanisms or the cell type-specificity of some neurodegenerative diseases.

DISCUSSION

Numerous reports over the last two decades have shown that miRNA-mediated posttranscriptional regulation is indispensable at basically all stages of brain assembly. Although the majority of these studies are focused on developmental transitions, here we argue that the same mechanisms also demonstrate that miRNAs are key determinant of cell identity. By reinforcing the transcriptional programs underlying lineage decisions, miRNAs instruct the emergence and maintenance of many cell types of the brain. Further, miRNAs are necessary building blocks in the molecular pathways controlling lamination, differentiation and proper connectivity, processes through which neurons take on the characteristics essential to their cell type. Despite this wealth of data, we believe that the field is still in its infancy. In fact, miRNA roles have only been tested in a small percentage of brain cell types. Even for the ones tested, detailed miRNA mechanisms are for the most part still missing. Finally, owing to advances in sequencing technologies, the field is rapidly progressing from studying a single miRNA and a few of its targets to identifying miRNA-target networks associated with distinct cell types and developmental stages (Nowakowski et al., 2018). This effort is complemented by new technologies that allow precise mapping of miRNA-target interactions (mTI) in specific cell types (Tan et al., 2013; Li et al., 2020). Integrating miRNA and target expression profile with mTI mapping will deliver, for the first time, the landscape of miRNA repression in specific cell types. The necessary next step will be to develop scalable tools that effectively manipulate mTI so that their functional roles in instructing cell identity can be tested. The combination of these technologies will reveal novel mechanisms driving cellular diversity in the brain and spawn a new era of miRNA research.

AUTHOR CONTRIBUTIONS

NZ and JD wrote the review with help from FZ and GL. All authors contributed to the article and approved the submitted version.

FUNDING

This work was supported by a grant from the Whitehall Foundation (2018-12-55) and by start-up money from The Scripps Research Institute (NIH NINDS 5R01NS121223).

REFERENCES

Åkerblom, M., Petri, R., Sachdeva, R., Klussendorf, T., Mattsson, B., Gentner, B., et al. (2014). microRna-125 distinguishes developmentally generated and adult-born olfactory bulb interneurons. *Development* 141, 1580–1588. doi: 10.1242/dev.101659

Amin, N. D., Bai, G., Klug, J. R., Bonanomi, D., Pankratz, M. T., Gifford, W. D., et al. (2015). Loss of motoneuron-specific microRNA-218 causes systemic neuromuscular failure. *Science* 350, 1525–1529. doi: 10.1126/science.aad2509

Bejarano, F., Chang, C. H., Sun, K., Hagen, J. W., Deng, W. M., and Lai, E. C. (2021). A comprehensive in vivo screen for anti-apoptotic miRNAs indicates

broad capacities for oncogenic synergy. *Dev. Biol.* 475, 10–20. doi: 10.1016/j.ydbio.2021.02.010

Bellon, A., Iyer, A., Bridi, S., Lee, F. C. Y., Ovando-Vázquez, C., Corradi, E., et al. (2017). miR-182 regulates Slit2-mediated axon guidance by modulating the local translation of a specific mRNA. *Cell Rep.* 18, 1171–1186. doi: 10.1016/j.celrep.2016.12.093

Bernstein, E., Kim, S. Y., Carmell, M. A., Murchison, E. P., Alcorn, H., Li, M. Z., et al. (2003). Dicer is essential for mouse development. *Nat. Genet.* 35, 215–217. doi: 10.1038/ng1253

Bremer, J., O'Connor, T., Tiberi, C., Rehrauer, H., Weis, J., and Aguzzi, A. (2010). Ablation of Dicer from murine Schwann cells increases their proliferation while blocking myelination. *PLoS One* 5:e12450. doi: 10.1371/journal.pone.0012450

Budde, H., Schmitt, S., Fitzner, D., Opitz, L., Salinas-Riester, G., and Simons, M. (2010). Control of oligodendroglial cell number by the miR-17-92 cluster. *Development* 137, 2127–2132. doi: 10.1242/dev.050633

Busskamp, V., Krol, J., Nelidova, D., Daum, J., Szikra, T., Tsuda, B., et al. (2014). MiRNAs 182 and 183 are necessary to maintain adult cone photoreceptor outer segments and visual function. *Neuron* 83, 586–600. doi: 10.1016/j.neuron.2014.06.020

Cadwell, C. R., Palasantza, A., Jiang, X., Berens, P., Deng, Q., Yilmaz, M., et al. (2016). Electrophysiological, transcriptomic and morphologic profiling of single neurons using Patch-seq. *Nat. Biotechnol.* 34, 199–203. doi: 10.1038/nbt.3445

Celli, J., Van Bokhoven, H., and Brunner, H. G. (2003). Feingold syndrome: clinical review and genetic mapping. *Am. J. Med. Genet.* 122A, 294–300. doi: 10.1002/ajmg.a.20471

Chen, T. H., and Chen, J. A. (2019). Multifaceted roles of microRNAs: from motor neuron generation in embryos to degeneration in spinal muscular atrophy. *Elife* 8:e50848. doi: 10.7554/eLife.50848

Cheng, L. C., Pastrana, E., Tavazoie, M., and Doetsch, F. (2009). miR-124 regulates adult neurogenesis in the subventricular zone stem cell niche. *Nat. Neurosci.* 12, 399–408. doi: 10.1038/nn.2294

Chmielarz, P., Konovalova, J., Najam, S. S., Alter, H., Piepponen, T. P., Erfle, H., et al. (2017). Dicer and microRNAs protect adult dopamine neurons. *Cell Death Dis.* 8:e2813. doi: 10.1038/cddis.2017.214

Choi, P. S., Zakhary, L., Choi, W. Y., Caron, S., Alvarez-Saavedra, E., Miska, E. A., et al. (2008). Members of the miRNA-200 family regulate olfactory neurogenesis. *Neuron* 57, 41–55. doi: 10.1016/j.neuron.2007.11.018

Cserép, C., Pósfai, B., and Dénes, Á (2021). Shaping neuronal fate: functional heterogeneity of direct microglia-neuron interactions. *Neuron* 109, 222–240. doi: 10.1016/j.neuron.2020.11.007

Cuellar, T. L., Davis, T. H., Nelson, P. T., Loeb, G. B., Harfe, B. D., Ullian, E., et al. (2008). Dicer loss in striatal neurons produces behavioral and neuroanatomical phenotypes in the absence of neurodegeneration. *Proc. Natl. Acad. Sci. U.S.A.* 105, 5614–5619. doi: 10.1073/pnas.0801689105

Davis, B. N., and Hata, A. (2009). Regulation of microRNA biogenesis: a miRiad of mechanisms. *Cell Commun. Signal.* 7:18. doi: 10.1186/1478-811X-7-18

de Chevigny, A., Coré, N., Follert, P., Gaudin, M., Barbry, P., Béclin, C., et al. (2012). MiR-7a regulation of Pax6 controls spatial origin of forebrain dopaminergic neurons. *Nat. Neurosci.* 15, 1120–1126. doi: 10.1038/nn.3142

de Pietri Tonelli, D., Pulvers, J. N., Haffner, C., Murchison, E. P., Hannon, G. J., and Huttner, W. B. (2008). miRNAs are essential for survival and differentiation of newborn neurons but not for expansion of neural progenitors during early neurogenesis in the mouse embryonic neocortex. *Development* 135, 3911–3921. doi: 10.1242/dev.025080

Diaz, J. L., Siththanandan, V. B., Lu, V., Gonzalez-Nava, N., Pasquina, L., MacDonald, J. L., et al. (2020). An evolutionarily acquired microRNA shapes development of mammalian cortical projections. *Proc. Natl. Acad. Sci. U.S.A.* 117, 29113–29122. doi: 10.1073/pnas.2006700117

Dong, Q., Meng, P., Wang, T., Qin, W., Qin, W., Wang, F., et al. (2010). MicroRNA let-7a inhibits proliferation of human prostate cancer cells in vitro and in vivo by targeting E2F2 and CCND2. *PLoS One* 5:e10147. doi: 10.1371/journal.pone.0010147

Dori, M., Cavalli, D., Lesche, M., Massalini, S., Alieh, L. H. A., De Toledo, B. C., et al. (2020). MicroRNA profiling of mouse cortical progenitors and neurons reveals miR-486-5p as a regulator of neurogenesis. *Development* 147:dev190520. doi: 10.1242/dev.190520

Dugas, J. C., Cuellar, T. L., Scholze, A., Ason, B., Ibrahim, A., Emery, B., et al. (2010). Dicer1 and miR-219 are required for normal oligodendrocyte differentiation and myelination. *Neuron* 65, 597–611. doi: 10.1016/j.neuron.2010.01.027

Dulcis, D., Lippi, G., Stark, C. J., Do, L. H., Berg, D. K., and Spitzer, N. C. (2017). Neurotransmitter switching regulated by miRNAs controls changes in social preference. *Neuron* 95, 1319–1333.e5. doi: 10.1016/j.neuron.2017.08.023

Ebert, M. S., and Sharp, P. A. (2012). Leading edge review roles for MicroRNAs in conferring robustness to biological processes. *Cell* 149, 515–524. doi: 10.1016/j.cell.2012.04.005

Ekins, T. G., Mahadevan, V., Zhang, Y., D'Amour, J. A., Akgül, G., Petros, T., et al. (2020). Emergence of non-canonical parvalbumin-containing interneurons in hippocampus of a murine model of type I lissencephaly. *Elife* 9:e62373. doi: 10.7554/eLife.62373

Fernández, V., Martínez−Martínez, M. Á, Prieto−Colomina, A., Cárdenas, A., Soler, R., Dori, M., et al. (2020). Repression of Irs2 by let−7 miRNAs is essential for homeostasis of the telencephalic neuroepithelium. *EMBO J.* 39:e105479. doi: 10.15252/embj.2020105479

Fineberg, S. K., Datta, P., Stein, C. S., and Davidson, B. L. (2012). MiR-34a represses Numbl in murine neural progenitor cells and antagonizes neuronal differentiation. *PLoS One* 7:e38562. doi: 10.1371/journal.pone.0038562

Földy, C., Darmanis, S., Aoto, J., Malenka, R. C., Quake, S. R., and Südhof, T. C. (2016). Single-cell RNAseq reveals cell adhesion molecule profiles in electrophysiologically defined neurons. *Proc. Natl. Acad. Sci. U.S.A.* 113, E5222–E5231. doi: 10.1073/pnas.1610155113

Fuzik, J., Zeisel, A., Mate, Z., Calvigioni, D., Yanagawa, Y., Szabo, G., et al. (2016). Integration of electrophysiological recordings with single-cell RNA-seq data identifies neuronal subtypes. *Nat. Biotechnol.* 34, 175–183. doi: 10.1038/nbt.3443

Georgi, S. A., and Reh, T. A. (2010). Dicer is required for the transition from early to late progenitor state in the developing mouse retina. *J. Neurosci.* 30, 4048–4061. doi: 10.1523/JNEUROSCI.4982-09.2010

Ghosh, T., Aprea, J., Nardelli, J., Engel, H., Selinger, C., Mombereau, C., et al. (2014). MicroRNAs establish robustness and adaptability of a critical gene network to regulate progenitor fate decisions during cortical neurogenesis. *Cell Rep.* 7, 1779–1788. doi: 10.1016/j.celrep.2014.05.029

Giusti, S. A., Vogl, A. M., Brockmann, M. M., Vercelli, C. A., Rein, M. L., Trümbach, D., et al. (2014). MicroRNA-9 controls dendritic development by targeting REST. *Elife* 3:e02755. doi: 10.7554/eLife.02755

Gouwens, N. W., Sorensen, S. A., Baftizadeh, F., Budzillo, A., Lee, B. R., Jarsky, T., et al. (2020). Toward an integrated classification of neuronal cell types: morphoelectric and transcriptomic characterization of individual GABAergic cortical neurons. *bioRxiv* [Preprint]. doi: 10.1101/2020.02.03.932244

Gouwens, N. W., Sorensen, S. A., Berg, J., Lee, C., Jarsky, T., Ting, J., et al. (2019). Classification of electrophysiological and morphological neuron types in the mouse visual cortex. *Nat. Neurosci.* 22, 1182–1195. doi: 10.1038/s41593-019-0417-0

Guo, Y., Hong, W., Wang, X., Zhang, P., Körner, H., Tu, J., et al. (2019). MicroRNAs in microglia: how do MicroRNAs affect activation, inflammation, polarization of microglia and mediate the interaction between microglia and glioma? *Front. Mol. Neurosci.* 12:125. doi: 10.3389/fnmol.2019.00125

Hamzei Taj, S., Kho, W., Riou, A., Wiedermann, D., and Hoehn, M. (2016). MiRNA-124 induces neuroprotection and functional improvement after focal cerebral ischemia. *Biomaterials* 91, 151–165. doi: 10.1016/j.biomaterials.2016.03.025

Han, J., Kim, H. J., Schafer, S. T., Paquola, A., Clemenson, G. D., Toda, T., et al. (2016). Functional implications of miR-19 in the migration of newborn neurons in the adult brain. *Neuron* 91, 79–89. doi: 10.1016/j.neuron.2016.05.034

Han, J., Lavigne, C. A., Jones, B. T., Zhang, H., Gillett, F., and Mendell, J. T. (2020). A ubiquitin ligase mediates target-directed microRNA decay independently of tailing and trimming. *Science* 370:eabc9546. doi: 10.1126/science.abc9546

Hancock, M. L., Preitner, N., Quan, J., and Flanagan, J. G. (2014). MicroRNA-132 is enriched in developing axons, locally regulates Rasa1 mRNA, and promotes axon extension. *J. Neurosci.* 34, 66–78. doi: 10.1523/JNEUROSCI.3371-13.2014

He, M., Liu, Y., Wang, X., Zhang, M. Q., Hannon, G. J., and Huang, Z. J. (2012). Cell-type-based analysis of microRNA profiles in the mouse brain. *Neuron* 73, 35–48. doi: 10.1016/j.neuron.2011.11.010

Heimberg, A. M., Sempere, L. F., Moy, V. N., Donoghue, P. C. J., and Peterson, K. J. (2008). MicroRNAs and the advent of vertebrate morphological complexity. *Proc. Natl. Acad. Sci. U.S.A.* 105, 2946–2950. doi: 10.1073/pnas.0712259105

Hemmat, M., Rumple, M. J., Mahon, L. W., Strom, C. M., Anguiano, A., Talai, M., et al. (2014). Short stature, digit anomalies and dysmorphic facial features are

associated with the duplication of miR-17 ∼ 92 cluster. *Mol. Cytogenet.* 7:27. doi: 10.1186/1755-8166-7-27

Hong, J., Zhang, H., Kawase-Koga, Y., and Sun, T. (2013). MicroRNA function is required for neurite outgrowth of mature neurons in the mouse postnatal cerebral cortex. *Front. Cell. Neurosci.* 7:151. doi: 10.3389/fncel.2013.00151

Hsu, R., Schofield, C. M., Dela Cruz, C. G., Jones-Davis, D. M., Blelloch, R., and Ullian, E. M. (2012). Loss of microRNAs in pyramidal neurons leads to specific changes in inhibitory synaptic transmission in the prefrontal cortex. *Mol. Cell. Neurosci.* 50, 283–292. doi: 10.1016/j.mcn.2012.06.002

Jessen, K. R., and Mirsky, R. (2016). The repair Schwann cell and its function in regenerating nerves. *J. Physiol.* 594, 3521–3531. doi: 10.1113/JP270874

Johnson, C. D., Esquela-Kerscher, A., Stefani, G., Byrom, M., Kelnar, K., Ovcharenko, D., et al. (2007). The let-7 microRNA represses cell proliferation pathways in human cells. *Cancer Res.* 67, 7713–7722. doi: 10.1158/0008-5472.CAN-07-1083

Jovičić, A., Roshan, R., Moisoi, N., Pradervand, S., Moser, R., Pillai, B., et al. (2013). Comprehensive expression analyses of neural cell-type-specific miRNAs identify new determinants of the specification and maintenance of neuronal phenotypes. *Ann. Intern. Med.* 158, 5127–5137. doi: 10.1523/JNEUROSCI.0600-12.2013

Kim, J., Inoue, K., Ishii, J., Vanti, W. B., Voronov, S. V., Murchison, E., et al. (2007). A microRNA feedback circuit in midbrain dopamine neurons. *Science* 317, 1220–1224. doi: 10.1126/science.1140481

Kosik, K. S. (2009). MicroRNAs tell an evo-devo story. *Nat. Rev. Neurosci.* 10, 754–759. doi: 10.1038/nrn2713

Krichevsky, A. M., Sonntag, K.-C., Isacson, O., and Kosik, K. S. (2006). Specific microRNAs modulate embryonic stem cell-derived neurogenesis. *Stem Cells* 24, 857–864. doi: 10.1634/stemcells.2005-0441

Kuang, Y., Liu, Q., Shu, X., Zhang, C., Huang, N., Li, J., et al. (2012). Dicer1 and MiR-9 are required for proper Notch1 signaling and the Bergmann glial phenotype in the developing mouse cerebellum. *Glia* 60, 1734–1746. doi: 10.1002/glia.22392

La Torre, A., Georgi, S., and Reh, T. A. (2013). Conserved microRNA pathway regulates developmental timing of retinal neurogenesis. *Proc. Natl. Acad. Sci. U.S.A.* 110, E2362–E2370. doi: 10.1073/pnas.1301837110

Lee, S. W., Oh, Y. M., Lu, Y. L., Kim, W. K., and Yoo, A. S. (2018). MicroRNAs overcome cell fate barrier by reducing EZH2-controlled REST stability during neuronal conversion of human adult fibroblasts. *Dev. Cell* 46, 73–84.e7. doi: 10.1016/j.devcel.2018.06.007

Leucht, C., Stigloher, C., Wizenmann, A., Klafke, R., Folchert, A., and Bally-Cuif, L. (2008). MicroRNA-9 directs late organizer activity of the midbrain-hindbrain boundary. *Nat. Neurosci.* 11, 641–648. doi: 10.1038/nn.2115

Li, X., Pritykin, Y., Concepcion, C. P., Lu, Y., La Rocca, G., Zhang, M., et al. (2020). High-resolution in vivo identification of miRNA Targets by Halo-Enhanced Ago2 pull-down. *Mol. Cell* 79, 167–179.e11. doi: 10.1016/j.molcel.2020.05.009

Lim, L., Mi, D., Llorca, A., and Marín, O. (2018). Development and functional diversification of cortical interneurons. *Neuron* 100, 294–313. doi: 10.1016/j.neuron.2018.10.009

Lin, S. T., and Fu, Y. H. (2009). miR-23 regulation of lamin B1 is crucial for oligodendrocyte development and myelination. *DMM Dis. Model. Mech.* 2, 178–188. doi: 10.1242/dmm.001065

Lippi, G., Fernandes, C. C., Ewell, L. A., John, D., Romoli, B., Curia, G., et al. (2016). MicroRNA-101 regulates multiple developmental programs to constrain excitation in adult neural networks. *Neuron* 92, 1337–1351. doi: 10.1016/j.neuron.2016.11.017

Liu, C., Mallick, B., Long, D., Rennie, W. A., Wolenc, A., Carmack, C. S., et al. (2013). CLIP-based prediction of mammalian microRNA binding sites. *Nucleic Acids Res.* 41, e138. doi: 10.1093/nar/gkt435

Magill, S. T., Cambronne, X. A., Luikart, B. W., Lioy, D. T., Leighton, B. H., Westbrook, G. L., et al. (2010). MicroRNA-132 regulates dendritic growth and arborization of newborn neurons in the adult hippocampus. *Proc. Natl. Acad. Sci. U.S.A.* 107, 20382–20387. doi: 10.1073/pnas.1015691107

Makeyev, E. V., Zhang, J., Carrasco, M. A., and Maniatis, T. (2007). The microRNA miR-124 promotes neuronal differentiation by triggering brain-specific alternative pre-mRNA splicing. *Mol. Cell* 27, 435–448. doi: 10.1016/j.molcel.2007.07.015

Meares, G. P., Rajbhandari, R., Gerigk, M., Tien, C.-L., Chang, C., Fehling, S. C., et al. (2018). MicroRNA-31 is required for astrocyte specification. *Glia* 66, 987–998. doi: 10.1002/glia.23296

Memczak, S., Jens, M., Elefsinioti, A., Torti, F., Krueger, J., Rybak, A., et al. (2013). Circular RNAs are a large class of animal RNAs with regulatory potency. *Nature* 495, 333–338. doi: 10.1038/nature11928

Men, Y., Ye, L., Risgaard, R. D., Promes, V., Zhao, X., Paukert, M., et al. (2020). Astroglial FMRP deficiency cell-autonomously up-regulates miR-128 and disrupts developmental astroglial mGluR5 signaling. *Proc. Natl. Acad. Sci. U.S.A.* 117, 25092–25103. doi: 10.1073/pnas.2014080117

Nowakowski, T. J., Fotaki, V., Pollock, A., Sun, T., Pratt, T., and Price, D. J. (2013). MicroRNA-92b regulates the development of intermediate cortical progenitors in embryonic mouse brain. *Proc. Natl. Acad. Sci. U.S.A.* 110, 7056–7061. doi: 10.1073/pnas.1219385110

Nowakowski, T. J., Rani, N., Golkaram, M., Zhou, H. R., Alvarado, B., Huch, K., et al. (2018). Regulation of cell-type-specific transcriptomes by microRNA networks during human brain development. *Nat. Neurosci.* 21, 1784–1792. doi: 10.1038/s41593-018-0265-3

Ohana, R., Weiman-Kelman, B., Raviv, S., Tamm, E. R., Pasmanik-Chor, M., Rinon, A., et al. (2015). MicroRNAs are essential for differentiation of the retinal pigmented epithelium and maturation of adjacent photoreceptors. *Development* 142, 2487–2498. doi: 10.1242/dev.121533

O'Toole, S. M., Ferrer, M. M., Mekonnen, J., Zhang, H., Shima, Y., Ladle, D. R., et al. (2017). Dicer maintains the identity and function of proprioceptive sensory neurons. *J. Neurophysiol.* 117, 1057–1069. doi: 10.1152/jn.00763.2016

Parchem, R. J., Moore, N., Fish, J. L., Parchem, J. G., Braga, T. T., Shenoy, A., et al. (2015). miR-302 is required for timing of neural differentiation, neural tube closure, and embryonic viability. *Cell Rep.* 12, 760–773. doi: 10.1016/j.celrep.2015.06.074

Peng, C., Furlan, A., Zhang, M.-D., Su, J., Lübke, M., Lönnerberg, P., et al. (2018). Termination of cell-type specification gene programs by the miR-183 cluster determines the population sizes of low-threshold mechanosensitive neurons. *Development* 145:dev165613. doi: 10.1242/dev.165613

Peng, C., Li, L., Zhang, M. D., Gonzales, C. B., Parisien, M., Belfer, I., et al. (2017). MIR-183 cluster scales mechanical pain sensitivity by regulating basal and neuropathic pain genes. *Science* 356, 1168–1172. doi: 10.1126/science.aam7671

Pereira, J. A., Baumann, R., Norrmén, C., Somandin, C., Miehe, M., Jacob, C., et al. (2010). Dicer in Schwann cells is required for myelination and axonal integrity. *J. Neurosci.* 30, 6763–6775. doi: 10.1523/JNEUROSCI.0801-10.2010

Pogue, A. I., Cui, J. G., Li, Y. Y., Zhao, Y., Culicchia, F., and Lukiw, W. J. (2010). Micro RNA-125b (miRNA-125b) function in astrogliosis and glial cell proliferation. *Neurosci. Lett.* 476, 18–22. doi: 10.1016/j.neulet.2010.03.054

Pong, S. K., and Gullerova, M. (2018). Noncanonical functions of microRNA pathway enzymes – Drosha, DGCR8, Dicer and Ago proteins. *FEBS Lett.* 592, 2973–2986. doi: 10.1002/1873-3468.13196

Ponomarev, E. D., Veremeyko, T., Barteneva, N., Krichevsky, A. M., and Weiner, H. L. (2011). MicroRNA-124 promotes microglia quiescence and suppresses EAE by deactivating macrophages via the C/EBP-α-PU.1 pathway. *Nat. Med.* 17, 64–70. doi: 10.1038/nm.2266

Prodromidou, K., Vlachos, I. S., Gaitanou, M., Kouroupi, G., Hatzigeorgiou, A. G., and Matsas, R. (2020). MicroRNA-934 is a novel primate-specific small non-coding RNA with neurogenic function during early development. *Elife* 9:e50561. doi: 10.7554/eLife.50561

Qiu, F., Mao, X., Liu, P., Wu, J., Zhang, Y., Sun, D., et al. (2020). MicroRNA deficiency in VIP+ interneurons leads to cortical circuit dysfunction. *Cereb. Cortex* 30, 2229–2249. doi: 10.1093/cercor/bhz236

Rago, L., Beattie, R., Taylor, V., and Winter, J. (2014). miR379-410 cluster miRNAs regulate neurogenesis and neuronal migration by fine-tuning N-cadherin. *EMBO J.* 33, 906–920. doi: 10.1002/embj.201386591

Rani, N., Nowakowski, T. J., Zhou, H., Godshalk, S. E., Lisi, V., Kriegstein, A. R., et al. (2016). A primate lncRNA mediates Notch signaling during neuronal development by sequestering miRNA. *Neuron* 90, 1174–1188. doi: 10.1016/j.neuron.2016.05.005

Reichenstein, I., Eitan, C., Diaz-Garcia, S., Haim, G., Magen, I., Siany, A., et al. (2019). Human genetics and neuropathology suggest a link between miR-218 and amyotrophic lateral sclerosis pathophysiology. *Sci. Transl. Med.* 11:eaav5264.

Rybak, A., Fuchs, H., Smirnova, L., Brandt, C., Pohl, E. E., Nitsch, R., et al. (2008). A feedback loop comprising lin-28 and let-7 controls pre-let-7 maturation during neural stem-cell commitment. *Nat. Cell Biol.* 10, 987–993. doi: 10.1038/ncb1759

Sarangdhar, M. A., Chaubey, D., Srikakulam, N., and Pillai, B. (2018). Parentally inherited long non-coding RNA Cyrano is involved in zebrafish neurodevelopment. *Nucleic Acids Res.* 46, 9726–9735. doi: 10.1093/nar/gky628

Saunders, A., Macosko, E. Z., Wysoker, A., Goldman, M., Krienen, F. M., de Rivera, H., et al. (2018). Molecular diversity and specializations among the cells of the adult mouse brain. *Cell* 174, 1015–1030.e16. doi: 10.1016/j.cell.2018.07.028

Saurat, N., Andersson, T., Vasistha, N. A., Molnár, Z., and Livesey, F. J. (2013). Dicer is required for neural stem cell multipotency and lineage progression during cerebral cortex development. *Neural Dev.* 8:14. doi: 10.1186/1749-8104-8-14

Scala, F., Kobak, D., Shan, S., Bernaerts, Y., Laturnus, S., Cadwell, C. R., et al. (2019). Layer 4 of mouse neocortex differs in cell types and circuit organization between sensory areas. *Nat. Commun.* 10:4174. doi: 10.1038/s41467-019-12058-z

Schaefer, A., O'Carroll, D., Chan, L. T., Hillman, D., Sugimori, M., Llinas, R., et al. (2007). Cerebellar neurodegeneration in the absence of microRNAs. *J. Exp. Med.* 204, 1553–1558. doi: 10.1084/jem.20070823

Shekhar, K., Lapan, S. W., Whitney, I. E., Tran, N. M., Macosko, E. Z., Kowalczyk, M., et al. (2016). Comprehensive classification of retinal bipolar neurons by single-cell transcriptomics. *Cell* 166, 1308–1323.e30. doi: 10.1016/j.cell.2016.07.054

Shen, Q., Zhong, W., Jan, Y. N., and Temple, S. (2002). Asymmetric Numb distribution is critical for asymmetric cell division of mouse cerebral cortical stem cells and neuroblasts. *Development* 129, 4843–4853.

Shibata, M., Kurokawa, D., Nakao, H., Ohmura, T., and Aizawa, S. (2008). MicroRNA-9 modulates Cajal-Retzius cell differentiation by suppressing Foxg1 expression in mouse medial pallium. *J. Neurosci.* 28, 10415–10421. doi: 10.1523/JNEUROSCI.3219-08.2008

Shibata, M., Nakao, H., Kiyonari, H., Abe, T., and Aizawa, S. (2011). MicroRNA-9 regulates neurogenesis in mouse telencephalon by targeting multiple transcription factors. *J. Neurosci.* 31, 3407–3422. doi: 10.1523/JNEUROSCI.5085-10.2011

Shu, P., Wu, C., Ruan, X., Liu, W., Hou, L., Fu, H., et al. (2019). Opposing gradients of microRNA expression temporally pattern layer formation in the developing neocortex. *Dev. Cell* 49, 764–785.e4. doi: 10.1016/j.devcel.2019.04.017

Smith, K. N., Starmer, J., Miller, S. C., Sethupathy, P., and Magnuson, T. (2017). Long noncoding RNA moderates microRNA activity to maintain self-renewal in embryonic stem cells. *Stem Cell Rep.* 9, 108–121. doi: 10.1016/j.stemcr.2017.05.005

Soldatov, R., Kaucka, M., Kastriti, M. E., Petersen, J., Chontorotzea, T., Englmaier, L., et al. (2019). Spatiotemporal structure of cell fate decisions in murine neural crest. *Science* 364:eaas9536. doi: 10.1126/science.aas9536

Sun, C., Zhu, L., Ma, R., Ren, J., Wang, J., Gao, S., et al. (2019). Astrocytic miR-324-5p is essential for synaptic formation by suppressing the secretion of CCL5 from astrocytes. *Cell Death Dis.* 10:141. doi: 10.1038/s41419-019-1329-3

Sun, G., Ye, P., Murai, K., Lang, M. F., Li, S., Zhang, H., et al. (2011). MiR-137 forms a regulatory loop with nuclear receptor TLX and LSD1 in neural stem cells. *Nat. Commun.* 2:529. doi: 10.1038/ncomms1532

Sundermeier, T. R., Zhang, N., Vinberg, F., Mustafi, D., Kohno, H., Golczak, M., et al. (2014). DICER1 is essential for survival of postmitotic rod photoreceptor cells in mice. *FASEB J.* 28, 3780–3791. doi: 10.1096/fj.14-254292

Tan, C. L., Plotkin, J. L., Venø, M. T., Von Schimmelmann, M., Feinberg, P., Mann, S., et al. (2013). MicroRNA-128 governs neuronal excitability and motor behavior in mice. *Science* 342, 1254–1258. doi: 10.1126/science.1244193

Tao, J., Wu, H., Lin, Q., Wei, W., Lu, X. H., Cantle, J. P., et al. (2011). Deletion of astroglial dicer causes non-cell autonomous neuronal dysfunction and degeneration. *J. Neurosci.* 31, 8306–8319. doi: 10.1523/JNEUROSCI.0567-11.2011

Tasic, B., Menon, V., Nguyen, T. N., Kim, T. K., Jarsky, T., Yao, Z., et al. (2016). Adult mouse cortical cell taxonomy revealed by single cell transcriptomics. *Nat. Neurosci.* 19, 335–346. doi: 10.1038/nn.4216

Tasic, B., Yao, Z., Graybuck, L. T., Smith, K. A., Nguyen, T. N., Bertagnolli, D., et al. (2018). Shared and distinct transcriptomic cell types across neocortical areas. *Nature* 563, 72–78. doi: 10.1038/s41586-018-0654-5

Telley, L., and Jabaudon, D. (2018). A mixed model of neuronal diversity. *Nature* 555, 452–454. doi: 10.1038/d41586-018-02539-4

Thiebes, K. P., Nam, H., Cambronne, X. A., Shen, R., Glasgow, S. M., Cho, H. H., et al. (2015). MiR-218 is essential to establish motor neuron fate as a downstream effector of Isl1-Lhx3. *Nat. Commun.* 6:7718. doi: 10.1038/ncomms8718

Thion, M. S., and Garel, S. (2020). Microglial ontogeny, diversity and neurodevelopmental functions. *Curr. Opin. Genet. Dev.* 65, 186–194. doi: 10.1016/j.gde.2020.06.013

Tuncdemir, S. N., Fishell, G., and Batista-Brito, R. (2015). MiRNAs are essential for the survival and maturation of cortical interneurons. *Cereb. Cortex* 25, 1842–1857. doi: 10.1093/cercor/bht426

Varol, D., Mildner, A., Blank, T., Shemer, A., Barashi, N., Yona, S., et al. (2017). Dicer deficiency differentially impacts microglia of the developing and adult brain. *Immunity* 46, 1030–1044.e8. doi: 10.1016/j.immuni.2017.05.003

Viader, A., Chang, L. W., Fahrner, T., Nagarajan, R., and Milbrandt, J. (2011). MicroRNAs modulate Schwann cell response to nerve injury by reinforcing transcriptional silencing of dedifferentiation-related genes. *J. Neurosci.* 31, 17358–17369. doi: 10.1523/JNEUROSCI.3931-11.2011

Vo, N., Klein, M. E., Varlamova, O., Keller, D. M., Yamamoto, T., Goodman, R. H., et al. (2005). A cAMP-response element binding protein-induced microRNA regulates neuronal morphogenesis. *Proc. Natl. Acad. Sci. U.S.A.* 102, 16426–16431. doi: 10.1073/pnas.0508448102

Wu, C., Zhang, X., Chen, P., Ruan, X., Liu, W., Li, Y., et al. (2019). MicroRNA-129 modulates neuronal migration by targeting Fmr1 in the developing mouse cortex. *Cell Death Dis.* 10:287. doi: 10.1038/s41419-019-1517-1

Yang, D., Li, T., Wang, Y., Tang, Y., Cui, H., Tang, Y., et al. (2012). miR-132 regulates the differentiation of dopamine neurons by directly targeting Nurr1 expression. *J. Cell Sci.* 125, 1673–1682. doi: 10.1242/jcs.086421

Yang, S., Toledo, E. M., Rosmaninho, P., Peng, C., Uhlén, P., Castro, D. S., et al. (2018). A Zeb2-miR-200c loop controls midbrain dopaminergic neuron neurogenesis and migration. *Commun. Biol.* 1:75. doi: 10.1038/s42003-018-0080-0

Yang, Z., Xu, J., Zhu, R., and Liu, L. (2017). Down-regulation of miRNA-128 contributes to neuropathic pain following spinal cord injury via activation of P38. *Med. Sci. Monit.* 23, 405–411. doi: 10.12659/MSM.898788

Yoo, A. S., Sun, A. X., Li, L., Shcheglovitov, A., Portmann, T., Li, Y., et al. (2011). MicroRNA-mediated conversion of human fibroblasts to neurons. *Nature* 476, 228–231. doi: 10.1038/nature10323

Yun, B., Anderegg, A., Menichella, D., Wrabetz, L., Feltri, M. L., and Awatramani, R. (2010). MicroRNA-deficient Schwann cells display congenital hypomyelination. *J. Neurosci.* 30, 7722–7728. doi: 10.1523/JNEUROSCI.0876-10.2010

Zeisel, A., Ḿòz-Manchado, A. B., Codeluppi, S., Lönnerberg, P., La Manno, G., Juréus, A., et al. (2015). Cell types in the mouse cortex and hippocampus revealed by single-cell RNA-seq. *Science* 347, 1138–1142. doi: 10.1126/science.aaa1934

Zeisel, A., Hochgerner, H., Lönnerberg, P., Johnsson, A., Memic, F., van der Zwan, J., et al. (2018). Molecular architecture of the mouse nervous system resource molecular architecture of the mouse nervous system. *Cell* 174, 999–1014. doi: 10.1016/j.cell.2018.06.021

Zhao, C., Sun, G., Li, S., and Shi, Y. (2009). A feedback regulatory loop involving microRNA-9 and nuclear receptor TLX in neural stem cell fate determination. *Nat. Struct. Mol. Biol.* 16, 365–371. doi: 10.1038/nsmb.1576

Zhao, X., He, X., Han, X., Yu, Y., Ye, F., Chen, Y., et al. (2010). MicroRNA-mediated control of oligodendrocyte differentiation. *Neuron* 65, 612–626. doi: 10.1016/j.neuron.2010.02.018

Zhao, X., Wu, J., Zheng, M., Gao, F., and Ju, G. (2012). Specification and maintenance of oligodendrocyte precursor cells from neural progenitor cells: involvement of microRNA-7a. *Mol. Biol. Cell* 23, 2867–2877. doi: 10.1091/mbc.e12-04-0270

Conflict of Interest: The authors declare that the research was conducted in the absence of any commercial or financial relationships that could be construed as a potential conflict of interest.

frontiers in Molecular Neuroscience

REVIEW
published: 20 May 2021
doi: 10.3389/fnmol.2021.670303

Neuropeptide Localization in *Lymnaea stagnalis*: From the Central Nervous System to Subcellular Compartments

Ellen A. Wood[1], Sylwia A. Stopka[2], Linwen Zhang[1], Sara Mattson[1], Gabor Maasz[3,4], Zsolt Pirger[3] and Akos Vertes[1]**

[1] Department of Chemistry, The George Washington University, Washington, DC, United States, [2] Department of Neurosurgery, Brigham and Women's Hospital, Harvard Medical School, Boston, MA, United States, [3] Balaton Limnological Research Institute, Eötvös Loránd Research Network (ELKH), Tihany, Hungary, [4] Soós Ernő Research and Development Center, University of Pannonia, Nagykanizsa, Hungary

Due to the relatively small number of neurons (few tens of thousands), the well-established multipurpose model organism *Lymnaea stagnalis*, great pond snail, has been extensively used to study the functioning of the nervous system. Unlike the more complex brains of higher organisms, *L. stagnalis* has a relatively simple central nervous system (CNS) with well-defined circuits (e.g., feeding, locomotion, learning, and memory) and identified individual neurons (e.g., cerebral giant cell, CGC), which generate behavioral patterns. Accumulating information from electrophysiological experiments maps the network of neuronal connections and the neuronal circuits responsible for basic life functions. Chemical signaling between synaptic-coupled neurons is underpinned by neurotransmitters and neuropeptides. This review looks at the rapidly expanding contributions of mass spectrometry (MS) to neuropeptide discovery and identification at different granularity of CNS organization. Abundances and distributions of neuropeptides in the whole CNS, eleven interconnected ganglia, neuronal clusters, single neurons, and subcellular compartments are captured by MS imaging and single cell analysis techniques. Combining neuropeptide expression and electrophysiological data, and aided by genomic and transcriptomic information, the molecular basis of CNS-controlled biological functions is increasingly revealed.

Keywords: ***Lymnaea stagnalis*, mass spectrometry, neuropeptide, central nervous system, single neuron analysis**

OPEN ACCESS

Edited by:
Miao He,
Fudan University, China

Reviewed by:
Etsuro Ito,
Waseda University, Japan
Elena V. Romanova,
University of Illinois at Urbana-Champaign, United States

***Correspondence:**
Zsolt Pirger
pirger.zsolt@blki.hu
orcid.org/0000-0001-9039-6966
Akos Vertes
vertes@gwu.edu
orcid.org/0000-0001-5186-5352

Received: *22 February 2021*
Accepted: *09 April 2021*
Published: *20 May 2021*

Citation:
Wood EA, Stopka SA, Zhang L, Mattson S, Maasz G, Pirger Z and Vertes A (2021) Neuropeptide Localization in Lymnaea stagnalis: From the Central Nervous System to Subcellular Compartments. Front. Mol. Neurosci. 14:670303. doi: 10.3389/fnmol.2021.670303

INTRODUCTION

Neuropeptides in *Lymnaea stagnalis*

Lymnaea stagnalis, also known as the great pond snail, is an excellent model organism used for research in neuroscience, aging, ecotoxicology, parasite-host interactions, and evolution and development (Jimenez et al., 2004; Hoek et al., 2005; Benjamin, 2008; Pirger et al., 2014; Fodor et al., 2020a,b, 2021). Specifically, the central nervous system (CNS) of *L. stagnalis* is highly characterized at multiple levels. It is composed of eleven interconnected ganglia, each containing their own unique sub-populations of large and brightly colored neurons with specific functions and

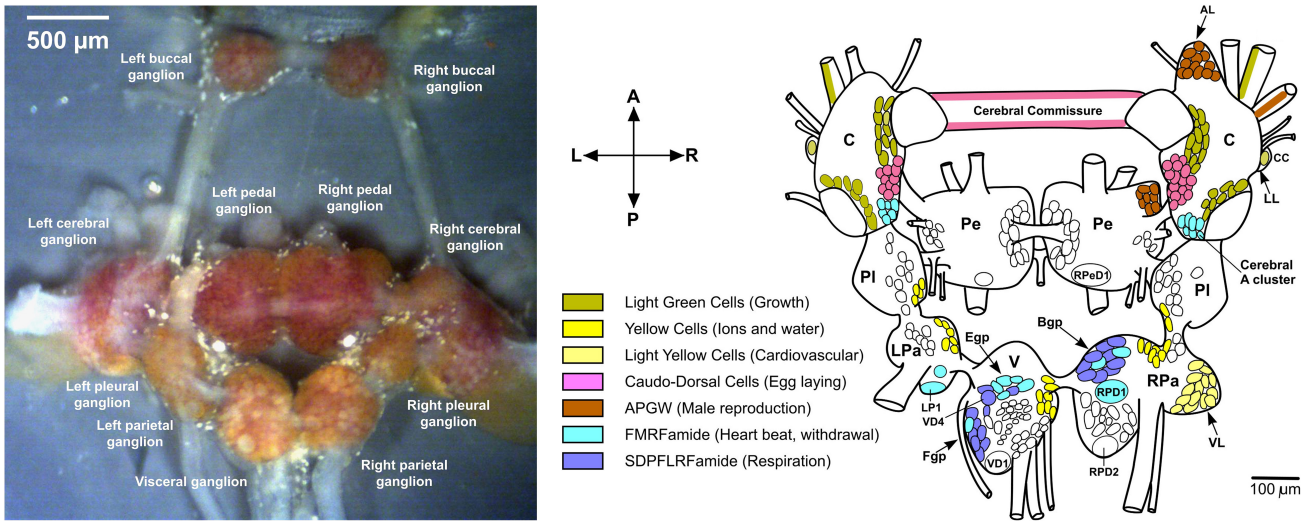

FIGURE 1 | Dissected *Lymnaea* CNS and distribution of some neuropeptides. **(left)** Dissected *L. stagnalis* CNS (Zhang et al., 2018). **(right)** Localization of some peptides to identified neurons (Benjamin and Kemenes, 2013). The anterior lobe (AL) hosts some APGW neurons. Abbreviations: C, cerebral ganglion; CC, Canopy Cell; B/Egp, B/E group; LL, lateral lobe; LP1, left parietal 1; LPa, left parietal ganglion; Pe, pedal ganglion; Pl, pleural ganglion; RPa, right parietal ganglion; RPD1/2, right parietal dorsal 1/2; RPeD1, right pedal dorsal 1; V, visceral ganglion; VD1, visceral dorsal 1; VD4, visceral dorsal 4; and VL ventral lobe.

expressing a set of neuropeptides, as shown in **Figure 1** (Benjamin and Kemenes, 2013; Rivi et al., 2020). In comparison to vertebrates, the CNS of *L. stagnalis* is considered more accessible because of the vastly lower number of neurons (∼20,000 compared to, e.g., 86,060,000,000 for humans; Azevedo et al., 2009), and partially elucidated neuronal circuits for specific functions. Functioning of the CNS, ganglia, neuronal circuits, and individual neurons relies in part on spatial and temporal variations in their chemical composition. From the early 1980s, neuropeptides have become a focal point for research due to their direct role in modulating neuronal circuit functions (that also occurs in the vertebrate nervous system) within the CNS (Schot et al., 1981; Patel et al., 2005).

The sensory system of *L. stagnalis* responds to a variety of external stimuli (e.g., a chemical stimulus – smell), signaling a modulatory response to the central pattern generator (CPG) networks that initiate the motor system (e.g., feeding motoneurons in buccal ganglia), and induces an observable physical response (e.g., feeding behavior – radula movement). Once a stimulus is received in the sensory system, a signal is sent to the modulatory system where neuropeptides convey the signal, further cascading it to the motor system (Kemenes et al., 2001). Extensive research has revealed biochemical processes associated with external stimuli and intracellular components such as learning and memory systems, whole-body withdrawal, heartbeat, feeding, and respiratory motor circuits (Buckett et al., 1990a,b; Brierley et al., 1997; Fulton et al., 2005). For example, strong correlation between the abundance of insulin in the CNS and long-term memory has been established (Kojima et al., 2015; Totani et al., 2019). Understanding the correlation between an introduced external stimulus, such as a tactile, photoreceptive, or food-related excitation, and an observed behavior of *L. stagnalis* in response, has been the driving force for continued research into the molecular profiling of CNS circuits. By identifying the neuropeptide profiles and localization in the CNS, a better consensus on the correlation between their composition, biochemical processes, and physiology can be achieved.

With the recent availability of the unannotated draft genome for *L. stagnalis* (Stevens et al., 2016), and the emerging transcript information (see the four major transcriptome databases), finding the sequences for neuropeptide precursor proteins (prohormones) is accelerating (Davison and Blaxter, 2005; Feng et al., 2009; Bouetard et al., 2012; Sadamoto et al., 2012). Comprehensive inventories of prohormones and predicted neuropeptides for other mollusks are being constructed. For example, for the gray garden slug (*Deroceras reticulatum*), 65 neuropeptide precursor genes and more than 330 neuropeptides were putatively identified (Ahn et al., 2017), or for the common the Roman snail (*Helix pomatia*), 12 neuropeptide precursor genes and more than 100 neuropeptides (clustered in 26 distinct peptide families) were predicted (Kiss and Pirger, 2006). Similar to these, approximately 100 (neuro)peptides have been identified in *L. stagnalis* so far (Benjamin and Kemenes, 2020) encoded by genes involved in various regulatory processes. The collection of 98 *L. stagnalis* neuropeptides listed in **Supplementary Table 1**, is assembled from other data collections (Wang et al., 2015) and the literature. Most of them are clustered according to their prohormone (protein precursor). In addition, families based on sequence homologies and similarity of function are also indicated. The latter include the FMRFamide, FMRFamide-related, small cardioactive peptides (SCP), insulin, molluscan ELH, myomodulin, LYC, α, FxRI, LYCEP, LIP, and vasopressin/oxytocin families.

Initially, the distribution of highly expressed neuropeptides was explored by oligonucleotide probes that hybridized to the mRNA coding for the relevant segments of the prohormone and

carried a fluorescent tag. For example, such studies indicated that the APGW-amide tetrapeptide was highly expressed in the right anterior lobe of the cerebral ganglia (Smit et al., 1992). An alternative approach relied on immunocytochemistry based on antisera raised against the peptides of interest (Santama et al., 1994a). Systematic studies revealed expression level variations with cellular resolution.

In the early 1990s, single cell level molecular analysis was enabled by the large size of some neurons (>50 μm) readily accessible in *L. stagnalis* and the emerging high spatial resolution and sensitivity of mass spectrometry (MS). Matrix-assisted laser desorption ionization (MALDI) MS made possible some of the earliest neuropeptide analysis experiments in single neurons (Vanveelen et al., 1993; Jimenez et al., 1994; Kellett et al., 1996). This extended molecular profiling, neuropeptide discovery and identification from whole CNS samples to single neurons and ultimately cellular compartments (Rubakhin et al., 2000, 2003; Altelaar et al., 2005; McDonnell et al., 2005). Multilevel understanding of neuropeptide distributions from the whole CNS to subcellular detail is critical to provide new insight into biochemical processes associated with the functioning CNS (Buckett et al., 1990b; Fodor et al., 2020a). Following the multilevel approach (from behavior to circuits, and molecules) in *L. stagnalis* research, **Figure 2** shows the four levels of organization in the CNS, the corresponding mass spectra, and the localization of some neuropeptides.

Advances in Mass Spectrometry Bring Neuropeptide Localization in Focus

The analysis of neuropeptides within the CNS of *L. stagnalis* has been an area of interest for decades, and new methodologies to improve detection are continually being introduced. Early neuropeptide research used a variety of techniques, such as the hybridization to DNA/RNA with exons coding for the targeted peptides, cloning, fluorescence, and immunohistochemistry (IHC) (Linacre et al., 1990; Bright et al., 1993; Santama et al., 1993). For example, the early recognition of molluscan insulin-related peptides was based on screening of a large cDNA library that revealed coding for preproinsulin (Smit et al., 1991). Neuropeptide discovery by some of these techniques was a time-consuming endeavor and required large sample sizes. For example, to discern neuropeptide primary structures in *L. stagnalis* required up to 500 ganglia and 1 million large neurons (Li et al., 1994a).

Initially, MS was an auxiliary method to indicate the expression of peptides predicted from cDNA sequences and partially verified by IHC (Santama et al., 1994b). The introduction of MALDI-MS to invertebrate neuroscience dramatically decreased the amount of sample required for peptide analysis and rapidly reached single neuron resolution (Jimenez et al., 1994). Due to instrumental limitations, however, these MALDI mass spectra only reported the nominal mass of the predicted peptide, in some cases only with a few Dalton (Da) accuracy.

With the application of tandem MS and improvements in instrument characteristics in the following decade, MS became a workhorse for the detection, identification, and quantitation of neuropeptides in a variety of biological samples, including invertebrates (Chaurand et al., 1999; Hummon et al., 2003, 2006). Improved mass accuracy and tandem MS enhanced the identification of neuropeptides, whereas MS imaging (MSI) helped to determine their distributions and localization in the organism (Caprioli et al., 1997). The ability to elucidate the primary structure of novel neuropeptides, and to reveal their localization in the CNS made MS an important tool for molecular exploration in *L. stagnalis*. In some cases, peptide sequencing by tandem MS pinpointed potential errors in the cDNA sequence and demonstrated the expression of an unexpected peptide in a particular cell type (Zhang et al., 2018).

Early on, tandem MS techniques helped with the de novo sequencing of the detected peptides to establish their relationship with the underlying genes, transcripts, and precursor proteins (Dreisewerd et al., 1997; Li et al., 1997; Jimenez et al., 1998). To reduce the complexity of tissue extracts, high-performance liquid chromatography (HPLC) was combined with MS techniques (Dewith and Vanderschors, 1992; Santama et al., 1995). However, for volume limited samples, i.e., single cells and subcellular compartments, HPLC is not suitable. Instead, the application of ion mobility separation (IMS) is being introduced (Zhang et al., 2018). Combining IMS with MS reduces the sample volume requirement for separation, and dramatically shortens the separation times from 10s of minutes to the ms timescale.

Neuropeptide imaging by MSI techniques became of interest to further elucidate neuropeptide distributions and colocalizations within the CNS. They include MALDI-MSI and matrix-enhanced secondary ion mass spectrometry (ME-SIMS) that are highly sensitive and used to spatially map neuropeptides within the CNS of *L. stagnalis* (Altelaar et al., 2005; McDonnell et al., 2005; Chen and Li, 2010). MSI techniques, including MADLI-MSI and ME-SIMS, have expanded the analysis of neuropeptides by tracking ions of interest and showing their distribution throughout the sample, which assists in determining localization within the CNS. As the name suggests, ME-SIMS combines the use of matrix for sample preparation and the imaging capabilities of SIMS. An MS image is produced by sputtering the surface of the sample with a focused primary ion beam, then collecting and analyzing ejected secondary ions (Altelaar et al., 2005; McDonnell et al., 2005; Chen and Li, 2010). The sensitivity of SIMS for higher mass molecules is improved by the addition of a matrix, thus the motivation behind the combination of techniques for ME-SIMS is to combine the high mass capabilities of MALDI with the high spatial resolution of SIMS (Altelaar et al., 2005; McDonnell et al., 2005; Chen and Li, 2010). With the use of ME-SIMS, high resolution molecular ion maps of the neuropeptide APGW were created, thus finding localization predominantly in the right anterior lobe of the right cerebral ganglia. Neurons in this region are known to regulate male copulation behavior in *L. stagnalis* (Altelaar et al., 2005). These findings help to correlate the localization of neuropeptides in the CNS to their biological role. Upon new imaging findings and improved instrumentation, these techniques have shown that direct molecular imaging of *L. stagnalis* nervous tissue is

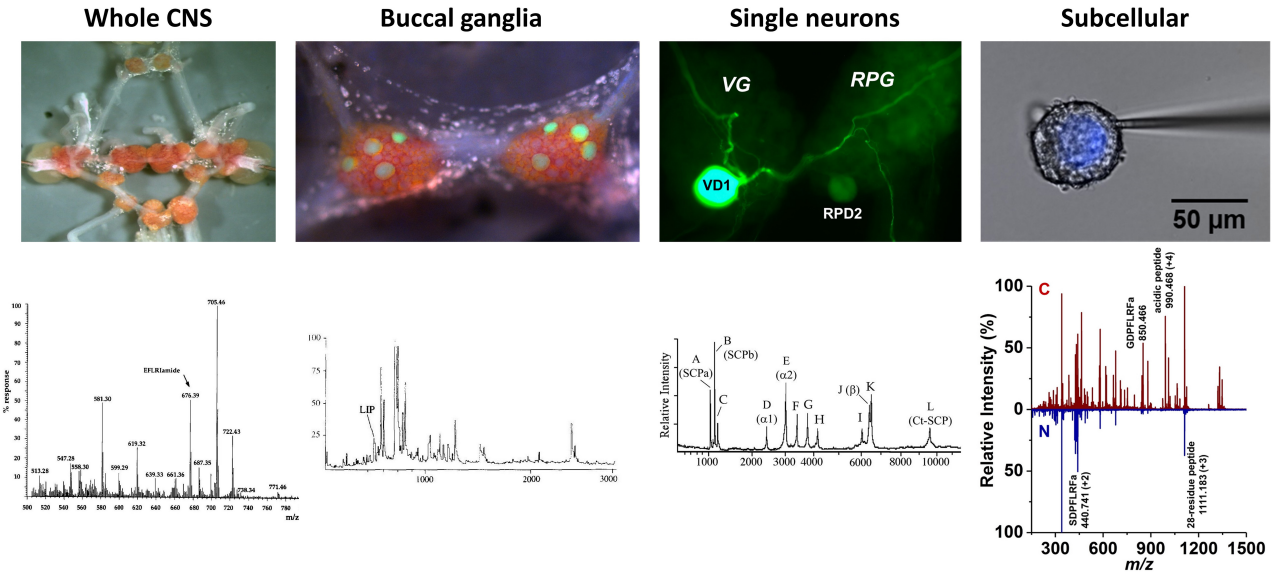

FIGURE 2 | Neuropeptide localization and mass spectra at four levels of organization. Images of whole CNS, buccal ganglia with identified feeding motoneurons, B1–B4, highlighted by lucifer-yellow intracellular filling, single visceral dorsal 1 (VD1) and right parietal dorsal 2 (RPD2) neurons with intracellular filling, and nucleus of Type 2 Fgp neuron and corresponding mass spectra (Santama et al., 1995, Li et al., 1996, Jimenez et al., 2006, and Zhang et al., 2018), respectively, revealed the expression of specific peptides.

possible and that the continued development of MS techniques will further accelerate neuropeptide profiling.

Here we present an account of recent developments in the analysis of neuropeptides by MS in the nervous system of *L. stagnalis* with granularity spanning from the whole CNS to subcellular details in identified cells.

WHOLE CNS STUDIES

Early research using *L. stagnalis* focused on neuropeptide identifications and distributions within the entire CNS. Non-MS techniques, such as immunocytochemistry and intracellular dye filling reported on the spatial distributions of multiple neuropeptide families including FMRFamide related, myomodulin, and SCP, whereas DNA/RNA hybridization and DNA extractions helped with predicting the amino acid sequence. The ability to link biological functions to the presence of these peptides in *L. stagnalis*, e.g., heart modulation, feeding behavior, and male copulation, made them attractive for early CNS analyses (Ebberink et al., 1987; Santama et al., 1994a,b; Benjamin, 2008).

Leading up to MS analysis of *L. stagnalis*, other mollusk model organisms, for example, *Aplysia californica*, were studied for neuropeptide identification, using both non-MS and MS techniques (Weiss et al., 1984; Sweedler et al., 2002). The FMRFamide peptides and the feeding circuit activating peptides (FCAPs) had been previously identified in the nervous system of *A. californica*, thus raising the possibility of their presence or the presence of their homologues in *L. stagnalis* due to similarities between the two invertebrates. The FMRFamide related peptide family was linked to heart modulation (Benjamin, 2008; Fodor et al., 2020a), making it of interest for early neuropeptide research. This neuropeptide class consisted of tetrapeptides (FMRF/FLRF) and heptapeptides (SDPFLRF/GDPFLRF) (Ebberink et al., 1987). In addition, other neuropeptide classes of biological importance, such as myomodulin and SCP, previously found in other mollusks (Kiss and Pirger, 2006), were also studied in *L. stagnalis* to further explore their role in gut modulation and male copulation. Using IHC, the distributions of these peptides throughout the CNS, e.g., myomodulin A (PMSMLRL) and SCP (SGYLAFPRM), were tentatively determined (Santama et al., 1994a,b; Benjamin and Kemenes, 2013).

Mass spectrometry techniques validated previous discoveries, as well as identified novel neuropeptides. With the addition of MS techniques, neuropeptide identifications expanded into a variety of functionally identified classes (see **Supplementary Table 1**), as well as the elucidation of new unlabeled neuropeptides (Fodor et al., 2020a). For example, analysis was done on multiple neuropeptides encoded on the FMRFamide locus of the snail. By combining HPLC and continuous-flow fast atom bombardment MS, three novel peptides, EFLRIamide, pQFYRIamide, and pQFLRIamide, were identified within an extract of 20 CNS samples (Santama et al., 1995). Additionally, MS analysis of the CNS tentatively recognized three novel peptides SKPYMRFamide, HDYMRFamide, and SSFPRYamide (Kellett et al., 1994). Taken together with earlier work, these findings expanded the biologically important FMRFamide neuropeptide class.

As neuropeptide classes, like FMRFamide-related peptides, were being explored, interest in their distribution within the CNS was growing. IHC indicated the preferential expression of particular neuropeptides in certain cell types (see, e.g.,

Santama et al., 1994b). In the coming years, this motivated the implementation of MSI techniques for molecular imaging and the targeted analysis of individual ganglia and neuronal clusters. **Figure 3** shows the distributions of six identified and two unidentified neuropeptides, GDPFLRFamide (*m/z* 850.4633), ILGGGYKFamide (*m/z* 853.4535), SDPFLRFamide (*m/z* 880.4734), SKPYMRFamide (*m/z* 927.4935), SGYLAFPRMamide (*m/z* 1040.5428), *m/z* 1144.9945, GPSRSSFPRYamide (*m/z* 1152.6086), and *m/z* 1396.6872, in the CNS as they are reported by MALDI-MSI.

INDIVIDUAL GANGLIA AND NEURONAL CLUSTERS

The CNS of *L. stagnalis* contains 11 interconnected ganglia, each with their own unique subpopulations of neurons on the surface of the ganglia. Previous whole CNS neuropeptide analyses have given rise to identification and validation of specific neuropeptide classes with important biological functions. Analysis of individual ganglia revealed neuropeptide localization within the CNS in greater detail.

Molecular components linked to reproduction in *L. stagnalis* have been of interest due to the hermaphroditic behavior and the abundance of correlated neuropeptide messengers (El Filali et al., 2006; Koene, 2010). Research has located multiple ganglia, numerous neuron clusters, and diverse neuropeptides associated with both male and female reproduction. Peptides involved in male copulation include APGW, conopressin, *C*-terminally located anterior lobe peptide, DEILSR, EFLRI, FLRF, FVRIs, G/SDPFLRF, gonadotropin releasing hormone, LIP A, B, and C, Lymnaea neuropeptide Y, myomodulins, pedal peptide, pQFYRI, and SEEPLY (Koene, 2010). In females, HF(FH)FYGPYDVFQRDV, 5895 Da peptide, amino terminal peptide, calfluxin, carboxyl terminal peptide, CDCH, α-CDCP, β1-CDCP, β2-CDCP, β3-CDCP, dorsal body hormone, LFRF, gonadotropin releasing hormone, γ-, δ-, and ε-peptides were found to be involved (Koene, 2010). For example, specific neuron clusters have been located in the right cerebral ganglia, specifically in the ventral and anterior lobe, which have a role in the male copulation behavior, and contain APGW (De Boer et al., 1997; Li et al., 1997). Another neuropeptide of interest due to its role in male copulation is myomodulin A (Li et al., 1994b). One of the first studies for myomodulin A using MS aimed to validate the presence of this neuropeptide, found in *A. californica*, also in *L. stagnalis*. After establishing its presence, IHC and MS suggested that myomodulin A is synthesized in neurons of the ventral lobe, located in the right cerebral ganglion (Li et al., 1994b). MS analysis of the right cerebral ganglion, specifically the cluster of neurons in the ventral lobe, revealed two more unique neuropeptides, SCP A and SCP B (Dreisewerd et al., 1997). It was also determined that none of these neuropeptides were found in the anterior lobe of this ganglion, further supporting a specific localization within a cluster of neurons involved in male copulation.

Previously unidentified neuropeptide classes and their localization were discovered using MALDI-MS. The

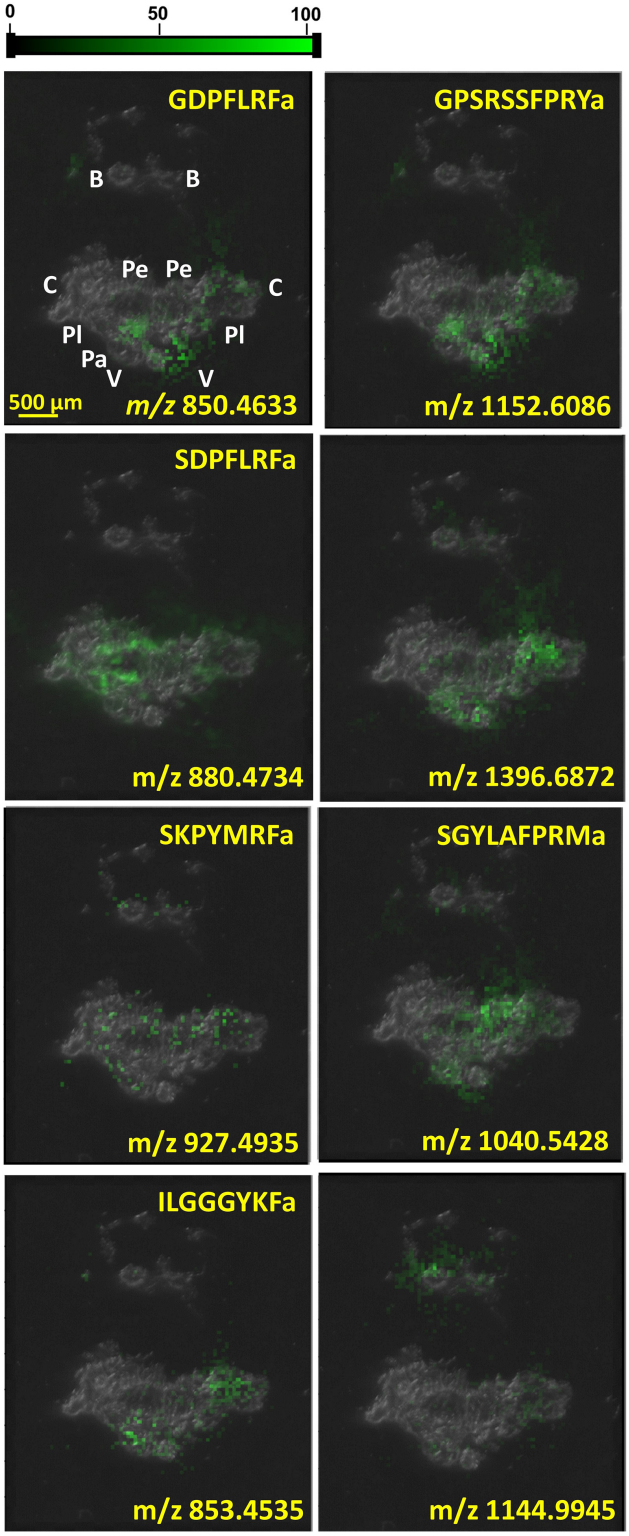

FIGURE 3 | Neuropeptide distributions in CNS based on MALDI-MSI overlaid on top of optical microscope image of CNS section. Several other peptides were uniformly distributed throughout the whole CNS, whereas the six known and two unknown peptides depicted above were significantly more abundant in specific ganglia.

neuropeptide, GAPRFVamide, once labeled as *L. stagnalis* inhibitory peptide (LIP), was found in the buccal ganglia (BG), and the ventral lobe, along with two other -FVamide neuropeptides (LIP B and C). GAPRFVamide is now labeled as LIP A and is included within the LIP neuropeptide class linked to the inhibitory effect on the spontaneous contraction and relaxation cycle in male copulation (Smit et al., 2003). Analysis of the neuropeptide APGW, and the myomodulin, SCP, and LIP neuropeptide classes within the specific ventral lobe cluster of neurons verified that localization of neuropeptides could correlate with their biological roles (van Tol-Steye et al., 1999).

MALDI-MSI of the whole CNS in **Figure 3** indicates the localization of some neuropeptides to specific ganglia and neuronal clusters. The neuropeptide GPSRRSSFPRYamide is localized in the left parietal, visceral, and cerebral ganglia, which correlates with its diverse functions. Neuropeptide SCP A (SGYLAFPRMamide) is detected in the right pedal cluster of neurons, where it aids locomotion, whereas FMRF-like neuropeptides, e.g., SDPFLRFamide and GDPFLRFamide, are important cardioactive species that act as neurotransmitters (Linacre et al., 1990). Increasing the spatial resolution in these MSI experiments from molecular mapping of neuronal clusters to the length scale of single neurons opens the possibility of additional insight into neuronal circuits.

SINGLE NEURONS

As neuropeptide profiling by MS made headway from whole CNS to the individual ganglia, single neuron analysis became the new frontier for understanding the functioning of the *L. stagnalis* nervous system. In the early 1990s, microsampling by a focused laser beam became an efficient tool to target the relatively large cells in this organism (Vanveelen et al., 1993; Jimenez et al., 1994). The ability to explore the differences in composition, abundances, and localization of neuropeptides with single cell resolution by MS brought the field to a new level (Li et al., 2000; Rubakhin et al., 2011; Comi et al., 2017; Zhang et al., 2018). In combination with results accumulating from patch clamp studies, a more detailed picture of the biological function of individual neurons has started to emerge.

Prior to MS analysis, neuropeptide expression and localization were tentatively identified throughout neuron clusters and individual neurons in the CNS using in situ hybridization and fluorescent tags. These studies revealed the presence of tetrapeptides (FMRF/FLRF) in multiple behaviorally important networks, such as moto-neurons, whole body withdrawal response moto-neurons, and penis moto-neurons, as well as giant identified neurons (left parietal 1 [LPa1] and right parietal dorsal 1 [RPaD1]) (Bright et al., 1993). Additionally, heptapeptides (GDPFLRF/SDPFLRF) were identified in B group (Bgp) and F group (Fgp) neuron clusters in visceral ganglion (VG). Analysis of the FMRFamide-like neuropeptides using DNA hybridization elucidated a 22 amino acid sequence neuropeptide, SEEPLY. Localization of SEEPLY in the BG of CNS exhibited similar neuronal distributions to the FMRFamide neuropeptide class. The co-expression of the FMRF neuropeptide class and SEEPLY gave rise to interest in more sensitive analytical techniques for neuropeptide mapping (Santama et al., 1993).

One of the first MALDI-MS single neuron studies focused on two neuronal groups, yellow cells and light-yellow cells, and two identified giant neurons, the visceral dorsal 1 (VD1) and right parietal dorsal 2 (RPaD2) (Vanveelen et al., 1993). The yellow cells are located in the right parietal ganglion (RPaG), as well as in the VG. They are known to be involved in the regulation of ion and water metabolism. MADLI-MS analysis of a single yellow cell detected a peptide containing 76 amino acid residues, closely related to the 77-residue sodium influx stimulating peptide (SIS), although this assertion was only supported by the nominal *m/z* 8,891 of the corresponding $[M+H]^+$ ion. The light-yellow cells, with a known role in heart modulation, are found in the RPaG and VG. Multiple light-yellow cell peptides (LYCP) were identified based on the nominal *m/z* values of the corresponding ions (Vanveelen et al., 1993; Li et al., 1994b). The VD1 and RPaD2 neurons are located within the VG and RPaG. MALDI-MS analysis showed the presence of α1, α2, and β peptides, where the α peptides were known to modulate heartbeat.

Peptide identification in these early single cell studies could not be purely attributed to the MS results. Nominal mass in itself is insufficient to uniquely identify these large molecules. Invariably, identification relied on known cDNA sequences of the corresponding prohormones and Edman degradation-based sequencing. For example, translating the genetic code to the prepro-SIS protein precursor showed the presence of two components, a signaling peptide and an active 77-residue SIS neuropeptide (see the corresponding entry in **Supplementary Table 1**). This peptide contained an extra lysine at the carboxyl terminus compared to the 76-residue peptide found by Edman degradation (Vanveelen et al., 1991; de With et al., 1993). Interestingly, the *m/z* 8,891 value detected by MALDI-MS was close to the calculated average *m/z* 8,887 for the protonated 76-residue peptide (Vanveelen et al., 1993). The mass difference of 4 Da between calculated and detected *m/z* in the mass spectrum reflected the limited mass accuracy of the MS instruments at the time. The most important contribution of the MS results in these studies was the information gleaned about the processing of the protein precursors to produce the active peptides.

Significant progress was made when tandem MS became available for single neuron studies. For example, the α1, α2, and β, peptide species that had been detected in VD1 and RPaD2 neurons were verified, and additional peptides were detected in these cells (Jimenez et al., 1998). Some of these peptides were sequenced and assigned as members of the SCP family. More recently, capillary microsampling electrospray ionization (ESI) tandem MS was used to identify the complete primary structure of an unknown 28-residue peptide, and verify the presence of the acidic peptide in the Fgp neuron cluster (see top panel of **Figure 4**) (Zhang et al., 2018).

Single neuron MS analyses of different neuropeptide classes in combination with patch clamp data enhanced our understanding of the role specific neurons and their neuropeptides play in relation to biological functions. The FMRFamide neuropeptide family was associated with heart modulation, thus their presence in cardio-regulatory neurons was explored. MALDI-MS analysis

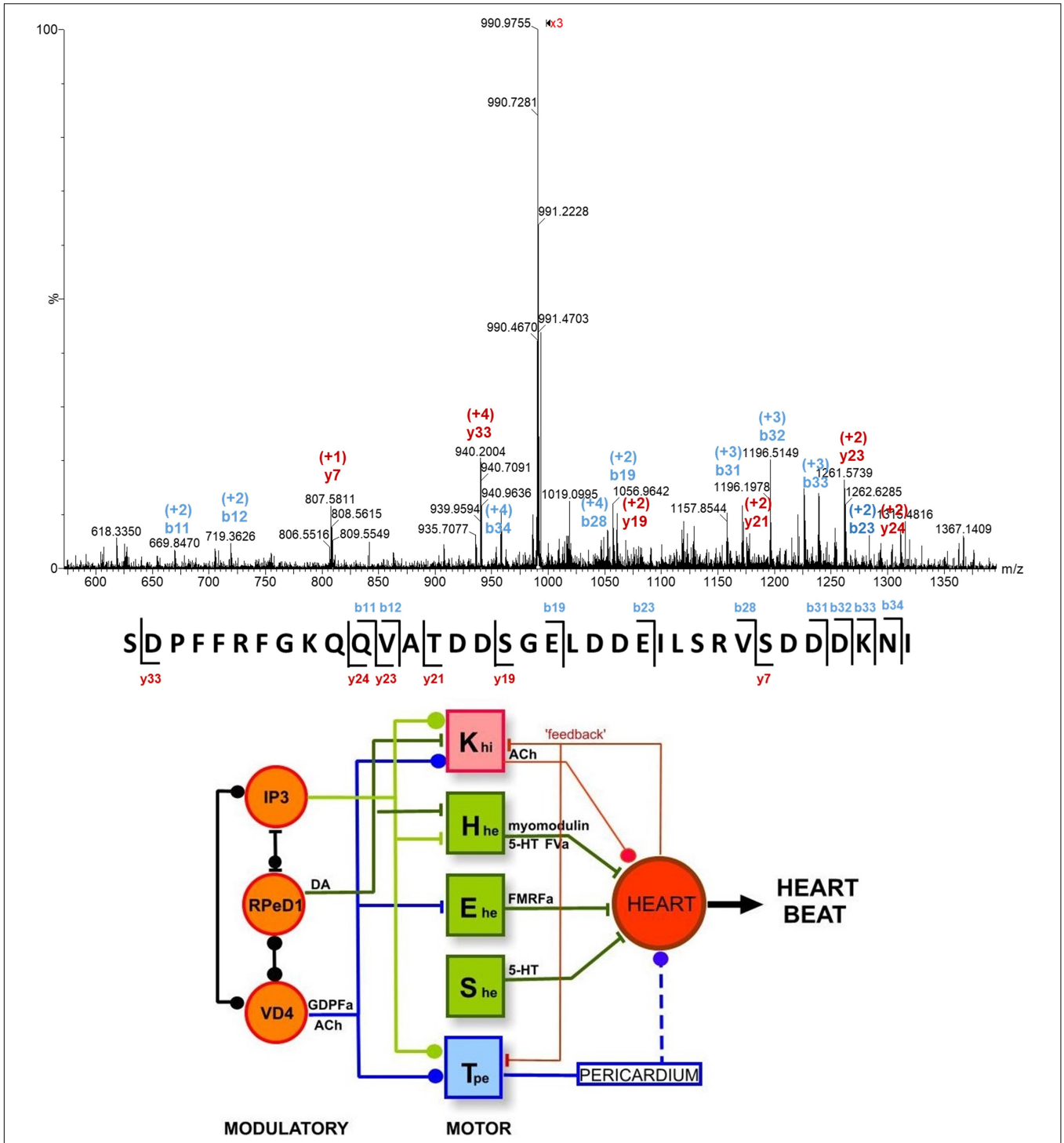

FIGURE 4 | (Top) Single cell tandem mass spectrum for a peptide ion with *m/z* 990.468 and a charge state of +4, assigned as a 35-residue acidic peptide, based on its fragmentation pattern and cDNA predicted peptide sequence (Zhang et al., 2018). **(Bottom)** The heartbeat network of *Lymnaea* consists of modulatory and motoneurons connected through excitatory and inhibitory regulation through the release of neuropeptides (Benjamin, 2008). See text for abbreviations.

of an excitatory moto-neuron, E_{he}, and an E group (Egp) neuron found that these cells expressed tetrapeptides (FMRF/FLRF) from this family, and the peptide pQFLRLI, whereas the visceral white interneuron (VWI) and Bgp single neurons were shown to express the heptapeptides GDPFLRF and SDPFLRF. The dissimilarities found between the cardio-regulatory neurons suggest differences in peptide functions, revealing the necessity of single neuron analysis within the cardio-regulatory system

(Vanveelen et al., 1993; Jimenez et al., 1994; Worster et al., 1998; Santama and Benjamin, 2000).

The accumulating compositional data on single neurons taken together with electrophysiological information enabled the identification of neuronal networks responsible for physiological functions, including the networks for heartbeat, whole-body withdrawal, feeding, and respiration (Benjamin, 2008). The heartbeat network of *L. stagnalis* consists of three interconnected modulatory neurons (IP3, RPeD1, and VD4), four excitatory (H_{he}, E_{he}, S_{he}, and T_{pe}) and one inhibitory (K_{hi}) moto-neurons (see bottom panel of **Figure 4**). Excitatory and inhibitory regulation of these neurons and the heart occurs through the release of specific neuropeptides and transmitters. For example, FMRFamide released by the E_{he} moto-neuron increases the rate of heartbeat. Conversely, acetylcholine released by the K_{hi} moto-neuron inhibits heartbeat.

Another biological function of interest in *L. stagnalis* is gut modulation. Analysis of single giant moto-neuron (B2) in the BG revealed the presence of both SCP A and SCP B peptides. With the use of in situ hybridization followed by MS analysis, it was determined that the SCP neuropeptides have a role in the co-modulation of gut motility (Perry et al., 1999). Analysis of single B2 cells also revealed the presence of four of the five myomodulin neuropeptides: SLSMLRLamide, SMSMLRLamide, PMSMLRLamide, and pQIPMLRLamide. Correlating their presence to their biological role, it was determined that the application of these four neuropeptides modulated contraction frequency and relaxation (Perry et al., 1998).

A uniquely useful tool to explore neuronal circuits and select unidentified neurons for analysis is retrograde tracing. It uses a dye, e.g., nickel-lysine, which is introduced into a neuron in the circuit of interest. The dye is then taken up by the connected neurons, thus labeling them for visual identification and sampling (El Filai et al., 2003). By combining retrograde filling and MALDI-MS analysis, multiple connected neurons from the RPaG were analyzed for their neuropeptide components. It was determined that neurons connected to the male copulation circuit in the RPaG can be divided into two groups: neurons that express FMRF heptapeptides and neurons that do not (El Filali et al., 2015). The combination of retrograde filling with MS technologies is becoming a powerful tool in exploring chemical communication within neuronal circuits.

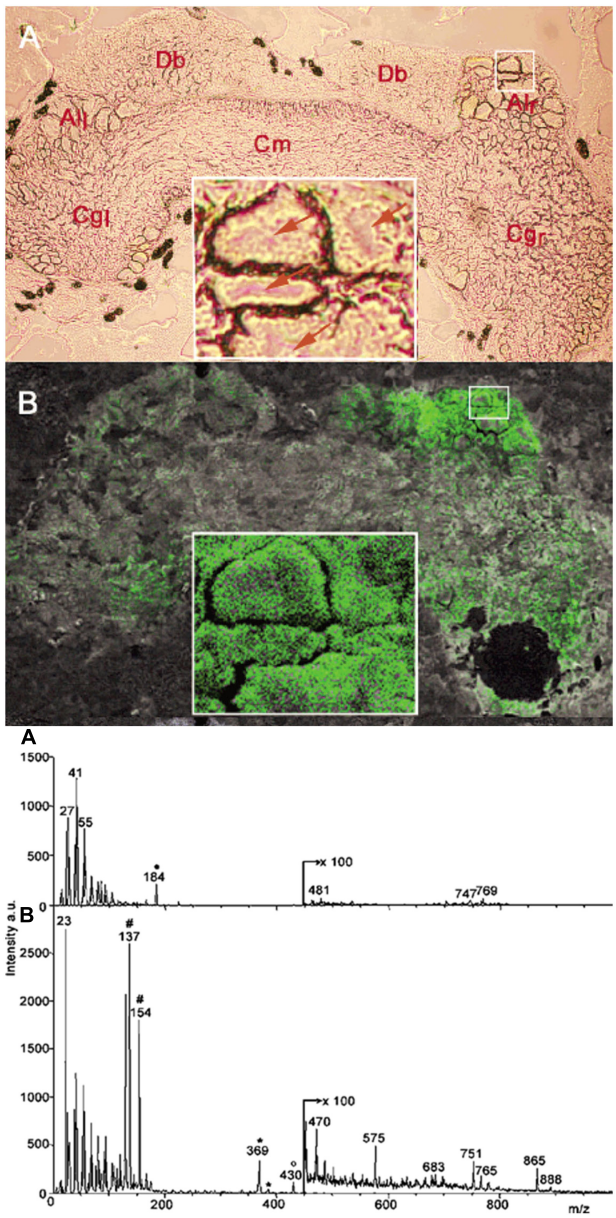

FIGURE 5 | Optical micrograph and ME-SIMS based MSI of cerebral ganglia, and mass spectra of CNS from *L. stagnalis*. Top panel A and B show the morphology and distribution of APGWamide in the left (Cgl) and right (Cgr) ganglia, respectively, with individual neurons in the right anterior lobe (Alr) shown in the insets (Altelaar et al., 2005). Bottom panel A and B compares the SIMS and ME-SIMS mass spectra, respectively. Only the latter detects the protonated APGWamide at *m/z* 430.

SUBCELLULAR LOCALIZATION

Biomolecules can play distinct roles and participate in different sometimes conflicting processes in cells based on their subcellular localization and compartmentalization (Villalobos et al., 2009; Martin, 2010; Diekmann and Pereira-Leal, 2013). With improved sampling techniques and more sensitive mass spectrometers, subcellular MS analysis of organelles, e.g., secretory granules, has become possible (Rubakhin et al., 2000, 2003; Miao et al., 2005). Profiling metabolites and neuropeptides on a subcellular level can face multiple challenges, such as fast molecular turnover rates, low sample volumes, limited amounts of analytes as well as the difficulties of isolating individual compartments with high purity. A novel family of approaches is based on subcellular sampling via laser ablation, microdissection, and extraction through microcapillaries. The combination of microdissection and selective laser ablation revealed large metabolite gradients between the nucleus and the cytoplasm (Stolee et al., 2012). Other studies showed that subcellular compartments can be captured by a nanoelectrospray tip inserted into the cell and the extracted

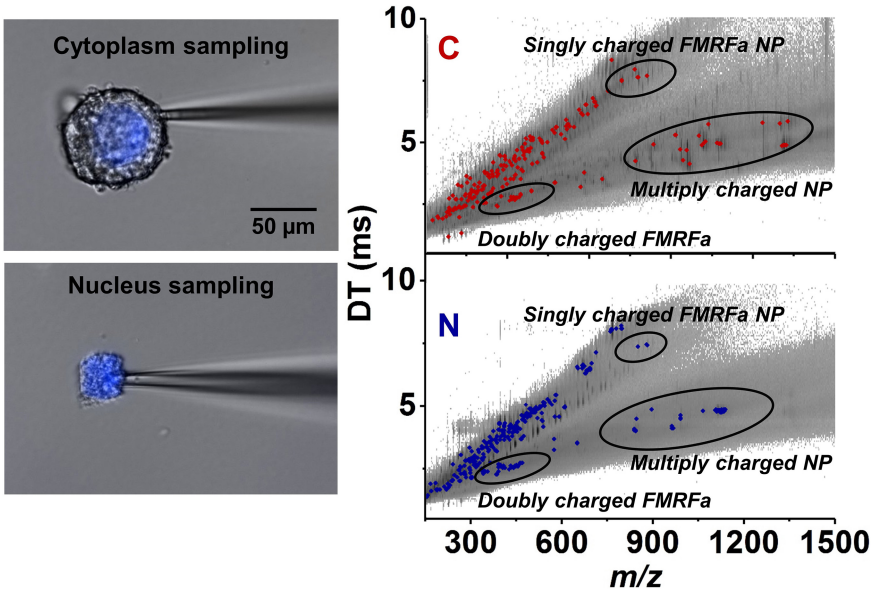

FIGURE 6 | Selective capillary microsampling of cytoplasm (top left panel) and nucleus (bottom left panel) of an Fgp neuron followed by IMS and MS (comparative right panel) (Zhang et al., 2018). The latter reveals the differences in neuropeptide compositions and abundances between the two subcellular compartments.

material can be directly electrosprayed (Mizuno et al., 2008), e.g., to study the subcellular metabolism of a drug (Date et al., 2012).

The submicrometer spatial resolution of secondary ion MS (SIMS) made this technique uniquely positioned to study subcellular chemical composition. A major obstacle for neuropeptide analysis by SIMS was the significant fragmentation of the produced ions. This problem was alleviated by the introduction of matrix-enhanced SIMS (ME-SIMS) that significantly reduced fragmentation (Altelaar et al., 2005; McDonnell et al., 2005). The method was based on combining the high spatial resolution of SIMS with the organic matrix-based sample preparation techniques in MALDI. Distributions of cholesterol, lipids, and the APGWamide peptide (see **Figure 5**) within neurons in the cerebral ganglia were captured using ME-SIMS and the mass spectra were compared to MALDI-MS. Results from ME-SIMS exhibited subcellular spatial resolution and the spectra up to m/z 2,500 were consistent with MALDI-MS data.

Capillary microsampling followed by ESI-IMS-MS showed an improved ability to carry out the identification and quantitation of neuropeptides from subcellular samples of *L. stagnalis* neurons (Zhang et al., 2018). Subcellular analysis conducted on Fgp moto-neurons in the visceral ganglion found differences in neuropeptide composition and abundances between the nucleus and the cytoplasm. The nucleus contained six neuropeptides at different abundances within the FMRFamide-like class, whereas the cytoplasm contained nine (see **Figure 6**). The differences in neuropeptide composition between the nucleus and cytoplasm indicated the presence of active transport, and/or differences in neuropeptide production and degradation rates in each compartment (Zhang et al., 2018).

Comparison of the different techniques and recent improvements in the methods suggest that there is a significant capacity to advance neuropeptide analysis and imaging enabling molecular profiling at the subcellular level.

CONCLUSION

The neurons, neuronal circuits, ganglia, and the entire CNS of *L. stagnalis* present an opportunity for MS based exploration of neuropeptide expression and localization. Discovery and profiling of neuropeptides by MS at the single neuron level is facilitated by the relatively large 60 pL to 2 nL soma volumes of their neurons. The new insights on peptide expression are synergistic with the emerging genomic and transcriptomic information, and a wealth of electrophysiological data. Therefore, *L. stagnalis*, next to *A. californica*, remains an important model organism for neuroscience.

Moving forward, a closer integration of genomic information and MS-based peptide discovery is envisioned along the lines of peptidogenomics (Kersten et al., 2011). With the advent of spatially resolved single cell transcriptomics based on multiplexed error-robust fluorescence in-situ hybridization (MERFISH) cell types are identified with unprecedented specificity (Close et al., 2021). Correlations between spatial distributions of transcript-defined cell types and neuropeptides can shed new light complex CNS functions.

Mass spectrometry offers the advantage of untargeted exploration of peptides, ultimately covering the entire peptidome of the CNS (Jimenez et al., 2006; Li and Smit, 2010). A full complement of the expressed peptides and their posttranslational modifications will help to unravel the chemical determinants of the neuronal state. It is expected that sampling protocols and techniques will continue to progress such that single cell and subcellular analysis, and molecular imaging of neuropeptides

are refined, and become available to the study of species with more complex CNS.

AUTHOR CONTRIBUTIONS

AV and ZP conceived the study, designed the experiments, and conducted the data analysis. EW and LZ raised the snails and performed the dissection of the animals. EW, GM, SS, and LZ conducted the mass spectrometry experiments and evaluated the data. EW, ZP, and AV wrote the manuscript with input from all authors. All authors contributed to the article and approved the submitted version.

FUNDING

Funding from the Distinguished Guest Scientists Fellowship Programme of the Hungarian Academy of Sciences (2349/4/2019/KP) to AV and ZP is gratefully acknowledged. Single neuron analysis experiments conducted at the BLI in Tihany, Hungary, were supported by Hungarian Brain Research Project (2017–1.2.1-NKP-2017–00002).

ACKNOWLEDGMENTS

We thank John Young in the Tabin Lab at Harvard Medical School, Department of Genetics, for providing the initial cohort of experimental animals.

SUPPLEMENTARY MATERIAL

The Supplementary Material for this article can be found online at: https://www.frontiersin.org/articles/10.3389/fnmol.2021.670303/full#supplementary-material

REFERENCES

Ahn, S. J., Martin, R., Rao, S., and Choi, M. Y. (2017). Neuropeptides predicted from the transcriptome analysis of the gray garden slug Deroceras reticulatum. *Peptides* 93, 51–65. doi: 10.1016/j.peptides.2017.05.005

Altelaar, A. F. M., van Minnen, J., Jimenez, C. R., Heeren, R. M. A., and Piersma, S. R. (2005). Direct molecular Imaging of Lymnaea stagnalis nervous tissue at subcellular spatial resolution by mass spectrometry. *Anal. Chem.* 77, 735–741. doi: 10.1021/ac048329g

Azevedo, F. A. C., Carvalho, L. R. B., Grinberg, L. T., Farfel, J. M., Ferretti, R. E. L., Leite, R. E. P., et al. (2009). Equal numbers of neuronal and nonneuronal cells make the human brain an isometrically scaled-up primate brain. *J. Comp. Neurol.* 513, 532–541. doi: 10.1002/cne.21974

Benjamin, P. R. (2008). *Lymnaea. Scholarpedia [Online], 3(1)*. Available online at: http://www.scholarpedia.org/article/Lymnaea (accessed 24, January, 2021)

Benjamin, P. R., and Kemenes, I. (2013). *Lymnaea Neuropeptide Genes. Scholarpedia [Online], 8(7)*. Available online at: http://www.scholarpedia.org/article/Lymnaea_neuropeptide_genes (accessed 24, January, 2021)

Benjamin, P. R., and Kemenes, I. (2020). "Peptidergic systems in the pond snail lymnaea: from genes to hormones and behavior," in *Advances in Invertebrate (Neuro) Endocrinology*, eds A. B. Lange, S. Saleuddin, and I. Orchard (Palm Bay, FL: Apple Academic Press).

Bogerd, J., Li, K. W., Jimenez, C. R., Vanderschors, R. C., Ebberink, R. H. M., and Geraerts, W. P. M. (1994). Processing, axonal-transport and cardioregulatory functions of peptides derived from 2 related prohormones generated by alternative splicing of a single-gene in identified neurons VD1 and RPD2 of Lymnaea. *Mol. Brain Res.* 23, 66–72. doi: 10.1016/0169-328x(94)90212-7

Bouetard, A., Noirot, C., Besnard, A. L., Bouchez, O., Choisne, D., Robe, E., et al. (2012). Pyrosequencing-based transcriptomic resources in the pond snail Lymnaea stagnalis, with a focus on genes involved in molecular response to diquat-induced stress. *Ecotoxicology* 21, 2222–2234. doi: 10.1007/s10646-012-0977-1

Brierley, M. J., Yeoman, M. S., and Benjamin, P. R. (1997). Glutamatergic N2v cells are central pattern generator interneurons of the Lymnaea feeding system: new model for rhythm generation. *J. Neurophysiol.* 78, 3396–3407.

Bright, K., Kellett, E., Saunders, S. E., Brierley, M., Burke, J. F., and Benjamin, P. R. (1993). Mutually exclusive expression of alternatively spliced FMRFamide transcripts in identified neuronal systems of the snail Lymnaea. *J. Neurosci.* 13, 2719–2729.

Buckett, K. J., Peters, M., and Benjamin, P. R. (1990a). Excitation and inhibition of the heart of the snail, Lymnaea, by non-FMRFamidergic motoneurons. *Journal of Neurophysiology* 63, 1436–1447.

Buckett, K. J., Peters, M., Dockray, G. J., Vanminnen, J., and Benjamin, P. R. (1990b). Regulation of heartbeat in Lymnaea by motoneurons containing FMRFamide-like peptides. *J. Neurophysiol.* 63, 1426–1435.

Caprioli, R. M., Farmer, T. B., and Gile, J. (1997). Molecular imaging of biological samples: localization of peptides and proteins using MALDI-TOF MS. *Anal. Chem.* 69, 4751–4760. doi: 10.1021/ac970888i

Chaurand, P., Stoeckli, M., and Caprioli, R. M. (1999). Direct profiling of proteins in biological tissue sections by MALDI mass spectrometry. *Anal. Chem.* 71, 5263–5270. doi: 10.1021/ac990781q

Chen, R. B., and Li, L. J. (2010). Mass spectral imaging and profiling of neuropeptides at the organ and cellular domains. *Anal. Bioanal. Chem.* 397, 3185–3193. doi: 10.1007/s00216-010-3723-7

Close, J. L., Long, B. R., and Zeng, H. (2021). Spatially resolved transcriptomics in neuroscience. *Nat. Methods* 18, 23–25. doi: 10.1038/s41592-020-01040-z

Comi, T. J., Do, T. D., Rubakhin, S. S., and Sweedler, J. V. (2017). Categorizing cells on the basis of their chemical profiles: progress in single-cell mass spectrometry. *J. Am. Chem. Soc.* 139, 3920–3929. doi: 10.1021/jacs.6b12822

Date, S., Mizuno, H., Tsuyama, N., Harada, T., and Masujima, T. (2012). Direct drug metabolism monitoring in a live single hepatic cell by video mass spectrometry. *Anal. Sci.* 28, 201–203. doi: 10.2116/analsci.28.201

Davison, A., and Blaxter, M. L. (2005). An expressed sequence tag survey of gene expression in the pond snail Lymnaea stagnalis, an intermediate vector of trematodes [corrected]. *Parasitology* 130(Pt 5), 539–552. doi: 10.1017/s0031182004006791

De Boer, P., Ter Maat, A., Pieneman, A. W., Croll, R. P., Kurokawa, M., and Jansen, R. F. (1997). Functional role of peptidergic anterior lobe neurons in male sexual behavior of the snail Lymnaea stagnalis. *J. Neurophysiol.* 78, 2823–2833.

de With, N. D., van der Schors, R. C., Boer, H. H., and Ebberink, R. H. M. (1993). The sodium influx stimulating peptide of the pulmonate freshwater snail Lymnaea stagnalis. *Peptides* 14, 783–789. doi: 10.1016/0196-9781(93)90114-V

Dewith, N. D., and Vanderschors, R. C. (1992). SKPYMRFamide, a novel FMRFamide-related peptide in the snail Lymnaea-stagnalis. *Neuroreport* 3, 612–614. doi: 10.1097/00001756-199207000-00017

Diekmann, Y., and Pereira-Leal, J. B. (2013). Evolution of intracellular compartmentalization. *Biochem. J.* 449, 319–331. doi: 10.1042/bj20120957

Dreisewerd, K., Kingston, R., Geraerts, W. P. M., and Li, K. W. (1997). Direct mass spectrometric peptide profiling and sequencing of nervous tissues to identify peptides involved in male copulatory behavior in Lymnaea stagnalis. *Int. J. Mass Spectr.* 169, 291–299. doi: 10.1016/s0168-1176(97)00220-6

Ebberink, R. H. M., Price, D. A., Vanloenhout, H., Doble, K. E., Riehm, J. P., Geraerts, W. P. M., et al. (1987). The brain of Lymnaea contains a family

of FMRFamide-like peptides. *Peptides* 8, 515–522. doi: 10.1016/0196-9781(87)90018-0

El Filai, Z., Hornshaw, M., Smit, A. B., and Li, K. W. (2003). Retrograde labeling of single neurons in conjunction with MALDI high-energy collision-induced dissociation MS/MS analysis for peptide profiling and structural characterization. *Anal. Chem.* 75, 2996–3000. doi: 10.1021/ac034057q

El Filali, Z., de Boer, P., Pieneman, A. W., de Lange, R. P. J., Jansen, R. F., Ter Maat, A., et al. (2015). Single-cell analysis of peptide expression and electrophysiology of right parietal neurons involved in male copulation behavior of a simultaneous hermaphrodite. *Invertebrate Neurosci.* 15:7. doi: 10.1007/s10158-015-0184-x

El Filali, Z., Van Minnen, J., Liu, W. K., Smit, A. B., and Li, K. W. (2006). Peptidomics analysis of neuropeptides involved in copulatory behavior of the mollusk Lymnaea stagnalis. *J. Proteome Res.* 5, 1611–1617. doi: 10.1021/pr060014p

Feng, Z. P., Zhang, Z., van Kesteren, R. E., Straub, V. A., van Nierop, P., Jin, K., et al. (2009). Transcriptome analysis of the central nervous system of the mollusc Lymnaea stagnalis. *BMC Genomics* 10:451. doi: 10.1186/1471-2164-10-451

Fodor, I., Hussein, A. A. A., Benjamin, P. R., Koene, J. M., and Pirger, Z. (2020a). The unlimited potential of the great pond snail. *Lymnaea stagnalis*. *Elife* 9:e56962. doi: 10.7554/eLife.56962

Fodor, I., Svigruha, R., Kemenes, G., Kemenes, I., and Pirger, Z. (2021). The great pond snail (Lymnaea stagnalis) as a model of ageing and age-related memory impairment: an overview. *J. Gerontol A Biol. Sci. Med. Sci.* doi: 10.1093/gerona/glab014 [Epup ahead of print],

Fodor, I., Urban, P., Scott, A. P., and Pirger, Z. (2020b). A critical evaluation of some of the recent so-called 'evidence' for the involvement of vertebrate-type sex steroids in the reproduction of mollusks. *Mol. Cell. Endocrinol.* 516:110949. doi: 10.1016/j.mce.2020.110949

Fulton, D., Kemenes, I., Andrew, R. J., and Benjamin, P. R. (2005). A single time-window for protein synthesis-dependent long-term memory formation after one-trial appetitive conditioning. *Eur. J. Neurosci.* 21, 1347–1358. doi: 10.1111/j.1460-9568.2005.03970.x

Hoek, R. M., Li, K. W., van Minnen, J., Lodder, J. C., de Jong-Brink, M., Smit, A. B., et al. (2005). LFRFamides: a novel family of parasitation-induced -RFamide neuropeptides that inhibit the activity of neuroendocrine cells in Lymnaea stagnalis. *J. Neurochem.* 92, 1073–1080. doi: 10.1111/j.1471-4159.2004.02927.x

Hummon, A. B., Amare, A., and Sweedler, J. V. (2006). Discovering new invertebrate neuropeptides using mass spectrometry. *Mass Spectr. Rev.* 25, 77–98. doi: 10.1002/mas.20055

Hummon, A. B., Sweedler, J. V., and Corbin, R. W. (2003). Discovering new neuropeptides using single-cell mass spectrometry. *Trac-Trends Anal. Chem.* 22, 515–521. doi: 10.1016/s0165-9936(03)00901-4

Jimenez, C. R., Li, K. W., Dreisewerd, K., Spijker, S., Kingston, R., Bateman, R. H., et al. (1998). Direct mass spectrometric peptide profiling and sequencing of single neurons reveals differential peptide patterns in a small neuronal network. *Biochemistry* 37, 2070–2076. doi: 10.1021/bi971848b

Jimenez, C. R., Spijker, S., de Schipper, S., Lodder, J. C., Janse, C. K., Geraerts, W. P. M., et al. (2006). Peptidomics of a single identified neuron reveals diversity of multiple neuropeptides with convergent actions on cellular excitability. *J. Neurosci.* 26, 518–529. doi: 10.1523/jneurosci.2566-05.2006

Jimenez, C. R., ter Maat, A., Pieneman, A., Burlingame, A. L., Smit, A. B., and Li, K. W. (2004). Spatio-temporal dynamics of the egg-laying-inducing peptides during an egg-laying cycle: a semiquantitative matrix-assisted laser desorption/ionization mass spectrometry approach. *J. Neurochem.* 89, 865–875. doi: 10.1111/j.1471-4159.2004.02353.x

Jimenez, C. R., Vanveelen, P. A., Li, K. W., Wildering, W. C., Geraerts, W. P. M., Tjaden, U. R., et al. (1994). Neuropeptide expression and processing as revealed by direct matrix-assisted laser-desorption ionization mass-spectrometry of single neurons. *J. Neurochem.* 62, 404–407.

Kellett, E., Perry, S. J., Santama, N., Worster, B. M., Benjamin, P. R., and Burke, J. F. (1996). Myomodulin gene of Lymnaea: structure, expression, and analysis of neuropeptides. *J. Neurosci.* 16, 4949–4957.

Kellett, E., Saunders, S. E., Li, K. W., Staddon, J. W., Benjamin, P. R., and Burke, J. F. (1994). Genomic organization of the FMRFamide gene in Lymnaea - multiple exons encoding novel neuropeptides. *J. Neurosci.* 14, 6564–6570.

Kemenes, G., Staras, K., and Benjamin, P. R. (2001). Multiple types of control by identified interneurons in a sensory-activated rhythmic motor pattern. *J. Neurosci.* 21, 2903–2911. doi: 10.1523/jneurosci.21-08-02903.2001

Kersten, R. D., Yang, Y. L., Xu, Y. Q., Cimermancic, P., Nam, S. J., Fenical, W., et al. (2011). A mass spectrometry-guided genome mining approach for natural product peptidogenomics. *Nat. Chem. Biol.* 7, 794–802. doi: 10.1038/nchembio.684

Kiss, T., and Pirger, Z. (2006). *Neuropeptides as Modulators and Hormones in Terrestrial Snails: Their Occurence, Distribution and Physiological Significance*. Kerala: Transworld Research Network.

Koene, J. M. (2010). Neuro-endocrine control of reproduction in hermaphroditic freshwater snails: mechanisms and evolution. *Front. Behav. Neurosci.* 4:167. doi: 10.3389/fnbeh.2010.00167

Kojima, S., Sunada, H., Mita, K., Sakakibara, M., Lukowiak, K., and Ito, E. (2015). Function of insulin in snail brain in associative learning. *J. Comp. Physiol. Neuroethol. Sensory Neural Behav. Physiol.* 201, 969–981. doi: 10.1007/s00359-015-1032-5

Li, K. W., Van Minnen, J., Van Veelen, P. A., Van der Greef, J., and Geraerts, W. P. M. (1996). Structure, localization and action of a novel inhibitory neuropeptide involved in the feeding of Lymnaea. *Mol. Brain Res.* 37, 267–272. doi: 10.1016/0169-328x(95)00333-n

Li, K. W., Jimenez, C. R., Vanveelen, P. A., and Geraerts, W. P. M. (1994a). Processing and targeting of a molluscan egg-laying peptide prohormone as revealed by mass-spectrometric peptide fingerprinting and peptide sequencing. *Endocrinology* 134, 1812–1819. doi: 10.1210/en.134.4.1812

Li, K. W., Kingston, R., Dreisewerd, K., Jimenez, C. R., vanderSchors, R. C., Bateman, R. H., et al. (1997). Structural elucidation of a peptide from a single neuron by matrix-assisted laser desorption/ionization employing a tandem double focusing magnetic-orthogonal acceleration time-of-flight mass spectrometer. *Anal. Chem.* 69, 563–565. doi: 10.1021/ac9609440

Li, K. W., and Smit, A. B. (2010). "Mass spectrometric analysis of molluscan neuropeptides," in *Peptidomics: Methods and Protocols*, ed. M. Soloviev (Totowa, NJ: Humana Press), 49–56.

Li, K. W., Vangolen, F. A., Vanminnen, J., Vanveelen, P. A., Vandergreef, J., and Geraerts, W. P. M. (1994b). Structural identification, neuronal synthesis, and role in male copulation of myomodulin-a of Lymnaea - a study involving direct peptide profiling of nervous-tissue by mass-spectrometry. *Mol. Brain Res.* 25, 355–358. doi: 10.1016/0169-328x(94)90172-4

Li, L. J., Garden, R. W., and Sweedler, J. V. (2000). Single-cell MALDI: a new tool for direct peptide profiling. *Trends Biotechnol.* 18, 151–160. doi: 10.1016/s0167-7799(00)01427-x

Linacre, A., Kellett, E., Saunders, S., Bright, K., Benjamin, P. R., and Burke, J. F. (1990). Cardioactive neuropeptide PHE-MET-ARG-PHE-NH2 (FMRFamide) and novel related peptides are encoded in multiple copies by a single gene in the snail Lymnaea-stagnalis. *J. Neurosci.* 10, 412–419.

Martin, W. (2010). Evolutionary origins of metabolic compartmentalization in eukaryotes. *Philos. Trans. R. Soc. B Biol. Sci.* 365, 847–855. doi: 10.1098/rstb.2009.0252

McDonnell, L. A., Piersma, S. R., Altelaar, A. F. M., Mize, T. H., Luxembourg, S. L., Verhaert, P., et al. (2005). Subcellular imaging mass spectrometry of brain tissue. *J. Mass Spectr.* 40, 160–168. doi: 10.1002/jms.735

Miao, H., Rubakhin, S. S., and Sweedler, J. V. (2005). Subcellular analysis of D-Aspartate. *Anal. Chem.* 77, 7190–7194. doi: 10.1021/ac0511694

Mizuno, H., Tsuyama, N., Harada, T., and Masujima, T. (2008). Live single-cell video-mass spectrometry for cellular and subcellular molecular detection and cell classification. *J. Mass Spectr.* 43, 1692–1700. doi: 10.1002/jms.1460

Nagle, G. T., de Jong-Brink, M., Painter, S. D., and Li, K. W. (2001). Structure, localization and potential role of a novel molluscan trypsin inhibitor in Lymnaea. *Eur. J. Biochem.* 268, 1213–1221. doi: 10.1046/j.1432-1327.2001.01972.x

Patel, B. A., Arundell, M., Parker, K. H., Yeoman, M. S., and O'Hare, D. (2005). Simple and rapid determination of serotonin and catecholamines in biological tissue using high-performance liquid chromatography with electrochemical detection. *J. Chromatogr. B Anal. Technol. Biomed. Life Sci.* 818, 269–276. doi: 10.1016/j.jchromb.2005.01.008

Perry, S. J., Dobbins, A. C., Schofield, M. G., Piper, M. R., and Benjamin, P. R. (1999). Small cardioactive peptide gene: structure, expression and mass spectrometric analysis reveals a complex pattern of co-transmitters in a snail feeding neuron. *Eur. J. Neurosci.* 11, 655–662.

Perry, S. J., Straub, V. A., Kemenes, G., Santama, N., Worster, B. M., Burke, J. F., et al. (1998). Neural modulation of gut motility by myomodulin peptides and acetylcholine in the snail Lymnaea. *J. Neurophysiol.* 79, 2460–2474.

Pirger, Z., Naskar, S., Laszlo, Z., Kemenes, G., Reglodi, D., and Kemenes, I. (2014). Reversal of age-related learning deficiency by the vertebrate PACAP and IGF-1 in a novel invertebrate model of aging: the pond snail (Lymnaea stagnalis). *J. Gerontol. A Biol. Sci. Med. Sci.* 69, 1331–1338. doi: 10.1093/gerona/glu068

Rivi, V., Benatti, C., Colliva, C., Radighieri, G., Brunello, N., Tascedda, F., et al. (2020). Lymnaea stagnalis as model for translational neuroscience research: From pond to bench. *Neurosci. Biobehav. Rev.* 108, 602–616. doi: 10.1016/j.neubiorev.2019.11.020

Rubakhin, S. S., Garden, R. W., Fuller, R. R., and Sweedler, J. V. (2000). Measuring the peptides in individual organelles with mass spectrometry. *Nat. Biotechnol.* 18, 172–175. doi: 10.1038/72622

Rubakhin, S. S., Greenough, W. T., and Sweedler, J. V. (2003). Spatial profiling with MALDI MS: distribution of neuropeptides within single neurons. *Anal. Chem.* 75, 5374–5380. doi: 10.1021/ac034498

Rubakhin, S. S., Romanova, E. V., Nemes, P., and Sweedler, J. V. (2011). Profiling metabolites and peptides in single cells. *Nat. Methods* 8, S20–S29. doi: 10.1038/nmeth.1549

Sadamoto, H., Takahashi, H., Okada, T., Kenmoku, H., Toyota, M., and Asakawa, Y. (2012). De novo sequencing and transcriptome analysis of the central nervous system of mollusc Lymnaea stagnalis by deep RNA sequencing. *PLoS One* 7:e42546. doi: 10.1371/journal.pone.0042546

Santama, N., and Benjamin, P. R. (2000). Gene expression and function of FMRFamide-related neuropeptides in the snail Lymnaea. *Microscopy Res. Tech.* 49, 547–556. doi: 10.1002/1097-0029(20000615)49:6<547::aid-jemt5<3.0.co;2-y

Santama, N., Brierley, M., Burke, J. F., and Benjamin, P. R. (1994a). Neural-network controlling feeding in Lymnaea-stagnalis - immunocytochemical localization of myomodulin, small cardioactive peptide, buccalin, and FMRFamide-related peptides. *J. Comp. Neurol.* 342, 352–365. doi: 10.1002/cne.903420304

Santama, N., Li, K. W., Bright, K. E., Yeoman, M., Geraerts, W. P. M., Benjamin, P. R., et al. (1993). Processing of the FMRFamide precursor protein in the snail Lymnaea-stagnalis - characterization and neuronal localization of a novel peptide, SEEPLY. *Eur. J. Neurosci.* 5, 1003–1016. doi: 10.1111/j.1460-9568.1993.tb00952.x

Santama, N., Wheeler, C. H., Burke, J. F., and Benjamin, P. R. (1994b). Neuropeptides myomodulin, small cardioactive peptide, and buccalin in the central-nervous-system of Lymnaea-stagnalis - purification, immunoreactivity, and artifacts. *J. Comp. Neurol.* 342, 335–351. doi: 10.1002/cne.903420303

Santama, N., Wheeler, C. H., Skingsley, D. R., Yeoman, M. S., Bright, K., Kaye, I., et al. (1995). Identification, distribution and physiological-activity of 3 novel neuropeptides of Lymnaea - EFLRLamide and PQFYRLamide encoded by the FMRFamide gene, and a related peptide. *Eur. J. Neurosci.* 7, 234–246. doi: 10.1111/j.1460-9568.1995.tb01059.x

Saunders, S. E., Bright, K., Kellett, E., Benjamin, P. R., and Burke, J. F. (1991). Neuropeptides GLY-ASP-PRO-PHE-LEU-ARG-PHE-amide (GDPFLRFamide) and SERASP-PRO-PHE-LEU-ARG-PHE-amide (SDPFLRFamide) are encoded by an exon 3' to PHE-MET-ARG-PHE-NH2 (FMRFamide) in the snail Lymnaea-stagnalis. *J. Neurosci.* 11, 740–745.

Schot, L. P. C., Boer, H. H., Swaab, D. F., and Vannoorden, S. (1981). Immunocytochemical demonstration of peptidergic neurons in the central nervous-system of the pond snail lymnaea-stagnalis with antisera raised to biologically-active peptides of vertebrates. *Cell Tissue Res.* 216, 273–291. doi: 10.1007/bf00233620

Smit, A. B., Geraerts, W. P. M., Meester, I., Vanheerikhuizen, H., and Joosse, J. (1991). Characterization of a cdna clone encoding molluscan insulin-related peptide-ii of lymnaea-stagnalis. *Eur. J. Biochem.* 199, 699–703. doi: 10.1111/j.1432-1033.1991.tb16173.x

Smit, A. B., Jimenez, C. R., Dirks, R. W., Croll, R. P., and Geraerts, W. P. M. (1992). Characterization of a cDNA clone encoding multiple copies of the neuropeptide APGWamide in the mollusk Lymnaea-stagnalis. *J. Neurosci.* 12, 1709–1715.

Smit, A. B., Spijker, S., Van Minnen, J., Burke, J. F., De Winter, F., Van Elk, R., et al. (1996). Expression and characterization of molluscan insulin-related peptide VII from the molluscLymnaea stagnalis. *Neuroscice* 70, 589–596. doi: 10.1016/0306-4522(95)00378-9

Smit, A. B., Thijsen, S. F. T., and Geraerts, W. P. M. (1993). cDNA cloning of the sodium-influx-stimulating peptide in the mollusc, Lymnaea stagnalis. *Eur. J. Biochem.* 215, 397–400. doi: 10.1111/j.1432-1033.1993.tb18046.x

Smit, A. B., van Kesteren, R. E., Spijker, S., Van Minnen, J., van Golen, F. A., Jimenez, C. R., et al. (2003). Peptidergic modulation of male sexual behavior in Lymnaea stagnalis: structural and functional characterization of -FVamide neuropeptides. *J. Neurochem.* 87, 1245–1254. doi: 10.1046/j.1471-4159.2003.02086.x

Stevens, L., Kumar, S., and Blaxter, L. M. (2016). *Lymnaea Stagnalis, Whole Genome Shotgun Sequencing Project*.

Stolee, J. A., Shrestha, B., Mengistu, G., and Vertes, A. (2012). Observation of Subcellular Metabolite Gradients in Single Cells by Laser Ablation Electrospray Ionization Mass Spectrometry. *Angewandte Chemie Int. Edn.* 51, 10386–10389. doi: 10.1002/anie.201205436

Sweedler, J. V., Li, L., Rubakhin, S. S., Alexeeva, V., Dembrow, N. C., Dowling, O., et al. (2002). Identification and characterization of the feeding circuit-activating peptides, a novel neuropeptide family of Aplysia. *J. Neurosci.* 22, 7797–7808.

Tensen, C. P., Cox, K. J. A., Smit, A. B., van der Schors, R. C., Meyerhof, W., Richter, D., et al. (1998). The Lymnaea cardioexcitatory peptide (LyCEP) receptor: a G-proteincoupled receptor for a novel member of the RFamide neuropeptide family. *J. Neurosci.* 18, 9812–9821.

Totani, Y., Aonuma, H., Oike, A., Watanabe, T., Hatakeyama, D., Sakakibara, M., et al. (2019). Monoamines, insulin and the roles they play in associative learning in pond snails. *Front. Behav. Neurosci.* 13:65. doi: 10.3389/fnbeh.2019.00065

van Tol-Steye, H., Lodder, J. C., Mansvelder, H. D., Planta, R. J., van Heerikhuizen, H., and Kits, K. S. (1999). Roles of G-protein beta gamma, arachidonic acid, and phosphorylation in convergent activation of an S-like potassium conductance by dopamine, Ala-Pro-Gly-Trp-NH2, and Phe-Met-Arg-Phe-NH2. *J. Neurosci.* 19, 3739–3751.

Van Kesteren, R., Smit, A., De Lange, R., Kits, K., Van Golen, F., Van Der Schors, R., et al. (1995). Structural and functional evolution of the vasopressin/oxytocin superfamily: vasopressin-related conopressin is the only member present in Lymnaea, and is involved in the control of sexual behavior. *J. Neurosci.* 15, 5989–5998. doi: 10.1523/jneurosci.15-09-05989.1995

Van Kesteren, R. E., Carter, C., Dissel, H. M. G., van Minnen, J., Gouwenberg, Y., Syed, N. I., et al. (2006). Local synthesis of actin-binding protein β-thymosin regulates neurite outgrowth. *J. Neurosci.* 26, 152–157. doi: 10.1523/jneurosci.4164-05.2006

van Kesteren, R. E., Smit, A. B., Dirks, R. W., de With, N. D., Geraerts, W. P., and Joosse, J. (1992). Evolution of the vasopressin/oxytocin superfamily: characterization of a cDNA encoding a vasopressin-related precursor, preproconopressin, from the mollusc Lymnaea stagnalis. *Proc. Natl. Acad. Sci.* 89, 4593–4597. doi: 10.1073/pnas.89.10.4593

Vanveelen, P. A., Jimenez, C. R., Li, K. W., Wildering, W. C., Geraerts, W. P. M., Tjaden, U. R., et al. (1993). Direct peptide profiling of single neurons by matrix-assisted laser-desorption ionization mass-spectrometry. *Organic Mass Spectr.* 28, 1542–1546. doi: 10.1002/oms.1210281229

Vanveelen, P. A., Tjaden, U. R., Vandergreef, J., and Dewith, N. D. (1991). Sequence-informative fragmentation in an 8.9 kda oligopeptide using plasma desorption mass-spectrometry. *Organic Mass Spectr.* 26, 345–346. doi: 10.1002/oms.1210260429

Villalobos, C., Alonso, M. T., and Garcia-Sancho, J. (2009). "Bioluminescence imaging of calcium oscillations inside intracellular organelles," in *Bioluminescence: Methods and Protocols*, Second Edn, eds P. B. Rich and C. Douillet (Totowa, NJ: Humana Press), 203–214.

Wang, Y., Wang, M., Yin, S., Jang, R., Wang, J., Xue, Z., et al. (2015). NeuroPep: a comprehensive resource of neuropeptides. *Database (Oxford)* 2015: bav038.

Weiss, S., Goldberg, J. I., Chohan, K. S., Stell, W. K., Drummond, G. I., and Lukowiak, K. (1984). Evidence for FMRFamide as a neurotransmitter in the gill of Aplysia-californica. *J. Neurosci.* 4, 1994–2000.

Worster, B. M., Yeoman, M. S., and Benjamin, P. R. (1998). Matrix-assisted laser desorption/ionization time of flight mass spectrometric analysis of the pattern of peptide expression in single neurons resulting from alternative mRNA splicing of the FMRFamide gene. *Eur. J. Neurosci.* 10, 3498–3507. doi: 10.1046/j.1460-9568.1998.00361.x

Zhang, L. W., Khattar, N., Kemenes, I., Kemenes, G., Zrinyi, Z., Pirger, Z., et al. (2018). Subcellular peptide localization in single identified neurons by capillary microsampling mass spectrometry. *Sci. Rep.* 8:12227. doi: 10.1038/s41598-018-29704-z

Conflict of Interest: The authors declare that the research was conducted in the absence of any commercial or financial relationships that could be construed as a potential conflict of interest.

frontiers in Cellular Neuroscience

ORIGINAL RESEARCH
published: 09 June 2021
doi: 10.3389/fncel.2021.673439

Oxytocin Regulates Synaptic Transmission in the Sensory Cortices in a Developmentally Dynamic Manner

Jing Zhang[1,2†], Shu-Jing Li[1†], Wanying Miao[1†], Xiaodi Zhang[1†], Jing-Jing Zheng[1], Chen Wang[3] and Xiang Yu[1,4*]*

[1]*Institute of Neuroscience, State Key Laboratory of Neuroscience, Center for Excellence in Brain Science and Intelligence Technology, Chinese Academy of Sciences, Shanghai, China,* [2]*Department of Clinical Pharmacology, Pharmacy College, Nanjing Medical University, Nanjing, China,* [3]*CAS Key Laboratory of Biological Effects of Nanomaterials and Nanosafety, CAS Center for Excellence in Nanoscience, National Center for Nanoscience and Technology, Beijing, China,* [4]*School of Life Sciences, Peking-Tsinghua Center for Life Sciences, and Peking University McGovern Institute, Peking University, Beijing, China*

OPEN ACCESS

Edited by:
Miao He,
Fudan University, China

Reviewed by:
Ji Hu,
ShanghaiTech University, China
Nan-Jie Xu,
Shanghai Jiao Tong University, China
Elizabeth Hammock,
Florida State University, United States

****Correspondence:***
Jing Zhang
zj1984@njmu.edu.cn
Xiang Yu
yuxiang01@pku.edu.cn

†These authors share first authorship

Specialty section:
This article was submitted to Cellular Neurophysiology, a section of the journal Frontiers in Cellular Neuroscience

Received: *27 February 2021*
Accepted: *10 May 2021*
Published: *09 June 2021*

Citation:
Zhang J, Li S-J, Miao W, Zhang X, Zheng J-J, Wang C and Yu X (2021) Oxytocin Regulates Synaptic Transmission in the Sensory Cortices in a Developmentally Dynamic Manner. Front. Cell. Neurosci. 15:673439. doi: 10.3389/fncel.2021.673439

The development and stabilization of neuronal circuits are critical to proper brain function. Synapses are the building blocks of neural circuits. Here we examine the effects of the neuropeptide oxytocin on synaptic transmission in L2/3 pyramidal neurons of the barrel field of the primary somatosensory cortex (S1BF). We find that perfusion of oxytocin onto acute brain slices significantly increases the frequency of miniature excitatory postsynaptic currents (mEPSC) of S1BF L2/3 pyramidal neurons at P10 and P14, but reduces it at the later ages of P22 and P28; the transition occurs at around P18. Since oxytocin expression is itself regulated by sensory experience, we also examine whether the effects of oxytocin on excitatory synaptic transmission correlate with that of sensory experience. We find that, indeed, the effects of sensory experience and oxytocin on excitatory synaptic transmission of L2/3 pyramidal neurons both peak at around P14 and plateau around P18, suggesting that they regulate a specific form of synaptic plasticity in L2/3 pyramidal neurons, with a sensitive/critical period ending around P18. Consistently, oxytocin receptor (*Oxtr*) expression in glutamatergic neurons of the upper layers of the cerebral cortex peaks around P14. By P28, however, *Oxtr* expression becomes more prominent in GABAergic neurons, especially somatostatin (SST) neurons. At P28, oxytocin perfusion increases inhibitory synaptic transmission and reduces excitatory synaptic transmission, effects that result in a net reduction of neuronal excitation, in contrast to increased excitation at P14. Using oxytocin knockout mice and *Oxtr* conditional knockout mice, we show that loss-of-function of oxytocin affects baseline excitatory synaptic transmission, while *Oxtr* is required for oxytocin-induced changes in excitatory synaptic transmission, at both P14 and P28. Together, these results demonstrate that oxytocin has complex and dynamic functions in

regulating synaptic transmission in cortical L2/3 pyramidal neurons. These findings add to existing knowledge of the function of oxytocin in regulating neural circuit development and plasticity.

Keywords: oxytocin, oxytocin receptor, synaptic transmission, pyramidal neurons, primary somatosensory cortex, critical period, sensitive period

INTRODUCTION

The wiring of neural circuits is an intricate developmental process, regulated by a combination of intrinsic and extrinsic cues (Katz and Shatz, 1996; Crair, 1999; Sur and Rubenstein, 2005; Blankenship and Feller, 2010). In rodents, wiring of the cerebral cortex occurs mostly during the first 4 weeks of postnatal development (Micheva and Beaulieu, 1996). This process is regulated by genetic programming, in combination with environmental factors (Feldman and Brecht, 2005; Fox and Wong, 2005; Nithianantharajah and Hannan, 2006; Sale et al., 2009). The anatomical and functional properties of neurons in the sensory cortices are particularly sensitive to modification by environmental stimuli during a limited developmental window, known as the "sensitive period" (Knudsen, 2004; Luby et al., 2020). An extreme form of sensitive period is the "critical period", where appropriate experience is essential for the normal development of a pathway or set of connections (Hensch, 2004). The most well-studied example of the critical period is the formation of ocular dominance columns in the visual cortex (Wiesel and Hubel, 1963). Subsequent studies showed that different aspects of visual cortical development have different sensitive/critical periods (Hensch, 2004; Hooks and Chen, 2007). Other cortical regions also have various sensitive/critical periods for different aspects of their development (Neville and Bavelier, 2002; Erzurumlu and Gaspar, 2012; Kral, 2013).

In previous work, we identified a new form of experience-dependent cross-modal plasticity in the sensory cortices, by showing that deprivation of sensory inputs in one modality cross-modally delayed the development of other sensory cortices (Zheng et al., 2014). Specifically, we showed that deprivation of somatosensory inputs through whisker deprivation (WD) reduced excitatory synaptic transmission in L2/3 pyramidal neurons of both the barrel field of the primary somatosensory cortex (S1BF), and the primary visual cortex (V1), at both P7 and P14. We further showed that the neuropeptide oxytocin, mostly synthesized in the paraventricular nuclei of the hypothalamus (PVH) and the supraoptic nuclei (SON), is an important mediator of this form of plasticity. Specifically, at P14, oxytocin knockout mice had reduced excitatory synaptic transmission, similar to the effects of WD, while perfusion of oxytocin onto acute brain slices or *in vivo* injection of oxytocin enhanced excitatory synaptic transmission (Zheng et al., 2014).

An important remaining question is whether this form of experience- and oxytocin-dependent plasticity has a sensitive/critical period. Here, we address this question by examining the effect of experience and oxytocin on synaptic transmission on L2/3 pyramidal neurons at different developmental time points. Our results show that this experience-dependent plasticity in the sensory cortices has a critical period ending around P18. We further show that the effect of oxytocin on excitatory and inhibitory synaptic transmission, as well as the expression of oxytocin receptors in the cerebral cortex, change during cortical development. Together, these results demonstrate that the developmental effects of oxytocin on excitatory and inhibitory synaptic transmission are dynamic and complex.

MATERIALS AND METHODS

Animals

All animal procedures complied with the animal care standards set forth by the US National Institutes of Health and were approved by the Institutional Animal Care and Use Committee at the Institute of Neuroscience, Chinese Academy of Sciences, and of Peking University. Mice on C57BL/6 background were raised in a specific pathogen-free (SPF) environment and group-housed under a 12h–12 h light-dark cycle with food and water provided *ad libitum* from the cage lid. Their health status was monitored routinely.

GAD67-GFP mice [also known as Gad1$^{tm1.1Tama}$; GAD67-GFP (delta neo)] (Tamamaki et al., 2003) were gifts of Yuchio Yanagawa (Department of Genetic and Behavioral Neuroscience, Gunma University Graduate School of Medicine, Maebashi, Japan). The *Oxt*$^{+/-}$ mice (*B6; 129S-Oxt*^{tm1Wsy}*/J*; JAX: 002713, RRID: IMSR_JAX:002713) on C57/BL6 background (Young et al., 1996) were gifts of Dr. Scott Young (US National Institute of Mental Health). *E2a-Cre* mice [B6.FVB-Tg (EIIa-cre) C5379Lmgd/J; JAX: 003724, RRID: IMSR_JAX:003724] express Cre recombinase in the early embryo, prior to implantation (Lakso et al., 1996). *Nex-Cre* mice (gift of Prof. Klaus Nave, Max Planck Institute, Goettingen, Germany) express Cre recombinase in excitatory neurons of the cerebral cortex and hippocampus starting from the late embryo (Goebbels et al., 2006). Oxytocin receptor conditional knockout mice (*Oxtr*$^{flox/flox}$; full name: B6.129 (SJL)-Oxtr$^{tm1.1Wsy}$/J; JAX:008471, RRID:IMSR_JAX:(008471) (Lee et al., 2008) were crossed with *E2a-Cre* or *Nex-Cre* to generate homozygous floxed and heterozygous Cre mice. Littermate homozygous floxed mice not expressing Cre were used as controls. The P7 group consists of P7–P9 mice, the P10 group consists of P9–P11 mice, the P14 group consists of P14–P15 mice, the P18 group consists of P17–P19 mice, the P21 group consists of P21–P22 mice, the P28 group consists of P26–P30 mice, and the adult group consists of 2–4 month-old mice. For data presented in **Figure 1G**, mice in the P18 and P22 groups were of exact ages. Both male and female mice were used for all experiments.

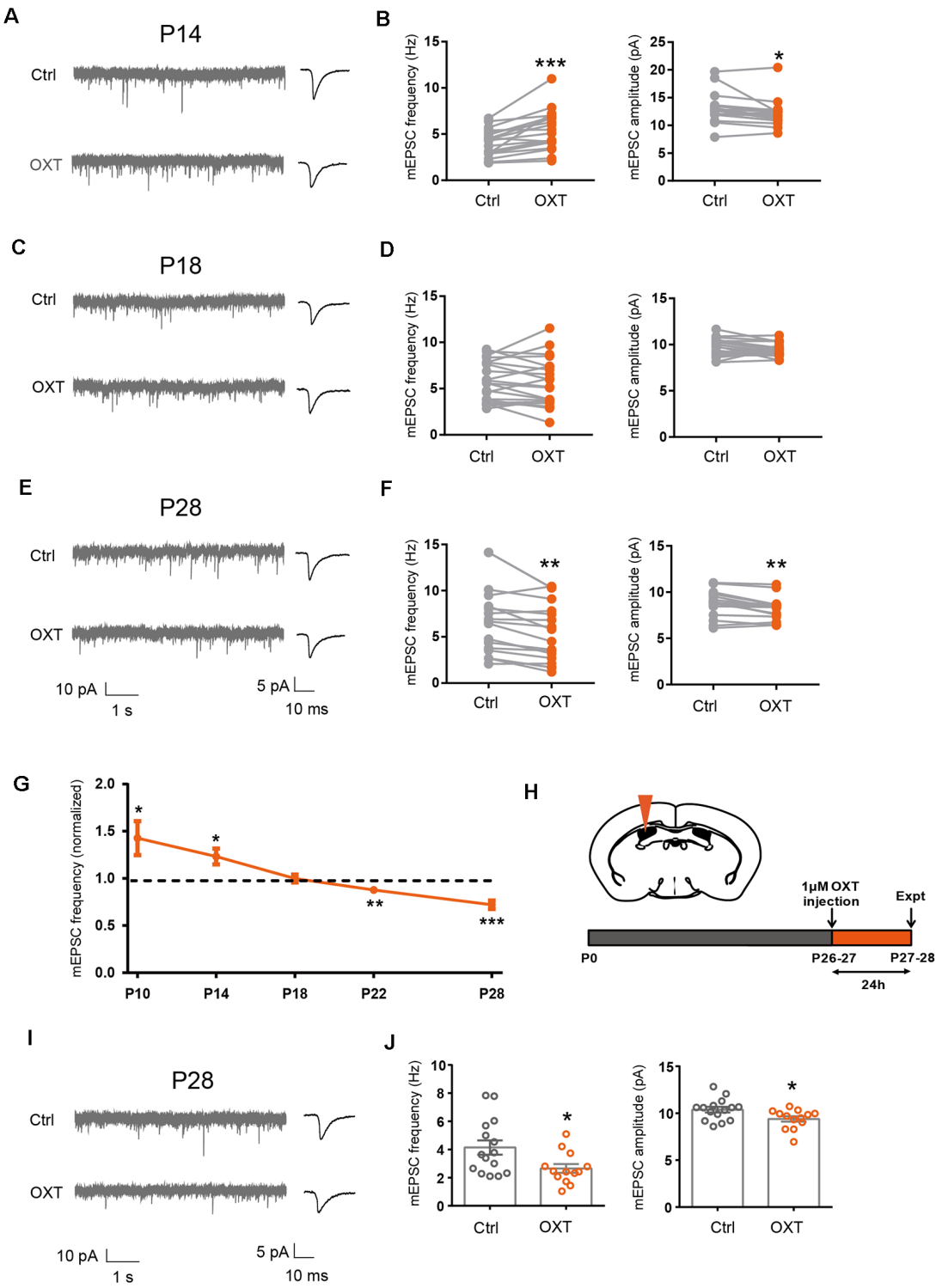

FIGURE 1 | Dynamic regulation of excitatory synaptic transmission by oxytocin. **(A,C,E)** Representative mEPSC recordings (left) and average waveforms (right) from S1BF L2/3 pyramidal neurons before (Ctrl) and after oxytocin (OXT) application, age as indicated. **(B)** Oxytocin application increased mEPSC frequency but reduced mEPSC amplitude in P14 mice (frequency: Ctrl, 4.10 ± 0.35 Hz; OXT, 5.43 ± 0.52 Hz; $n = 18$; $P < 0.001$, paired t-test; amplitude: Ctrl, 13.01 ± 0.63 pA; OXT, 12.17 ± 0.58 pA; $P < 0.05$, paired t-test). **(D)** Oxytocin application did not significantly affect mEPSC frequency or amplitude at P18 (frequency: Ctrl, 5.80 ± 0.47 Hz; OXT, 5.65 ± 0.57 Hz; $n = 21$; $P = 0.60$, paired t-test; amplitude: Ctrl, 9.71 ± 0.21 pA; OXT, 9.39 ± 0.15 pA; $P = 0.08$, paired

(*Continued*)

FIGURE 1 | Continued
t-test). **(F)** Oxytocin application reduced both mEPSC frequency and amplitude in P28 mice (frequency: Ctrl, 6.35 ± 0.82 Hz; OXT, 5.40 ± 0.76 Hz; $n = 16$; $P < 0.01$, paired *t*-test; amplitude: Ctrl, 8.75 ± 0.36 pA; OXT, 8.24 ± 0.31 pA; $P < 0.01$, paired *t*-test). **(G)** Developmental effects of oxytocin on mEPSC frequency (effect of oxytocin application normalized to before application control; P10: 1.43 ± 0.18; $n = 10$; $P < 0.05$; P14: 1.23 ± 0.08; $n = 9$; $P < 0.05$; P18: 0.96 ± 0.03; $n = 12$; $P = 0.21$; P22: 0.88 ± 0.04; $n = 16$; $P < 0.01$; P28: 0.72 ± 0.05; $n = 12$; $P < 0.001$, paired *t*-test at each time point). **(H)** Schematic of experimental procedure for *in vivo* oxytocin injection. **(I)** Representative mEPSC recordings (left) and average waveforms (right) for conditions as indicated in P28 mice. **(J)** mEPSC frequency and amplitude 24 h following *in vivo* oxytocin injection in P28 mice (frequency: Ctrl, 4.14 ± 0.50 Hz, $n = 15$; OXT, 2.66 ± 0.31 Hz, $n = 13$; $P < 0.05$, unpaired *t*-test; amplitude: Ctrl, 10.38 ± 0.30 pA; OXT, 9.40 ± 0.29 pA; $P < 0.05$, unpaired *t*-test). In this and subsequent figures, error bars represent SEM; $^*P < 0.05$, $^{**}P < 0.01$, $^{***}P < 0.001$.

For whisker deprivation (WD) experiments, littermates were randomly assigned to the control or WD group. All pups underwent anesthesia (isoflurane), but only mice assigned to the WD group had their whiskers trimmed from P0–P3 and plucked every other day from P4 until the time of the experiment. For dark-rearing (DR) experiments, pregnant dams were randomly placed in a cage completely covered by thick black plastic 1–4 days before delivery, and mice were cared for under dim red light. Mice were dark-reared until the time of experiment; control mice were from litters raised in parallel, under standard lighting conditions.

Acute Brain Slice Preparation

Brain slices from deeply anesthetized mice (0.14 g/kg sodium pentobarbital) were essentially prepared as previously described (Zheng et al., 2014). Brains were rapidly removed and immersed in ice-cold dissection solution. For young mice (P7–P21), choline-based dissection buffer contained (in mM): CholineCl 110, KCl 2.5, NaH_2PO_4 1.3, $MgCl_2$ 7, $CaCl_2$ 0.5, $NaHCO_3$ 25, glucose 20, bubbled with 95%O_2/5% CO_2, pH 7.4. Brains slices of adolescent mice (P21–P28) were cut in N-Methyl-D-glucamine (NMDG) based solution containing (in mM): NMDG 93, KCl 2.5, NaH_2PO_4 1.2, $MgSO_4$ 10, $CaCl_2$ 0.5, $NaHCO_3$ 30, HEPES 20, glucose 25, sodium pyruvate 3, titrated to pH 7.3–7.4 by adding approximately 8.5 ml of 10 M HCl to 1 liter of solution, and bubbled with 95%O_2/5% CO_2. Coronal slices were cut at 300–350 μm using a Vibratome 3000 (Leica, Germany) microslicer. Brain slices cut in choline solution were allowed to recover in a submersion holding chamber with artificial cerebral spinal fluid (aCSF) consisting of (in mM): NaCl 125, KCl 2.5, NaH_2PO_4 1.3, $MgCl_2$ 1.3, $CaCl_2$ 2, $NaHCO_3$ 25, glucose 20, bubbled with 95%O_2/5% CO_2 for 30 min at 37°C and a further 60 min at 25–28°C prior to recordings. Brain slices cut in NMDG allowed to recover in a submersion holding chamber with bubbled with 95%O_2/5% CO_2NMDG-based dissection buffer for 7 min, followed by a further 60 min in aCSF at 25–28°C prior to recordings. Brain slices of P21 mice cut with choline or NMDG-based solutions yielded similar results and were pooled.

Whole-Cell Recordings

Whole-cell recordings of L2/3 pyramidal neurons were made with a MultiClamp 700B amplifier (Molecular Devices, Sunnyvale, CA, USA), as previously described (Zheng et al., 2014). Signals were low-pass filtered at 2 kHz and digitized at 10 kHz using Digidata 1332A (Molecular Devices). Cells were visualized with an upright microscope (Nikon FN1, Japan) and a 40x water immersion objective under infrared optics. Slices were perfused with oxygenated aCSF at a rate of 4–6 ml/min at 28–30°C and used within 6 h of the first recording. S1BF and V1 were identified according to standard stereotaxic coordinates. For mEPSC recordings, Cs^+-based internal solution containing $CsMeSO_4$ 130, CsCl 5, HEPES 10, EGTA 0.5, Na_2ATP 15, MgATP 4 and Na_3GTP 0.3 and sodium phosphocreatine 10 (pH 7.4, 270–280 mOsm) was used. For mIPSC recordings, high chloride Cs^+-based internal solution containing (in mM): CsCl 110, NaCl 10, $MgCl_2$ 5, EGTA 0.5, MgATP 2, Na_3GTP 0.3 and HEPES 40 (pH 7.4, 270–280 mOsm) was used.

Recordings were made from 2–3 cells per slice, and 2–3 slices per mouse; for drug bath application experiments, one cell per slice was recorded. For mEPSC recordings, cells were held at −70 mV in voltage-clamp, with pipette resistance of 3–4 MΩ in the presence of tetrodotoxin (TTX, 0.5 μM) and picrotoxin (50 μM) to block Na^+ channels and $GABA_AR$, respectively. For mIPSC recordings, cells were held at −60 mV in the presence of TTX (0.5 μM) and NBQX (10 μM) to block Na^+ channels and AMPAR respectively. A brief hyperpolarization (10 mV, 100 ms) was given to monitor series and input resistances every 10 s. Cells with changes of input or series resistance greater than 20% were excluded from analyses. All cells analyzed had a series resistance <25 MΩ. Liquid junction potential and series resistance were uncompensated. Data were analyzed in MiniAnalysis (Synaptosoft, Fort Lee, NJ) with detection thresholds of 5 pA and 6 pA, for mEPSC and mIPSC, respectively. Data were analyzed blinded to the experimental condition.

All salts and drugs were obtained from Sigma or Tocris, except for TTX obtained from the Hebei Fisheries Science and Technology Development Company (Qinhuangdao, Hebei Province, China), and oxytocin from Guoping Pharmaceutical (Hefei, Anhui Province, China). *In vivo* stereotaxic injections were performed as previously described (Zheng et al., 2014). Oxytocin (1 μM, 3 μl, unilateral) was injected into the lateral ventricle (bregma: −0.3 mm; lateral: 1.3 mm; ventral: 1.7 mm). FITC-oxytocin (CYIQNCPLG[DD-miniPEG]-K(FITC)-NH2, 1 μM, 1 μl, unilateral) was injected into to the PVH (bregma: −0.7 mm; lateral: 1.7 mm; ventral: 4.0 mm; offset angel: 7°C) using a stereotaxic instrument (RWD Life Science, Shenzhen, China) and a syringe pump (Harvard Apparatus), at a speed of 0.2 μl/min. Sections were cut 24 h after injection and recordings were made from the injected side.

Fluorescent *In situ* Hybridization, Immunohistochemistry, and Quantitation

In situ hybridization was performed as previously described (Wu et al., 2009; Xiu et al., 2014; Duan et al., 2018). *Oxtr* probes were cloned into the BamHI and

EcoRI sites of pBluescript vector using forward primer cgcggatccGTTGGCACGGGTCAGTAGT, and reverse primer ccggaattcAATGCTTTCTGGGATGTCCTAA. RNA probes were labeled using DIG RNA Labeling Mix (Roche, Cat# 11277073910). Anti-Digoxigenin-AP Fab fragments (Roche, Cat# 11093274910, RRID: AB_514497) were used for DIG labeling of *Oxtr*. For colocalization with various cell type markers, the following primary antibodies were co-incubated with anti-digoxigenin-AP: CaMKIIβ (Abcam, Cat# ab34703, RRID: AB_2275072) and Somatostatin (SST, Santa Cruz, Cat# sc-7819, RRID: AB_2302603). The following secondary antibodies were used: Donkey anti-Rabbit Alexa Fluor 488 (Thermo Fisher Scientific, Cat# A-21206, RRID: AB_2535792), Donkey anti-Goat Alexa Fluor 488 (Thermo Fisher Scientific, Cat# A-11055, RRID: AB_2534102), both diluted 1:1,000. Fast red (Roche, Cat# 11496549001) was used for visualization of *in situ* hybridization. GAD67-GFP transgenic mice were used to label GABAergic neurons. Sections were mounted with Fluoromount medium (Sigma–Aldrich, Cat# F4680).

S1 Layer 2/3 images (1,024 × 1,024) were acquired on a Nikon A1 confocal microscope with S Fluor 40× Oil DIC H N2 Optics (N.A. = 1.3). Image analysis was performed using Image-Pro Plus (Media Cybernetics, Rockville, MD, USA), blinded to the experimental condition. For colocalization analysis, images of each channel were separately thresholded, and colocalization was defined as one or more pixels of overlap between the two conditions. *Oxtr* in each cell type was measured as a ratio of total *Oxtr* area in the section. For measuring the percentage of *Oxtr* positive marker, the area of *Oxtr* colocalizing with each marker was ratioed over that of total marker area. Image analysis was carried out with no post-acquisition modifications. For example images, brightness/contrast was adjusted with linear ranges using ImageJ (N.I.H., Bethesda, MD, USA). P14 and P28 sections were adjusted with the same parameters.

Oxytocin Binding in N2a Cells

Cultured N2a cells were transfected with pCS2 or pCS2-HAmOXTR. Live cells were then incubated with aCSF containing 1 mM oxytocin (GL Biochem) for 20 min, and then fixed in 4% PFA for 1 h. As control, cells were incubated in aCSF containing 1 mM Vasopressin (GL Biochem). Immunostaining was performed with the following antibodies: Oxytocin (Phoenix Pharmaceuticals, Cat# G-051–01, RRID: AB_2876858; 1:250), HA (Covance, Cat# MMS-101P, RRID: AB_2314672; 1:200), Donkey anti-rabbit Alexa Fluor 488 (Thermo Fisher Scientific, Cat# A-21206, RRID:AB_2535792; 1:500) and Donkey anti-mouse Alexa Fluor 568 (Thermo Fisher Scientific, Cat# A10037; 1:500). For the antibody block experiment, the oxytocin antibody was pre-incubated with 10 mM oxytocin. Sections were incubated with 640/660 Deep-Red Fluorescent Nissl Stain (Thermo Fisher Scientific Cat# N21483) for 20 min at room temperature, washed, and mounted onto glass slides in 70% glycerol. Images were acquired on a Nikon A1 confocal microscope with a Plan Apo VC 20× DIC N2 (N.A. = 0.8) objective.

Oxytocin Binding in Acute Brain Slices

To visualize the ability of cells to bind to oxytocin, acute brain slices (sectioned as in "Acute Brain Slice Preparation") were incubated in aCSF containing 1 mM oxytocin (GL Biochem) or 1 mM FITC-oxytocin (Guoping Pharmaceutical, Hefei, Anhui Province, China) for 20 min, then fixed in 4% PFA overnight. As control, brain slices were incubated in aCSF containing 1 mM Vasopressin (GL Biochem). Immunostaining was performed the following day after brain sections were washed in PBS. The following antibodies were used: Oxytocin (Phoenix Pharmaceuticals, Cat# G-051–01, RRID: AB_2876858; 1:250), NeuN (Millopore Cat# MAB377, RRID: AB_2298772; 1:250), Donkey anti-rabbit Alexa Fluor 568 (Thermo Fisher Scientific, Cat# A10042 RRID: AB_2534017; 1:500) and Donkey anti-mouse Alexa Fluor 647 (Thermo Fisher Scientific, Cat# A-31571, RRID: AB_162542; 1:500). Sections were incubated with DAPI (Thermo Fisher Scientific Cat# D1306 RRID: AB_2629482) for 15 min at room temperature, washed and mounted onto glass slides in 70% glycerol. Images were acquired on a Nikon A1 confocal microscope with a Plan Apo 10× DIC L (N.A. = 0.45) or a Plan Apo VC 20× DIC N2 (N.A. = 0.75) objective.

Perfusion of P14 S1BF brain slices with FITC-oxytocin (1 μM) significantly increased mEPSC frequency (Ctrl: 5.10 ± 0.27 Hz, FITC-OXT: 6.66 ± 0.39 Hz; $P < 0.001$) and reduced mEPSC amplitude (Ctrl: 12.00 ± 0.29 pA, OXT: 11.39 ± 0.32 pA; $P < 0.05$), similar to the effects of untagged oxytocin (**Figures 1A,B**), suggesting that the FITC tag did not significantly interfere with the function of oxytocin in regulating excitatory synaptic transmission.

Real-Time qPCR and Oxytocin Peptide Measurements

Total mRNA was extracted from the cerebral cortex, hippocampus, and hypothalamus, using TRIzol reagent (Invitrogen, Cat# 15596018). First-strand cDNA was generated using the M-MLV reverse transcriptase (Promega, Cat# M1701) according to the manufacturer's protocols. Real-time qPCR was performed using SYBR Green Master Mix (TaKaRa, Cat# RR420A) on a LightCycler 480 (Roche Applied Science). All reactions were carried out in duplicates, and the comparative C_T method was used for comparisons between samples. The following primers were used: *Oxtr*-1-F CCGCACAGTGAAGATGACCT; *Oxtr*-1-R AGCATGGCAATGATGAAGGCAG; *Gapdh*-F CTGCC CAGAACATCATCCCT; *Gapdh*-R TGAAGTCGCAGGAGAC AACC.

Oxytocin peptide concentration from S1, V1 and plasma were measured using an ELISA kit (Pheonix Pharmaceutics, EK-051–01), as previously described (Zheng et al., 2014).

Statistical Analysis

Statistical analysis was performed using GraphPad Prism 7 (GraphPad Software, La Jolla, CA, USA). Data are presented as mean ± SEM. Unpaired two-tailed Student's *t*-test (for sample pairs) or one-way ANOVA (for three or more samples) followed by Tukey's multiple comparison tests

were used, depending on the number of samples. For oxytocin perfusion experiments, paired two-tailed Student's *t*-test were used. For electrophysiological experiments, *n* represents the number of neurons. For *in situ* hybridization experiments, *n* represents the number of brain sections. For other experiments, *n* represents the number of mice. Typically, three or more mice were used for each experimental condition. Data were analyzed blinded to the experimental condition.

RESULTS

Experience- and Oxytocin-Dependent Regulation of Excitatory Synaptic Transmission Has a Sensitive/Critical Period

In previous work, we showed that whisker deprivation (WD) from birth (see "Materials and Methods" section) significantly reduced the frequency of miniature excitatory postsynaptic currents (mEPSC) of L2/3 pyramidal neurons in both S1BF and V1, at both P7 and P14 (Zheng et al., 2014). L2/3 pyramidal neurons of the cerebral cortex receive excitatory synaptic inputs from L4 ascending axons, as well as from other L2/3 neurons (Petersen, 2007), and thus functioning as important integrators of inputting sensory information. Here recording from L2/3 neurons of P18 mice, we found no significant differences in mEPSC frequency between WD mice and their whisker intact littermates (**Supplementary Figures 1A,B**), in both S1BF (Ctrl: 1.95 ± 0.34 Hz; WD: 1.90 ± 0.30 Hz; $P = 0.93$) and V1 (Ctrl: 1.81 ± 0.25 Hz; WD: 1.91 ± 0.29 Hz; $P = 0.78$).

Following dark-rearing (DR), another unimodal sensory deprivation paradigm, similar results were obtained. DR litters showed a significant reduction in mEPSC frequency at the earlier time points of P7 and P14 (Zheng et al., 2014); at P18, however, mEPSC frequency was not different between DR mice and those reared under standard lighting conditions (Ctrl; **Supplementary Figures 1C,D**), in both S1BF (Ctrl: 1.71 ± 0.27 Hz; DR: 1.52 ± 0.23 Hz; $P = 0.62$) and V1 (Ctrl: 1.83 ± 0.40 Hz; WD: 1.56 ± 0.28 Hz; $P = 0.57$). Together, these results suggest that experience-dependent synaptic plasticity in the sensory cortices has a sensitive/critical period ending around P18.

Since we have previously shown that sensory experience regulated excitatory synaptic transmission *via* the neuropeptide oxytocin (Zheng et al., 2014), we asked if oxytocin regulated excitatory synaptic transmission with a similar sensitive/critical period. We thus bath applied oxytocin (1 μM) onto acute S1BF brain slices of P14, P18, and P28 mice, and measured mEPSC frequency and amplitude of S1BF L2/3 pyramidal neurons, before and after oxytocin application. Consistent with our previous report (Zheng et al., 2014), in P14 mice, oxytocin significantly increased mEPSC frequency (Ctrl: 4.10 ± 0.35 Hz, OXT: 5.43 ± 0.52 Hz; $P < 0.001$; **Figures 1A,B**). We also observed a small, but significant, reduction in mEPSC amplitude (Ctrl: 13.01 ± 0.63 pA, OXT: 12.17 ± 0.58 pA; $P < 0.05$; please see "Discussion" section for discussion on all mEPSC amplitude changes). mEPSC frequency, reflecting release probability of individual synapses and total synapse number of the cell, and mEPSC amplitude, reflecting the size of individual synapses, both contribute to total synaptic strength. To more directly measure the effect of oxytocin on the total synaptic inputs of L2/3 neurons, we calculated the total charge transfer per second and found it to be significantly higher following oxytocin application (Ctrl: 148.32 ± 11.23 pAms; OXT: 193.10 ± 16.35 pAms; $P < 0.01$), consistent with oxytocin increasing total excitatory synaptic input of L2/3 pyramidal neurons at this developmental stage.

In P18 mice, oxytocin application had no significant effects on mEPSC frequency (Ctrl: 5.80 ± 0.47 Hz, OXT: 5.65 ± 0.57 Hz; $P = 0.60$) or amplitude (Ctrl: 9.71 ± 0.21 pA, OXT: 9.39 ± 0.15 pA; $P = 0.08$; **Figures 1C,D**). This result suggested that the effect of oxytocin on promoting excitatory synaptic transmission also had a critical period ending around P18, similar to the sensitive/critical period observed following sensory deprivation by WD or DR (**Supplementary Figures 1A–D**). Consistently, at P18-P21, sensory deprivation by WD or DR did not significantly reduce oxytocin peptide level, in S1 or V1 (**Supplementary Figures 1E,F**). This contrasts with significantly reduced oxytocin levels in S1 and V1 of P14 mice following WD or DR (Zheng et al., 2014).

At P28, oxytocin perfusion significantly reduced mEPSC frequency (Ctrl: 6.35 ± 085 Hz, OXT: 5.40 ± 0.76 Hz; $P < 0.01$) and amplitude (Ctrl: 8.75 ± 0.36 pA, OXT: 8.24 ± 0.31 pA; $P < 0.01$; **Figures 1E,F**).

To confirm the above results, we performed an additional set of experiments, with five time points between P10 to P28. At the earlier time points of P10 and P14, oxytocin significantly increased mEPSC frequency, while at the later time points of P22 and P28, it significantly reduced it; at the P18 transition point, oxytocin did not significantly affect excitatory synaptic transmission (all results shown as fold changes following oxytocin application, normalized to before application value; P10: 1.43 ± 0.18, $P < 0.05$; P14: 1.23 ± 0.08; $P < 0.05$; P 18: 0.96 ± 0.03; $P = 0.21$; P22: 0.88 ± 0.04, $P < 0.01$; P28: 0.72 ± 0.05, $P < 0.001$; **Figure 1G**).

In previous work, we showed that *in vivo* administration of oxytocin into the S1 of P12/13 mice significantly increased mEPSC frequency of L2/3 pyramidal neurons measured 24 h later (Zheng et al., 2014). We performed the same assay in P26/27 mice (**Figure 1H**), by injecting oxytocin into the lateral ventricle and recording from L2/3 pyramidal neurons 24 h later. We found significant reduction in mEPSC frequency (Ctrl: 4.14 ± 0.50 Hz, OXT: 2.66 ± 0.31 Hz; $P < 0.05$) and amplitude (Ctrl: 10.38 ± 0.30 pA, OXT: 9.40 ± 0.29 pA; $P < 0.05$) in mice injected with oxytocin, as compared to control mice injected with saline (**Figures 1I,J**).

Together, the above results show that regulation of excitatory synaptic transmission in L2/3 neurons by experience and oxytocin has sensitive/critical periods ending around P18. Furthermore, oxytocin regulates excitatory synaptic transmission

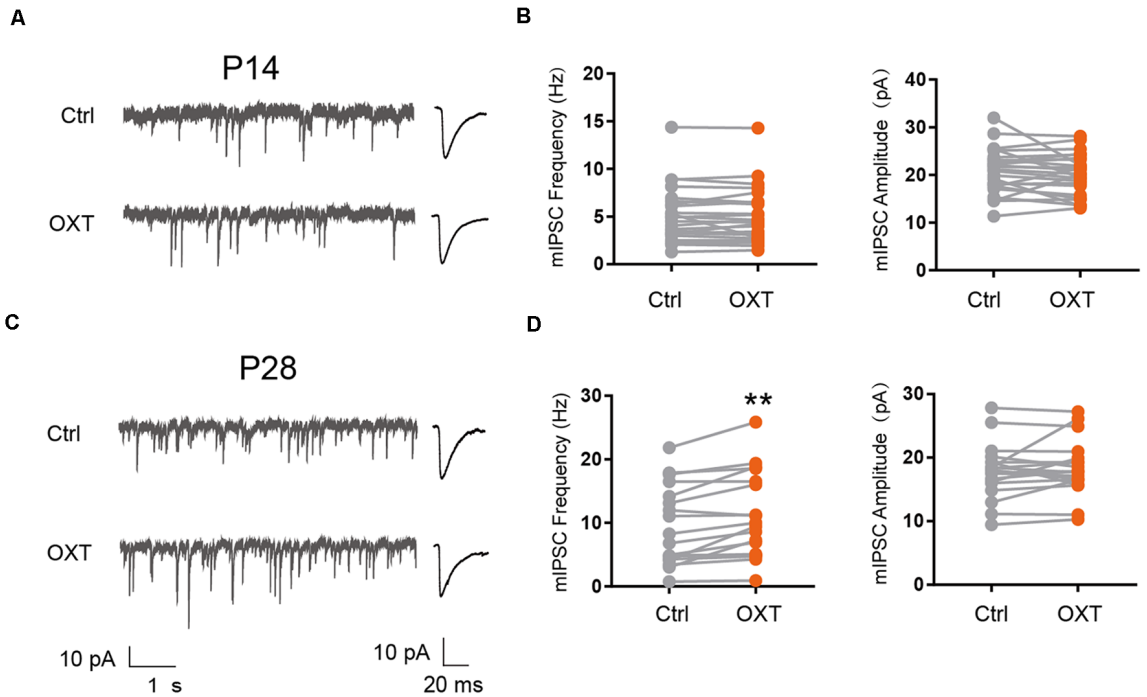

FIGURE 2 | Developmental effects of oxytocin application on inhibitory synaptic transmission. **(A–C)** Representative mIPSC recordings (left) and average waveforms (right) from S1BF L2/3 pyramidal neurons before (Ctrl) and after oxytocin (OXT) application, age as indicated. **(B)** Oxytocin application did not significantly affect mIPSC frequency or amplitude in P14 mice (frequency: Ctrl, 5.02 ± 0.58 Hz; OXT, 5.0 ± 0.58 Hz; $n = 25$; $P = 0.87$, paired t-test; amplitude: Ctrl, 20.82 ± 0.94 pA; OXT, 20.17 ± 0.85 pA; $P = 0.31$, paired t-test). **(D)** Oxytocin application increased mIPSC frequency but did not affect mIPSC amplitude in P28 mice (frequency: Ctrl, 9.17 ± 1.41 Hz; OXT, 10.77 ± 1.53 Hz; $n = 19$; $^{**}P < 0.01$, paired t-test; amplitude: Ctrl, 17.82 ± 0.99 pA; OXT, 18.38 ± 0.99 pA; $P = 0.33$, paired t-test). $^{**}P < 0.01$.

with a dynamic time course, increasing excitatory synaptic strength at P14 and reducing it at the later time point of P28.

Developmental Effects of Oxytocin on Inhibitory Synaptic Transmission

We next examined the effect of oxytocin on inhibitory synaptic transmission, by measuring the frequency and amplitude of miniature inhibitory post-synaptic currents (mIPSC). At P14, oxytocin application did not significantly affect mIPSC amplitude (Ctrl: 20.82 ± 0.94 pA, OXT: 20.17 ± 0.85 pA; $P = 0.31$) or frequency (Ctrl: 5.02 ± 0.58 Hz, OXT: 5.0 ± 0.58 Hz; $P = 0.87$; **Figures 2A,B**). At P28, however, oxytocin application significantly increased mIPSC frequency (Ctrl: 9.17 ± 1.41 Hz, OXT: 10.77 ± 1.53 Hz; $P < 0.01$), but did not affect mIPSC amplitude (Ctrl: 17.82 ± 0.99 pA, OXT: 18.38 ± 0.99 pA; $P = 0.33$; **Figures 2C,D**). Thus, the effect of oxytocin on inhibitory synaptic transmission also changes over the course of cortical development.

Developmental Changes in Oxytocin Receptor Expression in Different Neuronal Types

What biological changes may account for, or at least contribute to, dynamic changes in the effect of oxytocin on synaptic transmission? Oxytocin primarily signals through the oxytocin receptor (OXTR), a G protein-coupled receptor expressed widely in the brain (Gimpl and Fahrenholz, 2001; Jurek and Neumann, 2018). OXTR expression is developmentally dynamic and is regulated by experience (Vaidyanathan and Hammock, 2017). In the mouse cerebral cortex, *Oxtr* mRNA and OXTR protein expression, as well as radioligand labeling of receptors, all showed peak receptor expression at P14 (Hammock and Levitt, 2013; Zheng et al., 2014; Mitre et al., 2016). However, it is not known if *Oxtr* expression is mostly in glutamatergic or GABAergic neurons at this age. We thus performed *in situ* hybridization of *Oxtr* mRNA, in combination with immunohistochemistry for the beta subunit of Ca^{2+}/calmodulin-dependent protein kinase II (CaMKIIβ) or somatostatin (SST), respectively labeling glutamatergic (excitatory) neurons or a subclass of GABAergic (inhibitory) neurons previously shown to express *Oxtr* (Nakajima et al., 2014). *Oxtr in situ* hybridization was also carried out using *GAD67-GFP* mice, in which GABAergic neurons are labeled with the green fluorescent protein (GFP; Tamamaki et al., 2003).

In S1, at both P14 and P28, *Oxtr* mRNA partially colocalized with all three markers (**Figures 3A–C**); colocalization was defined as the overlap between the two signals at the pixel level. Between P14 and P28, the distribution of *Oxtr* mRNA changed, from mostly colocalizing with CaMKIIβ at P14 (CaMKIIβ:

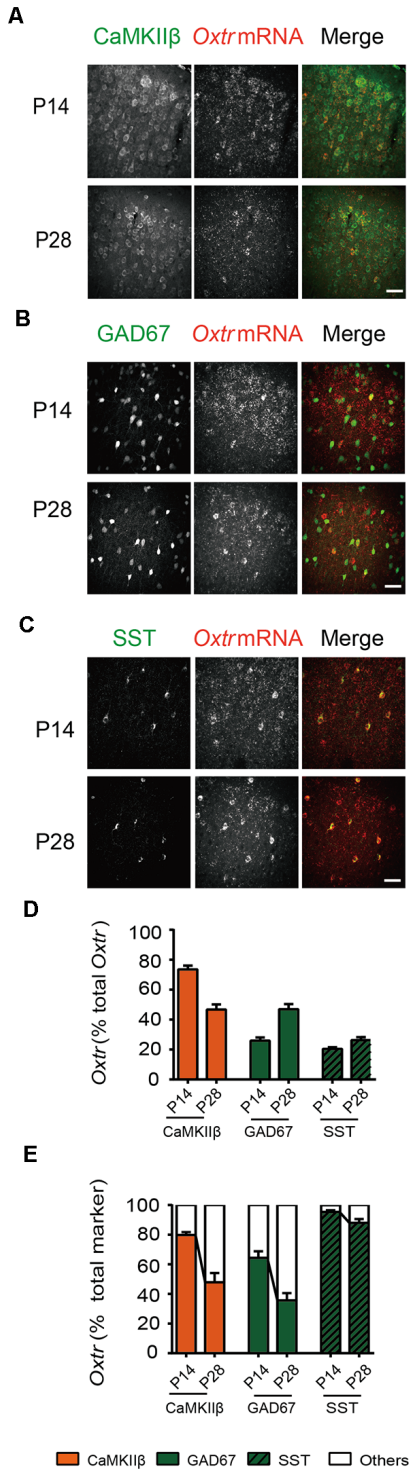

FIGURE 3 | *Oxtr* mRNA expression in glutamatergic and GABAergic neurons. **(A)** Representative images of *Oxtr* mRNA co-labeling with the glutamatergic neuron marker CaMKIIβ, age of mice as indicated in this and subsequent panels. **(B)** Representative images of *Oxtr* mRNA co-labeling with the GABAergic neuron marker GAD67. **(C)** Representative images of *Oxtr* mRNA co-labeling with SST, a marker for a subtype of GABAergic neurons. **(D)** *Oxtr* mRNA expression in different cell types in P14 and P28 mice, normalized to total *Oxtr* expression (P14: CaMKIIβ, 73.56 ± 2.51%; *n* = 22; GAD67, 26.0 ± 2.06%; *n* = 30; SST, 20.45 ± 1.07%; *n* = 30; P28: CaMKIIβ, 46.69 ± 3.42%; *n* = 20; GAD67, 46.99 ± 3.39%; *n* = 28; SST, 26.28 ± 1.98%; *n* = 30). **(E)** *Oxtr* mRNA colocalizing with marker as labeled (CaMKIIβ: P14, 79.79 ± 2.04%; *n* = 22; P28, 47.98 ± 6.17%; *n* = 20; GAD67: P14, 64.39 ± 4.43%; *n* = 30; P28, 35.74 ± 4.86%; *n* = 28; SST: P14, 95.39 ± 1.12% *n* = 30; P28: 87.96 ± 2.66%; *n* = 30). **(A–C)** Scale bar: 50 μm.

73.56 ± 2.51%; GAD67: 26.0 ± 2.06%; SST: 20.45 ± 1.07%), to relatively even distribution between glutamatergic and GABAergic neurons at P28 (CaMKIIβ: 46.69 ± 3.42%; GAD67: 46.99 ± 3.39%; SST: 26.28 ± 1.98%; **Figure 3D**). In addition, the ratio of *Oxtr*-expressing cells decreased from P14 to P28 in both glutamatergic neurons (P14: 79.79 ± 2.04%; P28: 47.98 ± 6.17%) and GABAergic neurons (P14: 64.39 ± 4.43%; P28: 35.74 ± 4.86%; **Figure 3E**), consistent with previous reports showing peak *Oxtr* expression in the cerebral cortex at P14. At both time points, a very high proportion of SST neurons expressed *Oxtr* (P14: 95.39 ± 1.12%; P28: 87.96 ± 2.66%; **Figure 3E**). These results show that *Oxtr* expression is dynamic during development, and has distinct expression patterns at P14 and P28.

Not having a specific OXTR antibody on hand, we confirmed our *in situ* results using the "oxytocin binding" method. Persistent activation of OXTR, a G protein-coupled receptor, leads to its endocytosis and internalization, together with its ligand oxytocin (Gimpl and Fahrenholz, 2001); thus cells expressing functional OXTR have significant oxytocin binding capacity and can be labeled using an antibody against oxytocin following ligand binding. In N2a cells, application of oxytocin resulted in specific labeling of OXTR-expressing cells with oxytocin antibody, but not neighboring cells not expressing OXTR; this effect was blocked by pre-incubation with oxytocin antibody and did not occur upon incubation with the closely related neuropeptide vasopressin (**Supplementary Figure 2**). We then treated acute brain slices with oxytocin for 20 min, fixed the brain slices, and immunostained for oxytocin and the pan-neuronal marker NeuN (**Figure 4**). In S1 of P14 mice, oxytocin immunoreactivity, marking cells with internalized OXTR, colocalized significantly with NeuN and was relatively high in the superficial layers of the cerebral cortical (layers 2/3), as compared to the deeper layer (layer 5; **Figure 4A**). As a control for specificity, cortical brain slices incubated with the closely related neuropeptide vasopressin were not labeled with oxytocin antibody (**Figure 4B**). In S1 of adult mice, the oxytocin immune-reactive cells distributed relatively evenly across superficial and deeper layers (**Figure 4C**). This dynamic pattern of OXTR expression in different cortical layers during development is consistent with a recent report using an OXTR reporter mouse line (Newmaster et al., 2020). The results of these oxytocin labeling experiments are also consistent with those of our *Oxtr in situ* hybridization experiments, although the labeling efficiency is lower. Specifically, the proportion of oxytocin immune-reactive cells that are GAD67-positive increased from 15.31 ± 0.30% at P14 to 29.17 ± 4.17% in adult mice. In both age

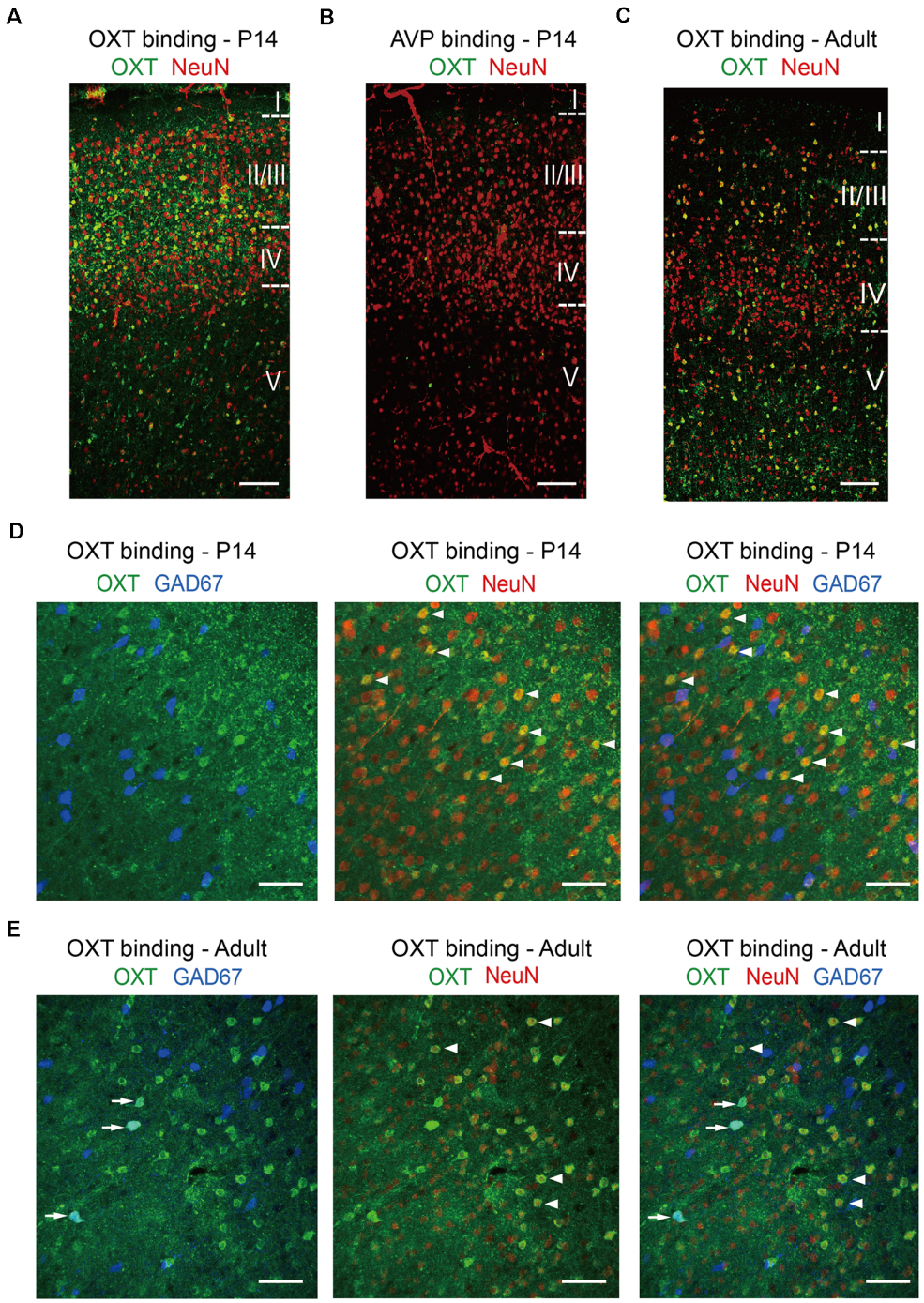

FIGURE 4 | Oxytocin binding in glutamatergic and GABAergic neurons. **(A)** Incubation of P14 acute brain slice with oxytocin leads to significant oxytocin binding and oxytocin antibody labeling (green) in neurons, co-labeled with NeuN (red). **(B)** As a negative control, incubation of P14 acute brain slice with vasopressin does not result in oxytocin antibody labeling. **(C)** Application of oxytocin to an adult brain slice leads to oxytocin antibody labeling (green) with a different pattern, as compared to P14. **(D)** Colocalization of oxytocin (green), NeuN (red), and GAD67 (blue) in the P14 cerebral cortex. **(E)** Colocalization of oxytocin (green), NeuN (red), and GAD67 (blue) in the adult cerebral cortex. Arrows indicate colocalization of oxytocin and GAD67; arrowheads indicated the colocalization of oxytocin and NeuN. **(A–C)** Cortical layers are delineated by dashed lines. Scale bar: 100 μm. **(D,E)** Scale bar: 50 μm.

groups, over 90% (P14: 90.30 ± 3.33%; adult: 90.28 ± 1.39%) of oxytocin immune-reactive cells co-labeled with NeuN, consisting with high OXTR expression in neurons (**Figures 4D,E**). In addition to the cerebral cortex, internalized oxytocin also colocalized with NeuN in the hippocampus, amygdala, and lateral septum of P14 mice (**Supplementary Figures 3A–C**).

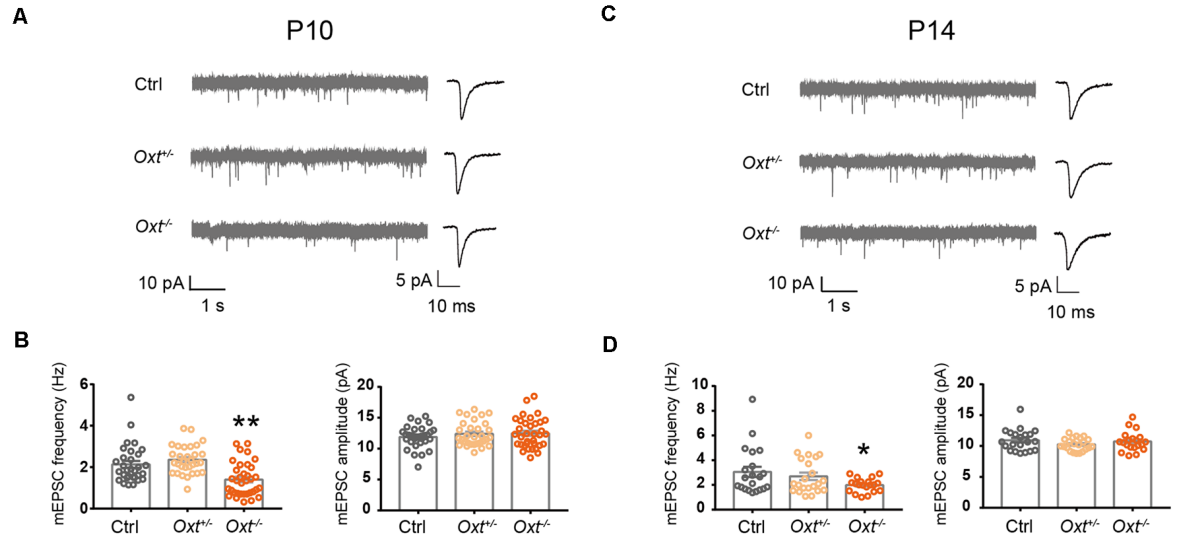

FIGURE 5 | Reduced excitatory synaptic transmission in oxytocin knockout mice. **(A–C)** Representative mEPSC recording (left) and average waveforms (right) of $Oxt^{+/-}$, $Oxt^{-/-}$ mice and littermate Ctrl mice at P10 and P14. **(B)** mEPSC frequency is reduced in P10 $Oxt^{-/-}$ mice (Ctrl, 2.13 ± 0.17 Hz; n = 31; $Oxt^{+/-}$, 2.36 ± 0.12 Hz; n = 31; $Oxt^{-/-}$, 1.40 ± 0.14 Hz; n = 35; $P < 0.01$ vs. Ctrl), while mEPSC amplitude is not significantly affected (Ctrl, 11.88 ± 0.32 pA; $Oxt^{+/-}$, 12.39 ± 0.35 pA; $Oxt^{-/-}$, 12.48 ± 0.41 pA). **(D)** mEPSC frequency is reduced in P14 $Oxt^{-/-}$ mice (Ctrl, 3.06 ± 0.42 Hz; n = 21; $Oxt^{+/-}$, 2.69 ± 0.30 Hz; n = 22; $Oxt^{-/-}$, 1.98 ± 0.12 Hz; n = 20; $P < 0.05$ vs. Ctrl), while mEPSC amplitude is not significantly affected (Ctrl, 10.95 ± 0.38 pA; $Oxt^{+/-}$, 10.25 ± 0.22 pA; $Oxt^{-/-}$, 10.74 ± 0.35 pA). One-way ANOVA followed by Tukey's multiple comparison test for all panels. $^{*}P < 0.05$, $^{**}P < 0.01$, unpaired t-test.

Labeling of cortical neurons was also achieved using FITC-oxytocin (see "Materials and Methods" section for details; **Supplementary Figure 4A**). Importantly, FITC-oxytocin did not label cells in the PVH of *EIIa-Cre; Oxtr*$^{fl/fl}$ (*EIIa-Cre*; *Oxtr* cKO) mice, where *Oxtr* is removed from the very early embryo (Lakso et al., 1996; Lee et al., 2008), thus demonstrating the requirement of OXTR for oxytocin binding *in vivo* (**Supplementary Figures 4B,C**).

Altered Excitatory Synaptic Transmission in Oxytocin and OXTR Knockout Mice

Having shown the sufficiency of oxytocin to regulating excitatory synaptic transmission, as well as expression of OXTR in a large proportion of L2/3 pyramidal neurons at P14, we next asked if oxytocin and OXTR are required for regulation of excitatory synaptic transmission under basal conditions and/or following oxytocin application. In homozygous oxytocin knockout mice (homo, $Oxt^{-/-}$, Young et al., 1996), mEPSC frequency was significantly reduced, as compared with littermate wildtype (WT, $Oxt^{+/+}$) or heterozygous (het, $Oxt^{+/-}$) mice, at both P10 (WT: 2.13 ± 0.17 Hz, het: 2.36 ± 0.12 Hz, homo: 1.40 ± 0.14 Hz; WT vs. het, P = 0.52; WT vs. homo $P < 0.01$) and P14 (WT: 3.06 ± 0.42 Hz, het: 2.69 ± 0.30 Hz, homo: 1.98 ± 0.12 Hz; WT vs. het: P = 0.68; WT vs. homo: $P < 0.05$; **Figure 5**). mEPSC frequency of heterozygous mice was not significantly different from wildtype littermates at both ages, and mEPSC amplitude was not significantly different between all genotypes at both ages (**Figure 5**). Thus, oxytocin's loss-of-function affects excitatory synaptic transmission as early as P10.

In complementary experiments, we examined excitatory synaptic transmission in *EIIa-Cre;Oxtr*$^{fl/fl}$ (*EIIa-Cre*;*Oxtr* cKO) mice. *Oxtr* mRNA level was significantly reduced in cortex, hippocampus, and hypothalamus of *EIIa-Cre;Oxtr* cKO mice (**Supplementary Figure 4D**). At P10, mEPSC frequency (loxP: 2.16 ± 0.18 Hz, cKO: 2.30 ± 0.15 Hz, P = 0.54) and amplitude (loxP: 12.55 ± 0.23 pA, cKO: 12.50 ± 0.28 pA, P = 0.90) were not significantly different between *EIIa-Cre*;*Oxtr* cKO mice, and *Oxtr*$^{fl/fl}$ (loxP) littermates (**Figures 6A,B**). At P14, while the baseline mEPSC frequency (P = 0.78) and amplitude (P = 0.15) were not different between the two groups, oxytocin perfusion onto acute brain slices from *EIIa-Cre*;*Oxtr* cKO mice led to a significant reduction in mEPSC frequency (cKO Ctrl: 5.91 ± 0.48 Hz, cKO OXT: 5.56 ± 0.45 Hz, $P < 0.05$), as compared to a significant increase observed in loxP littermates (loxP Ctrl: 5.69 ± 0.27 Hz, loxP OXT: 6.78 ± 0.33 Hz, $P < 0.001$; **Figures 6C,D**) and in wildtype mice (**Figures 1A,B**). In both conditions, mEPSC amplitude was reduced following oxytocin application (loxP Ctrl: 11.61 ± 0.37 pA, loxP OXT: 11.0 ± 0.41 pA, $P < 0.05$; cKO Ctrl: 10.58 ± 0.34 pA, cKO OXT: 10.24 ± 0.34 pA, $P < 0.05$; **Figures 6C,D**).

We further confirmed these results using *Nex-Cre; Oxtr*$^{fl/fl}$ (*Nex-Cre; Oxtr* cKO) mice, where Cre is expressed in all excitatory neurons of the cerebral cortex and hippocampus from the late embryo (Goebbels et al., 2006). In P14 *Nex-Cre; Oxtr* cKO mice, oxytocin application also reduced mEPSC frequency (cKO Ctrl: 5.44 ± 0.55 Hz, cKO OXT: 4.98 ± 0.50 Hz, $P < 0.05$) and amplitude (cKO Ctrl: 9.99 ± 0.31 pA, cKO OXT: 9.56 ± 0.31 pA, $P < 0.05$), while the same treatment increased mEPSC frequency (loxP Ctrl: 6.22 ± 0.49 Hz, loxP OXT: 7.25 ± 0.53 Hz, $P < 0.001$)

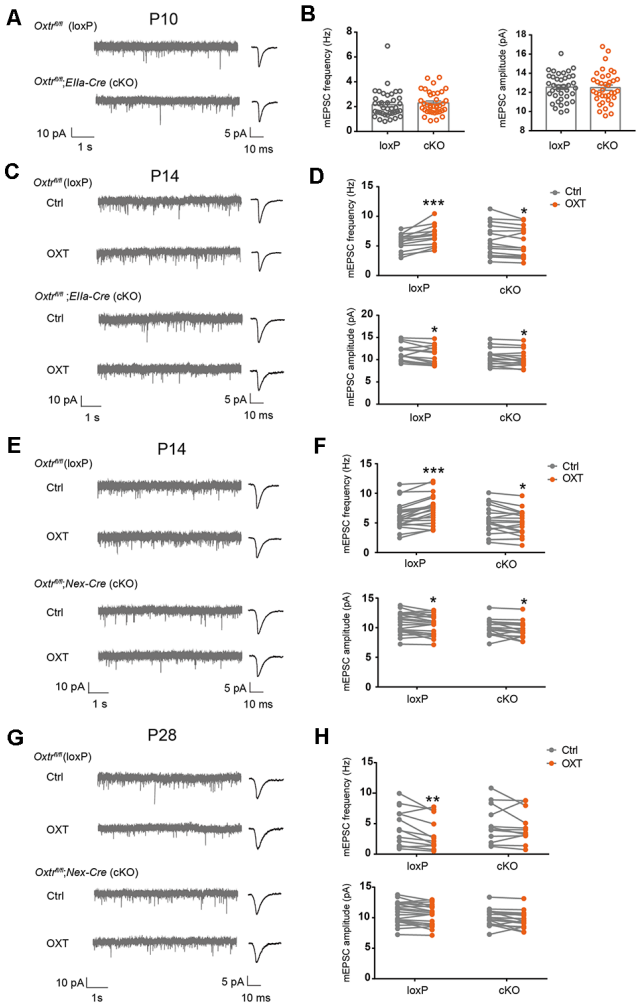

FIGURE 6 | Blockade of oxytocin-induced changes in excitatory synaptic transmission in *Oxtr*cKO mice. **(A)** Representative mEPSC recording (left) and average waveforms (right) of P10 *Ella-Cre;Oxtr* cKO mice and littermate loxP controls. **(B)** mEPSC frequency (Ctrl, 2.16 ± 0.18 Hz, n = 38; cKO, 2.30 ± 0.15 Hz, n = 37; P = 0.54, unpaired t-test) and amplitude (Ctrl: 12.55 ± 0.23 pA; cKO, 12.50 ± 0.28 pA; P = 0.90, unpaired t-test) were similar between *Ella-Cre;Oxtr* cKO mice and loxP littermates. **(C,E,G)** Representative mEPSC recordings (left) and average waveforms (right) before (Ctrl) and after (OXT) oxytocin application, age and genotype as indicated. **(D)** Oxytocin application increased mEPSC frequency but reduced mEPSC amplitude in P14 control mice, while its application reduced both mEPSC frequency and amplitude in P14 *Ella-Cre;Oxtr* cKO mice (frequency: loxP, Ctrl, 5.69 ± 0.27 Hz, OXT, 6.78 ± 0.33 Hz, n = 14; P < 0.001, paired t-test; cKO, Ctrl, 5.91 ± 0.48 Hz, OXT, 5.56 ± 0.45 Hz, n = 16; P < 0.05, paired t-test; amplitude: loxP, Ctrl, 11.61 ± 0.37 pA, OXT, 11.0 ± 0.41 pA; P < 0.05, paired t-test; cKO: Ctrl, 10.58 ± 0.34 pA, OXT, 10.24 ± 0.34 pA; P < 0.05, paired t-test). **(F)** Oxytocin application increased mEPSC frequency, but reduced mEPSC amplitude in P14 loxP mice, while its application reduced both mEPSC frequency and amplitude in *Nex-Cre;Oxtr* cKO mice (frequency: loxP, Ctrl, 6.22 ± 0.49 Hz, OXT, 7.25 ± 0.53 Hz, n = 21; P < 0.001, paired t-test; cKO: Ctrl, 5.44 ± 0.55 Hz, OXT, 4.98 ± 0.50 Hz, n = 19; P < 0.05, paired t-test; amplitude: loxP, Ctrl, 10.79 ± 0.39 pA, OXT, 10.43 ± 0.37 pA; P < 0.05, paired t-test; cKO: Ctrl, 9.99 ± 0.31 pA, OXT, 9.56 ± 0.31 pA; P < 0.05, paired t-test). **(H)** Oxytocin application reduced mEPSC frequency, without affecting mEPSC amplitude in P28 loxP mice; its application did not

(*Continued*)

FIGURE 6 | Continued
affect mEPSC frequency or amplitude in *Nex-Cre;Oxtr* cKO mice (frequency: loxP, Ctrl, 4.49 ± 0.81 Hz, OXT, 3.30 ± 0.70 Hz, n = 14; P < 0.01, paired t-test; cKO: Ctrl, 4.92 ± 0.89 Hz, OXT, 4.49 ± 0.78 Hz, n = 12; P = 0.35, paired t-test; amplitude: loxP, Ctrl, 8.12 ± 0.39 pA, OXT, 7.96 ± 0.47 pA; P = 0.48, paired t-test; cKO: Ctrl, 8.62 ± 0.37 pA, OXT, 8.53 ± 0.36 pA; P = 0.72, paired t-test). *P < 0.05, **P < 0.01, ***P < 0.001.

and reduced mEPSC amplitude (loxP Ctrl: 10.79 ± 0.39 pA, loxP OXT: 10.43 ± 0.37, pA, P < 0.05) in loxP littermates (**Figures 6E,F**). Baseline mEPSC frequency (P = 0.29) and amplitude (P = 0.12) were not significantly different between the two genotypes. Since *Nex-Cre* is only expressed in glutamatergic neurons, these results further confirm requirement for *Oxtr* expression in glutamatergic neurons for oxytocin-dependent regulation of excitatory synaptic transmission.

Measuring excitatory synaptic transmission in *Nex-Cre; Oxtr* cKO mice at P28, we found that baseline mEPSC frequency (P = 0.72) and amplitude (P = 0.36) were not significantly different between loxP and cKO groups. Oxytocin application to loxP mice reduced mEPSC frequency (loxP Ctrl: 4.49 ± 0.81 Hz, loxP OXT: 3.30 ± 0.70 Hz, P < 0.01; **Figures 6G,H**), similar to its effects on wildtype mice at this age (**Figures 1E,F**). In contrast, oxytocin application in *Nex-Cre; Oxtr* cKO did not significantly affect mEPSC frequency (cKO Ctrl: 4.92 ± 0.89 Hz, cKO OXT: 4.49 ± 0.78 Hz, P = 0.35; **Figures 6G,H**). In both genotypes, mEPSC amplitude was not affected by oxytocin application (loxP Ctrl: 8.12 ± 0.39 pA, loxP OXT: 7.96 ± 0.47, pA, P = 0.48; cKO Ctrl: 8.62 ± 0.37 pA, cKO OXT: 8.53 ± 0.36 pA, P = 0.72; **Figures 6G,H**). Together, these results show that while conditional knockout of *Oxtr* does not affect baseline excitatory synaptic transmission, it inhibits the effect of acute oxytocin application onto brain slices, at both P14 and P28.

DISCUSSION

Oxytocin and Sensory Experience Have Similar Sensitive/Critical Periods in Regulating Excitatory Synaptic Transmission of L2/3 Neurons

Here, we found that sensory experience and oxytocin regulate excitatory synaptic transmission in L2/3 pyramidal neurons of the sensory cortices with a similar sensitive/critical period, peaking around P14 and ending around P18 (**Figure 1** and **Supplementary Figures 1A–D**; Zheng et al., 2014). Consistently, sensory experience regulates oxytocin expression with a similar time course, elevation at P14, and essentially no changes at P18 (**Supplementary Figures 1E,F**; Zheng et al., 2014). Curiously, we observed an increase in oxytocin level in S1 of DR mice (**Supplementary Figure 1F**), possibly due to homeostatic compensation. The effects of sensory experience and oxytocin on excitatory synaptic transmission are both directional, with sensory deprivation and loss-of-function of oxytocin reducing excitatory synaptic transmission, and environmental enrichment and exogenous oxytocin

application increasing synaptic transmission (**Figures 1, 5** and **Supplementary Figure 1**; Zheng et al., 2014). The above evidence suggests that oxytocin may function as a mediator of early experience-dependent plasticity in L2/3 pyramidal neurons of the sensory cortices.

As to what biological change ends the sensitive/critical period, we can only speculate. Oxytocin expression in the hypothalamus increases steadily between P7 and P60 (Zheng et al., 2014), thus it is unlikely that a sharp change in oxytocin expression leads to closure of this sensitive/critical period. *Oxtr* mRNA, OXTR protein, oxytocin binding capacity, and OXTR reporter expression in the sensory cortices has been reported to peak around P14 and drops significantly at P21 and P28 (Hammock and Levitt, 2013; Mitre et al., 2016; Newmaster et al., 2020; **Figure 3**). Thus, a reduction in *Oxtr* expression may contribute to the closure of the sensitive/critical period. It is probably one of many factors that contribute. To better understand this form of experience-dependent plasticity in the sensory cortices, more mechanistic studies, as well as a deeper understanding of the physiological function of this sensitive/critical period is needed.

Effects of Oxytocin on Synaptic Transmission at P14

At P14 (and the earlier time point of P10), loss-of-function of oxytocin reduces mEPSC frequency of S1BF L2/3 pyramidal neurons, while its application to acute brain slices increases mEPSC frequency (**Figures 1, 5**). Furthermore, loss-of-function of *Oxtr* blocks oxytocin-induced increase in mEPSC frequency (**Figure 6**). *Oxtr* expression is high in L2/3 glutamatergic neurons and low in GABAergic neurons at this age (**Figures 3, 4**). Consistently, oxytocin application does not significantly affect inhibitory synaptic transmission. Increased excitatory synaptic transmission and no change in inhibition add to an increase in total excitatory input of L2/3 pyramidal neurons.

An interesting fine point is the difference between the effect of $Oxt^{-/-}$ knockout and *Oxtr* cKO: $Oxt^{-/-}$ mice have reduced excitatory synaptic transmission under baseline conditions, at both P10 and P14 (**Figure 5**), while in *EIIa-Cre; Oxtr* cKO or *Nex-Cre; Oxtr* cKO mice, baseline excitatory synaptic transmission is unaffected, but the effect of oxytocin application is blocked (**Figure 6**). Given that *EIIa-Cre* is expressed from the early embryo, before implantation (Lakso et al., 1996), *EIIa-Cre; Oxtr* cKO mice should have completely or near complete knockout of *Oxtr*. This opens up the possibility that oxytocin may have developmental effects independent of its receptors.

Another subject of interest is whether oxytocin affects mEPSC amplitude, a parameter that correlates with the size of individual synapses. In $Oxt^{-/-}$ mice, and in *Oxtr* cKO mice, mEPSC amplitude was similar between knockout mice and littermate controls (**Figures 5, 6**). Thus loss-of-function of *Oxt* or *Oxtr* does not affect mEPSC amplitude. In all oxytocin application experiments, however, a small but significant reduction in mEPSC amplitude was often observed (**Figures 1, 6**). A small reduction in mEPSC amplitude, in addition to being a biological phenomenon, could also be an artifact due to increased serial resistance during the course of whole cell patch-clamp recordings. To minimize this problem, we only analyzed recordings in which series and input resistances changed by less than 20% over the course of the experiment. Also, in P18 mice, neither mEPSC amplitude nor frequency was affected by oxytocin application (**Figures 1C,D**). Thus, the small reduction in mEPSC amplitude following oxytocin application is likely to be a *bona fide* biological phenomenon. However, since the magnitude of the increase in mEPSC frequency is much larger than the reduction in mEPSC amplitude, the total charge transfer, representing total excitatory input of the neuron, is increased following oxytocin application at P14.

Effects of Oxytocin on Synaptic Transmission at P28

In P28 mice, oxytocin application reduces mEPSC frequency and increases mIPSC frequency (**Figures 1, 2**) of S1BF L2/3 pyramidal neurons. The effect of acute oxytocin application on reducing mEPSC frequency was confirmed by *in vivo* oxytocin injection (**Figures 1H–J**) and blocked in *Nex-Cre; Oxtr* cKO mice (**Figures 6G,H**).

These results, together with those of P14, suggest that oxytocin has distinct effects on synaptic transmission at P14 and P28: increasing total excitatory inputs (increased mEPSC frequency and no changes in inhibition) of L2/3 pyramidal neurons at P14, and reducing it (reduced mEPSC frequency and increased mIPSC frequency) at P28. What physiological changes may underlie these switches? As discussed above, oxytocin expression increases steadily between P7 and P60 (Zheng et al., 2014), and thus is unlikely to account for the above described switch. Our *in situ* hybridization and oxytocin binding results, together with published data using a variety of approaches to measure OXTR level (Hammock and Levitt, 2013; Mitre et al., 2016; Newmaster et al., 2020), suggest that OXTR level is higher at P14, as compared to P21 and P28. It is relatively straightforward for high receptor expression to be associated with a higher level of signal transduction and increased transmission (e.g., P10 and P14), and lower receptor expression to be associated with no changes (e.g., P18); however, the change from increase at P14 to reduction at P28 presumably requires additional alterations in downstream signal transduction components.

In terms of GABAergic synaptic transmission, our results (**Figures 3, 4**) suggest increased relative expression of OXTR in GABAergic neurons in P28 and older mice, as compared to P14. An increase in OXTR expression in GABAergic cells would presumably increase OXTR-dependent signaling in these cells. Since we observed an increase in GABAergic input to L2/3 pyramidal neurons at P28, the increased OXTR expression likely enhanced the synaptic output of GABAergic neurons onto pyramidal neurons. A recent study indeed showed that oxytocin can enhance the excitability of SST neurons, thereby reducing the level of spontaneous activity (Maldonado et al., 2021).

Thus, combining the results on glutamatergic and GABAergic transmission, it seems that lower expression of OXTR is associated with no effects on synaptic transmission, while higher

OXTR expression is associated with increased transmission. The exception is excitatory synaptic transmission in P28 and older mice, where oxytocin application significantly reduces excitatory synaptic transmission in neurons expressing a low level of OXTR. We hypothesize that change in the level of one or more OXTR downstream signaling component mediates this effect.

We focused in S1 L2/3 pyramidal neurons for this study. Recent work showed that oxytocin affects spontaneous network events differentially in S1 and V1 (Maldonado et al., 2021). Given the complexity of the effects of oxytocin, studies on more cell types, more brain regions, and at more developmental stages, as well as more in-depth investigations of OXTR downstream signaling under these different conditions, are needed for a full understanding of its function.

Implications for Neural Circuit Development and Plasticity

Oxytocin has been shown to affect many aspects of neural circuit development and function, including regulating excitatory or inhibitory synaptic transmission, altering neuronal firing rates and patterns, and modulating the transition of GABA from excitatory to inhibitory (Stoop, 2012; Hammock, 2015; Marlin and Froemke, 2017; Ben-Ari, 2018). Our study adds to existing knowledge by showing that oxytocin regulates the excitatory and inhibitory synaptic transmission of L2/3 pyramidal neurons in a developmentally dynamic manner. An immediate implication of this finding is that giving the same dose of oxytocin to an individual may have different effects, sometimes opposite, depending on the developmental stage of the individual.

Because oxytocin can promote trust, eye contact, and facial memory, it has been proposed as a therapy for the treatment of autism spectrum disorders (ASD), a developmental disorder with deficits in social communication (Green and Hollander, 2010; Insel, 2010; Meyer-Lindenberg et al., 2011; Yamasue et al., 2012; Miller, 2013). A very large proportion of individuals with ASD also are hypo- or hypersensitive to sensory inputs (Marco et al., 2011; Suarez, 2012), consistent with the function of oxytocin in regulating cortical neural circuit wiring. However, clinical trials investigating the effectiveness of oxytocin as a treatment for ASD reported mixed results (Guastella and Hickie, 2016; Ooi et al., 2017; Keech et al., 2018; Huang et al., 2021). The dynamic developmental effects of oxytocin likely add to the difficulty of obtaining consistent results. Given the heterogeneity of ASD, the developmental switch point at which oxytocin function shifts from being overall excitatory in L2/3 pyramidal neurons to overall inhibitory may be different for different individuals. If we consider that oxytocin regulates the function of many types of neurons and that many of these functions may be developmentally dynamic and brain-region specific, the situation becomes exceedingly complex.

In addition to identifying complexity, what potential directions do we see moving forward? First, a deeper understanding of oxytocin-OXTR downstream signaling, as well as of other pathways mediating oxytocin signaling, would be important to understand the diversity of its physiological functions. Second, taking developmental stage/age into account may contribute towards more consistent results in both animal and human studies. The developmental stage/age may need to be defined functionally, and therapies may have to optimize treatment windows. Third, especially for patient studies, attempts to subtype or subclass may reduce the heterogeneity of outcomes. In the end, we hope that deeper mechanistic insights eventually translate to effective therapies for patients.

DATA AVAILABILITY STATEMENT

The raw data supporting the conclusions of this article will be made available by the authors, without undue reservation.

ETHICS STATEMENT

The animal study was reviewed and approved by Institutional Animal Care and Use Committee at the Institute of Neuroscience, Chinese Academy of Sciences and of Peking University.

AUTHOR CONTRIBUTIONS

JZ, S-JL, WM, XZ, and J-JZ performed experiments. JZ and XY wrote the manuscript. CW designed and provided reagents. All authors designed experiments, revised and approved the manuscript. All authors contributed to the article and approved the submitted version.

FUNDING

This work was supported by grant from the Key-Area Research and Development Program of Guangdong Province (2019B030335001 to XY), the National Natural Science Foundation of China (31530030 to XY), the National Key R&D Program of China (2016YFA0501000 to XY) and the China Postdoctoral Science Foundation (2017M621544 to JZ). The funders were not involved in the study design, collection, analysis, interpretation of data, the writing of this article or the decision to submit it for publication.

ACKNOWLEDGMENTS

We thank Drs. Klaus Nave, Yuchio Yanagawa and Scott Young for transgenic mice. We thank Shajin Huang and Yuan Lu for excellent technical assistance. We are grateful to colleagues at the Institute of Neuroscience, and members of the Yu laboratory for suggestions and comments.

SUPPLEMENTARY MATERIAL

The Supplementary Material for this article can be found online at: https://www.frontiersin.org/articles/10.3389/fncel.2021.673439/full#supplementary-material.

REFERENCES

Ben-Ari, Y. (2018). Oxytocin and vasopressin and the GABA developmental shift during labor and birth: friends or foes? *Front. Cell. Neurosci.* 12:254. doi: 10.3389/fncel.2018.00254

Blankenship, A. G., and Feller, M. B. (2010). Mechanisms underlying spontaneous patterned activity in developing neural circuits. *Nat. Rev. Neurosci.* 11, 18–29. doi: 10.1038/nrn2759

Crair, M. C. (1999). Neuronal activity during development: permissive or instructive? *Curr. Opin. Neurobiol.* 9, 88–93. doi: 10.1016/s0959-4388(99)80011-7

Duan, L., Zhang, X. D., Miao, W. Y., Sun, Y. J., Xiong, G., Wu, Q., et al. (2018). PDGFR? cells rapidly relay inflammatory signal from the circulatory system to neurons *via* chemokine CCL2. *Neuron* 100, 183.e188–200.e188. doi: 10.1016/j.neuron.2018.08.030

Erzurumlu, R. S., and Gaspar, P. (2012). Development and critical period plasticity of the barrel cortex. *Eur. J. Neurosci.* 35, 1540–1553. doi: 10.1111/j.1460-9568.2012.08075.x

Feldman, D. E., and Brecht, M. (2005). Map plasticity in somatosensory cortex. *Science* 310, 810–815. doi: 10.1126/science.1115807

Fox, K., and Wong, R. O. (2005). A comparison of experience-dependent plasticity in the visual and somatosensory systems. *Neuron* 48, 465–477. doi: 10.1016/j.neuron.2005.10.013

Gimpl, G., and Fahrenholz, F. (2001). The oxytocin receptor system: structure, function and regulation. *Physiol. Rev.* 81, 629–683. doi: 10.1152/physrev.2001.81.2.629

Goebbels, S., Bormuth, I., Bode, U., Hermanson, O., Schwab, M. H., and Nave, K. A. (2006). Genetic targeting of principal neurons in neocortex and hippocampus of NEX-Cre mice. *Genesis* 44, 611–621. doi: 10.1002/dvg.20256

Green, J. J., and Hollander, E. (2010). Autism and oxytocin: new developments in translational approaches to therapeutics. *Neurotherapeutics* 7, 250–257. doi: 10.1016/j.nurt.2010.05.006

Guastella, A. J., and Hickie, I. B. (2016). Oxytocin treatment, circuitry and autism: a critical review of the literature placing oxytocin into the autism context. *Biol. Psychiatry* 79, 234–242. doi: 10.1016/j.biopsych.2015.06.028

Hammock, E. A. (2015). Developmental perspectives on oxytocin and vasopressin. *Neuropsychopharmacology* 40, 24–42. doi: 10.1038/npp.2014.120

Hammock, E. A., and Levitt, P. (2013). Oxytocin receptor ligand binding in embryonic tissue and postnatal brain development of the C57BL/6J mouse. *Front. Behav. Neurosci.* 7:195. doi: 10.3389/fnbeh.2013.00195

Hensch, T. K. (2004). Critical period regulation. *Annu. Rev. Neurosci.* 27, 549–579. doi: 10.1146/annurev.neuro.27.070203.144327

Hooks, B. M., and Chen, C. (2007). Critical periods in the visual system: changing views for a model of experience-dependent plasticity. *Neuron* 56, 312–326. doi: 10.1016/j.neuron.2007.10.003

Huang, Y., Huang, X., Ebstein, R. P., and Yu, R. (2021). Intranasal oxytocin in the treatment of autism spectrum disorders: a multilevel meta-analysis. *Neurosci. Biobehav. Rev.* 122, 18–27. doi: 10.1016/j.neubiorev.2020.12.028

Insel, T. R. (2010). The challenge of translation in social neuroscience: a review of oxytocin, vasopressin and affiliative behavior. *Neuron* 65, 768–779. doi: 10.1016/j.neuron.2010.03.005

Jurek, B., and Neumann, I. D. (2018). The oxytocin receptor: from intracellular signaling to behavior. *Physiol. Rev.* 98, 1805–1908. doi: 10.1152/physrev.00031.2017

Katz, L. C., and Shatz, C. J. (1996). Synaptic activity and the construction of cortical circuits. *Science* 274, 1133–1138. doi: 10.1126/science.274.5290.1133

Keech, B., Crowe, S., and Hocking, D. R. (2018). Intranasal oxytocin, social cognition and neurodevelopmental disorders: a meta-analysis. *Psychoneuroendocrinology* 87, 9–19. doi: 10.1016/j.psyneuen.2017.09.022

Knudsen, E. I. (2004). Sensitive periods in the development of the brain and behavior. *J. Cogn. Neurosci.* 16, 1412–1425. doi: 10.1162/0898929042304796

Kral, A. (2013). Auditory critical periods: a review from system's perspective. *Neuroscience* 247, 117–133. doi: 10.1016/j.neuroscience.2013.05.021

Lakso, M., Pichel, J. G., Gorman, J. R., Sauer, B., Okamoto, Y., Lee, E., et al. (1996). Efficient *in vivo* manipulation of mouse genomic sequences at the zygote stage. *Proc. Natl. Acad. Sci. U S A* 93, 5860–5865. doi: 10.1073/pnas.93.12.5860

Lee, H. J., Caldwell, H. K., Macbeth, A. H., Tolu, S. G., and Young, W. S. 3rd (2008). A conditional knockout mouse line of the oxytocin receptor. *Endocrinology* 149, 3256–3263. doi: 10.1210/en.2007-1710

Luby, J. L., Baram, T. Z., Rogers, C. E., and Barch, D. M. (2020). Neurodevelopmental optimization after early-life adversity: cross-species studies to elucidate sensitive periods and brain mechanisms to inform early intervention. *Trends Neurosci.* 43, 744–751. doi: 10.1016/j.tins.2020.08.001

Maldonado, P. P., Nuno-Perez, A., Kirchner, J. H., Hammock, E., Gjorgjieva, J., and Lohmann, C. (2021). Oxytocin shapes spontaneous activity patterns in the developing visual cortex by activating somatostatin interneurons. *Curr. Biol.* 31, 322–333.e325.doi: 10.1016/j.cub.2020.10.028

Marco, E. J., Hinkley, L. B., Hill, S. S., and Nagarajan, S. S. (2011). Sensory processing in autism: a review of neurophysiologic findings. *Pediatr. Res.* 69, 48R–54R. doi: 10.1203/PDR.0b013e3182130c54

Marlin, B. J., and Froemke, R. C. (2017). Oxytocin modulation of neural circuits for social behavior. *Dev. Neurobiol.* 77, 169–189. doi: 10.1002/dneu.22452

Meyer-Lindenberg, A., Domes, G., Kirsch, P., and Heinrichs, M. (2011). Oxytocin and vasopressin in the human brain: social neuropeptides for translational medicine. *Nat. Rev. Neurosci.* 12, 524–538. doi: 10.1038/nrn3044

Micheva, K. D., and Beaulieu, C. (1996). Quantitative aspects of synaptogenesis in the rat barrel field cortex with special reference to GABA circuitry. *J. Comp. Neurol.* 373, 340–354. doi: 10.1002/(SICI)1096-9861(19960923)373:3<340::AID-CNE3>3.0.CO;2-2

Miller, G. (2013). Neuroscience. The promise and perils of oxytocin. *Science* 339, 267–269. doi: 10.1126/science.339.6117.267

Mitre, M., Marlin, B. J., Schiavo, J. K., Morina, E., Norden, S. E., Hackett, T. A., et al. (2016). A distributed network for social cognition enriched for oxytocin receptors. *J. Neurosci.* 36, 2517–2535. doi: 10.1523/JNEUROSCI.2409-15.2016

Nakajima, M., Görlich, A., and Heintz, N. (2014). Oxytocin modulates female sociosexual behavior through a specific class of prefrontal cortical interneurons. *Cell* 159, 295–305. doi: 10.1016/j.cell.2014.09.020

Neville, H., and Bavelier, D. (2002). Human brain plasticity: evidence from sensory deprivation and altered language experience. *Prog. Brain Res.* 138, 177–188. doi: 10.1016/S0079-6123(02)38078-6

Newmaster, K. T., Nolan, Z. T., Chon, U., Vanselow, D. J., Weit, A. R., Tabbaa, M., et al. (2020). Quantitative cellular-resolution map of the oxytocin receptor in postnatally developing mouse brains. *Nat. Commun.* 11:1885. doi: 10.1038/s41467-020-15659-1

Nithianantharajah, J., and Hannan, A. J. (2006). Enriched environments, experience-dependent plasticity and disorders of the nervous system. *Nat. Rev. Neurosci.* 7, 697–709. doi: 10.1038/nrn1970

Ooi, Y. P., Weng, S. J., Kossowsky, J., Gerger, H., and Sung, M. (2017). Oxytocin and autism spectrum disorders: a systematic review and meta-analysis of randomized controlled trials. *Pharmacopsychiatry* 50, 5–13. doi: 10.1055/s-0042-109400

Petersen, C. C. H. (2007). The functional organization of the barrel cortex. *Neuron* 56, 339–355. doi: 10.1016/j.neuron.2007.09.017

Sale, A., Berardi, N., and Maffei, L. (2009). Enrich the environment to empower the brain. *Trends Neurosci.* 32, 233–239. doi: 10.1016/j.tins.2008.12.004

Stoop, R. (2012). Neuromodulation by oxytocin and vasopressin. *Neuron* 76, 142–159. doi: 10.1016/j.neuron.2012.09.025

Suarez, M. A. (2012). Sensory processing in children with autism spectrum disorders and impact on functioning. *Pediatr. Clin. North Am.* 59, 203–214. doi: 10.1016/j.pcl.2011.10.012

Sur, M., and Rubenstein, J. L. (2005). Patterning and plasticity of the cerebral cortex. *Science* 310, 805–810. doi: 10.1126/science.1112070

Tamamaki, N., Yanagawa, Y., Tomioka, R., Miyazaki, J., Obata, K., and Kaneko, T. (2003). Green fluorescent protein expression and colocalization with calretinin, parvalbumin and somatostatin in the GAD67-GFP knock-in mouse. *J. Comp. Neurol.* 467, 60–79. doi: 10.1002/cne.10905

Vaidyanathan, R., and Hammock, E. A. (2017). Oxytocin receptor dynamics in the brain across development and species. *Dev. Neurobiol.* 77, 143–157. doi: 10.1002/dneu.22403

Wiesel, T. N., and Hubel, D. H. (1963). Single-cell responses in striate cortex of kittens deprived of vision in one eye. *J. Neurophysiol.* 26, 1003–1017. doi: 10.1152/jn.1963.26.6.1003

Wu, D., Vu, Q., Nguyen, A., Stone, J. R., Stubbs, H., Kuhlmann, G., et al. (2009). *In situ* genetic analysis of cellular chimerism. *Nat. Med.* 15, 215–219. doi: 10.1038/nm.1862

Xiu, J., Zhang, Q., Zhou, T., Zhou, T. T., Chen, Y., and Hu, H. (2014). Visualizing an emotional valence map in the limbic forebrain by TAI-FISH. *Nat. Neurosci.* 17, 1552–1559. doi: 10.1038/nn.3813

Yamasue, H., Yee, J. R., Hurlemann, R., Rilling, J. K., Chen, F. S., Meyer-Lindenberg, A., et al. (2012). Integrative approaches utilizing oxytocin to enhance prosocial behavior: from animal and human social behavior to autistic social dysfunction. *J. Neurosci.* 32, 14109–14117. doi: 10.1523/JNEUROSCI.3327-12.2012

Young, W. S., 3rd, Shepard, E., Amico, J., Hennighausen, L., Wagner, K. U., LaMarca, M. E., et al. (1996). Deficiency in mouse oxytocin prevents milk ejection, but not fertility or parturition. *J. Neuroendocrinol.* 8, 847–853. doi: 10.1371/journal.pmed.1003641

Zheng, J. J., Li, S. J., Zhang, X. D., Miao, W. Y., Zhang, D., Yao, H., et al. (2014). Oxytocin mediates early experience-dependent cross-modal plasticity in the sensory cortices. *Nat. Neurosci.* 17, 391–399. doi: 10.1038/nn.3634

Conflict of Interest: The authors declare that the research was conducted in the absence of any commercial or financial relationships that could be construed as a potential conflict of interest.

frontiers in Neuroscience

CASE REPORT
published: 14 July 2021
doi: 10.3389/fnins.2021.697167

Case Report: Mutant *SCN9A* Susceptible to Charcot Neuroarthropathy in a Patient With Congenital Insensitivity to Pain

*Xiao-hui Xie[1], Jian-guang Tang[2], Zhong-hua Liu[3], Shui-jiao Peng[3], Zhuang-zhuang Yuan[4], Heng Gu[1], Yi-qiao Hu[4] and Zhi-ping Tan[1]**

[1] Clinical Center for Gene Diagnosis and Therapy, Department of Cardiovascular Surgery, The Second Xiangya Hospital of Central South University, Changsha, China, [2] Department of Neurology, The Second Xiangya Hospital of Central South University, Changsha, China, [3] The National and Local Joint Engineering Laboratory of Animal Peptide Drug Development, College of Life Sciences, Hunan Normal University, Changsha, China, [4] Department of Cell Biology, School of Life Sciences, Central South University, Changsha, China

Charcot neuroarthropathy is a systemic disease with pathological changes in the musculoskeletal system, which leads to fractures, dislocations, and deformities involving multiple bones and joints, particularly those of the feet. While the common underlying cause of Charcot neuroarthropathy is diabetes mellitus, it is also associated with congenital insensitivity to pain (CIP). CIP is a rare disorder caused by loss-of-function mutations in *SCN9A* encoding Nav1.7. In this study, we report a patient with CIP from a consanguineous family susceptible to Charcot neuroarthropathy with a novel *SCN9A* mutation. This report involves the case of a middle-aged man who suffered from CIP, had repeated painless fractures, and developed bone and joint destruction. The physical and radiological examinations revealed that multiple joints were swollen and deformed, and soft-tissue trauma was evident. We identified a novel homozygous *SCN9A* mutation (p.Cys1339Arg) by whole-exome sequencing (WES), which was verified using Sanger sequencing. In addition, the wild-type (WT) and mutated p. Cys1339Arg were assessed in HEK293 cells expressing Nav1.7, and the results showed that p. Cys1339Arg almost abolished the Nav1.7 sodium current. In conclusion, Charcot neuroarthropathy associated with CIP demonstrated a wider spectrum of Charcot neuroarthropathy than was previously recognized or documented. In addition, this finding is conducive to understanding the critical amino acids for maintaining the function of Nav1.7, thus contributing to the development of Nav1.7-targeted analgesics.

Keywords: Charcot neuroarthropathy, bone destruction, joint destruction, congenital insensitivity to pain, *SCN9A*

OPEN ACCESS

Edited by:
Giordano Lippi, The Scripps Research Institute, United States

Reviewed by:
Lee Rogers, American Board of Medical Specialties, United States
Sulayman D. Dib-Hajj, Yale University, United States

****Correspondence:***
Zhi-ping Tan
zhipingtan@csu.edu.cn

Specialty section:
This article was submitted to Neurogenomics, a section of the journal Frontiers in Neuroscience

Received: *19 April 2021*
Accepted: *21 June 2021*
Published: *14 July 2021*

Citation:
Xie X-h, Tang J-g, Liu Z-h, Peng S-j, Yuan Z-z, Gu H, Hu Y-q and Tan Z-p (2021) Case Report: Mutant SCN9A Susceptible to Charcot Neuroarthropathy in a Patient With Congenital Insensitivity to Pain. Front. Neurosci. 15:697167. doi: 10.3389/fnins.2021.697167

INTRODUCTION

Charcot neuroarthropathy is a systemic disease with pathological changes in the musculoskeletal system, which lead to fractures, dislocations, and deformities involving multiple bones and joints, particularly those of the foot (Dodd and Daniels, 2018). In 1868, the famous neuropathologist Jean-Martin Charcot first described the condition of "Charcot neuroarthropathy," based on his clinical

Abbreviations: CIP, congenital insensitivity to pain; VGSC, voltage-gated sodium channel; WES, whole-exome sequencing; PCR, polymerase chain reaction; WT, wild-type; DRG, dorsal root ganglion.

observation of a patient with neurosyphilis and peripheral joint destruction (Hubault, 1982). Nowadays, with the increase in the incidence of diabetes, the common underlying cause of Charcot neuroarthropathy is diabetes mellitus (Watts et al., 2016). However, Charcot neuroarthropathy is also associated with congenital insensitivity to pain (CIP), which has rarely been reported (Cassidy and Shaffer, 2008).

Pain sensation is an essential protective mechanism to minimize tissue and cellular damage. CIP, a rare autosomal-recessive disorder, is characterized by the lack of protective mechanisms of pain against noxious stimuli, predisposing patients to self-mutilations, burns, and painless fractures (Waxman et al., 2014). Anosmia is also a common clinical feature of patients with CIP. Cox et al. (2006) reported that loss-of-function mutations in *SCN9A*, which encodes the voltage-gated sodium channel (VGSC) Nav1.7, caused congenital inability to experience pain and anosmia. While self-mutilation and anosmia are common, Charcot joints are not common features of Nav1.7-related CIP. The progression of Charcot neuroarthropathy is generally attributed to repetitive microtrauma in patients with impaired pain sensation and proprioception.

The development of Charcot neuroarthropathy in patients with CIP is rare, with few cases reported in the literature. Both clinical and genetic observations of Charcot neuroarthropathy are significant in improving the understanding of this condition. In this report, we have described a Chinese Han man who developed Charcot neuroarthropathy secondary to CIP. We identified a novel *SCN9A* mutation by whole-exome sequencing (WES), which was verified using Sanger sequencing. In addition, we detected the changes in electrophysiological activity using whole-cell patch-clamp recordings.

CASE DESCRIPTION

In the present consanguineous Chinese family, the proband was a 42-year-old man who presented with Charcot neuroarthropathy. He was the fourth child of parents with normal pregnancy and childbirth (**Figure 1A**). Although his older brother had similar symptoms, we were unable to collect the data because he died from a severe accident in the previous year. The proband had no history of diabetes mellitus, hypertension, and syphilis, which are common risk factors for Charcot neuroarthropathy. However, he reported that he had been unable to respond to pain since birth. When he was 1 year old, he often bit his fingers without any sensation of pain; later, his parents noticed that he was incapable of experiencing pain. When he was 10 years old, he repeatedly suffered painless fractures and got burned unknowingly. When he started smoking, he often burned his fingers with lit cigarettes but did not experience pain (**Figure 1C**). Furthermore, he did not experience pain due to extreme heat or cold, although he could distinguish between hot and cold sensations. However, the proband had a complete sense of smell as he could distinguish smells of water, alcohol, or white vinegar. In his 30 s, he developed multiple joint swelling, instability, and deformities caused by repetitive microtrauma and painless fractures (**Figures 1D,E**). Bone and joint destruction induced a severe negative impact on the quality of his life.

Detailed physical examination revealed swelling in the right knee, left ankle, and right elbow joint; reduced right knee flexion; valgus deformity; and left ankle varus. Skin ulcers were noted on the right knee and on the lateral side of the left ankle (**Figure 1D**). A neurological examination indicated normal cognitive function (**Table 1**). In addition, radiography of the right knee joint showed narrowing of the right knee joint space, blurring of the joint surface, bone destruction, and uneven density (**Figure 1F**). Three-dimensional CT scan of the left foot demonstrated that the structures of the left ankle joint, left tarsometatarsal joint, and the intertarsal joint were disordered, and the left ankle exhibited varus and subluxation (**Figure 1G**). After various evaluations, the proband underwent focus debridement and fusion external fixation of the left knee. Postoperative radiographic examination of the bilateral knee joints revealed that the internal fixation device was in place after correction of the valgus of the right knee, and there were no apparent signs of loosening or fracture (**Figure 1H**). During postoperative, the proband recovered well and could walk with crutches.

Mutation Analysis

Whole peripheral blood samples were collected and stored in ethylenediaminetetraacetic acid (EDTA) tubes. Genomic DNA was extracted using a QIAamp DNA Blood Mini Kit (250) (Qiagen, Valencia, CA, United States). WES was performed at the Berry Genomics bioinformatics institute (Beijing, China). The exomes were captured using Agilent SureSelect Human All Exon V6 kits and sequenced on a NovaSeq 6000 system (Illumina, Inc., San Diego, CA, United States). The WES data were filtered by three criteria: (1) variations outside the coding regions (e.g., intergenic, intronic, and untranslated regions) and synonymous mutations were excluded; (2) high allele frequencies relative to population databases ($>0.01\%$) (e.g., 1,000 Genomes Project, ESP, and gnomAD) were excluded; and (3) prediction of a deleterious functional effect by bioinformatics programs (e.g., MutationTaster; Polyphen2; Combined Annotation Dependent Depletion, CADD; and SIFT), loss of function, and deleterious mutations were considered.

Sanger sequencing was performed to verify the identified variant. The primers were designed by Primer Quest Tool (F:5′-GCTGGTTGGTTTGATGTCTTAG, R:5′-GGAACTTGA CTTGCAGGAAAC). The PCR conditions were set as follows: 95°C for 30 s, 56°C for 30 s, and 72°C for 1 min, for a total of 35 cycles using T3 Super PCR Mix (TSINGKE, Beijing, China). The PCR products were electrophoresed on a 2% agarose gel. The PCR fragments were subsequently cut, and the purified fragments were sequenced on a 3730 XL sequencer (Applied Biosystems).

Identification of a Novel *SCN9A* Mutation

Whole exome sequencing, a high-throughput sequencing technique, was performed to generate 12 Gb of data with 99% coverage and a depth of >100X. After filtration of the WES data, we finally identified a missense homozygous mutation (c.T4015C; Cys1339Arg) in exon 21 of *SCN9A*, which was further confirmed by Sanger sequencing (**Figure 1B**). The

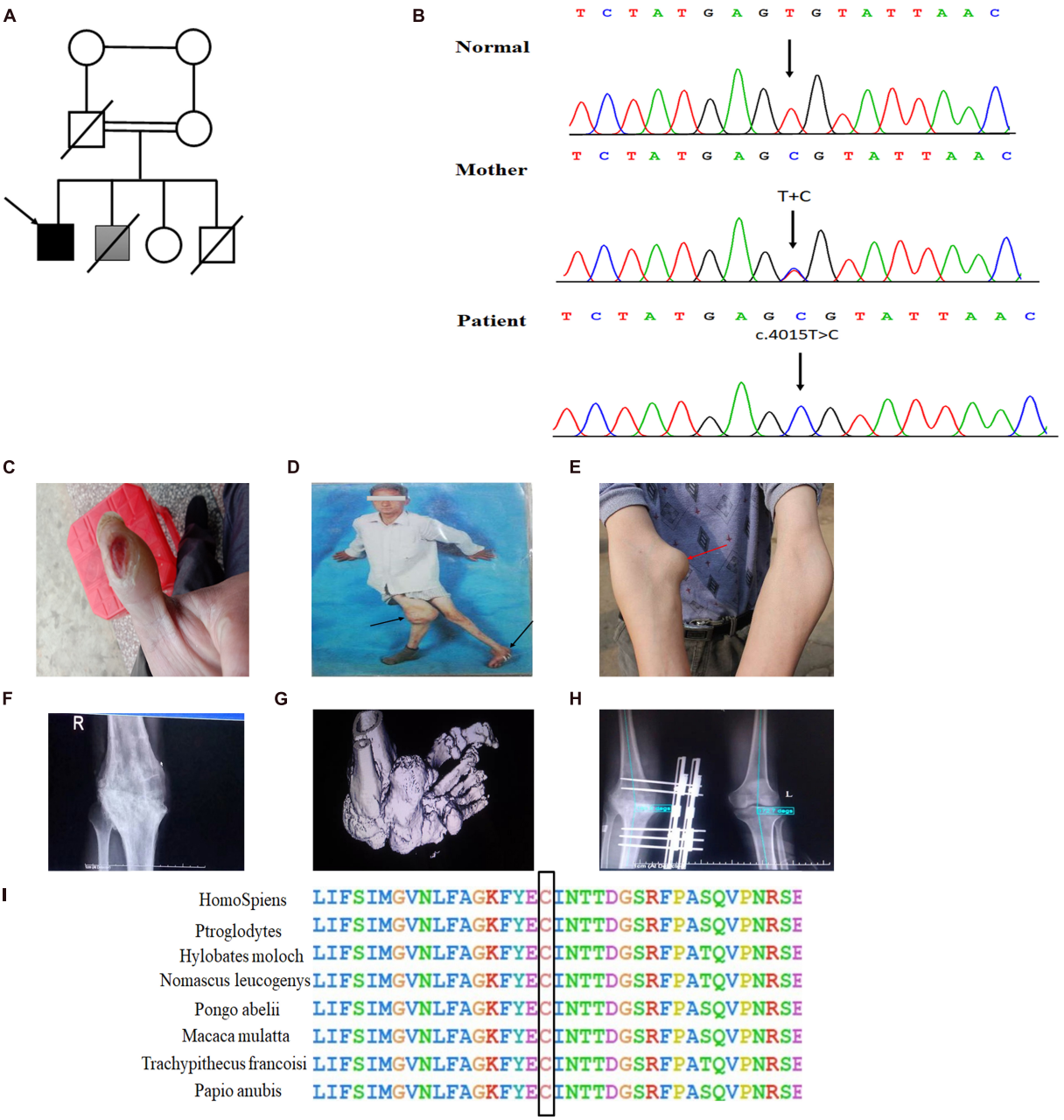

FIGURE 1 | Novel homozygous *SCN9A* mutation and the clinical phenotypes in the proband with Charcot neuroarthropathy. **(A)** Family pedigree. The proband is indicated by a black arrow. The shaded box represents a suspect patient who is presented with Charcot neuroarthropathy. The genetic relationship of parents is them being first cousins. **(B)** DNA sequence electropherograms demonstrating c.4015T > C (p. Cys1339Arg) homozygous mutation in the proband. **(C)** Burns on the finger by a lit cigarette. **(D,E)** Arrows of different colors represent swollen and deformed joints. **(F)** Plain radiographs of the right knee joint showed narrowing of the right knee joint space, blurring of the joint surface, bone destruction, and uneven density. The knee is swollen, distorted, and painless. **(G)** The three-dimensional CT of the left foot showed that the structures of the left ankle joint, the left tarsometatarsal joint, and the intertarsal joint were disordered, and the left ankle showed varus and subluxation. **(H)** The postoperative x-ray examination of bilateral knee joints showed that the internal fixation device was in place after the correction of the valgus of the right knee. **(I)** Conservation of residues Cys1339 among different species.

variant was predicted to be "disease-causing" by MutationTaster and was not found in the 1,000 Genome Browser, ExAC Browser, Exome Variant Server, or in 500 unrelated ethnically matched healthy controls. The controls were individuals presenting for routine health checkups or volunteers without similar symptoms or any positive family history of musculoskeletal system disorders and CIP.

The Nav1.7 mutation was predicted to result in amino acid substitutions p. Cys1339Arg in the extracellular linker joining S5 and S6 of domain III, outside the end of S5 (**Figure 2B**).

Multiple alignments of *SCN9A* orthologs in other animal species indicated that the amino acid at position 1339 was highly conserved (**Figure 1I**).

Electrophysiological Properties of Mutant Nav1.7 Channels

To determine the genotype and clinical phenotype correlation in the patient, we investigated the effect of the variation on the electrophysiological activity of Nav1.7 by performing whole-cell patch-clamp recordings in HEK cells inward sodium channel traces of wild-type (WT) and p.C1339R mutant Nav1.7 channels. First, to construct the Nav1.7 expression plasmid, the cDNA of human Nav1.7 (NM_002977.3) was subcloned into the pcDNA3.1mod vector, and mutations (c.4015T > C, p. Cys1339Arg) (referred to as C1339R) were introduced using overlap extension PCR with primers and verified by Sanger sequencing. There was no other modification of the pcDNA3.1mod vector. HEK293 cells were cultured in 3.5 cm plastic dishes (NEST) in Dulbecco's Modified Eagle Medium (Invitrogen, Beijing, China) supplemented with 10% fetal bovine serum, glutamine, and Penicillin-Streptomycin solution (Invitrogen). In addition, cells were grown under standard conditions (37°C, 5% CO_2) for approximately 12 h. Subsequently, cells were co-transfected with WT or mutant *SCN9A* plus *SCN1B* plus *SCN2B* plus *EGFP* using the Lipofectamine 2000 transfection reagent (Invitrogen, Carlsbad, CA, United States) according to the instructions of the manufacturer and incubated for 24 h.

Finally, custom-designed Exclamp software was used at 22 ± 2°C. The recording platform was EPC10 USB Amplifier (HEKA), and the control software was PatchMaster (HEKA). The extracellular bath solution included 140 mM NaCl, 5 mM KCl, 2 mM $CaCl_2$, 10 mM HEPES, 1 mM $MgCl_2$, and 10 mM glucose (pH 7.4, adjusted with NaOH). The pipette solution contained the following in mM concentrations: 105 CsF, 35 NaCl, 10 HEPES, and 10 EGTA (pH 7.4, adjusted with CsOH). The glass electrode was created using a microelectrode glass capillary (Wuhan Microprobe Scientific Instrument Co., Ltd., China, PC-10 electrode drawing instrument) using a two-step method, and the resistance of the electrode to water was controlled at 2–3 mΩ. An activation protocol was used whereby cells were voltage-clamped at a holding potential of −90 mV, followed by a 50 ms step to the activating step (−90 mV to +80 mV, 10 mV steps). The peak inward current at each activating step was quantified and presented as current-voltage curves. Finally, the data were analyzed using Igor pro6.10A and GraphPad Prism 8. Representative inward sodium channel traces of WT and p.C1339R are shown in **Figures 3A,B**. The results showed that the average peak current density of the p.C1339R channels was almost abolished compared with that of the WT channels (−9.3 ± 1.5 pA/pF, $N = 10$. vs. −119.1 ± 16.0 pA/pF, $N = 22$, $P < 0.05$) (**Figure 3C**).

DISCUSSION

In this study, we identified a novel homozygous missense mutation, Cys1339Arg, in *SCN9A* in the proband susceptible to Charcot neuroarthropathy by WES, which was verified by Sanger sequencing. The mutation was located in the extracellular linker joining S5 and S6 of domain III, outside the mouth of the pore. In addition, the patch-clamp recordings revealed that p.Cys1339Arg of Nav1.7 is a non-functional channel because of the almost non-existent inward charge density.

The proband from a consanguineous family exhibited CIP, but not anosmia, and presented with bone and joint destruction. Although CIP is most common in childhood (Shorer et al., 2014), this is a rare case of Charcot neuroarthropathy in a middle-aged patient with congenital inability to experience pain. The proband was diagnosed with Charcot neuroarthropathy based on thorough medical history and examinations, including clinical features, such as the loss of pain sensation; the presence of ulcers; and a warm and swollen foot, ankle, and knee (**Figures 1C–E**). The physical and radiological examinations showed that multiple joints were swollen and deformed, and soft-tissue trauma was evident (**Figures 1D–H**). While other causes of Charcot neuroarthropathy cannot be ruled out, CIP is likely to be a contributing factor in this case.

Previous studies emphasized that diabetes mellitus is the common underlying cause of Charcot neuroarthropathy, and nearly 1% of patients with diabetes presented neuropathic changes in the foot (McInnes, 2012); however, CIP is a rare risk factor of neuropathic arthropathy. The proband did not receive careful supervision from his parents when he was diagnosed with CIP in his childhood, and repetitive painless fractures are one of the factors that induce Charcot neuroarthropathy. To further explore the relationship between CIP and Charcot neuroarthropathy, we collected clinical data and carried out WES and patch-clamp recordings. As a result, a novel missense homozygous *SCN9A* variant (c.4015T > C; p.Cys1339Arg) was identified and predicted to be a disease-causing variant by MutationTaster and CADD. In addition, the electrophysiological tests showed that p.Cys1339Arg of Nav1.7 almost abolished current density. Considering that the Nav1.7

TABLE 1 | Summary of clinical findings in the proband.

Clinical features	
Age	**Symptoms**
1	Self-mutilation (bit fingers)
10	Painless injuries (fractures, burns)
30	Charcot joints
42	Bone and joint destruction
Examinations	
Examination	**Y or N**
Anosmia	N
Normal cognitive development	Y
Joint deformity	Y
Soft-tissue ulcer	Y

N, no; Y, yes.

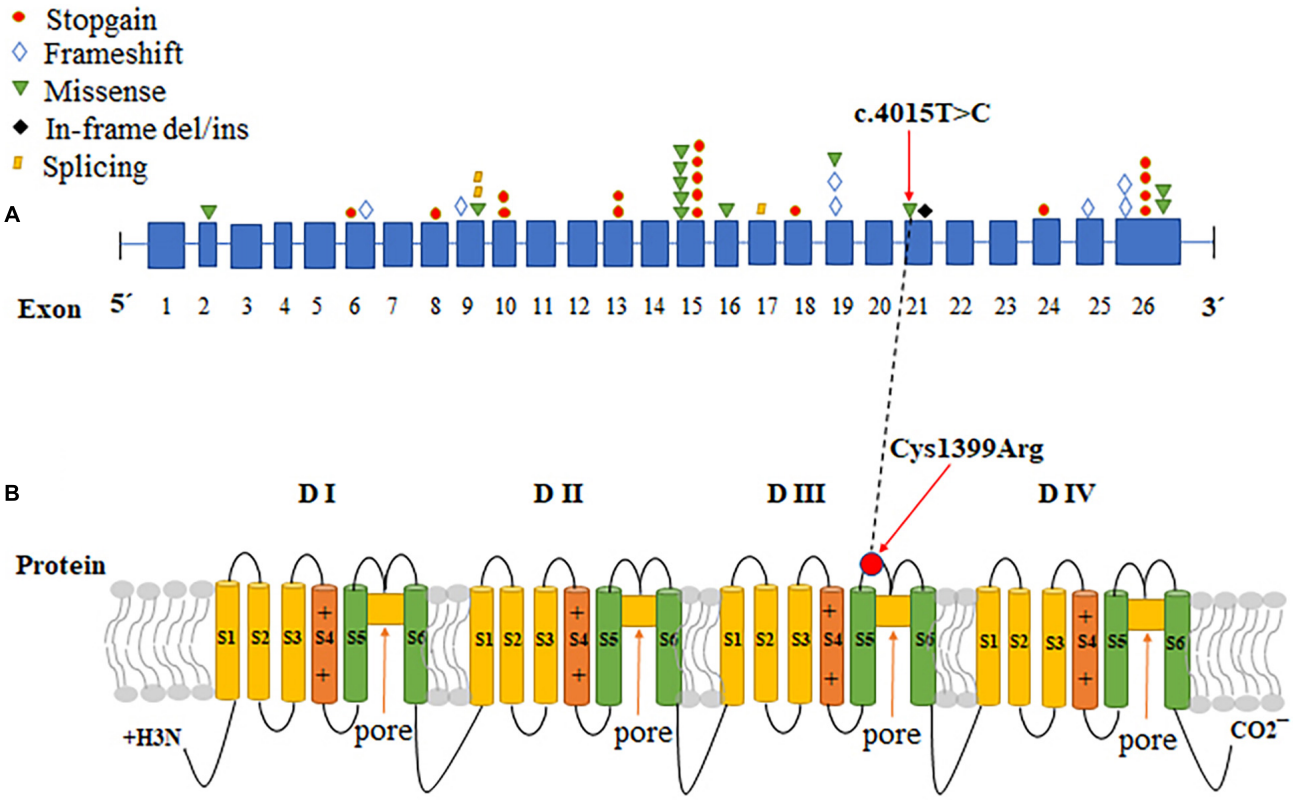

FIGURE 2 | The CDS sequence and protein structure pattern of *SCN9A*. **(A)** A variety of mutations in different exons in *SCN9A* cause CIP. The red circles: stopgain; blue diamonds: frameshift; green inverted triangles: missense; black diamonds: in-frame del/ins; yellow parallelograms: splicing. **(B)** Schematic representation of Nav1.7, the voltage-gated sodium channel (VGSC) a-subunit encoded by *SCN9A*, and the locations of the identified mutation. *SCN9A* encodes a plasma membrane protein, Nav1.7, which consisted of four similar domains with each domain comprising six a-helical transmembrane segments (labeled 1–6). Transmembrane segments 5 and 6 are the pore-lining segments and the voltage sensor is located in transmembrane segment 4 of each domain (depicted by a plus symbol). The red arrows indicate the location of the missense mutation identified in this study. The black dotted line correlates the change of CDS with protein change in SCN9A.

plays a vital role in signal pathways in nociceptive neurons (Haberberger et al., 2019), the mutant Nav1.7 completely abolishes its function as a VGSC in nociceptors. Therefore, the clinical feature of insensitivity to pain in the proband seemed well explained. Charcot neuroarthropathy may attribute to long-term impaired pain sensation, unnoticed damage, and repetitive microtrauma to the weight-bearing joints (Callaghan et al., 2015).

SCN9A, found at 2q24.3, is a 26-exon gene that encodes the VGSC Nav1.7, which is highly expressed in peripheral sensory neurons, most notably in nociceptive small-diameter DRG neurons and sympathetic ganglion neurons (Klugbauer et al., 1995; Toledo-Aral et al., 1997; Rush et al., 2006). VGSCs comprises pore-forming α-subunits and auxiliary β-subunits. Each α-subunit consists of four homologous domains (DI-DIV), with each containing six transmembrane segments (S1–S6), connected by intracellular loops (L1, L2, and L3) and cytoplasmic N- and C-terminal regions (Catterall, 2000). Mutations that cause a gain of function in NaV1.7 have been shown to cause autosomal-dominant pain disorders, such as primary erythermalgia. Conversely, loss-of-function mutations in *SCN9A* contribute to CIP (Klein et al., 2013). To date, more than 100 mutations in *SCN9A* have been reported, but only 42 have been associated with CIP (Baker and Nassar, 2020; **Supplementary Table 1** and **Figure 2A**). Among the *SCN9A* mutations identified in CIP patients, most were non-sense, frameshift, or splicing mutations, all of which produced non-functional and truncated Nav1.7 proteins; however, we identified a novel homozygous missense mutation (c.4015T > C, p. Cys1339Arg) in *SCN9A* in a patient with CIP, which abolished the current density and the Nav1.7 function. The variant site was localized in exon 21 of *SCN9A*, and the protein change was located in the extracellular linker joining S5 and S6 of domain III, which has not been reported previously (**Figure 2**). S5-P, P loop, and P-S6 are vital for the selective permeation of sodium ions (Catterall, 2017). Residue Cys1339 mapped to the S5-P, domain III of Nav1.7, is highly conserved among different species (**Figure 1I**) and plays a role in filtering sodium ions.

Loss-of-function mutations in the VGSC Nav1.7 cause CIP in human, making Nav1.7 an important target for novel analgesics. For humans, in most patients with CIP, the perception of non-noxious touch and warmth is not affected, whereas the perception of noxious heat, pressure, and injury pain is completely lost. Therefore, loss of Nav1.7 did not lead to lethality or any disability

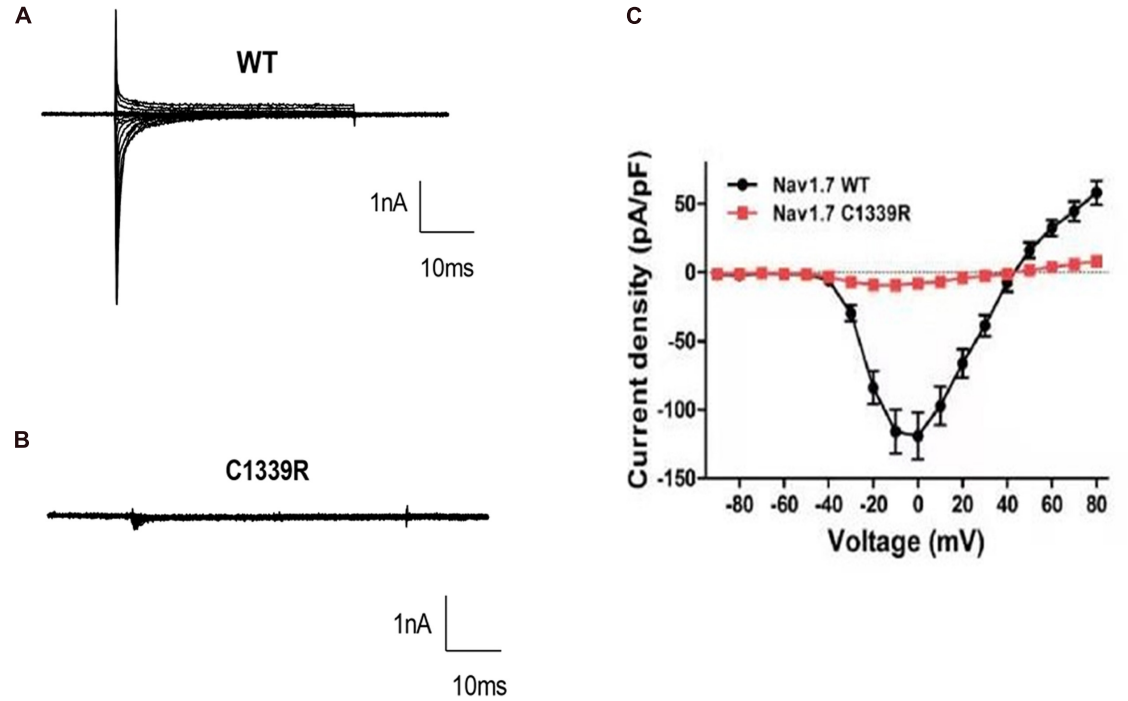

FIGURE 3 | Biophysical characterization of WT and mutant Nav1.7 channels in HEK293 cells. **(A,B)** Representative inward current traces were recorded from HEK293 cells expressing WT, and mutant p. Cys1339Arg Nav1.7 channels, respectively. **(C)** Current-voltage relationship of WT and mutant p. Cys1339Arg channels. Peak current density normalized to membrane capacitance is presented as the mean ± SEM.

(Zufall et al., 2012). Selective Nav1.7 channel blockers, as potential painkillers with improved safety and reduced unwanted side effects, will be increasingly favored by doctors and patients. For mice, a study indicated that mice with selective knockout of Nav1.7 in nociceptive neurons showed deficits in acute and inflammatory pain sensation, whereas a global knockout (KO) of Nav1.7 was neonatal lethal because the animals are anosmic and cannot feed (Nassar et al., 2004). Indeed, a global KO mouse was generated on a different genetic background that partially alleviated anosmia and allowed the mice to survive, which provides a powerful tool for pre-clinical experiments in the analgesic field (Grubinska et al., 2019). To determine the maximum effect of a theoretically perfect selective Nav1.7 inhibitor, a research team generated a tamoxifen-inducible KO mouse model that enabled the genetic deletion of Nav1.7 in adult mice (Shields et al., 2018). The selective blocker site of the NaV1.7 channel, with minimal side effects, is a significant target for analgesic drugs. According to the structure of Nav1.7, S4 carries gating charges in the sliding helix or helical screw model of voltage sensing. Amino acid residues in the short segments between S5 and S6 form the receptor site for the pore blocker tetrodotoxin (Catterall, 2017). The novel mutation p.Cys1339Arg is located in the extracellular linker joining S5 and S6 of domain III, outside the mouth of the pore-forming region, which is a significant part of Nav1.7. In addition, the patient in this study with the p.Cys1339Arg variant in Nav1.7 developed Charcot neuroarthropathy in conjunction with CIP, which may arise attention in pain drugs development programs.

In summary, the novel missense homozygous variant p.Cys1339Arg is a loss-of-function mutation in Nav1.7, which constitutes a novel mutation susceptible to neuroarthropathy. Charcot neuroarthropathy associated with CIP demonstrated a wider spectrum of Charcot arthropathy of the foot and ankle than that which has previously been recognized or documented. In addition, these findings help in understanding the critical amino acid for maintaining the function of Nav1.7, thus contributing to the development of Nav1.7-targeted analgesics.

DATA AVAILABILITY STATEMENT

The datasets presented in this study can be found in online repositories. The names of the repository/repositories and accession number(s) can be found below: ClinVar, SCV001572593.

ETHICS STATEMENT

The studies involving human participants were reviewed and approved by the Ethics Committee of The Second Xiangya Hospital of Central South University. The patients/participants provided their written informed consent to participate in this study. Written informed consent was obtained from the individual(s) for the publication of any potentially identifiable images or data included in this article.

AUTHOR CONTRIBUTIONS

Z-PT designed the overall study and performed the data analysis. X-HX processed the WES data, validated the mutation, and drafted the manuscript. J-GT enrolled the subjects. Z-HL and S-JP carried out the electrophysiological analysis. Z-ZY analyzed the data and edited the manuscript. Y-QH and HG conducted the cell culture and transfection. All authors read and approved the final version of the manuscript, contributed to the article, and approved the submitted version.

FUNDING

This study was supported by the National Natural Science Foundation of China (81970268 and 81470445).

ACKNOWLEDGMENTS

The authors are grateful to the patient and his family for their support and cooperation. The authors also thank Editage (www.editage.cn) for English language editing.

SUPPLEMENTARY MATERIAL

The Supplementary Material for this article can be found online at: https://www.frontiersin.org/articles/10.3389/fnins.2021.697167/full#supplementary-material

Supplementary Table 1 | *SCN9A* mutations that cause congenital insensitivity to pain (CIP): in order of their publications.

REFERENCES

Baker, M. D., and Nassar, M. A. (2020). Painful and painless mutations of SCN9A and SCN11A voltage-gated sodium channels. *Pflugers Archiv* 472, 865–880. doi: 10.1007/s00424-020-02419-9

Callaghan, B. C., Price, R. S., Chen, K. S., and Feldman, E. L. (2015). The Importance of Rare Subtypes in Diagnosis and Treatment of Peripheral Neuropathy: A Review. *JAMA Neurol.* 72, 1510–1518. doi: 10.1001/jamaneurol.2015.2347

Cassidy, R. C., and Shaffer, W. O. (2008). Charcot arthropathy because of congenital insensitivity to pain in an adult. *Spine J.* 8, 691–695. doi: 10.1016/j.spinee.2007.04.005

Catterall, W. A. (2000). From ionic currents to molecular mechanisms: the structure and function of voltage-gated sodium channels. *Neuron* 26, 13–25.

Catterall, W. A. (2017). Forty Years of Sodium Channels: Structure, Function, Pharmacology, and Epilepsy. *Neurochem. Res.* 42, 2495–2504. doi: 10.1007/s11064-017-2314-9

Cox, J. J., Reimann, F., Nicholas, A. K., Thornton, G., Roberts, E., Springell, K., et al. (2006). An SCN9A channelopathy causes congenital inability to experience pain. *Nature* 444, 894–898. doi: 10.1038/nature05413

Dodd, A., and Daniels, T. R. (2018). Charcot Neuroarthropathy of the Foot and Ankle. *J. Bone Joint Surg. Am.* 100, 696–711. doi: 10.2106/jbjs.17.00785

Grubinska, B., Chen, L., Alsaloum, M., Rampal, N., Matson, D. J., Yang, C., et al. (2019). Rat Na1.7 loss-of-function genetic model: Deficient nociceptive and neuropathic pain behavior with retained olfactory function and intra-epidermal nerve fibers. *Mole. Pain* 15:1744806919881846. doi: 10.1177/1744806919881846

Haberberger, R. V., Barry, C., Dominguez, N., and Matusica, D. (2019). Human Dorsal Root Ganglia. *Front. Cell Neurosci.* 13:271. doi: 10.3389/fncel.2019.00271

Hubault, A. (1982). Nervous arthropathies. *Rev. Neurol.* 138, 1009–1017.

Klein, C., Wu, Y., Kilfoyle, D., Sandroni, P., Davis, M., Gavrilova, R., et al. (2013). Infrequent SCN9A mutations in congenital insensitivity to pain and erythromelalgia. *J. Neurol. Neurosurg. Psychiatry.* 84, 386–391. doi: 10.1136/jnnp-2012-303719

Klugbauer, N., Lacinova, L., Flockerzi, V., and Hofmann, F. J. (1995). Structure and functional expression of a new member of the tetrodotoxin-sensitive voltage-activated sodium channel family from human neuroendocrine cells. *EMBO J.* 14, 1084–1090.

McInnes, A. D. (2012). Diabetic foot disease in the United Kingdom: about time to put feet first. *J. Foot Ankle Res.* 5:26. doi: 10.1186/1757-1146-5-26

Nassar, M. A., Stirling, L. C., Forlani, G., Baker, M. D., Matthews, E. A., Dickenson, A. H., et al. (2004). Nociceptor-specific gene deletion reveals a major role for Na(v)1.7 (PN1) in acute and inflammatory pain. *Proc. Natl. Acad. Sci. U. S. A.* 101, 12706–12711. doi: 10.1073/pnas.0404915101

Rush, A., Dib-Hajj, S., Liu, S., Cummins, T., Black, J., and Waxman, S. A. (2006). A single sodium channel mutation produces hyper- or hypoexcitability in different types of neurons. *PNAS* 103, 8245–8250. doi: 10.1073/pnas.0602813103

Shields, S., Deng, L., Reese, R., Dourado, M., Tao, J., Foreman, O., et al. (2018). Insensitivity to Pain upon Adult-Onset Deletion of Nav1.7 or Its Blockade with Selective Inhibitors. *J. Neurosci.* 38, 10180–10201. doi: 10.1523/jneurosci.1049-18.2018

Shorer, Z., Wajsbrot, E., Liran, T. H., Levy, J., and Parvari, R. (2014). A novel mutation in SCN9A in a child with congenital insensitivity to pain. *Pediatr. Neurol.* 50, 73–76. doi: 10.1016/j.pediatrneurol.2013.09.007

Toledo-Aral, J., Moss, B., He, Z., Koszowski, A., Whisenand, T., Levinson, S., et al. (1997). Identification of PN1, a predominant voltage-dependent sodium channel expressed principally in peripheral neurons. *Neurbiology* 94, 1527–1532. doi: 10.1073/pnas.94.4.1527

Watts, C. D., Martin, J. R., Houdek, M. T., Abdel, M. P., Lewallen, D. G., and Taunton, M. J. (2016). The Charcot foot Pathophysiology, Diagnosis and Classification. *Bone Joint J.* 98, 1155–1159. doi: 10.1302/0301-620X.98B9

Waxman, S. G., Merkies, I. S. J., Gerrits, M. M., Dib-Hajj, S. D., Lauria, G., Cox, J. J., et al. (2014). Sodium channel genes in pain-related disorders: phenotype–genotype associations and recommendations for clinical use. *Lancet Neurol.* 13, 1152–1160. doi: 10.1016/s1474-4422(14)70150-4

Zufall, F., Pyrski, M., Weiss, J., and Leinders-Zufall, T. (2012). Link Between Pain and Olfaction in an Inherited Sodium Channelopathy. *Archiv. Neurol.* 69, 1119–1123. doi: 10.1001/archneurol.2012.21

Conflict of Interest: The authors declare that the research was conducted in the absence of any commercial or financial relationships that could be construed as a potential conflict of interest.

frontiers in Cellular Neuroscience

REVIEW
published: 13 September 2021
doi: 10.3389/fncel.2021.743353

Role of Exosomes in Brain Diseases

Nan Zhang[1†], *Fengling He*[1†], *Ting Li*[1], *Jinzhi Chen*[1], *Liping Jiang*[1,2], *Xin-Ping Ouyang*[1,3*] *and Lielian Zuo*[1*]

[1] *Hengyang Key Laboratory of Neurodegeneration and Cognitive Impairment, Department of Physiology, Hengyang Medical School, Institute of Neuroscience Research, University of South China, Hengyang, China,* [2] *Hunan Taihe Hospital, Changsha, China,* [3] *Hunan Province Cooperative Innovation Center for Molecular Target New Drug Study, University of South China, Hengyang, China*

Exosomes are a subset of extracellular vesicles that act as messengers to facilitate communication between cells. Non-coding RNAs, proteins, lipids, and microRNAs are delivered by the exosomes to target molecules (such as proteins, mRNAs, or DNA) of host cells, thereby playing a key role in the maintenance of normal brain function. However, exosomes are also involved in the occurrence, prognosis, and clinical treatment of brain diseases, such as Alzheimer's disease, Parkinson's disease, stroke, and traumatic brain injury. In this review, we have summarized novel findings that elucidate the role of exosomes in the occurrence, prognosis, and treatment of brain diseases.

Keywords: clinical treatment, biomarkers, cargo, brain diseases, exosomes, miRNAs

OPEN ACCESS

Edited by:
Giordano Lippi,
The Scripps Research Institute, United States

Reviewed by:
Chiara Porro,
University of Foggia, Italy
Yvette Wooff,
Australian National University, Australia

***Correspondence:**
Xin-Ping Ouyang
y1655@163.com
Lielian Zuo
799515733@qq.com

[†] *These authors have contributed equally to this work and share first authorship*

Specialty section:
This article was submitted to Cellular Neurophysiology, a section of the journal Frontiers in Cellular Neuroscience

Received: *18 July 2021*
Accepted: *10 August 2021*
Published: *13 September 2021*

Citation:
Zhang N, He F, Li T, Chen J, Jiang L, Ouyang X-P and Zuo L (2021) Role of Exosomes in Brain Diseases. Front. Cell. Neurosci. 15:743353. doi: 10.3389/fncel.2021.743353

INTRODUCTION

Extracellular vesicles are vesicles with a diameter range of 3 nm−1 μm secreted by cells into the extracellular space, which can be divided into exosomes (30–100 nm), microvesicles (100 nm−1 μm in diameter), and apoptotic bodies (50–5,000 nm) (Beeraka et al., 2020). According to the MISEV guidelines, extracellular vesicles measuring <100 nm in diameter, are termed as small extracellular vesicles (sEVs). Small extracellular vesicles (SEVs) originating from late endosomes are termed as exosomes, whereas other Small extracellular vesicles (SEVs) originate from the cell surface (plasma membrane) (Thery et al., 2018). Traditional methods of vesicle extraction and isolation are limited to in their ability to isolate different subtypes of EVs. Therefore, the terms "EV," "sEV," and "exosome" are used interchangeably in some studies (He et al., 2021b). This review focused on the function of exosomes.

Exosomes originate from the endomembrane system, and their envelope is continuously invaginated during early endosomal maturation to form intraluminal vesicles within the endosome. During this time, proteins, nucleic acids, and lipids are screened and enter the intraluminal vesicles. Late endosomes containing a large number of intraluminal vesicles are also called multivesicular bodies (Zhang et al., 2020; Nieland et al., 2021). Multivesicular bodies have two metabolic pathways. One is to be degraded by binding to lysosomes, and the other is to be transported to cell membranes, where the multivesicular membrane fuses with cell membranes and releases the inner vesicles into the extracellular space to form exosomes, which are loaded with proteins, non-coding RNAs, lipids and other biologically active substances (Ratajczak and Ratajczak, 2020). The endosome sorting complex is required for transport, with tetraspanins, ALG2-interacting protein X (Alix), heat shock protein (Hsp70), tumor susceptibility gene 101 protein, etc. being the accepted biomarkers for identifying exosomes (Budnik et al., 2016).

Exosomes carry various bioactive compounds as cargo, such as proteins, non-coding RNAs, lipids, etc. after being secreted from cells, thus facilitating communication between cells (Nieland et al., 2021). This function of exosomes forms the basis for their role in the development of various

diseases, and altering the cargoes carried by exosomes or changing their surface molecules may hold therapeutic potential (Jafari et al., 2020). Exosomes are secreted by different types of cells and since the cargoes of exosomes secreted by the same type of cells differ in different disease processes suggests that studying the cargo of exosomes may be beneficial in predicting the course of a disease and for disease diagnosis (Zhang et al., 2020).

The brain is considerably intricate in its structure and function. The study of the molecular mechanisms underlying the development of brain disease is still in its infancy, creating limitations for clinical treatment. Brain diseases impose many social and economic burdens on society (Wang et al., 2020b). In recent years, exosomes have attracted considerable interest in the study of brain diseases, such as Alzheimer's disease, Parkinson's disease, stroke, and traumatic brain injury, due to their critical importance in the disease process and potential value for clinical application. The role and molecular mechanisms of exosomes carrying proteins related to the brain diseases [amyloid precursor protein (APP), α-synuclein (α-syn), mHtt, PrPsc] have been emphatically explored (Hartmann et al., 2017; Leblanc et al., 2017; Wang J. K. T. et al., 2017; Hill, 2019; Li B. et al., 2020; Pan et al., 2020; Perez-Gonzalez et al., 2020; Singh and Muqit, 2020; Tsunemi et al., 2020, 2021; Ananbeh et al., 2021; Soares Martins et al., 2021a). Notably, their ability to transport cargo is a key mechanism involved in the spread of disease. Compared to traditional therapeutic drugs, exosomes carrying drugs are more likely to pass through the blood-brain barrier (BBB), which helps the drugs to reach the target tissue (Azarmi et al., 2020). Due to the prevalence and easy availability of exosomes in the organism, as well as their involvement in various biomodulatory effects, exosomes have been considered as potential biomarker candidates for the clinical diagnosis and prognosis of diseases (He et al., 2021b). Over recent years, an increasing number of studies have explored the specific mechanisms of exosome involvement in brain disease (Soares Martins et al., 2021b). Here, we summarize novel findings that elucidate the role of exosomes in the occurrence, prognosis, and treatment of brain disease.

Abbreviations: EVs, Extracellular vesicles; Alix, ALG2-interacting protein X; APP, amyloid precursor protein; α-syn, α-synuclein; BBB, blood-brain barrier; GBM, glioblastoma; mTOR, mammalian target of rapamycin; CSF, cerebrospinal fluid; TAM, tumor-associated macrophages; L1CAM, cell adhesion molecule L1; PTRF, transcript release factor; miRNA, microRNA; KLF2, Kruppel-like factors 2; KLF4, Kruppel-like factors 4; VEGF, vascular endothelial growth factor; LncRNA, long non-coding RNA; TMZ, Temozolomide; BMSCs, bone marrow-derived mesenchymal stem cells; AD, Alzheimer's disease; Aβ, Amyloid beta; iPSC, induced pluripotent stem cell; mTau, mutant tau; ANP32A, acidic nuclear phosphoprotein 32 family member A; ADEs, astrocyte-derived exosomes; CR1, complement receptor type 1; GAC, glutaminase C; piRNAs, PIWI-interacting RNAs; GAP43, growth associated protein 43; MSCs, mesenchymal stem cells; LTP, long-term potentiation; CA1, cornu ammonis 1; PD, Parkinson's disease; DA, dopaminergic; ASO, antisense oligonucleotides; ALS, Amyotrophic lateral sclerosis; SOD1, superoxide dismutase 1; TDP, TDR DNA-binding protein; IL, Interleukin; NIR, INHAT repressor; ADSCs, adipose-derived stem cells; MS, Multiple sclerosis; IGF1R, growth factor 1 receptor; PBMC, peripheral mononuclear blood cells; HD, Huntington's disease; Prpc, cellular prion protein; LPS, lipopolysaccharides; HMGBM1, high-mobility group box 1; TBI, Traumatic brain injury; BDPs, breakdown products; mTBI, mild TBI; ApoE, apolipoprotein E; GJA1, gap junction Alpha 1; SCZ, schizophrenia; BD, bipolar disorder; BDNF, brain-derived neurotrophic factor; MDD, major depressive disorder; IRS-1, insulin receptor substrate−1.

EXOSOMES AND NEURAL TUMORS

Nervous system tumors include primary and metastatic tumors that originate in the brain, spinal cord, or meninges. As a highly malignant neural tumor, glioblastoma (GBM) has a high clinical mortality rate due to its poor prognosis, drug resistance, and susceptibility to hematologic metastasis. In recent years it has been closely studied in the field of exosome researches (De Leo et al., 2020; Ou et al., 2020).

Exosomes take part in the complicated inflammatory and immune responses of GBM. The inflammatory response present in GBM can alter the tumor microenvironment and promote tumor angiogenesis, cell proliferation, and invasive metastasis through a variety of active factors (Baig et al., 2020). Meanwhile, exosomes have been found to be involved in the inflammatory response in GBM and can alter the tumor microenvironment in GBM and promote tumor aggressiveness (Azambuja et al., 2020). Brain tumor-initiating cells transport tenascin-C through exosomes, which interacts with integrin α5β1 and αVβ6 to inhibit the mammalian target of rapamycin (mTOR) signaling pathway and further inhibit T cell activity (Mirzaei R. et al., 2018). LGALS9, a protein found in cerebrospinal fluid (CSF) exosomes derived from patients with GBM inhibits dendritic cell antigen presentation and cytotoxic T cell immunity (Yang et al., 2020). GBM cell-derived exosomes can promote the conversion of normal macrophages to tumor-associated macrophages (TAM), and TAM subsequently release large amounts of tumor growth-promoting exosomes. It has been further revealed that the inhibition of arginase-1+ TAM is a potential therapeutic target for GBM (Azambuja et al., 2020).

Exosomes and their cargo boost tumor proliferation and invasion in addition to altering the tumor microenvironment. Exosomes with cell adhesion molecule L1 (L1CAM) have been observed to stimulate the invasiveness and proliferation of GBM cells (Pace et al., 2019). The antisense transcript of hypoxia-inducible factor-1α is upregulated in exosomes of GBM cells, which can promote tumor viability, invasiveness, and radiation resistance (Dai et al., 2019). Polymerase I and transcript release factor (PTRF) in GBM cells accelerates the secretion of exosomes to transform the microenvironment and induces malignancy of adjacent cells. In both tumor tissue exosomes and blood exosomes isolated from GBM patients, tumor grade is positively correlated with the expression of PTRF in exosomes, and the expression of PTRF in blood exosomes decreases in patients after surgery (Huang K. et al., 2018).

Exosomal miR-301a derived from hypoxia-treated GBM cells can target TCEAL7 genes, thereby activating the Wnt/β-catenin signaling pathway and promoting the anti-radiation ability of the tumor (Yue et al., 2019). miR-182-5p is significantly upregulated in exosomes produced by GBM cells in a hypoxic environment, and this microRNA (miRNA) can inhibit the expression of Kruppel-like factors 2 and 4 (KLF2 and KLF4), leading to the accumulation of vascular

endothelial growth factor (VEGF) receptor and promotion of tumor angiogenesis. Additionally, exosome-mediated miR-182-5p inhibits tight junction-related proteins (such as ZO-1, occludin, and claudin-5), thereby boosting vascular permeability and tumor transendothelial migration. Moreover, knockdown of miR-182-5p reduces angiogenesis and tumor proliferation (Li J. et al., 2020).

An abundance of abnormal nucleic acids in exosomes has been reported in GBM patients. A fragment of SOX2 DNA can be detected in exosomes, which is an important gene in embryonic stem cells (Vaidya and Sugaya, 2020). By measuring the serum exosomes in several patients with GBM, researchers found that the long non-coding RNA (lncRNA) HOTAIR 12q13 fragment, an RNA associated with GBM proliferation, is upregulated in exosomes, demonstrating that this RNA could be a new biomarker for GBM (Tan et al., 2018). However, these effects need to be explored further.

Temozolomide (TMZ) is an oral capsule preparation for the treatment of GBM and overcoming resistance to this drug is of paramount importance. After treatment with TMZ, GBM cells produce exosomes containing miR-93 and miR-193 to target cyclinD1, which shortens the cell cycle and accelerates cell proliferation, thereby leading to drug resistance (Munoz et al., 2019). Exosomal miR-151a *in vitro* can improve the sensitivity of GBM cells to TMZ and have a therapeutic effect (Zeng et al., 2018). Recent studies have revealed that exosomes released from human bone marrow-derived mesenchymal stem cells (BMSCs) that are loaded with miR-34a alleviate the malignancy of tumors by silencing MYCN, thus promoting the sensitivity of GBM cells to TMZ (Wang et al., 2019a) (**Figure 1A**).

EXOSOMES AND ALZHEIMER'S DISEASE

Among brain diseases, Alzheimer's disease is one of the most popular diseases studied in the field of exosome researches. The disparate modification of Amyloid beta (Aβ) peptide and tau protein in the damaged brain regions are considered characteristic features of Alzheimer's disease (AD). The former is degraded by APP (Luciunaite et al., 2020; Zhao et al., 2020). Over phosphorylation of tau proteins can lead to dissociation of tau proteins from microtubules and aggregation with each other, forming neurofibrillary tangles and deposition in neuronal cell bodies as well as axons and dendrites (Vandendriessche et al., 2020). The aggregation of abnormal proteins activates microglia and astrocytes, which in turn triggers a chronic inflammatory response, producing a variety of cytokines that can directly induce neuronal apoptosis and further Aβ accumulation in neurons. Therefore, neuroinflammation is an important factor in the development of AD disease (Soares Martins et al., 2021b).

Exosomes are involved in the complex mechanisms of secretion, spread, and degradation of Aβ or tau proteins. Researchers have investigated the physical properties of individual exosomes using electrostatic force microscopy, and observed that when higher concentrations of Aβ42 oligomers are fed to the neuroblastoma cells, the exosomes contained more Aβ42, implying that exosomes act as transport vesicles for Aβ42 (Choi et al., 2021). By constructing tau-containing N2a neurons, the researchers found that tau propagation between neuronal cells is facilitated by exosomes, and tau-containing exosomes are taken up by neurons and microglia, but not astrocytes. Additionally, on analyzing the CSF of patients with AD, it was discovered that the CSF exosomes contained tau in monomeric and oligomeric forms (Wang Y. et al., 2017). Among the exosomes generated from human induced pluripotent stem cell (iPSC)-derived neurons expressing mutant tau (mTau), there were a variety of unique proteins not found in normal exosomes, such as acidic nuclear phosphoprotein 32 family member A (ANP32A). In electrophysiological studies in human tau transgenic mice, knockdown of ANP32A rescued memory deficits and restored synaptic neurotransmission (Podvin et al., 2020).

Exosomes may play a role in the neuroinflammation observed in AD. Compared with healthy controls, patients with AD have higher levels of complement proteins in astrocyte-derived exosomes (ADEs), such as C1q, C46, and factor B. The mean levels of complement proteins in ADEs are significantly higher in the moderate dementia stage than in the preclinical stage. However, the complement regulatory proteins CD59, CD46, decay accelerating factor, and complement receptor type 1 (CR1) are lower in the ADEs of patients with AD than in healthy controls and decrease further with disease progression. This study suggests that measuring complement protein level in the exosomes may predict the progression of the disease (Goetzl et al., 2018). The exosomes produced by SHSWe cells contain miR-21 and can be internalized by microglia to promote an inflammatory response (Fernandes et al., 2018). AD mice demonstrate a high expression of glutaminase C (GAC) in their microglia, and previous studies have shown that GAC promotes exosome secretion and changes the exosome content to pro-inflammatory miRNAs, thereby activating the microglia (Gao et al., 2019).

Nucleic acids and proteins contained in the exosomes can be used as biomarkers for AD. miR-125b-5p, miR-451a, and miR-605-5p in CSF exosomes of patients with early dementia and elderly dementia are different from those in normal individuals (Mckeever et al., 2018). Additionally, miR-212 and miR-132 levels are decreased in the neural derived plasma exosomes from patients with AD (Cha et al., 2019). Synaptosomal-associated-protein-25 and the receptor for advanced glycation end products are expected to become the new biomarkers for AD (Agliardi et al., 2019). Additionally, some researchers are considering PIWI-interacting RNAs (piRNAs) as candidate biomarkers for AD (Jain et al., 2019). Growth associated protein 43 (GAP43), neurogranin, synaptotagmins, Rab3A, and synaptosome associated protein 25 in neuronal-derived exosomes are expected to serve as blood biomarkers for AD and mild cognitive impairment. Those proteins when used in combination can detect preclinical AD 5–7 years before the onset of cognitive impairment (Jia et al., 2021).

Many experiments have demonstrated that exosomes and the cargoes they carry can improve the symptoms of AD, but the specific molecular mechanisms still need to be investigated further (Soares Martins et al., 2021b). The expression of miR-21

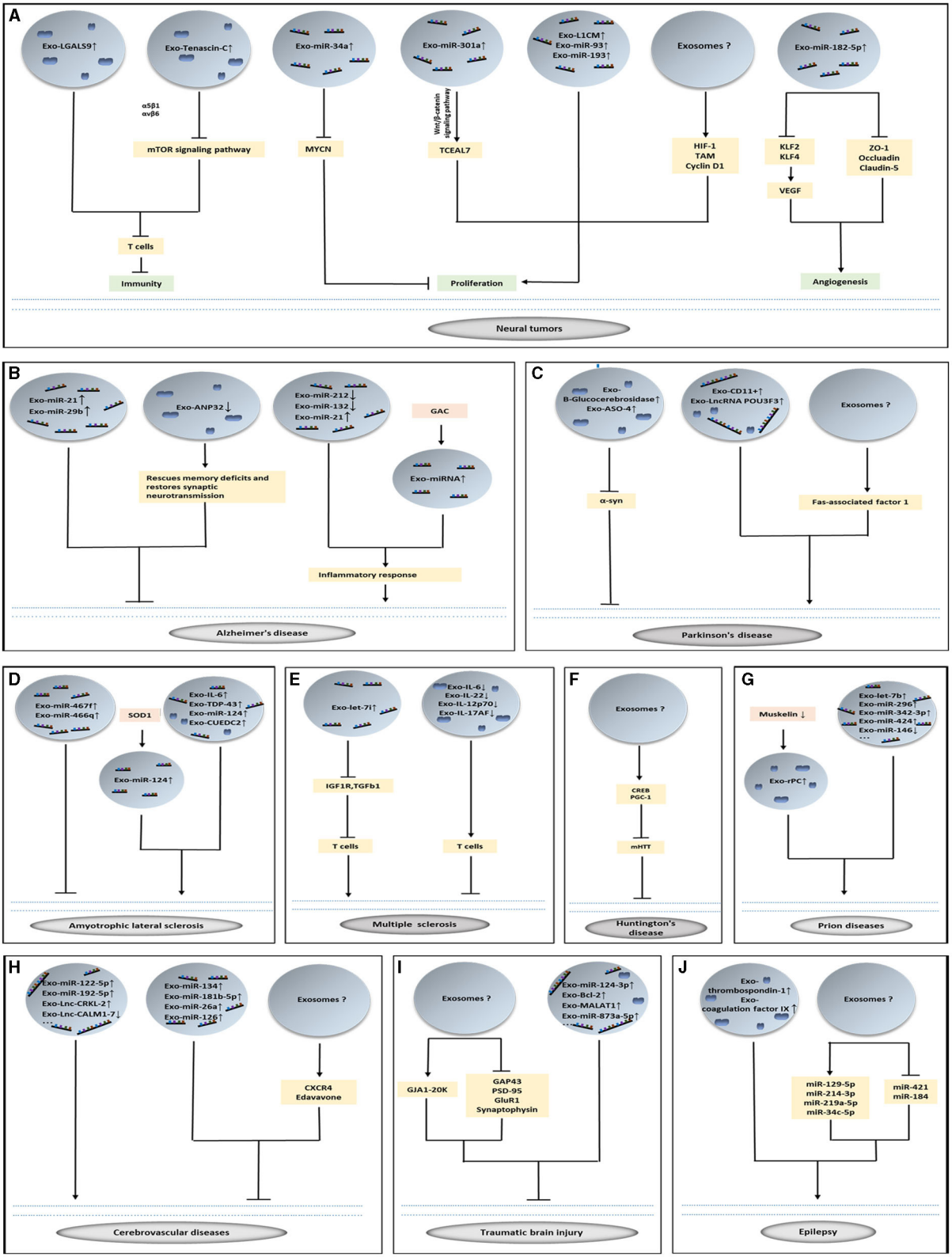

FIGURE 1 | The role of exosomes in brain diseases. **(A–J)** Exosomes loading with vital cargoes promote or inhibit the occurrence of disease and play a therapeutic role in nervous system diseases.

was increased in exosomes produced by hypoxia pretreated mesenchymal stem cells (MSCs) suggesting that miR-21 can restore cognitive deficits in mice and prevent pathological features of AD (Cui et al., 2018). Delivery of MSC-derived EVs (including exosomes and microvesicles) to the brain *via* the intranasal route of administration (a non-invasive modality) can result in the inhibition of microglial activation and increase the density of dendritic spines (Losurdo et al., 2020). The exosomes produced by hippocampal neural stem cells protect the synapses in the hippocampus against the toxicity of Aβ oligomers and restore their long-term potentiation (LTP) and memory functions, which is a new method for the treatment of AD (Kim et al., 2020). Interestingly, exosomes produced by mature hippocampal neurons do not have this therapeutic function (Micci et al., 2019). Researchers have developed a neutral sphingomyelinase 2 inhibitor, called PDDC, which inhibits exosome release and is associated with the pathologic processes of exosomes (Sala et al., 2020). The oral administration of P2X purinoceptor 7 inhibitors in AD mice led to a significant improvement in the working and environmental memory, which may be due to inhibition of the release of microglial exosomes (Ruan et al., 2020). Injection of exosomes carrying miR-29b into the cornu ammonis 1 (CA1) region of the brains of AD mice resulted in reduced Aβ and improved performance in spatial learning and memory (Jahangard et al., 2020). Exosomes carrying quercetin demonstrate superior alleviation of the AD symptoms of mice than free quercetin by inhibiting cyclin-dependent kinase 5-mediated tau phosphorylation and reducing the formation of insoluble neurofibrillary tangles (Qi et al., 2020) (**Figure 1B**).

EXOSOMES AND PARKINSON'S DISEASE

The prominent pathological changes in Parkinson's disease (PD) are the degenerative death of dopaminergic neurons (DA) in the substantia nigra, a significant decrease in striatal DA content, and the appearance of Lewy bodies in the cytoplasm of residual nigrostriatal neurons (Singh and Muqit, 2020). α-synis a soluble protein expressed presynaptically and perinuclearly in the central nervous system and is associated with the pathogenesis and dysfunction of PD, and is a major component of Lewy bodies (Pinnell et al., 2021). α-syn is secreted in an exosome-dependent or non-exosome-dependent manner (Sun et al., 2020; Pinnell et al., 2021).

There is substantial evidence suggesting a strong link between exosomes and the development of PD. New research has revealed that exosomes can contribute to the intercellular spread of Fas-associated factor 1, which leads to the death of adjacent dopamine neurons, and is closely related to the disease progression of PD (Park et al., 2020). More direct evidence suggests that the presence of α-syn oligomers in CD11b+ exosomes produced by microglia/macrophages in the CSF of patients with PD induces α-syn aggregation within neurons (Guo et al., 2020).

Non-coding RNAs and proteins are abnormally expressed in the serum and CSF of patients with PD. Exosomal lnc-MKRN2-42:1 in the plasma has been positively correlated with the MDS-UPDRS III score in patients with PD (Wang et al., 2019b). lncRNA POU3F3 and α-syn in plasma L1CAM exosomes of patients with PD are increased, and this increase is related to a decrease in β-Glucocerebrosidase, as well as the disease severity of PD. The discovery of these three molecules may shed light on the mechanism of the autophagic-lysosomal system involved in PD pathogenesis (Zou et al., 2020). A new study shows that the exosomes released from neurons in the serum can be used to distinguish PD from atypical parkinsonism. Meanwhile, the concentration of α-syn in exosomes shows an increase with the disease progression of PD. This method of differential diagnosis can precede the clinical presentation (Jiang et al., 2020).

Some new findings demonstrate that exosomes may be beneficial in the treatment of PD (Sun et al., 2020; Yang et al., 2021). Some researchers have designed shRNA minicircles to treat PD (Li et al., 2020a). These RNAs are delivered by RVG-exosomes to act on the dopaminergic neurons and halt α-syn aggregation. Their data demonstrate that this kind of therapy is a long-term treatment for PD. Among the several PD treatments, the ideal treatment should be minimally invasive and effective in the long-term. Consequently, exosomal transport genes and the blocking of α-syn hold clear potential in this regard (Izco et al., 2019). Blood-derived exosomes from healthy volunteers attenuated dopaminergic neuronal damage in the substantia nigra and striatum of PD mice, resulting in improved motor coordination (Sun et al., 2020). Intracerebroventricular injection of exosomes loaded with antisense oligonucleotides (ASO)-4 into PD mice significantly ameliorated α-syn aggregation while attenuating the degeneration of dopaminergic neurons, resulting in significant improvements in motor function (Yang et al., 2021) (**Figure 1C**).

EXOSOMES AND AMYOTROPHIC LATERAL SCLEROSIS

Amyotrophic lateral sclerosis (ALS) is a disease that causes muscle weakness and atrophy of the limbs, trunk, and chest after a motor neuron injury. The pathogenesis of ALS includes an imbalance of protein homeostasis in the nervous system, prion-like proliferation and propagation of abnormal proteins, mitochondrial dysfunction, and an inflammatory cascade response. Mutations in the SOD1 gene lead to abnormal folding of superoxide dismutase 1 (SOD1) mutants *in vivo* and the eventual formation of toxic aggregates is responsible for the pathogenesis of ALS. TDP (TDR DNA-binding protein)-43 is the pathological marker protein of ALS, which causes re-entry of mature motor neurons into the cell cycle and induces apoptosis (Andjus et al., 2020).

Exosomes are engaged in the neuroinflammation observed in ALS. Interleukin (IL)-6 levels in plasma exosomes of astrocytes have been shown to be increased in patients with ALS, and IL-6 is positively correlated with disease progression within 12 months (Chen et al., 2019b). Motor neurons transfected with SOD1 can secrete exosomes containing inflammatory miR-124, and their co-culture with microglia *in vitro* can cause microglia to transform into the M1 type (Pinto et al., 2017). Exosomes produced by MSCs suppress the microglial pro-inflammatory

phenotype in ALS mice *via* miR-467f and miR-466q (Giunti et al., 2021).

New studies have identified biomarkers in the exosomes of patients with ALS (Iguchi et al., 2016). TDP-43, a major component of ubiquitinated and hyper phosphorylated cytoplasmic aggregates observed in postmortem tissues of patients with ALS, is commonly found in the brains and is a major protein in the pathogenesis of ALS (De Boer et al., 2020; Suk and Rousseaux, 2020). The ratio of TAR DNA-binding protein-43 in the plasma exosomes demonstrated an increase with increasing follow-up time in patients with ALS (Chen P. C. et al., 2020). EVs, which contain exosomes, produced by the spinal cord tissue in ALS mouse models and ALS patients are rich in misfolded and non-native disulfide-cross-linked aggregates of SOD1, and the central nervous system-derived EVs in ALS mouse models are secreted by astrocytes and neurons, but not microglia (Silverman et al., 2019). The gene CUEDC2 in the CSF exosomes of patients serves as a biomarker for ALS (Otake et al., 2019). Proteomic analysis of CSF exosomes from ALS patients demonstrated a high level of novel INHAT repressor (NIR), while NIR is reduced in the nucleus of motor neurons (Hayashi et al., 2019) (**Figure 1D**).

Exosomes also play a role in the treatment of ALS. Exosomes derived from adipose-derived stem cells (ADSCs) could recover coupling efficiency, complex I activity, and mitochondrial membrane potential in an *in vitro* experiment related to ALS (Calabria et al., 2019). Repeated administration of ADSC-derived exosomes by intravenous and intranasal administration to ALS mice improved their motor performance, protected the lumbar motor neurons and neuromuscular junctions, and reduced microglial activation (Bonafede et al., 2020).

EXOSOMES AND MULTIPLE SCLEROSIS

Multiple sclerosis (MS) is a type of autoimmune demyelinating disease caused by the loss of tolerance to a self-protein (myelin antigen) (Jackle et al., 2020). Its main pathological manifestations are the disruption of BBB integrity and infiltration of peripheral immune cells into the central nervous system to form inflammatory lesions, which in turn initiate autoimmune mechanisms leading to myelin destruction and axonal damage, as well as motor, sensory, and autonomic dysfunction (Martinez and Peplow, 2020).

Proteins and nucleic acids are connected with the pathogenesis of MS. Let-7i in circulating exosomes inhibits insulin like growth factor 1 receptor (IGF1R) and transforming growth factor beta receptor 1, thus inhibiting the differentiation of regulatory T cells and promoting the development of MS (Kimura et al., 2018). Exosomes in the CSF of patients with MS may contain high levels of ceramide and acid phosphatase, which are associated with axonal neurological dysfunction (Pieragostino et al., 2018). Myelin basic protein, proteolipid protein, and myelin oligodendrocyte glycoprotein are expressed in the serum exosomes of patients. Accordingly, exosomes may enhance and/or maintain the antimyelin immune response in MS (Galazka et al., 2018). Several researchers have summarized the miRNAs that are abnormally up or down regulated in the exosomes present in the CSF or blood of patients with MS, and have indicated that further studies will investigate their usefulness as biomarkers for determining the prognosis and therapeutic effects of MS.

Recently, researchers have also explored the role of exosomes in the treatment of MS. Exosomes secreted by human MSCs [stimulated by interferon gamma (IFN-γ)] can alleviate demyelination in MS mice, decrease the levels of proinflammatory Th1 and Th17 cytokines (including IL-6, IL-12p70, IL-17AF, and IL-22), increase the levels of immunosuppressive cytokines, and upregulate CD4+CD25+FOXP3+ regulatory T cells in the spinal cord of MS mice. These findings make cell-free therapy for MS a distinct possibility (Riazifar et al., 2019). It has been shown that exosomes produced by human umbilical cord blood-derived MSCs can inhibit the proliferation of peripheral mononuclear blood cells (PBMCs) when co-cultured with PBMCs *in vitro* (Baharlooi et al., 2021) (**Figure 1E**).

EXOSOMES AND HUNTINGTON'S DISEASE

Huntington's disease (HD) is caused by a mis-expression of multiple CAG repeats (thus leading to Htt protein variation) on the *HTT* gene (He et al., 2021a).

The delivery of pathological proteins and miRNAs in different species is carried out through exosomes (a non-cell form), and these proteins and miRNAs trigger or inhibit HD-related behavior and pathology (Jeon et al., 2016). When fibroblasts from patients with HD were injected into the ventricles of newborn mice and induced pluripotent stem cells carrying CAG repeat sequences, researchers found the specific exosomal mHtt derived from the fibroblasts of patients with HD in these mice (Didiot et al., 2016). Meanwhile, mouse embryonic fibroblasts (MEFs) overexpressing exon 1 of the *HTT* gene showed that mHTT was found to be present in glutaminase 2-mediated exosomes when bound to exosomal structural proteins Alix and TSG101(Beatriz et al., 2021). Exosomal miRNAs have been found in HD, such as miR-22, miR-214, miR-150, miR-146a, and miR-125b (Wang J. K. T. et al., 2017; Reed et al., 2018). However, the mechanism of these miRNAs needs to be further investigated.

Exosomes can cross the blood-brain barrier and affect the nervous system to regulate mHtt aggregation, mitochondrial dysfunction, cell death and cell viability in HD (Lee et al., 2021). Exosomes secreted by ADSCs are considered critical for relieving HD phenotypes, which up-regulate phosphorylated CREB, PGC-1, and expedite non-apoptotic protein levels (Lee et al., 2016), notably alleviating mHtt aggregation in R6/2 mouse neurons (Deng et al., 2019; Lee et al., 2021). Thus, exosome-carried mHTT propagation is thought to be a novel mechanism for HD pathology, providing a potential therapeutic target for

alleviating this neurodegenerative disease (Ananbeh et al., 2021) (**Figure 1F**).

EXOSOMES AND PRION DISEASES

Prion diseases are a group of neurodegenerative diseases caused by mutated prions. Prions protein-infecting factors, virulent prions or infectious proteins, and the cellular prion protein (PrPc), a cell surface protein encoded by the PRNP gene, is most abundantly expressed in the nervous system, and its misfolded isomer PrP (PrPSc) is key to the development of prion diseases (Ryskalin et al., 2019; Lopez-Perez et al., 2020).

There is plenty of evidence that supports the intercellular transfer of prion proteins *via* exosomes (Cheng et al., 2018). Cellular prion protein (Prpc) regulates cell adhesion and signaling in the brain (Hartmann et al., 2017). Prpc binds to dynein, muskelin, and KIF5C in exosomes, while muskelin coordinates the bidirectional transport of Prpc between the extracellular space and lysosomes. Accumulation of Prpc on the neuronal surface and in secretory exosomes is increased in Muskelin knockout mice. When researchers injected pathogenic prions into Muskelin knockout mice, they found that the onset of prion disease was accelerated (Heisler et al., 2018). On performing miRNA sequencing of the exosomes released from prion-infected neurons, it was revealed that the expression of let-7b, let-7i, miR-21, miR-222, miR-29b, miR-342-3p, and miR-424 were upregulated, whereas miR-146 expression was downregulated (Bellingham et al., 2012; Boese et al., 2016). However, biomarkers for the diagnosis of prion diseases need to be explored further (**Figure 1G**).

EXOSOMES AND CEREBROVASCULAR DISEASES

Cerebrovascular diseases are divided into cerebral hemorrhagic diseases and cerebral ischemic diseases according to their pathogenesis. Stroke is a cerebrovascular disease that is characterized by a focal neurological deficit due to impaired brain blood circulation. Energy depletion and a hypoxic state after stroke can lead to neuronal damage, which activates resident glial cells and promotes the invasion of peripheral immune cells into the ischemic area of the brain; these immune cells can further necrotize neurons and exacerbate ischemic brain injury, and likewise promote neuronal repair, differentiation, and neural regeneration (Wang et al., 2020a; Xing and Bai, 2020).

The non-coding RNA in exosomes of stroke patients show significant changes. The level of lnc-CRKL-2 and lnc-NTRK3-4 in the serum exosomes of patients with acute minor stroke are increased, while those of RPS6KA2-AS1 and lnc-CALM1-7 are decreased (Xu et al., 2020). Studies have identified important roles for miRNAs in anti-angiogenic mechanisms and cerebrovascular disease (Xin et al., 2017). Some researchers sequenced the blood exosomes from patients with intracranial atherosclerotic disease (associated with high susceptibility to strokes) who did not respond to intensive medical management and found the specific expression of 10 miRNAs, including miR-122-5p, miR-192-5p, and miR-27b-3p. These miRNAs have the potential to be molecular markers for cerebrovascular diseases (Jiang et al., 2019).

Increasing evidence shows that exosomes can play a therapeutic role in stroke (Mirzaei H. et al., 2018; Jafarzadeh-Esfehani et al., 2020; Rahmani et al., 2020). ADEs can mitigate neuronal damage in mice by inhibiting the autophagy of neurons, suggesting that these exosomes can alleviate ischemic stroke (Pei et al., 2019). A similar study revealed that exosomes from MSCs can alleviate the inflammation of astrocytes stimulated by lipopolysaccharides (LPS) in mice, and exosomes can also mitigate LPS-induced abnormal calcium signaling and mitochondrial dysfunction (Xian et al., 2019). Exosomes from BMSCs with high expression of the chemokine receptor CXCR4 promote proliferation and angiogenesis of microvascular endothelial cells in rats with stroke and exert anti-apoptotic effects *via* the Wnt-3a/β-linked protein pathway (Li et al., 2020b).

Increasing number of miRNAs therapeutic targets have been discovered in exosomes. Researchers have attempted to treat stroke by improving the hypoxic state of neuronal cells, promoting vascular regeneration, and modulating the inflammatory response (Chamorro et al., 2021). A recent study has uncovered that exosomes derived from mouse brain vascular endothelial cells can deliver higher levels of miR-126 that can be used to treat mice stroke models with type 2 diabetes, and ease their cognitive function and inflammatory response (Rahmani et al., 2020). Additionally, endothelium-derived exosomes containing miR-126 enrichment are more therapeutically effective than exosomes without miR-126 enrichment (Venkat et al., 2019; Ueno et al., 2020). The exosomes produced by astrocytes carry miR-190b and inhibit the autophagy of nerve cells (from the mouse hippocampus) that are deprived of oxygen and glucose by targeting Atg7 (Pei et al., 2020). In an *in vitro* experiment, the targeting of transient receptor potential melastatin 7 resulted in ADSC-derived exosomal miR-181b-5p inducing an increase in the levels of hypoxia-inducible factor 1α and VEGF, while decreasing the protein expression of the tissue inhibitor of metalloproteinase 3, thereby improving angiogenesis (Yang et al., 2018). BMSCs secrete exosomes loaded with miR-134 that targets caspase-8 to prevent rat oligodendrocyte apoptosis *in vitro*, and it might be a new potential therapeutic target for the treatment of ischemic stroke (Xiao et al., 2018). Exosomes derived from human urine-derived stem cells carry miR-26a (Ling et al., 2020). Researchers injected them into the vein of mice stroke models and found that they can promote functional recovery of stroke by inhibiting histone deacetylase 6 *via* miR-26a (Ling et al., 2020). Secretion of exosomes in multipotent mesenchymal stromal cells transfected with miR-17-92 enhances axonal-myelin remodeling and electrophysiological recovery in mice when injected intravenously, probably due to the downregulation of PTEN by miR-17-92 leading to the activation of the PI3K/Akt/mTOR pathway (Xin et al., 2021) (**Figure 1H**).

A few studies have attempted to treat an animal stroke model using manually assembled exosomes. They constructed RVG-exosomes loaded with HMGBM1 (high-mobility group

box 1) -siRNA and delivered them into the ischemic brain of animal models by intravenous administration. This method could alleviate the inflammation associated with stroke (Kim et al., 2019). The use of macrophage-derived exosomes to deliver edaravone makes it easier to reach ischemic sites. Furthermore, the use of exosomes to deliver edaravone significantly increases its bioavailability, prolongs its half-life, and enhances its original therapeutic effects (Li F. et al., 2020).

EXOSOMES AND TRAUMATIC BRAIN INJURY

Traumatic brain injury (TBI), also referred to as brain injury or head injury, is a kind of brain tissue damage caused by trauma (Beard et al., 2020).

In recent years, the changes in the exosomal content during the development of disease in patients with TBI have been extensively studied. Brain-injury biomarkers were detected in the CSF exosomes of patients with TBI, such as αII-spectrin breakdown products (BDPs), glial fibrillary acidic protein and its BDPs, ubiquitin C-terminal hydrolase-L1, synaptophysin, and Alix (Manek et al., 2018). This study found that after the occurrence of TBI, changes in the levels of exosomes and their markers in the plasma or CSF does not just diagnose TBI but also stages patients with TBI (Beard et al., 2020; Peltz et al., 2020). In patients with mild TBI (mTBI), the concentration of neuron-derived exosomes in the plasma is reduced by 45% in the acute phase but not in the chronic phase, and the elevation of neuropathological proteins in these exosomes depicts phase-specificity (Peltz et al., 2020). This study suggested that exosomal proteins differed during different periods of TBI (Goetzl et al., 2019). An updated study on exosomes from 195 army veterans showed that compared to controls without TBI, the number of times the veteran was subjected to mTBI correlated with the NfL levels in plasma exosomes. An increase in the number of years since the most recent trauma was correlated with higher plasma exosomal NfL levels, and an increase in the number of years since the first trauma was also correlated with higher plasma exosomal NfL levels. Therefore, NfL level in plasma exosomes can act as a prognostic biomarker for remote symptoms after mTBI (Guedes et al., 2020).

Some exosomal miRNAs play a protective role in TBI (Zhang et al., 2021). Microglial exosomes with upregulated miR-124-3p can improve the neurodegeneration after repetitive mTBI. Microglia have a dual role in the inflammatory response after TBI, inducing a rapid shift from M1 to M2 microglia after the start of the recovery process or promoting microglia M2 polarization, which can suppress the brain inflammatory response and improve neuroprognosis. Microglia exhibited M1 pro-inflammatory phenotype and M2 anti-inflammatory phenotype. miRNA microarray analysis revealed that the expression level of miR-124-3p was most significantly increased. In the TBI mouse model, exosomal miR-124-3p levels gradually increased from the acute to chronic phase. The upregulated exosomal miR-124-3p derived from microglial cells improved the neurodegeneration after repetitive mTBI, promoted microglia anti-inflammatory M2 polarization, inhibited neuronal inflammation, and promoted axonal growth by targeting Rela, which is an inhibitory transcription factor for apolipoprotein E (ApoE) (Huang S. et al., 2018; Li et al., 2019). Exosomal miR-124-3p has been considered a potential treatment option for TBI, and various studies have explored its therapeutic effects (Ge et al., 2020). Recent studies proved that miR-21-5p containing exosomes secreted by neurons mitigate neuroinflammation after TBI by boosting microglial M2 polarization (Yin et al., 2020). miR-873a-5p carried by ADEs inhibits neuroinflammation by inhibiting the NF-κB signaling pathway of neurons after TBI (Long et al., 2020). Researchers co-cultured exosomes from microglia with artificially stretched neurons *in vitro*, while *in vivo* exosomes were administered into the tail vein of mice that had undergone fluid shock damage. The results showed that exosomes from the microglia were absorbed, the dendritic complexity of exosome-treated injured neurons was reduced *in vivo* and *in vitro*, motor function in mice was improved, and the protein levels of GAP43, PSD-95, GluR1, and synaptophysin were reduced in the neurons *in vitro*. However, exosomes produced by the stretch-injured microglia were found to impair motor coordination in TBI mice, which was largely associated with decreased miR-5121 in the exosomes (Zhao et al., 2021).

Meanwhile, the nucleic acids and proteins carried by exosomes can enter the BBB to exert therapeutic effects (Andjus et al., 2020). Damage to the BBB by TBI can be repaired by exosomes derived from human umbilical cord blood-derived endothelial colony-forming cells. These exosomes can also promote the migration of tissue-resident endothelial cells and reduce PTEN expression in endothelial cells incubated under hypoxic conditions, as well as increase AKT phosphorylation and tight junction protein expression (Gao et al., 2018). The exosomes of ADSCs contain MALAT1, a long-chain non-coding RNA, which is required for regulating the cell cycle, cell death, regenerative molecular pathways, and expression of snoRNAs, and is capable of significantly restoring the motor function in mice and reducing cortical brain damage (Patel et al., 2018). ADEs contain GJA1 (gap junction Alpha 1)-20k which they deliver to TBI neurons, thereby decreasing the apoptosis rate, increasing mitochondrial function, and alleviating neuron damage (Chen et al., 2019a). Swine models of TBI that were administered early single-dose exosomes shed from human MSCs showed reduced brain swelling, decreased lesion size, and improved BBB integrity (Williams et al., 2020).

Researchers have utilized modified exosomes to alleviate the symptoms of TBI. Exosomes incorporating plasmids expressing Bcl-2 and Bax shRNA (which can cause Bcl-2 overexpression and inhibit Bax expression) can reduce the levels of Mcl-1, XIAP, and survivin proteins in the brain and release cytochrome C from the mitochondria. Meanwhile, they can also reduce the damage to miniature excitatory postsynaptic current in mice and LTP after TBI, and enhance the motor and cognitive behavior of mice (Wang and Han, 2019) (**Figure 1I**).

In short, there is sufficient evidence to assert the therapeutic role of exosomes in stroke and TBI. However, before practical clinical applications, the mechanisms by which the exosomes participate in treatment and their exact contents need to be further elucidated. Multiple exosome-related human trials

related to the use of exosomes for transporting drugs in stroke models should be performed in the future.

EXOSOMES AND MENTAL DISEASE

Depression, schizophrenia (SCZ), bipolar disorder (BD), autism, etc. comprise the mental diseases discussed in this section.

Intravenous injection of blood exosomes from patients with major depression into the tail of healthy mice causes them to show depression-like behaviors. It has been shown that this effect is mediated by hsa-miR-139-5p (which decreases hippocampal neurogenesis) in the exosomes (Wei et al., 2020). Exosomal miR-207 derived from natural killer cells alleviates the symptoms of depression in mice by targeting the TLR4 interaction with leucine-rich repeats and decreasing NF-κB signaling of astrocytes (Li D. et al., 2020). In one study, brain-derived neurotrophic factor (BDNF) in the serum exosomes of the experimental group (patients with major depression) was significantly reduced compared to healthy controls; however, after 7 weeks of antidepressant treatment, BDNF in the serum exosomes of patients in the experimental group was not significantly different from that in healthy controls. Contrastingly, pro-BDNF was higher in the experimental group compared to the control group before treatment, but was not significantly different after treatment. This study suggests that BDNF may be an effective biomarker for the treatment of depression (Gelle et al., 2021). Compared to healthy controls, the number of L1CAM rich exosomes was increased in patients with major depressive disorder (MDD), and these patients had increased concentrations of insulin receptor substrate −1 (IRS-1) in L1CAM+ exosomes, which is associated with suicidality and anhedonia. Sex differences were observed in serine-312 phosphorylation of IRS-1 in L1CAM+ exosomes of patients with MDD. These findings may provide a basis for the effective treatment of MDD (Nasca et al., 2020).

The miRNA sequencing of plasma exosomes from BD patients and healthy individuals identified 13 abnormal miRNAs. Among them, the level of miR-484, miR-652-3p, and miR-142-3p were significantly decreased, while that of miR-185-5p was significantly increased (Ceylan et al., 2020). On transplanting exosomes secreted by human BMSCs into the lateral ventricles of BTBR mice, their autism-like behavior was reported to be attenuated. These exosomes were found to be capable of ameliorating the symptoms of autism spectrum disorder effectively by nasal injection (Perets et al., 2018). The Shank3B knockout model of autism was treated by intranasal administration of exosomes secreted from MSCs, and after 3 weeks of treatment, it was found that the mice had improved social behavior, increased vocalization, and reduced repetitive behaviors (Perets et al., 2020). This finding may be useful in patients with Shank3B-deficient autism (Perets et al., 2020). Additionally, miR-206, which suppresses the expression of BDNF mRNA and protein, and is used as a latent biomarker for SCZ, was found to be significantly up-regulated in the blood exosomes of patients with SCZ (Du et al., 2019).

Despite numerous studies on the mechanisms of these mental diseases, few have investigated the role of exosomes in depth.

EXOSOMES AND EPILEPSY

Epilepsy is a chronic disease in which sudden abnormal discharges of neurons in the brain lead to transient brain dysfunction (Perucca et al., 2020).

Researchers have found that 42 exosomal miRNAs are differentially expressed in patients with mesial temporal lobe epilepsy with hippocampal sclerosis. Among them, hsa-miR-129-5p,−214-3p,−219a-5p, and−34c-5p are increased, while hsa-miR-421 and−184 are decreased. These aberrantly expressed miRNAs can be used as potential targets for disease diagnosis and treatment (Chen S. D. et al., 2020; Huang et al., 2020). Measurement of proteins in serum exosomes from patients with epilepsy revealed that coagulation factor IX (F9) and thrombospondin-1 represent potential new markers for the diagnosis of epilepsy (Lin et al., 2020). This was the first time that exosomal proteins have been measured in epileptic patients, and conducting further exosomal studies in the field of epilepsy is essential (Lin et al., 2020) (**Figure 1J**).

EXOSOMES AND MENINGITIS

Meningitis, which is caused by multiple biological pathogenic factors invading the pia mater and spinal membranes, is considered a diffuse inflammation of the meninges. Long-term sequelae comprise the primary concern during the treatment of this disease.

Researchers have shown that proteins that take part in the immune response and exosome signal transduction are enriched in the CSF of patients with streptococcal meningitis, supporting the potential role of exosomes in the progression of meningitis. Exosomes can potentially provide a non-invasive and accurate method for detecting variations in the central nervous system after meningitis, and guide optimal treatment. However, little relevant research has been undertaken thus far in this area (Gomez-Baena et al., 2017).

FUTURE PERSPECTIVES

Exosomes are inextricably linked to the progression of nervous system disease, as they can convey pathological proteins to various neurons and accelerate the progression of disease. Exosomes are also involved in the self-rescue of neurons, and neurons can remove detrimental substances by the secretion of exosomes. Nevertheless, whether exosomes allow neurons to save themselves or transmit proteins to other neurons to resulting in more serious consequences, needs to be explored further.

Exosomes have been used as a diagnostic and treatment tool in animal experiments. Due to their ability to reflect the course of the disease, exosomes in the blood, CSF, urine, and saliva, which contain diverse biomarkers, are convenient and non-invasive tools for the early detection of diseases as well as

for developing therapeutic strategies. Recent studies have shown that Aβ42, T-tau, and P-T181-tau in blood exosomes can be used to diagnose AD and amnestic mild cognitive impairment (Jia et al., 2019). Exosomes can also serve as carriers for drug delivery, and some studies have modified their surface to improve their targeting ability, which enables better drug absorption compared to the traditional routes of administration. Compared to a direct injection of MSCs, exosomes can pass through the BBB and minimize immune rejection, leading to improved drug absorption and treatment in patients with AD or PD (Jin et al., 2021).

However, there are some problems that need to be conclusively resolved in this field. Although exosomes transporting drugs were found to be fully absorbed by the target cells *in vitro* and achieved the desired results, whether this effect is the same *in vivo*, and is not associated with any side-effects, is an issue that still needs further exploration. The artificial synthesis of exosome-like nanovesicles with the retention of the key exosome molecules can help avoid the disadvantages mentioned above and make better use of exosomes; moreover, this has become a research hotspot (Lu and Huang, 2020). Furthermore, the modification of the exosome surface to increase its targeting ability and the construction of a better exosome separation and purification system have also been attracting research interest recently. Furthermore, prior to using the cargo carried by exosomes as biomarkers for clinical diagnosis, we require more supporting data with higher accuracy. Beyond this, the relationship between the abnormal rise or decline of biomarkers and disease progression needs further study, and it is hoped that exosomes can provide a foundation for clinical staging of certain diseases.

AUTHOR CONTRIBUTIONS

LZ proposed and revised the manuscript. NZ and FH co-wrote this manuscript. All authors reviewed the manuscript and approved of the final version.

FUNDING

This work was supported by grants from the National Natural Science Foundation of China (No. 81903030), Outstanding Young Aid Program for Education Department of Hunan Province (Grant No. 18B274), the Natural Science Foundation of Hunan Province, China (Nos. S2021JJQNJJ1153, 2019JJ40249, and 2018JJ3455), Cooperative Education Program of Ministry of Education (No. 202002138007), and Key Project of Hunan Provincial Department of Education (20A427).

ACKNOWLEDGMENTS

We would like to express our gratitude to all those helped me during the writing of this manuscript. We apologize to all researchers whose relevant contributions were not cited due to space limitations.

REFERENCES

Agliardi, C., Guerini, F. R., Zanzottera, M., Bianchi, A., Nemni, R., and Clerici, M. (2019). SNAP-25 in serum is carried by exosomes of neuronal origin and is a potential biomarker of Alzheimer's disease. *Mol. Neurobiol.* 56, 5792–5798. doi: 10.1007/s12035-019-1501-x

Ananbeh, H., Vodicka, P., and Kupcova Skalnikova, H. (2021). Emerging roles of exosomes in Huntington's disease. *Int. J. Mol. Sci.* 22:4085. doi: 10.3390/ijms22084085

Andjus, P., Kosanović, M., Milićević, K., Gautam, M., Vainio, S. J., Jagečić, D., et al. (2020). Extracellular vesicles as innovative tool for diagnosis, regeneration and protection against neurological damage. *Int. J. Mol. Sci.* 21:6859. doi: 10.3390/ijms21186859

Azambuja, J. H., Ludwig, N., Yerneni, S. S., Braganhol, E., and Whiteside, T. L. (2020). Arginase-1+ exosomes from reprogrammed macrophages promote glioblastoma progression. *Int. J. Mol. Sci.* 21:3990. doi: 10.3390/ijms21113990

Azarmi, M., Maleki, H., Nikkam, N., and Malekinejad, H. (2020). Transcellular brain drug delivery: a review on recent advancements. *Int. J. Pharm.* 586:119582. doi: 10.1016/j.ijpharm.2020.119582

Baharlooi, H., Nouraei, Z., Azimi, M., Moghadasi, A. N., Tavassolifar, M. J., Moradi, B., et al. (2021). Umbilical cord mesenchymal stem cells as well as their released exosomes suppress proliferation of activated PBMCs in multiple sclerosis. *Scand. J. Immunol.* 93:e13013. doi: 10.1111/sji.13013

Baig, M. S., Roy, A., Rajpoot, S., Liu, D., Savai, R., Banerjee, S., et al. (2020). Tumor-derived exosomes in the regulation of macrophage polarization. *Inflammation Res.* 69, 435–451. doi: 10.1007/s00011-020-01318-0

Beard, K., Meaney, D. F., and Issadore, D. (2020). Clinical applications of extracellular vesicles in the diagnosis and treatment of traumatic brain injury. *J. Neurotrauma* 37, 2045–2056. doi: 10.1089/neu.2020.6990

Beatriz, M., Vilaca, R., and Lopes, C. (2021). Exosomes: innocent bystanders or critical culprits in neurodegenerative diseases. *Front. Cell Dev. Biol.* 9:635104. doi: 10.3389/fcell.2021.635104

Beeraka, N. M., Doreswamy, S. H., Sadhu, S. P., Srinivasan, A., Pragada, R. R., Madhunapantula, S. V., et al. (2020). The role of exosomes in stemness and neurodegenerative diseases-chemoresistant-cancer therapeutics and phytochemicals. *Int. J. Mol. Sci.* 21:6818. doi: 10.3390/ijms21186818

Bellingham, S. A., Coleman, B. M., and Hill, A. F. (2012). Small RNA deep sequencing reveals a distinct miRNA signature released in exosomes from prion-infected neuronal cells. *Nucleic Acids Res.* 40, 10937–10949. doi: 10.1093/nar/gks832

Boese, A. S., Saba, R., Campbell, K., Majer, A., Medina, S., Burton, L., et al. (2016). MicroRNA abundance is altered in synaptoneurosomes during prion disease. *Mol. Cell. Neurosci.* 71, 13–24. doi: 10.1016/j.mcn.2015.12.001

Bonafede, R., Turano, E., Scambi, I., Busato, A., Bontempi, P., Virla, F., et al. (2020). ASC-exosomes ameliorate the disease progression in SOD1(G93A) murine model underlining their potential therapeutic use in human ALS. *Int. J. Mol. Sci.* 21:3651. doi: 10.3390/ijms21103651

Budnik, V., Ruiz-Canada, C., and Wendler, F. (2016). Extracellular vesicles round off communication in the nervous system. *Nat. Rev. Neurosci.* 17, 160–172. doi: 10.1038/nrn.2015.29

Calabria, E., Scambi, I., Bonafede, R., Schiaffino, L., Peroni, D., Potrich, V., et al. (2019). ASCs-exosomes recover coupling efficiency and mitochondrial membrane potential in an *in vitro* model of ALS. *Front. Neurosci.* 13:1070. doi: 10.3389/fnins.2019.01070

Ceylan, D., Tufekci, K. U., Keskinoglu, P., Genc, S., and Ozerdem, A. (2020). Circulating exosomal microRNAs in bipolar disorder. *J. Affect. Disord.* 262, 99–107. doi: 10.1016/j.jad.2019.10.038

Cha, D. J., Mengel, D., Mustapic, M., Liu, W., Selkoe, D. J., Kapogiannis, D., et al. (2019). miR-212 and miR-132 are downregulated in neurally

derived plasma exosomes of Alzheimer's patients. *Front. Neurosci.* 13:1208. doi: 10.3389/fnins.2019.01208

Chamorro, A., Lo, E. H., Renu, A., Van Leyen, K., and Lyden, P. D. (2021). The future of neuroprotection in stroke. *J. Neurol. Neurosurg. Psychiatry* 92, 129–135. doi: 10.1136/jnnp-2020-324283

Chen, P. C., Wu, D., Hu, C. J., Chen, H. Y., Hsieh, Y. C., and Huang, C. C. (2020). Exosomal TAR DNA-binding protein-43 and neurofilaments in plasma of amyotrophic lateral sclerosis patients: a longitudinal follow-up study. *J. Neurol. Sci.* 418:117070. doi: 10.1016/j.jns.2020.117070

Chen, S. D., Pan, H. Y., Huang, J. B., Liu, X. P., Li, J. H., Ho, C. J., et al. (2020). Circulating MicroRNAs from serum exosomes may serve as a putative biomarker in the diagnosis and treatment of patients with focal cortical dysplasia. *Cells* 9:1867. doi: 10.3390/cells9081867

Chen, W., Zheng, P., Hong, T., Wang, Y., Liu, N., He, B., et al. (2019a). Astrocytes-derived exosomes induce neuronal recovery after traumatic brain injury via delivering gap junction alpha 1-20 k. *J. Tissue Eng. Regen. Med.* 14, 412–423. doi: 10.1002/term.3002

Chen, Y., Xia, K., Chen, L., and Fan, D. (2019b). Increased interleukin-6 levels in the astrocyte-derived exosomes of sporadic amyotrophic lateral sclerosis patients. *Front. Neurosci.* 13:574. doi: 10.3389/fnins.2019.00574

Cheng, L., Zhao, W., and Hill, A. F. (2018). Exosomes and their role in the intercellular trafficking of normal and disease associated prion proteins. *Mol. Aspects Med.* 60, 62–68. doi: 10.1016/j.mam.2017.11.011

Choi, Y., Kim, S. M., Heo, Y., Lee, G., Kang, J. Y., and Yoon, D. S. (2021). Nanoelectrical characterization of individual exosomes secreted by Abeta42-ingested cells using electrostatic force microscopy. *Nanotechnology* 32:025705. doi: 10.1088/1361-6528/abba58

Cui, G. H., Wu, J., Mou, F. F., Xie, W. H., Wang, F. B., Wang, Q. L., et al. (2018). Exosomes derived from hypoxia-preconditioned mesenchymal stromal cells ameliorate cognitive decline by rescuing synaptic dysfunction and regulating inflammatory responses in APP/PS1 mice. *FASEB J.* 32, 654–668. doi: 10.1096/fj.201700600R

Dai, X., Liao, K., Zhuang, Z., Chen, B., Zhou, Z., Zhou, S., et al. (2019). AHIF promotes glioblastoma progression and radioresistance via exosomes. *Int. J. Oncol.* 54, 261–270. doi: 10.3892/ijo.2018.4621

De Boer, E. M. J., Orie, V. K., Williams, T., Baker, M. R., De Oliveira, H. M., Polvikoski, T., et al. (2020). TDP-43 proteinopathies: a new wave of neurodegenerative diseases. *J. Neurol. Neurosurg. Psychiatry.* 92, 86–95. doi: 10.1136/jnnp-2020-322983

De Leo, A., Ugolini, A., and Veglia, F. (2020). Myeloid cells in glioblastoma microenvironment. *Cells* 10:18. doi: 10.3390/cells10010018

Deng, S., Zhou, X., Ge, Z., Song, Y., Wang, H., Liu, X., et al. (2019). Exosomes from adipose-derived mesenchymal stem cells ameliorate cardiac damage after myocardial infarction by activating S1P/SK1/S1PR1 signaling and promoting macrophage M2 polarization. *Int. J. Biochem. Cell Biol.* 114:105564. doi: 10.1016/j.biocel.2019.105564

Didiot, M. C., Hall, L. M., Coles, A. H., Haraszti, R. A., Godinho, B. M., Chase, K., et al. (2016). Exosome-mediated delivery of hydrophobically modified siRNA for Huntingtin mRNA silencing. *Mol. Ther.* 24, 1836–1847. doi: 10.1038/mt.2016.126

Du, Y., Yu, Y., Hu, Y., Li, X. W., Wei, Z. X., Pan, R. Y., et al. (2019). Genome-wide, integrative analysis implicates exosome-derived microRNA dysregulation in schizophrenia. *Schizophr. Bull.* 45, 1257–1266. doi: 10.1093/schbul/sby191

Fernandes, A., Ribeiro, A. R., Monteiro, M., Garcia, G., Vaz, A. R., and Brites, D. (2018). Secretome from SH-SY5Y APPSwe cells trigger time-dependent CHME3 microglia activation phenotypes, ultimately leading to miR-21 exosome shuttling. *Biochimie* 155, 67–82. doi: 10.1016/j.biochi.2018.05.015

Galazka, G., Mycko, M. P., Selmaj, I., Raine, C. S., and Selmaj, K. W. (2018). Multiple sclerosis: serum-derived exosomes express myelin proteins. *Mult. Scler.* 24, 449–458. doi: 10.1177/1352458517696597

Gao, G., Zhao, S., Xia, X., Li, C., Li, C., Ji, C., et al. (2019). Glutaminase C regulates microglial activation and pro-inflammatory exosome release: relevance to the pathogenesis of Alzheimer's disease. *Front. Cell. Neurosci.* 13:264. doi: 10.3389/fncel.2019.00264

Gao, W., Li, F., Liu, L., Xu, X., Zhang, B., Wu, Y., et al. (2018). Endothelial colony-forming cell-derived exosomes restore blood-brain barrier continuity in mice subjected to traumatic brain injury. *Exp. Neurol.* 307, 99–108. doi: 10.1016/j.expneurol.2018.06.001

Ge, X., Guo, M., Hu, T., Li, W., Huang, S., Yin, Z., et al. (2020). Increased microglial exosomal miR-124-3p alleviates neurodegeneration and improves cognitive outcome after rmTBI. *Mol. Ther.* 28, 503–522. doi: 10.1016/j.ymthe.2019.11.017

Gelle, T., Samey, R. A., Plansont, B., Bessette, B., Jauberteau-Marchan, M. O., Lalloue, F., et al. (2021). BDNF and pro-BDNF in serum and exosomes in major depression: evolution after antidepressant treatment. *Prog. Neuropsychopharmacol. Biol. Psychiatry* 109:110229. doi: 10.1016/j.pnpbp.2020.110229

Giunti, D., Marini, C., Parodi, B., Usai, C., Milanese, M., Bonanno, G., et al. (2021). Role of miRNAs shuttled by mesenchymal stem cell-derived small extracellular vesicles in modulating neuroinflammation. *Sci. Rep.* 11:1740. doi: 10.1038/s41598-021-81039-4

Goetzl, E. J., Elahi, F. M., Mustapic, M., Kapogiannis, D., Pryhoda, M., Gilmore, A., et al. (2019). Altered levels of plasma neuron-derived exosomes and their cargo proteins characterize acute and chronic mild traumatic brain injury. *FASEB J.* 33, 5082–5088. doi: 10.1096/fj.201802319R

Goetzl, E. J., Schwartz, J. B., Abner, E. L., Jicha, G. A., and Kapogiannis, D. (2018). High complement levels in astrocyte-derived exosomes of Alzheimer disease. *Ann. Neurol.* 83, 544–552. doi: 10.1002/ana.25172

Gomez-Baena, G., Bennett, R. J., Martinez-Rodriguez, C., Wnek, M., Laing, G., Hickey, G., et al. (2017). Quantitative proteomics of cerebrospinal fluid in paediatric pneumococcal meningitis. *Sci. Rep.* 7:7042. doi: 10.1038/s41598-017-07127-6

Guedes, V. A., Kenney, K., Shahim, P., Qu, B. X., Lai, C., Devoto, C., et al. (2020). Exosomal neurofilament light: a prognostic biomarker for remote symptoms after mild traumatic brain injury? *Neurology* 94, e2412–e2423. doi: 10.1212/WNL.0000000000009577

Guo, M., Wang, J., Zhao, Y., Feng, Y., Han, S., Dong, Q., et al. (2020). Microglial exosomes facilitate alpha-synuclein transmission in Parkinson's disease. *Brain* 143, 1476–1497. doi: 10.1093/brain/awaa090

Hartmann, A., Muth, C., Dabrowski, O., Krasemann, S., and Glatzel, M. (2017). Exosomes and the prion protein: more than one truth. *Front. Neurosci.* 11:194. doi: 10.3389/fnins.2017.00194

Hayashi, N., Doi, H., Kurata, Y., Kagawa, H., Atobe, Y., Funakoshi, K., et al. (2019). Proteomic analysis of exosome-enriched fractions derived from cerebrospinal fluid of amyotrophic lateral sclerosis patients. *Neurosci. Res.* 160, 43–49. doi: 10.1016/j.neures.2019.10.010

He, M., Zhang, H. N., Tang, Z. C., and Gao, S. G. (2021a). Diagnostic and therapeutic potential of exosomal microRNAs for neurodegenerative diseases. *Neural Plast.* 2021:8884642. doi: 10.1155/2021/8884642

He, X., Kuang, G., Wu, Y., and Ou, C. (2021b). Emerging roles of exosomal miRNAs in diabetes mellitus. *Clin. Transl. Med.* 11:e468. doi: 10.1002/ctm2.468

Heisler, F. F., Pechmann, Y., Wieser, I., Altmeppen, H. C., Veenendaal, L., Muhia, M., et al. (2018). Muskelin coordinates PrP(C) lysosome versus exosome targeting and impacts prion disease progression. *Neuron* 99, 1155–1169 e1159. doi: 10.1016/j.neuron.2018.08.010

Hill, A. F. (2019). Extracellular vesicles and neurodegenerative diseases. *J. Neurosci.* 39, 9269–9273. doi: 10.1523/jneurosci.0147-18.2019

Huang, K., Fang, C., Yi, K., Liu, X., Qi, H., Tan, Y., et al. (2018). The role of PTRF/Cavin1 as a biomarker in both glioma and serum exosomes. *Theranostics* 8, 1540–1557. doi: 10.7150/thno.22952

Huang, L. G., Luo, Y. H., Xu, J. W., and Lu, Q. C. (2020). Plasma exosomal MiRNAs expression profile in mesial temporal lobe epilepsy with hippocampal sclerosis: case-control study and analysis of potential functions. *Front. Mol. Neurosci.* 13:584828. doi: 10.3389/fnmol.2020.584828

Huang, S., Ge, X., Yu, J., Han, Z., Yin, Z., Li, Y., et al. (2018). Increased miR-124-3p in microglial exosomes following traumatic brain injury inhibits neuronal inflammation and contributes to neurite outgrowth via their transfer into neurons. *FASEB J.* 32, 512–528. doi: 10.1096/fj.201700673R

Iguchi, Y., Eid, L., Parent, M., Soucy, G., Bareil, C., Riku, Y., et al. (2016). Exosome secretion is a key pathway for clearance of pathological TDP-43. *Brain* 139(Pt 12), 3187–3201. doi: 10.1093/brain/aww237

Izco, M., Blesa, J., Schleef, M., Schmeer, M., Porcari, R., Al-Shawi, R., et al. (2019). Systemic exosomal delivery of shRNA minicircles prevents parkinsonian pathology. *Mol. Ther.* 27, 2111–2122. doi: 10.1016/j.ymthe.2019.08.010

Jackle, K., Zeis, T., Schaeren-Wiemers, N., Junker, A., Van Der Meer, F., Kramann, N., et al. (2020). Molecular signature of slowly expanding lesions in progressive multiple sclerosis. *Brain* 143, 2073–2088. doi: 10.1093/brain/awaa158

Jafari, D., Shajari, S., Jafari, R., Mardi, N., Gomari, H., Ganji, F., et al. (2020). Designer exosomes: a new platform for biotechnology therapeutics. *BioDrugs* 34, 567–586. doi: 10.1007/s40259-020-00434-x

Jafarzadeh-Esfehani, R., Soudyab, M., Parizadeh, S. M., Jaripoor, M. E., Nejad, P. S., Shariati, M., et al. (2020). Circulating exosomes and their role in stroke. *Curr. Drug Targets* 21, 89–95. doi: 10.2174/1389450120666190821153557

Jahangard, Y., Monfared, H., Moradi, A., Zare, M., Mirnajafi-Zadeh, J., and Mowla, S. J. (2020). Therapeutic effects of transplanted exosomes containing miR-29b to a rat model of Alzheimer's disease. *Front. Neurosci.* 14:564. doi: 10.3389/fnins.2020.00564

Jain, G., Stuendl, A., Rao, P., Berulava, T., Pena Centeno, T., Kaurani, L., et al. (2019). A combined miRNA-piRNA signature to detect Alzheimer's disease. *Transl. Psychiatry* 9:250. doi: 10.1038/s41398-019-0579-2

Jeon, I., Cicchetti, F., Cisbani, G., Lee, S., Li, E., Bae, J., et al. (2016). Human-to-mouse prion-like propagation of mutant huntingtin protein. *Acta Neuropathol.* 132, 577–592. doi: 10.1007/s00401-016-1582-9

Jia, L., Qiu, Q., Zhang, H., Chu, L., Du, Y., Zhang, J., et al. (2019). Concordance between the assessment of Abeta42, T-tau, and P-T181-tau in peripheral blood neuronal-derived exosomes and cerebrospinal fluid. *Alzheimers. Dement.* 15, 1071–1080. doi: 10.1016/j.jalz.2019.05.002

Jia, L., Zhu, M., Kong, C., Pang, Y., Zhang, H., Qiu, Q., et al. (2021). Blood neuro-exosomal synaptic proteins predict Alzheimer's disease at the asymptomatic stage. *Alzheimers. Dement.* 17, 49–60. doi: 10.1002/alz.12166

Jiang, C., Hopfner, F., Katsikoudi, A., Hein, R., Catli, C., Evetts, S., et al. (2020). Serum neuronal exosomes predict and differentiate Parkinson's disease from atypical parkinsonism. *J Neurol. Neurosurg. Psychiatry* 91, 720–729. doi: 10.1136/jnnp-2019-322588

Jiang, H., Toscano, J. F., Song, S. S., Schlick, K. H., Dumitrascu, O. M., Pan, J., et al. (2019). Differential expression of circulating exosomal microRNAs in refractory intracranial atherosclerosis associated with antiangiogenesis. *Sci. Rep.* 9:19429. doi: 10.1038/s41598-019-54542-y

Jin, Q., Wu, P., Zhou, X., Qian, H., and Xu, W. (2021). Extracellular vesicles: novel roles in neurological disorders. *Stem Cells Int.* 2021:6640836. doi: 10.1155/2021/6640836

Kim, E., Otgontenger, U., Jamsranjav, A., and Kim, S. S. (2020). Deleterious alteration of glia in the brain of Alzheimer's disease. *Int. J. Mol. Sci.* 21:6676. doi: 10.3390/ijms21186676

Kim, M., Kim, G., Hwang, D. W., and Lee, M. (2019). Delivery of high mobility group box-1 siRNA using brain-targeting exosomes for ischemic stroke therapy. *J. Biomed. Nanotechnol.* 15, 2401–2412. doi: 10.1166/jbn.2019.2866

Kimura, K., Hohjoh, H., Fukuoka, M., Sato, W., Oki, S., Tomi, C., et al. (2018). Circulating exosomes suppress the induction of regulatory T cells via let-7i in multiple sclerosis. *Nat. Commun.* 9:17. doi: 10.1038/s41467-017-02406-2

Leblanc, P., Arellano-Anaya, Z. E., Bernard, E., Gallay, L., Provansal, M., Lehmann, S., et al. (2017). Isolation of exosomes and microvesicles from cell culture systems to study prion transmission. *Methods Mol. Biol.* 1545, 153–176. doi: 10.1007/978-1-4939-6728-5_11

Lee, M., Im, W., and Kim, M. (2021). Exosomes as a potential messenger unit during heterochronic parabiosis for amelioration of Huntington's disease. *Neurobiol. Dis.* 155:105374. doi: 10.1016/j.nbd.2021.105374

Lee, M., Liu, T., Im, W., and Kim, M. (2016). Exosomes from adipose-derived stem cells ameliorate phenotype of Huntington's disease *in vitro* model. *Eur. J. Neurosci.* 44, 2114–2119. doi: 10.1111/ejn.13275

Li, B., Liu, J., Gu, G., Han, X., Zhang, Q., and Zhang, W. (2020). Impact of neural stem cell-derived extracellular vesicles on mitochondrial dysfunction, sirtuin 1 level, and synaptic deficits in Alzheimer's disease. *J. Neurochem.* 154, 502–518. doi: 10.1111/jnc.15001

Li, D., Huang, S., Yin, Z., Zhu, J., Ge, X., Han, Z., et al. (2019). Increases in miR-124-3p in microglial exosomes confer neuroprotective effects by targeting FIP200-mediated neuronal autophagy following traumatic brain injury. *Neurochem. Res.* 44, 1903–1923. doi: 10.1007/s11064-019-02825-1

Li, D., Wang, Y., Jin, X., Hu, D., Xia, C., Xu, H., et al. (2020). NK cell-derived exosomes carry miR-207 and alleviate depression-like symptoms in mice. *J. Neuroinflammation* 17:126. doi: 10.1186/s12974-020-01787-4

Li, F., Zhao, L., Shi, Y., and Liang, J. (2020). Edaravone-loaded macrophage-derived exosomes enhance neuroprotection in the rat permanent middle cerebral artery occlusion model of stroke. *Mol. Pharm.* 17, 3192–3201. doi: 10.1021/acs.molpharmaceut.0c00245

Li, J., Yuan, H., Xu, H., Zhao, H., and Xiong, N. (2020). Hypoxic cancer-secreted exosomal miR-182-5p promotes glioblastoma angiogenesis by targeting kruppel-like factor 2 and 4. *Mol. Cancer Res.* 18, 1218–1231. doi: 10.1158/1541-7786.MCR-19-0725

Li, X., Zhang, J., Zhang, X., and Dong, M. (2020a). Puerarin suppresses MPP(+)/MPTP-induced oxidative stress through an Nrf2-dependent mechanism. *Food Chem Toxicol.* 144:111644. doi: 10.1016/j.fct.2020.111644

Li, X., Zhang, Y., Wang, Y., Zhao, D., Sun, C., Zhou, S., et al. (2020b). Exosomes derived from CXCR4-overexpressing BMSC promoted activation of microvascular endothelial cells in cerebral ischemia/reperfusion injury. *Neural Plast.* 2020:8814239. doi: 10.1155/2020/8814239

Lin, Z., Gu, Y., Zhou, R., Wang, M., Guo, Y., Chen, Y., et al. (2020). Serum exosomal proteins F9 and TSP-1 as potential diagnostic biomarkers for newly diagnosed epilepsy. *Front. Neurosci.* 14:737. doi: 10.3389/fnins.2020.00737

Ling, X., Zhang, G., Xia, Y., Zhu, Q., Zhang, J., Li, Q., et al. (2020). Exosomes from human urine-derived stem cells enhanced neurogenesis via miR-26a/HDAC6 axis after ischaemic stroke. *J. Cell. Mol. Med.* 24, 640–654. doi: 10.1111/jcmm.14774

Long, X., Yao, X., Jiang, Q., Yang, Y., He, X., Tian, W., et al. (2020). Astrocyte-derived exosomes enriched with miR-873a-5p inhibit neuroinflammation via microglia phenotype modulation after traumatic brain injury. *J. Neuroinflammation* 17:89. doi: 10.1186/s12974-020-01761-0

Lopez-Perez, O., Badiola, J. J., Bolea, R., Ferrer, I., Llorens, F., and Martin-Burriel, I. (2020). An update on autophagy in prion diseases. *Front Bioeng Biotechnol.* 8:975. doi: 10.3389/fbioe.2020.00975

Losurdo, M., Pedrazzoli, M., D'agostino, C., Elia, C. A., Massenzio, F., Lonati, E., et al. (2020). Intranasal delivery of mesenchymal stem cell-derived extracellular vesicles exerts immunomodulatory and neuroprotective effects in a 3xTg model of Alzheimer's disease. *Stem Cells Transl. Med.* 9, 1068–1084. doi: 10.1002/sctm.19-0327

Lu, M., and Huang, Y. (2020). Bioinspired exosome-like therapeutics and delivery nanoplatforms. *Biomaterials* 242:119925. doi: 10.1016/j.biomaterials.2020.119925

Luciunaite, A., Mcmanus, R. M., Jankunec, M., Racz, I., Dansokho, C., Dalgediene, I., et al. (2020). Soluble Abeta oligomers and protofibrils induce NLRP3 inflammasome activation in microglia. *J. Neurochem.* 155, 650–661. doi: 10.1111/jnc.14945

Manek, R., Moghieb, A., Yang, Z., Kumar, D., Kobeissy, F., Sarkis, G. A., et al. (2018). Correction to: protein biomarkers and neuroproteomics characterization of microvesicles/exosomes from human cerebrospinal fluid following traumatic brain injury. *Mol. Neurobiol.* 55:6129. doi: 10.1007/s12035-018-0909-z

Martinez, B., and Peplow, P. V. (2020). MicroRNAs as disease progression biomarkers and therapeutic targets in experimental autoimmune encephalomyelitis model of multiple sclerosis. *Neural Regen Res.* 15, 1831–1837. doi: 10.4103/1673-5374.280307

Mckeever, P. M., Schneider, R., Taghdiri, F., Weichert, A., Multani, N., Brown, R. A., et al. (2018). MicroRNA expression levels are altered in the cerebrospinal fluid of patients with young-onset Alzheimer's disease. *Mol. Neurobiol.* 55, 8826–8841. doi: 10.1007/s12035-018-1032-x

Micci, M. A., Krishnan, B., Bishop, E., Zhang, W. R., Guptarak, J., Grant, A., et al. (2019). Hippocampal stem cells promotes synaptic resistance to the dysfunctional impact of amyloid beta oligomers via secreted exosomes. *Mol. Neurodegener.* 14:25. doi: 10.1186/s13024-019-0322-8

Mirzaei, H., Momeni, F., Saadatpour, L., Sahebkar, A., Goodarzi, M., Masoudifar, A., et al. (2018). MicroRNA: relevance to stroke diagnosis, prognosis, and therapy. *J. Cell. Physiol.* 233, 856–865. doi: 10.1002/jcp.25787

Mirzaei, R., Sarkar, S., Dzikowski, L., Rawji, K. S., Khan, L., Faissner, A., et al. (2018). Brain tumor-initiating cells export tenascin-C associated with exosomes to suppress T cell activity. *Oncoimmunology* 7:e1478647. doi: 10.1080/2162402X.2018.1478647

Munoz, J. L., Walker, N. D., Mareedu, S., Pamarthi, S. H., Sinha, G., Greco, S. J., et al. (2019). Cycling quiescence in temozolomide resistant glioblastoma cells is partly explained by microRNA-93 and−193-mediated decrease of cyclin D. *Front. Pharmacol.* 10:134. doi: 10.3389/fphar.2019.00134

Nasca, C., Dobbin, J., Bigio, B., Watson, K., De Angelis, P., Kautz, M., et al. (2020). Insulin receptor substrate in brain-enriched exosomes in subjects with major

depression: on the path of creation of biosignatures of central insulin resistance. *Mol. Psychiatry*. doi: 10.1038/s41380-020-0804-7. [Epub ahead of print].

Nieland, L., Morsett, L. M., Broekman, M. L. D., Breakefield, X. O., and Abels, E. R. (2021). Extracellular vesicle-mediated bilateral communication between glioblastoma and astrocytes. *Trends Neurosci.* 44, 215–226. doi: 10.1016/j.tins.2020.10.014

Otake, K., Kamiguchi, H., and Hirozane, Y. (2019). Identification of biomarkers for amyotrophic lateral sclerosis by comprehensive analysis of exosomal mRNAs in human cerebrospinal fluid. *BMC Med. Genomics*. 12:7. doi: 10.1186/s12920-019-0473-z

Ou, A., Yung, W. K. A., and Majd, N. (2020). Molecular mechanisms of treatment resistance in glioblastoma. *Int. J. Mol. Sci*. 22. doi: 10.3390/ijms22010351

Pace, K. R., Dutt, R., and Galileo, D. S. (2019). Exosomal L1CAM stimulates glioblastoma cell motility, proliferation, and invasiveness. *Int. J. Mol. Sci.* 20:3982. doi: 10.3390/ijms20163982

Pan, J., He, R., Huo, Q., Shi, Y., and Zhao, L. (2020). Brain microvascular endothelial cell derived exosomes potently ameliorate cognitive dysfunction by enhancing the clearance of abeta through up-regulation of P-gp in mouse model of AD. *Neurochem. Res*. 45, 2161–2172. doi: 10.1007/s11064-020-03076-1

Park, G., Kim, B. S., and Kim, E. (2020). A novel function of FAF1, which induces dopaminergic neuronal death through cell-to-cell transmission. *Cell Commun. Signal*. 18:133. doi: 10.1186/s12964-020-00632-8

Patel, N. A., Moss, L. D., Lee, J. Y., Tajiri, N., Acosta, S., Hudson, C., et al. (2018). Long noncoding RNA MALAT1 in exosomes drives regenerative function and modulates inflammation-linked networks following traumatic brain injury. *J. Neuroinflammation* 15:204. doi: 10.1186/s12974-018-1240-3

Pei, X., Li, Y., Zhu, L., and Zhou, Z. (2019). Astrocyte-derived exosomes suppress autophagy and ameliorate neuronal damage in experimental ischemic stroke. *Exp. Cell Res*. 382:111474. doi: 10.1016/j.yexcr.2019.06.019

Pei, X., Li, Y., Zhu, L., and Zhou, Z. (2020). Astrocyte-derived exosomes transfer miR-190b to inhibit oxygen and glucose deprivation-induced autophagy and neuronal apoptosis. *Cell Cycle* 19, 906–917. doi: 10.1080/15384101.2020.1731649

Peltz, C. B., Kenney, K., Gill, J., Diaz-Arrastia, R., Gardner, R. C., and Yaffe, K. (2020). Blood biomarkers of traumatic brain injury and cognitive impairment in older veterans. *Neurology* 95:e1126–e1133. doi: 10.1212/WNL.0000000000010087

Perets, N., Hertz, S., London, M., and Offen, D. (2018). Intranasal administration of exosomes derived from mesenchymal stem cells ameliorates autistic-like behaviors of BTBR mice. *Mol. Autism* 9:57. doi: 10.1186/s13229-018-0240-6

Perets, N., Oron, O., Herman, S., Elliott, E., and Offen, D. (2020). Exosomes derived from mesenchymal stem cells improved core symptoms of genetically modified mouse model of autism Shank3B. *Mol. Autism* 11:65. doi: 10.1186/s13229-020-00366-x

Perez-Gonzalez, R., Kim, Y., Miller, C., Pacheco-Quinto, J., Eckman, E. A., and Levy, E. (2020). Extracellular vesicles: where the amyloid precursor protein carboxyl-terminal fragments accumulate and amyloid-beta oligomerizes. *FASEB J*. 34, 12922–12931. doi: 10.1096/fj.202000823R

Perucca, P., Bahlo, M., and Berkovic, S. F. (2020). The Genetics of Epilepsy. *Annu. Rev. Genomics Hum. Genet*. 21, 205–230. doi: 10.1146/annurev-genom-120219-074937

Pieragostino, D., Cicalini, I., Lanuti, P., Ercolino, E., Di Ioia, M., Zucchelli, M., et al. (2018). Enhanced release of acid sphingomyelinase-enriched exosomes generates a lipidomics signature in CSF of Multiple Sclerosis patients. *Sci. Rep*. 8:3071. doi: 10.1038/s41598-018-21497-5

Pinnell, J. R., Cui, M., and Tieu, K. (2021). Exosomes in Parkinson disease. *J. Neurochem*. 157, 413–428. doi: 10.1111/jnc.15288

Pinto, S., Cunha, C., Barbosa, M., Vaz, A. R., and Brites, D. (2017). Exosomes from NSC-34 cells transfected with hSOD1-G93A are enriched in miR-124 and drive alterations in microglia phenotype. *Front. Neurosci*. 11:273. doi: 10.3389/fnins.2017.00273

Podvin, S., Jones, A., Liu, Q., Aulston, B., Ransom, L., Ames, J., et al. (2020). Dysregulation of exosome cargo by mutant tau expressed in human-induced pluripotent stem cell (iPSC) neurons revealed by proteomics analyses. *Mol. Cell. Proteomics*. 19, 1017–1034. doi: 10.1074/mcp.RA120.002079

Qi, Y., Guo, L., Jiang, Y., Shi, Y., Sui, H., and Zhao, L. (2020). Brain delivery of quercetin-loaded exosomes improved cognitive function in AD mice by inhibiting phosphorylated tau-mediated neurofibrillary tangles. *Drug Deliv*. 27, 745–755. doi: 10.1080/10717544.2020.1762262

Rahmani, A., Saleki, K., Javanmehr, N., Khodaparast, J., Saadat, P., and Nouri, H. R. (2020). Mesenchymal stem cell-derived extracellular vesicle-based therapies protect against coupled degeneration of the central nervous and vascular systems in stroke. *Ageing Res. Rev*. 62:101106. doi: 10.1016/j.arr.2020.101106

Ratajczak, M. Z., and Ratajczak, J. (2020). Extracellular microvesicles/exosomes: discovery, disbelief, acceptance, and the future? *Leukemia* 34, 3126–3135. doi: 10.1038/s41375-020-01041-z

Reed, E. R., Latourelle, J. C., Bockholt, J. H., Bregu, J., Smock, J., Paulsen, J. S., et al. (2018). MicroRNAs in CSF as prodromal biomarkers for Huntington disease in the PREDICT-HD study. *Neurology* 90:e264–e272. doi: 10.1212/WNL.0000000000004844

Riazifar, M., Mohammadi, M. R., Pone, E. J., Yeri, A., Lasser, C., Segaliny, A. I., et al. (2019). Stem cell-derived exosomes as nanotherapeutics for autoimmune and neurodegenerative disorders. *ACS Nano* 13, 6670–6688. doi: 10.1021/acsnano.9b01004

Ruan, Z., Delpech, J. C., Venkatesan Kalavai, S., Van Enoo, A. A., Hu, J., Ikezu, S., et al. (2020). P2RX7 inhibitor suppresses exosome secretion and disease phenotype in P301S tau transgenic mice. *Mol. Neurodegener*. 15:47. doi: 10.1186/s13024-020-00396-2

Ryskalin, L., Busceti, C. L., Biagioni, F., Limanaqi, F., Familiari, P., Frati, A., et al. (2019). Prion protein in glioblastoma multiforme. *Int. J. Mol. Sci*. 20:5107. doi: 10.3390/ijms20205107

Sala, M., Hollinger, K. R., Thomas, A. G., Dash, R. P., Tallon, C., Veeravalli, V., et al. (2020). Novel human neutral sphingomyelinase 2 inhibitors as potential therapeutics for Alzheimer disease. *J. Med. Chem*. 63, 6028–6056. doi: 10.1021/acs.jmedchem.0c00278

Silverman, J. M., Christy, D., Shyu, C. C., Moon, K. M., Fernando, S., Gidden, Z., et al. (2019). CNS-derived extracellular vesicles from superoxide dismutase 1 (SOD1) (G93A) ALS mice originate from astrocytes and neurons and carry misfolded SOD1. *J. Biol. Chem*. 294, 3744–3759. doi: 10.1074/jbc.RA118.004825

Singh, P. K., and Muqit, M. M. K. (2020). Parkinson's: a disease of aberrant vesicle trafficking. *Annu. Rev. Cell Dev. Biol*. 36, 237–264. doi: 10.1146/annurev-cellbio-100818-125512

Soares Martins, T., Marcalo, R., Ferreira, M., Vaz, M., Silva, R. M., Martins Rosa, I., et al. (2021a). Exosomal abeta-binding proteins identified by "*in silico*" analysis represent putative blood-derived biomarker candidates for Alzheimer's disease. *Int. J. Mol. Sci*. 22:3933. doi: 10.3390/ijms22083933

Soares Martins, T., Trindade, D., Vaz, M., Campelo, I., Almeida, M., Trigo, G., et al. (2021b). Diagnostic and therapeutic potential of exosomes in Alzheimer's disease. *J. Neurochem*. 156, 162–181. doi: 10.1111/jnc.15112

Suk, T. R., and Rousseaux, M. W. C. (2020). The role of TDP-43 mislocalization in amyotrophic lateral sclerosis. *Mol. Neurodegener*. 15:45. doi: 10.1186/s13024-020-00397-1

Sun, T., Ding, Z. X., Luo, X., Liu, Q. S., and Cheng, Y. (2020). Blood exosomes have neuroprotective effects in a mouse model of Parkinson's disease. *Oxid. Med. Cell. Longev*. 2020:3807476. doi: 10.1155/2020/3807476

Tan, S. K., Pastori, C., Penas, C., Komotar, R. J., Ivan, M. E., Wahlestedt, C., et al. (2018). Serum long noncoding RNA HOTAIR as a novel diagnostic and prognostic biomarker in glioblastoma multiforme. *Mol. Cancer* 17:74. doi: 10.1186/s12943-018-0822-0

Thery, C., Witwer, K. W., Aikawa, E., Alcaraz, M. J., Anderson, J. D., Andriantsitohaina, R., et al. (2018). Minimal information for studies of extracellular vesicles 2018 (MISEV2018): a position statement of the International Society for Extracellular Vesicles and update of the MISEV2014 guidelines. *J. Extracell. Vesicles* 7:1535750. doi: 10.1080/20013078.2018.1535750

Tsunemi, T., Ishiguro, Y., Yoroisaka, A., and Hattori, N. (2021). Analysis of alpha-synuclein in exosomes. *Methods Mol. Biol*. 2322, 41–45. doi: 10.1007/978-1-0716-1495-24

Tsunemi, T., Ishiguro, Y., Yoroisaka, A., Valdez, C., Miyamoto, K., Ishikawa, K., et al. (2020). Astrocytes protect human dopaminergic neurons from alpha-synuclein accumulation and propagation. *J. Neurosci*. 40, 8618–8628. doi: 10.1523/JNEUROSCI.0954-20.2020

Ueno, Y., Hira, K., Miyamoto, N., Kijima, C., Inaba, T., and Hattori, N. (2020). Pleiotropic effects of exosomes as a therapy for stroke recovery. *Int. J. Mol. Sci*. 21:6894. doi: 10.3390/ijms21186894

Vaidya, M., and Sugaya, K. (2020). Differential sequences and single nucleotide polymorphism of exosomal SOX2 DNA in cancer. *PLoS ONE* 15:e0229309. doi: 10.1371/journal.pone.0229309

Vandendriessche, C., Bruggeman, A., Van Cauwenberghe, C., and Vandenbroucke, R. E. (2020). Extracellular vesicles in Alzheimer's and Parkinson's disease: small entities with large consequences. *Cells* 9:2485. doi: 10.3390/cells9112485

Venkat, P., Cui, C., Chopp, M., Zacharek, A., Wang, F., Landschoot-Ward, J., et al. (2019). MiR-126 mediates brain endothelial cell exosome treatment-induced neurorestorative effects after stroke in type 2 diabetes mellitus mice. *Stroke*. 50, 2865–2874. doi: 10.1161/STROKEAHA.119.025371

Wang, B., and Han, S. (2019). Modified exosomes reduce apoptosis and ameliorate neural deficits induced by traumatic brain injury. *ASAIO J*. 65, 285–292. doi: 10.1097/MAT.0000000000000810

Wang, B., Wu, Z. H., Lou, P. Y., Chai, C., Han, S. Y., Ning, J. F., et al. (2019a). Human bone marrow-derived mesenchymal stem cell-secreted exosomes overexpressing microRNA-34a ameliorate glioblastoma development via down-regulating MYCN. *Cell Oncol*. 42, 783–799. doi: 10.1007/s13402-019-00461-z

Wang, J. K. T., Langfelder, P., Horvath, S., and Palazzolo, M. J. (2017). Exosomes and homeostatic synaptic plasticity are linked to each other and to huntington's, parkinson's, and other neurodegenerative diseases by database-enabled analyses of comprehensively curated datasets. *Front. Neurosci*. 11:149. doi: 10.3389/fnins.2017.00149

Wang, M. M., Feng, Y. S., Tan, Z. X., Xing, Y., Dong, F., and Zhang, F. (2020a). The role of exosomes in stroke. *Mol. Biol. Rep*. 47, 6217–6228. doi: 10.1007/s11033-020-05569-2

Wang, Q., Han, C. L., Wang, K. L., Sui, Y. P., Li, Z. B., Chen, N., et al. (2019b). Integrated analysis of exosomal lncRNA and mRNA expression profiles reveals the involvement of lnc-MKRN2-42:1 in the pathogenesis of Parkinson's disease. *CNS Neurosci. Ther*. 26, 527–537. doi: 10.1111/cns.13277

Wang, X., Zhou, Y., Gao, Q., Ping, D., Wang, Y., Wu, W., et al. (2020b). The role of exosomal microRNAs and oxidative stress in neurodegenerative diseases. *Oxid. Med. Cell. Longev*. 2020:3232869. doi: 10.1155/2020/3232869

Wang, Y., Balaji, V., Kaniyappan, S., Kruger, L., Irsen, S., Tepper, K., et al. (2017). The release and trans-synaptic transmission of Tau via exosomes. *Mol. Neurodegener*. 12:5. doi: 10.1186/s13024-016-0143-y

Wei, Z. X., Xie, G. J., Mao, X., Zou, X. P., Liao, Y. J., Liu, Q. S., et al. (2020). Exosomes from patients with major depression cause depressive-like behaviors in mice with involvement of miR-139-5p-regulated neurogenesis. *Neuropsychopharmacology*. 45, 1050–1058. doi: 10.1038/s41386-020-0622-2

Williams, A. M., Bhatti, U. F., Brown, J. F., Biesterveld, B. E., Kathawate, R. G., Graham, N. J., et al. (2020). Early single-dose treatment with exosomes provides neuroprotection and improves blood-brain barrier integrity in swine model of traumatic brain injury and hemorrhagic shock. *J. Trauma Acute Care Surg*. 88, 207–218. doi: 10.1097/TA.0000000000002563

Xian, P., Hei, Y., Wang, R., Wang, T., Yang, J., Li, J., et al. (2019). Mesenchymal stem cell-derived exosomes as a nanotherapeutic agent for amelioration of inflammation-induced astrocyte alterations in mice. *Theranostics* 9, 5956–5975. doi: 10.7150/thno.33872

Xiao, Y., Geng, F., Wang, G., Li, X., Zhu, J., and Zhu, W. (2018). Bone marrow-derived mesenchymal stem cells-derived exosomes prevent oligodendrocyte apoptosis through exosomal miR-134 by targeting caspase-8. *J. Cell Biochem*. doi: 10.1002/jcb.27519. [Epub ahead of print].

Xin, H., Katakowski, M., Wang, F., Qian, J. Y., Liu, X. S., Ali, M. M., et al. (2017). MicroRNA cluster miR-17-92 cluster in exosomes enhance neuroplasticity and functional recovery after stroke in rats. *Stroke* 48, 747–753. doi: 10.1161/STROKEAHA.116.015204

Xin, H., Liu, Z., Buller, B., Li, Y., Golembieski, W., Gan, X., et al. (2021). MiR-17-92 enriched exosomes derived from multipotent mesenchymal stromal cells enhance axon-myelin remodeling and motor electrophysiological recovery after stroke. *J. Cereb. Blood Flow Metab*. 41, 1131–1144. doi: 10.1177/0271678X20950489

Xing, Y., and Bai, Y. (2020). A review of exercise-induced neuroplasticity in ischemic stroke: pathology and mechanisms. *Mol. Neurobiol*. 57, 4218–4231. doi: 10.1007/s12035-020-02021-1

Xu, X., Zhuang, C., and Chen, L. (2020). Exosomal long non-coding RNA Expression from serum of patients with acute minor stroke. *Neuropsychiatr. Dis. Treat*. 16, 153–160. doi: 10.2147/NDT.S230332

Yang, J., Luo, S., Zhang, J., Yu, T., Fu, Z., Zheng, Y., et al. (2021). Exosome-mediated delivery of antisense oligonucleotides targeting alpha-synuclein ameliorates the pathology in a mouse model of Parkinson's disease. *Neurobiol. Dis*. 148:105218. doi: 10.1016/j.nbd.2020.105218

Yang, Y., Cai, Y., Zhang, Y., Liu, J., and Xu, Z. (2018). Exosomes secreted by adipose-derived stem cells contribute to angiogenesis of brain microvascular endothelial cells following oxygen-glucose deprivation *in vitro* through MicroRNA-181b/TRPM7 axis. *J. Mol. Neurosci*. 65, 74–83. doi: 10.1007/s12031-018-1071-9

Yang, Z., Wang, T., Wu, D., Min, Z., Tan, J., and Yu, B. (2020). RNA N6-methyladenosine reader IGF2BP3 regulates cell cycle and angiogenesis in colon cancer. *J Exp Clin Cancer Res*. 39:203. doi: 10.1186/s13046-020-01714-8

Yin, Z., Han, Z., Hu, T., Zhang, S., Ge, X., Huang, S., et al. (2020). Neuron-derived exosomes with high miR-21-5p expression promoted polarization of M1 microglia in culture. *Brain Behav. Immun*. 83, 270–282. doi: 10.1016/j.bbi.2019.11.004

Yue, X., Lan, F., and Xia, T. (2019). Hypoxic glioma cell-secreted exosomal miR-301a activates wnt/beta-catenin signaling and promotes radiation resistance by targeting TCEAL7. *Mol Ther*. 27, 1939–1949. doi: 10.1016/j.ymthe.2019.07.011

Zeng, A., Wei, Z., Yan, W., Yin, J., Huang, X., Zhou, X., et al. (2018). Exosomal transfer of miR-151a enhances chemosensitivity to temozolomide in drug-resistant glioblastoma. *Cancer Lett*. 436, 10–21. doi: 10.1016/j.canlet.2018.08.004

Zhang, Y., Bi, J., Huang, J., Tang, Y., Du, S., and Li, P. (2020). Exosome: a review of its classification, isolation techniques, storage, diagnostic and targeted therapy applications. *Int. J. Nanomed*. 15, 6917–6934. doi: 10.2147/IJN.S264498

Zhang, Y., Zhang, Y., Chopp, M., Pang, H., Zhang, Z. G., Mahmood, A., et al. (2021). MiR-17-92 cluster-enriched exosomes derived from human bone marrow mesenchymal stromal cells improve tissue and functional recovery in rats after traumatic brain injury. *J. Neurotrauma* 38, 1535–1550. doi: 10.1089/neu.2020.7575

Zhao, C., Deng, Y., He, Y., Huang, X., Wang, C., and Li, W. (2021). Decreased level of exosomal mir-5121 released from microglia suppresses neurite outgrowth and synapse recovery of neurons following traumatic brain injury. *Neurotherapeutics*. doi: 10.1007/s13311-020-00999-z. [Epub ahead of print].

Zhao, J., Liu, X., Xia, W., Zhang, Y., and Wang, C. (2020). Targeting amyloidogenic processing of APP in Alzheimer's disease. *Front. Mol. Neurosci*. 13:137. doi: 10.3389/fnmol.2020.00137

Zou, J., Guo, Y., Wei, L., Yu, F., Yu, B., and Xu, A. (2020). Long noncoding RNA POU3F3 and alpha-synuclein in plasma L1CAM exosomes combined with beta-glucocerebrosidase activity: potential predictors of Parkinson's disease. *Neurotherapeutics*. 17, 1104–1119. doi: 10.1007/s13311-020-00842-5

Conflict of Interest: The authors declare that the research was conducted in the absence of any commercial or financial relationships that could be construed as a potential conflict of interest.

Publisher's Note: All claims expressed in this article are solely those of the authors and do not necessarily represent those of their affiliated organizations, or those of the publisher, the editors and the reviewers. Any product that may be evaluated in this article, or claim that may be made by its manufacturer, is not guaranteed or endorsed by the publisher.

Advantages of publishing in Frontiers

OPEN ACCESS
Articles are free to read for greatest visibility and readership

FAST PUBLICATION
Around 90 days from submission to decision

HIGH QUALITY PEER-REVIEW
Rigorous, collaborative, and constructive peer-review

TRANSPARENT PEER-REVIEW
Editors and reviewers acknowledged by name on published articles

Frontiers
Avenue du Tribunal-Fédéral 34
1005 Lausanne | Switzerland

Visit us: www.frontiersin.org
Contact us: frontiersin.org/about/contact

REPRODUCIBILITY OF RESEARCH
Support open data and methods to enhance research reproducibility

DIGITAL PUBLISHING
Articles designed for optimal readership across devices

FOLLOW US
@frontiersin

IMPACT METRICS
Advanced article metrics track visibility across digital media

EXTENSIVE PROMOTION
Marketing and promotion of impactful research

LOOP RESEARCH NETWORK
Our network increases your article's readership